VOLUME 105 – NO. 1/4 – MARCH 1992 Complete Volume ISSN 0025-3227

MARINE GEOLOGY

INTERNATIONAL JOURNAL OF MARINE GEOLOGY, GEOCHEMISTRY AND GEOPHYSICS

EDITORS-IN-CHIEF: H. CHAMLEY, LILLE
D.A. MCMANUS, SEATTLE, WASH.

ELSEVIER

MARINE GEOLOGY

Editorial Board

F. Barbieri, Parma
W. Berger, La Jolla, Calif.
A.H. Bouma, Baton Rouge, La.
A.J. Bowen, Halifax, N.S.
B. Carson, Bethlehem, Pa.
L. Carter, Wellington
D.S. Cronan, London
J.R. Curray, La Jolla, Calif.
P.J. Davies, Canberra, A.C.T.
M.L. Delaney, Santa Cruz, Calif.
R.V. Dingle, Cape Town
S.L. Eittreim, Menlo Park, Calif.
M.E. Field, Menlo Park, Calif.
J. Francheteau, Paris
G.P. Glasby, Wellington
D.S. Gorsline, Los Angeles, Calif.
M. Grant Gross, Baltimore, Md.
A. Guilcher, Brest
J.R. Hails, Adelaide, S.A.
E.L. Hamilton, San Diego, Calif.
D.M. Hanes, Gainesville, Fla.
W.W. Hay, Boulder, Colo.
A.C. Hine, St. Petersburg, Fla.
H. Holtedahl, Bergen
D. Jongsma, O'Connor, A.C.T.
M.J. Keen, Dartmouth, N.S.
N.H. Kenyon, Godalming
E.M. Klein, Durham, N.C.
H.J. Knebel, Woods Hole, Mass.
I.N. McCave, Cambridge
R.E. McDuff, Seattle, Wash.
A.R.M. Nowell, Seattle, Wash.
R.Q. Oaks, Jr., Logan, Utah
E. Olausson, Gothenburg
O.H. Pilkey, Durham, N.C.
H. Postma, Texel
A.I. Rees, Godalming
H.E. Reineck, Wilhelmshaven
D.A. Ross, Woods Hole, Mass.
W.F. Ruddiman, Charlottesville, Va.
E. Seibold, Freiburg
J.-C. Sempéré, Seattle, Wash.
J.M. Skei, Oslo
D.J. Stanley, Washington, D.C.
A.H.B. Stride, Godalming
D. Stüben, Wellington
D.J.P. Swift, Norfolk, Va.
S. Uyeda, Tokyo
J.T. Wells, Morehead City, N.C.
R.A. Wheatcroft, Woods Hole, Mass.
L.D. Wright, Gloucester Point, Va.

Scope of the journal
Marine Geology is an international medium for the publication of original studies and comprehensive reviews in the field of Marine Geology, Geochemistry and Geophysics. The editors endeavour to maintain a high scientific level and it is hoped that with its international coverage the journal will contribute to the sound development of this field.
A *letter section* is provided as a publication outlet for short papers which require *rapid* publication.

Publication schedule and subscription information – 1992
Marine Geology (ISSN 0025–3227) is published as six volumes (24 issues) a year. The subscription price for 1992 (Volumes 102–107) is Dfl. 1800 + Dfl. 186 p.h. = Dfl. 1986 (approx. US$983). The Dutch guilder price is definitive. The U.S. dollar price is subject to exchange-rate fluctuations and is given only as a guide. Subscriptions are accepted on a prepaid basis only, unless different terms have previously been agreed upon. Personal subscription rates and conditions are available upon request from the Publisher. Subscription orders can be entered only by calendar year (Jan.–Dec.) and should be sent to Elsevier Science Publishers, Journal Department, P.O. Box 211, 1000 AE Amsterdam, The Netherlands, tel. 31.20.5803642, fax 31.20.5803598, or to your usual subscription agent. Postage & handling (p.h.) charges include surface delivery, except to the following countries where air delivery via S.A.L. (Surface Air Lift) mail is ensured: Argentina, Australia, Brazil, Canada, Hong Kong, India, Israel, Japan*, Malaysia, Mexico, New Zealand, Pakistan, PR China, Singapore, South Africa, South Korea, Taiwan, Thailand and the USA. *For Japan, air delivery (S.A.L.) requires an additional charge of 25% of the normal postage and handling charge. For all other countries, airmail rates are available upon request. Claims for missing issues must be made within three months of publication (mailing) date; otherwise, such claims cannot be honoured free of charge. For further information, or a free sample copy of this or any other Elsevier Science Publishers journal, readers in the USA and Canada can contact the following address: Elsevier Science Publishing Co. Inc., Journal Information Center, 655 Avenue of the Americas, New York, NY 10010, U.S.A., tel. 212.63337502. Back issues can be ordered. For further information regarding prices etc., please contact Elsevier Science Publishers, Journal Department, P.O. Box 211, 1000 AE Amsterdam, The Netherlands, tel. 31.20.5803642, fax 31.20.5803598.

Journal Information Center
For customers in the U.S.A. and Canada wishing additional bibliographic information on this and other Elsevier journals, please contact: Elsevier Science Publishing Co. Inc., Journal Information Center, 655 Avenue of the Americas, New York, NY 10010, U.S.A., Tel: (212) 633-3750.

Publication of abstracts and contents lists
Abstracts and/or contents lists of this journal are published in the following journals: *Geoscience Contents, Geo Abstracts, Current Contents, Bulletin Signalétique, Chemical Abstracts, Marine Science Contents Tables, A.G.I.'s Bibliography and Index of Geology, Aquatic Sciences and Fisheries Abstracts and Oceanic Abstracts.*

(continued on inside back cover)

© 1992, ELSEVIER SCIENCE PUBLISHERS B.V., ALL RIGHTS RESERVED 0025-3227/92/$05.00

No part of this publication may be reproduced, stored in a retrieval system or transmitted in any form or by any means, electronic, mechanical, photocopying, recording or otherwise, without the prior written permission of the publisher, Elsevier Science Publishers B.V., Copyright and Permissions Department, P.O. Box 521, 1000 AM Amsterdam, The Netherlands.
Upon acceptance of an article by the journal, the author(s) will be asked to transfer copyright of the article to the publisher. The transfer will ensure the widest possible dissemination of information.
Submission of an article for publication entails the author(s) irrevocable and exclusive authorization of the publisher to collect any sums or considerations for copying or reproduction payable by third parties (as mentioned in article 17 paragraph 2 of the Dutch Copyright Act of 1912 and in the Royal Decree of June 20, 1974 (S. 351) pursuant to article 16b of the Dutch Copyright Act of 1912) and/or to act in or out of Court in connection therewith.
Special regulations for readers in the U.S.A. — This journal has been registered with the Copyright Clearance Center, Inc. Consent is given for copying of articles for personal or internal use, or for the personal use of specific clients. This consent is given on the condition that the copier pays through the Center the per-copy fee for copying beyond that permitted by Sections 107 or 108 of the U.S. Copyright Law. The per-copy fee is stated in the code-line at the bottom of the first page of each article. The appropriate fee, together with a copy of the first page of the article, should be forwarded to the Copyright Clearance Center, Inc., 27 Congress Street, Salem, MA 01970, U.S.A. If no code-line appears, broad consent to copy has not been given and permission to copy must be obtained directly from the author(s). All articles published prior to 1980 may be copied for a per-copy fee of US $2.25, also payable through the Center. This consent does not extend to other kinds of copying, such as for general distribution, resale, advertising and promotion purposes, or for creating new collective works. Special written permission must be obtained from the publisher for such copying.
No responsibility is assumed by the Publisher for any injury and/or damage to persons or property as a matter of products liability, negligence or otherwise, or from any use or operation of any methods, products, instructions or ideas contained in the material herein.
Although all advertising material is expected to conform to ethical (medical) standards, inclusion in this publication does not constitute a guarantee or endorsement of the quality or value of such a product or of the claims made of it by its manufacturer.

This issue is printed on acid-free paper.

PRINTED IN THE NETHERLANDS

MARINE GEOLOGY

VOL. 105 (1992)

MARINE GEOLOGY

International Journal of Marine Geology, Geochemistry and Geophysics

VOL. 105 (1992)

Editors-in-Chief

D. A. McManus, Seattle, Wash.
H. Chamley, Lille

Editorial Board

F. Barbieri, Parma
W. Berger, La Jolla, Calif.
A.H. Bouma, Baton Rouge, La.
A.J. Bowen, Halifax, N.S.
B. Carson, Bethlehem, Pa.
L. Carter, Wellington
D.S. Cronan, London
J.R. Curray, La Jolla, Calif.
P.J. Davies, Canberra, A.C.T.
M.L. Delaney, Santa Cruz, Calif.
R.V. Dingle, Cape Town
S.L. Eittreim, Menlo Park, Calif.
M.E. Field, Menlo Park, Calif.
J. Francheteau, Paris
G.P. Glasby, Wellington
D.S. Gorsline, Los Angeles, Calif.
M. Grant Gross, Baltimore, Md.
A. Guilcher, Brest
J.R. Hails, Adelaide, S.A.
E.L. Hamilton, San Diego, Calif.
D.M. Hanes, Gainesville, Fla.
W.W. Hay, Boulder, Colo.
A.C. Hine, St. Petersburg, Fla.
H. Holtedahl, Bergen
D. Jongsma, O'Connor, A.C.T.
M.J. Keen, Dartmouth, N.S.
N.H. Kenyon, Godalming
E.M. Klein, Durham, N.C.
H.J. Knebel, Woods Hole, Mass.
I.N. McCave, Cambridge
R.E. McDuff, Seattle, Wash.
A.R.M. Nowell, Seattle, Wash.
R.Q. Oaks, Jr., Logan, Utah
E. Olausson, Gothenburg, Sweden
O.H. Pilkey, Durham, N.C.
H. Postma, Texel
A.I. Rees, Godalming
H.E. Reineck, Wilhelmshaven
D.A. Ross, Woods Hole, Mass.
W.F. Ruddiman, Charlottesville, Va.
E. Seibold, Freiburg
J.-C. Sempéré, Seattle, Wash.
J.M. Skei, Oslo
D.J. Stanley, Washington, D.C.
A.H.B. Stride, Godalming
D. Stüben, Wellington
D.J.P. Swift, Norfolk, Va.
S. Uyeda, Tokyo
J.T. Wells, Morehead City, N.C.
R.A. Wheatcroft, Woods Hole, Mass.
L.D. Wright, Gloucester Point, Va.

ELSEVIER
AMSTERDAM – LONDON – NEW YORK – TOKYO

© 1992, ELSEVIER SCIENCE PUBLISHERS B.V. ALL RIGHTS RESERVED

0025-3227/92/$05.00

No part of this publication may be reproduced, stored in a retrieval system or transmitted in any form or by any means, electronic, mechanical, photocopying, recording or otherwise, without the prior written permission of the publisher, Elsevier Science Publishers B.V., Copyright and Permissions Department, P.O. Box 521, 1000 AM Amsterdam, The Netherlands.

Upon acceptance of an article by the journal, the author(s) will be asked to transfer copyright of the article to the publisher. The transfer will ensure the widest possible dissemination of information.

Submission of an article for publication entails the author(s) irrevocable and exclusive authorization of the publisher to collect any sums or considerations for copying or reproduction payable by third parties (as mentioned in article 17 paragraph 2 of the Dutch Copyright Act of 1912 and in the Royal Decree of June 20, 1974 (S. 351) pursuant to article 16b of the Dutch Copyright Act of 1912) and/or to act in or out of Court in connection therewith.

Special regulations for readers in the U.S.A. — This journal has been registered with the Copyright Clearance Center, Inc. Consent is given for copying of articles for personal or internal use, or for the personal use of specific clients. This consent is given on the condition that the copier pays through the Center the per-copy fee for copying beyond that permitted by Sections 107 or 108 of the U.S. Copyright Law. The per-copy fee is stated in the code-line at the bottom of the first page of each article. The appropriate fee, together with a copy of the first page of the article, should be forwarded to the Copyright Clearance Center, Inc., 27 Congress Street, Salem, MA 01970, U.S.A. If no code-line appears, broad consent to copy has not been given and permission to copy must be obtained directly from the author(s). All articles published prior to 1980 may be copied for a per-copy fee of US $2.25, also payable through the Center. This consent does not extend to other kinds of copying, such as for general distribution, resale, advertising and promotion purposes, or for creating new collective works. Special written permission must be obtained from the publisher for such copying.

No responsibility is assumed by the Publisher for any injury and/or damage to persons or property as a matter of products liability, negligence or otherwise, or from any use or operation of any methods, products, instructions or ideas contained in the material herein.

Although all advertising material is expected to conform to ethical (medical) standards, inclusion in this publication does not constitute a guarantee or endorsement of the quality or value of such a product or of the claims made of it by its manufacturer.

This issue is printed on acid-free paper.

PRINTED IN THE NETHERLANDS

Marine Geology, 105 (1992) 1–21
Elsevier Science Publishers B.V., Amsterdam

Model simulations of tsunamis generated by the Storegga Slides

C.B. Harbitz

Department of Mathematics, Mechanics Division, University of Oslo, P.O. Box 1053 Blindern, 0316 Oslo 3, Norway

(Received July 10, 1991; revision accepted October 29, 1991)

ABSTRACT

Harbitz, C.B., 1992. Model simulations of tsunamis generated by the Storegga Slides. Mar. Geol., 105: 1–21.

A mathematical model based on the hydrodynamic shallow water equations is developed for numerical simulation of water waves generated by the submarine Storegga Slides on the Norwegian continental slope. The equations are solved numerically by a finite difference technique. Computations of wave amplification effects reveal run-up heights for the Second Storegga Slide between 3 and 5 m in exposed areas along the eastern coast of Greenland, Iceland and Scotland and the western coast of Norway. The calculated run-up heights agree remarkably well with possible tsunami wave heights deduced from geological evidences along the eastern coast of Scotland. The generated wave heights are strongly dependent on the acceleration of the slide. The effects of shear stress at the interface between the water and the slide body, has turned out to be important.

1 Introduction

1.1 Introductory remarks

This paper is motivated by the reports by Dawson et al. (1988) and Long et al. (1989), where the occurrence of a marine sand layer interbedded in terrestrial peat along the eastern coast of Scotland were interpreted as evidence of a tsunami, probably generated by a submarine slide occurring on the Norwegian continental slope around 7000 B.P. If the slide caused tsunamis of such a magnitude as indicated by Dawson et al. (1988) and Long et al. (1989), then the coast of western Norway must also have been affected. Svendsen and Mangerud (1990) describe two sites south of Ålesund with possible tsunami deposits. At the first of the Norwegian sites, sand layers with marine influence are interbedded in the lower part of the Holocene lacustrine gyttja. The threshold of this basin is 4 m above the Tapes transgression maximum. At the second locality, situated 5 m above the Tapes level and 6 m above the 7000 B.P. level, a disturbed layer including terrestrial turf is apparently the result of slumping triggered by an external source such as a tsunami. Furthermore Hansom and Briggs (1991) describe a beach ridge full of marine taxa, possibly caused by a tsunami 6900 B.P., on top of freshwater peats ca. 6 m above present sea level at the Vestfirðir peninsula, NW Iceland.

It is of interest to calculate the run-up heights generated by one of the world's largest known submarine slides, which occurred in the Storegga area on the continental shelf off the coast of Møre, Mid-Norway, and compare these with the possible tsunami wave run-up heights deduced from the geological evidences mentioned above. The calculations are also of interest in view of coastal activity and the large number of off-shore oil installations in the Norwegian Sea and the North Sea.

Edgers and Karlsrud (1982) report that submarine slides might be triggered on slopes with an inclination less than 1°, and comprise enormous volumes in comparison to most terrestrial slides.

Correspondence to: C.B. Harbitz, Department of Mathematics, Mechanics Division, University of Oslo, P.O. Box 1053 Blindern, 0316 Oslo 3, Norway.

0025-3227/92/$05.00 © 1992 — Elsevier Science Publishers B.V. All rights reserved

Heezen and Ewing (1952) report submarine slide velocities of 20–30 m/s, based upon the sequence of downslope cable breaks on Grand Banks, Newfoundland, in 1929.

Tsunamis are intermediate between tides and swell waves in the spectrum of gravity water waves, with periods between 2 and 200 min, and with an initial surface elevation above the tsunami source of the order of one meter (Voit, 1987). From the studies on tsunamis by Hammack (1973) it is known that the wave structure for relatively slow bed motions, as for submarine slides, is strongly dependent on the time-displacement history of the movement.

1.2 Geological data

The Storegga ("great-edge") Slide involved a total of about 5580 km^3 of sediment. The 290 km long headwall is located at the shelf edge 100 km off the coast (Fig.1). The slide scar, which covers an area of 34,000 km^2, extends down-slope for 200–250 km, narrowing slightly towards the depositional area at the base of the continental slope below 2700 m. Slide deposits have been mapped for a further 500–550 km beyond this point. The total run-out distance could therefore be more than 750 km. The present maximum thickness of the deposits is 450 m. The average gradient of the whole slide scar is about 0.5°. The slope of the surface of the depositional area to the northwest is about 0.1° (Bugge et al., 1988).

The available data indicate that the Storegga Slide was formed by three major events. Estimated area, thickness and volume of the three slides are shown in Table 1. The First Slide event probably occurred 30,000–50,000 yrs B.P., and comprised the whole 290 km wide slide scar. The volume of this slide was about 3880 km^3, deposited both within and beyond the slide scar, i.e. 350–400 km from the headwall. The average thickness of the slide was about 114 m (Bugge et al., 1987, 1988).

The Second Slide took place in the central part of the slide scar about 6000–8000 yrs B.P. The slide cut deeper into the seabed and probably developed retrogressively, such that the headwall retreated 6–8 km onto the continental shelf, leaving the steep edge called Storegga. The slide travelled well out into the abyssal plain, probably more than 750 km from the headwall (Bugge et al., 1988).

The Third Storegga Slide was limited to the upper part of the Second Slide scar (Bugge et al., 1988). Jansen et al. (1987) date the Third Slide to 6000 B.P., and states that there was a very small age difference between the Second and the Third Slides.

The volume of the last two slides was about 1700 km^3. This does not include any deposits of the First Slide removed by the later ones (Bugge et al., 1988). The average thickness of the First Slide deposits left in the Second Slide Scar of 19,200 km^2, was about 40 m (T. Bugge, pers. commun., 1991). Hence the Second Slide also redistributed a volume of about 770 km^3 in addition to the above mentioned 1700 km^3.

A partially liquified debris flow with enhanced pore water pressure was probably dominant in the First Slide, which mainly comprised poorly consolidated, soft clayey sediments. During the Second and Third slides (involving more consolidated sediments) the sliding sediments probably flowed down the gentle slope (as low as 0.1°) on liquified layers where excess pore pressure allowed the layers to act as lubricants. Turbidties, resulting mainly from the Second Slide, are also widely recognized through the immediate slide area, and a very thick distal turbidite found in the Norway basin 750 km from the headwall is related to the Second Slide (Bugge et al., 1987, 1988; Jansen et al., 1987).

The seismic activity in the area suggests that the primary triggering mechanism was earthquakes, together with associated increases in pore water pressure, and perhaps decomposition of gas hydrates which liberate gas and water (resulting in further excess pore water pressures). Other factors, such as ice loading (for the First Slide) may have contributed (Jansen et al., 1987; Bugge et al., 1988).

Since the available information about volume, extension and run-out distance is most reliable for the First Storegga Slide, most of the presented simulations are for this event. As the geological evidences are dated back to the time of the Second Storegga Slide, additional simulations are made with slide dimensions corresponding to this second event. The large run-out distance of the Second

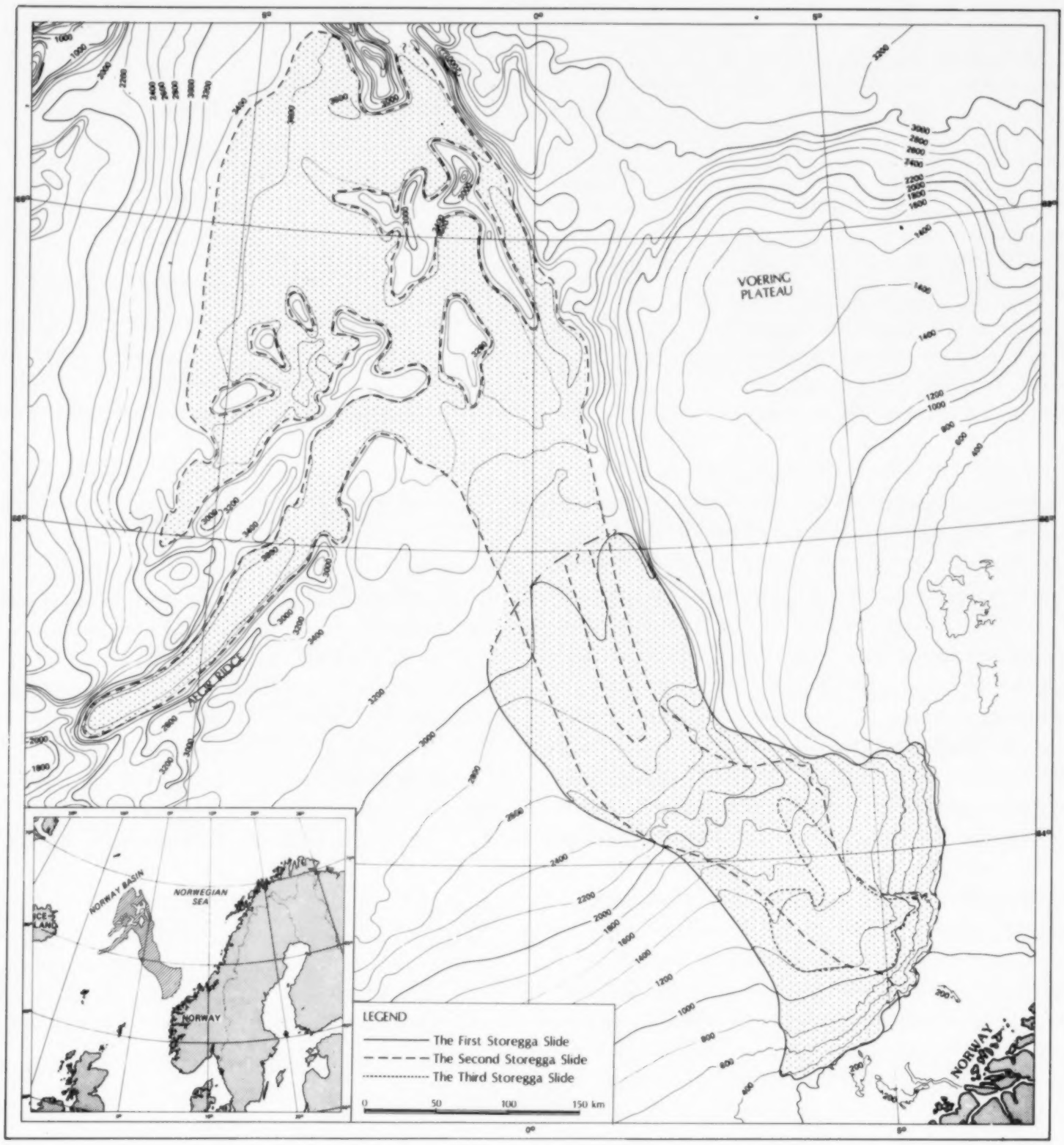

Fig.1. Areal distribution of the Storegga Slides (by courtesy of Dr. Bugge, IKU).

Slide was due to the transformation of less compacted sediments into a large turbidity current. However, the primary and highest waves were generated during the initial stages of the slide motion before transition to a turbidity current occurred (cf. discussion in sec. 4.1). Hence simulations of the Second Slide are made with the same progress of slide motion as for the First Slide.

2 Hydrodynamic equations

Waves generated by landslides in fjords of western Norway have been successfully simulated by a numerical model (Harbitz et al., 1991). The simulations presented herein are based on the same model, except for modifications due to a completely submarine slide motion starting from rest.

TABLE 1

Estimated area, thickness and volume of the three slide events (from Bugge et al., 1988)

	First Slide	Second Slide	Third Slide	Total
Total run-out distance (km)	350–380	800–850	100–130	850
Area of slide scar (km^2)	34000	19200	6000	34000
Total slide-influenced area (km^2)	52000	88000	6000	112500
Maximum thickness (m)	280	330		430
Average thickness (m)	114	88		160
Volume (km^3)	3880	1700		5580
Volume of deposits left in slide scar today (km^3)	400	950		1350
Volume of deposits below 2700 m (km^3)	3480	750		4230

Gross features of the primary wave leaving the wave generation area may be determined for a submarine slide when the magnitudes of parameters which characterize the bed displacement are known. This was first done by Hammack (1973), who used the results to derive a scaled set of equations for tsunamis. By means of this scaled set, Ichiye (1983) gives criteria for the linear long wave assumptions to be valid, based on the parameters which characterize the bed displacement. With slide dimensions and time scale as proposed in sec. 4.3, these criteria will be fulfilled also within the wave generation region for the Storegga Slide. Furthermore we find the wave lengths to be much less than the Rossby radius of deformation. Hence we do not expect the waves generated by the Storegga Slide to be substantially influenced by Coriolis' effects.

The equations are formulated in a Cartesian coordinate system with horizontal axes, Ox and Oy in the undisturbed water level and the vertical axis, Oz, pointing upwards. The fluid is confined to $-h<z<\eta$ where h is the depth referred to the datum $z=0$, η the water surface displacement and we denote the total water depth by $H=h+\eta$. Since the slide introduces bathymetric changes, h will be a function of time (t). In terms of the averaged horizontal velocity, $\vec{u}=u\vec{i}+v\vec{j}$, where $\vec{i}$ and $\vec{j}$ denote the unit vectors in the x- and y-directions respectively, we obtain a linearized continuity equation of the form:

$$\frac{\partial H}{\partial t} = -\nabla\cdot(h\vec{u}) \tag{1}$$

Provided the pressure is hydrostatic and the nonlinear terms can be neglected the momentum equation becomes:

$$\frac{\partial \vec{u}}{\partial t} = -g\nabla\eta + \frac{\vec{\tau}}{\rho h} \tag{2}$$

where g is the acceleration of gravity, ρ is the density of the fluid and $\vec{\tau}$ is the bottom shear stress. The relative errors introduced are described in Harbitz et al. (1991, sec. 2.1).

The equations are solved numerically by a finite difference technique. For the Storegga Slide event we will consider the influence of $\vec{\tau}$ (see sec. 4.2). The implementation of this term is made by first computing the velocity components $u^{n+1/2}_{i+1/2,j}$ and $v^{n+1/2}_{i,j+1/2}$ with $\vec{\tau}$ omitted. Subsequently the terms $[\tau_x \Delta t/(\rho \bar{h}^x)]^{n+1/2}_{i+1/2,j}$ and $[\tau_y \Delta t/(\rho \bar{h}^y)]^{n+1/2}_{i,j+1/2}$ are added to $u^{n+1/2}_{i+1/2,j}$ and $v^{n+1/2}_{i,j+1/2}$ respectively. The explicit expression for $\vec{\tau}=\tau_x\vec{i}+\tau_y\vec{j}$ is given by eqn. (8). $f^{\kappa}_{\beta,\gamma}$ denotes the numerical approximation to a parameter f at a grid-point with coordinates ($\beta\Delta x$, $\gamma\Delta y$, $\kappa\Delta t$) where Δx, Δy and Δt are the grid increments. For further details see Harbitz et al. (1991).

3 The slide model

The process of water wave generation by slides is found to be controlled by the global characteristics of the slide (Harbitz et al., 1991, sec. 3). We shall therefore focus only on the total water displacement and the shear stress acting between the slide masses and the fluid.

The total water displacement is determined by the aggregated displacement thickness of the slide. The slide will therefore be described as one body with a prescribed motion. This corresponds to a

time dependent water depth:

$$h(x, y, t) = h_0(x, y) - h_s(x - x_s(t),\ y - y_s(t)) \tag{3}$$

where $h_0(x, y)$ represents the rigid seafloor, and h_s describes the water displacement by the slide body. By assuming a simple functional relation for the slide motion, the coordinates $(x_s(t), y_s(t))$ defined by:

$$\left.\begin{aligned} x_s &= x_0 + \left\{\frac{1}{2} R\left(1 - \cos\frac{\pi t}{T}\right)\right\} \cos\varphi \\ y_s &= y_0 + \left\{\frac{1}{2} R\left(1 - \cos\frac{\pi t}{T}\right)\right\} \sin\varphi \end{aligned}\right\} \quad 0 < t < T \tag{4}$$

specify the motion of the slide. φ is the angle between the propagation direction of the slide and the x-axis. (x_0, y_0) is the position of the front of the slide when the movement starts ($t = 0.0$ s). R is the total horizontal displacement during the time interval T. We shall refer to R as the frontal run-out distance and to T as the running time of the slide. The maximum velocity of the slide is U_{max} and from eqn. (4) we have:

$$T = \frac{\pi}{2} \frac{R}{U_{max}} \tag{5}$$

The velocity profile of the slide will be discussed further in sec. 4.1.

The shape of the slide is represented by a box form of length L, width B and maximum thickness Δh. To avoid sharp gradients in h, the edges of the box form is smoothed along both sides over a distance equal to B from the central line, and in the front and rear end over a distance S, by an exponential function of the form:

$$h_s = \begin{cases} \Delta h \exp\left(-\left(2\dfrac{x' + S + L}{S}\right)^4 - \left(2\dfrac{y'}{B}\right)^4\right) \\ \qquad \text{for } -(L + 2S) < x' < -(L + S), \\ \Delta h \exp\left(-\left(2\dfrac{y'}{B}\right)^4\right) \\ \qquad \text{for } -(L + S) \leqslant x' < -S, \\ \Delta h \exp\left(-\left(2\dfrac{x' + S}{S}\right)^4 - \left(2\dfrac{y'}{B}\right)^4\right) \\ \qquad \text{for } -S \leqslant x' < 0, \end{cases} \tag{6}$$

where

$$x' = (x - x_s)\cos\phi + (y - y_s)\sin\phi$$

$$y' = -(x - x_s)\sin\phi + (y - y_s)\cos\phi$$

The x'-axis is directed along the direction of the slide motion, and the y'-axis in the transverse direction, with the origin in the front of the slide (confer Harbitz et al., 1991, fig.3).

The width of the slide, B, and the total length of the slide, $L + S$, constitutes the width of that part of the box which is thicker than $0.37\Delta h$. With this definition of h_s the slide volume V is:

$$V = 0.90 B \Delta h (L + 0.90 S) \tag{7}$$

where the factor 0.90 arises due to the smoothening.

The bottom shear stress acting on the water is expressed by:

$$\vec{\tau} = \frac{1}{2} c_D^u \rho [(\dot{x}_s - u)^2 + (\dot{y}_s - v)^2]^{1/2} [(\dot{x}_s - u)\vec{i} + (\dot{y}_s - v)\vec{j}] \tag{8}$$

where c_D^u is the drag coefficient (the dot denotes differentiating with respect to t).

4 The First and Second Storegga Slides

4.1 The slide motion

Edgers and Karlsrud (1982) point out that geological evidence of submarine soil flows, in which the slide debris moves as a more or less concentrated fluid, has been found in a number of areas. Turbidity currents were previously emphasized as the predominant mechanism in very large and rapid submarine slides. However, Edgers and Karlsrud find it difficult to see how the main body of a flowing mass will become sufficiently dilute to turn into a low density current. The viscous flow analysis of slide run-out velocity by the same authors (Edgers and Karlsrud, 1981), provides good agreement with available field observations. For the back calculated soil viscosities, the Reynolds number indicates laminar conditions at the soil/water interface. This precludes the large amount of turbulent mixing necessary to maintain

the flow primarily as a turbidity current. The soil viscosities also agree remarkably with viscosities of clearly viscous sub-aerial quick clay slides.

The tangential gradient of the slide thickness is assumed to be small (as for the Storegga Slides). The resultant active pressure acting on one single element of the slide from the neighbouring elements will therefore be small compared to gravitational forces (see Norem et al., 1989). This suggests a rigid body description of the slides. As long as the dense flow is accelerating, it will not be surpassed by a turbidity current generated by the initial slides.

The internal velocity gradient normal to the slope will also be small for a submarine flowslide with dimensions like the Storegga Slides. Hence viscous shear stresses are of importance only on the upper surface and along the base of the slide. The viscous shear stresses are described by a dynamic drag proportional to the slide velocity squared. As the slide consists of blocks that slide and bounce, the resistive forces along the base of the slide should also include a Coulomb friction term. Wave energy considerations have revealed that the contribution to the total wave energy from displacement effects clearly exceeds the contribution from shear stress effects, especially in the initial stages of the slide motion. Hence a wave resistance must be included in the forces acting upon the slide.

The slide velocity U for a slide moving on a linear slope with inclination angle α, assuming that there is no mass entrainment along the path, is consequently determined by the momentum equation:

$$\frac{dU}{dt} = \frac{\bar{\rho}-\rho_t}{\bar{\rho}} g(\sin\alpha - \mu\cos\alpha) - \frac{1}{2}(c_D^u + c_D^b)\frac{\rho_t}{\bar{\rho}\bar{h}} U^2 - \frac{R_w}{\bar{\rho}\bar{h}} \tag{9}$$

where $\bar{\rho}$ is the average density of the slide masses, ρ_t is the density of the turbidity current surrounding the slide masses, $\bar{h}$ is the average thickness of the slide and R_w is the wave resistance per unit area. c_D^u and c_D^b are the drag coefficients along the upper surface and along the base of the slide respectively and μ is the Coulomb friction coefficient.

For a numerical solution R_w can be found by integrating the pressure along the surface of the slide at each time step. Following Norem et al. (1989) the value of c_D^u averaged over the slide length $L+S=225$ km, for turbulent flow along a flat rough plate moving with slowly varying velocity, is defined through the equation proposed by Schlichting (1968):

$$c_D^u = \left[1.89 + 1.62 \log\frac{(L+S)}{k}\right]^{-5/2} \tag{10}$$

where k is a roughness length in the range 0.01–0.1 m. Hence c_D^u will be between 0.0014 and 0.0019. The upper value is selected for the simulations in sec. 4.3. There is uncertainty connected to the values of all parameters appearing in eqn. (9), as well as to possible mass entrainment. The parameters can not be determined exactly by core samples from the slide deposits, as the present structure is significantly altered from when the slides were moving. Samples of materials affected only by the First Slide don't even exist (Jansen et al., 1987). Thus predictions of the velocities of the Storegga Slides will never be more than very rough estimates, even though the main contributing physical effects are included.

If the wave resistance is ignored and the friction and drag coefficients are considered to be constants, the terminal slide velocity is expressed by:

$$U_{term} = \sqrt{\frac{(\bar{\rho}-\rho_t) g\bar{h}(\sin\alpha - \mu\cos\alpha)}{\frac{1}{2}(c_D^u + c_D^b)\rho_t}} \tag{11}$$

Excess pore pressure will reduce the Coulomb friction coefficient significantly. For a slide scar with inclination angle $\alpha = 0.5°$, μ is determined by $\tan 0.5° > \mu > \tan 0.1°$ (the inclination angle of the depositional area). An average value of 0.005 is selected. Finally ignoring the viscous drag along the base of the slide ($c_D^b = 0.0$), the terminal slide velocity U_{term} is estimated to 48.9 m/s for a slide flowing on an infinite path length with parameter values as given in Table 2 for the First Storegga Slide. The corresponding value for the Second Slide is 55.0 m/s. The terminal slide velocity will be reduced if a viscous drag along the base is

TABLE 2

Parameter values used to determine terminal slide velocity

		First Slide	Second Slide
$\bar{h}$	average thickness of slide (m)	114.0	144.0
α	inclination angle of slope (deg.)	0.5	
$\bar{\rho}$	average density of slide masses (kg/m^3)	1.7×10^3	
ρ_t	density of turbidity current (kg/m^3)	1.1×10^3	
μ	Coulomb friction coefficient	5×10^{-3}	
c_D^u	drag coefficient	1.9×10^{-3}	

included. The wave resistance will initially reduce the slide velocity. Since the slide motion is clearly sub-critical (i.e. $U_{max}/\sqrt{gh} < 1$),the primary waves, mainly caused by displacement effects during the early stages of the slide motion, will advance faster than the slide and leave the slide area, and it may easily be shown that for a slide moving with slowly varying velocity on a slowly varying seabed (as is the case during the following stages of the slide motion), the wave resistance due to displacement effects will be negligible. In this case the waves generated by shear stress effects will cause a negative wave resistance (confer the analytical solutions by Harbitz et al., 1991), which will again increase the slide velocity. In the subsequent analysis, $U_{max} = 50.0$ m/s will be applied as an absolute upper limit of the maximum slide velocity.

For the 1929 Grand Banks Slide, Newfoundland, which comprised 760 km^3 and travelled on a slope with depth profile comparable with the Storegga one, a sequence of downslope cable breaks revealed slide velocities of 20–30 m/s within the first 100–200 km of the run-out distance (Heezen and Ewing, 1952). $U_{max} = 20.0$ m/s will therefore be applied as a lower limit of the maximum slide velocity, while an intermediate value of 35.0 m/s will be applied as the most likely maximum velocity of the slides. The general observation referred by Edgers and Karlsrud (1982) that the ratio of total run-out distance to total height difference increases with the volume of submarine slides, supports the choice of a somewhat higher maximum velocity for the Storegga Slides than for the Grand Banks Slide.

With the same limitations and parameter values as used to determine the terminal slide velocity, a

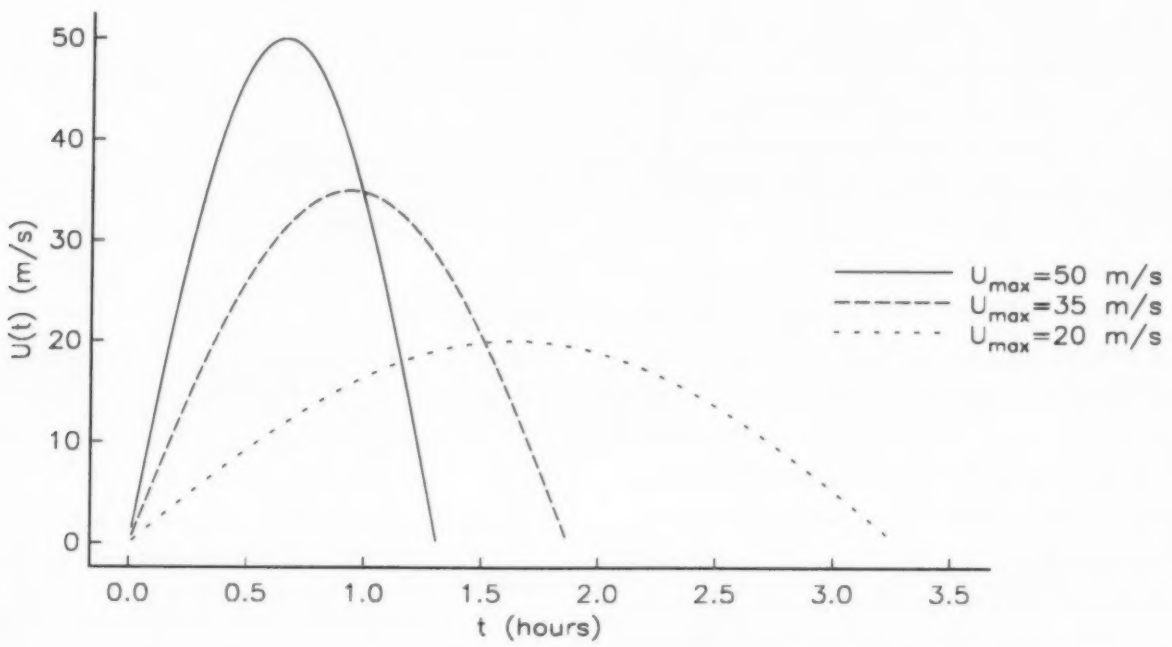

Fig.2. Velocity profiles defined by eqn. (4) (with $R = 150.0$ km).

velocity of 35 m/s is reached when the slides have travelled approximately a distance $R/2 = 75.0$ km, which is less than the distance for the gravity centre of the slides to reach the depositional area where the slope is less than 1°. If this was not the case, the retardation would have started before the slides obtained a velocity of 35 m/s.

By simulations with different variation of the slide velocity in time, i.e. different velocity profiles of the slide motion, it is established that the form of the velocity profile during the retardation phase of the slides is of minor importance. This is a consequence of the sub-critical slide motion, and supports the choice of the most simple curve reproducing both an acceleration phase and a retardation phase of the slides, given by eqn. (4). Simulations also reveal that the wave heights increase significantly with the acceleration of the slides. The velocity profile defined by eqn. (4) with $U_{max} = 35.0$ m/s and $R = 150.0$ km approximately reproduces the initial acceleration defined by eqn. (9) with the same limitations and parameter values as used to find U_{term} (the viscous drag is anyhow initially negligible). Simultaneously the slides reach a velocity of 35.0 m/s when they have travelled a distance $R/2$. Thus we consider this velocity profile to represent an estimate as good as any during the acceleration phase of the slides. The velocity profile is depicted in Fig.2. $U(t)$ is here defined as $|\dot{x}_s\vec{i} + \dot{y}_s\vec{j}|$.

To demonstrate the significance of the velocity profile, the wave heights generated by the First Slide with velocity profiles defined by eqn. (4) with $U_{max} = 20.0$ m/s and $U_{max} = 50.0$ m/s ($R = 150.0$ km) (Fig.2) will also be presented in sec. 4.3.

The initial acceleration of the slides defined by eqn. (4) is 0.005 m/s^2 and 0.033 m/s^2 with $U_{max} = 20$ m/s and $U_{max} = 50$ m/s respectively. Simulations with $U_{max} = 35$ m/s, but with other velocity profiles than defined by eqn. (4), reveal wave heights between the results obtained with $U_{max} = 20$ m/s and $U_{max} = 50$ m/s in eqn. (4), as long as the initial acceleration of the slides is between the two values mentioned above. Hence the wave heights resulting from the latter profiles are assumed to represent the absolute upper and lower limits of the wave heights generated by the First and Second Storegga Slides.

4.2 Effects of shear stress on the fluid/slide interface

In order to estimate the effect of shear stress on the wave height, we shall use the analytical solutions discussed by Harbitz et al. (1991). If η^{τ}_{max} and η^{d}_{max} denote the maximum surface elevation due to bottom shear stress and volume displacement respectively, we have $\frac{\eta^{\tau}_{max}}{\eta^{d}_{max}} = c^{u}_{D}\frac{U/\sqrt{gh_0}(L+S)}{2\Delta h}$, for a two-dimensional slide with total length $L+S$ and maximum thickness Δh moving on a horizontal bottom at depth h_0 with constant velocity U. The bottom shear stress is here expressed by $\tau = \frac{1}{2}c^{u}_{D}\rho U^2$. With $L+S = 225.0$ km, $\Delta h = 114.0$ m (as the First Storegga Slide), $h_0 = 2700.0$ m, $U = 35.0$ m/s and $c^{u}_{D} = 0.0019$, we find $(\eta^{\tau}_{max})/(\eta^{d}_{max}) = 0.4$. This implies that the effects of shear stress at the interface between the water and the slide body can not be

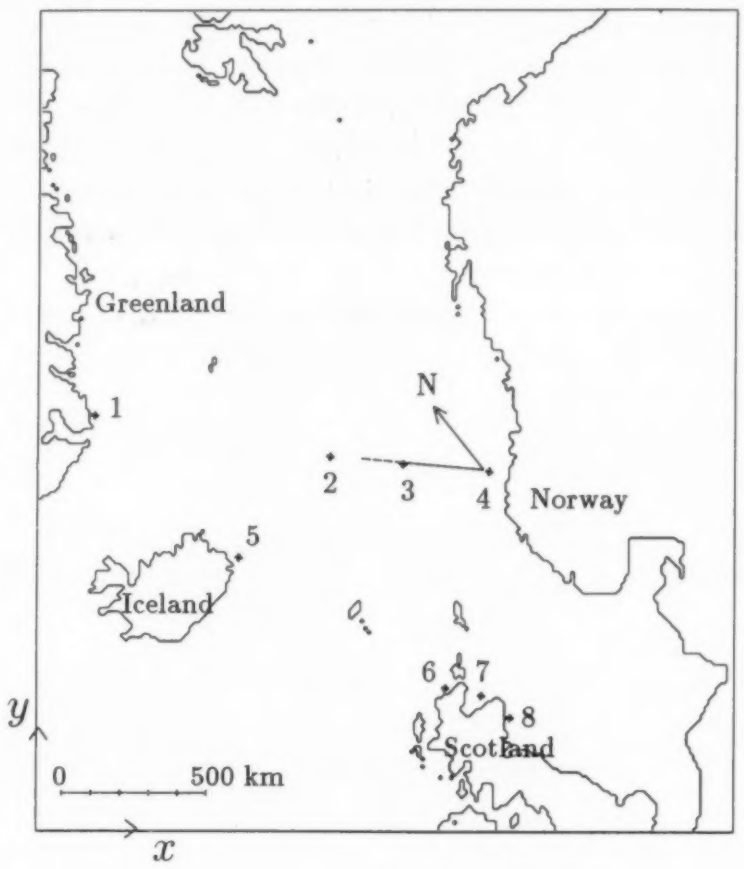

Fig.3. Model domain on a stereographic map projection. ——: Initial location of the central line of the slide, — —: frontal run-out distance, ↑: northward direction from rear end of slide, *1–8*: location of the 8 stations where time series of sea surface displacement are analysed. The precise location of the eight stations are referred in Table 4.

neglected when considering the wave formation ascribed to the Storegga Slides, as confirmed by the results referred in Table 4. Hence the effect of the bottom shear stress is included in the numerical simulations.

4.3 The simulated wave structure

The model domain with coordinate axes, initial location of the slide and the location of the eight stations where we analyse time series of the surface elevation, are shown in Fig.3. The precise location of each site is referred in Table 4. The depth profile for the slide area is shown in Fig.4. Estimated values of the slide parameters, based on the information in sec. 1.2, are listed in Table 3. The model domain constitutes 192×220 grid cells. The grid increments are $\Delta x = \Delta y = 12.5$ km. The depth matrix is based on the present bathymetry of the Norwegian Sea and the North Sea. Even though bathymetric changes due to reduced ice loading, rising sea level and crustal motions have occurred, the difference between the present water level and the water level at the time of the sand layer deposition (7000 yrs B.P.), is only of the order of 10 m along the coast of western Norway (Sørensen et al., 1987). At the locations inside point 8, eastern coast of Scotland, the corresponding difference is less than 6 m (Long et al., 1989). These differences may only slightly affect the wave propagation in shallow water regions. In the Storegga area the water depth was less at the time of the Second Slide than at present. This probably caused that the landward propagating waves were somewhat higher than the simulated wave heights. In deep sea regions, including the generation area for the seaward propagating waves, the effect of water level changes is insignificant. Thus we expect the

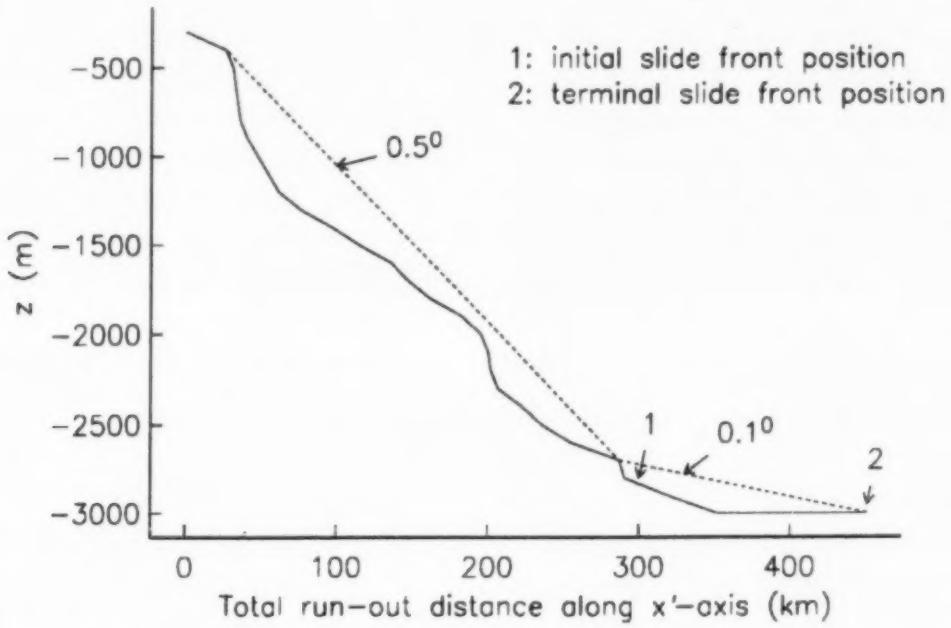

Fig.4. Solid line: Present depth profile in the slide area. Dotted lines: Average gradients of the slide scar and the depositional area.

TABLE 3

Parameters for slide volume and path of slide motion

		First Slide	Second Slide
B	width of the slide (km)	175.0	85.0
Δh	height of the slide (m)	114.0	144.0
L	length of the slide (km)	150.0	
S	smoothing distance, front and rear end (km)	75.0	
ϕ	direction of the slide motion relative to the x-axis (deg.)	174.9	
R	frontal run-out distance (km)	150.0	

TABLE 4

Maximum and minimum values of sea surface displacements η^{τ} ($\Delta h = 0.0$ m) and η^{d} ($c_D^u = 0.000$) in stations (1–8) for the First Slide with $U_{max} = 35.0$ m/s.

Station no.	Location		η^{τ}_{max}	η^{τ}_{min}	η^{d}_{max}	η^{d}_{min}
1	70°50′N	21°7′W	2.4	−2.1	4.0	−7.1
2	66°41′N	3°9′W	1.8	−0.7	2.9	−3.4
3	65°12′N	1°14′E	2.4	−1.5	5.8	−6.7
4	63°19′N	5°53′E	2.9	−6.1	12.0	−9.9
5	65°12′N	12°54′W	2.7	−2.6	4.7	−7.6
6	58°46′N	4°17′W	1.1	−2.8	8.3	−4.0
7	57°59′N	2°41′W	1.9	−3.0	5.7	−3.9
8	56°57′N	1°56′W	1.3	−2.2	4.0	−3.5

applied depth matrix to be appropriate for the waves generated by the Second Storegga Slide in spite of the water level changes. The sea level at the time of the First Slide is more uncertain.

In order to compare η^{τ} and η^{d}, the values have been calculated separately for the First Slide with $U_{max} = 35.0$ m/s (by choosing $c_D^u = 0.0019$, $\Delta h = 0.0$ m, i.e. no volume displacement, for η^{τ}, and $c_D^u = 0.000$, $\Delta h = 114.0$ m for η^{d}) (Table 4). In accordance with the discussion in sec. 4.1, the significance of the velocity profile is demonstrated by setting maximum slide velocity $U_{max} = 20.0$, 35.0 and 50.0 m/s in the profile defined by eqn. (4), see Fig.2. The extremes of the sea surface displacement at the eight stations are referred in Table 5. Figures 5 and 11 show the complete time series of η for $U_{max} = 35.0$ m/s for the First and Second Slides respectively. A secondary wave of 7.1 m for the First Slide and 4.5 m for the Second Slide in station 6 would probably not occur with open boundary conditions along the boundaries of the computational domain located at sea.

For relatively slow submarine slide motion, the height of the primary wave increases approximately in proportion to the velocity of the slide, given by U_{max}, for a fixed value of T. In this case we will from eqn. (4) find the initial acceleration of the slide to be proportional to U_{max} for $t \ll T$. For real slide events the value of R can often be estimated, as for the First Storegga Slide. With R

TABLE 5

Maximum and minimum values of sea surface displacement η in stations (1–8) for the First Slide with $U_{max} = 20$, 35, 50 m/s, and for the Second Slide with $U_{max} = 35.0$ m/s

Station no.	First Slide						Second Slide	
	$U_{max} = 20.0$ m/s		$U_{max} = 35.0$ m/s		$U_{max} = 50.0$ m/s		$U_{max} = 35.0$ m/s	
	η_{max} (m)	η_{min} (m)	η_{max} (m)	η_{min} (m)	η_{max} (m)	η_{min} (m)	η_{max} (m)	η_{min} (m)
1	1.4	−1.1	5.1	−6.9	12.4	−17.7	2.8	−3.8
2	0.9	−1.1	3.6	−3.3	8.8	−8.9	2.1	−2.0
3	1.8	−1.7	7.0	−5.9	13.6	−14.2	5.2	−3.7
4	2.9	−4.7	10.5	−11.6	12.4	−19.1	7.0	−7.3
5	2.6	−2.3	5.6	−8.1	13.1	−12.9	3.3	−4.6
6	1.5	−2.9	7.1	−5.4	13.0	−10.6	4.5	−3.2
7	2.0	−2.8	4.8	−5.5	6.7	−7.0	3.3	−3.2
8	1.2	−1.8	3.5	−4.1	4.9	−6.4	2.5	−2.6

First Slide

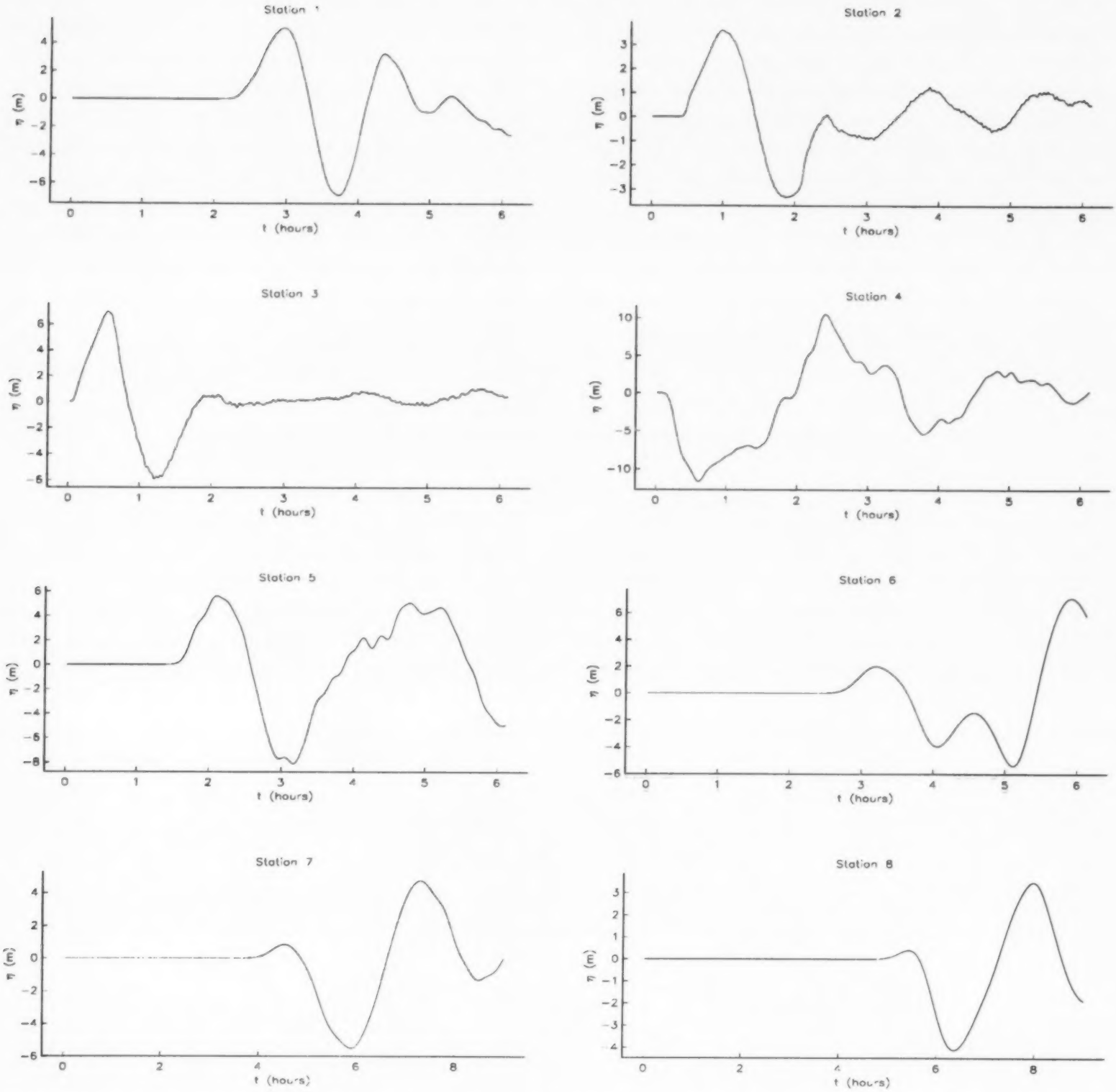

Fig.5. Simulated time series of sea surface displacement η at the eight stations depicted in Fig.3 for the First Slide with $U_{max} = 35.0$ m/s.

fixed, the value of T will have to decrease while U_{max} is increased. Hence the initial acceleration of the slide will be proportional to U_{max}^2 for $t \ll T$. This explains why the height of the primary wave seems to be approximately proportional to U_{max}^2 rather than U_{max}, as indicated by the results in Table 5. In fact it may be deduced from eqn. (1) that the surface elevation initially increases in time

in proportion to U_{max}^2. The validity of the results is therefore strongly dependent on a correct estimate of the maximum slide velocity.

The simulated wave pattern for the First Slide with $U_{max} = 35.0$ m/s is shown in Figs.6–10. The sea surface displacement introduced by the slide appears at $t = 1.0$ h as a characteristic, symmetric wave pattern consisting of a sickle shaped surface elevation with a maximum height of about 3 m, followed by a surface depression with a minimum height of about -15 m (Figs.6 and 7). At $t = 2.0$ h, the primary wave has reached the eastern coast of Iceland, and the wave height outside the shore is about 5 m (Figs.8 and 9). Simultaneously there is a wave strongly affected by refraction, possibly an edge wave, propagating northwards along the Norwegian coast with its crest approximately perpendicular to shore line. At $t = 3.0$ h, the wave height east of Greenland is about 5 m, while the wave height north of Scotland is 1.5m only (Fig.10).

The corresponding wave pattern for the Second Slide is shown in Figs.12–14. At $t = 1.0$ h the maximum height of the surface elevation is about 2 m, followed by a surface depression with a minimum height of -8 m (Fig.12). At $t = 2.0$ h, the wave height outside the eastern coast of Iceland is 3 m (Fig.13). At $t = 3.0$ h, the wave height east of Greenland is about 3 m, while the wave height north of Scotland is about 1 m (Fig.14). We conclude that most of the wave energy induced by the slide propagates towards Greenland and Iceland, rather than Scotland.

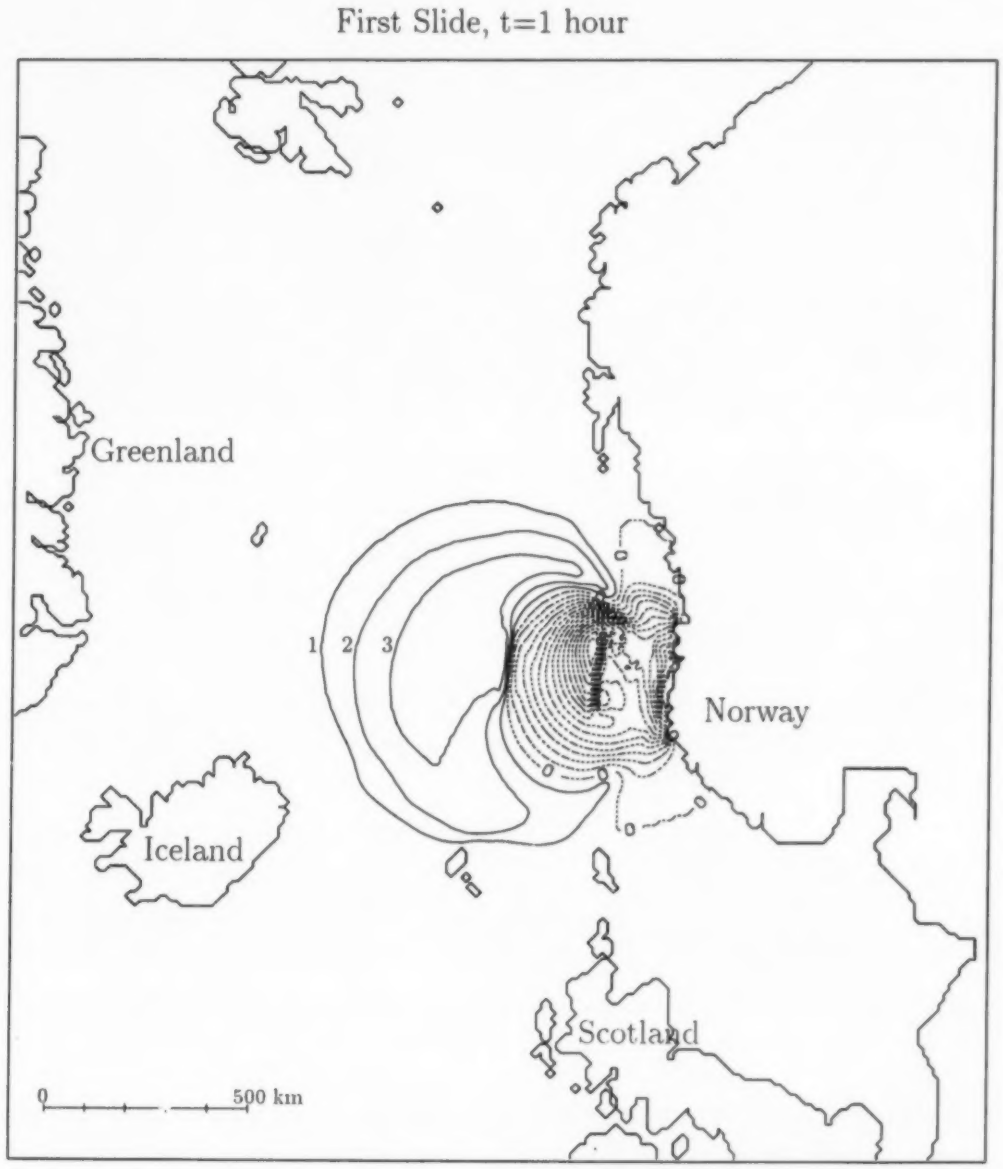

Fig.6. Simulated wave pattern at $t = 1$ h after the release of the First Slide with $U_{max} = 35.0$ m/s. Contour lines for wave height with interval 1.0 m. Solid lines indicate surface elevation. Maximum height of outward propagating primary wave: 3 m.

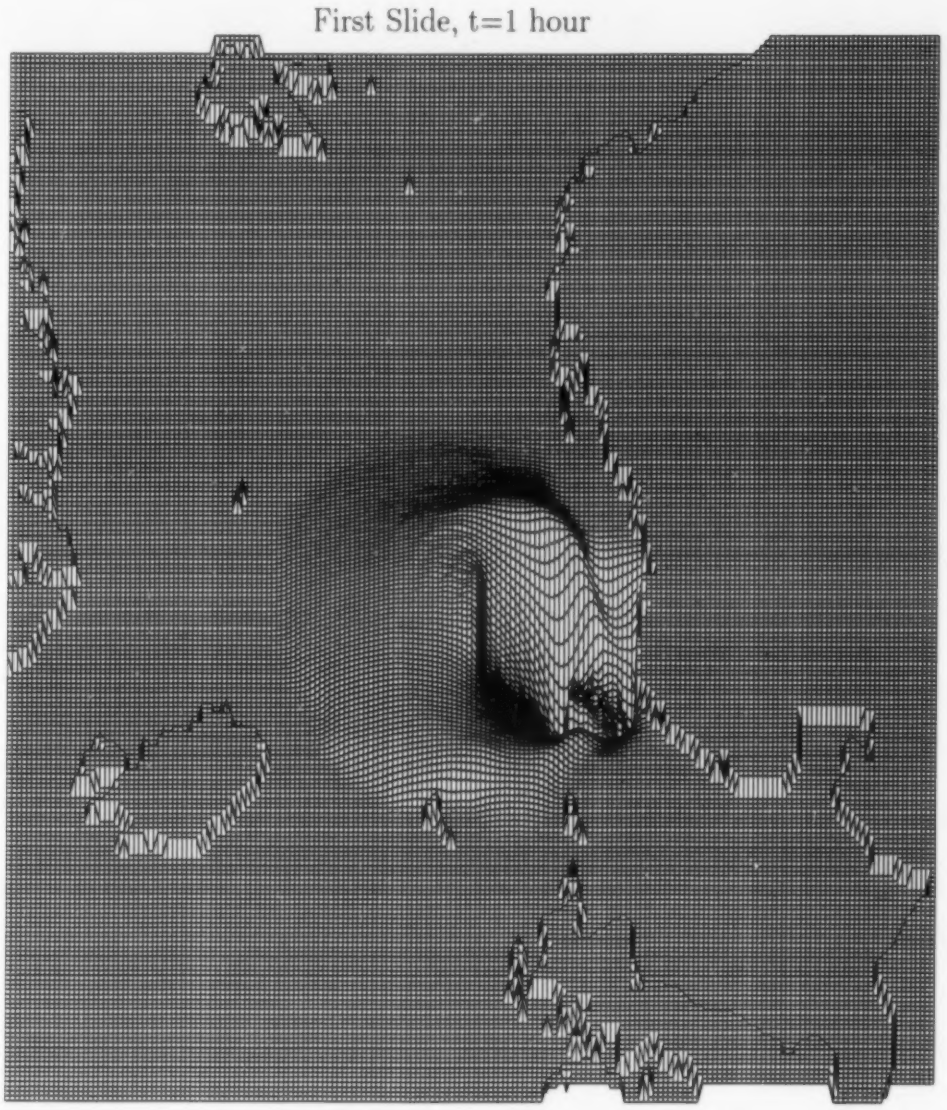

Fig.7. Perspective view of sea surface displacement at $t = 1.0$ h after the release of the First Slide. Parameter values as in Fig.6.

4.4 Estimated run-up heights

Waves approaching the shore line will amplify and wash up the beach slope. By the method described by Harbitz et al. (1991, appendix) rough estimates for the maximum run-up height may be found from the calculated height η^p and the period T^p of the primary waves at stations off the coast of Greenland, Iceland and Scotland (insignificant precursors in stations 7 and 8 are disregarded). The final amplification is assumed to take place along a linear slope with inclination angle θ between the point of depth h_0 where η^p is read, and the shore line. The periods of the incident waves are estimated directly from the time series. Values for the run-up computation are presented in Table 6. An estimate of the run-up height inside station 7 is omitted due to the critical location outside Moray Firth. The beach slopes of this estuary are exposed for significant run-up heights which can only be found by a detailed analysis including local effects.

Along the Norwegian coast a precursor with downward displacement of the sea surface occurred, as indicated by the time series from station 4 (Figs.5 and 11). The time series together with the contour plots in Figs.10 and 14 reveal that the subsequent positive sea surface displacement caused run-up heights of 10–15 m for the First Slide and 5–8 m for the Second Slide.

The estimated amplification factor for the waves between the stations where η^p is read and the shore line, varies from 1.1 to 3.1 (except for one special occasion described below). The small values are a direct consequence of the large wave lengths with

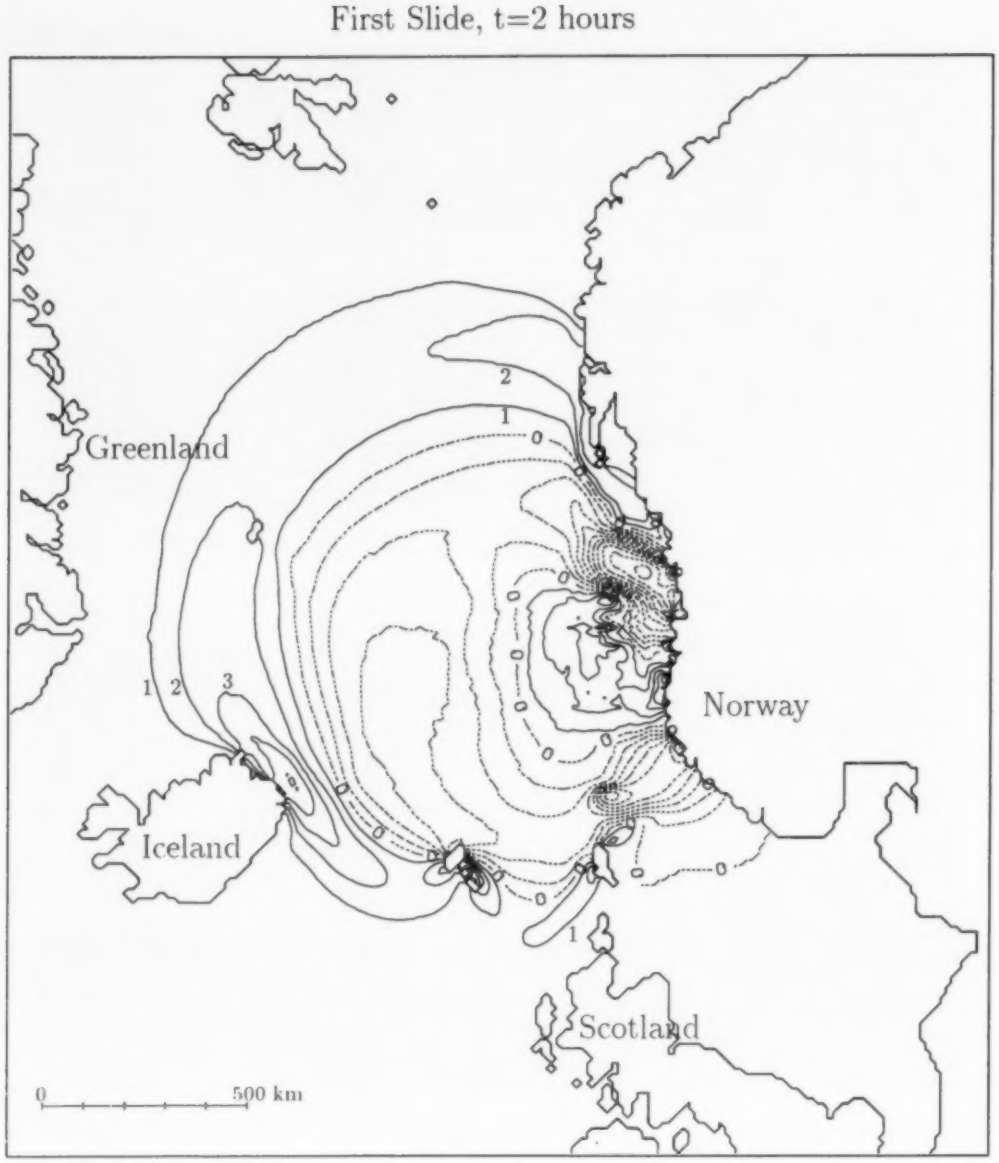

Fig.8. Simulated wave pattern at $t = 2$ h after the release of the First Slide. Parameter values and contour line interval as in Fig.6. Maximum height of wave approaching Iceland: 5 m.

TABLE 6

Estimated run-up heights, R^p, for primary wave. $U_{max} = 35.0$ m/s

Locations	Stations	h_0 (m)	θ (deg.)	First Slide			Second Slide		
				T^p (h)	η^p (m)	R^p (m)	T^p (h)	η^p (m)	R^p (m)
East Greenland	1	233	0.71	2.20	5.1	5.6	2.13	2.8	3.1
East Iceland	5	157	0.34	2.17	5.6	7.8	2.05	3.3	4.6
North Scotland	6	61	0.13	2.27	2.0	5.0	2.10	1.2	3.7
East Scotland	7	72	0.05	3.03	4.8	–	2.83	3.3	–
East Scotland	8	76	0.23	2.57	3.5	4.6	2.57	2.5	3.3

corresponding wave periods much longer than normally reported in tsunami events. Where the continental shelf is narrow, landward propagating waves will experience the continental slope and the shore line almost as one vertical wall, causing the amplification factor between a station outside the continental shelf and the shore line to be approximately 2.

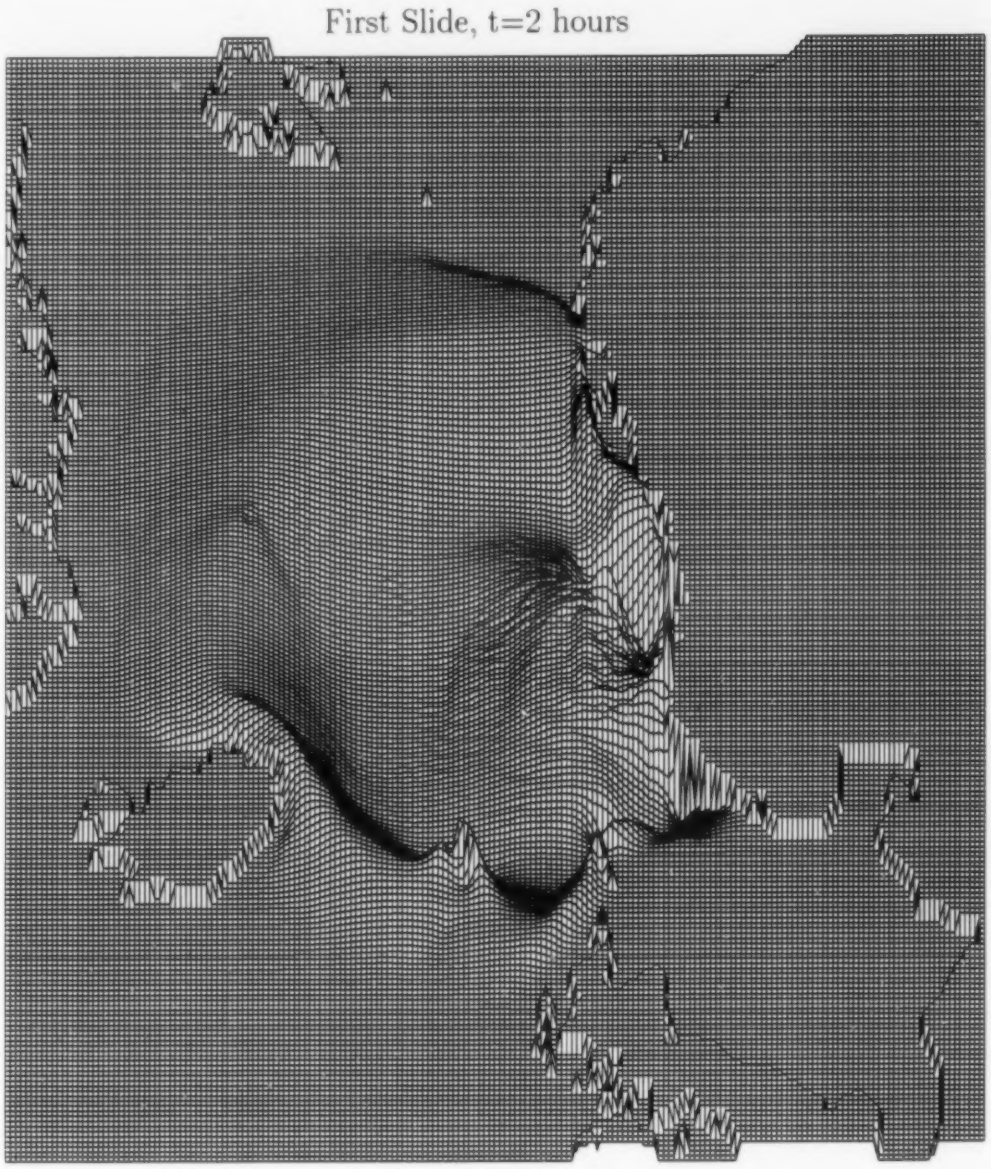

Fig.9. Perspective view of sea surface displacement at $t = 2.0$ h after the release of the First Slide. Parameter values as in Fig.6.

In the applied method for estimating run-up heights (Harbitz et al., 1991, appendix), the incident wave is replaced by a single periodic harmonic with period T^p and amplitude η^p. Normally the periodic wave in its entirety will reach higher than the primary wave alone. The difference between the run-up height for a single crested wave and for a single periodic wave is however small for long waves (see Pedersen, 1987). In station 8, eastern coast of Scotland, there will hardly be any difference at all, as the situation with a surface depression preceding the primary wave is more closely related to a periodic wave.

By reducing the maximum slide velocity to 20 m/s, the run-up heights for the First Slide are reduced to 1.8 m on the eastern coast of Iceland, and about 1.5 m on the eastern coast of Greenland and the coast of northern Scotland. A maximum slide velocity of 50 m/s reveals run-up heights for the First Slide of 21 m along the eastern coast of Iceland, 12.0 m along the eastern coast of Greenland and 13.3 and 6.9 m along the northern and eastern coast of Scotland respectively.

The calculated run-up heights for the Second Slide with $U_{max} = 35$ m/s, agree remarkably well with the run-up heights from the Second Slide deduced by Dawson et al. (1988), recording that "the tsunami struck the eastern coast of Scotland and reached a height of at least 4 m above contemporary high water mark in some inlets", whilst smaller values were recorded at more open locations. At the most open site (at the mouth of the river Ythan, about 50 km NE along the coast from station 8, Fig.3) the maximum height of the sand

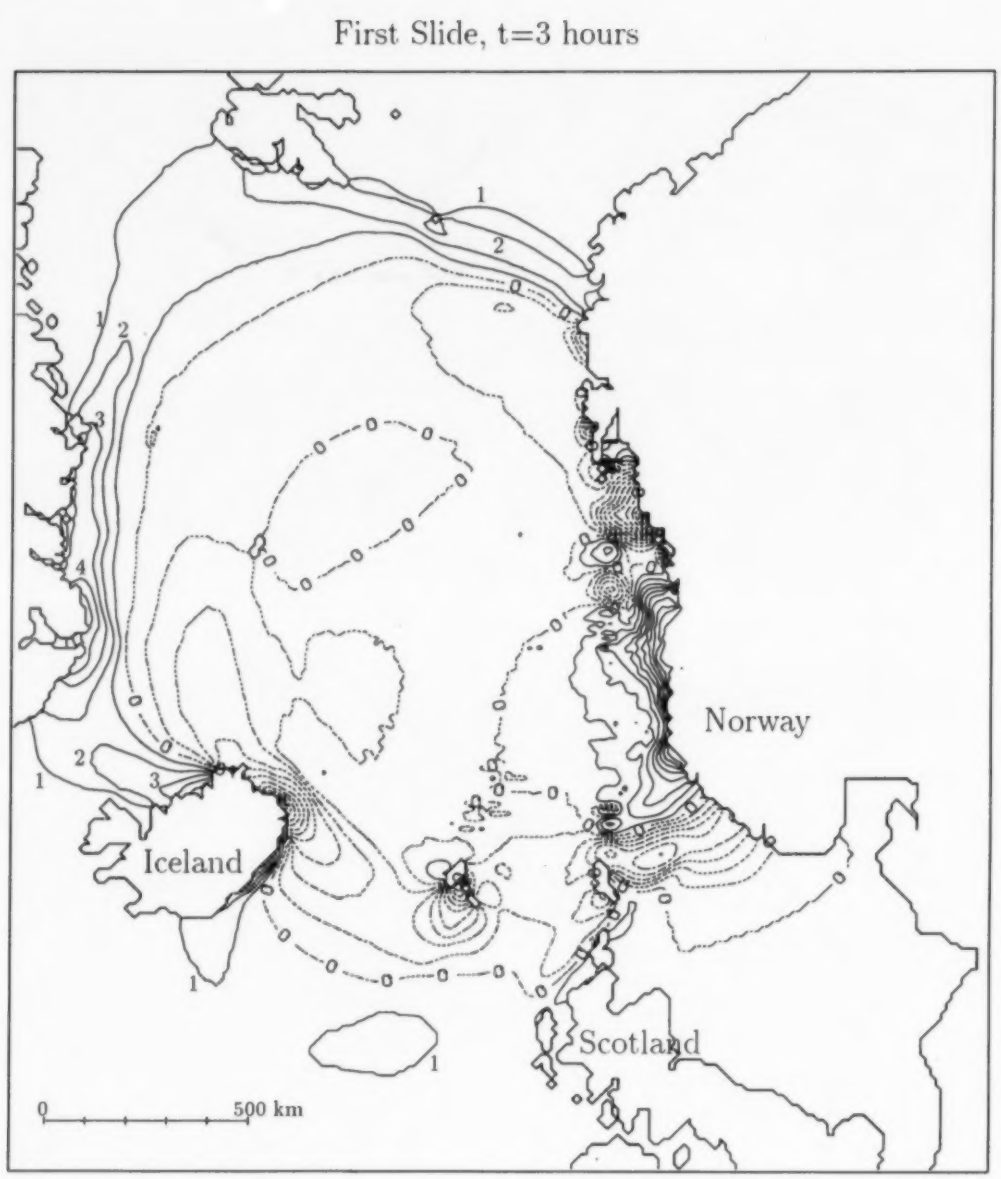

Fig.10. Simulated wave pattern at $t = 3$ h after the release of the First Slide. Parameter values and contour line interval as in Fig.6. Maximum height of wave approaching Scotland: 1.5 m, Greenland: 5 m.

layer is 1.0–1.5 m above contemporary high water mark (Smith et al., 1983). According to Dawson et al. (1988) the measured run-up values "can be regarded as minima because the tsunami wave run-up may have reached above the level of sand deposition. Also, the tsunami may have struck the coast when the tide was not at the contemporary high water mark". With a maximum slide velocity of 20 m/s, the run-up heights for the Second Slide are reduced to 1.8 m on the eastern coast of Iceland, 0.9 m on the eastern coast of Greenland, and 1.0 m on the coast of northern Scotland. A maximum slide velocity of 50 m/s reveals run-up heights for the Second Slide of 13.7 m along the eastern coast of Iceland, 11.5m along the eastern coast of Greenland and 18 and 5.3 m along the northern and eastern coast of Scotland respectively. The large value of 18 m occurs because the incident wave is relatively short, $T^{\mathrm{p}} = 1.8$ h. This gives an amplification factor of 8.2 for an average slope $\theta = 0.13°$. The wave would probably break before this value is reached.

It should be emphasized that run-up heights may be significantly increased by local topographical effects causing resonance phenomena as well as interference, focusing or trapping of the incident waves (e.g. Liu, 1981). Traces of larger run-up heights resulting from these effects may possibly be found in a few peculiar places, but will not be recognizable in a larger region. Oblique angles of incidence as well as wave breaking will generally reduce the amplification.

In exposed areas traces of the tsunami might have been washed away by waves from regular

Second Slide

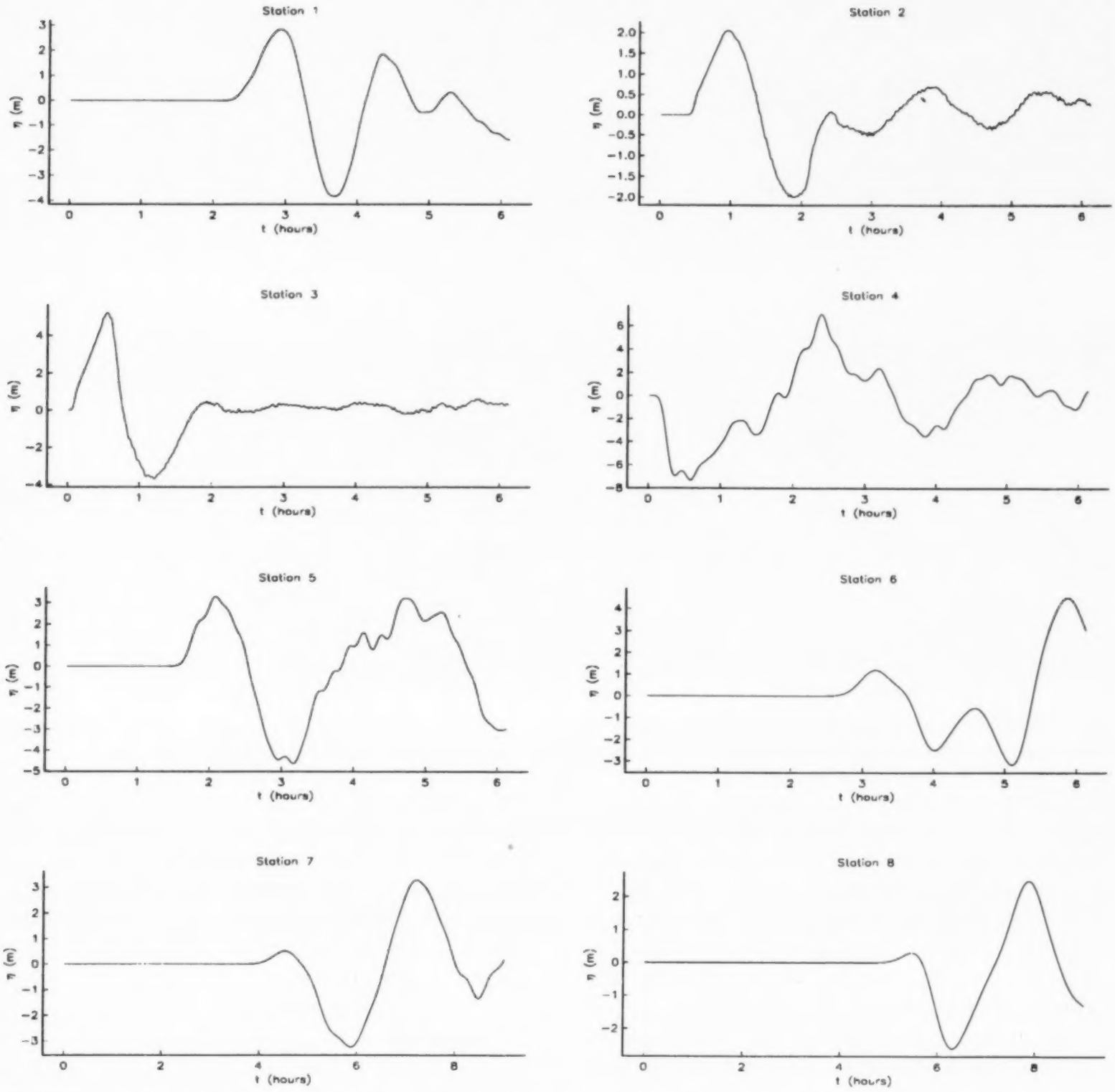

Fig.11. Simulated time series of sea surface displacement η at the eight stations depicted in Fig.3 for the Second Slide with U_{max} = 35.0 m/s.

storms. Tsunamis will however propagate for long distances into bays and fjord systems, and thereby leave well-defined traces in otherwise sheltered areas.

4.5 Some remarks on the numerical computations

The slides are assumed to move upon the existing sea bed, i.e. upon the real slide deposits. The error

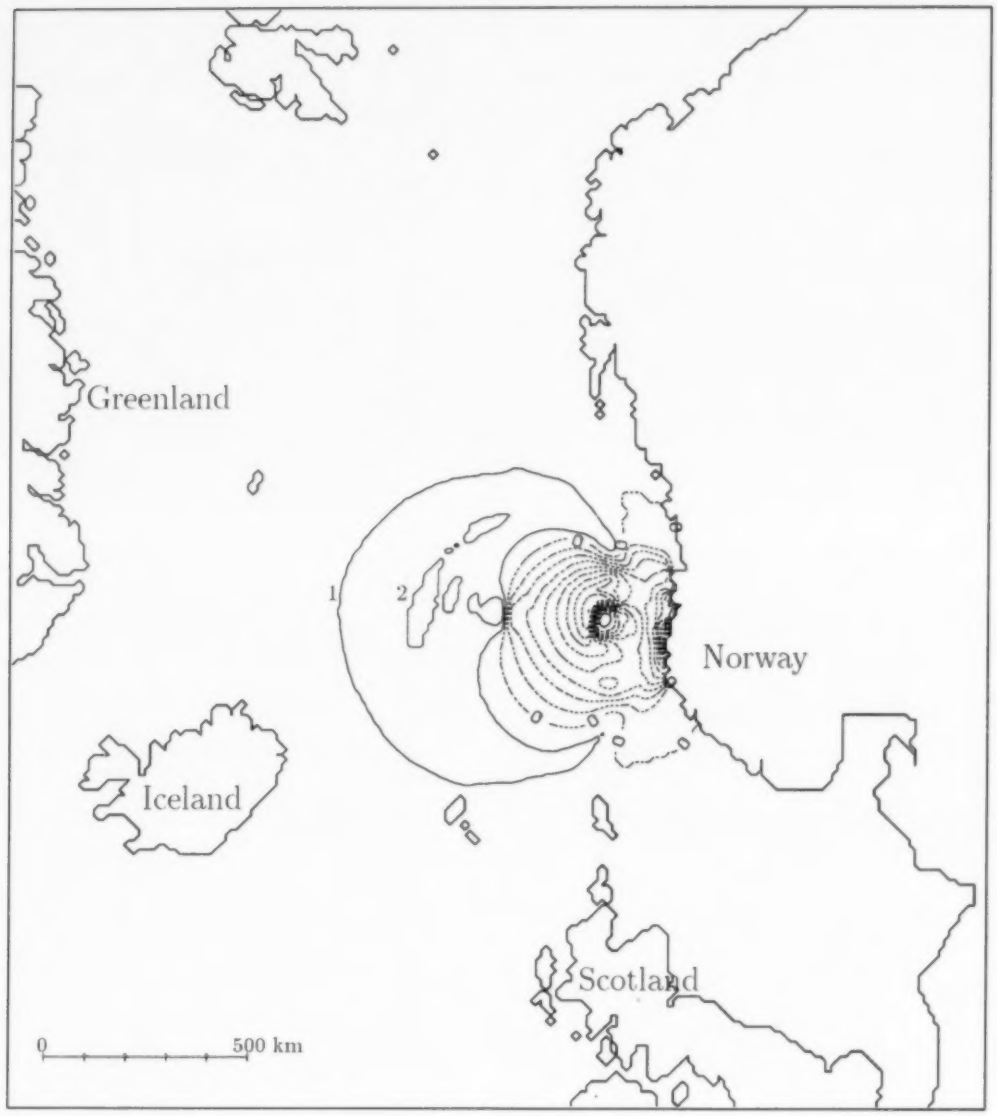

Fig.12. Simulated wave pattern at $t = 1$ h after the release of the Second Slide with $U_{max} = 35.0$ m/s. Contour lines for wave height with interval 1.0 m. Solid lines indicate surface elevation. Maximum height of outward propagating primary wave: 2 m.

introduced by this simplification will be small since the thickness of the deposits and the moving slides is relatively small compared to the water depth. The effect of a retrogressive slide movement is omitted. This is probably more important for the Second Slide, but will by no means affect the primary seaward propagating wave.

As stated above, tsunamis are not influenced by Coriolis' effects. However, it should not be concealed that these effects might originate Kelvin waves where the width of the continental shelf is at least 300 km. If such waves arose, they slightly affected the wave heights in the coastal areas.

The exponential smoothing function, eqn. (6), is favoured because little high frequency numerical noise is introduced compared to other smoothing functions. A reduced smoothing distance S will introduce more high frequency noise, and increase the steepness of the primary wave. However, the main characteristics and the wave heights are approximately unchanged as long as the total slide volume is kept constant.

5 Conclusions

Wave run-up heights generated by the First and Second Storegga Slides are computed on the basis of a numerical model. The results for the Second Slide are in remarkably good agreement with wave heights deduced from possible deposits of the Second Slide tsunami in northern Scotland (Dawson et al., 1988). The simulated wave heights along

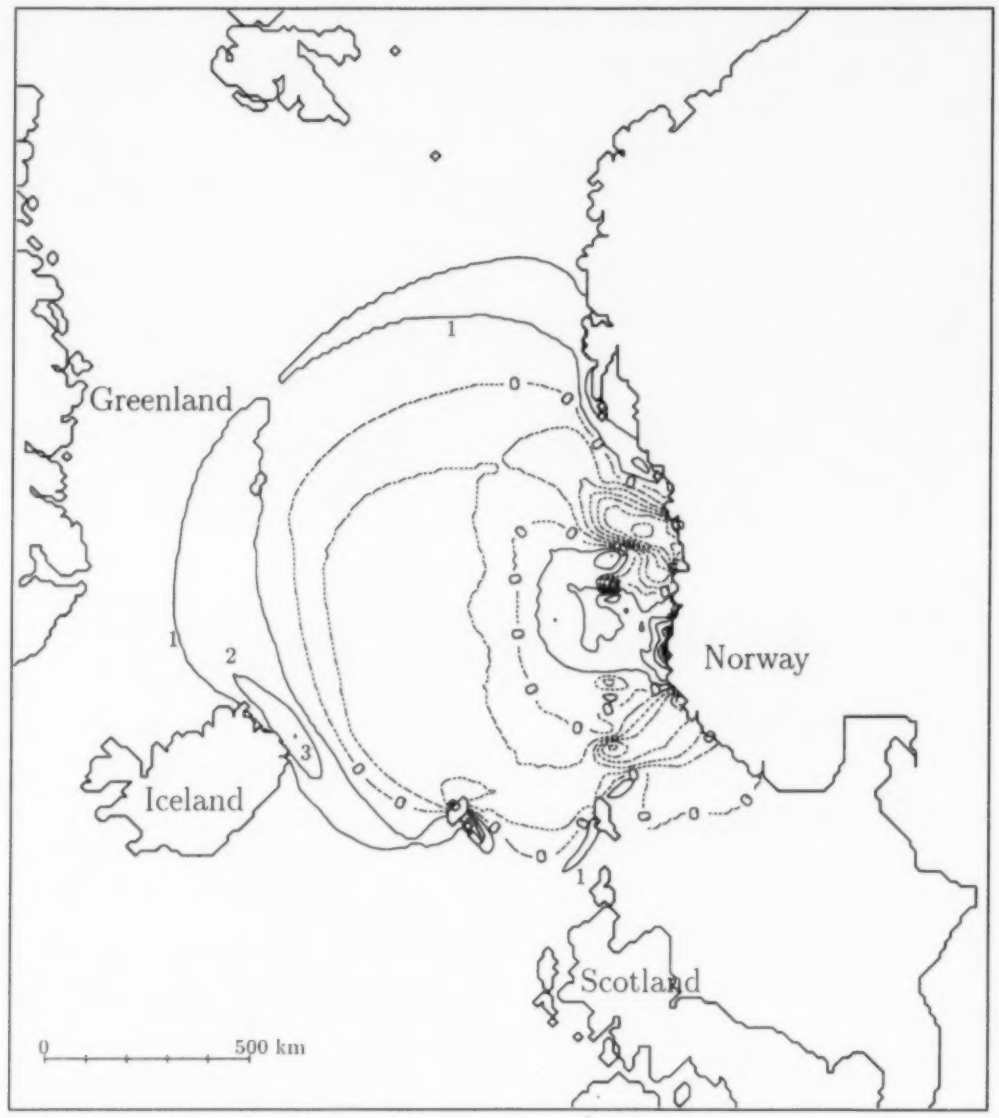

Fig.13. Simulated wave pattern at $t=2$ h after the release of the Second Slide. Parameter values and contour line interval as in Fig.12. Maximum height of wave approaching Iceland: 3 m.

the western coast of Norway also support Svendsen and Mangerud's (1990) conjecture about tsunami deposits south of Ålesund.

The model is based on the linearized hydrostatic shallow water equations for wave propagation in open sea regions and a slide model for describing the dynamics of the slide body. The wave energy induced by the slide propagates mainly towards Greenland and Iceland (i.e. in the direction of the slide motion). The generated wave heights increase significantly with the acceleration of the slide, and a slide with a smaller volume may easily cause higher waves than a bigger one, if the smaller slide has a sufficiently higher initial acceleration. For a fixed run-out distance the selected velocity profile, i.e. the variation of the slide velocity in time, is determined simply by the maximum slide velocity. A correct estimate of this parameter is therefore essential. From considerations of a slide moving on a linear slope, sec. 4.1, giving an upper limit of the maximum slide velocity of about 50 m/s, and from comparisons with the recorded velocities of the 1929 Grand Banks Slide, Newfoundland, giving a lower limit of 20 m/s (Heezen and Ewing, 1952), an intermediate value of 35 m/s is applied as the most likely maximum slide velocity.

Local wave amplification in the wave run-up zone are estimated by comparing results from an idealized numerical run-up model using a no-flux boundary condition with an analytical model for calculation of run-up heights on a gentle beach slope. The large scale run-up heights for the First Slide are found to be 7.8 m on the eastern coast of Iceland, 5.6 m on the eastern coast of Greenland

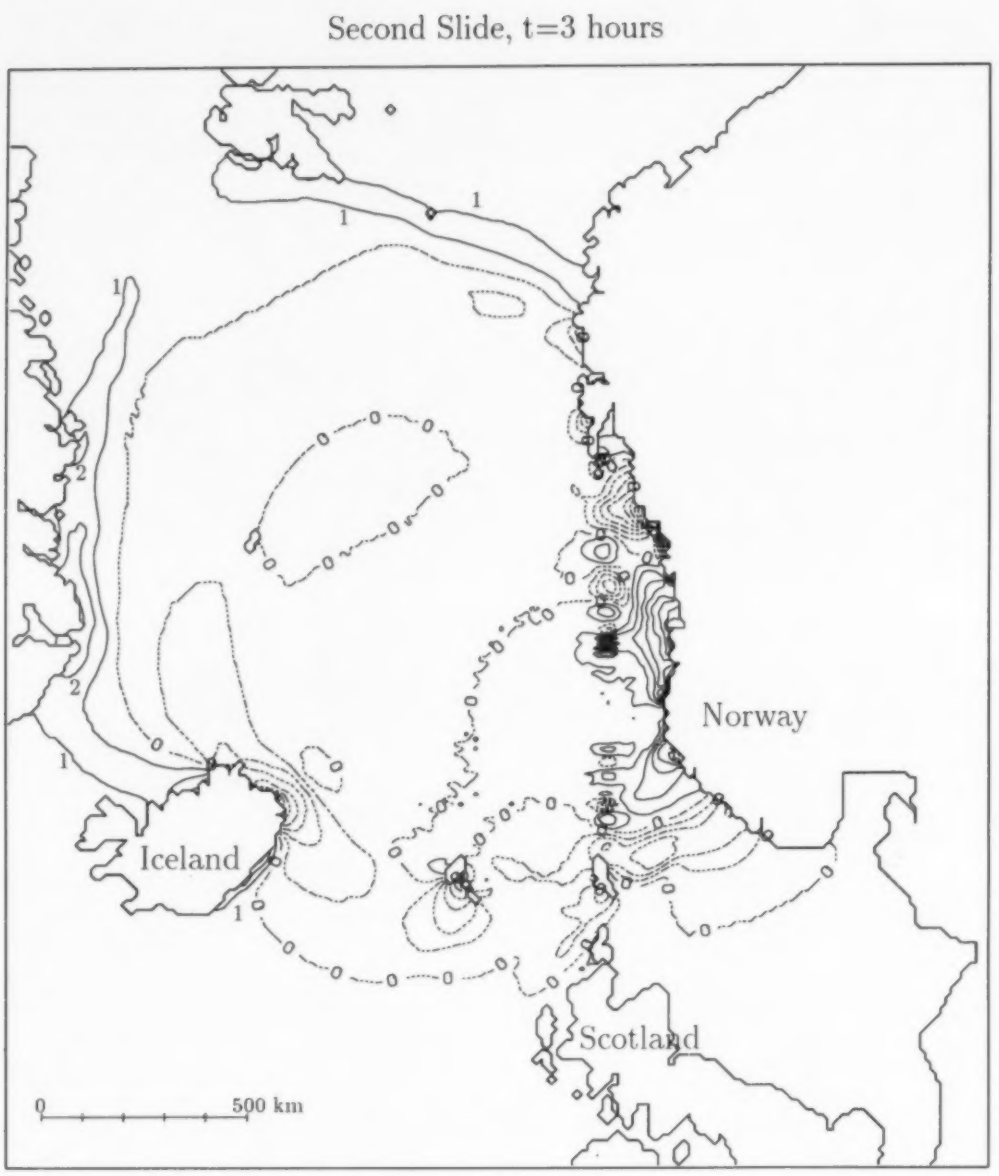

Fig.14. Simulated wave pattern at $t = 3$ h after the release of the Second Slide. Parameter values and contour line interval as in Fig.12. Maximum height of wave approaching Scotland: 1.0 m, Greenland: 3 m.

and about 5 m on the coast of northern Scotland for a maximum slide velocity of 35 m/s. For the Second Slide the calculated large scale run-up heights are 4.6 m on the eastern coast of Iceland, 3.1 m on the eastern coast of Greenland and about 3.5 m on the coast of northern Scotland. However, the run-up heights may be significantly increased by local effects. Along the Norwegian coast there was primarily a precursor with downward displacement. The subsequent positive sea surface displacement caused run-up heights exceeding 10 m for the First Slide and 5 m for the Second Slide. By reducing the maximum slide velocity to 20 m/s, the run-up heights of the First Slide are reduced to 1.8 m on the eastern coast of Iceland, and about 1.5 m on the eastern coast of Greenland and the coast of northern Scotland. A maximum slide velocity of 50 m/s reveals run-up heights for the First Slide of 21 m along the eastern coast of Iceland, 12.0 m along the eastern coast of Greenland and 13.3 and 6.9 m along the northern and eastern coast of Scotland respectively. For the Second Slide, a maximum slide velocity of 20 m/s reveals run-up heights of 1.8 m on the eastern coast of Iceland, 0.9 m on the eastern coast of Greenland, and 1.0 m on the coast of northern Scotland. The limited amplification is a direct consequence of the large wave lengths with corresponding wave periods much longer than normally reported in tsunami events.

In view of the predicted run-up heights, the eastern coast of Iceland and the western coast of

Norway were most exposed to the tsunami. Traces of a tsunami are therefore most likely to be detected in these regions.

Analysis of the effects of shear stress at the interface between the water and the slide body, has proved that this effect must be included. Except for run-up zones with gentle beach slopes, the assumptions of linear long wave propagation are fulfilled in the entire computational domain.

Acknowledgements

This work was supported by the Royal Norwegian Council for Scientific and Industrial Research. The author wishes to thank Harald Norem at Norwegian Geotechnical Institute (NGI), for contributing with valuable information about submarine slide motion. Dr. Tom Bugge, Continental Shelf and Petroleum Technology Research Institute (IKU), is thanked for supplying unpublished information. Dr. Alastair G. Dawson, Department of Geography, Coventry Polytechnic (England, U.K.), is thanked for constructive comments and advice.

References

Bugge, T., Befring, S., Belderson, R.H., Eidvin, T., Jansen, E., Kenyon, N.H., Holtedahl, H. and Sejrup, H.P., 1987. A giant three-stage submarine slide off Norway. Geo-Mar. Lett., 7: 191–198.

Bugge, T., Belderson, R.H. and Kenyon, N.H., 1988. The Storegga Slide. Philos. Trans. R. Soc. London, A 325 (1988): 357–388.

Dawson, A.G., Long, D. and Smith, D.E., 1988. The Storegga Slides: Evidence from eastern Scotland for a possible tsunami. Mar. Geol., 82: 271–276.

Edgers, L. and Karlsrud, K., 1981. Viscous analysis of submarine flows — Field case studies. Norw. Geotech. Inst., Rep. 52207-8.

Edgers, L. and Karlsrud, K., 1982. Soil flows generated by submarine slides — Case studies and consequences. Norw. Geotech. Inst., Publ. 143.

Hammack, J.L., 1973. A note on tsunamis: Their generation and propagation in an ocean of uniform depth. J. Fluid Mech., 60(4): 769–799.

Hansom, J.D. and Briggs, D.J., 1991. Sea-level changes in Vestfirðir, north west Iceland. In: J.K. Maizels and C. Caseldine (Editors), Environmental Change in Iceland: Past and Present. Glaciol. Quat. Geol., 7: 79–91.

Harbitz, C., Pedersen, G. and Gjevik, B., 1991. Model simulations of large water waves due to landslides. Preprint Ser., Dep. Math., Univ. Oslo, 3.

Heezen, B.C. and Ewing, M., 1952. Turbidity currents and submarine slumps, and the 1929 Grand Banks earthquake. Am. J. Sci., 250: 849–873.

Ichiye, T., 1983. Tsunami generation as finite depth Cauchy-Poisson problem or long wave problem. In: K. Iida and T. Iwasaki (Editors), Tsunamis—Their Science and Engineering. pp. 265–274.

Jansen, E., Befring, S., Bugge, T., Eidvin, T., Holtedahl, H. and Sejrup, H.P., 1987. Large submarine slides on the Norwegian continental margin: Sediments, transport and timing. Mar. Geol., 78: 77–107.

Liu, P.L.-F., 1981. Effects of the continental shelf on harbor resonance. In: K. Iida and T. Iwasaki (Editors), Tsunamis — Their Science and Engineering. pp.303–314.

Long, D., Smith, D.E. and Dawson, A.G., 1989. A Holocene tsunami deposit in eastern Scotland. J. Quat. Sci., 4: 61–66.

Norem, H., Locat, J. and Schieldrop, B., 1989. An approach to the physics and the modelling of submarine flowslides. Norw. Geotech. Inst., Rep. 522090-2.

Pedersen, G., 1987. Run-up of cnoidal waves. Preprint Ser., Dep. Math., Univ. Oslo, 4.

Schlichting, H., 1968. Boundary Layer Theory. McGraw-Hill, New York.

Sørensen, R., Bakkelid, S. and Torp, B., 1987. Landhevning (Land Uplift). Nasjonalatlas for Norge. Kartblad (map sheet) 2.3.3.

Svendsen, J.I. and Mangerud, J., 1990. Sea-level changes and pollen stratigraphy on the outer coast of Sunnmøre, western Norway. Nor. Geol. Tidsskr., 70: 111–134.

Voit, S.S., 1987. Tsunamis. Annu. Rev. Fluid Mech. 1987. 19: 217–236.

Marine Geology, 105 (1992) 23–36
Elsevier Science Publishers B.V., Amsterdam

Recent environmental changes recorded in anoxic Barsnesfjord sediments: Western Norway

Matthias Paetzel and Hans Schrader

University of Bergen, Department of Geology, Section B, Allégt. 41, N-5007 Bergen, Norway

(Received January 16, 1991; revision accepted October 22, 1991)

ABSTRACT

Paetzel, M. and Schrader, H., 1992. Recent environmental changes recorded in anoxic Barsnesfjord sediments: Western Norway. Mar. Geol., 105: 23–36.

Four high quality gravity cores and five box cores, up to 2.3 m long, from the land-locked, silled and anoxic Barsnesfjord in western Norway contained three different sediment sequences. These were alternating thick dark and light layers, fine scaled laminated sections and grayish/brownish layers dominated by minerogenic grains.

Accurate sedimentation rates over the last 150 years were determined using three different techniques: ^{137}Cs dating, occurrence of historically documented slide/slump events and counting of seasonal sediment layers.

Bulk sediment- and organic carbon accumulation rates in the outer and inner fjord basin decreased by over 30% when values of the last century (pre-1904) are compared with those of this century (1904–1986). This significant change is attributed to the damming of the Hafslovatn in 1904. No significant change in these values was observed after regulation of the Veitastrondsvatn in 1982 and after the 2nd damming of the Hafslovatn in connection with the construction of the Årøy electrical power plant in 1983. Zn and Cu accumulation over the same time periods remained constant.

Introduction

Accurate dating of both marine and freshwater sediments deposited over historical time is crucial in the detailed analysis of sediment *bulk* and *individual* component accumulation. Any study that tries to detect recent changes in the sediment column in relation to anthropogenic or natural causes depends on an accurate chronology. Sediments retrieved from areas with high accumulation rates are ideal recorders of these most recent changes if their chronology is well constrained.

The "exact" modelling of environmental changes from marine sediments depends on undisturbed deposition preserving primary sedimentary structures and high sedimentation rates over 0.5 cm/year. Such sediments can be found in the highly productive coastal upwelling areas off Peru (Schrader, 1991), off Namibia (Calvert and Price, 1971), off Somalia (Prell et al., 1989), in shelf areas close to large river estuaries (the northern Adriatic: Puškarić et al., 1990) and in some anoxic fjords (Skei and Melsom, 1982; Nagy and Alve, 1987; Sancetta and Calvert, 1988).

Shallow sills effectively limit circulation and exchange of deep bottom waters. Renewal of deeper water including renewal of dissolved oxygen is thus strongly reduced. High primary production coupled with high organic matter flux from the photic zone causes high consumption of oxygen by organic matter degradation in the deeper waters and at the sediment–water interface. Therefore anoxic conditions may prevail at the bottom if exchange processes of bottom waters are reduced.

High new production and high supply of terrigenous matter result in high sedimentation rates that are deposited without vertical bioturbation under anoxic bottom condition. New production (Dugdale and Goering, 1967; Eppley and Peterson,

Correspondence to: M. Paetzel, University of Bergen, Department of Geology, Section B, Allegaten 41, N-5007 Bergen, Norway.

0025-3227/92/$05.00 © 1992 — Elsevier Science Publishers B.V. All rights reserved

1979) is that portion of photosynthesis which depends on inorganic nitrate supply from below the photic zone or from land. The new production delivers the export of biological material to deeper waters and, ultimately, the supply to the seafloor and to the sediments.

The other major advantage of land-locked fjord basins is that they contain a complete sediment sequence only occasionally interrupted by the insertion of slump material. Erosional events in the deeper fjord basins do not occur. All sediments derived from primary production in the photic zone via new production, from precipitation, from fluvial runoff and from local slide events will be caught in these natural sediment traps. Anoxic fjords with an estuarine circulation are ideal small scale "ocean" models where input, residence and sedimentary output can be monitored and modeled (Syvitski et al., 1987). These high resolution sediment sequences contain tracers of climatical and environmental changes through historical and geological times in much more detail than pelagic sediments. The understanding of the sedimentary record of natural and man induced input into fjords will lead to an input model where most parameters can be assessed.

It is the aim of this contribution to document historical changes in sedimentation rates, in bulk accumulation rates and in selected component accumulation of pre-industrial (19th century) and industrial (20th century) times and relate these changes to changes in the surrounding environment.

Environmental setting

The Barsnesfjord in western Norway is a northeast tributary of the Sogndalsfjord which is connected with the Sognefjord further to the south (Fig. 1). The 5 km long fjord consists of two basins with smooth and flat bottoms. An inner, 62 m deep, basin in the north stretches from the river Årøy to the peninsula of Barsnes and Kvam, and an outer, 75 m deep, basin in the south extends to the small town of Sogndal. Both basins are separated by a 29 m deep sill. Another 7.5 m deep sill separates the outer basin from the Sogndalsfjord.

The main freshwater supply is from the Jostedalsbre in the north (Fig. 1). Meltwater from this glacier passes through two lakes, the Veitastrondsvatn and Hafslovatn, which trap fine and coarse grained sedimentary material originating from the glacier. Only clay and silt sized material reaches the Barsnesfjord via the Årøy river.

Dissolved oxygen concentrations are uniformly high in the surface waters throughout the year. The deeper part of the outer basin is periodically anoxic whereas the inner basin is permanently anoxic below ca. 60 m water depth (Hovgaard, 1988; Paetzel and Schrader, 1991). Sewage release from the neighbouring town of Sogndal does not reach and affect benthic and planktonic environments in the Barsnesfjord (Hovgaard, 1985; P. Hovgaard, pers. commun., 1989). The surrounding rocks are dominated by granite, mica-schist, phyllite and Caledonian nappe rocks (mainly gneiss).

Methods

Five box cores and four gravity cores were retrieved from the Barsnesfjord in the summer of 1988 (Fig. 1; Table 1). A modified OSU (Oregon State University, Corvallis, Oregon) gravity corer with a 2.5 m long, thick walled plastic barrel (110 mm diameter) and a brass lemon core catcher was used. A box corer with a $30 \times 30 \times 50$ cm box was used to retrieve short surficial sediments. 50 cm long sub-samples were taken from these sediments by thin walled plastic tubes. Bulk density, water content and porosity were determined from freshly sampled material.

X-ray photography was done on a Philips K 140 BE X-ray machine. These X-ray photographs revealed internal sediment structures and helped

Fig. 1. Map of Southern Norway (upper right) and Sogndal–Barsnesfjord area (upper left). The Barsnesfjord receives its freshwater supply from the Jostedalsbre glacier in the north via the lakes Veitastrondsvatn and Hafslovatn and the river Årøy. Lower right: Bathymetry of the Barsnesfjord, equidistance of lines is 20 m. Crosses indicate the shallowest parts of the two sills and the deepest parts of the inner, northern and the outer, southern basin. Core locations are indicated by black stars.

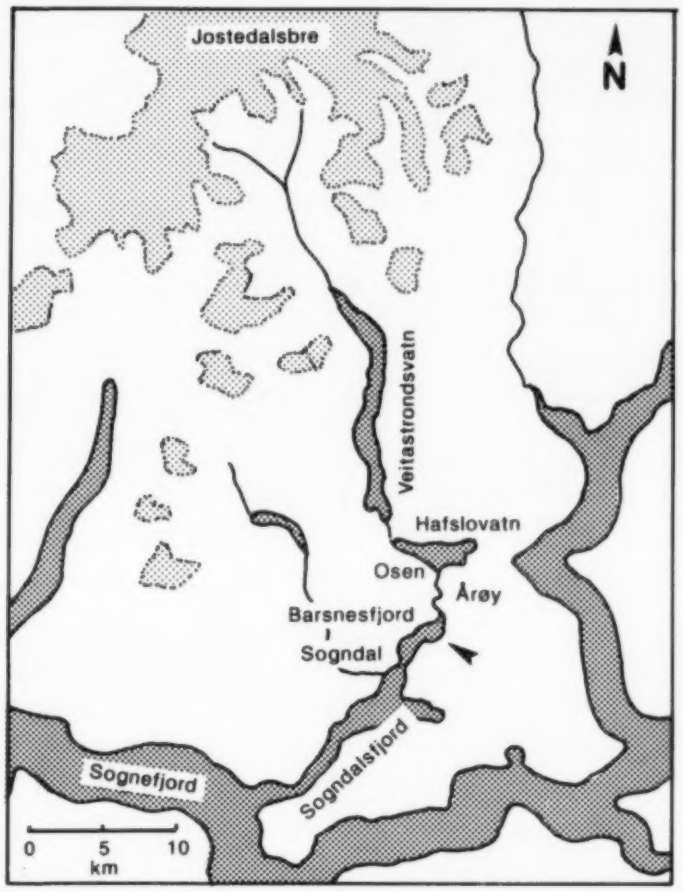
Jostedalsbre
N
Veitastrondsvatn
Hafslovatn
Osen
Årøy
Barsnesfjord
Sogndal
Sognefjord
Sogndalsfjord
0
5
10
km

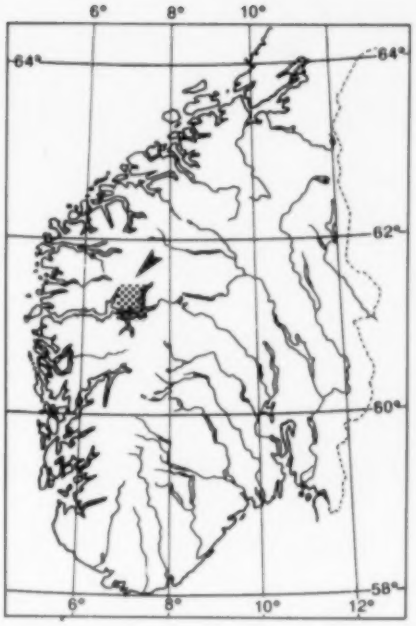
6°
8°
10°
64°
62°
60°
58°
12°

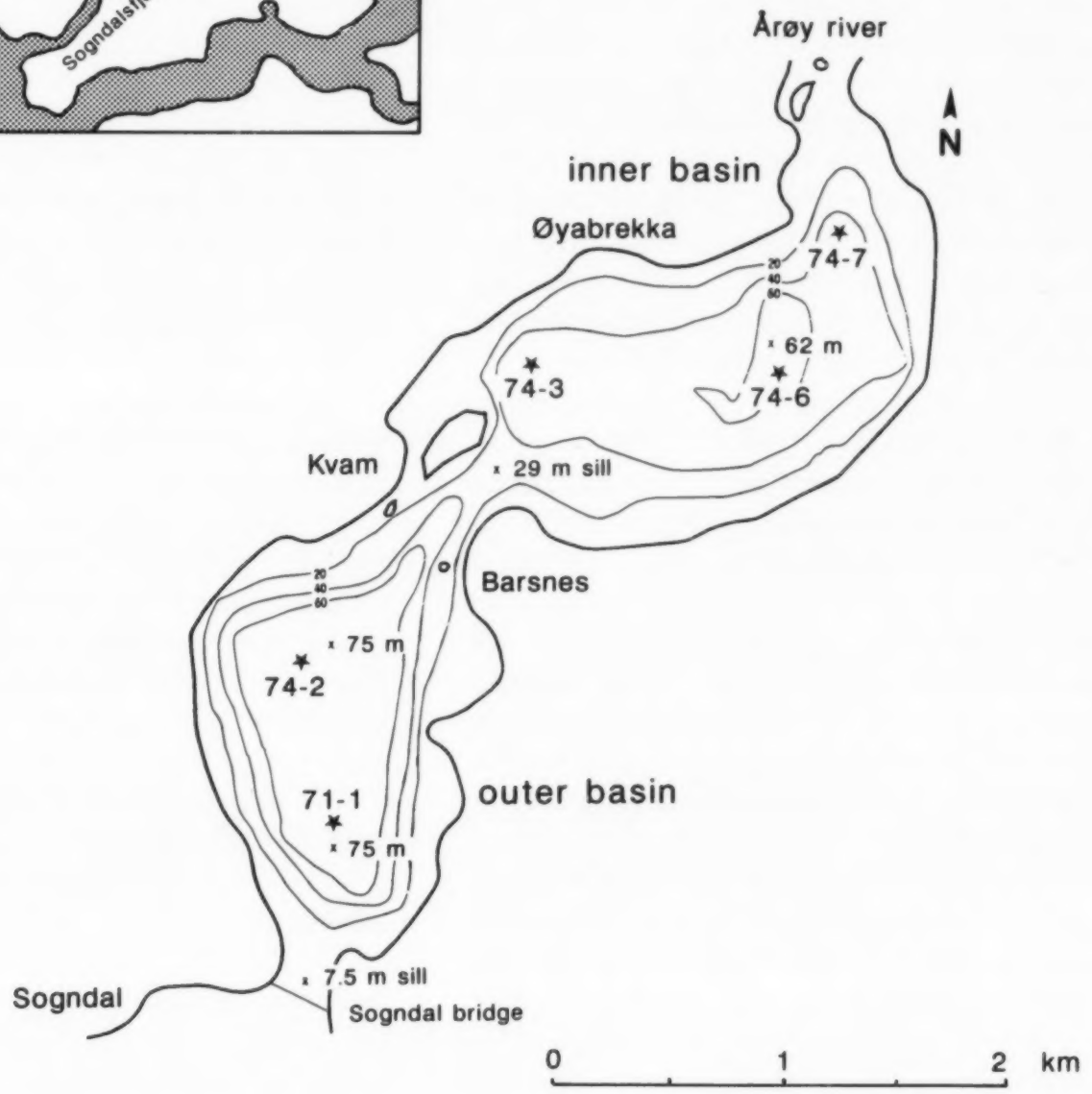
Årøy river
N
inner basin
Øyabrekka
74-7
20
40
60
x 62 m
74-3
74-6
Kvam
x 29 m sill
Barsnes
x 75 m
74-2
71-1
outer basin
x 75 m
x 7.5 m sill
Sogndal
Sogndal bridge
0
1
2
km

TABLE 1

Position, water depth, core length and coring instrument (box and gravity corer) used during cruise 1988-74 in the Barsnesfjord, western Norway

No.	Latitude (N)	Longitude (E)	Corer	Depth (m bsl[1])	Recovery (cm bsf[2])
74-1	61°14′17″	07°07′50″	box	75	37
			gravity	75	202
74-2	61°14′41″	07°07′45″	box	75	40
			gravity	75	208
74-3	61°15′22″	07°08′31″	box	55	45
			gravity	56	213
74-6	61°15′26″	07°09′50″	box	62	33
			gravity	62	211
74-7	61°15′39″	07°10′08″	box	52	47

[1]m bsl = meters below sea level;
[2]cm bsf = centimeters below seafloor.

to identify laminated, bioturbated intervals and intervals with unusually larger grains. Total organic carbon and $CaCO_3$ content were measured on a LECO carbon detector E-C 12.

Minerogenic grain sizes were determined by wet sieving through >1 mm and 500, 250, 125, 63, and <45 μm sieves and subsequent dry weighing of individual size classes. Transmitted polarized light microscopy was used for quantitative and qualitative analysis of grain size and type of both, the inorganic and organic fraction.

X-ray diffraction analysis (XRD) was done on a Philips X-ray generator (PW 1730/10) for whole rock and clay mineral samples (pressed sediment powder). Three measurements using different sediment preparation techniques (untreated, glycolized with ethylene glycol and heated at 550°C, after Carroll, 1970) were carried out in order to differentiate the clay minerals illite, chlorite, kaolinite and smectite. Heavy metals were analyzed from organic carbon free samples on a Philips PW 1450 automatic XRF spectrometer (Paetzel and Schrader, 1991).

The following diatoms were used to differentiate different environmental photic zone conditions and presence of allochthonous material derived from the shallower parts of the fjord (after Hustedt, 1930–1966):

(1) Displaced shallow water forms which were robust, large and belonged to the pennate genera of *Diploneis*, and *Nitzschia*.

(2) Freshwater planktonic species including *Tabellaria flocculosa*, *Eunotieae* sp., and *Ceratoneis arcus*.

(3) Saltwater planktonic species including *Sceletonema costatum*, *Thalassiosira nordenskioeldii*, *Thalassionema nitzschioides*, and *Chaetoceros* sp.

(4) Photic zone conditions during stress situations (less light or nutrients, lower salinity) were identified by the common occurrence of *Chaetoceros* resting stages.

Organic matter and its separation into marine and terrestrial part was microscopically estimated from smear slides. All brownish-dark particles with well confined shapes, cuticular fragments and terrestrial pollen/spores were classified as terrestrial organic matter and all light brownish-yellowish, diffuse material that contained minerogenic grains (pyrite, clay and silt) and biogenic opaline skeletons (diatoms and silicoflagellates) and was loosely packed into aggregates was termed marine organic matter.

The equation of Dymond and Veeh (1975) was used for calculation of accumulation rates.

Results

Sediment physical properties

Water content and porosity were high (>60–70%) in the upper 50 cm of all cores (Fig. 2 example of core BC-74-3; Table 3); they decrease

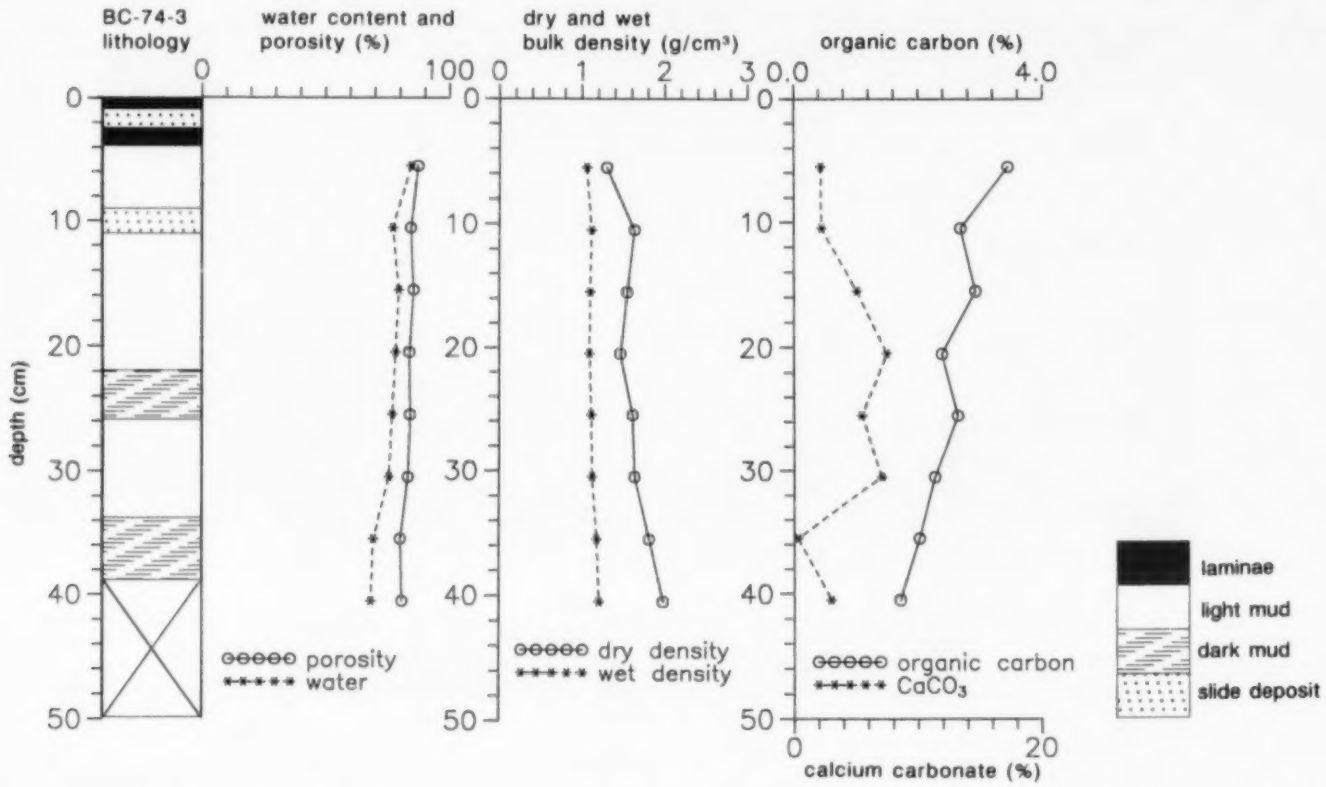

Fig. 2. Box core BC-74-3, lithology and color, porosity and water content (%), density (g cm^{-3}), organic carbon (scale at top) and carbonate (scale at bottom, % dry weight).

downcore due to compaction. Organic carbon (Fig. 2) decreased from 3.45% at the top to 1.71% at 40.5 cm in core BC-74-3. Mean organic carbon accumulation rates ($C_{org}AR$) were 40–80 gC m^{-2} a^{-1} over this interval in both basins (Table 3), with the highest value (184) found near the mouth of the river Årøy.

Averaged bulk sediment accumulation rates (BAR) of the upper 40 cm (Fig. 3) were 1.7 to 3.2 in the outer and 1.7 to 2.1 kg m^{-2} a^{-1} in the inner basin (Table 3) with a maximum value of 6.2 at the river Årøy delta. Minimum BAR values occurred at location 74-3 (Fig. 1); here $C_{org}AR$ were lowest (Table 3). The high $CaCO_3$ values (up to 7.5%) are due to the occasional occurrence of mollusk shell fragments.

Mineralogy

No major changes in the composition of minerogenic grains were observed downcore through all sediment sequences (0 to 2.3 m bsf). Quartz was dominant with 90%, biotite and plagioclase were subordinate with $<10\%$, some quartzite ($<1\%$) was found in some grayish/brownish layers. Pyrite occurred primarily in the cavities of diatom frustules.

The composition of the clay mineral fraction was rather uniform with depth with 93–95% illite, small amounts of chlorite (2–3%) and kaolinite (2–5%).

The distribution of organic and inorganic grains as determined from smear slides analysis is illustrated in Fig. 3. Both the smear slide grain size analysis and the wet sieving grain size analysis gave similar results. The wet sieving grain size analysis differed slightly in underestimating the silt and sand sized particles made up of organic matter matrices. The proportions of sand (2–5%), silt (15–30%) and clay (65–80%) were similar in both basins. A marked change in these proportions was found in the northernmost core BC-74-7. Here the proportions were 4% sand, 35–50% silt and 40–60% clay. Grain size was smallest in BC-74-3, and total bulk accumulation rates were also lowest in this core.

Sedimentology

Three distinctly different sediment sequences were distinguished in all cores: Alternating dark

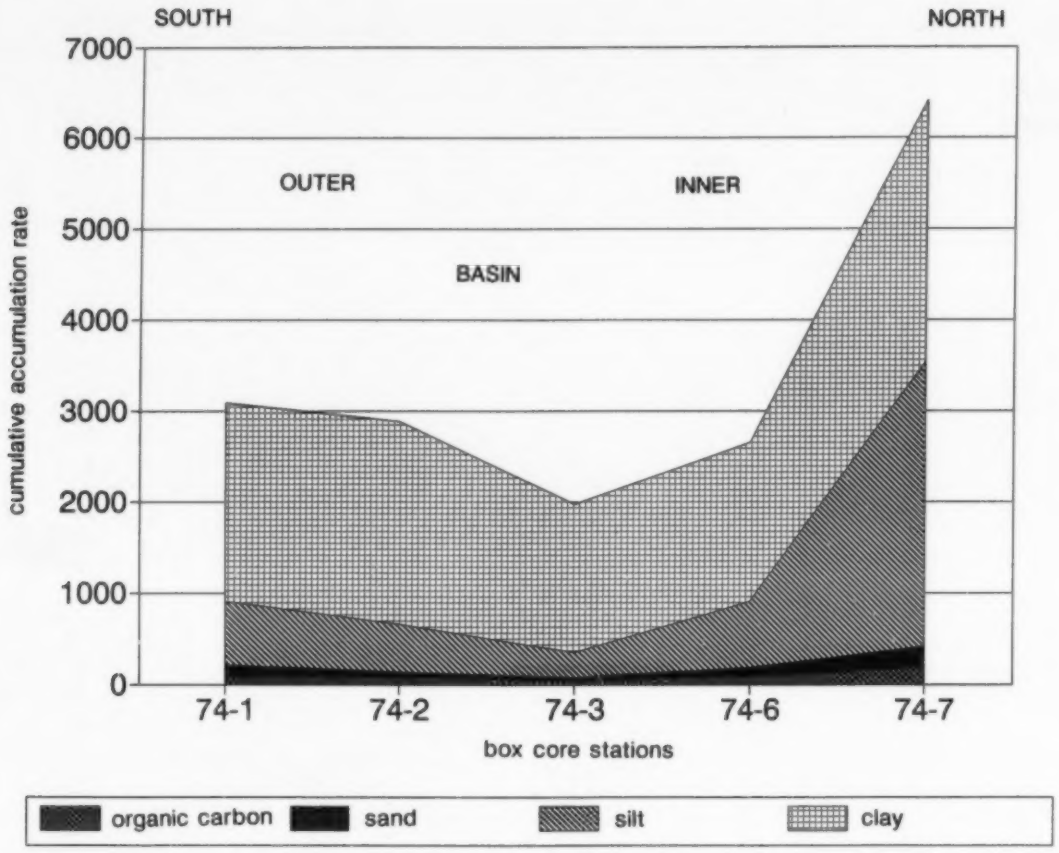

Fig. 3. Averaged cumulative grain class accumulation (g m^{-2} a^{-1}) in the upper 40 cm of cores. Grain sizes sand, silt and clay determined from smear slides include both, the inorganic and the organic fraction. Accumulation of organic carbon is plotted closest to the *x*-axis. Note remark caption Table 3.

and light layers, alternating laminae, and grayish/brownish layers. The main part of the sediment consists of centimeter thick, alternating, homogenous, dark and light layers. No density variations occurred nor were internal structures visible within these individual layers (Figs. 2 and 4). More than 70% by volume of the grains were irregularly shaped organic matter rich particles (this value decreases to less than 5% if calculated by weight). The organic matter grains consisted of aggregates that were made up of marine organic matter (brown and diffuse in smear slides) and enclosed micro-organism skeletons, as well as very little terrestrial organic matter (determined by its black color and by its well defined sharp edges) and inorganic (minerogenic) material. The degree of bioturbation was low within the dark layers showing fewer traces of bioturbation compared to the lighter layers. The color difference may be due to variation in anoxic bottom conditions.

The second sediment type are packets of millimeter thick alternating laminae. The laminae were found in the top 10 cm of most box cores (Figs. 2 and 5) and were more distinct over the 35 to 65 cm interval in core GC-74-6 (Fig. 4). Box core BC-74-6 (Fig. 5) displayed the best defined lamination. Sediment type 2 is similar in its composition to sediment type 1 but without any bioturbation traces representing deposition under permanent anoxic bottom conditions.

Different diatom assemblages were observed in the individual laminae. Usually one lamina was dominated by freshwater diatoms, followed by 3 laminae dominated by marine, marine to brackish and brackish assemblages. This diatom assemblage succession represents biological productivity seasons in the photic zone over a years period with an early and a late spring bloom, a low production summer period and a fall bloom.

The third sediment type consists of centimeter thick alternating grayish/brownish layers; it was found in distinct horizons in some box and all gravity cores. The layers had higher density, lower porosity and less organic carbon content than the neighboring sediments of type 1 or 2 (Fig. 4). The minerogenic fraction dominated (also by volume)

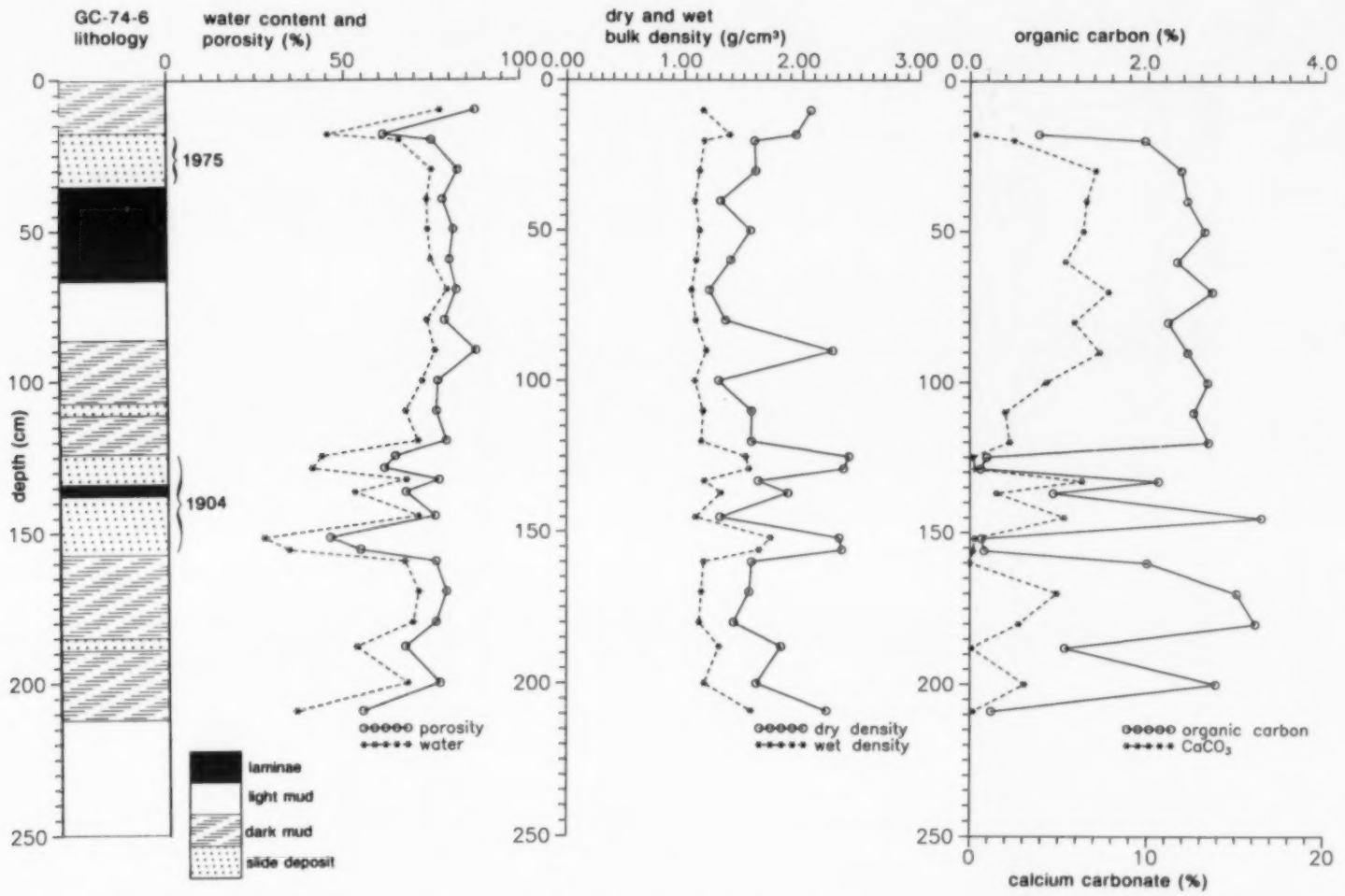

Fig. 4. Gravity core GC-74-6, lithology and color, porosity and water content (%), density (g cm^{-3}), organic carbon (scale at top) and carbonate (scale at bottom, % of dry weight). Note the sharp decreases in porosity, water content, and organic carbon and the increase in density at 17 cm and 130–155 cm representing deposits of the 1975 slide event at Øyabrekka and the 1904 slide event when the river Årøy was dammed up at Osen.

and consisted predominantly of quartz. These sections were distinctly upward graded and the grain size was either more silty or more clayey compared with the under- and over-laying mud.

Type (3) sediment represents slide and slump material from 4 major slide events of 1873, 1904, 1975 and 1982. The slide direction and its source area were traced by mapping the decrease in thickness and in grain size within the sedimentary column of each core. Both thickness and grain sizes decreased from the slide point source within the grayish/brownish layers of the different cores.

The best preserved event is that of 1982. At that time a water tunnel for a hydro-power plant was built stretching from the lake Hafslovatn to the lower Årøy river (Fig. 1) through the gneissic bedrock. The tunnel material was crushed into gravel and stored in large piles at the mouth of the river. In the summer of 1982 one of these piles slid into the inner fjord basin. Core BC-74-7 (Fig. 6) was collected in the vicinity of the slide event and a distinct horizon could be recognized between 9–18 cm. This horizon consisted of gravel sized gneiss of 2–3 cm diameter at the bottom covered with upward grading finer material and organic matter of grassy composition at the top. The grassy organic matter mats form a well defined boundary to the overlying hemipelagic mud sequence.

Another event occurred in April 1904 when several 100 m^3 of block-, stone- and soil-masses where accidently blasted into the inlet of the river Årøy at Osen (Fig. 1) during road work (Aftenposten, 1904). The Hafslovatn was dammed up by more than 1 m for the rest of the year. Only the large blocks were removed from the inlet in the following winter (1904/1905) leaving the remainder of the blast material in the inlet. The deeper parts

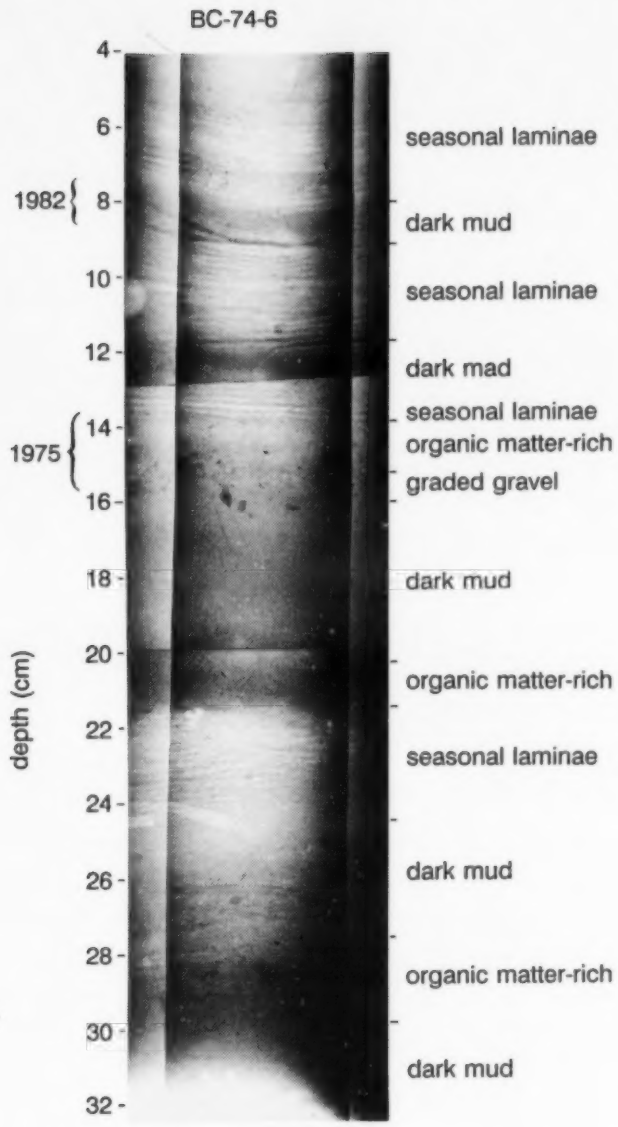

Fig. 5. Whole core X-ray photograph (positive print) of the top 4 to 32 cm of box core BC-74-6.

of the inlet are still barricaded (N. Kvam, pers. commun., 1987) and an artificial sill was formed between lake and river.

Sediment material was deposited in the Årøy river-bed during a short period after the accident because of reduced river flow. This material was washed out during the following meltwater season in, 1905. Sediment traces of this event are preserved in GC-74-6 at 125 cm core depth (Fig. 4).

Sedimentation rates

All sedimentation rates (Table 2) represent linear rates between two dated events (^{137}Cs and or dated slides). Sections of slide and slump disturbance within these sequences are subtracted. The major slide events left a relatively easy to detect sediment

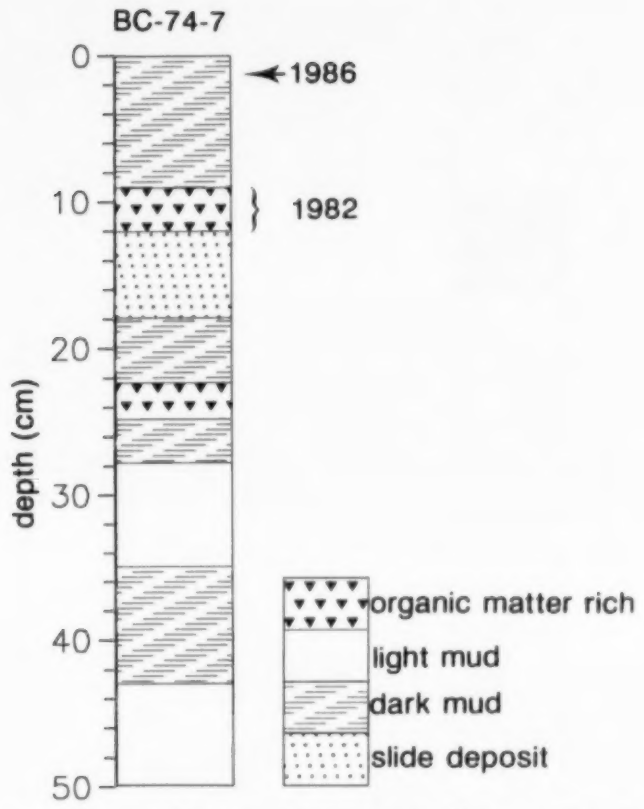

Fig. 6. Lithology of box core BC-74-7. Arrow/bracket encloses the point to the maximum ^{137}Cs fallout from Chernobyl in 1986 and the sequence of the 1982 Årøy gravel slide.

TABLE 2

Sedimentation rates of all box and gravity cores. Years for events are: 1986—Chernobyl fallout, 1982—gravel slide at the river mouth, 1975—sand and silt slide from road work, 1963—second cesium maximum during Pacific nuclear testings, 1959—first cesium maximum during Pacific nuclear tests, 1904—blast accident, and 1873—major land slide at Sogndal

Core	Interval (years of events)	Sedimentation rate (cm/year)
74-1	1873–1986	0.96
74-2	1873–1986	1.02
74-3	1873–1986	0.85
	1873–1963	0.69
	1959–1986	0.75
	1959–1975	0.64
	1959–1963	0.68
	1963–1986	0.76
	1963–1975	0.63
	1975–1986	0.91
74-6	1904–1986	1.18
	1904–1982	1.16
	1904–1975	1.19
	1975–1986	1.09
	1975–1982	0.86
	1982–1986	1.50
	seasonal layers	>0.40–0.50
74-7	1982–1986	2.00

trace. The smaller, less dramatic events on the other hand and long lasting increased runoff from land may have been underestimated when calculating sedimentation rates.

High levels of ^{137}Cs from the Chernobyl atomic power-plant accident were found in all box core surfaces (Paetzel and Schrader, 1991) indicating that we did not successfully recover youngest sediments or material from the sediment–water interface that should represent sedimented material of 1987 and 1988 (the year of collection). Another possibility might be that we mixed the very watery top sediments during recovery and subsequent handling.

Increased levels of ^{137}Cs activities derived from the worldwide fallouts of the 1959 and the 1963 Pacific nuclear weapon testing experiments (Cambray et al., 1971; Degens, 1989) were found at certain horizons in some cores and were used for sedimentation rate calculations (Table 2).

The downcore sequences of grayish/brownish layers aided in core to core correlation of contemporaneous events. These layers represent recent and well documented catastrophic events that occurred in historical time around the Barsnesfjord. These events include the 1982 gravel dump slide at the mouth of the river Årøy, the 1975 slide event of Øyabrekka during road work, the 1904 blast event at Osen and the 1873 major land slide event at Sogndal.

The 1986 ^{137}Cs maximum level was found at 1 cm depth in core BC-74-7 and the top of the gravel slide event of 1982 occurred at 9 cm (Fig. 6), resulting in a linear sedimentation rate of 2.0 cm/year near the mouth of the river Årøy (Figs. 2 and 6). The equivalent event did occur at 8 cm in core BC-74-6 (Fig. 4) which has a slightly smaller sedimentation rate.

The finely laminated sections in some cores provided additional age control. These layers are seasonal deposits and we postulate that four layers represent sedimentation over one year. Using the number of laminae per unit length averaged sedimentation rates of >0.4–0.5 cm/year were calculated in core BC-74-6. This sedimentation rate is about 50% lower than that estimated from ^{137}Cs and slide events in the same core (ca. 0.86 to 1.19 cm/year). Two possible explanations may account for this discrepancy: (1) Additional small scale slide horizons may exist which were not recognized. These will increase the linear sedimentation rate, and the estimated value of 0.86 to 1.19 cm/year is then too high. (2) The assumption of 4 sediment laminae to represent one year may be in error and additional seasonal layers may be present that were either not distinguishable or could not be sampled.

The average sedimentation rate (values from Table 2) for both basins is 0.91 cm/year over the last 100 years.

Discussion

Sedimentation rates

High average linear sedimentation rates of 0.91 cm/year characterize deposition of both marine derived and land derived particulate matter in the deeper parts of the anoxic Barsnesfjord during the last 150 years. These rates increase towards the mouth of the river Årøy due to the increased input of terrigenous fine grained loads and to a possible fertilization effect by river loaded nutrient-rich waters enhancing primary production.

Other Norwegian fjords with comparable hydrographic and topographic conditions reveal similar high sedimentation rates (Skei and Melsom, 1982; Nagy and Alve, 1987). Normal marine hemipelagic sedimentation rates and sedimentation rates in fjords with well ventilated and thus dissolved oxygen-rich bottom waters are smaller and usually do not exceed rates of <0.1 to 0.2 cm/year.

Organic carbon

Accumulation rates (over the last 80 years) of organic carbon are 40 to 80 gC m^{-2} a^{-1} in the Barsnesfjord. Primary production rates of organic carbon in the surface waters of the deeper and oxic Sogndalsfjord south of the Barsnesfjord (Fig. 1) are 100 gC m^{-2} a^{-1} (Hovgaard, 1988). These rates are similar or even higher in the Barsnesfjord, indicating a very effective transfer of carbon fixed in the photic zone to the deeper parts of the fjord with little alteration and recycling

during settling and deposition. Smear-slide analysis revealed that more than 90% of the organic material is of marine origin.

The deposition and burial of more than half of the photic zone produced organic carbon in the Barsnesfjord agrees with sediment trap measurements of Wassmann (1983) carried out in various Norwegian land-locked fjords. In general 30 to 70% of the surface water produced organic carbon gets sedimented. Wassmann and Aadnesen (1984) found organic carbon production rates of 180 to 230 gC m^{-2} a^{-1} in the Raunefjord, the Kviturvikpollen and the Vagsböpollen (western Norway) which have similar environmental settings. More than 35 to 44% of the organic carbon reached the sediment surface (Wassmann, 1985a). Carbon accumulation rates of 48 gC m^{-2} a^{-1} are found in the anoxic sediments of the Bunnefjord (Magnusson et al., 1988), but here total sediment accumulation rates are considerable lower than in the Barsnesfjord (by a factor of 8, i.e. 0.34 kg m^{-2} a^{-1} compared with 2.5 to 3.0 kg m^{-2} a^{-1} in the Barsnesfjord). This difference may be attributed to higher production of organic carbon (and organic carbon derived from sewage), to reduced input of inorganic material, or to reduced carbon oxidation both in the water column, across the sediment–water interface and in the sediment.

The fact that about half of the production reaches the sediment, is buried and actually is being preserved, may be explained by the shallow depth and a fast vertical transport mechanism and anoxic bottom water conditions.

The autochthonous Barsnesfjord sediments consist mainly of organic matter rich, diffuse and loosely packed aggregates. These aggregates are the result of flocculation, aggregation (Syvitski et al., 1987) and pelletization processes (Schrader, 1971) during settling through the water column and through the sediment–water interface. Primary production is the main source of organic matter in the Barsnesfjord. Because of its high volume this organic matter is also the main contributor to the high sedimentation rates.

Seasonal layers

Erga (1989b) distinguished four major seasons per year in the coastal surface waters at Lista (southern Norway) characterized by salinity and temperature. Similar seasonalities occur in the surface waters of the Boknafjord (Erga, 1989a), the Korsfjord (Erga and Heimdal, 1984) and the Barsnesfjord (Hovgaard, 1988). These four seasons are not only distinguishable by temperature and salinity but also by the presence of characteristic diatom phytoplankton associations. Within the finely laminated autochthonous intervals in the Barsnesfjord sediments four different diatom assemblages are found which are related to these seasons.

They are (1) reduced salinity (26‰) and low temperature (< 5°C) in surface waters representing brackish conditions at the end of March. Improving light conditions result in increased photosynthesis and produce the first spring bloom under brackish water conditions.

(2) Snow melting increases towards the end of May. Salinities decrease to < 5‰ in the surface waters, temperatures increase to about 10°C and light conditions are optimal. Now the second spring phytoplankton bloom occurs under "freshwater" conditions.

(3) High surface water temperatures (12°–16°C) and high salinities (30°–33°C) prevail in the Boknafjord during the summer. The hydrographic record of the Barsnesfjord over the summer indicates more freshwater influence in August. Marine to brackish conditions may prevail during the summer. An increase in the abundance of *Chaetoceros* resting stages in the sedimentary record indicates that primary production is lower during the warm summer season compared to the other seasons.

(4) Surface water temperature and salinity decrease in the beginning of October due to the increasing autumn rainfall. This results in a fall phytoplankton bloom under marine to brackish conditions.

Surface water temperatures are low during the winter, salinities are greater than 32‰ and the shortening of day light becomes a limiting productivity factor resulting in minimal or no production.

Similar seasonal diatom productivity cycles are found in other western Norwegian fjords including the Hardangerfjord (Braarud et al., 1974), the Lindåspollen and Kviturvikpollen (Wassmann,

1983, 1985a) and the Nordåsvannet (Wassmann, 1985b; Wassmann et al., 1986).

Sancetta and Calvert (1988) and Sancetta (1989) recognized seasonal cycles in the siliceous microfossil sedimentation in sediment traps from Saanich and Jervis Inlet (British Columbia).

Primary productivity is not only controlled by light but also by the availability of dissolved nutrients. The availability of dissolved nutrients may account for different onset of the different blooms in the different fjords. The fall phytoplankton bloom occurs in September in the Lindåspollen, in October in the Barsnesfjord and in November in the Hardangerfjord.

Slide events

The grayish/brownish layers represent four major slide and slump events. These events are: the 1982 gravel pile slide at the mouth of the river Årøy, the 1975 slide event at Øyabrekka that occurred during road work, the 1904 accident at Osen when part of the river Årøy and part of the lake Hafslovatn was dammed during road work and the 1873 slide event at the town of Sogndal (N. Kvam, pers. commun., 1989).

Accumulation rates during the last 100 years

BAR and $C_{org}AR$ have changed during the last 100 years in both basins (Fig. 7; Table 3). The outer basin BAR (core 74-1 and 74-2) are not reliable because of poor chronostratigraphic control. However, similar trends are detectable in the outer cores compared with the inner basin cores (74-3 and 74-6).

The inner basin cores are characterized by a decrease in BAR from 2.8–4.3 during the last century to 1.6–3.6 kg m^{-2} a^{-1} after 1904 (Fig. 7). A similar reduction (from 77–119 gC m^{-2} a^{-1} before 1900 to 48–91 gC m^{-2} a^{-1} in this century) took place for organic carbon. The decline in BAR can be explained by the accidental damming of the Hafslovatn at the upper part of the river Årøy in 1904. The Årøy is the main tributary to the Barsnesfjord. The unremoved fill-in acted like a shallow sill between the lake and the river. This artificial sill reduced the transport of suspensoids carried from the Jostedalsbre to the Barsnesfjord decreasing BAR in both basins by almost 50% trapping suspensoids in the Hafslovatn.

This sill may also be responsible for the 30% reduction of $C_{org}AR$ in the Barsnesfjord during

TABLE 3

Bulk sediment (BAR) and organic carbon ($C_{org}AR$) accumulation rates of cores 74-1, 74-2, 74-3 and 74-6 in pre-industrial (older than 1904) and industrial times (1904–1986). Sedimentation rate (*sr*, cm/year), wet density (ρ, g/cm^3), water content (w%) and organic carbon (% C_{org}). Note BAR values plotted in Fig. 3 are integrated over the top 0 to 40 cm and therefore are different from the BAR values in this table

		Concentrations				Accumulation rates	
		sr	ρ	w%	% C_{org}	BAR	$C_{org}AR$
74-1	before 1873	0.96	1.25	60	2.54	4800	122
	1873–1986	0.96	1.17	67	2.58	3707	96
74-2	before 1873	1.02	1.23	61	2.64	4893	129
	1873–1986	1.02	1.15	71	2.60	3402	88
74-3	before 1873	0.85	1.12	70	2.69	2856	77
	1873–1963	0.69	1.10	76	2.62	1822	48
	1963–1975	0.63	1.10	79	2.66	1455	39
	1975–1986	0.91	1.06	84	3.45	1543	53
74-6	before 1900	1.17	1.15	68	2.76	4306	119
	1904–1975	1.19	1.12	73	2.52	3599	91
	1975–1982	0.86	1.12	78	2.93	2119	62
	1982–1986	1.50	1.06	87	3.24	2067	67

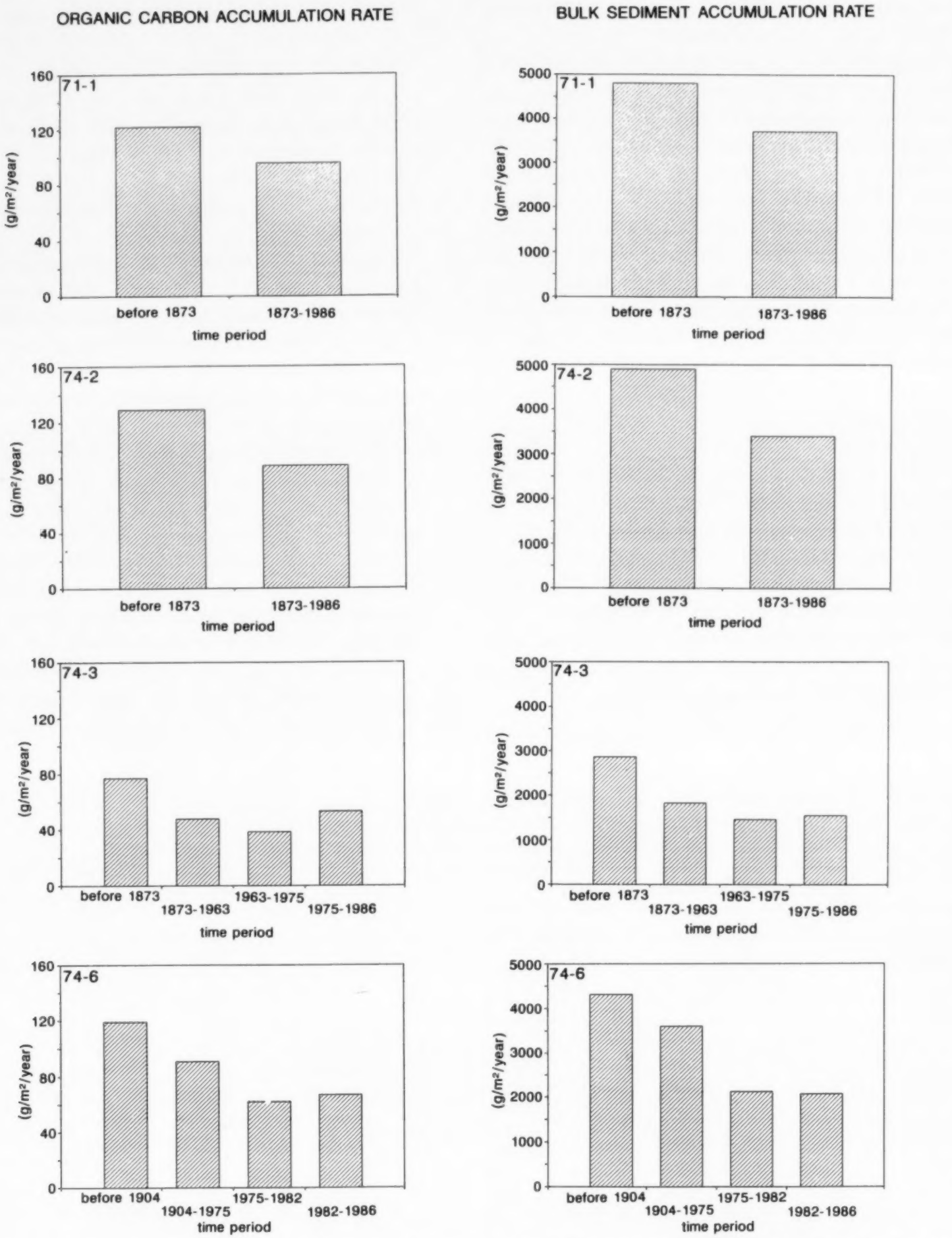

Fig. 7. Accumulation rates of bulk sediment and organic carbon (in g m^{-2} a^{-1}) for cores 74-1, 74-2 (outer basin) and cores 74-3, 74-6 (inner basin) in pre-industrial (1873–1904) and industrial times (1904–1986). Time periods are those from Table 2. Note the different time intervals in the cores and the lack of dated sequences in the outer basin cores for the last century.

this century. The supply of dissolved nutrients via the river Årøy was reduced due to the sill. After the accident nutrients were stripped in the Hafslovatn by primary production in the "dammed" lake due to longer residence times of the by-passing waters. Fewer amounts of dissolved nutrients were transported down the river Årøy into the Barsnesfjord. This reduction in nutrient supply resulted in lower primary production and decreased $C_{org}AR$.

Accumulation of Cu and Zn has remained the same during pre- and post-industrial times (Table 4). This indicates that no increase in the accumulation of these metals due to anthropogenic influence has occurred in the Barsnesfjord area (Paetzel and Schrader, 1991).

Two damming events occurred after 1904. The Veitastrondsvatn was regulated in 1982 and the Hafslovatn was dammed at Osen in 1983. Since 1983 the water flows through a tunnel from the Hafslovatn down to an electrical power station, is then released into the lower part of the river Årøy and finally moves into the Barsnesfjord. Both damming and regulations did not influence sedimentation in the fjord (Fig. 7).

Conclusion

The Barsnesfjord sediments were accurately dated by ^{137}Cs, historical sliding events and seasonal layers. Linear sedimentation rates were used to calculate bulk sediment, organic carbon and heavy metal accumulation rates. A major change in the sedimentary environment occurred after the accidental blast that dammed the Hafslovatn in 1904, causing the bulk sediment and organic carbon accumulation rates to decrease in the Barsnesfjord. Two additional damming events and regulation in 1982 and 1983 had no influence on the sediment composition. Heavy metal accumulation rates remained constant throughout the last two centuries.

TABLE 4

Zn and Cu concentrations and accumulation rates (AR) in core 74-3 for the period before 1873 and around 1986

Time	Zn (%)	Cu (%)	Zn (AR)	Cu (AR)
<1873	137	28	0.39	0.08
ca. 1986	144	30	0.29	0.06

Acknowledgements

We thank Ole Tumyr (University of Bergen) for XRD analysis, Peter Hovgaard (Marine Biological Station, Sogndal) and Nils Kvam (Sogndal) for hydrographic and historical data. We acknowledge the help of Stein Kjetil Helle, Tim Schrader and the crew of the RV *Fridtjof Nansen* during the cruise. NAVF (*Norges Allmennvitenskapelige Forskningsråd*, Oslo) and NGU (*Norges Geologiske Undersøkelse*, Trondheim) funded part of this work.

References

Aftenposten, 1904. Oversvømmelse voldt ved veibygning. Article in daily paper from 11 July 1904, Kristiania (Oslo), Norway.

Braarud, T., Föyn, B., Hofsvang, P. and Överland, A.K., 1974. The natural history of the Hardangerfjord. 10. The phytoplankton in 1955–56. The quantitative phytoplankton cycle in the fjord waters and in the offshore coastal waters. Sarsia, 55: 63–98.

Calvert, S.E. and Price, N.B., 1971. Recent sediments of the South West African shelf. In: F.M. Delaney (Editor), The Geology of the East Atlantic Continental Margin. Inst. Geol. Sci., London, Rep. 70/16, pp. 171–185.

Cambray, R.S., Fisher, E.M.R., Brooks, W.L. and Peirson, D.H., 1971. Radioactive fallout in air and rain: Results to the middle of 1971. AERE-R 6923, HMSO, London.

Carroll, D., 1970. Clay minerals: A guide to their X-ray identification. Geol. Soc. Am., Spec. Pap., 126: 1–80.

Degens, E.T., 1989. Perspectives on biochemistry. Springer, Berlin, 423 pp.

Dugdale, R.C. and Goering, J.J., 1967. Uptake of new and regenerated forms of nitrogen in primary productivity. Limnol. Ocean., 12: 196–206.

Dymond, J. and Veeh, H., 1975. Metal accumulation rates in the southeast Pacific and the origin of metalliferous sediments. Earth Planet. Sci. Lett., 28: 13–22.

Eppley, R.W. and Peterson, B.J., 1979. Particulate organic matter flux and planktonic new production in the deep ocean. Nature, 282: 677–680.

Erga, S.R., 1989a. Ecological studies on the phytoplankton of Boknafjorden, Western Norway. 1. The effect of water exchange processes and environmental factors on temporal and vertical variability of biomass. Sarsia, 74: 161–176.

Erga, S.R., 1989b. The importance of external physical controls on vertical distribution of phytoplankton and primary production in fjords of Western Norway. Dr.Sc. Thesis, Univ. Bergen.

Erga, S.R. and Heimdal, B.R., 1984. Ecological studies on the phytoplankton of Korsfjorden, western Norway. The dynamics of a spring bloom seen in relation to hydrographical conditions and light regime. J. Plankton Res., 6: 67–90.

Hovgaard, P., 1985. Resipientforhold i Sogndal kommune—En vurdering. Sogn Fjordane Distriktshøgskole, Sogndal, Norway, 35 pp.

Hovgaard, P., 1988. Vannkvalitet i Sogndalsfjorden, betydning for akvakultur. Sogn Fjordane Distriktshøgskole, Skrifter, 2: 68–81.

Hustedt, F., 1930–1966. Die Kieselalgen Deutschlands, Österreichs und der Schweiz unter Berücksichtigung der übrigen Länder Europas, sowie der angrenzenden Meeresgebiete. In: L. Rabenhorst (Editor), Kryptogamenflora von Deutschland, Österreich und der Schweiz. Akademische Verlagsgesellschaft m.b.H., Leipzig.

Magnusson, J., Andersen, T., Efraimsen, U. and Næs, K., 1988. Overvåking av forurensninssituasjonen i Indre Oslofjord 1987. Norw. Inst. Water Res. Annu. Rep. 1988, No. 0-71160.

Nagy, J. and Alve, E., 1987. Temporal changes in foraminiferal faunas and impact of pollution in Sandebukta, Oslofjord. Mar. Micropaleontol., 12: 109–128.

Paetzel, M. and Schrader, H., 1991. Heavy metal (Zn, Cu, Pb) accumulation in the Barsnesfjord: Western Norway. Nor. Geol. Tidsskr., 71: 65–73.

Prell, W.L., Niitsuma, N. and Shipboard Scientific Party, 1989. Proc. ODP, Init. Rep., 117, 1236 pp.

Puškarić, S., Berger, G.W. and Jorissen, F.J., 1990. Successive appearance of subfossil phytoplankton species in Holocene sediments of the northern Adriatic and its relation to increased eutrophication pressure. Estuarine Coastal Shelf Sci., 31: 177–187.

Sancetta, C., 1989. Spatial and temporal trends of diatom flux in British Columbian fjords. J. Plankton Res., 11: 503–520.

Sancetta, C. and Calvert, S.E., 1988. The annual cycle of sedimentation in Saanich Inlet, British Columbia: Implications for the interpretation of diatom fossil assemblages. Deep-Sea Res., 35: 71–90.

Schrader, H., 1971. Fecal pellets: Role in sedimentation of pelagic diatoms. Science, 174: 55–57.

Schrader, H., 1991. Peruvian coastal primary paleo-productivity during the last 160,000 years. In: C. Summerhayes, W. Prell and K. Emeis (Editors), Evolution of Upwelling Systems since the Early Miocene. Geol. Soc. London, in press.

Skei, J. and Melsom, S., 1982. Seasonal and vertical variation in the chemical composition of suspended particulate matter in an oxygen-deficient fjord. Estuarine Coastal Shelf Sci., 14: 61–78.

Syvitski, J.P.M., Burrell, D.C. and Skei, J.M., 1987. Fjords: Processes and products. Springer, New York, 379 pp.

Wassmann, P., 1983. Sedimentation of organic and inorganic particulate material in Lindåspollene, a stratified, land-locked fjord in Western Norway. Mar. Ecology-Progress Ser., 13: 237–248.

Wassmann, P., 1985a. Sedimentation of particulate material in two shallow, land-locked fjords in western Norway. Sarsia, 70: 317–331.

Wassmann, P., 1985b. Sedimentation of particulate material in Nordåsvannet, a hypertrophic, land-locked fjord in Western Norway. Mar. Ecology-Progress Ser., 22: 259–271.

Wassmann, P. and Aadnesen, A., 1984. Hydrography, nutrients, suspended organic matter, and primary production in a shallow fjord system on the west coast of Norway. Sarsia, 69: 139–153.

Wassmann, P., Naas, K.E. and Johannessen, P.J., 1986. Annual supply and loss of particulate organic carbon in Nordåsvannet, a eutrophic, land-locked fjord in Western Norway. Rapp. P.-V. Réun. Cons. Int. Explor. Mer, 186: 423–431.

Marine Geology, 105 (1992) 37–50
Elsevier Science Publishers B.V., Amsterdam

Organic carbon distribution in the North Atlantic Ocean during the last glacial maximum

Melissa L. Coppedge [1] and William L. Balsam
Department of Geology, Box 19049, University of Texas at Arlington, Arlington, TX 76019, USA

(Received June 27, 1991; revision accepted August 13, 1991)

ABSTRACT

Coppedge, M.L. and Balsam, W.L., 1992. Organic carbon distribution in the North Atlantic Ocean during the last glacial maximum. Mar. Geol., 105: 37–50.

The organic carbon content of eighty-two last glacial maximum (LGM) sediment samples from the North Atlantic Ocean was determined with a Coulometer. Organic carbon in these sediments averaged about 0.5% by weight, slightly higher than in modern sediments. Factors that control organic carbon distribution were examined in two ways: by mapping the spatial distribution of organic carbon during the LGM and by comparing organic carbon content to sediment characteristics. In general, sediment organic content increases with increasing sedimentation rate, increasing clay content, and decreasing carbonate content. The spatial distribution of LGM organic content is similar in most respects to the mapped modern distribution, the primary exception being areas of high organic content. One area of high organic content off northwest Africa is situated in the same area geographically but is larger than its modern counterpart perhaps indicating that wind-driven upwelling was more intense and/or widespread during the LGM. The two other areas of high organic carbon content, the North American margin and west of the Mid-Atlantic Ridge (MAR) at about 40°N, have no modern counterpart. On the North American margin, south of Cape Cod, organic carbon content is generally >0.6% and in several samples is >0.9%. The increased organic carbon content of sediment in this area appears to be related to an increase in sedimentation rate and the concomitant increase in inorganic nutrients. The area west of the MAR is more perplexing and appears to be related to changes in LGM surface circulation.

Introduction

Although deep-sea sediment contains many components, probably none has a more complex depositional history than organic carbon (C_{org}). Organic carbon preserved in sediment goes through a long, complex, and often poorly understood sequence of events. Preservation of organic material is influenced by numerous parameters including sea surface productivity, transit time through the water column, sea water and pore water chemistry, sedimentation rate, bioturbation, and sediment mineralogy.

That climate and the deep-sea environment are intimately related has been documented in numerous publications (for example Cline and Hays, 1976). Climatic changes have a synergistic effect on many of the factors that influence the preservation of organic matter in the deep sea. The relationship between climate and preservation of organic carbon should be most evident in the North Atlantic Ocean because of all oceans it was most influenced by the last glaciation (CLIMAP, 1976, 1981). During the last glacial maximum (LGM) the North Atlantic underwent many changes in response to global cooling and the associated glaciation. Changes in wind patterns and ocean surface circulation influenced areas of upwelling and hence sea surface productivity. Perhaps even more significant was the effect of changing surface circulation on deep circulation. Cooling in high latitudes shifted the polar front to the south. This shift steepened the thermal gradient, forcing the Gulf Stream to flow directly across the Atlantic at ~42°N, and

[1]Present address: 4004 49th St., Lubbock, TX 79413, USA.

0025-3227/92/$05.00 © 1992 — Elsevier Science Publishers B.V. All rights reserved

allowing the establishment of permanent ice-cover in the Norwegian, Greenland, and Labrador Seas (CLIMAP, 1976). This permanent ice-cover may have precluded the formation of North Atlantic Deep Water (NADW) as we know it today. With the primary source of NADW reduced or cut off, the chemistry of LGM deep water changed-CO_2 and ocean alkalinity increased while O_2 decreased (Boyle, 1988). These changes in LGM deep water chemistry were potentially important influences on the preservation rate of C_{org} in the deep sea.

In this paper we attempt to gain insight into the factors that influence organic carbon preservation by examining the relationship between C_{org} and factors suspected of influencing its concentration in sediment and by comparing modern and LGM accumulation patterns in the North Atlantic. We recognize that organic carbon in modern and LGM sediments have had different depositional and burial histories. For this reason we focus on differences in depositional patterns rather than the absolute value of sediment organic content.

Previous work

The distribution of organic carbon in bottom sediments of the world's oceans has been reported in several studies. These include reports by Lisitzin (1972), Bezrukov et al. (1977), Premuzic et al. (1982) and Demaison and Moore (1980). The results of these studies are far from uniform. In the North Atlantic, Lisitzin (1972) shows significant C_{org} concentrations at the base of most continental slopes and scattered throughout the Norwegian Sea. Most of the central and subpolar North Atlantic, according to Lisitzin, is characterized by C_{org} concentrations less than 0.25%. As plotted on Lisitzin's map, C_{org} distribution in the North Atlantic has a strong latitudinal component.

Bezrukov et al. (1977) also mapped the distribution of C_{org} in the world ocean. In the North Atlantic, like Lisitzin (1972), they indicate high concentrations on continental margins and in the Norwegian Sea. However, their map differs in several respects. Most important, the overall pattern indicated by Bezrukov et al. (1977) is longitudinal. Further, the absolute value of C_{org} contents differs significantly; Bezrukov's values are higher than those indicated by Lisitzin. Some of this variation is geographically distinct. Bezrukov et al. indicate that low values ($< \sim 0.25\%$) are restricted primarily to the Mid-Atlantic Ridge (MAR) while higher values (0.25–0.50%) are typical of the deep basins. Also, Bezrukov et al. indicate substantially higher C_{org} contents off eastern North America.

Premuzic et al. (1982) also charted the distribution of C_{org} in the world ocean. For sediments beyond the shelf in the North Atlantic their work is based primarily on the data of Bezrukov et al. (1977). Not surprisingly, their map shows great similarity to Bezrukov's. Likewise, Demaison and Moore's (1980) map of C_{org} in the Atlantic is based primarily on the data of Bezrukov et al. (1977).

Differences between the studies described above may be the result of several factors. First, while each of the above studies incorporates data from numerous other studies, the mixture of data sources differs causing the maps to vary in detail. Second, no standard method exists for determining C_{org}. Each method yields slightly different results. Combining data from numerous sources therefore frequently means incorporating data of differing quality and precision produced by several techniques. With these points in mind we note that (1) only the most general conclusions can be drawn from the modern corg distributions, and (2) our comparison of modern and LGM C_{org} values must be correspondingly general.

Sample location and analytic methods

We analyzed 82 LGM samples from the North Atlantic Ocean (Fig. 1; Table 1). This is a subset of the cores used by Balsam and McCoy (1987) and includes cores in which the LGM level was identified by CLIMAP Project Members (1976) as well as those identified by others. As Balsam and McCoy (1987) note, the CLIMAP data set favors cores with good biotic preservation, generally cores from quiescent pelagic settings exhibiting little significant down slope movement of extrabasinal sediment. To expand the depositional environments represented by the CLIMAP data set, Balsam and McCoy (1987) added 35 cores from basins and margins to the North Atlantic data set. The

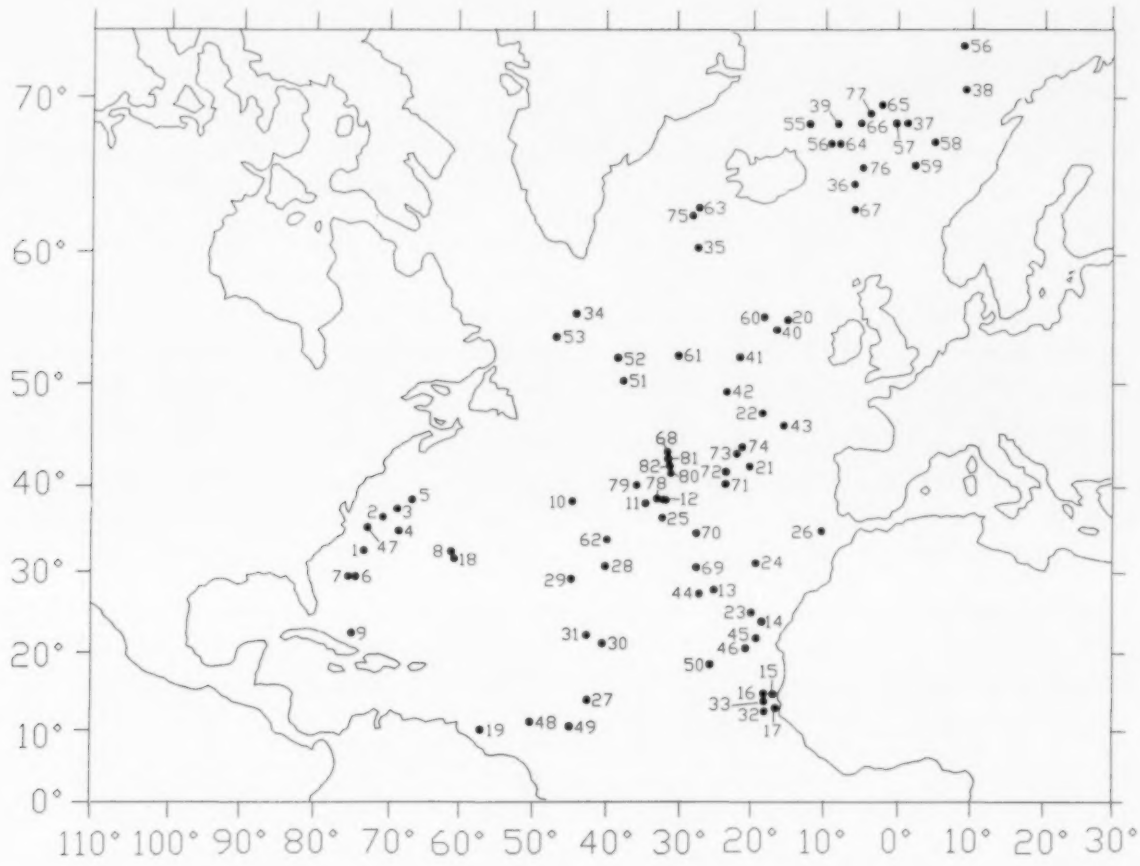

Fig. 1. Mapped distribution of core samples used in this study. The numbered data points correspond to the Map numbers on Table 1 which also contains additional information about the core samples.

cores range in depth from 1142 m to 4944 m and in latitude from 11°N to 72°N.

Samples were prepared for C_{org} analysis by grinding to $<38\mu$ with a mortar and pestle and drying in a controlled humidity environment. C_{org} in each LGM sample was analyzed with a Coulometer Carbon Analyzer. The Coulometer measures total carbon (TC), that is mineral carbon plus organic carbon, by combusting 15 to 30 mg of sample at 950°C in an O_2 stream and measuring the evolved CO_2 in an automatic titration cell. Mineral carbon (MC) is determined by digestion of 15 to 30 mg of sample in warm perchloric acid (2N) and automatic titration of the CO_2 generated. Organic carbon content (C_{org}) is calculated as the difference between TC and MC assuming all the mineral carbon is calcium carbonate.

Coulometric analysis, like other types of C_{org} analyses, does not distinguish between recently deposited or primary organic matter and second generation or redeposited organic matter (peat or lignite for example). According to Tissot and Welte (1978) redeposited organic matter is unlikely in modern marine sediments. If this assumption is correct, and most recent research with C_{org} in marine sediments makes this assumption, then our results should reflect the weight percentage of first generation or primary organic material. It must be noted that this assumption has recently been challenged. Stein (1991), in a study of a Baffin Bay core (ODP Site 645), notes that a substantial portion of the organic material in this particular setting is secondary. The importance of secondary organic material at this site is not surprising considering it is a narrow basin surrounded by continents. Because of the unique geographic setting these results (Stein, 1991) do not appear applicable to larger ocean basins; in most sediments beyond the edge of the continental shelf marine derived C_{org} appears to dominate (Walsh et al., 1985).

Replicate analyses were performed on U.S. Geological Survey (USGS) standard MRG-1. MRG-1 is known to have a TC value of 0.31% by weight. Our analytical values were identical to the known values of MRG-1 indicating the Coulometer was capable of a high degree of precision and accuracy. Replicate analyses were also performed on 34 of the 82 LGM samples; seven of the samples were

TABLE 1

Core locations and characteristics

Map no.	Core no.	Depth to LGM	Latitude	Longitude	Water depth (m)	C_{org} (%)	$CaCO_3$ (%)
1	A156-004	770	34°49'	74°41'	3015	1.11	8.8
2	A164-005	188	37°46'	71°14'	3244	0.75	4.9
3	A164-006	120	38°08'	69°52'	3591	0.74	11.8
4	A164-024	83	36°29'	69°00'	4304	0.82	3
5	A164-061	110	39°32'	68°47'	2567	1.20	8.2
6	A167-013	154	31°39'	75°21'	2795	0.81	15.4
7	A167-014	110	31°28'	76°28'	2548	1.04	14.3
8	A173-004	78	33°52'	62°32'	3847	0.49	11.5
9	A179-015	164	24°48'	75°56'	3024	0.36	68.3
10	A180-009	66	39°27'	45°57'	3975	1.04	12.7
11	A180-015	66	39°16'	36°42'	4525	1.40	74.9
12	A180-016	77	38°21'	32°29'	2183	0.32	75
13	A180-032	66	29°07'	26°15'	4944	0.39	41.3
14	A180-039	33	25°50'	19°18'	3385	0.23	65.7
15	A180-047	380	15°20'	17°56'	2110	0.71	15.1
16	A180-048	529	15°19'	18°06'	1365	2.12	15.1
17	A180-056	110	12°14'	17°46'	2512	0.94	6
18	RC8-145	39	33°35'	62°23'	2658	0.31	53.8
19	RC9-049	77	11°11'	58°36'	1766	0.65	30.5
20	RC9-225	149	54°59'	15°24'	2249	0.77	17.5
21	RE5-034	40	42°23'	21°58'	3665	0.43	44.3
22	RE5-036	73	46°55'	18°35'	4415	0.55	11
23	RE5-054	11	25°52'	19°03'	3210	0.35	59.1
24	SP8-004	33	32°50'	18°32'	3280	0.08	60
25	V4-008	55	37°14'	33°08'	1612	0.41	1.6
26	V4-032	370	35°03'	11°37'	2211	0.17	75.6
27	V16-205	74	15°24'	43°24'	3958	0.18	69.8
28	V17-165	21	32°45'	41°54'	3839	0.29	61.2
29	V19-309	110	31°10'	45°08'	4459	0.34	44
30	V20-241	55	22°08'	41°30'	4287	0.18	52.4
31	V20-242	66	23°22'	43°39'	4480	0.23	58.5
32	V22-196	88	13°50'	18°58'	3643	0.57	5.8
33	V22-197	79	14°10'	18°35'	3082	0.54	1.5
34	V23-023	95	56°05'	44°33'	3207	0.45	9.7
35	V23-042	77	62°11'	27°56'	1429	0.43	14.3
36	V23-058	66	65°46'	07°07'	1711	0.38	10.1
37	V23-059	55	68°02'	−00°01'	2998	0.47	9.6
38	V23-060	110	70°03'	−08°19'	2889	0.57	7.7
39	V23-074	99	68°11'	09°36'	1841	0.47	9.7
40	V23-081	300	54°15'	16°59'	2308	0.64	16.3
41	V23-082	115	52°35'	21°56'	3889	0.54	18.8
42	V23-083	109	49°52'	24°15'	3786	1.50	92.8
43	V23-084	89	46°00'	16°55'	4428	0.59	17.3
44	V23-091	33	29°35'	28°34'	2673	0.23	72
45	V23-098	77	23°07'	19°18'	3421	0.83	51.2
46	V23-100	46	21°18'	22°41'	4494	0.29	58.6
47	V24-001	292	36°30'	73°30'	2927	0.93	14.8
48	V25-042	66	12°33'	50°39'	4622	0.50	25.4
49	V25-044	33	11°30'	45°03'	3964	0.26	61.1
50	V26-041	47	19°20'	26°07'	4256	0.28	60.1
51	V27-017	39	50°06'	37°18'	3969	0.46	16.2
52	V27-019	37	52°06'	38°48'	3381	0.31	15.7
53	V27-020	88	54°00'	46°12'	3425	0.39	8.3

TABLE 1 (*continued*)

Map no.	Core no.	Depth to LGM	Latitude	Longitude	Water depth (m)	C_{org} (%)	$CaCO_3$ (%)
54	V27-046	77	67°35'	11°31'	1643	0.41	5.9
55	V27-047	55	68°28'	13°33'	16320	0.56	5.4
56	V27-060	121	72°11'	−08°35'	244	0.80	6.1
57	V27-084	66	68°38'	01°36'	33192	0.45	13.7
58	V27-085	44	67°22'	−04°02'	1145	0.47	9.8
59	V27-086	88	66°36'	−01°07'	281	0.37	7.6
60	V27-110	52	56°54'	18°30'	1179	0.38	26.1
61	V27-116	66	52°50'	30°20'	3117	0.29	20.4
62	V27-263	22	35°01'	40°55'	3619	0.42	57.2
63	V28-014	165	64°47'	29°34'	1770	0.22	5.3
64	V28-035	55	67°07'	09°34'	1291	0.27	13
65	V28-038	165	69°33'	04°24'	3326	0.38	9.8
66	V28-056	77	68°02'	06°07'	2856	1.28	8.3
67	V28-059	55	64°52'	07°52'	2537	0.10	3.4
68	V28-089	79	44°32'	32°35'	3558	0.47	16.2
69	V29-173	28	33°42'	29°23'	3198	0.21	75.6
70	V29-174	44	36°18'	29°22'	3335	0.18	58.8
71	V29-177	45	41°32'	25°43'	3306	0.24	59.3
72	V29-178	54	42°51'	25°09'	3363	0.29	62.4
73	V29-179	80	44°01'	24°32'	3242	0.42	36.5
74	V29-180	63	45°18'	23°52'	3094	0.20	36.9
75	V29-206	175	64°54'	29°17'	1539	0.27	7.3
76	V29-210	66	66°44'	06°44'	2375	0.31	9.6
77	V29-219K	55	68°23'	05°27'	3299	0.38	6.5
78	V30-096	68	39°56'	33°08'	3103	0.38	65.2
79	V30-097	83	41°00'	37°56'	3286	0.77	52.8
80	V30-099	35	43°09'	32°27'	3509	0.03	58.9
81	V30-100	72	44°06'	32°30'	3434	0.32	37.5
82	V30-101K	50	44°06'	32°30'	3419	0.68	27.2

selected at random while the remaining 27 samples had high TC. Because precision and accuracy fall as the weight percent carbon increases, replicate analyses of samples with high TC is essential. The difference between analyses of replicate samples ranged from 0 to 0.46% and averaged about 0.14%. Given the Coulometer's ability to reproduce TC values from MRG-1 precisely we can offer only one explanation for the lower reproducibility exhibited by our LGM samples—inhomogeneity. We therefore followed the practice of running multiple analyses on a single sample and using the mean value (Davis, 1986).

Results

The range of C_{org} values for all the samples analyzed is from 0.03 to 2.12% by weight. Most of the samples, about 60%, exhibit a narrow range of C_{org} values, from 0.2 to 0.5% (Fig. 2). Less than 10% of the samples exceed 0.9% C_{org} while an equally small percentage is less than 0.2% C_{org}. While the mean C_{org} value for the data set is about 0.5%, the distribution is asymmetric, skewed toward samples with a high C_{org} content (Fig. 2). The eight samples with the lowest C_{org} values have organic contents between 0.03 and 0.2% C_{org} while the eight samples with the highest C_{org} values have organic contents from 1 to 2.12%.

The distribution of C_{org} does not appear to be depth related. A plot of C_{org} versus water depth (Fig. 3) is extremely noisy and provides little evidence of a relationship. However, the mapped distribution of C_{org} indicates substantial geographic restriction of both high and low values (Fig. 4). Considering that the average C_{org} value of the data set is about 0.5%, high values are most common along continental margins. The highest

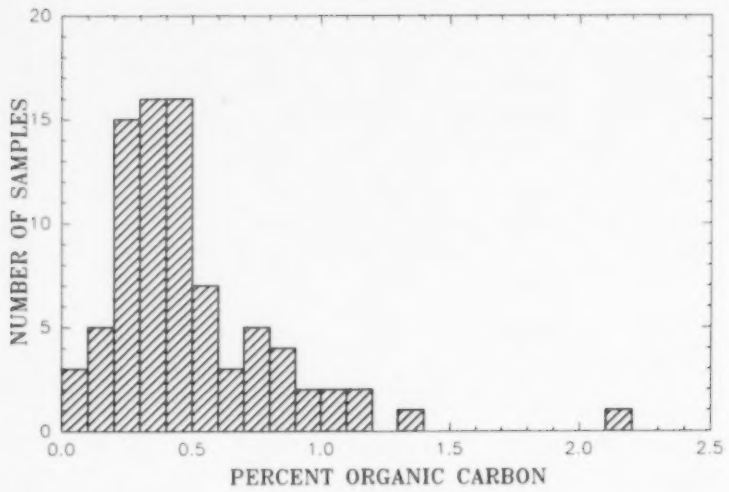

Fig. 2. Frequency histogram illustrating organic carbon content as a function of the number of samples. Note, most of the samples fall into a very narrow range of C_{org} values and that values are skewed towards higher organic content.

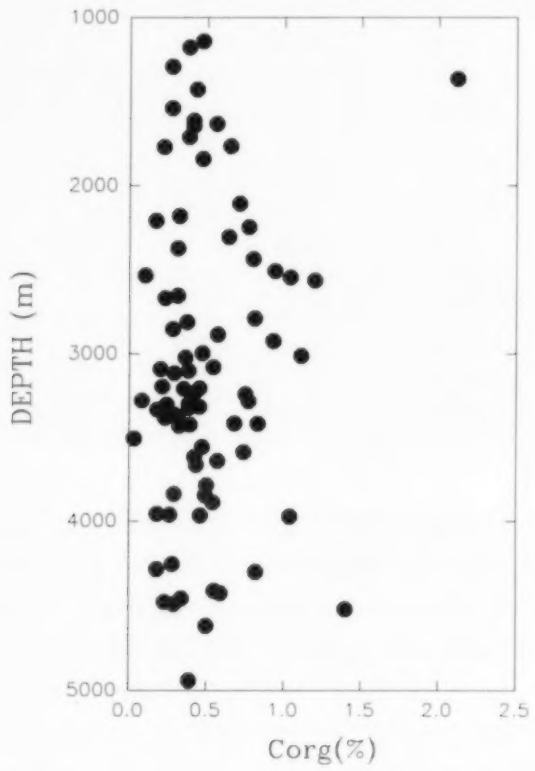

Fig. 3. Sample organic content as a function of water depth.

C_{org} values are present off northwest Africa between 10° and 20°N. In this region values reach the data set maximum of 2.12%. High values are also present off eastern North America where C_{org} concentrations generally exceed 0.6% and sometimes exceed 0.9%. Another zone of high C_{org} defined by several points is centered to the west of the MAR at 40°N and 40°W. Unlike all the other zones of high C_{org} content which occur on continental margins, this zone occurs in the mid-ocean. Three areas of high C_{org} values, off the coast of South America near the Amazon River outflow, west of Great Britain and the Bay of Biscaye, and in the Norwegian Sea are defined by either one or two points and require further analysis to fully document.

The remainder of the North Atlantic has values less then 0.6% C_{org}. Three areas exhibit very low values, less than 0.3%. The largest area extends from coastal Africa (20°–35°N) toward the southwest across the Atlantic to about 50°W. A second area of low C_{org} values occupies the region to the southwest of Iceland while the third area occurs just to the east of Iceland and extends into the Norwegian Sea.

Discussion

Any discussion of the LGM distribution of C_{org} is perhaps best undertaken with reference to modern distributions. When making this comparison it must be remembered that organic carbon in modern sediments has been subjected to less biogenic decomposition and diagenetic alteration than LGM C_{org}. If the only factor affecting organic content were time and the biogenic and diagenetic alteration that continues beneath the sediment water interface in the mixed layer, then one would expect modern C_{org} values to be higher than LGM. However, in the North Atlantic this is not the case; most LGM C_{org} values are as high as or slightly higher than C_{org} values from geographically comparable modern sediments. Higher LGM C_{org} values in spite of increased potential for biogenic and diagenetic degradation suggests that delivery (flux) and/or preservation rate of organic material increased during glacial time.

Increased flux of organic material typically is correlated with increased sea surface productivity. Productivity increases, however, are usually local in nature. They cannot explain the general increase in North Atlantic C_{org} values. Preservation changes are more likely to have a wide spread effect on C_{org} values. Several factors, either individually or in concert, may alter the preservation potential of organic material in LGM sediments compared to the present. These factors may be related to the chemistry of bottom or pore waters or to the

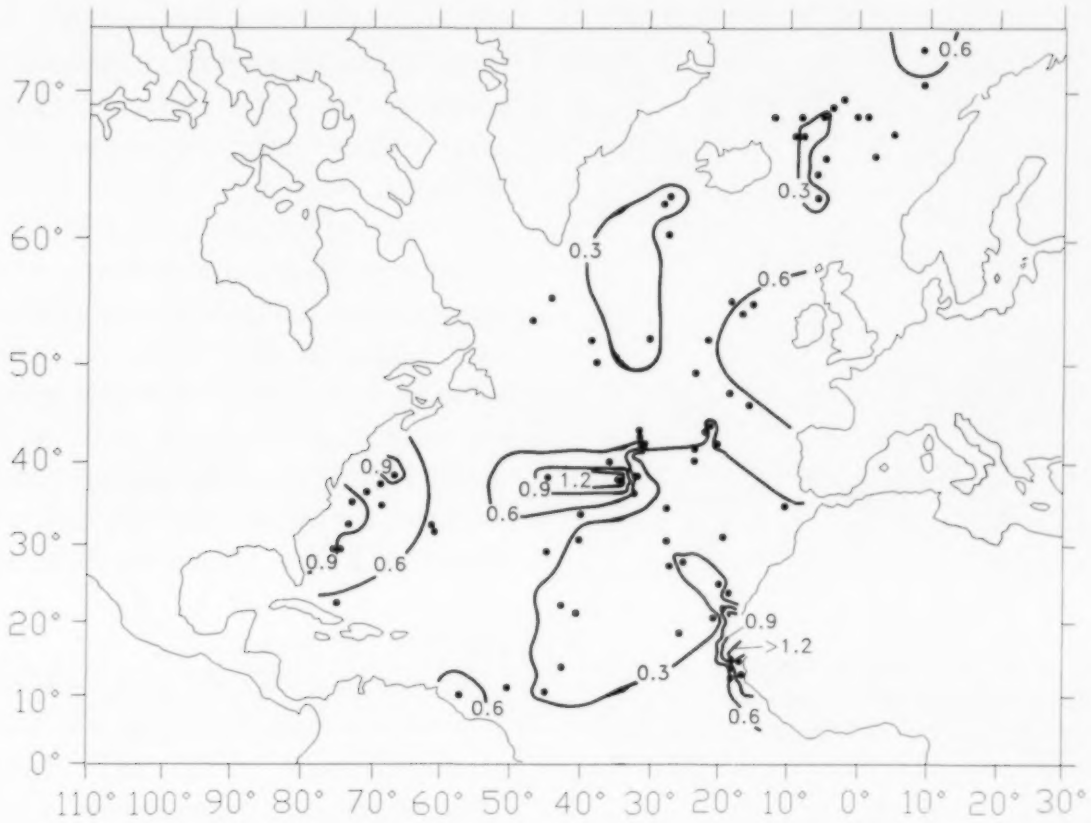

Fig. 4. Mapped distribution of sediment organic content in samples taken from the LGM stratigraphic level.

sediment, either through compositional differences or accumulation rate.

Sediment type is one factor that has been noted by numerous researchers as a possible influence on C_{org} distributions. Correlation of C_{org} to lithology usually takes one of two forms; either a relationship between carbonate content and C_{org} or a correlation between clay content and organic content. Carbonate content is usually thought of as being inversely related to organic content. However, generalizations based on data from different oceans do not always agree. For example, Heath et al. (1977) note a direct correlation between carbonate content and C_{org} in deep marine sediments of the northeast Pacific Ocean. In the Atlantic a direct relationship does not exist; Premuzic et al. (1982) note that carbonate content and C_{org} vary inversely. Further, Bezrukov et al.'s (1977) map of C_{org} distribution in the Atlantic also indicates an inverse relationship with carbonate content. Their map reveals that the lowest modern C_{org} concentrations are confined to the Mid-Atlantic Ridge where weight percent carbonate is highest (Biscaye et al., 1976; Balsam and McCoy, 1987). [Bezrukov et al. (1977) also note that on a carbonate-free basis nearshore oozes tend to have high organic contents. This is not surprising considering that nearshore productivity is high and that calculating C_{org} on a carbonate-free basis for an ooze would emphasize the remaining sediment, especially components that normally occur in low concentrations like C_{org}. Their observations of carbonate-free distribution does not nullify the fact that their map of C_{org} indicates low values where carbonate contents are high.]

Our plot of C_{org} versus carbonate content (Fig. 5), although noisy, tends to support an inverse correlation between these two variables in LGM Atlantic sediments. This diagram makes it clear that samples with carbonate contents exceeding about 65%, that is oozes (McCoy, 1983), with one exception, have an organic content less than or equal to 0.5%. For carbonate contents less than 65%, organic carbon content is much more variable but exhibits a poorly defined trend of increasing C_{org} with decreasing carbonate content. The C_{org} variability is well illustrated (Fig. 5) in samples that have carbonate contents ranging from 0 to 10%; for these samples C_{org} values range from 0.1 to 1.2%.

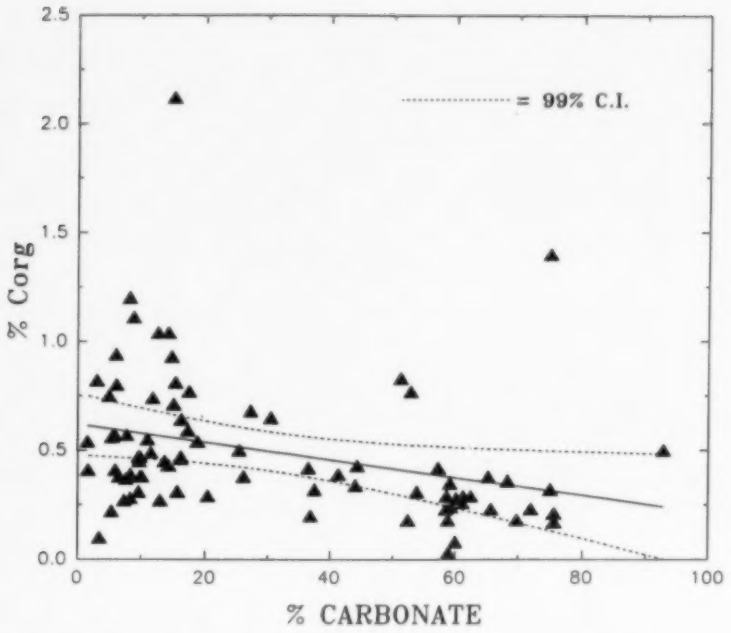

Fig. 5. Sediment organic carbon content as a function of weight percent carbonate. The results of a linear regression (solid line) indicates that with a large degree of uncertainty (dashed lines) organic content decreases as carbonate content increases.

Many workers have noted a correlation between C_{org} content and clay content or grain size (Bezrukov et al., 1977; Premuzic et al., 1982). Some researchers, notably Premuzic et al. (1982) and Tissot and Welte (1978), have suggested that organic matter preservation is enhanced by the presence of clay minerals. They indicate that the electrostatic forces associated with the surface of clays facilitate coprecipitation and flocculation of organic material thereby increasing its settling rate and potentially protecting it from destruction by metazoans and from microbial consumption. Nevertheless, the correlation of C_{org} to clay content or grain size is not straightforward. While grain size generally decreases from the shelf into deep ocean basins, C_{org} increases across the shelf to the mid-slope, reaching a maximum at a depth of 2000–3000 m and then decreases in the deeper ocean basins (Bezrukov et al., 1977; Premuzic et al., 1982).

Our data generally support the idea that C_{org} and clay content are directly related. For each of our samples Balsam and McCoy (1987) have analyzed sediment composition. For the purposes of this paper we considered the ooze and marl sediment categories to be carbonate-rich and calcareous clay and clay categories to be clay-rich. When lithology is superimposed on C_{org} frequency (Fig. 6) it becomes obvious that high C_{org} and a clay-rich lithology are correlated. Of the twenty seven samples that have a C_{org} concentration greater than 0.5%, only 3 samples are carbonate-rich.

As shown by Balsam and McCoy (1987) North Atlantic sediment composition underwent a major change from glacial to interglacial time. Carbonate rich sediments dominate the North Atlantic at present. At the LGM synoptic level, the carbonate component is decreased and the dominant sediment type shifts to clay and calcareous clay. Hence, changing sediment characteristics in the form of higher clay content may be responsible, at least in part, for the higher LGM C_{org} values when compared to the present.

Another factor that could influence organic carbon content is sediment accumulation rate. Several workers (Heath et al., 1977; Müller and Suess, 1979; Ibach, 1982) have noted that sedimentation rate and C_{org} are positively correlated. As the sedimentation rate increases the time organic matter is exposed to near seabed oxidation and biological decomposition is reduced. This positive relationship between weight percent organic carbon and sedimentation rate deteriorates for extremely high sediment accumulation rates because increased dilution exceeds increased preservation of C_{org}. In areas of high productivity, such as coastal upwelling zones, this basic pattern may be altered because the increased sedimentation

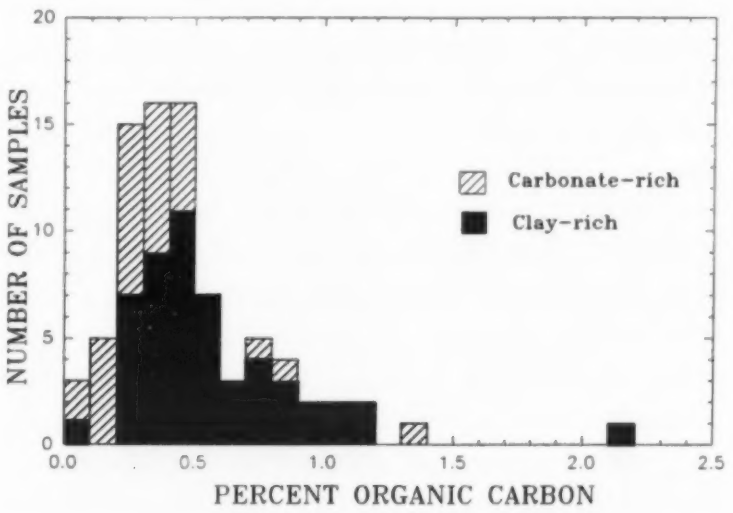

Fig. 6. Frequency histogram showing the relationship of carbonate versus clay-rich lithologies to organic content.

rate, at least in part, results from an increase in the flux of organic material to the seabed.

Diagrams that compare organic carbon/sedimentation rate (OCSR diagrams) frequently use log scales on both axes. Sedimentation rate in cm/1000 yrs is usually plotted on the *X*-axis while the mean C_{org} for that stratigraphic interval is plotted on the *Y*-axis. Log scales tend to diminish the importance of extremely high sedimentation rates and to emphasize low concentrations of C_{org}. Stein (1990) has indicated that in addition to documenting a relationship between C_{org} and sedimentation rate, these diagrams may also be useful for assessing bottom water chemistry and sea surface productivity. He subdivided OCSR diagrams into three overlapping fields (open-marine oxic, high productivity, and anoxic) and one subfield (open ocean upwelling) at the juncture of high productivity and open-marine oxic fields. In order to utilize OCSR diagrams we had to determine sedimentation rates for each of our LGM samples. Sedimentation rates were taken from Balsam and McCoy (1987). They calculated these rates from the down core position of the LGM (18,000 yrs B.P.) stratigraphic horizon assuming the core top sediment was modern. Balsam and McCoy (1987) note two potential problems concerning sedimentation rate calculations. First, the assumption regarding core top age was not verified and second, the late glacial to modern stratigraphic horizons over which the sedimentation rate was averaged includes times of highly varying depositional conditions. Nevertheless, we contend our data are adequate for comparison to published OCSR diagrams. These diagrams frequently are based on sedimentation rates averaged over substantially longer periods of time (Stein, 1990) with a higher degree of stratigraphic uncertainty then the LGM to modern stratigraphic interval we employ. When calculating sedimentation rates for older samples a correction for compaction is normally applied. Because of the shallow burial depth of our samples a compaction correction was not necessary.

The OCSR plot for our data (Fig. 7) indicates that as sedimentation rate increases so does organic content; in the North Atlantic sedimentation rate and C_{org} are correlated. As noted above, the OCSR

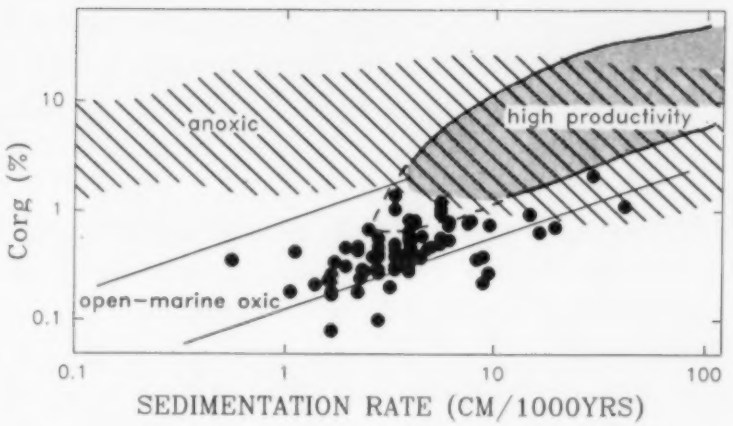

Fig. 7. OCSR diagram for our North Atlantic LGM core samples. This diagram is based on work by Stein (1990); the axes are scaled the same as Stein's for easy comparison. One sample, with a C_{org} content of 0.03%, could not be plotted at Stein's scale. The diagram is divided into three overlapping fields. Diagonally ruled areas indicate potential anoxia; shaded areas indicate high productivity; the zone between the two solid lines is generally open-marine oxic; and the area enclosed by dashed lines but not shaded is thought to be indicative of open-ocean upwelling (or in this case open-ocean high productivity).

diagram may also be a useful indicator of bottom water chemistry. When plotted on the OCSR diagram most of our data fall into the open-marine oxic field (Fig. 7), although some samples fall just below that field boundary. While samples below the open-marine oxic field are not discussed by Stein (1990) presumably they are still indicative of oxic conditions. [It must be noted that the field boundaries are empirically determined and therefore open to adjustment.] Stein's OCSR diagram (Stein 1990, fig. 2) for Atlantic Quaternary sediments (ODP Leg 108) also contains a few points beneath the open-marine oxic field. This data suggests that the variability we observe in our North Atlantic LGM data set (Fig. 7) is within the range of what others have observed and that points which fall below the open-marine oxic field are not uncommon.

It is perhaps surprising that most of our data fall into the open marine oxic field considering proposed deep circulation changes in North Atlantic during the LGM. During glacial times the polar front migrated to the south (CLIMAP, 1976), cutting off the present source of NADW causing deep circulation in the North Atlantic to be substantially reduced. With diminished or sluggish deep circulation the oxygen content of the deep water was reduced by biological consumption.

Thus, while the source of NADW certainly changed during the LGM, the deep ocean remained ventilated, and the oxygen content of the deep waters, while reduced, did not approach anoxia (Boyle and Keigwin, 1982, 1987; Boyle, 1988, 1990). Our organic carbon data is consistent with this view; that is, North Atlantic deep water was oxic during the LGM. While some of our data points fall into or near the area where the high productivity, anoxic, and oxic fields overlap (as defined by Stein, 1990), none of our samples fall into a region that is clearly anoxic. The use of OCSR diagrams for estimating bottom water oxygen content is imprecise. Our data only indicates that bottom waters in the North Atlantic were generally oxic. We cannot rule out the possibility that a decrease in LGM bottom water oxygen content enhanced the preservation of organic matter compared to the present.

Three regions—(1) off northwest Africa, (2) the American continental margin, and (3) west of the Mid-Atlantic Ridge at ~40°N—exhibit geographically constrained (Fig. 4) high C_{org} values in at least four samples (Fig. 8A–C). Some samples from all three areas fall into the field indicative of high productivity or occur near the lower boundary of the high productivity field where it overlaps the open-marine oxic and anoxic fields.

The area off northwest Africa is currently a region of high productivity (Diester-Haass, 1978; Sarnthein et al., 1982) with sediment organic content occasionally reaching 3.5% by weight. This region of high productivity is divided into two zones, each reflecting its origin. One zone is the result of nutrient influx from the Senegal River while the second zone is induced by wind-driven upwelling off Cape Blanc. During the LGM oceanographic and climatic conditions were substantially different than today. Nutrient influx from the Senegal River was substantially reduced during the LGM (Sarnthein et al., 1982) because aridity in the sub-Sahara increased. Further, both Pedersen (1983) and Sarnthein et al. (1982) suggest that the velocity of the winds blowing off the Sahara, the Harmattan Winds, increased during the LGM. Increased wind velocity would have led to increased upwelling. As Sarnthein et al. (1982) note, the nature of waters upwelled during the

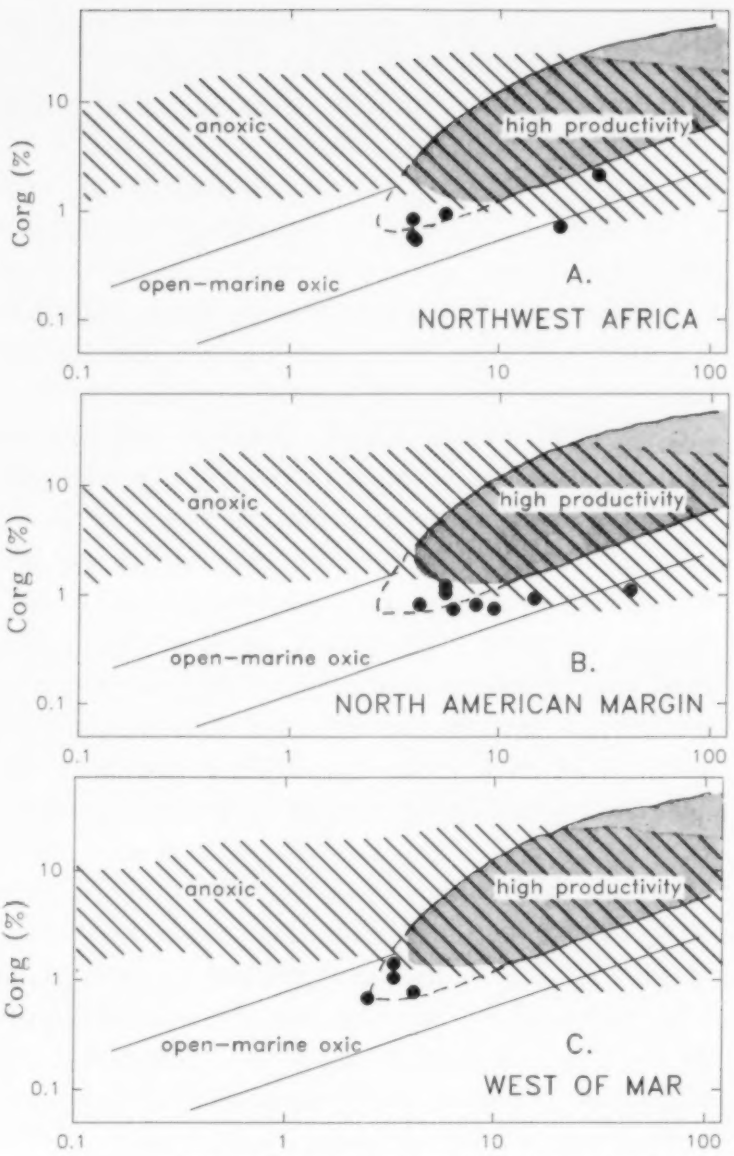

Fig. 8. OCSR diagrams for three mapped regions of high productivity. (A) Off Northwest Africa, (B) on the North American margin, and (C) west of the MAR. Additional description of OCSR diagrams may be found in the text and caption for Fig. 7.

LGM also may have influenced both the productivity and preservation of organic material. During the LGM South Atlantic Central Water (SACW) expanded (Sarnthein et al., 1982). When upwelled, this nutrient-rich water could promote extremely high sea surface productivity. Because LGM SACW was oxygen-poor compared to bottom waters currently occupying this site, it also may have enhanced the preservation potential of organic material once that material reached the bottom.

Our data indicate the zone of high sediment organic content off northwest Africa was larger

during the LGM (Fig. 4) than at present. This expansion is consistent with the results of other paleoceanographic studies (Sarnthein et al., 1982) which predict increased LGM wind-driven upwelling in this area. When our data from this area are plotted on an OCSR diagram most of the samples fall into or near the open-ocean upwelling zone (Fig. 8A). This is not surprising considering that most of our samples come from a substantial distance offshore. The shallowest samples generally have the highest C_{org} content in this group and fall near the high productivity field suggesting an upwelling zone may be located closer to shore.

A second area of moderately high LGM C_{org} values is located on the slope and rise off eastern North America (Fig. 4). At the present time sediments on the North American continental margin exhibit low to moderately high C_{org} values, that is, 0–1.0% (Bezrukov et al., 1977; Demaison and Moore, 1980; Premuzic et al., 1982). The present distribution is geographically dependent: from Cape Cod north to the Grand Banks C_{org} values are moderately high, from 0.5–1%, while south of Cape Cod C_{org} values are generally $<0.5\%$. The area surrounding the Grand Banks currently exhibits high sea surface productivity, comparable to the productivity off northwest Africa (Demaison and Moore, 1980). Nevertheless, sediment organic content is substantially lower than off northwest Africa (Emery and Uchupi, 1972) because deep waters off the Grand Banks are extremely rich in oxygen thereby impeding the accumulation of organic matter.

During the LGM the distribution of C_{org} off eastern North America was substantially different then at present. South of Cape Cod where present C_{org} values are low, LGM values are high, $>0.6\%$ and frequently in excess of 0.9%. Unfortunately our data set contains no samples off the Grand Banks making it impossible to assess the extent of sediment with high organic content. The OCSR diagram for this area (Fig. 8B) indicates that most samples are marginal to the high productivity field, either in the open-ocean upwelling field or high sedimentation rate end of the open-marine oxic field. Like the samples from off northwest Africa, the shallowest samples on the North American margin also exhibit the highest organic content, suggesting that a high productivity zone may be present closer to shore.

In part, the high C_{org} content of these American margin sediments may result from increased glacial sedimentation rates. Many studies (see for example Ericson et al., 1961; Balsam, 1981) indicate at least a factor of two increase in sedimentation rate from interglacial to glacial time. Factors related to productivity also may have influenced sediment organic content. Nutrient-rich meltwater from the Wisconsin Ice Sheet may have stimulated LGM productivity over a broad area. Further, LGM oceanographic conditions may have enhanced productivity. The southward migration of the polar front and concomitant steepening of thermal gradients off eastern North America (Balsam, 1981) probably led to an increase in Gulf Stream velocity enhancing coastal upwelling and further increasing LGM productivity.

The area west of the MAR at about 40°N is more difficult to explain and is somewhat perplexing. This region is represented by samples from four cores with C_{org} contents ranging from 0.68% to 1.4%. Sedimentation rates in these cores averages 3.7 cm/1000 yrs over the last 18,000 yrs, a figure that is typical of deep ocean settings in this area (Balsam and McCoy, 1987). The OCSR diagram for these samples (Fig. 8C) indicates that they all are in the open-ocean upwelling field. However, oceanographic conditions during the LGM make upwelling in this region unlikely. During the LGM this region was a transition zone separating the cold waters north of the polar front, about 2°N, from the warm water of the subtropical gyre immediately to the south (CLIMAP, 1976). Reconstructions of surface circulation during the glacial maximum (CLIMAP, 1976; Ruddiman, 1977) generally indicate that the transition zone is flanked by surface currents flowing to the east. Because both currents are flowing in the same direction, Coriolis forces cannot produce a divergence and the resulting upwelling. High productivity in this region, then, must result from something other than upwelling. However, deep circulation reconstructions based on $^{13}C/^{12}C$ indicate a probable divergence at about 55°N (Labeyrie and Duplessy, 1985; Duplessy et al., 1988). Although our data are scanty (Fig. 4), sediment

beneath the probable divergence does not have a high organic content suggesting enhancement of productivity by the divergence was limited.

Another line of evidence germane to the interpretation of C_{org} values in this region is the time/depth distribution of the benthic foraminifera. Benthic foraminiferal faunas analyzed in these cores and additional cores from this region lack a strongly dominant species, exhibit little down core variability, and are remarkable for their uniformity (Schnitker, 1980; Parsons, 1990). In most of the western North Atlantic benthic foraminiferal faunas exhibit rapid changes with both water depth and time (see e.g., Streeter, 1973; Schnitker, 1974, 1979; Streeter and Lavery, 1982); in this region all faunal changes are very gradual. During the LGM the same benthic foraminiferal fauna is present in this region from a water depth of 2500 m to almost 5000 m. In most of the western North Atlantic LGM core samples from this depth range are dominated by the foraminifera *Uvigerina perigrina* (Balsam, 1981; Balsam et al., 1987); west of the MAR *Uvigerina* is only a minor faunal constituent. [It must be noted that low numbers of *Uvigerina* in a region of moderately high organic content is in disagreement with the hypothesis (Miller and Lohmann, 1982) that this foraminifer's distribution is related to organic carbon content.] The uniformity of the LGM foraminiferal distribution with depth could indicate the water column in this region was not highly stratified. In a uniform, isopycnal water column nutrients could more easily be mixed from deep waters to the surface thereby supporting higher than normal productivity during much of the year. If a uniform benthic foraminiferal fauna is indicative of an isopycnal water column, this region also may have been one site of LGM deep water formation.

Conclusions

Analysis of 82 North Atlantic Ocean core samples indicates that during the last glacial maximum the average organic content of the sediment was about 0.5% by weight. Although comparison of modern and LGM samples is difficult because of differences in their depositional and diagenetic histories, LGM C_{org} values appear slightly higher. The mapped distribution of last glacial maximum sediment organic content indicates three areas of high values—off Northwest Africa, the North American margin, and west of the MAR at about 40°N. Only one of these areas, off Northwest Africa, also has high C_{org} values at the present. During the LGM this area was larger than at present, possibly because of increased wind-driven upwelling. On the North American margin the increased organic carbon content of LGM sediments may be the result of higher sedimentation rates increasing the preservation potential of the organic matter. West of the MAR the area of increased LGM organic carbon content appears related to glacial circulation patterns.

Organic carbon content also appears to be related to sediment composition. Samples with high C_{org} values generally are clay-rich. A plot of organic carbon versus sedimentation rate (OCSR diagram) indicates that organic carbon content increases with increasing sedimentation rate. This diagram also indicates that most of the samples are from an oxic open-marine environment suggesting that any possible decrease in LGM deep water oxygen content was minimal.

Thus, our data indicates that no one factor can explain the LGM increase in C_{org}. Rather, it appears that the increase in sediment organic content during the LGM resulted from a combination of factors including decreased carbonate content, increased clay content, increased sedimentation rate, and changing ocean circulation patterns.

Acknowledgements

This study is based on the senior author's Master of Science thesis at the University of Texas at Arlington. Comments and criticisms by B. Ellwood and J. Schieber helped clarify many of the ideas developed in this paper. A special debt of gratitude is owed J. Cooper for providing a wealth of scientific information concerning organic matter and T. Crowley for lengthy discussions of LGM paleocirculation. W. Ruddiman provided numerous thoughtful suggestions as a reviewer of this paper. The Texas Bureau of Economic Geology donated the use of their Coulometer Carbon Ana-

lyzer. Dr. Koppenal, director of the Mineral Laboratory, and T. Pinkston also provided instruction and assistance running the Coulometer. This project would have been impossible were it not for their help. All samples are from Lamont-Doherty Geological Observatory (LDGO). Support for the curating facilities of the LDGO Deep-Sea Sample Repository is provided by the National Science Foundation through Grant OCE88-00001 and the Office of Naval Research through Grant N00014-87-K-0204. Ms. Rusty Lotti, core curator at LDGO, provided invaluable assistance in obtaining core material.

References

Balsam, W.L., 1981. Late Quaternary sedimentation in the western North Atlantic: Stratigraphy and paleoceanography. Palaeogeogr., Palaeoclimatol., Palaeoecol., 35: 215–240.

Balsam, W.L. and McCoy, F.W. Jr., 1987. Atlantic sediments: Glacial/interglacial comparisons. Paleoceanography, 2: 531–542.

Balsam, W.L., Gary, A.C., Healy-Williams, N. and Williams, D., 1987. Morphology and time/depth distribution *Uvigerina peregrina*: continental slope, eastern U.S. margin. Palaios, 2: 172–177.

Bezrukov, P.L., Yemel'yanov, Y.E.M., Lisitsyn, A.P. and Romankevich, Y.E.A., 1977. Organic carbon in the upper sediment layer of the world ocean. Oceanology, 17: 561–564.

Biscaye, P.E., Kolla, V. and Turekian, K.K., 1976. Distribution of calcium carbonate in surface sediments of the Atlantic Ocean. J. Geophys. Res., 81: 2595–2603.

Boyle, E.A., 1988. Vertical oceanic nutrient fractionation and glacial/interglacial CO_2 cycles. Nature, 331: 55–56.

Boyle, E.A., 1990. Quaternary deepwater paleoceanography. Science, 249: 863–870.

Boyle, E.A. and Keigwin, L.D., 1982. Deep circulation of the North Atlantic: Geochemical evidence. Science, 218: 784–787.

Boyle, E.A. and Keigwin, L.D., 1987. North Atlantic thermohaline circulation during the past 20,000 years linked to high-latitude surface temperature. Nature, 330: 35–41.

CLIMAP Project Members, 1976. The surface of the ice-age earth. Science, 191: 1131–1137.

CLIMAP Project Members, 1981. Seasonal reconstructions of the Earth's surface at the last glacial maximum. Geol. Soc. Am. Map Chart Ser., MC-36.

Cline, R.M. and Hays, J.D. (Editors), 1976. Investigation of Late Quaternary Paleoceanography and Paleoclimatology. Geol. Soc. Am. Mem., 145, 464 pp.

Davis, J.C., 1986. Statistics and Data Analysis in Geology. 2nd ed. Wiley, New York, 646 pp.

Demaison, G.J. and Moore, G.T., 1980. Anoxic environments and oil source bed genesis. Am. Assoc. Pet. Geol., 64: 1179–1209.

Diester-Haass, L., 1978. Sediments as an indicator of upwelling. In: R. Boje and M. Tomczak (Editors), Upwelling Ecosystems. Springer, New York, pp. 261–281.

Duplessy, J.C., Shackleton, N.J., Fairbanks, R.G., Labeyrie, L., Oppo, D. and Kallel, N., 1988. Deepwater source variations during the last climatic cycle and their impact on global deepwater circulation. Paleoceanography, 3:343–360.

Emery, K.O. and Uchupi, E., 1972. Western North Atlantic Ocean: Topography, rocks, structure, water, life and sediments. Am. Assoc. Pet. Geol. Mem., 17, 532 pp.

Ericson, D.B., Ewing, M., Wollin, G. and Heezen, B.C., 1961. Atlantic deep-sea sediment cores. Geol. Soc. Am. Bull., 72: 193–286.

Heath, G.R., Moore, T.J. and Dauphin, J.P., 1977. Organic carbon in deep-sea sediments. In: N.R. Anderson and A. Malahoff (Editors), The Fate of Fossil Fuel CO_2 in the Oceans. Plenum, New York, pp. 605–625.

Ibach, L.E.J., 1982. Relationship between sedimentation rate and total organic carbon in ancient marine sediments. Am. Assoc. Pet. Geol. Bull., 66: 170–188.

Labeyrie, L.D. and Duplessy, J.C., 1985. Changes in the oceanic $^{13}C/^{12}C$ ratio during the last 140 000 years: high-latitude surface water records. Palaeogeogr., Palaeoclimatol., Palaeoecol., 50:217–240.

Lisitzin, A.P., 1972. Sedimentation in the World Oceans. Soc. Econ. Paleontol. Mineral., Spec. Publ., 17, 218 pp.

McCoy, F.W., 1983. Seafloor sediment: Map of the circum-Pacific region, northwest quadrant (1:10,000,000). In: K.J. Drummond (Editor), Circum-Pacific Map Project of the Circum-Pacific Council for Energy and Mineral Resources. Am. Assoc. Pet. Geol.

Miller, K.G. and Lohmann, G.P., 1982. Environmental distribution of recent benthic foraminifera on the northeast United States continental slope. Geol. Soc. Am. Bull., 93: 200–206.

Müller, P.J. and Suess, E., 1979. Productivity, sedimentation rate and sedimentary organic matter in the oceans—I. Organic carbon preservation. Deep-Sea Res., 26A: 1347–1362.

Parsons, A.L., 1990. Late Quaternary deep/intermediate water history: benthic foraminiferal evidence from the mid-Atlantic Ridge at 35° North. M.S. thesis, Univ. Texas, Arlington.

Pedersen, T.F., 1983. Increased productivity in the eastern equatorial Pacific during the last glacial maximum (19,000 to 14,000 yr BP). Geology, 11: 16–19.

Premuzic, E.T., Benkovitz, C.M., Gaffney, J.S. and Walsh, J.J., 1982. The nature and distribution of organic matter in the surface sediments of the world oceans and seas. Organic Geochem., 4: 63–77.

Ruddiman, W.F., 1977. Late Quaternary deposition of ice-rafted sand in the subpolar North Atlantic (lat 40° to 65°N). Geol. Soc. Am. Bull., 88: 1813–1827.

Sarnthein, M., Theide, J., Pflaumann, U., Erlenkeuser, H., Futterer, D., Koopmann, B., Lange, H. and Seibold, E., 1982. Atmospheric and oceanic circulation patterns of northwest Africa during the past 25 million years. In: U. von Rad, K. Hinz et al. (Editors), Geology of the Northwest African Continental Margin. Springer, Berlin, pp. 545–604.

Schnitker, D., 1974. West Atlantic abyssal circulation during the past 120,000 years. Nature, 248: 385–387.

Schnitker, D., 1979. The deep waters of the western North Atlantic during the past 24,000 years, and the re-initiation

of the Western Boundary Undercurrent. Mar. Micropaleontol., 4: 265–280.

Schnitker, D., 1980. Quaternary deep-sea benthic foraminifers and bottom water masses. Annu. Rev. Earth Planet. Sci. Lett., 8: 343–370.

Stein, R., 1990. Organic carbon content/sedimentation rate relationship and its paleoenvironmental significance for marine sediments. Geo-Mar. Lett., 10: 37–44.

Stein, R., 1991. Organic carbon accumulation in Baffin Bay and paleoenvironment in high latitudes during the past 20 m.y. Geology, 19: 356–359.

Streeter, S.S., 1973. Bottom water and benthonic foraminifera in the North Atlantic—glacial–interglacial contrasts. Quat. Res., 3: 131–141.

Streeter, S.S. and Lavery, S.A., 1982. Holocene and latest glacial benthic foraminifera from the slope and rise off eastern North America. Geol. Soc. Am. Bull., 93: 190–199.

Tissot, B.P. and Welte, D.H., 1978. Petroleum Formation and Occurrence. Springer, New York, 538 pp.

Walsh, J.J., Premuzic, E.G., Gaffney, J.S., Rowe, G.T., Harbottle, G., Stoenner, R.W., Balsam, W.L. and Betzer, P.R., 1985. Organic storage of CO_2 on the continental slope off the mid-Atlantic Bight, the southeastern Bering Sea, and the Peru Coast. Deep-Sea Res., 32:853–883.

Marine Geology, 105 (1992) 51–61
Elsevier Science Publishers B.V., Amsterdam

Early diagenesis of marine organic matter: Alteration of the carbon isotopic composition

J.M. M[c]Arthur[a], R.V. Tyson[b], J. Thomson[c] and D. Mattey[d]

[a]*Department of Geological Sciences, University College London, Gower Street, London WC1E 6BT, UK*
[b]*Newcastle Research Group, Fossil Fuels and Environmental Geochemistry, (Postgraduate Institute), Drummond Building, The University, Newcastle upon Tyne, NE1 7RU, UK*
[c]*Institute of Oceanographic Sciences, Brook Road, Wormley, Surrey GU8 5UB, UK*
[d]*Royal Holloway and Bedford New College, Egham, Surrey, TW20 0EX, UK*

(Received May 24, 1991; revision accepted September 16, 1991)

ABSTRACT

M[c]Arthur, J.M., Tyson, R.V., Thomson, J. and Mattey, D., 1992. Early diagenesis of marine organic matter; alteration of the carbon isotopic omposition. Mar. Geol., 105: 51–61.

In two distal carbonate turbidites (labelled *a* and *e*) from the Madeira Abyssal Plain oxidation of organic matter (OM) has been accompanied by a reduction in Hydrogen Index (HI) and change in the isotopic composition of carbon. Since the emplacement of turbidite *a* 0.5 ka ago 35% of the OM in the upper part has been oxidised by oxygen and nitrate diffusing from sea water into the sediment. There is an accompanying decrease of $\leq$ 0.3‰ in δ^{13}C-OM, and a decrease of 25% in HI. Turbidite *e* was emplaced about 73 ka and was exposed to bottom water for 12.3 ka before being buried beneath later turbidites. During exposure oxygen and nitrate diffused into its upper part and oxidised 50% of the TOC without an accompanying change in isotopic composition; further oxidation of the more refactory organic components decreased TOC by a further 25% and decreased δ^{13}C by 2.5‰. Oxidation also reduced HI by 50% from originally low values. Unless corrected for, the isotopic changes accompanying extended oxic and suboxic degradation of organic matter in sediments will give rise to erroneous estimates of marine–terrestrial OM ratios.

Introduction

The isotopic composition of organic matter (OM) in marine sediments is often used to identify its source, and for oil/source-rock and similar correlations (Gearing et al., 1984; Sackett, 1989; Dean et al., 1986, and refs. therein). Many workers have determined the relative proportions of marine and terrestrial OM in sediments from a study of its isotopic composition (e.g. Hedges and Parker, 1976; Schultz and Calder, 1976; Gearing et al., 1977; Tan and Strain, 1979; Showers and Angle, 1986; Kennicutt et al., 1987; Cai et al., 1988). In such studies a value of about −21‰ is often assumed for the δ^{13}C of Recent marine (non-seagrass) OM, and a value of about −26‰ for Recent terrestrial OM. A further assumption often made is that the isotopic composition of OM is a conservative property that is little affected by diagenetic fractionation. (e.g. Gearing et al., 1984; Lewan, 1986). Nevertheless, the isotopic composition of organic matter is an average of that of its components (e.g. lignins, lipids, proteins, carbohydrates, etc.), the isotopic composition of which may differ by as much as 5‰ (Deines, 1980; Spiker and Hatcher, 1984) and individual organic components, decaying at different rates during diagenesis, might be expected to change the isotopic composition of organic matter (Dean et al., 1986; Spiker and Hatcher, 1987). Downcore diagenetic fractionations of up to 4‰ caused by the selective degradation of carbohydrates have been documented in

Correspondence to: J.M. M[c]Arthur, Department of Geological Sciences, University College London, Gower Street, London WC1E 6BT, UK.

0025-3227/92/$05.00 © 1992 — Elsevier Science Publishers B.V. All rights reserved

lacustrine settings (Hatcher et al., 1983; Spiker and Hatcher, 1984, 1987).

Although the general significance of such diagenetic effects remains controversial (e.g. Dean et al., 1986; Sackett, 1989) they have been recognised as a potentially significant source of error in determining marine–terrestrial OM ratios (Spiker and Hatcher, 1984; Jasper and Gagosian, 1990). The controversy stems from the difficulty of isolating or constraining non-diagenetic sources of isotopic variation that may influence the vertical changes seen in sediment cores, especially those due to variations in organic matter type, that may result from changes in productivity and the variable supply of terrestrial-OM. In this paper we attempt to analyse the problem of diagenetic fractionation by studying sediments that were uniform in composition when deposited and which have subsequently been altered by diagenetic processes alone. Such sediments occur as distal, carbonate-rich turbidites on the Madeira Abyssal Plain beneath the eastern Atlantic off NW Africa. (Weaver and Kuijpers, 1983; Searle et al., 1985; Weaver et al., 1986; Thomson et al., 1986, 1987; Jarvis and Higgs, 1987; De Lange et al., 1987).

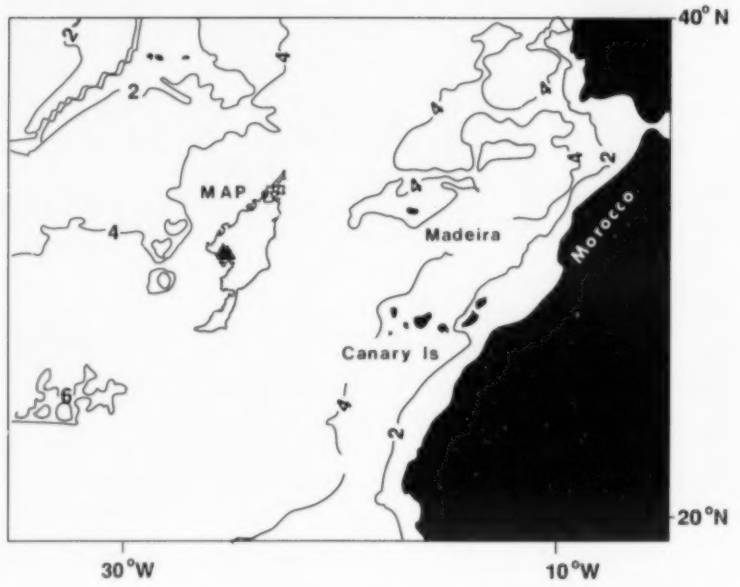

Fig. 1. Location of Madeira Abyssal Plain (MAP) shown stippled. Filled triangle show locations of core sites. Bathymetry in kilometres (adapted from Weaver et al., in press).

Sample location and description

Samples were recovered from the Madeira Abyssal Plain beneath the NE Atlantic Ocean 800 km WNW of the Canary Islands (Fig. 1). Turbidite *a* was collected from the uppermost 60+cm of box core BX 11327 taken from a depth of 5380 m at 31° 18.3′ N, 25° 23.4′ W. Turbidite *e* was sampled from piston core 11143, in which it was 270 cm thick, and occurred between 808 and 1078 cm sub-bottom depth. This core was recovered from 5424 m of water at 31° 12.0′ N, 25° 11.4′ W. Turbidite *a* contains 58% $CaCO_3$ and turbidite *e* contains 53% $CaCO_3$ (Jarvis and Higgs, 1987; McArthur, unpublished data).

In the study area turbidites on the Madeira Abyssal Plain, including a and e, are homogenous ungraded muds intercalated into a typical sequence of pelagic carbonate (Weaver et al., 1986; Thomson et al., 1988; Weaver et al., in press). Each turbidite, including *a* and *e*, is distinctive mineralogically and chemically (Jarvis and Higgs, 1987). Pelagic carbonate deposited subsequently to turbidite emplacement is mixed into turbidite tops by bioturbation. This has not altered the calcite contents of our samples from the upper part of turbidite *a* (Thomson et al., 1987; McArthur, 1989), but this process, or calcite dissolution, has reduced the calcite content of the the uppermost sample in turbidite *e* to 39%.

Diagenesis of OM is active now in turbidite *a*, which is currently exposed to bottom water, but has been arrested in turbidite *e* owing to its burial beneath later turbidites. As a consequence of this post-depositional oxic and post-oxic diagenesis turbidites *a* and *e* have different colours above and below their redox fronts. Turbidite *e* is light green in the upper 74 cm, darker green below 83 cm, and an intermediate but distinctive colour between 74 and 83 cm. The boundaries represent chemical interfaces and are termed redox fronts. They are caused by the progressive downward oxidation of the original OM by oxygen and nitrate diffusing into the turbidite when exposed to bottom water. The colour changes at 74 cm and 83 cm in turbidite *e* represent the maximum depths of penetration of O_2 and NO_3 respectively, prior to burial. Turbidite *a* is pale brown above 21 cm and light grey below. In this turbidite the oxygen and nitrate fronts are too close to be disinguished.

Analytical methods

Before analysis calcite was removed from all samples with 1 *M* HCl. Samples were then dried at 20°C. Methods of carbonate removal prior to isotopic analysis of OM vary widely (cf. Gearing et al., 1984; Lewan, 1986) and it seems that isotopic artefacts during sample preparation are not widely anticipated. We have tested superficially for such artefacts by analysing sub-samples of turbidite *a* from above (5–7 cm) and below (52–54 cm) the redox front following carbonate removal with 1*M* HCl, 5 *M* HCl, and 8.5 M H_3PO_4, and drying at various temperatures (Table 1). Isotopic measurements were made on a VG Isotech Prism gas-source mass spectrometer after the oxidation of TOC to CO_2. About 10 mg of accurately weighed sediment was mixed with copper oxide and silver wire and combusted at 950°C for 10 h in a quartz tube sealed under vacuum. Yields of CO_2 were measured, using a capacitance manometer, to an accuracy of ± 3%. Accuracy of the isotopic analysis was monitored with twelve analyses of NBS 21 (graphite), which gave −28.05 ± 0.10‰ (2σ) during the period of the analysis. Replicate sample analysis showed that the precision of the isotopic analysis of samples was ≤ 0.1‰; duplicates usually agreed to within 0.03‰ of a mean value. Measurements of carbonate-free TOC were made with a LECO C/S125 Determinator to a precision of ± 3%, and served as a check on the yield of CO_2 obtained by combustion during isotopic analysis; LECO data were systematically 0.07% lower than TOC measured from isotopic combustions. LECO data are reported here. The organic matter in four samples from above the redox boundaries of each core, and four from below, were subjected to examination by optical microscopy in order to determine the type of OM present. Samples were prepared for this examination by treatment with HCl and HF, and were then strew-mounted on glass slides. Nineteen samples were analysed using a LECO THA-200 Thermolytic Hydrocarbon Analyser, to characterise the OM further. Between 60 and 120 mg of dry sample were pyrolysed and Hydrogen Indices (HI) measured ($100S_2$/TOC). Duplicates agreed to within 20% and the means are given in Table 2. The poor reproducibility results from the low TOC of the samples. Reported HI may be systematically low because of matrix absorption at low TOC (Peters, 1986).

TABLE 1

$\delta^{13}C$ and carbonate-free TOC for samples given different preparations

Sample	Drying °C/h	Acid	[1]%TOC	$\delta^{13}C$‰
5–7	20/20	1*M* HCl	0.81	−19.71
			0.80	−19.72
5–7	50/16	8.5*M*	0.79	−19.92
		H_3PO_4	0.80	−19.97
5–7	110/4	5*M* HCl	0.83	−19.53
			0.84	−19.46
5–7	90/96	1*M* HCl	0.82	−20.01
			0.83	−19.97
52–54	20/20	1*M* HCl	1.29	−19.49
52–54	50/16	8.5*M*	1.29	−19.53
		H_3PO_4		
52–54	110/4	5*M* HCl	1.28	−19.35
			1.28	−19.38
52–54	90/96	1*M* HCl	1.24	−19.71
			1.25	−19.75

[1]TOC on a carbonate-free basis.

Results

Table 1 gives isotopic data and TOC on replicates of turbidite *a* from 5–7 cm and 52–54 cm after carbonate removal with acids of different composition and strength, and different drying conditions. Table 2 presents the results of analysis for $\delta^{13}C$, TOC, and HI for depth profiles through turbidites *a* and *e*. TOC data are presented on a carbonate-free basis, and a whole-sediment basis (recalculated from the carbonate-free data). The $\delta^{13}C$, TOC and HI data for turbidites *a* and *e* are also shown in Figs. 2 and 3.

Optical microscopic examination of the organic matter residues from both turbidites showed it consisted of brown amorphous organic matter and some undigested clay minerals. Also present are rare angiosperm pollen and rare fragments of opaque phytoclasts, the latter probably wind-blown charcoal. In turbidite *a* there is no clear difference in the appearance of the organic matter above and below the redox front. In turbidite *e*

TABLE 2

%TOC, $\delta^{13}C$, S_2, T_{max} and HI in turbidites *a* and *e*

[1]Depth (cm)	[2]%TOC	%TOC	$\delta^{13}C$	S_2 (mg/g)	T_{max}	[3]HI
Turbidite a. Core 11327						
1–2	0.94	0.39	−19.6			
2–3	0.90	0.38	−19.5			
5–7	0.84	0.35	−19.7	0.13	376	37
7–9	0.86	0.36	−19.4	0.17	373	47
11–13	0.92	0.39	−19.7	0.17	376	44
13–15	0.96	0.40	−19.3	0.24	376	60
15–17	1.10	0.46	−19.3			
17–19	1.20	0.50	−19.3	0.28	379	55
19–20	1.29	0.54	−19.3	0.33	387	61
		Redox front at 21 cm				
22–23	1.33	0.56	−19.3			
24–25	1.31	0.55	−19.3	0.36	404	66
36–38	1.30	0.55	−19.3			
40–42	1.32	0.55	−19.3	0.33	395	59
44–46	—		−19.2			
52–54	1.34	0.56	−19.4	0.32	408	56
60–62	1.32	0.55	−19.4			
Turbidite e. Core 11143						
1–2	0.26	0.16	−23.7			
4–5	0.29	0.14	−24.3			
7–8	0.32	0.15	−23.9			
10–11	0.27	0.13	−22.9			
18–19	0.34	0.16	−23.6			
23–24	0.31	0.15	−23.7	0.07	456	45
29–30	0.34	0.16	−23.5			
35–36	0.30	0.14	−23.6			
39–41	0.37	0.17	−23.9	0.07	397	40
43–44	0.36	0.17	−23.2			
47–48	0.38	0.18	−23.3			
53–54	0.50	0.24	−23.1	0.09	369	38
57–58	0.54	0.25	−22.2			
62–63	0.64	0.30	−22.0			
66–67	0.66	0.31	−21.5	0.18	382	58
68–69	0.68	0.32	−21.3	0.17	387	52
70–71	0.80	0.38	−21.6	0.18	377	47
		Oxygen front at 74 cm				
74–75	1.27	0.60	−21.6	0.25	389	42
78–79	1.26	0.59	−21.2			
82–83	1.33	0.63	−21.4	0.55	416	88
		Nitrate front at 83 cm				
98–90	1.29	0.61	−21.2			
103–104	1.29	0.61	−21.4	0.59	409	96
113–114	1.38	0.65	−21.2			
118–119				0.58	415	92
120–121	1.34	0.63	−22.2			

[1]Accurate to ±2 cm; bioturbation obscures the turbidite top.
[2]%TOC on a carbonate-free basis.
[3]100× (mg hydrocarbons [S_2]/g TOC).

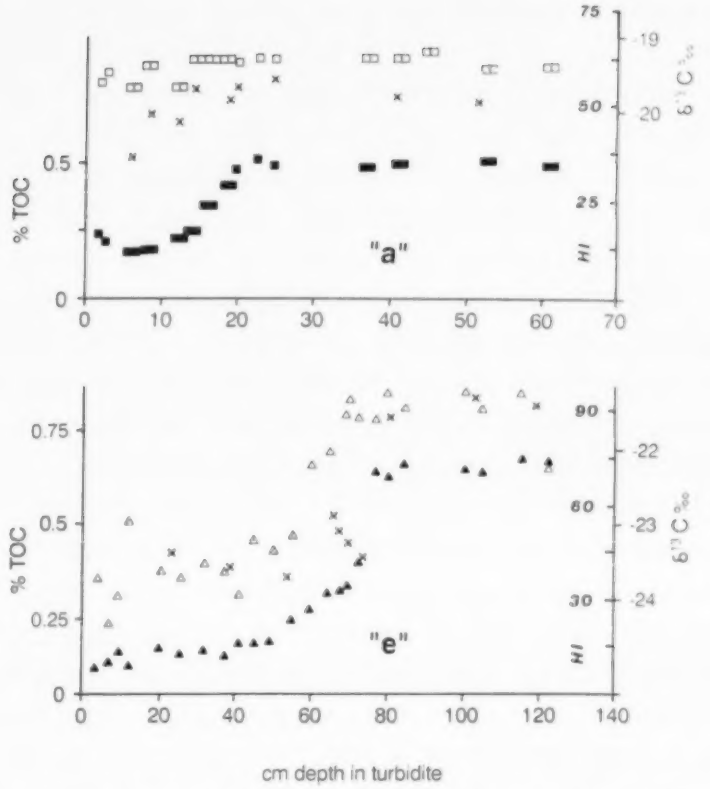

Fig. 2. Variation of %TOC, $\delta^{13}C$ and HI with depth from turbidite top in turbidites *a* and *e*. Open symbols are $\delta^{13}C$‰ (PDB); filled symbols are %TOC. Crosses are HI.

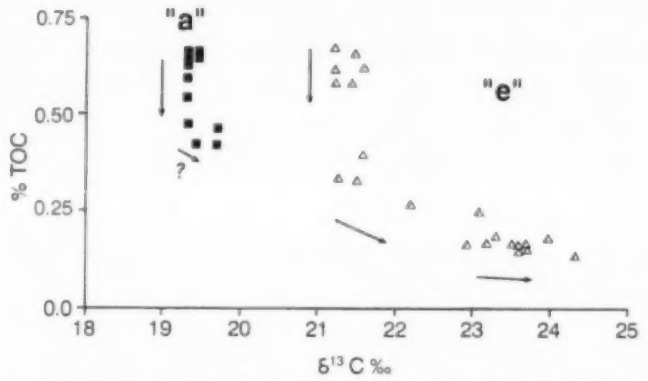

Fig. 3. Variation of $\delta^{13}C$ with TOC in turbidites *a* and *e*. Arrows highlight data trends. Uppermost two samples from turbidite *a* are not plotted as they are affected by bioturbation (see text).

that above the front is slightly darker in colour than that below. Our experience with ancient kerogens suggests such colour differences reflect partial oxidation, not a difference in organic matter type.

Characterisation of OM in both turbidites by pyrolysis showed it to have a Type IV, 'residual organic matter', inert or gas-prone composition (Tissot and Welte, 1984; Peters, 1986). This often consists of oxidised woody material, but it can also result from degradation of marine material, as is clearly the case in this study. The organic

matter type is the same above and below the redox fronts, but samples from below show higher HI, particularly in turbidite *e*, indicating that they are relatively less oxidised.

Discussion

Turbidite *a* was emplaced 0.5 ka ago (Thomson et al., 1988) and is at present undergoing oxic diagenesis. The sharp interface between oxic and anoxic parts of the turbidite is at 21 cm. Turbidite *e* was emplaced about 73 ka, at the boundary between Oxygen Isotope Stages 4 and 5 (Weaver et al., in press) and suffered oxic diagenesis for 12.3 ka (see later sections), during which time the redox front reached a depth of 74 cm below the sediment–water interface. The turbidite was then buried beneath 8 m of later turbidites and pelagic sediments. Burial terminated the supply of oxygen to the turbidite and oxic diagenesis ceased. Subsequently, anoxic conditions prevailed but sulphate reduction does not seem to occur in either turbidite (De Lange et al., 1987).

Source of the organic matter

Turbidites *a* and *e* are classified as organic-rich and have unusually high values of TOC for deep-sea sediments (Tables 1 and 2; De Lange et al., 1987; Jarvis and Higgs, 1987; Weaver et al., in press). This reflects their derivation from the NW African continental margin north of 20° N (Weaver and Kuijpers, 1983; De Lange et al., 1987; Weaver et al., in press), a region of upwelling where the OM in sediments is largely amorphous organic matter (AOM) derived predominantly from marine phytoplankton. A small amount of windblown charcoal is the only terrestrial input from the arid hinterland (Caratini et al., 1979; Summerhayes, 1983; De Leeuw et al., 1982, in De Lange et al., 1987). Organic matter does not accumulate on the continental shelf where the currents are strong but instead concentrates below 500 m at the first downslope occurrence of fine sediment (Diester-Haas and Müller, 1979; Diester-Haas, 1982; Fütterer, 1983; Summerhayes, 1983). Slumping on the margin triggers turbidity currents which lead to periodic re-sedimentation of the organic-rich slope sediment on the Madeira Abyssal Plain. AOM might be expected to concentrate in the upper portion of turbidites owing to its low density, but TOC profiles (Fig. 2; Jarvis and Higgs, 1987) suggest that it originally had a uniform vertical distribution in Madeira turbidites. The absence of appreciable woody input, the limited variation in grain size, and the overwhelming predominance of marine OM in the source area, are the main reasons for this uniformity.

In contrast to turbidites on the Madeira Abyssal Plain, many elsewhere show strong vertical variations, especially where terrestrial phytoclasts are concentrated in the coarser lower divisions because of their hydraulic equivalence to fine sand and silt grade clastics. The lower parts of many, even carbonate-rich, turbidites are thus woody, whilst the upper parts are richer in OM of algal origin (Tyson, 1984; Nwachukwu and Barker, 1985). Our optical characterisation of the organic matter as 'amorphous' is rather imprecise. Although AOM in marine settings may have a number of origins its isotopic composition usually indicates derivation from phytoplankton (Lewan, 1986). In view of our optical study, and the isotopic composition of AOM in the unoxidised part of the turbidites (-19.3 ± 0.1‰, -21.4 ± 0.2‰) we feel confident in ruling out other sources. Other studies have also indicated that the OM in the MAP turbidites is predominantly marine (De Leeuw et al., 1982, in De Lange et al., 1987).

Despite rapid deposition, and the large amounts of marine OM, sulphate reduction does not occur in most of the turbidites on the Madeira Abyssal Plain (Wilson et al., 1985; De Lange et al., 1987); only trace consumption of sulphate has been demonstrated, and this at depths below 17 m (De Lange, 1988). Reduction of iron and manganese do occur (Wilson et al., 1985, 1986; Thomson et al., 1986). Significant reduction of sulphate in deep-water sediments is often absent because the reactivity of OM is reduced by oxidation, prior to deposition (Jørgensen, 1982, 1983). Slow sulphate reduction has been noted in slope sediments at 2500 m of NW Africa (Hartmann et al., 1973), but only half the pore-water sulphate is reduced at 8 m below the sediment surface, despite the sediment containing 3–4% TOC. The slowness of this sul-

phate reduction probably reflects rapid transformation of much of the original AOM into stable humic substances (cf. Cronin and Morris, 1982), and also its partial oxidation during winnowing from the shelf and transport downslope (as noted earlier). Its partial oxidation is suggested by the high C/N weight ratios (mean 15, Hartmann et al., 1973), which are twice that of fresh planktonic detritus. An average C/N ratio of 17 has also been reported as characteristic of buried turbidites (5–18 m) from the Madeira Abyssal Plain (De Lange, 1988). The C/N ratios in the sandier shelf sediments, has been interpreted as being due to dilution by terrestrial OM (e.g. Diester-Haas and Muller, 1979; Stein et al., 1989), but in view of our optical observations and the low potential of the arid hinterland for supplying such an input, we consider partial oxidation more likely. Davis et al. (1988) suggest that significant sulphate reduction does not occur in sediments where the Hydrogen Index is less than 150. In our turbidites even the least oxidised organic matter, in the lower part of the units, has HI values less than 100 (Table 2). Thus it is not surprising that little sulphate reduction is seen in turbidites on the Madeira Abyssal Plain.

Sample preparation artefacts

Table 1 shows that variations in $\delta^{13}C$ OM of up to 0.5‰ can result from simple variations in the conditions of sample preparation prior to analysis. Similar responses to preparation method are seen in oxidised samples from above the redox front and in reduced samples from below it. In both cases the shortest drying time yields the heaviest samples (4 h at 110°C) and the most extreme drying conditions yields the lightest samples (96 hrs. at 90°C). The chemical methods used to separate organic matter from sediments differs between authors and are sometimes more severe than those reported here (cf. Lewan, 1986 and Dean et al., 1986). Sample preparation artefacts may therefore induce noise on isotopic signals of OM that may be larger than the 0.5‰ reported here.

Pyrolysis, TOC and $\delta^{13}C$ analysis

In both turbidites the first down-core colour change is taken to mark the position of maximum penetration of O_2. More deeply buried redox fronts mark the position at which NO_3 is completely reduced and reduction of Fe(III) begins (Potter et al., 1980; Lyle, 1983). In turbidite *a* these redox fronts are not separable. Below this joint redox front (at 21 cm) in turbidite *a* the TOC has a concentration of 0.55%–0.56%. In the oxic region of the turbidite TOC decreases exponentially to a minimum of 0.36% at about 5 cm after which it increases slightly in the 0–5 cm region because pelagic sedimentation and bioturbation are adding new organic matter from the sediment-water interface. In all, 35% of the TOC is oxidised. Values of $\delta^{13}C$ in Turbidite *a* are -19.3 ± 0.1‰ below the redox front and no more negative than -19.6‰ above it (Figs. 2 and 3) The oxidation of 35% of the TOC does not alter the carbon isotope composition of the OM by more than 0.3‰. In turbidite *e* about 75% of the TOC has been lost from above the upper redox front (at 74 cm) and this loss has been accompanied by a shift of about 2.5‰ in $\delta^{13}C$. The consumption of OM and the isotopic change in $\delta^{13}C$ do not coincide. At 66 cm, about 8 cm above the upper redox front, TOC has decreased by about 50% (from 0.61 to 0.31%) without an accompanying isotopic fractionation. A further decrease of TOC to 0.16% (i.e. a further decrease of 25% of the original amount) in the upper part of the turbidite is accompanied by an isotopic shift of 2.5‰. This is best seen in Fig. 3 where the co-variation of TOC and $\delta^{13}C$ is shown. The isotopic change is not coincident with the change in TOC, but the change in TOC is coincident at 74 cm with the upper of the two colour changes in this turbidite. Their is no observable change in either TOC or $\delta^{13}C$ in the interval 74-83 cm; metabolism of OM by NO_3 reducing bacteria is therefore not an important influence in our samples on either of these parameters.

The greater isotopic fractionation in turbidite *e* compared to turbidite *a*, and the greater loss of TOC is probably due to the difference in exposure time to oxic conditions experienced by the two

sediments. The O_2 redox front moves down in the cores at a rate that is diffusion-limited and decreases with depth. The O_2 front in turbidite *a* took 0.5 ka to reach its present depth of 21 cm (Thomson et al., 1988). Using the approximation $t_z = z^2/2D$ (McCorkle et al., 1985, where t_z is time to depth z and D is sediment bulk density), and also allowing for the different amounts of organic carbon consumed above the redox fronts in the turbidites, it can be calculated that the redox front in turbidite *e* took 12.3 ka to reach 74 cm. This calculation assumes that the concentration of dissolved oxygen in bottom water was the same during oxidation of both turbidites, which may not be correct. This estimate of time greatly exceeds the estimate of 4.5 ka made by Buckley and Cranston (1988), but is consistent with the observation that most of Isotope Stage 4 (12 ka) appears to be preserved in pelagic sediment overlying turbidite *e* (Weaver and Kuijpers, 1983; Jarvis and Higgs, 1987; Weaver et al., in press). Oxidation would have continued throughout this time interval, before being terminated by the emplacement of the overlying turbidite.

In turbidite *e* there is a 65% change in TOC and HI across the full thickness of the redox front. Hydrogen Index is normalised to TOC, so both independently indicate a similar magnitude of oxidation. The change in HI in turbidite *a* is about 30%. This data confirms that, above the redox front, turbidite *e* apparently suffered more oxidation than turbidite *a*.

It is clear that turbidite *e* was exposed to oxidation at least 20 times longer than turbidite *a*. This leads us to suggest that the OM in turbidite *a* had sufficient time to partially oxidise, but insufficient time for oxidation to cause isotopic fractionation. In turbidite *e* the offset step-functions in TOC and $\delta^{13}C$ (Figs. 2 and 3) suggest that above 66 cm enough time elapsed for both processes to occur; and that between 66 cm and 74 cm, a distance equivalent in time to 2.4 ka, oxidation occurred without isotopic fractionation. This time is longer than the time oxidation took to reach 21 cm in turbidite *a* because of the higher amount of reactive OM in turbidite *e* and the greater depth to the redox front.

The $\delta^{13}C$ data for turbidite *e* show a 2–3‰ shift in $\delta^{13}C$ from values of about −21.4‰ in the lower part to −23.8‰ in the upper oxidised part. The values below the redox front are typical for marine sediments at these latitudes (Newman et al., 1973; Dean et al., 1986), whilst those above the redox front are similar to those recorded from wood-rich marine deltaic sediments. A trend of $\delta^{13}C$ and TOC similar to that seen in turbidite *e* has been reported in a core from the Hatteras Abyssal Plain that contained a turbidity unit (Sackett, 1964). The OM in the core was not characterised and it was assumed that the turbidite introduced marine OM into a terrestrially dominated basin, thus explaining the lighter $\delta^{13}C$ at the top of the core. In view of the sharp decrease in TOC in the upper part of the core, we suspect that post-depositional oxic diagenesis is a viable alternative explanation of the chemical trends. Conversely, isotopic values similar to those seen in the upper part of turbidite *e* have been reported in turbiditic muds from the Gulf of Mexico (Newman et al., 1973). In view of the different nature of the sediment sources in the two areas, however, the isotopic similarity is probably fortuitous; sediments in the Gulf of Mexico *are* probably enriched in terrestrial OM, whilst those on the Madeira Abyssal Plain are not.

For turbidite *e* the $\delta^{13}C$-OM is about −21.4‰ in the lower part and −23.8‰ in the upper oxidised part. Conventional calculations of marine–terrestrial ratios of OM, based on isotopic data and using marine and terrestrial end-member values of −21 and −26‰, respectively (Popp et al., 1989; Sackett, 1989), suggest that the upper oxidised layer of the turbidite contains 50% terrestrial OM and the bottom very little. This is a trend opposite to that expected from hydraulic sorting of OM during deposition. Even if an unusually light value of −30‰ is assigned to a putative terrestrial component conventional calculation suggests 28% of terrestrial OM should be present in the upper part of the turbidite. Optical microscopy of OM residues failed to reveal any significant vertical change in the abundance of terrestrially-derived OM, and certainly none of the magnitude required to match a conventional isotopic interpretation of marine–terrestrial OM proportions. Thus the isotopic shift in turbidite *e* must result from the selective degradation of an isotopi-

cally heavy component of the marine organic matter which has left the residue isotopically light.

The isotopic composition of OM below the redox fronts in the turbidites is −21.4‰ in turbidite *e* and −19.3‰ in turbidite *a*. The 2‰ difference encompasses the range of $\delta^{13}C$ in planktonic OM at these latitudes. As the optical microscopy showed no real difference between the OM in the cores the $\delta^{13}C$ may have changed in the time between their deposition. Whether these values represent isotopic fractionations from the original AOM is not clear, but the degree of further oxidation in the turbidites needed to change $\delta^{13}C$ suggests not. Also, the OM in turbidite *e* (−21.4‰) may have experienced an isotopic shift (of about 2‰) prior to re-sedimentation on the abyssal plain, making the total isotopic fractionation as potentially as great as 4.5‰. A final complication in interpreting the 2‰ difference is that it might result from the mixing of AOM in the turbidite with AOM entrained from the sediment surface by passage across the abyssal plain.

Consequences of isotopic fractionation

The isotopic composition of dissolved inorganic carbon (DIC) in pore water is strongly influenced by inputs of CO_2 and HCO_3^- produced by oxidation of organic matter. The relation between $\delta^{13}C$ of OM in sediments and $\delta^{13}C$ of DIC in marine pore water in abyssal sediments is not well described by available pore-water models, which assume a bulk OM value for $\delta^{13}C$ in their calculations (McCorkle et al., 1985, 1988; Sayles and Curry, 1988; McArthur, 1989). Isotopic fractionation of organic matter during diagenesis may lead to DIC inputs with $\delta^{13}C$ different to that in bulk OM and enable measured and modelled values to be reconciled. Isotopic fractionation of OM was rejected by McArthur (1989) as a viable explanation for differences between measured and modelled values of $\delta^{13}C$-DIC in pore waters from turbidite *a* but on the basis of only a small number of analyses of $\delta^{13}C$-OM. The additional data presented here confirms the previous finding that little ($\leq$ 0.3‰) isotope fractionation *is now manifest* in the isotopic composition of the OM, but does not prove that it is not occurring. Isotopic fractionation in the solid phase would not yet be too apparent if the OM in turbidite *a* is only now entering a period of isotopic change after a prolonged period (0.5 ka) of oxidation without fractionation, as the step functions in $\delta^{13}C$, HI and TOC show happened in turbidite *e*.

Isotopic fractionation of OM may well be applicable to modelling $\delta^{13}C$-DIC in turbidites and in slowly accumulating pelagic sediments (McCorkle et al., 1985; Sayles and Curry, 1988). In slowly accumulating sediments (sedimentation rates of the order of 1 cm/ka) and sediments exposed to oxidation for long periods ($>10^3$ yrs), OM would have sufficient time to undergo isotopic fractionation. In turbidite *e* an isotopic fractionation of 2.5‰ accompanies the TOC decrease from 0.31 to 0.16% in the upper regions of the turbidite. The DIC added to pore water over this interval must have had an isotopic composition of -18.4‰, about 2‰ heavier than the OM. The fractionation required by McCorkle et al. (1985) to match measurement to modelled $\delta^{13}C$ in DIC was 1.5‰, (a figure well within the range our turbidite data suggests) and achievable by oxidation of OM. Furthermore, Sayles and Curry (1988) suggest that isotopic fractionation cannot easily explain the difference in measured and modelled values for DIC in their sediments because less than 2% of the OM reaching the sediment was preserved and buried. Our data suggest extensive oxidation can occur without fractionation, and be followed by a period of small loss in TOC but high isotopic fractionation. Isotopic fractionation of organic matter should be re-examined as a possible cause of the discrepancies between modelled and measured values of DIC in abyssal pore-waters.

We infer from our data that oxidation may be a significant source of variation of $\delta^{13}C$ in the OM of pelagic and turbiditic sediments. It certainly needs to be taken into account when calculating marine–terrestrial ratios of OM in slowly or discontinuously accumulating oxic facies. Long-term variation in bottom water oxygenation may also be a significant variable in determining whether oxidation is sufficiently intense to result in isotopic fractionation.

The possible time-variant nature of isotopic fractionation may introduce 'noise' into the iso-

topic record of marine-OM and hamper identification of trends in the data. $\delta^{13}C$ of terrestrial and marine OM differ by between 0 and 7‰ for different periods in the Phanerozoic (Dean et al., 1986; Hayes et al. 1989; Popp et al., 1989); the change in $\delta^{13}C$ we see on oxidation of OM in turbidite *e* is 35% of the maximum difference. The degree of isotopic fractionation may depend on concentrations of dissolved oxygen and these have not always been similar to those of today. Lower concentrations in the past may have resulted in different degrees of isotopic fractionation during oxic respiration.

Finally, the influence of time on isotopic fractionation of organic matter may be one reason (out of many) for the variety of conflicting reports in the literature regarding the occurrence, or non-occurrence of isotopic fractionation of organic matter during degradation. Published reports carry too little data to permit this idea to be tested.

Summary

Preparing samples for isotopic analysis by different methods can result in differences of up to 0.5‰ in $\delta^{13}C$, so caution must be exercised when comparing $\delta^{13}C$ data from different authors using different sample preparation techniques. Isotopic fractionation of marine-derived OM requires >0.5 ka to occur at abyssal temperatures and bacterial populations. A substantial component of OM can be oxidised without isotopic fractionation. Continued exposure to oxygen causes further degradation and substantial isotopic fractionation. This isotopic fractionation may be the reason why isotopic modelling of marine abyssal pore-water fails to predict their isotopic compositions. The time-variant nature of isotopic fractionation may partly explain some of the conflicting reports in the literature regarding the extent of isotopic fractionation on degradation of organic matter. Isotopic fractionation on organic matter degradation may also introduce noise into the isotopic record and obscure temporal trends in the isotopic composition of OM. In slowly, or discontinuously accumulating marine sediments oxidation of OM may result in isotopic compositions appearing terrestrial rather than marine. As with other bulk geochemical techniques (such as elemental analysis and pyrolysis) source characterisation with stable isotopic signatures of partially degraded marine organic matter may yield erroneous interpretations unless integrated with optical methods.

Acknowledgements

Samples were collected during cruises of RRS *Discovery* during 1985 and 1986. The crew are thanked for their assistance in sampling. The isotopic measurements were made by the first author in the Stable Isotope Laboratory of the Department of Geology at Royal Holloway and Bedford New College. The laboratory is partly funded by the University of London as an Intercollegiate Facility. We thank S. Wood (UCL/NRG) for preparing samples for optical microscopy of OM residues, A.O. Osborn for assistance with sample preparation and I. Harrison (NRG) for the pyrolysis measurements.

References

Buckley, D.E. and Cranston, R.E., 1988. Early diagenesis in deep sea turbidites: the imprint of paleo-oxidation zones. Geochim. Cosmochim. Acta, 52: 2925-2939.

Cai, D.L., Tan, F.C. and Edmond J.M., 1988. Sources and transport of particulate organic carbon in the Amazon River. Estuarine Coastal Shelf Sci., 26: 1-14.

Caratini, C., Bellet, J. and Tissot, C., 1979. Étude microscopique de la matière organique: palynologie et palynofaciès. In: Géochime Organique des Sediments Marins Profonds: ORGON III, Mauritanie-Sénégal-Isles du Cap-Vert. CNRS, Paris, pp 215–265.

Caratini, C., Bellet, J. and Tissot, C., 1983. Les palynofaciès: représentation graphique, intérêt de leur étude pour les reconstructions paléogéographiques. In: Géochime Organique des Sediments Marins d'ORGON à MISEDOR. CNRS, Paris, pp 3278–351.

Colley, S. and Thomson, J., 1985. Recurrent uranium relocations in distal turbidites emplaced in pelagic conditions. Geochim. Cosmochim. Acta, 49: 2339–48.

Cronin, J.R. and Morris, R.J., 1982. The occurrence of high molecular weight humic material in Recent organic-rich sediments from the Namibian shelf. Estuarine Coastal Shelf Sci., 15: 17–27.

Davis, H.R., Byers, C.W. and Dean, W.E., 1988. Pyrite formation in the Lower Cretaceous Maury Shale: effect of organic matter Type and reactive iron content. Am. J. Sci., 288: 873–890.

Dean, W., Arthur, M.A. and Claypool, G.E., 1986. Depletion of 13C in Cretaceous marine organic matter: source, diagenetic or environmental signal? Mar. Geol. 70: 119–157

Deines, P., 1980. The isotopic composition of reduced organic carbon. In: P. Fritz and J.-Ch. Fontes (Editors), Handbook of Environmental Isotope Geochemistry. Vol. 1: The Terrestrial Environment, (A). Elsevier, Amsterdam, pp. 329–406.

De Lange, G.J., 1986. Early diagenetic reactions in interbedded pelagic and turbiditic sediments in the Nares Abyssal Plain (western North Atlantic): consequences for the composition of sediment and interstitial water. Geochim. Cosmochim. Acta, 50: 2543–2561.

De Lange, G.J., Jarvis, I. and Kuijpers, A., 1987. Geochemical characteristics and provenance of late Quaternary sediments from the Madeira Abyssal Plain, N Atlantic. In: P.P.E. Weaver and J. Thomson (Editors), Geology and Geochemistry of Abyssal Plains. Geol. Soc. London Spec. Publ., 31: 147–165.

De Lange, G.J., 1988. Geochemical and early diagenetic aspects of interbedded pelagic-turbiditic sediments in two N. Atlantic Abyssal Plains. Geol. Ultraiectina, 157: 189 pp.

De Leeuw, J.W., Viets, T.C. and Schenck, P.A., 1982. Een vergelijkend onderzoek van 8 sedimentmonsters uit het Canary-Basin en 9 sedimentmonsters uit het Angola-Basin met Curie-punt Pyrolyse Massaspectrometrie. Rep. TH Delft FOM Inst. At. Mol. Phys., Amsterdam, pp 1–6.

Diester-Haas, L., 1982. Indicators of water depth in bottom sediments of the continental margin off West Africa. Mar. Geol., 49: 311–326.

Diester-Haas, L. and Müller, P.J., 1979. Processes influencing sand fraction composition and organic matter content in surface sediments off W Africa (12–19° N). 'Meteor' Forschungsergeb., Reihe C, 31: 21–47.

Fütterer, D.K., 1983. The upwelling record off northwest Africa. In: J. Thiede and E. Suess (Editors), Coastal Upwelling: Its sediment record. Part B: Sedimentary Records of Ancient Coastal Upwelling. Plenum, New York, pp. 105–121

Gearing, P.J., Plucker, F.E. and Parker, P.L., 1977. Organic carbon stable isotope ratios of continental margin sediments. Mar. Chem., 5: 251–266.

Gearing, J.N., Gearing, P.J., Rudnick, D.T., Requejo, A.G. and Hutchins, M.J., 1984. Isotopic variability of organic carbon in a phytoplankton based temperate estuary. Geochim. Cosmochim. Acta, 48: 1089-1098.

Goldhaber, M.B., Aller, R.C., Cochran, J.K., Rosenfeld, J.K., Martens, C.S. and Berner, R.A., 1977. Sulphate reduction, diffusion, and bioturbation in Long Island Sound sediments: Report of the FOAM Group. Am. J. Sci., 277: 193–237.

Hartmann, M., Muller, P., Suess, E. and Van der Weiden, C-H., 1973. Oxidation of organic matter in recent marine sediments. 'Meteor' Forschungsergeb., Reihe C, 12: 74–86.

Hatcher, P.G., Spiker, E.C., Szeverenyi, N.M. and Maciel, G.E., 1983. Selective preservation and origin of petroleum-forming aquatic kerogen. Nature, 305: 498–501.

Hedges, J.I. and Parker, P.L., 1976. Land-derived organic matter in surface sediments from the Gulf of Mexico. Geochim. Cosmochim Acta, 40: 1019–1029.

Jarvis, I. and Higgs N., 1987. Trace element mobility during early diagenesis in distal turbidites: late Quaternary of the Madeira Abyssal Plain, N Atlantic. In: P.P.E. Weaver and J. Thomson (Editors), Geology and Geochemistry of Abyssal Plains. Geol. Soc. London Spec. Pub., 31: 179–213.

Jasper, J.P. and Gagosian, R.B., 1990. The sources and deposition of organic matter in the Late Quaternary Pigmy Basin, Gulf of Mexico. Geochim. Cosmochim. Acta, 54: 1117–1132.

Jørgensen, B.B., 1982. Mineralisation of organic matter on the sea bed: the role of sulphate reduction. Nature, 296: 643–645.

Jørgensen, B.B., 1983. Processes at the sediment-water interface. In: B. Bolin and R.B. Cook (Editors), The Major Biogeochemical Cycles and their Interactions. Wiley, New York, pp. 477–515.

Kennicutt, M.C. II, Barker, C., Brooks, J.M., DeFreitas, D.A. and Zhu, G.H., 1987. Selected organic matter source indicators in the Orinoco, Nile and Changjiang deltas. Org. Geochem., 11: 41–51.

Lewan, M.D., 1986. Stable carbon isotopes of amorphous herogens from Phanerozoic sedimentary rocks. Geochim. Cosmochim. Acta, 50: 1583–1591.

Lyle, M., 1983. A brown-green color transition in marine sediments: a marker of the Fe(III)-Fe(II) redox boundary. Limnol. Oceanogr, 28: 1026–1033.

McArthur, J.M., 1989. Carbon isotope geochemistry of calcite, organic matter and pore water in turbidites on the Madeira Abyssal Plain. Geochim. Cosmochim. Acta, 53: 2997–3004.

McCorkle, D.C., Emerson, S.R. and Quay, P.D., 1985. Stable carbon isotopes in marine pore waters. Earth Planet. Sci. Lett., 74: 13–26.

Newman, J.W., Parker, P.L. and Behrens, E.W., 1973. Organic carbon isotope ratios in Quaternary cores from the Gulf of Mexico. Geochim. Cosmochim. Acta, 37: 225–238.

Nwachukwu, J.I. and Barker, C., 1985. Variations in kerogen densities of sediments from the Orinoco Delta. Chem. Geol., 51: 193–198.

Peters, K.E., 1986. Guidelines for evaluating petroleum source rocks using programmed pyrolysis. Am. Assoc. Pet. Geol. Bull., 70: 318–329.

Popp, B.N., Takigiku, R., Hayes, J.M., Louda, J.W. and Baker, E.W., 1989. The post-Paleozoic chronology and mechanism of δ^{13} depletion in primary marine organic matter. Am. J. Sci., 289: 436–454.

Potter, P.E., Maynard, J.B. and Pryor, W.A., 1980. Sedimentology of Shale. Springer, Berlin, pp 53–58.

Sackett, W.M., 1964. The depositional history and isotopic organic carbon composition of marine sediments. Mar. Geol., 2: 173–185.

Sackett, W.M., 1989. Stable carbon isotope studies on organic matter in the marine environment. In: P. Fritz and J.-Ch. Fontes, (Editors). Handbook of Environmental Isotope Geochemistry. Vol. 3. Elsevier, Amsterdam, p. 139–170.

Sayles, F.L. and Curry, W.B., 1988. δ^{13}C, TCO2, and the metabolism of organic carbon in deep sea sediments. Geochim. Cosmochim. Acta, 52: 2963–2978.

Schultz, D.J. and Calder, J.A., 1976. Organic carbon 13C/12C variations in estuarine sediments. Geochim. Cosmochim. Acta, 40: 381–385.

Searle, R.C., Schultheiss, P.J., Weaver, P.P.E., Noel, M., Kidd, R.B., Jacobs, C.L. and Huggett, Q.J., 1985. Great Meteor East (distal Madeira Abyssal Plain): geological studies of its suitability for disposal of heat-emitting radioactive wastes. Inst. Oceanogr. Sci. Rep. 193, 162 pp.

Showers, W.J. and Angle, D.G., 1986. Stable isotopic character-

isation of organic carbon accumulation on the Amazon continental shelf. In: C.A Nittrouer and D.J. DeMaster (Editors). Sedimentary Processes on the Amazon Continental Shelf. Cont. Shelf Res., 6: 227–244.

Spiker, E.C. and Hatcher, P.G., 1984. Carbon isotope fractionation of sapropelic organic matter during early burial diagenesis. Org. Geochem. 5: 238–290.

Spiker, E.C. and Hatcher, P.G., 1987. The effect of early burial diagenesis on the chemical and stable carbon isotopic composition of wood. Geochim. Cosmochim. Acta 51: 1385–1391.

Stein, R., Ten Haven, H.L., Littke, R., Rullkotter, J. and Welte, D.H., 1989. Accumulation of marine and terrigenous organic carbon at upwelling Site 658 and non-upwelling Sites 657 and 659: implications for the reconstruction of paleoenvironments in the eastern subtropical Atlantic through Late Cenozoic times. Proc. ODP, Sci. Results, 108: 361–385.

Summerhayes, C.P., 1983. Sedimentation of organic matter in upwelling regimes.In: J. Thiede and E. Suess (Editors), Coastal Upwelling: Its Sediment Record. Part B: Sedimentary Records of Ancient Coastal Upwelling. Plenum, New York, pp. 29–72.

Tan, F.C. and Strain, P.M., 1979. Organic carbon isotope ratios in Recent sediments in the St Lawrence Estuary and the Gulf of St Lawrence. Estuarine Coastal Mar. Sci., 8: 213–225.

Thomson, J., Higgs, N.C., Jarvis, I., Hydes, D.J., Colley, S. and Wilson, T.R.S., 1986. The behaviour of manganese in Atlantic carbonate sediments. Geochim. Cosmochim. Acta, 50: 1807–1818.

Thomson, J., Colley, S., Higgs, N.C., Hydes, D.J., Wilson, T.R.S. and Sørensen, J., 1987. Geochemical oxidation fronts in NE Atlantic distal turbidites and their effects in the sedimentary record. In: P.P.E. Weaver and J. Thomson (Editors), Geology and Geochemistry of Abyssal Plains. Geol. London Soc Spec. Pub, 31: 167–177.

Tissot, B.P. and Welte, D.H., 1984. Petroleum Formation and Occurrence. Springer, Berlin, 2nd ed., 699 pp.

Tyson, R.V., 1984. Palynofacies investigation of Callovian (Middle Jurassic) sediments from DSDP Site 534, Blake-Bahamas Basin, western Central Atlantic. Mar. Pet. Geol., 1: 3–13.

Weaver, P.P.E. and Kuijpers, A., 1983. Climatic control of turbidite deposition on the Madeira Abyssal Plain. Nature, 306: 360–363.

Weaver, P.P.E., Searle, R.C. and Kuijpers, A., 1986. Turbidite deposition and the origin of the Madeira Abyssal Plain. In: C.P. Summerhayes and N.J. Shackleton (Editors), North Atlantic Palaeoceanography. Geol. London Soc. Spec. Pub, 21: 131–143.

Weaver, P.P.E., Rothwell, R.G., Ebbing, J., Gunn, D. and Hunter, P.M., in press. Correlation, frequency of emplacement and source directions of megaturbidites on the Madeira Abyssal Plain. In: J. Middelburg and Nakashima (Editors), Geochemistry of North Atlantic Abyssal Plains. Mar. Geol.

Wilson, T.R.S., Thomson, J., Colley, S., Hydes, D.J. and Higgs, H.C., 1985. Early organic diagenesis: the significance of progressive subsurface oxidation fronts in pelagic sediments. Geochim. Cosmochim. Acta, 49: 811–822.

Wilson, T.R.S, Thomson, J., Hydes, D.J., Colley, S., Culkin, F. and Sorensen, J., 1986. Oxidation fronts in pelagic sediments: diagenetic formation of metal-rich layers. Science, 232: 972–975.

Marine Geology, 105 (1992) 63–76
Elsevier Science Publishers B.V., Amsterdam

Petrology and geochemistry of a dredged clinopyroxenite–dolerite basal complex from the Jan Mayen volcanic province, Norwegian–Greenland Sea

J.C. Bailey[a], J. Campsie[b], N. Hald[c], F. Dittmer[b], S. Fine[b] and M. Rasmussen[b]

[a]*Institute for Petrology, Copenhagen University, Øster Voldgade 10, DK 1350 Copenhagen K, Denmark*
[b]*Ocean Study Group, Borgergade 34, DK 1300 Copenhagen K, Denmark*
[c]*Geological Museum, Øster Voldgade 5–7, DK 1350 Copenhagen K, Denmark*

(Received February 19, 1991; revision accepted September 12, 1991)

ABSTRACT

Bailey, J.C., Campsie, J., Hald, N., Dittmer, F., Fine, S. and Rasmussen, M., 1992. Petrology and geochemistry of a dredged clinopyroxenite–dolerite basal complex from the Jan Mayen volcanic province, Norwegian–Greenland Sea. Mar. Geol., 105: 63–76.

Serpentinised plagioclase–olivine clinopyroxenite and dolerite fragments were dredged from the western Jan Mayen Fracture Zone, near its intersection with the Kolbeinsey Ridge. According to major and trace element analyses of the rocks and minerals (a) the clinopyroxenite represents cumulates which crystallised from a Jan Mayen-like alkaline magma at an intermediate basaltic stage in the uppermost mantle or lower crust, and (b) the dolerite fragments constitute an oceanic, within-plate tholeiitic series with alkaline affinities. These rocks have been subjected to serpentinization, low–medium grade metamorphism, metasomatism, brecciation and veining, part of which probably took place during fracture zone tectonism. By analogy with the geological development of the Canary Islands, they are considered to form part of a layered basal complex to the alkaline Jan Mayen volcanic province.

Geological setting

The Jan Mayen Fracture Zone (JMFZ) consists of two segments extending from the Vøring Plateau off the Norwegian coast to the Greenland shelf (Talwani and Eldholm, 1977). The western segment dextrally offsets the Mid-Atlantic Ridge (Kolbeinsey Ridge and Mohns Ridge) by ca. 200 km. Jan Mayen is located between the two offset parts.

In 1973, USNS *Lynch* conducted a seismic and dredging survey of the western JMFZ (Campsie, 1976) (Fig. 1). The Kolbeinsey Ridge axis yielded typical ocean ridge tholeiite (Dittmer et al., 1975), but around Jan Mayen the dredged igneous rocks were considered to define an extensive, alkaline Jan Mayen volcanic province (Campsie, 1976; Pedersen et al., 1976). Ankaramite and trachybasalt are the most common rock types, but trachyandesite, trachyte and tuff–agglomerate are also present. A close relationship may be inferred with the alkaline rocks of Jan Mayen which were described by Imsland (1984).

A depression in excess of 3000 m deep is found at the northern extension of Kolbeinsey Ridge. A seismic reflection line across the depression (Johnson and Campsie, 1976, fig. 3) indicates a lack of sediment accumulation and an irregular rough bottom indicating youth. The north escarpment of the Iceland Plateau (south wall of JMFZ) is also rough, suggesting faulting. From the rugged south wall of the depression, and ca. 45 km (crustal age ca. 4.5 Ma) east of the termination of the Kolbeinsey Ridge axis, dredging recovered 6 kg of rocks (dredge 13; 71°33.0'N, 11°36.2'W; depth 2500 m). The angular fragments have surfaces with thin films of ferric oxide; manganese crusts are absent. Among fragments larger than 5 cm, about 60% are coarse-grained clinopyroxenite and 40%

0025-3227/92/$05.00 © 1992 — Elsevier Science Publishers B.V. All rights reserved

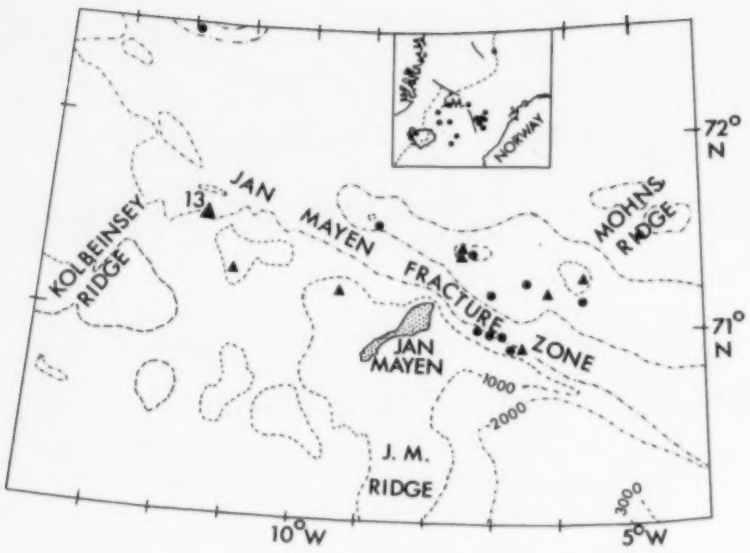

Fig. 1. Locality and topography map for dredge 13, western Jan Mayen Fracture Zone. Triangles (Campsie, 1976) and dots (Kharin, 1980; Neumann and Schilling, 1984) indicate other dredge stations where alkaline igneous rocks have been recovered. Inset shows regional setting (solid lines = fracture zones; dashed lines = Mid-Atlantic Ridge) and DSDP sites (dots).

are doleritic. Only individual fragments of other rock types (greenstone and ankaramite) are found.

Pedersen et al. (1976) found an $^{87}Sr/^{86}Sr$ ratio in a dredge 13 "microdiorite" (dolerite 26004) of 0.70344, similar to the values they determined elsewhere in the Jan Mayen volcanic province (0.70327–0.70364). An associated clinopyroxenite (26152) had a significantly higher value of 0.70435. The age determinations on the dredge 13 rocks (Campsie et al. (1990) are summarised below.

The object of this paper is to describe and interpret the origin of the dredge 13 rocks in relation to their geological setting.

Analytical methods

Seventeen rock fragments were analysed for major elements by the Geological Survey of Greenland (Copenhagen). Major elements, with the exception of Na and Mg, were analysed by X-ray fluorescence (Siemens SRS-1) on glass discs; Fe^{2+} was analysed by the metavanadate technique and H_2O^+ by the Penfield method. Na and Mg were obtained by flame photometry and atomic absorption. The authors analysed most trace elements on powder pellets (Norrish and Chappell, 1977) using a Philips PW 1400 X-ray spectrometer. Li was analysed by activation analysis and Cerenkov counting, and U by delayed neutron counting.

A Hitachi XMA-5B scanning electron microanalyser (microprobe) was used for the mineral analyses. The analyses have been corrected after Springer (1967) and Sweatman and Long (1969). The correction programme, EMSKOR, was written by J.G. Rønsbo (unpublished).

Petrography

Clinopyroxenite

The ultramafic fragments are greyish-green, coarse-grained rocks dominated by diopside (60–85 vol.%). Olivine, plagioclase and ore minerals together constitute less than 2%. The remainder is serpentine with subordinate chlorite and tremolite. The texture is allotriomorphic granular; no banding has been observed in thin section, but it is weakly visible in hand specimen. A few fragments are brecciated.

Pyroxene crystals in sample 26152 have a weak orientation of their *b*-axes (N.I. Christensen, pers. commun., 1979), which suggests weak flow in a fracture zone or the upper mantle, rather than well-oriented cumulus crystals.

The clinopyroxene is a diopside, $Mg_{46}Fe_7Ca_{47}$ (Table 1, Fig. 2A), with a fairly high concentration of Cr_2O_3 (0.45%) and a low content of Na_2O (0.25%). It can be matched exactly with diopside from Jan Mayen (Imsland, 1984) and thus also crystallised from a ne-normative basalt. In detail, the fit is best for diopside from the Jan Mayen intermediate stage of basalt fractionation.

The olivine is homogeneous (Fo_{86-84}), and is characterised by low concentrations of CaO (0.05%). Plagioclase (An_{85-90}) is sparse. Opaque minerals include magnetite, ilmenite and chromite. The chromite is Mg-poor, unlike the chromite from other ocean floor peridotite and clinopyroxenite samples (Nicholls et al., 1981; Michael and Bonatti, 1985). Chalcopyrite and cubanite are the most important sulphide minerals, but small grains of pyrite are also present. The ultramafic fragments can be classified as plagioclase–olivine clinopyroxenite (IUGS, 1973).

The serpentine forms irregular schlieren together

TABLE 1

Mineral analyses from dredge 13 rocks, western Jan Mayen Fracture Zone

Number:	26152	26153	26006	26152	26153	26163	26163	26004	26157	26153	26153	26153
Host rock:	Cpxite	Cpxite	Cpxite	Cpxite	Cpxite	Dolerite	Dolerite	Dolerite	Trem. vein	Cpxite	Cpxite	Cpxite
Mineral:	Olivine	Olivine	Diopside	Diopside	Diopside	Augite	Augite	Augite	Tremolite	Ilmenite	Chromite	Magnetite
SiO_2	40.1	40.0	51.1	51.1	51.2	51.4	50.3	51.9	56.6	0.15	0.75	0.45
TiO_2	0.04	0.05	0.70	0.84	0.80	0.75	1.1	0.08	0.10	51.8	1.0	0.25
Al_2O_3	<0.02	<0.02	3.5	4.1	4.1	3.3	3.6	0.55	1.60	0.10	19.3	0.35
Cr_2O_3	<0.02	<0.02	0.45	0.48	0.40	0.05	0.05	0.02	0.00	0.15	30.2	1.1
Fe_2O_3	–	–	–	–	–	–	–	–	–	3.43	13.74	67.16
FeO	14.8	15.5	4.6	4.8	4.7	5.5	9.3	10.8	2.9	37.91	29.84	29.09
MnO	0.25	0.25	0.15	0.10	0.15	0.15	0.20	0.57	0.10	2.4	0.50	0.10
MgO	44.9	44.3	16.2	15.8	15.8	16.7	14.9	12.6	22.1	3.6	4.1	1.8
CaO	<0.02	0.05	23.0	23.0	22.6	20.4	20.3	22.4	13.3	0.00	0.00	0.10
Na_2O	<0.02	<0.02	0.25	0.21	0.25	0.25	0.30	0.46	0.40	–	–	–
K_2O	<0.02	<0.02	<0.02	0.04	0.02	–	–	–	<0.02	–	–	–
Sum	100.15	100.15	99.95	100.5	100.0	98.5	100.05	99.4	97.1	99.5	99.4	100.4

Analyst: N. Hald. Fe_2O_3 in ilmenite, chromite and magnetite calculated on the basis of 4, 24 and 24 cations, respectively.

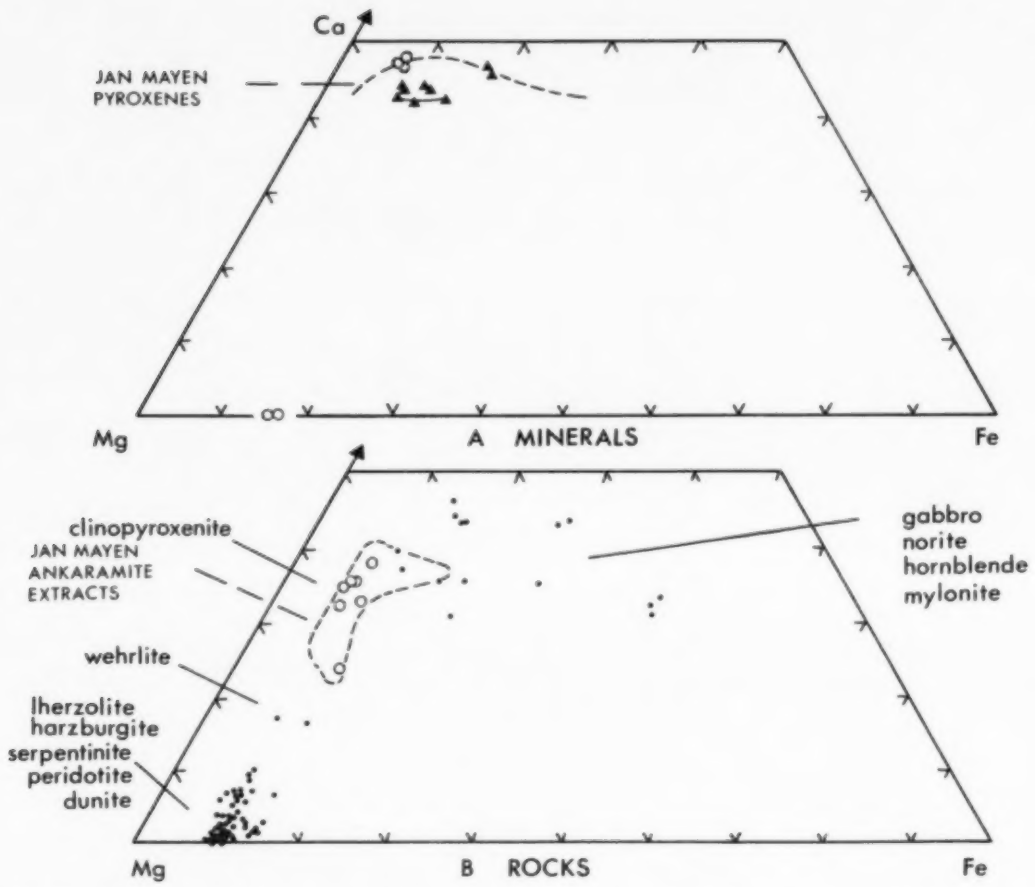

Fig. 2. Ca–Mg–Fe compositions. (A) Mafic minerals in dredge 13 rocks. Circles = clinopyroxenite; triangles = dolerite; tie lines join phenocrysts to Fe-richer groundmass crystals. The clinopyroxene trend for Jan Mayen is from Imsland (1984). (B) Rocks. Dredge 13 clinopyroxenite shown as circles. Ocean-floor ultramafic and associated rocks shown as dots: Engel and Fisher, 1969; Miyashiro et al., 1969; Vinogradov et al., 1969; Hekinian, 1970, 1982; Aumento and Loubat, 1971; Bonatti et al., 1971; Melson and Thompson, 1971; Melson et al., 1972; Hekinian and Aumento, 1973; Prinz et al., 1976; Michael and Bonatti, 1985; Shibata and Thompson, 1986. The field for crystal extracts from Jan Mayen ankaramite is calculated from Imsland (1984).

with small amounts of chlorite. In sample 26152, the schlieren are linked by many subparallel fractures also filled with serpentine. Of all the clinopyroxenite phases, the serpentine has the highest levels of K_2O (0.06%).

In some fragments the serpentine and margins of diopside grains are replaced by aggregates of tremolite, with subordinate serpentine, chlorite, hydrogarnet, sphene and ore minerals. Sample 26157 consists exclusively of tremolite (Table 1) plus chlorite, and possibly represents a vein filling.

A few veins of brown serpentine plus minor calcite cut the ultramafic fragments after the stage of tremolitization. Later brecciation associated with tremolite has also been noted in two samples.

We conclude that various degrees of metamorphism and tectonism were imposed on the clinopyroxenite following primary crystallization and serpentinization and that these few ultramafic fragments were derived from a fairly extensive body of clinopyroxenite.

Dolerite

The fragments gathered under this heading range from dolerite to amphibole-rich rocks of dioritic appearance. Plagioclase laths are generally less than 2 mm in length and the size of the other minerals is less than 1 mm. The samples are partially recrystallised under greenschist or lower amphibolite facies but lack foliation.

In dolerite 26163, the plagioclase laths are partly replaced by sericite, chlorite and small amounts of epidote. The pale brown augite is fresh, and it occurs as rare phenocrysts and as subhedral grains in the groundmass. The phenocrysts have the composition $Mg_{48}Fe_9Ca_{43}$, whereas the groundmass grains are richer in Fe/Mg but poorer in Ca,

as is typical for the tholeiitic series (Table 1, Fig. 2A). Fine-scale lamellar intergrowths of magnetite and ilmenite, rod-shaped ilmenite and irregular grains of haematite are important oxide phases. Interstitial quartz is present in subordinate amounts. Aggregates of chlorite, enclosing grains of epidote and hydroandradite–grossular (according to microprobe analysis), constitute almost 10% of the fragment.

In samples 26159, 26160 and 26164, the clinopyroxene ($Mg_{45}Fe_{11}Ca_{44}$) is usually completely replaced by chlorite and green amphibole. Plagioclase ranges from An_{61} to An_{50}. Tiny grains of sphene are common.

A "microdioritic" fragment, 26004, contains plagioclase (An_{57-25}), K-feldspar, quartz, clinopyroxene, green amphibole, biotite, apatite and ore minerals. The clinopyroxene ($Mg_{36}Fe_{18}Ca_{46}$) is largely replaced by chlorite and minor amphibole, probably actinolite. The pyroxene trend of dolerites 26163 to 26004 (Fig. 2A), an increase in Fe/Mg along with whole-rock ratios and an enrichment in Ca, is probably non-igneous and arises from progressive re-equilibration with the Ca-poorer metamorphic amphibole (magnesiohornblende). The biotite ($Mg_{51}Fe_{49}$) is rich in TiO_2 (4.8%). The opaque oxides are magnetite and ilmenite, usually coarsely intergrown, and haematite. Rare sulphides (pyrite and chalcopyrite) are generally surrounded by a rim of haematite. Irregular microsyenitic veins of quartz and alkali feldspar (Or_{90-84}, Ab_{16-10}) are present.

Another sample of similar appearance, 26166B, has a breccia-like structure with subangular dolerite fragments enclosed in a quartz microsyenite matrix. The microsyenite (26166A) consists of quartz, plagioclase and orthoclase together with green amphibole, biotite and opaques which are similar in appearance to the same minerals in the adjacent dolerite and are probably xenocrystal. A few sulphide–calcite–quartz veins with bleached (chloritised and sericitised) margins were introduced before the intrusion of the microsyenite. The microsyenite veins possess diffuse and wavy margins with no signs of a chilled contact.

A fractured greenstone sample, 26165, consists mainly of chlorite and green amphibole, but relics of olivine phenocrysts and ophitic texture can still be discerned.

Chemistry

Clinopyroxenite

The higher MgO samples of clinopyroxenite tend to carry more Ni and Co and also possess higher percentages of serpentine which most likely developed at the expense of olivine (originally 3–25 wt.%) (Table 2).

Because of the abundant diopside, the dredge 13 clinopyroxenite fragments differ from almost all other described ocean floor ultramafic rocks in their high contents of CaO (12.5–18.0 wt.%) (Fig. 2B). An analysis of clinopyroxenite from the Ob Trench in the Indian Ocean (Hekinian, 1970) is fairly close to the dredge 13 samples, but clinopyroxenite dredged southwest of Australia appears to have been recrystallised and metasomatised, forming Ti- and K-rich kaersutite and phlogopite (Nicholls et al., 1981). The dredge 13 samples possess low Rb, Sr, Ba, Na and K contents, suggesting that they have largely avoided LIL element metasomatism. Only trace amounts of K_2O are associated with the serpentine.

The diopside separated from fragment 26152 contains 212 ppm Ni and 2550 ppm Cr. Clinopyroxene in peridotite nodules and alpine-type intrusions, or as early cumulate horizons and phenocrysts derived from basalts, almost always contain more than 250 ppm Ni and 3000 ppm Cr (Brown, 1967; Frey et al., 1974). However, much lower levels of Ni and Cr are recorded in clinopyroxene from evolved basalt; thus the dredge 13 diopside should be assigned to an intermediate stage of basalt fractionation.

Various geochemical parameters can be used to determine the parental magma type and tectonic setting of the dredge 13 clinopyroxenite. Ti contents of igneous clinopyroxene depend both on the Ti content of the parental magma and its fractionation stage (Fig. 3). Diopside from dredge 13 clinopyroxenite falls in the ankaramitic and basaltic field of the Jan Mayen series and is thus richer in Ti than clinopyroxene in (a) MORB and island arc (orogenic) magma series, (b) peridotite

TABLE 2

Major and trace element analyses of dredge 13 clinopyroxenite, tremolite–chlorite vein and diopside separated from clinopyroxenite

Number	1 26152	2 26153	3 26007	4 26156	5 26262	6 26008	7 26006	8 26157	9 26152DIO
Major elements (%)									
SiO_2	45.2	47.6	50.4	47.7	47.4	51.3	49.8	47.2	51.3
TiO_2	0.56	0.55	0.60	0.63	0.66	0.61	0.65	0.44	0.77
Al_2O_3	2.34	3.18	4.22	3.70	3.98	3.10	4.60	5.80	3.65
Fe_2O_3	4.97	3.86	1.35	1.65	0.54	0.99	2.44	2.25	2.50
FeO	3.87	3.38	4.19	3.70	4.02	4.27	3.71	5.04	2.66
MnO	0.15	0.15	0.16	0.14	0.14	0.18	0.09	0.10	0.13
MgO	24.0	20.2	19.9	19.8	19.8	18.6	17.9	24.0	16.5
CaO	12.5	16.0	15.3	16.9	16.7	16.1	18.0	8.90	22.0
Na_2O	0.22	0.25	0.29	0.28	0.14	0.44	0.26	0.18	0.07
K_2O	0.063	0.060	0.049	0.059	0.041	0.045	0.27	0.023	0.02
P_2O_5	0.01	0.02	0.03	0.03	0.03	0.02	0.02	0.01	0.02
H_2O^-	0.63	0.60	0.41	1.03	1.30	0.92	0.50	1.05	0.15
H_2O^+	5.38	3.98	3.53	3.98	4.50	2.47	1.66	4.71	0.40
Sum	99.89	99.83	100.43	99.60	99.25	99.05	99.90	99.70	100.17
FeO*/MgO	0.35	0.34	0.27	0.26	0.23	0.28	0.33	0.29	0.30
Trace elements (ppm)									
Li	4.4	6.5	2.1	7.7	3.7	9.1	5.2	2.5	–
Rb	0.9	0.8	0.4	0.5	0.2	<0.2	4.1	0.4	0.9
Sr	24	33	22	49	53	24	40	5.2	37
Ba	21	24	17	25	18	18	144	7	10
Pb	5	<1	<1	7	3	<1	4	<1	<1
La	2	4	7	5	6	8	5	<1	3
Ce	6	7	9	5	7	9	7	4	6
Nd	5	6	7	5	5	7	6	4	7
Y	5	6	7	7	6	5	7	3	7
Zr	16	16	19	18	23	17	19	22	22
Nb	1	1	3	1	3	1	1	7	1
Th	<1	<1	<1	<1	<1	<1	<1	<1	<1
V	171	185	221	216	210	188	226	175	214
Cr	1720	1960	2180	1970	1620	2030	1970	264	2550
Ni	536	528	338	503	535	195	412	884	212
Co	86	90	50	65	68	38	67	50	36
Sc	74	72	86	86	91	81	92	20	99
Zn	40	43	38	35	35	38	35	30	62
Cu	37	119	49	141	278	27	188	31	48
Ga	5	4	7	6	7	6	6	10	6
Ge	1.6	1.7	1.6	1.6	–	1.5	1.5	1.6	1.7
Cl	390	610	690	610	420	1400	650	400	250
S	220	680	70	320	860	280	860	270	240

Analysts: Majors—Ib Sørensen (GGU); traces—J.C.Bailey, Li—R. Gwozdz.
1–7 = clinopyroxenites (ordered according to decreasing MgO contents); 8 = tremolite–chlorite vein; 9 = diopside separated from 26152.

from oceanic fracture zones, and (c) Alaskan-type (orogenic) cumulate bodies. Ti/V ratios range from 4 to 12 in island arc (orogenic) basaltic clinopyroxene (Irvine 1974; Dostal et al., 1983) and are thus distinctly lower than those in other basaltic magma types (Shervais 1982), including the dredge 13 diopside, which has a Ti/V ratio of 21.

The partition coefficient for Zr between clinopyr-

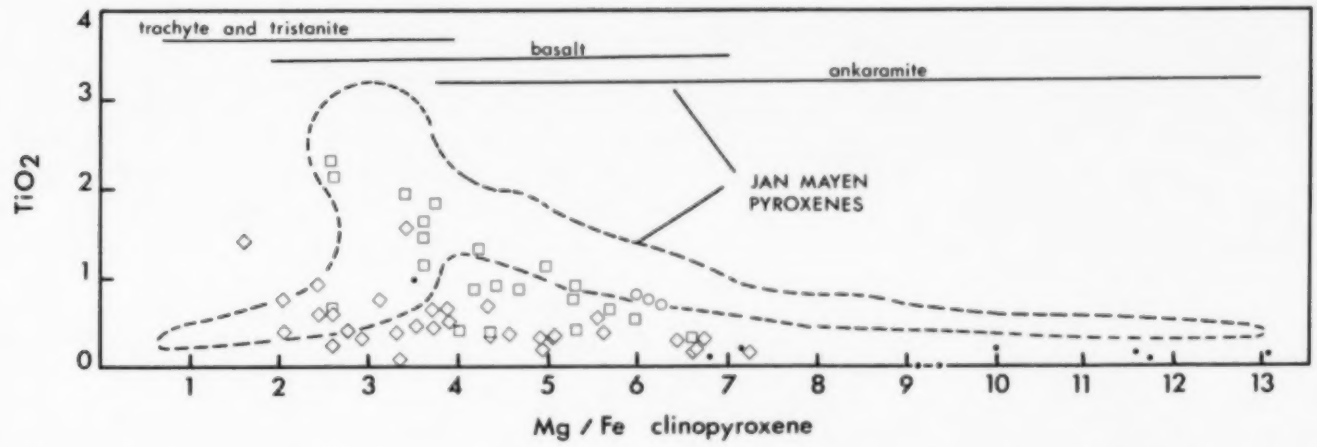

Fig. 3. TiO_2–Mg/Fe relationships in clinopyroxenes. Circles = dredge 13 clinopyroxenite; dots = ocean floor peridotite (Prinz et al., 1976; Hekinian, 1982; Michael and Bonatti, 1985; Shibata and Thompson, 1986); squares = Atlantic MORB (Frey et al., 1974; Shibata et al., 1979; Hekinian, 1982); diamonds = island arc/orogenic ultramafic rocks (James, 1971; Irvine, 1974; Snoke et al., 1981; Dostal et al., 1983; Conrad and Kay, 1984). Jan Mayen alkaline series from Imsland (1984).

oxene and low-Zr basaltic magmas is close to 0.12 (Fujimaki et al., 1984) and points to a Zr level of around 183 ppm in the basaltic magma coexisting with the dredge 13 diopside (22 ppm Zr). This is a relatively high Zr content, certainly above average values for MORB and island arc magmas (Holm, 1985). It is similar, however, to average levels in ocean island tholeiite (174 ppm) and perhaps enriched MORB (141 ppm). Ankaramitic basalt from Jan Mayen contains 130–270 ppm Zr (Imsland, 1984), and the dredge 13 dolerite contains 88–169 ppm Zr (Table 3).

Assuming a diopside/basalt partition coefficient of 0.19 for Y (Arth, 1976), the dredge 13 diopside coexisted with a magma containing 37 ppm Y, which is typical of many types of basalt. More significantly, the suggested Zr/Y ratio (which is largely independent of the fractionation stage) of the diopside's coexisting magma is 4.9, and this lies above the typical ratios seen in MORB and island arc tholeiite (2.4 and 2.7). It can be matched with the ratio for ocean island tholeiite (5.7) (Holm, 1985) and the dredge 13 dolerite (3.9–6.6, Table 3). Ratios are somewhat higher (7.3–13.5) in ankaramitic basalt from Jan Mayen (Imsland, 1984).

Clinopyroxene/basalt partition coefficients for Sr range from 0.0719 to 0.111 (Hart and Brooks, 1974) and for the separated diopside yield a parent basalt with 333–515 ppm Sr. Such Sr levels are higher than those from the nearby Kolbeinsey Ridge tholeiite (55–145 ppm; Dittmer et al., 1975) and the Iceland enriched MORB (plume) tholeiite (195–246 ppm; Bailey and Noe-Nygaard, 1976) but comparable with Jan Mayen ankaramite (231–590 ppm; Imsland, 1984). However, Sr levels in Jan Mayen ankaramitic basalt (509–844 ppm) and basalt (574–1236 ppm) are generally higher. The proposed Sr values overlap those in the dredge 13 dolerite (306–475 ppm, Table 3).

Dolerite

Despite their mineralogical and textural variations, the chemical spectrum displayed by the dolerite fragments is relatively narrow (Table 3). The differentiation index (FeO*/MgO) varies from 1.31–2.68, and all SiO_2 values fall in the range 48.5–50.7%. When plotted against the differentiation index, most major and trace elements exhibit regular and expected trends; for example, values of P, Ti, Zr, Nb, Th, Ga, REE and V all increase, whereas Mg, Ni, Co and Cr contents decrease (Fig. 4). The regular behaviour of the more "immobile" elements, such as Ti, Zr, Nb, V, Co, Sc, Cr and Ni (Pearce and Cann, 1973; Frey et al., 1974) could hardly have formed by accident and is taken as evidence of consanguinity of the dolerite fragments with each other. Distinctive geochemical features such as low Zr/Nb ratios (1.5–2.7) and low Zn contents (34–74 ppm) are common to all the samples and confirm their relationship to each other.

Even allowing for disturbed Fe_2O_3/FeO ratios

TABLE 3

Major and trace element analyses of dredge 13 dolerite, quartz microsyenite and greenstone

Number	1 26162	2 26163	3 26164	4 26160	5 26166B	6 26159	7 26004	8 26166A	9 26165
Major elements (%)									
SiO_2	50.4	49.4	49.5	49.7	48.5	50.6	50.7	64.5	41.1
TiO_2	1.95	1.73	2.30	2.43	2.90	2.77	2.70	1.09	1.40
Al_2O_3	14.1	14.5	14.3	14.3	14.7	14.7	13.1	15.4	14.2
Fe_2O_3	7.22	2.83	4.00	4.57	6.61	4.66	5.35	2.03	1.37
FeO	3.41	6.84	7.46	7.41	6.20	8.09	8.48	3.39	9.15
MnO	0.21	0.20	0.20	0.20	0.27	0.19	0.21	0.09	0.28
MgO	7.55	7.13	6.64	6.21	5.81	4.71	4.96	1.83	13.8
CaO	8.78	9.09	7.85	7.31	8.02	7.51	7.54	3.79	11.8
Na_2O	3.07	2.45	2.87	2.74	3.29	3.21	2.72	4.04	0.34
K_2O	1.48	1.67	1.56	1.92	1.96	1.63	1.99	2.34	0.10
P_2O_5	0.41	0.32	0.41	0.42	0.67	0.60	0.50	0.23	0.23
H_2O^-	0.80	0.86	0.44	0.47	0.35	0.70	0.89	0.63	1.11
H_2O+	1.21	2.71	2.84	2.71	1.08	1.01	1.35	0.99	5.25
Sum	100.59	99.73	100.37	100.39	100.36	100.38	100.49	100.35	100.13
FeO*/MgO	1.31	1.32	1.67	1.86	2.09	2.61	2.68	2.85	0.75
Trace elements (ppm)									
Li	5.3	9.1	7.7	7.3	7.8	6.4	4.5	3.4	18.2
Rb	47	39	38	8.2	60	36	46	43	<0.2
Sr	408	317	326	354	298	462	351	472	41
Ba	740	480	480	580	570	605	660	1200	14
Pb	41	20	50	31	16	14	5	1	32
La	31	25	28	27	65	45	37	66	30
Ce	45	42	51	52	92	73	68	79	43
Nd	28	22	28	32	49	41	35	39	23
Y	19	22	27	34	37	31	26	31	17
Zr	125	88	133	131	151	168	169	395	89
Nb	59	50	58	61	99	79	63	128	43
Th	2	2	2	2	3	3	5	7	2
U	0.95	0.73	1.03	1.05	1.34	1.36	1.63	2.34	0.72
V	392	339	448	454	464	468	570	128	330
Cr	205	135	117	93	79	8	16	22	78
Ni	84	99	66	51	51	24	35	22	119
Co	46	51	40	40	42	41	43	17	58
Sc	41	37	39	39	42	35	39	14	42
Zn	34	63	38	47	74	48	66	25	69
Cu	53	68	24	38	44	49	53	16	11
Ga	17	15	18	17	19	19	19	17	12
Ge	1.5	1.5	1.5	1.5	1.4	1.4	1.4	1.3	1.5
Cl	1100	160	330	320	880	750	700	560	530
S	340	70	290	760	200	910	2000	400	100

Analysts: Majors—Ib Sørensen (GGU); traces—J.C. Bailey, Li—R. Gwozdz, U—H. Kunzendorf.
1–7 = Dolerite (ordered according to increasing FeO*/MgO); 8 = quartz microsyenite vein; 9 = greenstone

and a small addition of secondary quartz, the dolerite fragments are tholeiitic, unlike the great bulk of Jan Mayen basaltic lavas which are ne-normative (Imsland 1984). On the FMA triangle (not shown), the dolerite samples form a well-defined tholeiitic trend with iron enrichment. The alkali basalt series of Jan Mayen exhibits a more abrupt advance toward alkali-rich compositions.

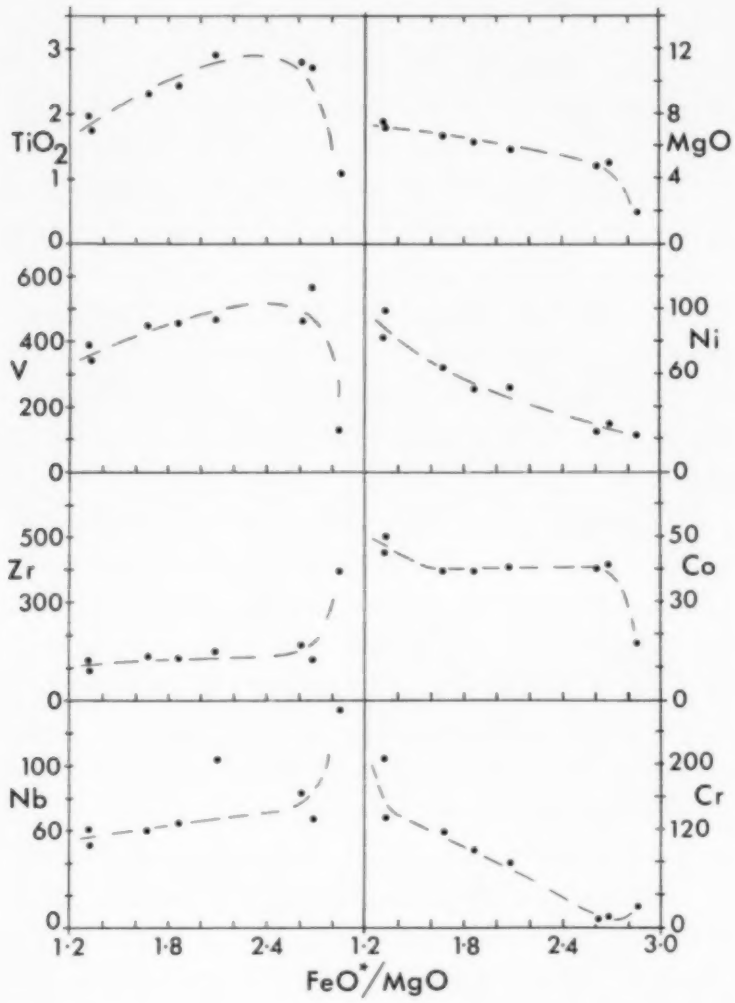

Fig. 4. Differentiation diagrams for dolerite and microsyenite, dredge 13, western Jan Mayen Fracture Zone.

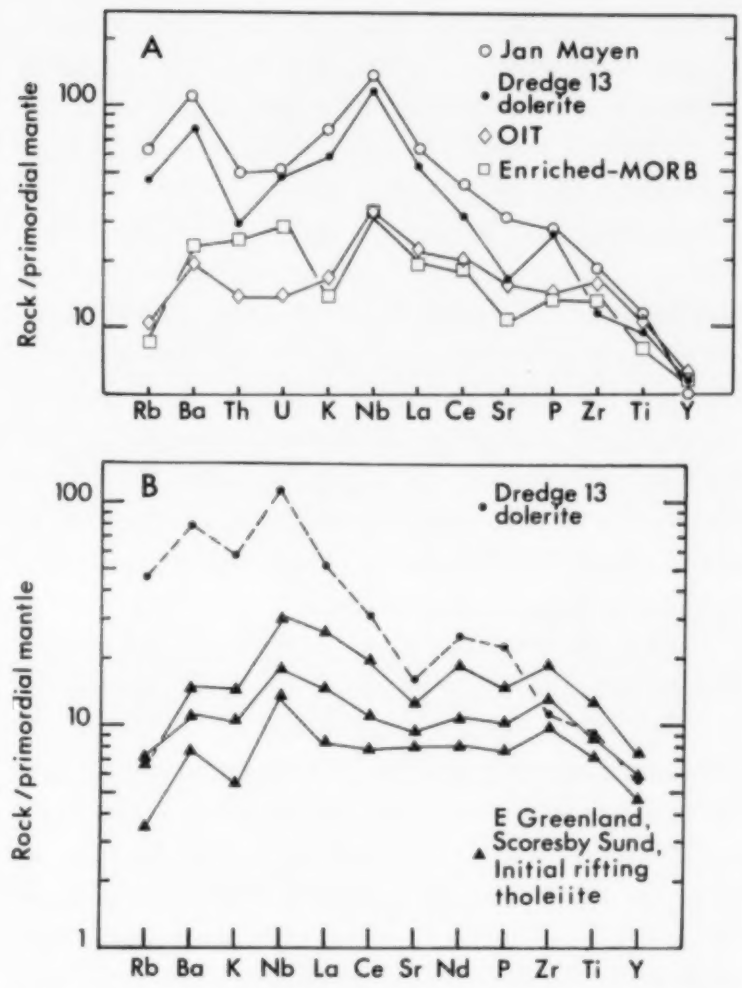
A
Jan Mayen
Dredge 13 dolerite
OIT
Enriched-MORB
Rock /primordial mantle
Rb Ba Th U K Nb La Ce Sr P Zr Ti Y
B
Dredge 13 dolerite
E Greenland, Scoresby Sund, Initial rifting tholeiite
Rb Ba K Nb La Ce Sr Nd P Zr Ti Y

Fig. 5. H-element diagrams (spidergrams) for dredge 13 dolerite samples normalised to primordial upper mantle (Wood et al., 1979). (A) Patterns for ocean island tholeiite (OIT) and enriched MORB from Holm (1985); Jan Mayen alkali basalt from Weigand et al. (1972), Imsland (1984) and authors' unpublished data. (B) Patterns for East Greenland (Scoresby Sund); initial rifting tholeiite from Larsen et al. (1989).

Relatively high K_2O/Na_2O ratios (av. = 1.6), if primary, are similar to Jan Mayen lavas (av. = 1.5), and the dredge 13 dolerite fragments are thus distinctly potassic.

The H-element pattern (spidergram) of the dredge 13 dolerite (Fig. 5) can be closely matched with that for ocean island tholeiite. The positive anomaly for Ba and K over Th–U sets it apart from the enriched MORB type, and the overall negative slope from Rb to Y rules out any similarity with initial rifting tholeiite lavas such as those in East Greenland.

The quartz microsyenite with 64.5% SiO_2 (26166A) is considerably more evolved than the dolerite it veins. Its low Zr/Nb (3.1) and Zn (25 ppm) values suggest that it is chemically related to the dolerite (see also Fig. 4). Contents of K, Sr, Ba, Zr, Nb, Th and REE are even higher than in the dolerite and confirm the alkaline affinities of the suite. The analysed specimen contains a significant percentage of doleritic microxenoliths and xenocrysts, so its original composition was almost certainly even more siliceous and rich in LIL elements.

The low Fe_2O_3/FeO ratio (0.15) and high water content of the single greenstone are typical of advanced recrystallization under greenschist facies (Floyd, 1976). Its relationship to the other dredge 13 rocks is far from clear, although the low Zr/Nb (2.1) and high normalised La/Y (10.7) ratios suggest it may be cogenetic with the dolerite.

Age determinations

Five dolerite samples (6.6–7.9 Ma) and a syenitic vein (7.5 Ma) have very similar K–Ar ages (Campsie et al., 1990), which is compatable with the close

relationship between these rocks based on geochemical data. It is possible that the ages are close enough to the proposed magnetic anomaly age for the dredge 13 area (4.5 Ma) to suggest that their formation can be linked to events connected with the accretionary history of the Kolbeinsey Ridge. However, because there are no petrological affinities between the dredge 13 rocks and typical ocean-ridge igneous rocks, we prefer to consider the dolerite and syenite vein as representing a slightly older event related to alkaline magmatism of the Jan Mayen province. Perhaps an older sliver of a dredge 13 alkaline igneous centre was preserved in the western JMFZ when younger mid-ocean ridge rocks slid past during faulting.

Although Campsie et al. (1990) argued that a K–Ar age of 529 ± 36 Ma for a single clinopyroxenite (26152) indicated the presence of Caledonian basement beneath dredge 13, this age cannot easily be matched with rock units in the East Greenland Caledonides (Rex and Higgins, 1985). Indeed, in view of the disturbed alkali element contents of the clinopyroxenites this age is not regarded here with any confidence. It is more likely that this date represents an excess argon age and that the source of the excess argon is older basement rocks beneath the oceanic crust of this area.

Plate tectonic setting

According to reconstructions of the opening of the Northeast Atlantic (Talwani and Eldholm, 1977; Nunns, 1983; Larsen, 1988) the main tectonic events in the area of dredge 13 were the following:

(1) Spreading started during anomalies 25 and 24R (56–59 Ma) when a spreading axis (southern Mohns Ridge) lay east of the dredge 13 area, which was attached to the East Greenland continental block in the area of Traill Island/Franz Joseph Fjord. This area consisted of a Caledonian basement overlain by Mesozoic sedimentary basins which became covered by a thick sequence of Lower Tertiary basalt.

(2) Spreading continued on the Mohns Ridge and its offset continuation to the south, the Aegir Ridge, until anomaly 7 (26 Ma). From about anomaly 13 (35 Ma), the main Northeast Atlantic spreading ridge (the Reykjanes Ridge) propagated into the East Greenland continental margin, eventually splitting off (around anomaly 6 or 7, 20–25 Ma) a continental sliver (Jan Mayen Ridge) and forming a new spreading axis (the Kolbeinsey Ridge). Also around anomaly 6 or 7 the new axis may have propagated beyond the early eastern JMFZ up to its present position against a newly formed western JMFZ; it is thus coeval with the youngest (24–29 Ma) alkaline plutonic activity in the Traill Island–Hold with Hope region (Beckinsale et al., 1970; Upton et al., 1984; Noble et al., 1988).

(3) Spreading has been active on the Kolbeinsey Ridge since about anomaly 6C (24 Ma). At about 4.5 Ma the area in or around the dredge 13 site lay beneath the Kolbeinsey spreading axis, and since then drifted about 45 km to the east.

Although exposures on Jan Mayen only date back to 0.49 Ma, volume-eruption frequency calculations extend this to the late middle Tertiary, say 15–20 Ma (Sylvester, 1975). Ashes in DSDP holes on Jan Mayen Ridge could be as old as early Pliocene (ca. 5 Ma) (Sylvester, 1978). Transitional alkaline basalt samples were dredged from the western JMFZ about 70 km east of Jan Mayen and have been dated at 30.1 ± 1.6 Ma (Campsie et al., 1990). These features suggest that alkaline magmatism of the Jan Mayen province has been active over the last 30 Ma, and that it includes the East Greenland centres and the dredge 13 area.

Discussion

The likely geological history of the dredge 13 area raises the possibility that the clinopyroxenite might be derived from the Caledonian orogenic belt of East Greenland. However, the rare ultramafic rocks of orogenic zones are Alpine-type bodies characterised by tectonized harzburgite–dunite and quite unlike the dredge 13 material. The Alaskan-type associations are distinguished (James, 1971; Irvine, 1974; Snoke et al., 1981) by their wide range of rock types (ultramafic, gabbroic, dioritic), the common presence of hornblende, and the lack of tectonism and serpentinization. Furthermore, the relatively high contents of TiO_2 in the Mg/Fe-rich diopside of the dredge 13 clinopyroxenite, its high Zr contents

and its high Ti/V and Zr/Y ratios have no affinities with island arc/orogenic magmas.

Along mid-ocean ridges and fracture zones, harzburgite, lherzolite and dunite are the most prevalent ultramafic rock types (see references in Fig. 2). Geochemical parameters such as the relatively high TiO_2, Zr and Zr/Y of the dredge 13 diopside and its likely coexisting basaltic magmas rule out petrological affinities with MORB.

As noted above, the diopside in the dredge 13 clinopyroxenite is similar to the clinopyroxene crystallizing from the intermediate basalt stages on Jan Mayen. Predicted levels of Zr, Y and Sr in the coexisting basaltic magma, based on partition coefficients, match those in Jan Mayen basic magmas. Setting aside the probably disturbed Sr isotope ratios, the dredge 13 clinopyroxenite matches all geochemical expectations for Jan Mayen cumulate rocks. Because dredge 13 lies 150 km west of Jan Mayen, a direct connection cannot be postulated, but it appears likely that a Jan Mayen-like volcanic centre once lay above the dredge 13 site.

Modelled extracts (Imsland, 1984) at the intermediate basaltic stage of Jan Mayen contain 59–94% clinopyroxene, 6–35% olivine, 0–7% magnetite and 0–5% plagioclase and are thus equivalent to the modes and chemistry of the clinopyroxenite in dredge 13 (Fig. 2B). Enormous volumes of cumulus clinopyroxenite are expected beneath Jan Mayen as they dominate the first 80% of its fractionation history.

The presence of bytownitic plagioclase in the dredge 13 clinopyroxenite restricts the rock's depth of formation to the crust or uppermost mantle, depths which are similar to those envisaged for the Hawaiian ultramafic xenoliths (White, 1966) and the basal complex of the Canary Islands (Frisch, 1974).

The dolerite fragments possess a grain size suggesting crystallization at moderate depth, perhaps in dykes. During post-magmatic cooling or a later thermal event the alteration of feldspars, pyroxene and ore minerals took place. Sulphide veins with bleached margins were introduced before local veining by a comagmatic residual syenitic magma.

A variety of mineralogical and geochemical criteria indicate that the dolerite fragments are best assigned to an ocean island tholeiitic, i.e. oceanic within-plate, magma type with notably high contents of LIL elements. A residual syenitic magma and possibly metamorphosed greenstone equivalents of the dolerite may be present.

Contact relationships between the clinopyroxenite and dolerite have not been observed in the present dredged materials. However, these two rock types and their tectono-thermal characteristics are only known from this single locality in the Jan Mayen region, and it is thus reasonable to attempt to link them in a single geological history.

The primary clinopyroxene crystallizing from the dolerite has tholeiitic affinities, whereas that accumulating in the clinopyroxenite was derived from a ne-normative basalt. Thus the dolerite cannot be the immediate parent magma for the cumulates. Differences in Sr-isotopic ratios (see section on geological setting) and LIL element ratios such as K/Rb also suggest that the two rock types are not cogenetic, although these differences could have arisen through secondary alteration (Pedersen et al., 1976). Nevertheless, the apparently primary Ti, Ti/V, Zr, Zr/Y and Sr levels of the cumulate diopside point to a parent magma with alkaline affinities similar in geochemistry to the dolerite.

Both the clinopyroxenite and dolerite have been variably metamorphosed in the greenschist or lower amphibolite facies. The presence of andradite–grossular implies thermal rather than regional metamorphism. Miyashiro et al. (1971) argued that amphibolite facies temperatures can be reached in the oceanic lower crust or uppermost mantle and that the metamorphic rocks are subsequently transferred to the surface by faulting. Transportation by faulting in the JMFZ is consistent with the clinopyroxenite passing through a stage of weak flowage which obliterated the high orientation of crystal cumulates and with the late-stage brecciation of the clinopyroxenite fragments. Tectonic adjustments continue along this fracture zone, as is evident from its recent seismic activity (Sylvester, 1975).

The geological history of the Canary Islands seems to be particularly relevant in helping to solve the problems presented by the Jan Mayen region. The Canary Islands have undergone a two-

stage development with an early, largely mid-Tertiary, basal complex overlain by Miocene–recent basaltic rocks (Stillman, 1987; Neumann 1991). The basal complex consists of plutonic mafic and ultramafic rocks and syenite together with submarine volcanic and sedimentary rocks. The plutonic rocks include peridotite, pyroxenite, dunite and wehrlite together with olivine and alkaline gabbro. They appear to be part of a large layered intrusion developed from a transitional alkaline–tholeiitic magma type. Younger syenite, as veins and small intrusive bodies, caused alkalinization of the complex. The basal complex is cut by a very dense basaltic and ankaramitic dyke swarm and then capped by the younger, more alkaline, subaerial basalt. Pillow lavas in the complex and the succeeding dyke swarm were extensively altered under greenschist facies.

The dredge 13 association of clinopyroxenite and greenschist facies dolerite, and the presence of cumulates and possible dykes with, respectively, alkaline and transitional alkaline–tholeiitic affinities suggests considerable overlap in the geological histories of the Canary Islands and the Jan Mayen region. Based on this analogy, we consider that the dredge 13 rocks represent samples of an extensive basal complex of the Jan Mayen volcanic province.

Conclusions

(1) Clinopyroxenite fragments dredged from the western JMFZ are cumulates which crystallized in the uppermost mantle or lower crust from an intermediate basaltic stage of an extensive Jan Mayen-like alkaline igneous centre.

(2) Associated dolerite and microsyenite fragments constitute a tholeiitic series with transitional alkaline affinities.

(3) These two rock types represent part of a basal complex of the Jan Mayen volcanic province. They underwent variable thermal metamorphism and metasomatism prior to fracture zone tectonism.

Acknowledgements

We thank the officers and crew of the USNS *Lynch* and Professor A. Noe-Nygaard and Dr. G.L. Johnson for their support. The Danish Natural Science Research Council (SNF) provided grants for the research equipment. We are grateful to I. Sørensen, R. Gwozdz and H. Kunzendorf for analytical results. Professor N.I. Christensen (University of Washington) kindly provided the fabric analysis of a clinopyroxenite fragment.

References

Arth, J.G., 1976. Behaviour of trace elements during magmatic processes—a summary of theoretical models and their applications. J. Res. U.S. Geol. Surv., 4: 41–47.

Aumento, F. and Loubat, H., 1971. The Mid-Atlantic Ridge near 45°N. XVI. Serpentinized ultramafic intrusions. Can. J. Earth Sci., 8: 631–663.

Bailey, J.C. and Noe-Nygaard, A., 1976. Chemistry of Miocene plume tholeiites from northwest Iceland. Lithos, 9: 185–201.

Beckinsale, R.D., Brooks, C.K. and Rex, D.C., 1970. K-Ar ages for the Tertiary of East Greenland. Geol. Soc. Den. Bull., 20: 27–35.

Bonatti, E., Honnorez, J. and Ferrara, G., 1971. Peridotite–gabbro–basalt complex from the equatorial Mid-Atlantic Ridge. Philos. Trans. R. Soc. London, A, 268: 385–402.

Brown, G.M., 1967. Mineralogy of basaltic rocks. In: H.H. Hess and A. Poldervaart (Editors), Basalts: The Poldervaart Treatise on Rocks of Basaltic Composition. 1. Interscience, New York, pp. 103–162.

Campsie, J., 1976. Vulkanske bjergarter fra oceanbunden omkring Jan Mayen. Dan. Geol. Foren. Årsskr., 1975: 37–39.

Campsie, J., Rasmussen, M.H., Kovacs, L.C., Dittmer, F., Bailey, J.C., Hansen, N.O., Laursen, J. and Johnson, L., 1990. Chronology and evolution of the northern Iceland Plateau. Polar Res., 8: 237–243.

Conrad, W.K. and Kay, R.W., 1984. Ultramafic and mafic inclusions from Adak Island: Crystallization history, and implications for the nature of primary magmas and crustal evolution in the Aleutian arc. J. Petrol., 25: 88–125.

Dittmer, F., Fine, S., Rasmussen, M., Bailey, J.C. and Campsie, J., 1975b. Dredged basalts from the mid-oceanic ridge north of Iceland. Nature, 254: 298–301.

Dostal, J., Dupuy, C., Carron, J.P., Le Guern de Kerneizon, M. and Maury, R.C., 1983. Partition coefficients of trace elements: application to volcanic rocks of St. Vincent, West Indies. Geochim. Cosmochim. Acta, 47: 525–533.

Engel, C.G. and Fisher, R.L., 1969. Lherzolite, anorthosite, gabbro and basalt dredged from the Mid-Indian Ocean Ridge. Science, 166: 1136–1141.

Floyd, P.A., 1976. Geochemical variation in the greenstones of S.W. England. J. Petrol., 17: 522–545.

Frey, F.A., Bryan, W.B. and Thompson, G., 1974. Atlantic Ocean floor: Geochemistry and petrology of basalts from Legs 2 and 3 of the Deep-Sea Drilling Project. J. Geophys. Res., 79: 5507– 5527.

Frisch, T., 1974. Clinopyroxenes as geobarometric indicators in mafic and ultramafic rocks from Canary Islands: a discussion. Contrib. Mineral. Petrol., 48: 315–316.

Fujimaki, H., Tatsumoto, M. and Aoki, K., 1984. Partition

coefficients of Hf, Zr and REE between phenocrysts and groundmass. J. Geophys. Res., 89(Suppl.): B662–B672.
Hart, S.R. and Brooks, C., 1974. Clinopyroxene–matrix partitioning of K, Rb, Cs, Sr and Ba. Geochim. Cosmochim. Acta, 38: 1799–1806.
Hekinian, R., 1970. Gabbro and pyroxenite from a deep sea core in the Indian Ocean. Mar. Geol., 9: 287–294.
Hekinian, R., 1982. Petrology of the Ocean Floor. Elsevier, Amsterdam, 393 pp.
Hekinian, R. and Aumento, F., 1973. Rocks from the Gibbs Fracture Zone and the Minia Seamount near 53°N in the Atlantic Ocean. Mar. Geol., 14: 463–473.
Holm, P.E., 1985. The geochemical fingerprints of different tectonomagmatic environments using hygromagmatophile element abundances of tholeiitic basalts and basaltic andesites. Chem. Geol., 51: 303–323.
Imsland, P., 1984. Petrology, mineralogy and evolution of the Jan Mayen magma system. Visindafelag Isl., 43: 332 pp.
Irvine, T.N., 1974. Petrology of the Duke Island ultramafic complex, Southeastern Alaska. Geol. Soc. Am. Mem., 138: 240 pp.
IUGS, 1973. Classification and nomenclature of plutonic rocks. Recommendations. Geol. Newslett., 1973: 110–127.
James, O.B., 1971. Origin and emplacement of the ultramafic rocks of the Emigrant Gap area, California. J. Petrol., 12: 523–560.
Johnson, G.L. and Campsie, J., 1976. Morphology and structure of the Western Jan Mayen Fracture Zone. Nor. Polarinst. Årb., 1974: 69–81.
Kharin, G.S., 1980. The basalts of the Kolbeinsey submarine ridge (Norwegian–Greenland Basin). Oceanology, 20(1): 50–55.
Larsen, H.C., 1988. A multiple and propagating rift model for the NE Atlantic. In: A.C. Morton and L.M. Parson (Editors), Early Tertiary Volcanism and the Opening of the NE Atlantic. Spec. Publ. Geol. Soc. London, 39: 95–114.
Larsen, L.M., Watt, W.S. and Watt, M., 1989. Geology and petrology of the Lower Tertiary plateau basalts of the Scoresby Sund region, East Greenland. Grœnl. Geol. Unders. Bull., 157: 164 pp.
Melson, W.G. and Thompson, G., 1971. Petrology of a transform fault and adjacent segments. Philos. Trans. R. Soc. London, A, 268: 423–441.
Melson, W.G., Hart, S.R. and Thompson, G., 1972. St. Paul's Rocks, equatorial Atlantic: Petrogenesis, radiometric ages, and implications for sea-floor spreading. Geol. Soc. Am. Mem., 132: 241–272.
Michael, P.J. and Bonatti, E., 1985. Peridotite composition from the North Atlantic: regional and tectonic variations and implications for partial melting. Earth Planet. Sci. Lett., 73: 91–104.
Miyashiro, A., Shido, F. and Ewing, M., 1969. Composition and origin of serpentinites from the Mid-Atlantic Ridge near 24° and 30° north. Contrib. Mineral. Petrol., 23: 117–127.
Miyashiro, A., Shido, F. and Ewing, M., 1971. Metamorphism in the Mid-Atlantic Ridge near 24° and 30°N. Philos. Trans. R. Soc. London, A, 268: 589–603.
Neumann, E.-R., 1991. Ultramafic and mafic xenoliths from Hierro, Canary Islands: evidence for melt infiltration in the upper mantle. Contrib. Mineral. Petrol., 106: 236–252.
Neumann, E.-R. and Schilling, J.-G., 1984. Petrology of basalts from the Mohns–Knipovich Ridge; the Norwegian–Greenland Sea. Contrib. Mineral. Petrol., 85: 209–223.
Nicholls, I.A., Ferguson, J., Jones, H., Marks, G.P. and Mutter, J.C., 1981. Ultramafic blocks from the ocean floor southwest of Australia. Earth Planet. Sci. Lett., 56: 362–374.
Noble, R.H., Macintyre, R.M. and Brown, P.E., 1988. Age constraints on Atlantic evolution: timing of magmatic activity along the E Greenland continental margin. In: A.C. Morton and L.M. Parson (Editors), Early Tertiary Volcanism and the Opening of the NE Atlantic. Geol. Soc. London Spec. Publ., 39: 201–214.
Norrish, K. and Chappell, B.W., 1977. X-ray fluorescence spectrometry. In: J. Zussman (Editor), Physical Methods in Determinative Mineralogy. Academic Press, London, pp. 201–272.
Nunns, A.G., 1983. Plate tectonic evolution of the Greenland–Scotland Ridge and surrounding regions. In: M.H.P. Bott et al. (Editors), Structure and Development of the Greenland–Scotland Ridge. New Methods and Concepts. Plenum, New York, pp. 11–30.
Pearce, J.A. and Cann, J.R., 1973. Tectonic setting of basic volcanic rocks determined using trace element analyses. Earth Planet. Sci. Lett., 19: 290–300.
Pedersen, S., Larsen, O., Hald, N., Campsie, J. and Bailey, J.C., 1976. Strontium isotope and lithophile element values from the submarine Jan Mayen province. Geol. Soc. Den. Bull., 25: 15–20.
Prinz, M., Keil, K., Green, J.A., Reid, A.M., Bonatti, E. and Honnorez, J., 1976. Ultramafic and mafic dredge samples from the equatorial mid-Atlantic ridge and fracture zones. J. Geophys. Res., 81: 4087–4103.
Rex, D.C. and Higgins, A.K., 1985. Potassium–argon mineral ages from the East Greenland Caledonides between 72° and 74°N. In: D.G. Gee and B.A. Sturt (Editors), The Caledonide Orogen—Scandinavia and Related Areas. Wiley, New York, pp. 1115–1124.
Shervais, J.W., 1982. Ti–V plots and the petrogenesis of modern and ophiolitic lavas. Earth Planet. Sci. Lett., 59: 101–118.
Shibata, T. and Thompson, G., 1986. Peridotites from the Mid-Atlantic Ridge at 43°N and their petrogenetic relation to abyssal tholeiites. Contrib. Mineral. Petrol., 93: 144–159.
Shibata, T., DeLong, S.E. and Walker, D., 1979. Abyssal tholeiites from the Oceanographer Fracture Zone, 1. Petrology and fractionation. Contrib. Mineral. Petrol., 70: 89–108.
Snoke, A.W., Quick, J.E. and Bowman, H.R., 1981. Bear Mountain igneous complex, Klamath Mountains, California: an ultrabasic to silicic calc-alkaline suite. J. Petrol., 22: 501–552.
Springer, G., 1967. Die Berechnung von Korrekturen fur die quantitative Elektronen-strahl-Mikroanalyse. Fortschr. Mineral., 45: 103–124.
Stillman, C.J., 1987. A Canary Island dyke swarm: implications for the formation of oceanic islands by extensional fissural volcanism. In: H.C. Halls and W.F. Fahrig (Editors), Mafic Dyke Swarms. Geol. Assoc. Can. Spec. Pap., 34: 243–256.
Sweatman, T.R. and Long, J.V.P., 1969. Quantitative electron-probe microanalyses of rock-forming minerals. J. Petrol., 10: 332–379.

Sylvester, A.G., 1975. History and surveillance of volcanic activity of Jan Mayen Island. Bull. Volcanol., 39: 313–335.

Sylvester, A.G., 1978. Petrography of volcanic ashes in deep-sea cores near Jan Mayen Island: Sites 338 and 345–350, DSDP Leg 38. Init. Rep. DSDP, 38(Suppl.): 101–109.

Talwani, M. and Eldholm, O., 1977. The evolution of the Norwegian–Greenland Sea. Geol. Soc. Am. Bull., 88: 969–999.

Upton, B.G.J., Emeleus, C.H., Beckinsale, R.D. and Macintyre, R.M., 1984. Myggbukta and Kap Broer Ruys: the most northerly of the East Greenland Tertiary igneous centres(?). Mineral. Mag., 48: 323–343.

Vinogradov, A.P., Udintsev, G.B., Dmitriev, L.V., Kanaev, V.F., Neprochnov, Y.P., Petrova, G.N. and Rikunov, L.N., 1969. The structure of the mid-oceanic rift zone of the Indian Ocean and its place in the world rift system. Tectonophysics, 8: 377–401.

Weigand, P.W., Brunfelt, A.O., Heier, K.S., Sundvoll, B. and Steinnes, E., 1972. Geochemistry of alkali olivine basalts from an eruption on Jan Mayen. Nature Phys. Sci., 235: 31–35.

White, R.W., 1966. Ultramafic inclusions in basaltic rocks from Hawaii. Contrib. Mineral. Petrol., 12: 245–314.

Wood, D.A., Joron, J.-L., Treuil, M., Norry, M. and Tarney, J., 1979. Elemental and Sr isotope variations in basic lavas from Iceland and the surrounding ocean floor. The nature of mantle source signatures. Contrib. Mineral. Petrol., 70: 319–339.

Marine Geology, 105 (1992) 77–94
Elsevier Science Publishers B.V., Amsterdam

Collapse and flow of lowstand shelf-margin deposits: An example from the eastern Tyrrhenian Sea, Italy

Fabio Trincardi[a] and Michael E. Field[b]

[a]*Istituto per la Geologia Marina, Via Zamboni 65, 40127 Bologna, Italy*
[b]*U.S. Geological Survey, 345 Middlefield Road, Menlo Park, CA 94025, USA*

(Received March 22, 1991; revision accepted August 26, 1991)

ABSTRACT

Trincardi, F. and Field, M.E., 1992. Collapse and flow of lowstand shelf-margin deposits: An example from the eastern Tyrrhenian Sea, Italy. Mar. Geol., 105: 77–94.

The upper slope of the eastern Tyrrhenian Sea margin has a complex morphology shaped by Quaternary tectonism and by sedimentation phases controlled by changing sea levels. Sediment slides of widely varying size and shape are common in Quaternary deposits of the upper slope, particularly where gradients are steep. Our study of a large sediment failure in lowstand prograded coastal deposits west of Cape Licosa indicates that the nature of shelf-margin deposition is an additional important control on failure.

The failure zone has a mobilization surface showing in-situ deformation in the sediment above it; an upper failure surface; a head scarp; and a zone of ponded sediment debris downslope from the exposed surface of failure. The basal mobilization surface is roughly parallel to the seafloor and coincident with a major downlap surface. The failed section is less than 20 m thick and local in extent, but deformation on the basal mobilization surface extends outside the immediate area of the failure. Directly downslope of the slide scarp are internally stratified mounds that show no evidence of deformation or movement. Most of the prograded deposit experienced in-situ deformation that evolved into the collapse of part of the sediment pile above the mobilization surface. A portion of the mobilized sediment flowed a few kilometers basinward and accumulated at the base of a slope-parallel ridge.

Sediment failure occurred on the Licosa shelf margin following a major pulse of coastal sedimentation along the lowstand shoreline. On many continental margins, sea-level lowering is thought to be an important cause of failure of unconsolidated sediment deposited during previous high-stand conditions. The Licosa slide demonstrates that sea-level fall has another, equally important but indirect, role in sediment failure. As sea level falls and reaches its lowstand position, streams are at their peak efficiency and a coarsening-upward clastic coastal wedge is rapidly emplaced at relatively steep gradients on the shelf margin, and these are conditions that inherently favor sediment instability and failure.

Introduction

Purpose

Sediment failure is a common phenomenon on continental margins particularly where earthquakes are common and sediment accumulation rates high (Moore, 1961; Field, 1987; Lee, 1989). Most studies of sediment failure emphasize either the physical and geotechnical properties of the sediment that failed (Lee et al., 1981; Twichell et al., 1992); aspects of the setting in which failure occurred (Hampton, in press; McGregor et al., 1992); the geometry of the failure deposit (Kenyon, 1987, Trincardi and Normark, 1989; Trincardi and Argnani, 1990; Edwards et al., in press); or the specific triggering process that induced failure (Almagor, 1980; Field et al., 1982; Perissoratis et al., 1984; Barnes and Lewis, 1991; Normark et al., 1992). Few studies have linked specific depositional systems with failure. Our purpose here is to present information from high-resolution seismic-reflection profiles and sediment samples from a shelf-margin failure that occurred on the upper slope off southwestern Italy (Fig. 1) affecting the seaward termination of a lowstand progradational deposit

0025-3227/92/$05.00 © 1992 — Elsevier Science Publishers B.V. All rights reserved

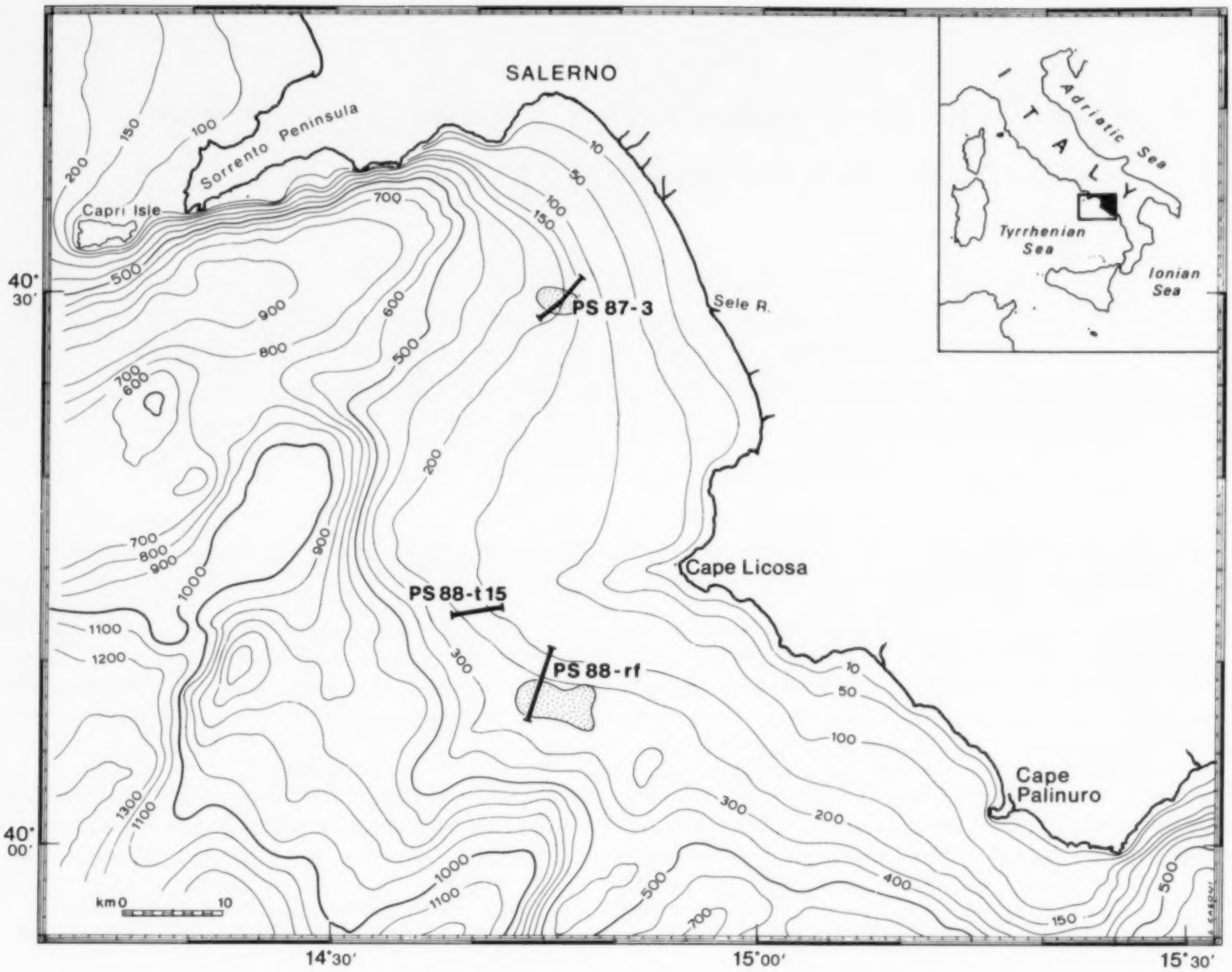

Fig. 1. Map of the study area showing the complex and irregular morphology of the eastern Tyrrhenian margin between the Sorrento Peninsula and Cape Palinuro, Italy. Profile *PS88-rf* crosses the Licosa slide (stippled); the profile is shown in Fig. 2 and a map view of the slide is shown in Fig. 3. Profiles *PS88-t15* and *PS87-3* are shown in Fig. 11. The 10-m contour is shown; from 50 to 200 m the contour interval is 50 m and at greater depths 100 m.

(Fig. 2). We examine the style of this failure and relate its development to the original depositional and sea-level setting of the deposit that failed. If certain types of sediment facies, such as downlapping shelf-margin deposits, are prone to failure, then regional analysis of margin sediment facies may be useful for identifying areas of potential sediment failure.

Geologic setting and its control on sediment failure

The study area lies on the eastern Tyrrhenian Sea margin of southwestern Italy (inset Fig. 1). The margin evolved during the late Neogene–Quaternary opening of the Tyrrhenian basin and bears evidence of differential vertical movements and widespread Quaternary faulting and folding (Fabbri et al., 1981; Trincardi and Zitellini, 1987; Marani et al., 1988; Sartori et al., 1987; Kastens et al., 1988). Intense Quaternary tectonic activity produced a morphologically-complex margin having a narrow shelf, steep slope, confined slope basins, and irregular slope ridges that vary in orientation, relief, and flank steepness (Fabbri et al., 1981; Argnani et al., 1989; Argnani and Trincardi, 1990). Local downwarping of the shelf and slope is evident in the study area from the marked variations in the depth of the shelf edge (ranging between 100 and 200 m).

This complex and irregular shelf/slope morphol-

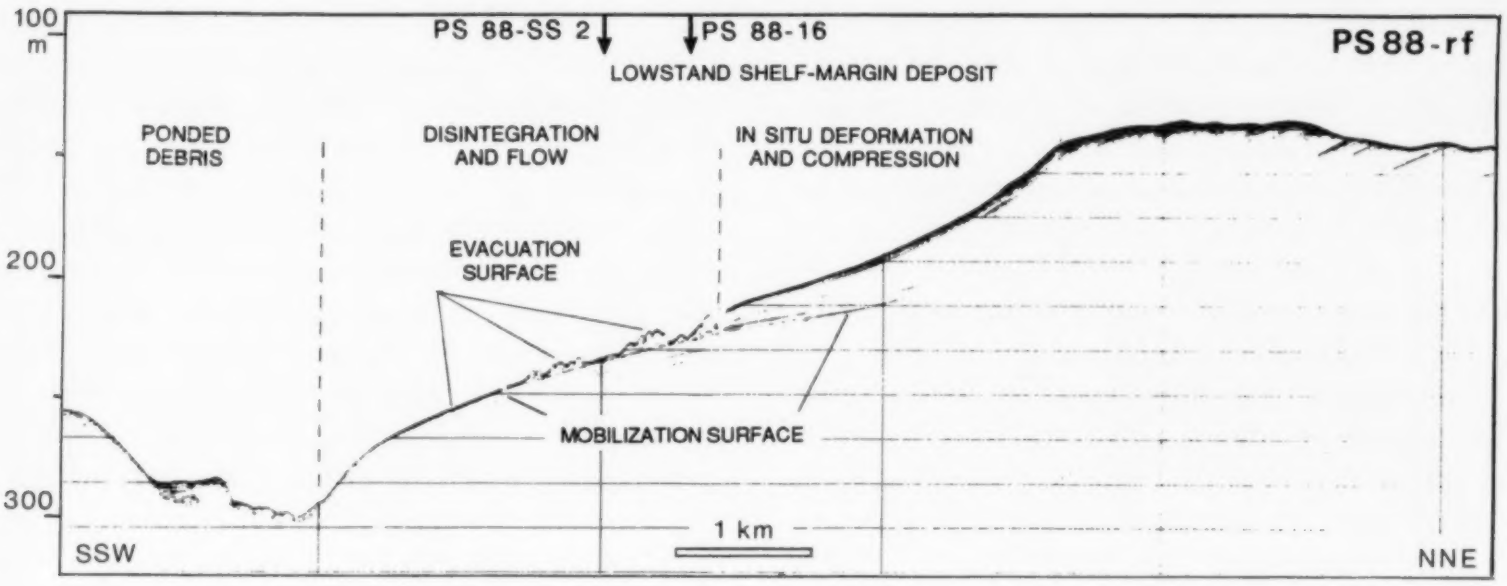

Fig. 2. High-resolution acoustic profile PS88-rf showing the main features common to the Licosa slide: a zone of remnant sediment mounds directly downslope from the slide scarp; an exposed mobilization surface; and a zone of slide blocks and other flow deposits piled against a slope ridge.

ogy, along with the local occurrence of tectonically oversteepened slopes, provides a potentially unstable setting for seafloor sediment. Furthermore, earthquakes occur both on the offshore margin and onshore in the Apennine chain (Rehault et al., 1987). The occurrence of large earthquakes, which are recognized as the most common triggering mechanism for submarine slope failures (Lee, 1989), is well-documented in the southern Italy/eastern Tyrrhenian Sea area and they are recognized to have been caused both by fault motion and by volcanic activity (Gabbianelli et al., 1990; Soloviev et al., 1990; Boschi et al., 1990).

Sediment accumulation rate is one of the most important controls on sediment failure (e.g. Field, 1981; Lee, 1989; Barnes and Lewis, 1991). Thus large deltaic regions around the world, such as the Mississippi River (Prior and Coleman, 1984) and the Alsek River (Schwab et al., 1987), are commonly sites of sediment failure, regardless of the occurrence of earthquakes or the gradient of the shelf and slope. In southern Italy, uplift in the Apennine chain has led to abundant sediment in the source region, and the rate of sediment accumulation on the eastern Tyrrhenian margin has been high throughout the Quaternary. A drill hole on the shelf off the Sele River recovered over 1000 m of Quaternary sediment (Bartole, 1983), implying an average deposition rate of nearly 50 cm/1000 yrs. This average rate excludes hiatuses and erosional losses, so actual sedimentation rates were correspondingly higher. Similar Quaternary sediment thicknesses were reported for the Sele Plain (Ortalani and Torre, 1981).

The combination of locally-steep gradients on the margin, abundant earthquakes and relatively high sedimentation rates on the eastern Tyrrhenian margin is conducive to causing sediment failure, and landslide deposits resulting from sediment slides and sediment gravity flows are common in Quaternary strata (Gallignani, 1982; Argnani et al., 1989; Trincardi and Normark, 1989). These deposits form an important contribution to deposition in the slope basins and on the floor of the Tyrrhenian Sea. Failure deposits occur on the margin as shallow-seated rotational and translational slides and on basin floors as a suite of flow deposits (Gallignani, 1982; Bartole et al., 1984; Trincardi and Normark, 1989; Canu and Trincardi, 1989). Many of the slope basins contain ponded flow deposits (Gallignani, 1982; Trincardi and Normark, 1989; Argnani et al., 1989) and slide and slump scars are common on the upper slope, particularly in steeper areas (Argnani et al., 1989).

Equipment and procedures

The data used in this study include one-kJoule sparkarray seismic profiles and 3.5-kHz echo-

sounding profiles (Fig. 3) acquired during three cruises aboard the R/V *Bannock* during October 1986, November 1987, and May 1988 as part of a multi-year survey program to investigate the Quaternary formation of sedimentary deposits on the eastern Tyrrhenian margin (Argnani et al., 1989; Bortoluzzi et al., 1989). One-kJ sparker profiles were acquired using a broad band (100–2000 Hz) sparkarray sound source pulsed every 2 seconds. Signals were filtered typically with a band-pass filter of 100–500 or 200–600 Hz and recorded on an analog recorder at a 2-s sweep. Depth conversions from time section were made using an assumed sound velocity (V_p) of 1625 m s^{-1} in the first one hundred meters of sediment, in accordance with Carlson et al. (1986). Echo-sounder (3.5 kHz) and bathymetric profiles (20 kHz) were obtained concurrently with the seismic data. Side-scan sonar data were acquired along selected profiles to investigate the nature of the slide head and surface. Samples were taken from the major features of the slide using a gravity corer, box corer, and a surface grab sampler.

Trackline positions are based on a Loran-C hyperbolic positioning system calibrated by GPS (Global Positioning System). Data were transformed on-line to geographic coordinates referred to the European Datum ED-50. Depth values were corrected for seasonal variations in water temperature and density to accurately compare data from different cruises.

The Licosa submarine slide

Shelf-margin sediment facies: Regressive downlapping deposits

During the last Pleistocene sea-level fall and lowstand, coastal deposits prograded seaward to the shelf-edge in many areas of the world (Field and Trincardi, 1992). Commonly these prograded deposits are only preserved at the shelf margin and in nearly all areas they attain their greatest thickness there. In the current study area, prograded coastal deposits are confined to a narrow sector of the shelf margin south and west of Cape Licosa where the physiographic shelf break is deeper than the low-stand shoreline (Trincardi and Field, 1991). Progradation occurred in this area apparently at a high rate of deposition relative to sedimentation rates during the succeeding transgressive and highstand phase. Sedimentation during the transgression and present highstand of sea level produced a very thin layer of sediment that is draped over the shelf surface. This layer, referred to as a condensed section (after Loutit et al., 1988; Posamentier and Vail, 1988), is generally equal to or less than the resolution (about 1 m in ideal conditions) of the geophysical equipment used for this study (Bortoluzzi et al., 1989).

High-resolution reflection profiles obtained from the shelf-edge and upperslope west of Cape Licosa (Figs. 1 and 3) show that sediment failure occurred at the seaward termination of the prograded sediment deposit (Trincardi and Field, 1991). Failure took place above a well-defined basal surface separating sedimentary units having different physical properties and lying roughly parallel to the seafloor (Fig. 2). The failed section is less than 20 m thick and has a regional extent of about 30 km^2.

Geometry of the slide

Representative profiles across the Licosa slide show it to consist of several geomorphic units (Fig. 2), each of which reflects both the style of failure and the preexisting margin morphology. The failure occurred on a gentle slope (about 1.0°), just seaward of the shelf-edge and upslope from a tectonic slope ridge that buttressed flow deposits

Fig. 3. Detailed maps of Licosa slide. (Top) Bathymetry of the outer shelf and upper slope at 10 m intervals. Tracklines show data available for this study; black dots give locations of sediment cores. South of the slide the slope ridge acted as a dam to sediment flows. (Bottom) Geologic map showing major morphological elements of the slide and the thickness distribution (TWTT, in milliseconds) of the recentmost and coarser-grained portion of the shelf margin deposit resting on the downlap surface (modified from Trincardi and Field, 1991). Numbered lines appear in subsequent figures. Note that evidence of slump folding and compression is reported upslope and adjacent to the slide scarp where sediment did not undergo mobilization into a gravity flow. (Inset) Schematic definition of the upper and lower failure surfaces active during the collapse and flow of lowstand shelf-margin deposits off Cape Licosa.

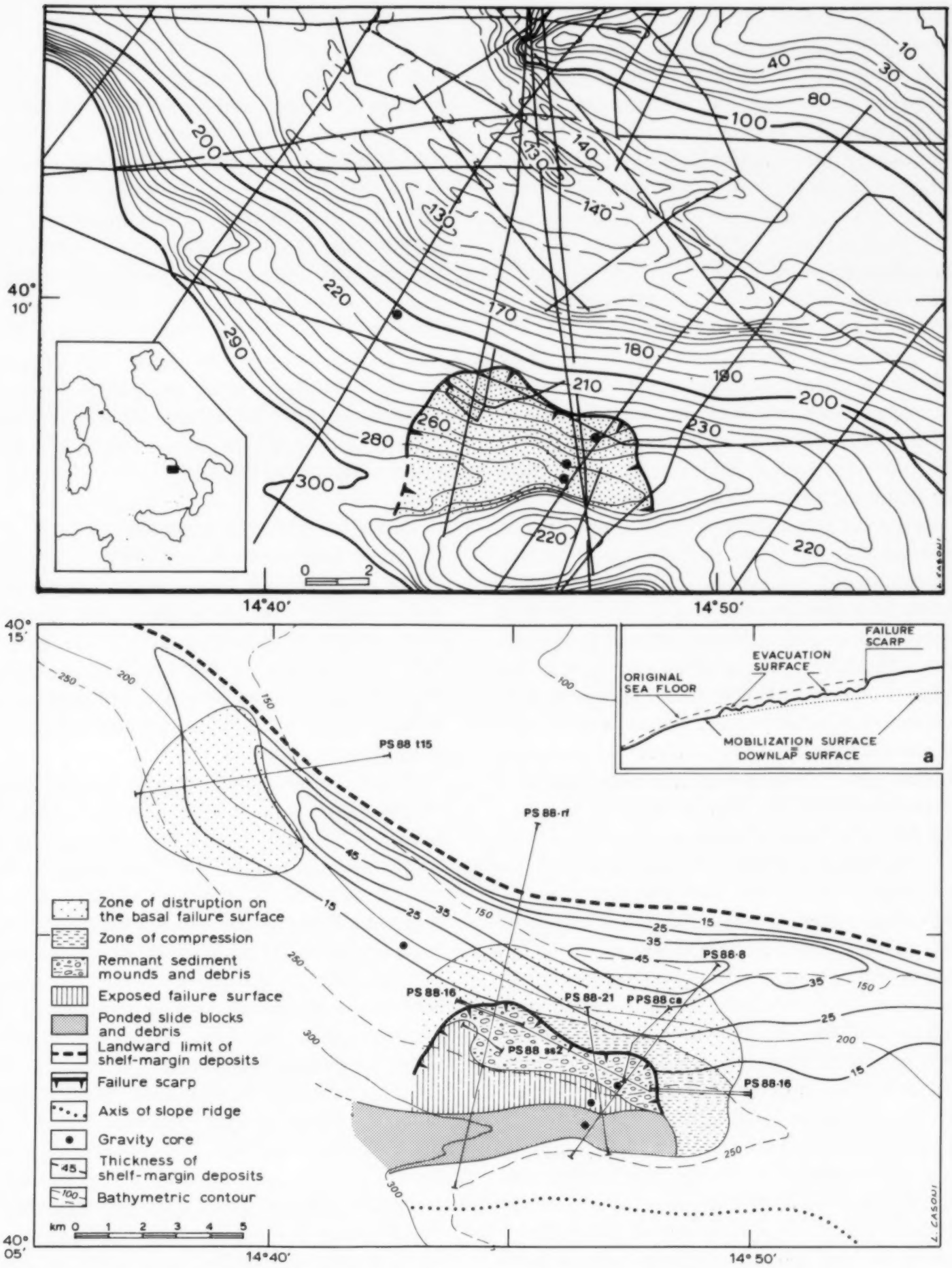
40° 10′
14°40′
14°50′
10
30
40
80
100
130
140
170
180
190
200
210
220
230
260
280
290
300
0 2
40° 15′
40° 05′
PS 88 t15
PS 88-rf
PS 88-8
PS 88-16
PS 88-21
PS 88 cs
PS 88 ss2
ORIGINAL SEA FLOOR
EVACUATION SURFACE
FAILURE SCARP
MOBILIZATION SURFACE
DOWNLAP SURFACE
a
Zone of distruption on the basal failure surface
Zone of compression
Remnant sediment mounds and debris
Exposed failure surface
Ponded slide blocks and debris
Landward limit of shelf-margin deposits
Failure scarp
Axis of slope ridge
Gravity core
Thickness of shelf-margin deposits
Bathymetric contour
km 0 1 2 3 4 5
L. CASOLI

from more extensive failure (Fig. 3). The scarp which defines the slide zone has an amphitheater shape with a radius of about 4 km. Through analysis of high-resolution seismic reflection profiles, we have defined the major geomorphic features and deposits that characterize the Licosa slide as: a buried and exposed surface of failure; a zone of compressional deformation; a zone of distintegration and flow; and ponded debris (Fig. 3).

The failure surfaces

The Licosa slide area is complex relative tc many submarine slides in that it is characterized by two surfaces of failure (inset Fig. 3): the lower mobilization surface and the upper evacuation surface (sensu Edwards et al., in press). The basal mobilization surface extends upslope and outside of the slide area and is the primary plane upon which failure occurred (Figs. 2 and 3).

Unlike slides that exhibit a single simple planar or concave surface of failure and dislocation, the upper evacuation surface in Licosa Slide is very irregular. It is contiguous with the slide scarp and becomes smooth and continuous 1 to 2 km downslope of the scarp, where it converges with the mobilization surface. Where the mobilization surface is exposed or only thinly veneered with sediment, the seafloor is smooth and regular and there is no evidence of hummocky or chaotic deposits, or low angle offsets or scarps (Fig. 4).

The sediment horizon that constitutes the mobilization surface is a major downlap surface within the progradational deposit and represents a correlatable stratigraphic marker in the study area (Trincardi and Field, 1991). On seismic reflection profiles, the downlap surface is everywhere characterized by a high amplitude reflector caused by a significant change in acoustic impedance. This surface marks a major change in sedimentation characterized by upward and seaward sediment coarsening accompanied by the increase of foreset steepness (Fig. 5). Discontinuous high-amplitude reflectors are present along the mobilization surface, possibly indicating the presence of bubble-phase gas. The gassy appearance of this reflector is common throughout the area and extends beyond the zone of failure (Figs. 4A and 6). The reflector locally shows indications of deformation and disruption marked by gentle bowing and increased dissipation of acoustic energy on 3.5-kHz profiles (Figs. 6 and 7).

Zone of in-situ compressional deformation

Upslope of the failure scarp there is abundant evidence of internal deformation, both along the mobilization surface and within the overlying deposits, that resulted from compressive forces. The surface of downlap, which corresponds with the surface of failure, has high-amplitude reflectors that are discontinuous and disrupted for distances of up to 3 to 4 km upslope of the scarp (Figs. 3 and 4A). Bedding in the upper 20 m of sediment shows evidence of bowing and gentle folding. Overall, the deformation is more pronounced on the eastern portion of the area immediately upslope of the slide scarp (Fig. 6).

Zone of disintegration and flow

The amphitheater-shaped failure scarp prominently defines the upslope boundary of the evacuation surface above which disintegration and flow of the sediment section occurred. The scarp typically is an abrupt 5–10 m high morphologic step (Figs. 6 and 8); elsewhere it is replaced by a 500 m wide zone of scarps and mounds of decreasing relief (Figs. 2 and 4A).

Individual sediment mounds in the zone of disintegration and flow are less than 10 m high, and most are less than 5 m high. They measure up to 100 m across (Fig. 4). The mounds become smaller in relief and fewer in number downslope (Fig. 4A). None of the mounds exceeds the height between the lower surface of failure and the top of the scarp. Internal beds are correlateable between mounds and conformable with undeformed subsurface strata adjacent to the slide (Figs. 4A, 6 and 7A), possibly indicating that no rotation occurred during failure. Internal structure of most of the mounds consists of undisrupted, plane-parallel bedding. The edges of the mounds have a smooth rounded appearance on side-scan sonar data (Bortoluzzi et al., 1989) suggesting that the sediment composing the mounds is relatively weak or non-cohesive and susceptible to deformation, as observed in other blocky areas within

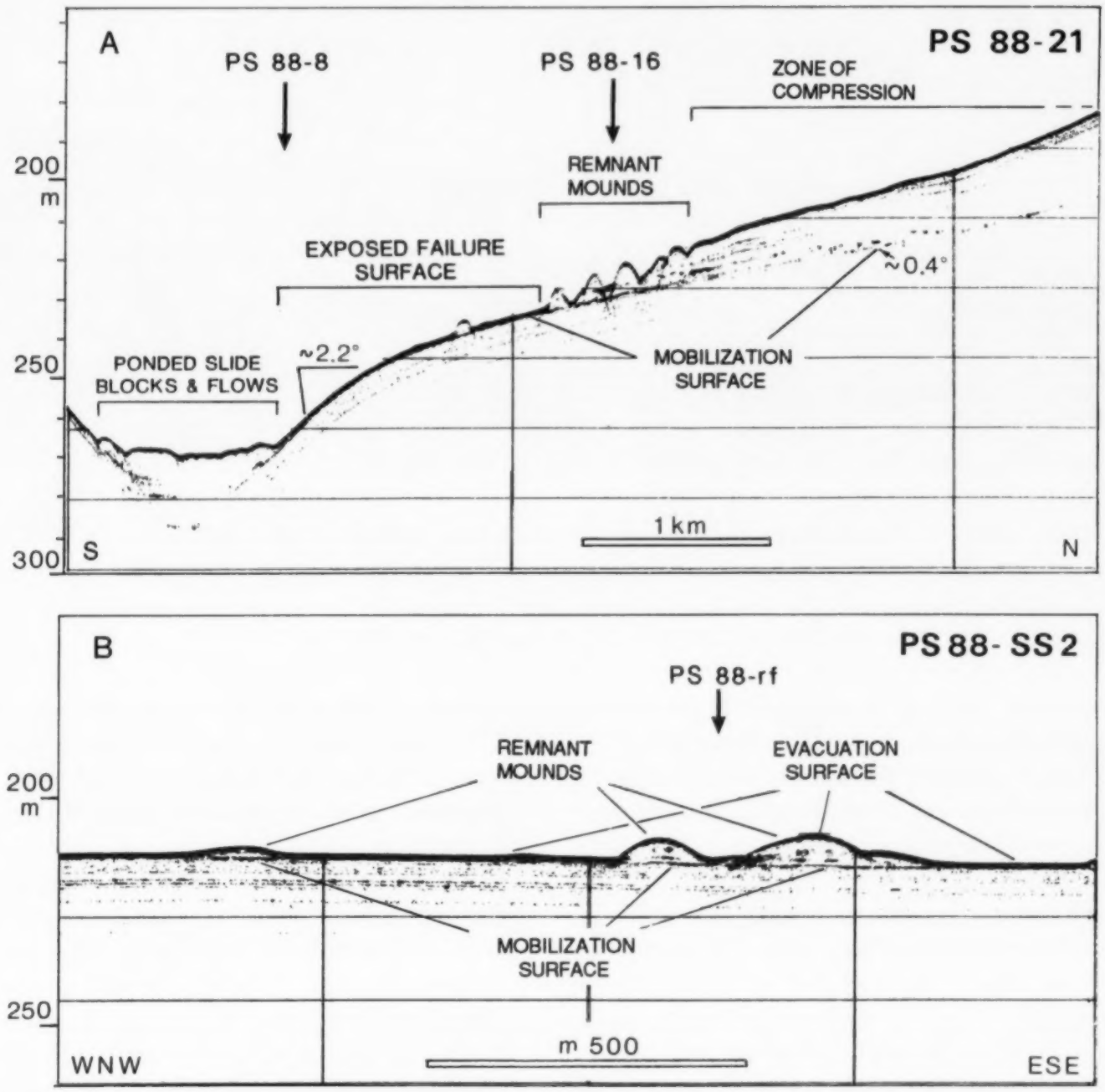

Fig. 4. High-resolution seismic-reflection dip (A) and strike (B) profiles across Licosa slide (locations in Fig. 3). The profiles show the extremely smooth nature of the exposed slide surface; the parallel internal bedding in sediment mounds downslope from the slide surface indicating that the mounds are in situ; and the evidence for deformation and folding updip from the failure scarp.

Quaternary slides (e.g. Normark, 1990). The mounds consistently decrease in height downslope, and this also suggests that translation of the mounds did not occur or was minor. The shelf-margin deposits form a sediment wedge that thins basinward, and decreasing mound height reflects this trend. We interpret the mounds as in-situ remnants of the collapsed section. The mounds are coalesced near the slide scarp and become more sparse downslope where sediment was removed across a wide area.

A strike section through the failure zone illustrates the lateral complexity of Licosa slide (Fig. 7). Because of the complicated morphology of the Licosa margin, the upper section of sediment responded differently at different locations during failure. In some places, the evacuation surface bounds the high-relief undeformed remnant sediment, as in profile PS88-16 (Fig. 7A and B). In adjacent locations subsurface deposits are deformed only along the mobilization surface in response to compressive stresses developed during translation (Fig. 7B). The mobilization surface is exposed in the zone of greatest slope (between 2°

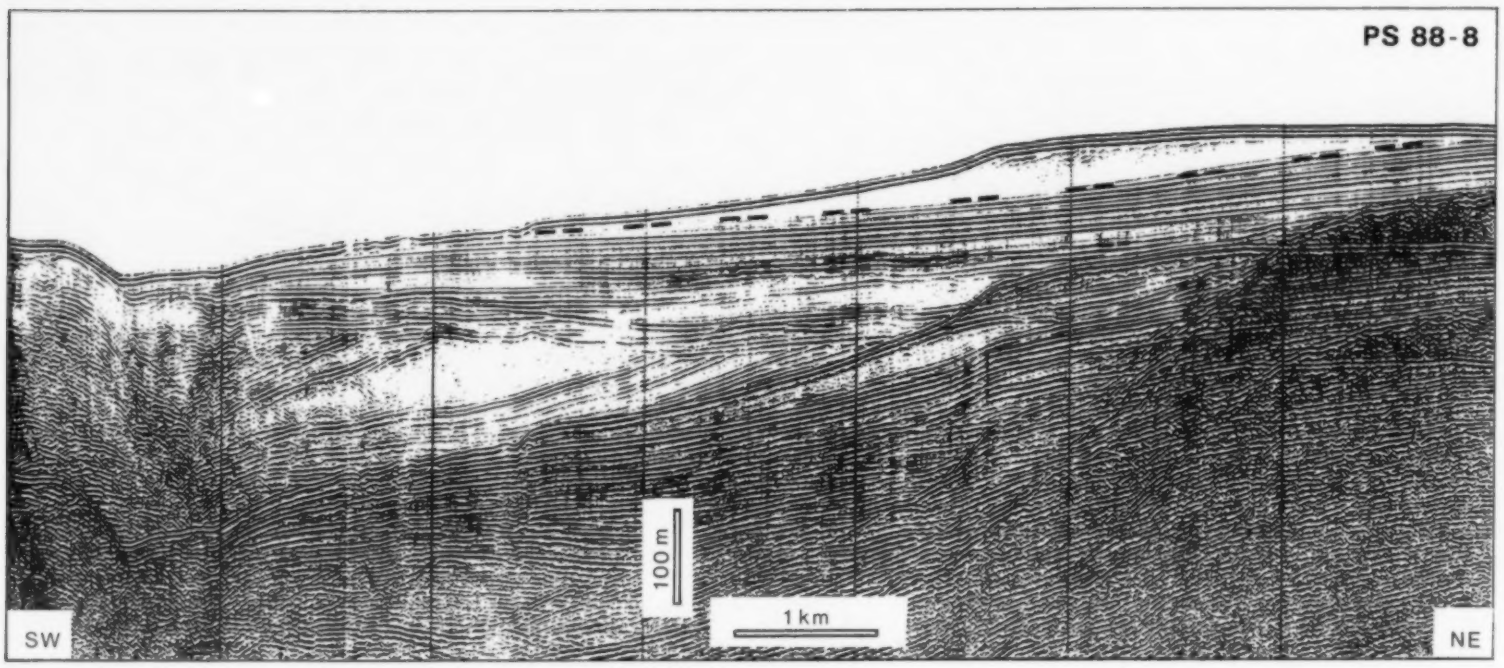

Fig. 5. One-kJ sparker seismic reflection profile showing the geometric character of the downlap surface on which mobilization of regressive deposits occurred. Note the seaward steepening of foresets and the "transparent" acoustic facies of the regressive deposit, both consistent with the seaward increase in sediment grain-size observed on gravity cores.

and 3°) within the slide area, probably as a result of complete mobilization and downslope transport of the failed section. The zone where sediment mobilized and flowed downslope is also referred to as the zone of evacuation (Edwards et al., in press).

Examples of large-scale mounds comparable with those observed in the area of Licosa slide come from areas characterized by high rates of progradation, such as modern deltaic systems. Mounds of relatively undisturbed sediment tens to hundreds of meters in diameter are found in the gully-head region on the Mississippi delta front (Roberts, 1980). There, as on the Licosa margin, the mounds decrease in size basinward and rest on a well defined basal bedding plane. In Alaska, a portion of the Alsek prodelta is characterized by a similar irregular mounded surface seaward of the major scarp (Schwab et al., 1987).

Ponded debris

A portion of the failed sediment is piled in the trough between the slope ridge and the upper slope, indicating a minimum transport distance of several hundred meters (Fig. 2). The deposit is 10 to 20 m thick and acoustically transparent, with no evidence of internal stratification. This, along with the hummocky upper surface, suggests significant remoulding of the transported sediment. The upper surface varies from flat-lying to tilted, indicating both downslope flow and local up-slope transport and deposition, probably by viscous flows. The sediment stopped flowing to the west down the trough when the shear strength exceeded the driving forces. Local small-scale hummocky relief, indicated by hyperbolic echoes from the upper surface, is probably caused by intact blocks that were rafted by the sediment flows. Rafted blocks of comparable size or larger have been observed in slide deposits in other locations (Hill, 1984; Carter and Carter, 1985; Shor and Piper, 1989; Normark, 1990). These and other studies have shown that blocks tend to decrease in size in the downslope direction by breaking apart during transport. In areas of high relief, such as fjords, blocks have been inferred to have outrun sediment gravity flows and be deposited in undeformed areas of the seafloor (Prior et al., 1984).

Timing and style of failure

Occurrence in mid-Holocene time

The timing of the Licosa slide is fairly well constrained by seismic-reflection data and core samples to be early to mid-Holocene time. High-

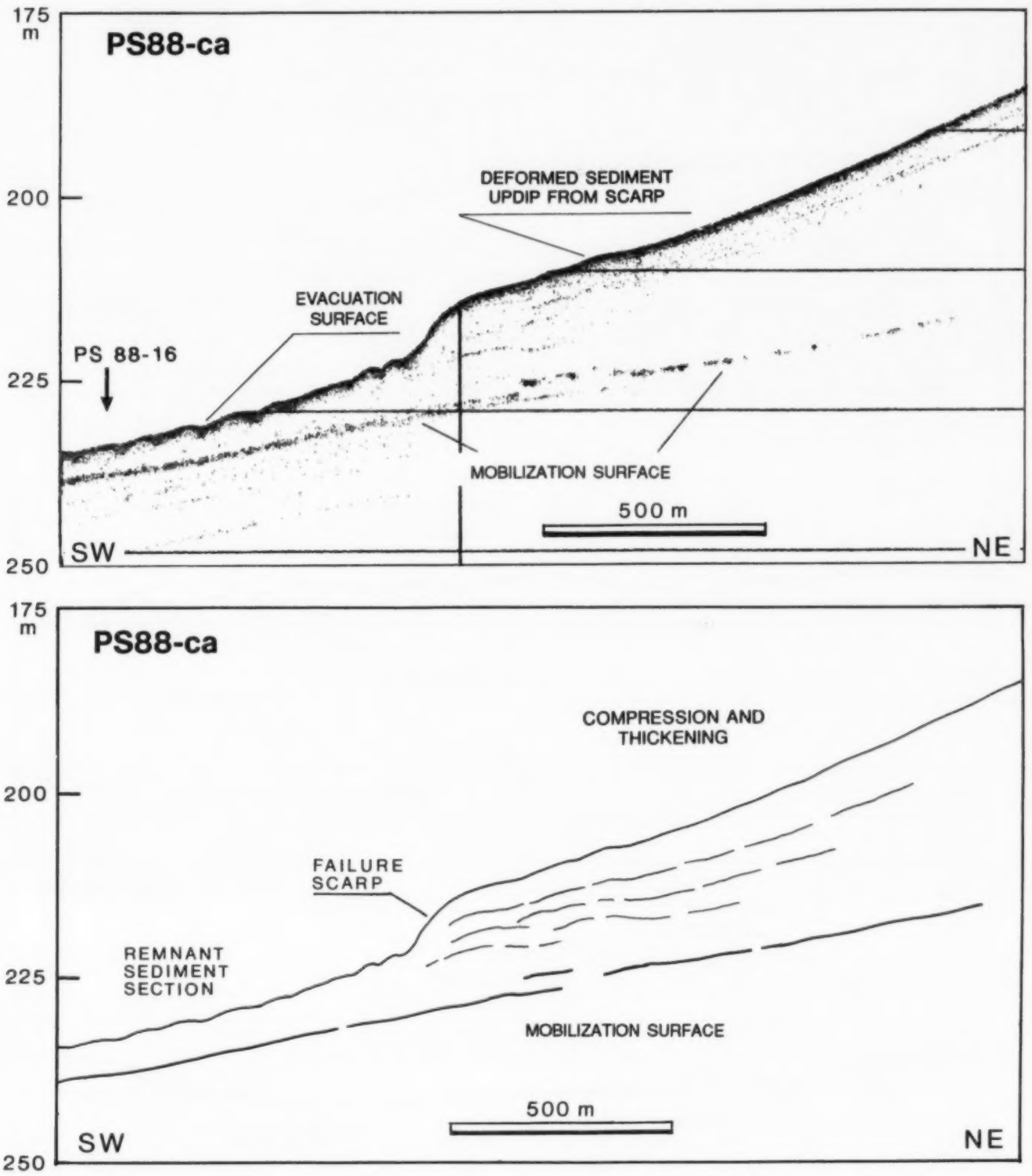

Fig. 6. High-resolution seismic-reflection profile PS88-ca and interpreted line drawing showing the nature of internal compressive deformation *upslope* from the scarp. Profile location in Fig. 3.

resolution reflection records show that failure took place following coastal progradation driven by a relative fall of sea level (Trincardi and Field, 1991). As no regressive beds cap the slide, failure must have occurred sometime after sea level reached its last lowstand position about 18,000 yrs B.P. The thin sediment veneer that drapes the slide is interpreted by Trincardi and Field (1991) to result from transgressive and highstand sedimentation on the outer shelf.

Core data collected in a transect across the slide zone substantiate a late Pleistocene to mid Holocene time of failure. Cores are shown schematically in Fig. 8; original logs and photographs are in Bortoluzzi et al. (1989). Within the slide area, transgressive and highstand sediment is distin-

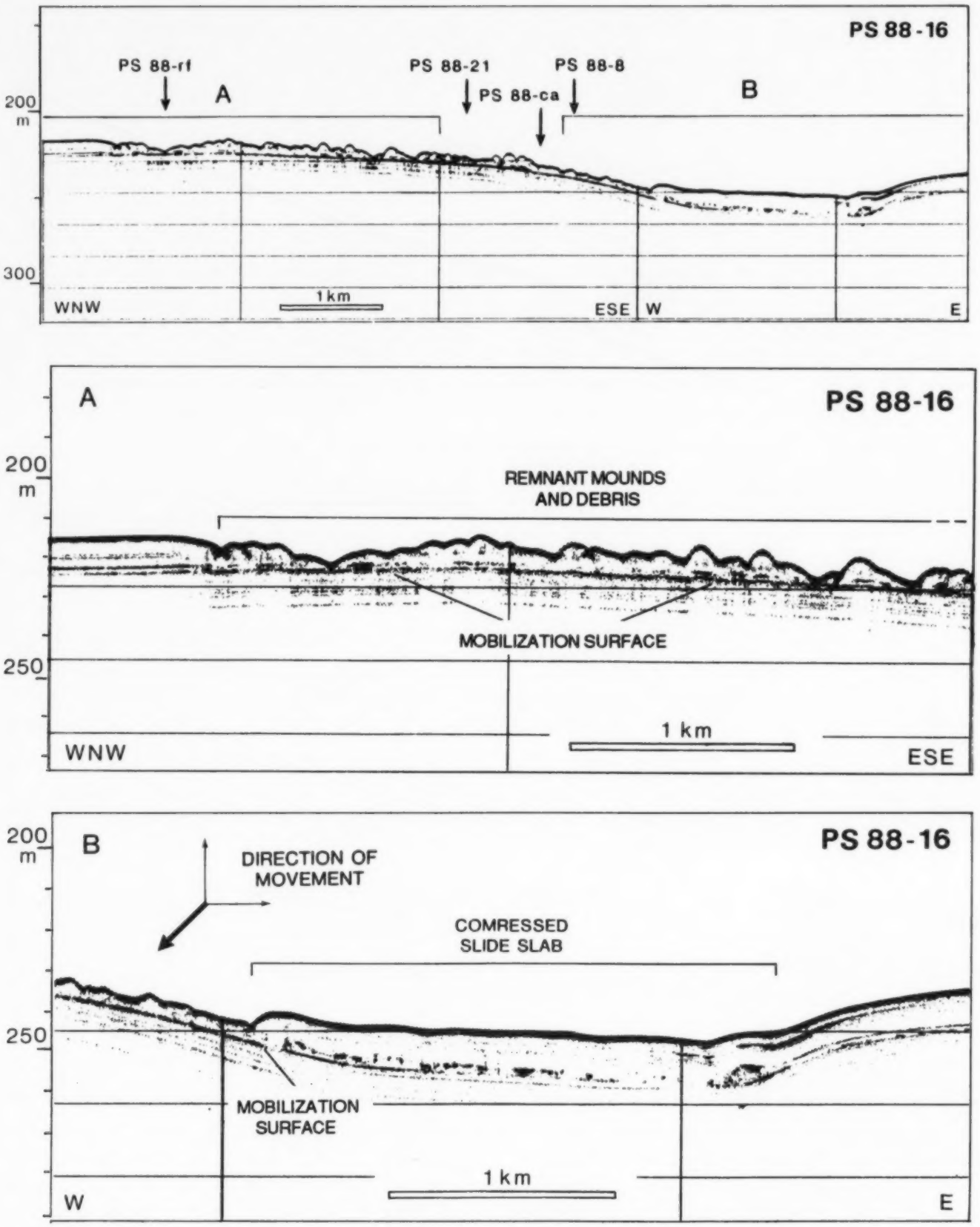

Fig. 7. High-resolution seismic-reflection profile PS88-16 crossing the slide subparallel to strike (location in Fig. 3). The top profile (A) shows that material left behind after the failure is essentially in place, as evident from continuity of internal bedding. The bottom profile (B) shows internal deformation of beds from compression of the slide slab.

guished from the underlying failure deposits by the absence of boreal (cold water) fauna and the presence of faunas in equilibrium with the present-day water depth and sediment texture. An ash layer resulting from the 79-A.D. *Plinian* eruption of the Vesuvius volcano (Bortoluzzi et al., 1989; Rosi et al., 1990) uniformly covered the entire study area. The *Plinian* ash layer lies at 20–40 cm

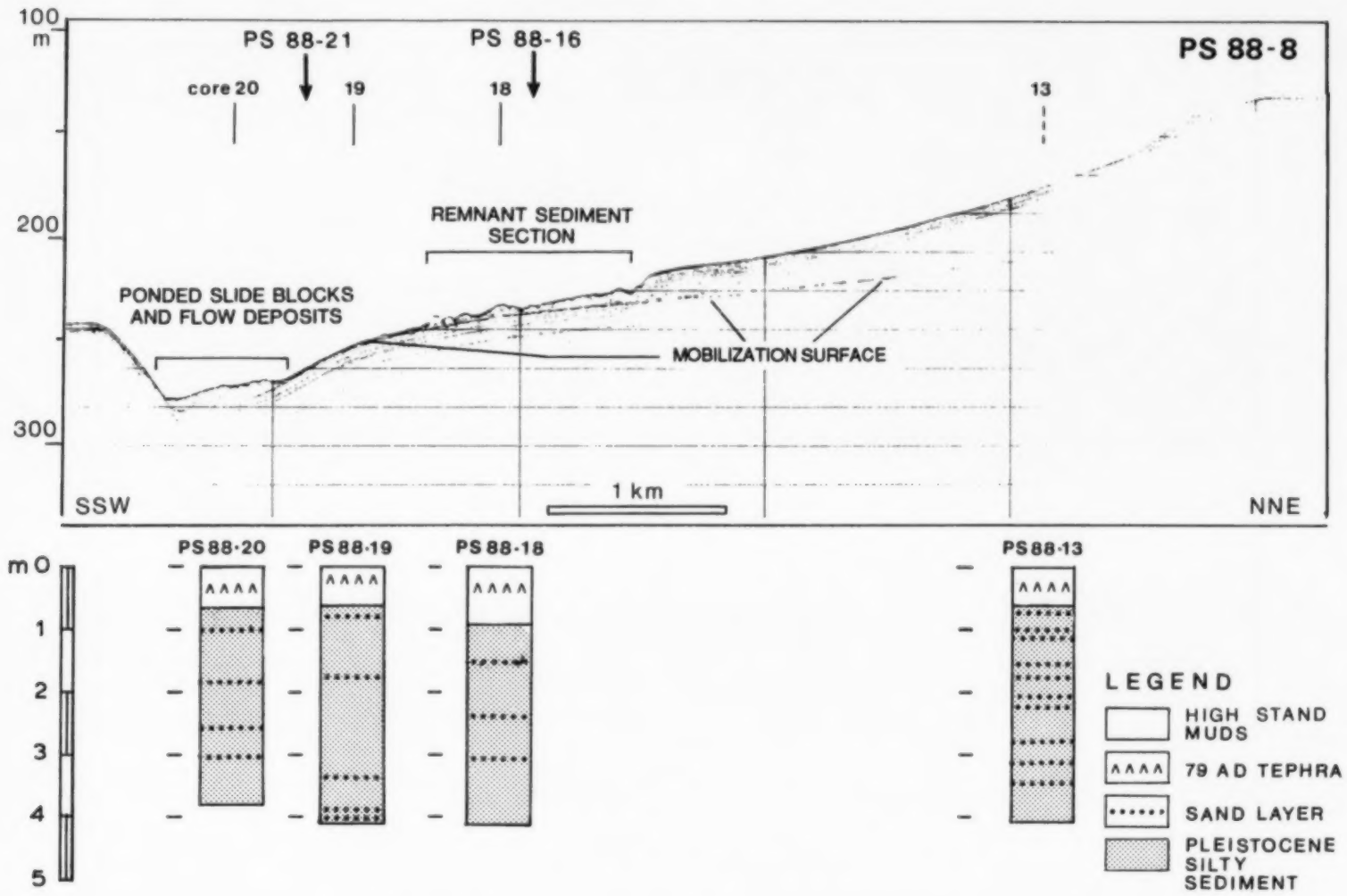

Fig. 8. High resolution acoustic profile PS88-8 across the slide showing location and lithology of gravity cores (location in Fig. 3). The profile is similar in detail to those shown in Figs. 2 and 4A with one addition: the slide surface can be traced beneath the ponded slide blocks and flow deposits. All four cores have a well-correlated 2 ky ash layer (Rosi et al., 1990) about half a meter from the surface.

below the surface in each core and is interbedded in highstand deposits composed dominantly of silty clay (Fig. 8). This surface layer of highstand sediment is about 75–100 cm thick and overlies coarser (sandy silt) deposits containing boreal fauna; in two cores (PS88-18 and 20) the interface is marked by the presence of corals and bryozoans (Fig. 8). Based on the burial depth of the tephra within the Holocene section, the surface layer has an approximate sedimentation rate of 10 to 20 cm/1000 yrs, and was deposited over roughly 3000 to 6000 years. This thin surface layer, not discernible on acoustic profiles, is interpreted to be the result of transgressive and highstand deposition across the margin. The presence of highstand sediment as an undisturbed drape across the exposed mobilization surface and failure deposits constrains the time of failure to mid-Holocene or older. The fact that failure postdates the last lowstand of relative sea level constrains it to be younger than late Pleistocene.

Initiation of failure

The surface we identify as the mobilization surface marks a major sequence-stratigraphic change and therefore a probable lithologic change as well. The surface of failure is the recent-most downlap surface within the shelf margin deposits and thus represents a hiatus, or significant change, in sedimentation (Fig. 9). The downlap surface is shown by coring to be composed of a thin drape of slowly deposited fine grained sediment, on to which coarser grained coastal facies rapidly prograded during the late stages of the last fall in sea level (Trincardi and Field, 1991). The pronounced change in sediment below and above the downlap surface results in marked differences in lithologic

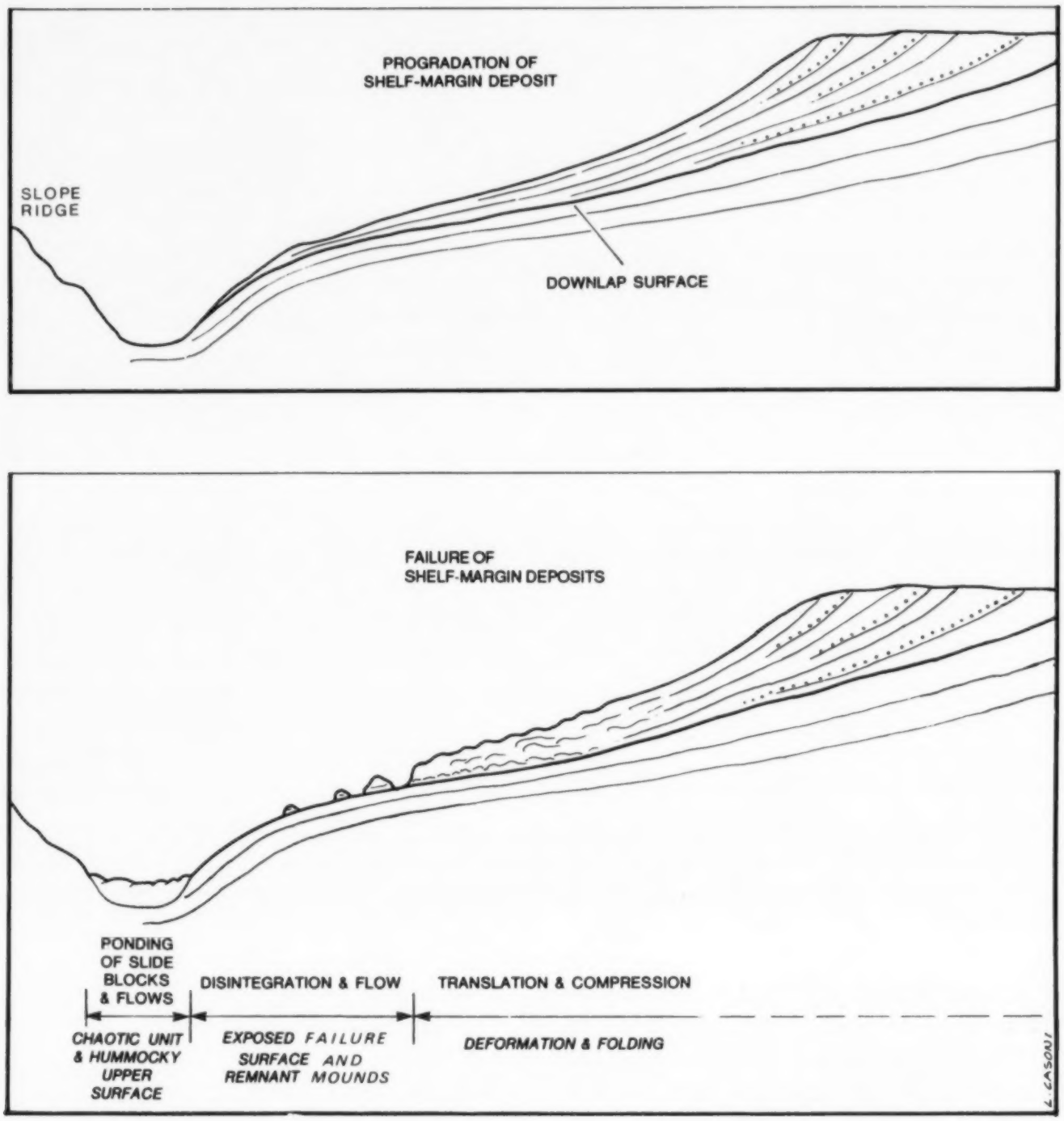

Fig. 9. Schematic diagram illustrating the pre- and post-failure cross sections of the seafloor. The sediment that failed is inferred to be fine-grained deposits formed in a nearshore environment during the last low stand of sea level (Trincardi and Field, 1991).

character and derivative physical properties, such as water content and shear strength.

The enhanced (high-amplitude) reflectors that define the mobilization surface indicate a local change in sediment properties along the failure surface (Figs. 6A and 7B). Without samples it is not possible to identify the nature of those changes, but comparable studies elsewhere have indicated that the presence of gas and the local densification of sediment due to fluid loss are two possible mechanisms to explain enhanced reflectors (Dobrin, 1976; Field and Jennings, 1987). Because the area where the mobilization surface appears deformed and acoustically enhanced is much larger than the slide itself (Figs. 3 and 4A), we assume that an increase of shear strength through this surface prevented the section underneath it from failing. Sediment mobilization and translation was limited to the weaker unit above this surface but developed over a broad area and may, in turn, have induced fluid escape.

The perturbations in the mobilization surface

upslope of the slide scarp indicate that compression occurred along and above the basal surface (Figs. 6 and 8). Crumpling of the beds was probably caused by the interaction between downslope transport and shear resistance on the basal surface (Fig. 10). The slide slab east of the failure zone (Fig. 7B) formed the same way as the folded section upslope of the slide scarp, but it shows more internal deformation, possibly because of more lateral confinement.

Disintegration and transport

All aspects of Licosa slide indicate that as failure occurred, the shelf margin deposits lost their internal strength and disintegrated into sediment gravity flows (Fig. 10). The chaotic, irregular surface and internal bedding of the sediment piled against the slope ridge shows that the sediment flows contained large blocks and clasts that were rafted along the surface. Additionally, the highly irregular character of the failure surface downslope from the scarp indicates that sediment was evacuated by flows rather than by large discrete blocks sliding over a smooth, uniform surface. No evidence of simple rotational slumps is found in the head region. No deep core samples are available from the ponded deposit to document the type of sediment flow that occurred, but as much of the sedimentary section above the failure surface was completely removed, it seems likely that the sediment flowed as either a turbidite or a cohesionless debris flow (Postma, 1986).

The sediment failure at Licosa shows the heterogeneity that occurs in failures and that results in a variety of clast sizes carried in a flow, as documented on video for example at Rissa, Norway (Gregersen, 1981) where glacial quick-clays failed. The Rissa documentation also shows the decreasing relief of the remnant sediment in the slide zone and shows large blocks and slabs of ground, some with houses and barns still intact, being carried on the surface of viscous sediment flows. The Licosa failure, like the Rissa failure and many others suggests a style of failure involving sediment reaching a critical state and disintegrating into flows in a continuous retrogressive sequence. Remnant sediment mounds and the main scarp at Licosa mark areas where sediment strength exceeded the tendency to fail, probably as a result of local inhomogeneities in the sediment (Fig. 10).

Liquefaction of seafloor deposits, typically initiated at shallow subsurface depths, leads to sediment failure and flowage (Field et al., 1982; Keefer,

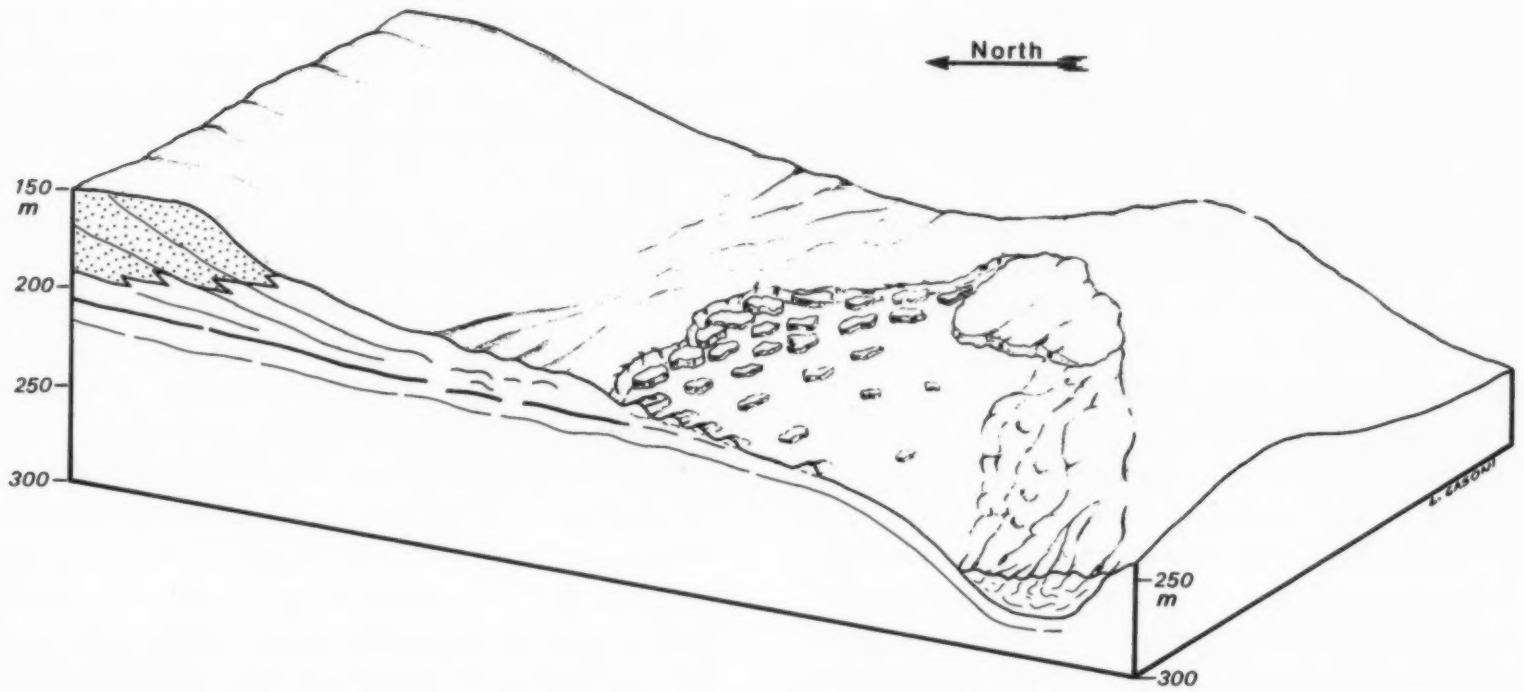

Fig. 10. Block diagram illustrating the setting and geometry of the Licosa shelf following the collapse and flow of regressive downlapping deposits.

1984; Einsele, 1990). The enhanced acoustic character of the basal mobilization surface may indicate that liquefaction occurred along that plane. Once failure was initiated along the basal plane, whether by liquefaction of a layer or by shearing, it caused a loss of sediment strength and initiated widespread failure on the shelf margin deposit (Fig. 9). Underneath the mobilization surface sediment strength increases preventing the failure of the older deposits. Thus Licosa slide represents an example of sediment collapse along the steeper part of the mobilization surface and failure that retrogressed upslope towards the margin sector where the mobilization surface becomes progressively gentler. Isolated mounds resting on this surface are interpreted to be remnant of the removed part of the section rather than translated material. As failure continued, it propagated upslope in response to the removal of downslope frictional resistance. The failure proceeded in this way until the strength of material overlying the mobilization surface exceeded the forces driving failure. Compressional deformation on the mobilization surface indicates that the overlying deposit remained potentially unstable after the downslope section was evacuated (Fig. 10).

Sediment failure in lowstand shelf margin deposits

Submarine sediment failures are commonly associated with particular sedimentary environments. For example, deltas, submarine canyons, and deep sea fans are settings where sediment failure is concurrent with active deposition (Moore, 1977). That is, instability occurs at the site of accumulation largely as a result of the particular physical properties exhibited by the deposits such as fluid pore-pressure, high accumulations of organic matter, and low shear strength (Field et al., 1982; Prior and Coleman, 1984; Lee, 1989).

Sediment failure in areas where active deposition has essentially ceased is thought to be controlled by earthquakes, slope steepening, and other tectonic processes (e.g., Moore, 1977; Hampton and Bouma, 1977). Relative falls of sea level also may be important (Coleman et al., 1983; Mutti, 1985) as they lead to high rates of deposition directly at the shelf edge where pre-existing deposits may be rapidly loaded and become unstable. Thus, sea-level falls and lowstands are thought to be characterized by an increase in frequency of sediment failures (Posamentier and Vail, 1988).

Shelf-edge failures are common to Quaternary deposits of many continental margins, particularly near major fluvial sources of sediment. Sediment failure offshore of large streams can be concurrent with deposition and commonly yields a variety of distinctive features, such as, growth faults. In areas where sediment failure follows active deposition, slump scarps tend to dominate seafloor morphology, because they are relatively high-angle and cut through older deposits (Coleman et al., 1983; Tesson et al., 1990). Rifted, tectonically-active, continental margins are particularly prone to shelf-margin failure resulting from the effects of sediment deposition on steeply dipping slopes (Argnani et al., 1989; Tesson et al., 1990; Ferran and Maldonado, 1990) seismic activity (Barnes and Lewis, 1991), and tectonic steepening of slopes (Ferentinos et al., 1981).

On the eastern Tyrrhenian Sea margin sediment failure is also a common phenomenon; where failure occurs on the seaward termination of progradational lowstand shelf-margin deposits we relate its occurrence to cycles of sedimentation forced by sea-level fluctuations. At places mobilization occurs on the basal surface of downlap and gives rise to a limited amount of deformation not followed by translation or disintegration and flow (Fig. 11A). Elsewhere, the style of failure and the amount of downslope desplacement are affected by the size and location of morphologic reliefs that, at places, can buttress the failed section preventing further translation (Fig. 11B). The Licosa failure, in particular, represents a case in which downslope mass transport occurred following a major pulse of coastal progradation (Fig. 10). Coastal progradation at the shelf edge into deepening water provided a thickened section of sand-rich sediment on a relatively steep slope. Failure occurred after the cessation of progradation and the landward shift of the sediment input, both caused by a relative rise in sea level. Hence, the role played by a sea-level fall, although somewhat indirect, is markedly significant in that it controls the rapid emplacement on shelf margins

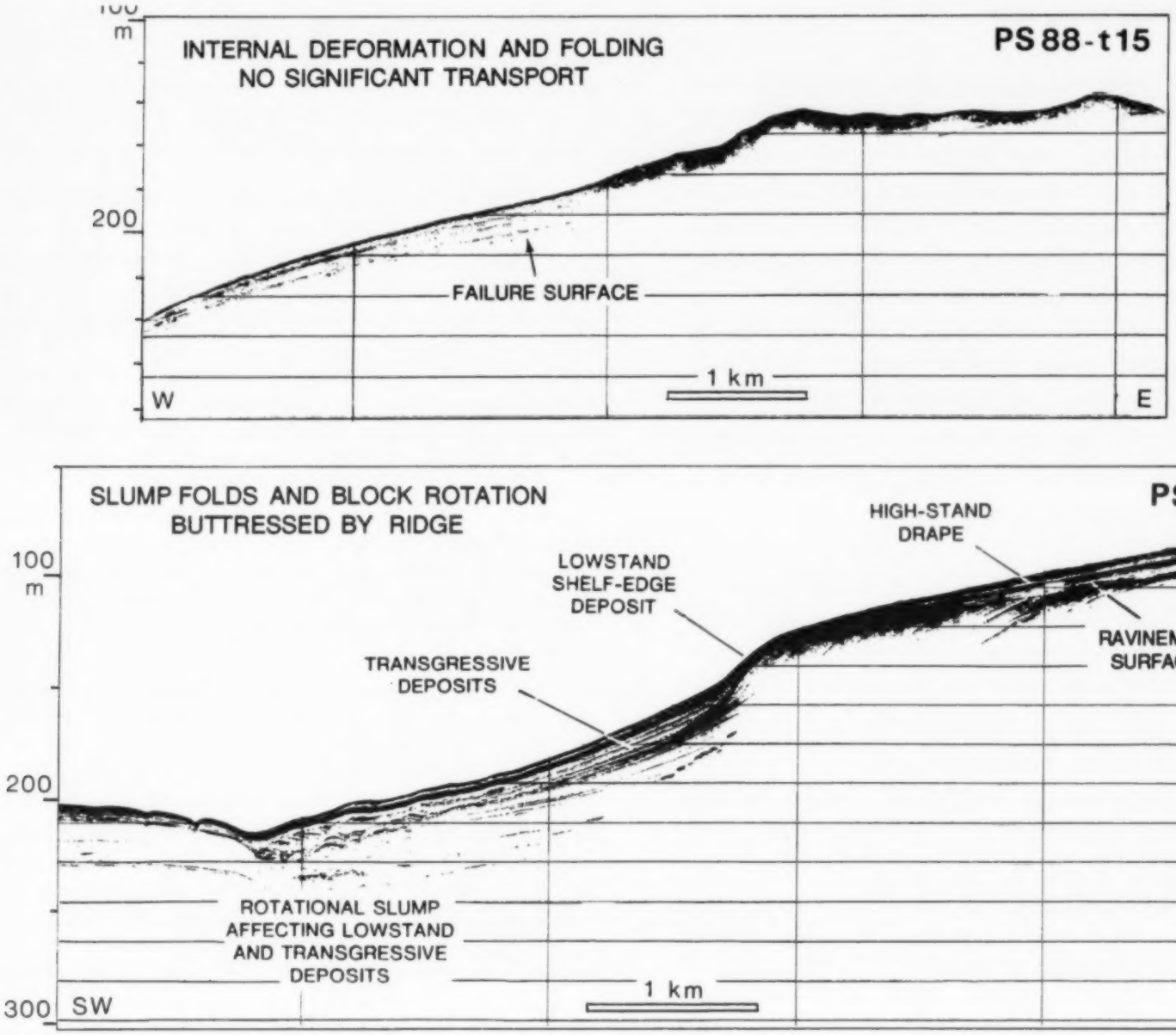

Fig. 11. High-resolution seismic-reflection profiles outside of the Licosa slide that indicate initial stages of failure but lack evidence of collapse into flows. Profile locations are in Fig. 1. (Top) Profile PS88-t15 shows deformation in beds downdip, but no significant lateral transport appears to have occurred. (Bottom) Profile PS87-3 shows rotational failures in low-stand and transgressive deposits. The slump blocks are buttressed against an offshore ridge, perhaps preventing further disintegration and translation.

of coarsening-upward sediment wedges that are prone to sediment failure by disintegration and flow.

Summary

(1) The Licosa failure occurred in a progradational coastal wedge that formed during the late Pleistocene relative sea-level fall and lowstand. Failure occurred in mid-Holocene time, after active progradation had ceased.

(2) The collapsed section was less than 15 m thick in the head region. Allochtonous remoulded debris and rafted blocks are found few kilometers south of the failure in 280 to 300 m of water. Remnant sediment mounds characterize the area immediately seaward of the scarp, indicating that downslope translation did not affect the entire sediment section above the mobilization surface.

(3) Slope instability occurred initially along a regional surface of downlap at the base of the lowstand progradational sedimentary unit. The surface may have been blanketed by unstable deposits that mobilized and caused the collapse and flow of the overlying section.

Acknowledgements

We thank Michael Marani and Marco Taviani for their stimulating comments on an earlier version of this paper, and Homa Lee and William Normark for their thoughtful and careful critical reviews. We also gratefully acknowledge Capitan Mario Piazza, officers and crew of the R/V *Bannock* for their skillful work during cruise PS88 and Marco Ligi and Marcello Canu for assisting us with navigation and digital bathymetric data. Luciano Casoni prepared the figures. This is contribution No. 878 of the *Istituto per la Geologia Marina*.

References

Almagor, G., 1980. Halokinetic deep-seated slumping on the Mediterranean slope of northern Sinai and southern Israel. Mar. Geotechnol., 4(1): 83–105.

Argnani, A. and Trincardi, F., 1990. Paola slope basin: evidence of regional contraction on the Eastern Tyrrhenian Margin. Mem. Soc. Geol. Ital., 44: 93–105.

Argnani, A., Bortoluzzi, G., Bozzani, A., Canepa, A., Ligi, M., Palumbo., Serracca, P. and Trincardi, F., 1989. Sedimentary dynamics on the Eastern Tyrrhenian Margin: preliminary report. G. Geol., 51(1): 165–178.

Barnes, P.M. and Lewis, K.B., 1991. Sheet slides and rotational failures on a convergent margin: the Kidnappers slide, New Zealand. Sedimentology, 38: 205–221.

Bartole, R., 1983. Tectonic structure of the Latian–Campanian shelf (Tyrrhenian Sea). Boll. Oceanol. Teor. Appl., 2: 197–230.

Bartole, R., Savelli, C., Tramontana, M. and Wezel, F.-C., 1984. Structural and sedimentary features in the Tyrrhenian margin off Campania, Southern Italy. Mar. Geol., 55: 163–180.

Bortoluzzi, G., Gasperini, L., Marozzi, G., Palumbo, V., Spagnoli, F., Taviani, M. and Trincardi, F., 1989. Studio pluridisciplinare di un margine continentale: rapporto sulla crociera PS 88 (margine tirrenico orientale da Capo Palinuro alla Penisola Sorrentina). Rapp. Tecnico Ist. Geol. Mar., Bologna, 23, 75 pp.

Boschi, E., Pantosti, D., and Valensise, G., 1990. Paradoxes of Italian seismicity. EOS, Trans. Am. Geophys. Union, 71: 1787–1788.

Canu, M. and Trincardi, F., 1989. Controllo eustatico e tettonico sui sistemi deposizionali del Bacino di Paola (Plio-Quaternario), margine tirrenico orientale. G. Geol., 51(2): 41–61.

Carlson, R.L., Gangi, A.F. and Snow, K.R., 1986. Empirical reflection travel time versus depth and velocity versus depth functions for the deep sea sediment column. J. Geophys. Res., 91: 8249–8266.

Carter, L. and Carter, R.M., 1985. Current modification of a mass failure deposit on the continental shelf, North Canterbury, New Zealand. Mar. Geol., 62: 193–211.

Coleman, J.M., Prior D.B. and Lindsay J.F., 1983. Deltaic influences on shelfedge instability processes. In: D.J. Stanley and G.T. Moore (Editors), The Shelfbreak: Critical Interface on Continental Margins. Soc. Econ. Paleontol. Mineral. Spec. Publ., 33: 121–137.

Dobrin, M.B., 1976. Introduction to Geophysical Prospecting. McGraw-Hill, New York, 3rd ed., pp. 339–356.

Edwards, B.D., Lee, H.J. and Field, M.E., in press. Mud flow generated by retrogressive slope failure, Santa Barbara Basin, California Borderland—Part I: geometry and processes. J. Sediment. Petrol.

Einsele, G., 1990. Deep-reaching liquefaction potential of marine slope sediments as a prerequisite for gravity mass flows? (Results from the DSDP). Mar. Geol., 91: 267–279.

Fabbri, A., Gallignani, P. and Zitellini, N., 1981. Geologic evolution of the peri-Tyrrhenian sedimentary basins. In: F.-C. Wezel (Editor), Sedimentary Basins of Mediterranean Margins. Tecnoprint, Bologna, pp. 101–126.

Ferentinos, G., Brooks, M. and Collins, M., 1981. Gravity-induced deformation on the North flank and floor of the Sphorades Basin of the North Aegean Sea Trough. Mar. Geol., 44: 289–302.

Ferran, M. and Maldonado, A, 1990. The Ebro continental shelf: Quaternary seismic stratigraphy and growth patterns. Mar. Geol., 95: 289–312.

Field, M.E., 1987. Sediment mass-transport in basins: controls and patterns. In: D.S. Gorsline (Editor), Depositional Systems in Active Margin Basins. Pacific Sec., Soc. Econ. Paleontol. Mineral., Los Angeles, 54: 1–23.

Field, M.E. and Jennings, A.E., 1987. Seafloor gas seeps triggered by a northern California earthquake. Mar. Geol., 77: 39–51.

Field, M.E. and Trincardi, F., 1992. Regressive coastal deposits on Quaternary continental shelves: preservation and legacy. In: R.H. Osborne (Editor). Soc. Econ. Paleontol. Mineral. Spec. Publ., 46.

Field, M.E., Gardner, J.V., Jennings, A.E. and Edwards, B.D., 1982. Earthquake-induced sediment failures on a 0.25 degrees slope, Klamath River delta, California. Geology, 10: 542–546.

Gabbianelli, G., Gillot, P.Y., Lanzafame, G., Romagnoli, C. and Rossi, P.L., 1990. Tectonic and volcanic evolution of Panarea (Aeolian Islands, Italy). Mar. Geol., 92: 313–326.

Gallignani, P., 1982. Recent sedimentation processes on the Calabrian continental shelf and slope (Tyrrhenian Sea Italy). Oceanol. Acta, 5: 493–500.

Gregersen, O., 1981. The quick clay landslide in Rissa, Norway. Proc. Tenth Int. Conf. Soil Mechanics Foundation Engineering. Stockholm, 3, pp. 421–426.

Hampton, M.A., 1992. Comparison of tectonic and stratigraphic control of submarine landslides on the Kodiak upper continental slope, Alaska. In: W.C. Schwab, H.J. Lee, D.C. Twichell and M.A. Hampton (Editors), Submarine Landslides: Selected Studies from the U.S. Exclusive Economic Zone. U.S. Geol. Surv. Bull., 2002, Pap. 13.

Hampton, M.A. and Bouma, A.H., 1977. Slope instability near the shelf break, western gulf of Alaska. Mar. Geotechnol., 2: 309–331.

Hill, P.R., 1984. Sedimentary facies of the Nova Scotian upper and middle slope, offshore eastern Canada. Sedimentology, 31: 293–309.

Kastens, K., Mascle, J., Auroux, C., Bonatti, E., Broglia, C., Channel, J., Curzi, P., Emeis, K., Glacon, G., Hasegawa, S., Hieke, W., Mascle, G., McCoy, F., McKenzie, J., Mendelson, J., Muller, C., Rehault, J., Robertson, A., Sartori, R., Sprovieri, R. and Torii, M., 1988. ODP Leg 107 in the Tyrrhenian sea: Insights into passive margin and back-arc basin evolution. Geol. Soc. Am. Bull., 100: 1140–1156.

Keefer, D.K., 1984. Landslides caused by eartthquakes. Bull. Geol. Soc. Am., 95: 406–421.

Kenyon, N.H., 1987. Mass-wasting features on the continental slope of northwest Europe. Mar. Geol., 74: 57–77.

Lee, H.J., 1989. Undersea landslides: extent and significance in the Pacific Ocean. In: E.E. Brabb and B.L. Harrod, (Editors), Landslides: Extent and Economic Significance. Proc. 28th IGC Symp. on Landslides. Balkema, Rotterdam, pp. 367–379.

Lee, H.J., Edwards, B.D. and Field, M.E., 1981. Geotechnical analysis of a submarine slump, Eureka, California. Proc. Offshore Technol. Conf., OTC-4121: 53–59.

Loutit, T.S., Hardenbol, J., Vail, P. and Baum, G.R., 1988. Condensed sections, the key to age determination and correlation of continental margin sequences. In: C.K. Wilgus, B.S. Hastings et al. (Editors,) Sea Level Changes—an Integrated Approach. Soc. Econ. Paleontol. Mineral. Spec. Publ., 42: 183–213.

Marani, M., Taviani, M., Trincardi, F., Argnani, A., Borsetti, A.M. and Zitellini, N., 1988. Pleistocene progradation and postglacial events of the NE Tyrrhenian continental shelf between the Tiber river delta and Capo Circeo. Mem. Soc. Geol. Ital., 36: 67–89.

McGregor, B., Rothwell, G., Kenyon, N.H. and Twichell, D.C., 1992. The effect of salt diapirsm on submarine slope failure: western gulf of Mexico. In: W.C. Schwab, H.J. Lee, D.C. Twichell and M.A. Hampton (Editors), Submarine Landslides: Selected Studies from the U.S. Exclusive Economic Zone. U.S. Geol. Surv. 2002, Bull., Pap. 10.

Middleton, G.V. and Hampton, M.A., 1973. Sediment gravity flows: mechanics of flow and deposition. In: G.V. Middleton and A.H. Bouma (Editors), Turbidites and Deep Water Sedimentation. Soc. Econ. Paleontol. Mineral. Pacific Sec. Short Course Notes, pp. 1–38.

Moore, D.G., 1961. Submarine slumps. J. Sediment. Petrol., 31: 343–357.

Moore, D.G., 1977. Submarine slides. In: B. Voight (Editor), Rockslides and Avalanches. (Developments in Geotechnical Engineering, 14A) Elsevier, Amsterdam, pp. 563–601.

Mutti, E., 1985. Turbidite systems and their relation to depositional sequences. In: G.G. Zuffa (Editor), Provenance of Arenites. Reidel, Boston, Mass., pp. 63–93.

Normark, W.R., 1990. Return to Ranger Submarine Slide, Baja California, Mexico. Geo-Mar. Lett., 10: 81–91.

Normark, W.R., Chase, T.E., Campbell, F., Tsutsui, B. and Wilde P., 1992. Hurricane slope failures induced by Hurricane Iwa, Kahe Point, Oahu, Hawaii. In: W.C. Schwab, H.J. Lee, D.C. Twichell and M.A. Hampton (Editors), Submarine Landslides: Selected Studies from the U.S. Exclusive Economic Zone. U.S. Geol. Surv. Bull., 2002, Pap. 23.

Ortolani, F. and Torre, M., 1981. Guida all'escursione nell'area interessata dal terremoto del 23.11.1980. Rend. Soc. Geol. Ital., 4.: 173–214.

Perissoratis, C., Mitropoulos, D. and Angelopoulos, I., 1984. The role of earthquakes in inducing sediment mass movements in the Korinthiakoc Gulf. An example from the February 24–March 4, 1981 activity. Mar. Geol., 55: 35–45.

Popenoe, P., Schmuck, E. and Dillon W., 1992. The Cape Fear landslide: slope failure associated with salt diapirism and gas hydrate decomposition. In: W.C. Schwab, H.J. Lee, D.C. Twichell and M.A. Hampton (Editors), Submarine Landslides: Selected Studies from the U.S. Exclusive Economic Zone. U.S. Geol. Surv. Bull., 2002, Pap. 5.

Posamentier, H.W. and Vail, P.R., 1988. Eustatic control on clastic deposition, II—sequence and systems tract models. In: C.K. Wilgus, B.S. Hastings, C.G.St.C. Kendall et al. (Editors), Sea-Level Changes—An Integrated Approach. Soc. Econ. Paleontol. Mineral. Spec. Publ., 42: 125–154.

Postma, G., 1986. Classification for sediment gravity-flow deposits based on flow conditions during sedimentation. Geology, 14: 291–294.

Prior, D.B. and Coleman, J.M., 1982. Active slides and flows in underconsolidated marine sediments on the slopes of the Mississippi delta. In: S. Saxov and J.K. Nieuwenhuis (Editors), Submarine Slides and Other Mass Movements. Plenum, New York, pp. 21–50.

Prior, D.B. and Coleman, J.M., 1984. Submarine slope instability. In: D. Brunsden and D.B. Prior (Editors), Slope Instability. Wiley, New York, pp. 419–455.

Prior, D.B., Bornhold, B.D. and Johns, B.D., 1984. Depositional characteristics of a submarine debris flow. J. Geol., 92: 707–727.

Rehault, J.P., Mascle, J., Fabbri, A., Moussat, E. and Thommeret, M., 1987. The Tyrrhenian Sea before leg 107. In: K. Kastens, J. Mascle et al. (Editors), Init. Rep. DSDP, 107: 9–35.

Roberts H.H., 1980. Sediment characteristics of Mississippi river deltafront mudflow deposits. Gulf Coast Am. Geol. Soc. Trans., 30: 485–495.

Rosi, M., Taviani, M. and Trincardi, F., 1990. The 79 AD Plinian event and its signature on the Eastern Tyrrhenian continental shelf. 13th Int. Sedimentol. Conf. (Nottingham). Int. Assoc. Sedimentol., p. 263. (abstract).

Sartori, R., Mascle, G. and Amaudric du Chaffaut, S., 1987. A review of circum-Tyrrhenian regional geology. In: K. Kastens, J. Mascle et al. (Editors), Init. Rep. DSDP, 107: 37–63.

Schwab, W.C., Lee, H.J. and Molnia, B.F., 1987. Causes of varied sediment gravity flow types on the Alsek prodelta, northeast Gulf of Alaska. Mar. Geotechnol., 7: 317–342.

Shor, A.N. and Piper, D.J.W., 1989. A large Late Pleistocene blocky debris flow on the central Scotian Slope. Geo-Mar. Lett., 9: 153–160.

Soloviev, S.L., Kuzin, I.P., Kovachev, S.A., Ferri, M., Guerra, I. and Luongo, G., 1990. Microearthquakes in the Tyrrhenian Sea as revealed by joint land and sea-bottom seismographs. Mar. Geol., 94: 131–146.

Tesson, M., Gensous, B., Allen, G.P. and Ravenne, Ch., 1990. Late Quaternary deltaic lowstand wedges on the Rhone continental shelf, France. Mar. Geol., 91: 325–332.

Trincardi, F. and Argnani, A., 1990. Gela submarine slide: a major basin-wide event in the Plio-Quaternary foredeep of Sicily. Geo-Mar. Lett., 10: 13–21.

Trincardi, F. and Field, M.E., 1991. Geometry, lateral variation, and preservation of downlapping regressive shelf deposits: Eastern Tyrrhenian Margin, Italy. J. Sediment. Petrol., 61(5): 775–790.

Trincardi, F. and Normark, W.R., 1989. The Suvero Pleistocene slide, Paola basin, Southern Italy. Mar. Pet. Geol., 6(4): 324–335.

Trincardi, F. and Zitellini, N., 1987. The rifting of the Tyrrhenian basin. Geo-Mar. Lett., 7: 1–6.

Twichell, D., Valentine, P. and Parson, L., 1992. Slope failure of carbonate sediments on the west Florida slope. In: W.C. Schwab, H.J. Lee, D.C. Twichell and M.A. Hampton (Editors), Submarine Landslides: Selected Studies from the U.S. Exclusive Economic Zone. U.S. Geol. Surv. Bull., 2002, Pap. 8.

Marine Geology, 105 (1992) 95–118
Elsevier Science Publishers B.V., Amsterdam

The western Grand Banks of Newfoundland: Transgressive Holocene sedimentation under the combined influence of waves and currents

Robert W. Dalrymple[a], Eric M. LeGresley[a,1], Gordon B.J. Fader[b] and Brian D. Petrie[c]

[a]*Department of Geological Sciences, Queen's University, Kingston, Ont. K7L 3N6, Canada*
[b]*Atlantic Geoscience Centre, Bedford Institute of Oceanography, Dartmouth, NS B2Y 4A2, Canada*
[c]*Department of Fisheries and Oceans, Bedford Institute of Oceanography, Dartmouth, NS B2Y 4A2, Canada*

(Received June 5, 1991; revision accepted October 7, 1991)

ABSTRACT

Dalrymple, R.W., LeGresley, E.M., Fader, G.B.J. and Petrie, B.D., 1992. The western Grand Banks of Newfoundland: Transgressive Holocene sedimentation under the combined influence of waves and currents. Mar. Geol., 105: 95–118.

The surficial sediments on the western Grand Banks of Newfoundland have been reworked from older deposits (primarily late Wisconsinan glacial and glaciomarine sediments) during the post-glacial sea-level fall and Holocene rise. Winnowed medium to coarse sands and lag gravels that are generally less than 0.5 m thick characterize the areas above the lowstand elevation at −110 to −120 m. The Holocene sediments which have accumulated in the deeper interbank channels, isolated basins and on the upper continental slope are thicker and consist of the fine sands and muds that were removed from the banks. The deposits below the lowstand elevation coarsen upward because little deposition occurred during the sea-level rise. In general, the Holocene succession becomes thicker and finer grained to the south.

Active sediment movement occurs at all depths less than about 110 m. Wave ripples composed of sandy gravel form to depths in excess of 100 m in response to long-period (15 s) surface waves, but the predominant bedforms consist of current-generated sand ribbons, megaripples and sandwaves which exhibit unidirectional migration azimuths toward the southwest, even though the storm-current directions are highly variable and the maximum sediment-transport rates are directed toward the east or southeast. The bedform orientation and resultant transport are instead parallel to the southerly and southwesterly storm currents which occur during the prolonged, post-storm spin-down period, and to the weak (<0.1 m s^{-1}) Labrador Current and the orbital motion associated with the largest waves. Thus, the interaction of the oceanic current and wave-orbital motion with the directionally-variable storm currents is responsible for the consistent orientation of the current-generated bedforms, and for the distribution of Holocene deposits.

Introduction

Marine geologists and sedimentologists have become increasingly aware in recent years of the complexity of sedimentation processes on continental shelves (Vincent et al., 1981; Swift and Niedoroda, 1985; Cacchione and Drake, 1990). The complex interactions which occur when waves and currents are superimposed during storms are the subject of growing interest from the fluid-mechanical point of view (e.g., Grant and Madsen, 1979, 1982; Davies et al., 1988), but relatively little is known about the nature of the bedforms and sedimentary structures produced by combined flows (Arnott and Southard, 1990; Southard et al., 1990), or even about the relative importance of the waves and currents in bedform generation (Duke, 1990). Many more flume and field observations are needed before these questions can be answered.

In a contribution toward this objective, we describe here the Holocene sediments on the central and western Grand Banks of Newfound-

[1] Present address: 513 Roosevelt Avenue, Ottawa, Ont. K2A 1Z9, Canada.

0025-3227/92/$05.00 © 1992 — Elsevier Science Publishers B.V. All rights reserved

land (Fig. 1), where sedimentation occurs under the combined influence of an inshore branch of the permanent Labrador Current and the large waves and strong wind-driven currents associated with intense winter storms. This complex assemblage of processes acts on sediments whose textural characteristics are also profoundly influenced by post-glacial sea-level changes.

Most of the previous work in the study area consists of reconnaissance surveys (Slatt, 1977; Fader and King, 1981; Fader et al., 1982; Barrie et al., 1985; Fader and Miller, 1986a,b; Fader, 1989a,b); the only detailed descriptions of the modern depositional processes have dealt with the Hibernia hydrocarbon discovery area on the northeastern portion of Grand Bank (Fig. 1; Barrie et al., 1984, 1985; Fader et al., 1985; Barrie and Collins, 1989). An overview of sediment transport on the entire eastern Canadian shelf is provided by Amos and Judge (1991).

Data base

The findings reported below are based on an integration of all publically-available information collected up to 1987 (LeGresley, 1988). Most of the data, including the majority of the sediment grab samples and all of the sidescan sonar and seismic reflection data, were collected on Bedford Institute of Oceanography (BIO) cruises 73-006 (King, 1973), 80-010 (Fader, 1980), 84-024 (Lewis, 1984), 85-005 (Fader, 1985) and 86-017 (Fader, 1986); some additional samples were also collected by Amoco Canada (Slatt, 1977).

A total of 315 sediment grab samples were analyzed texturally. The majority of these came from St. Pierre Bank, the adjacent Halibut Channel, the eastern portion of Whale Bank, Whale Deep and the southwestern part of Grand Bank (Fig. 1). Three piston cores from Halibut Channel and 2 cores from Whale Deep were also examined.

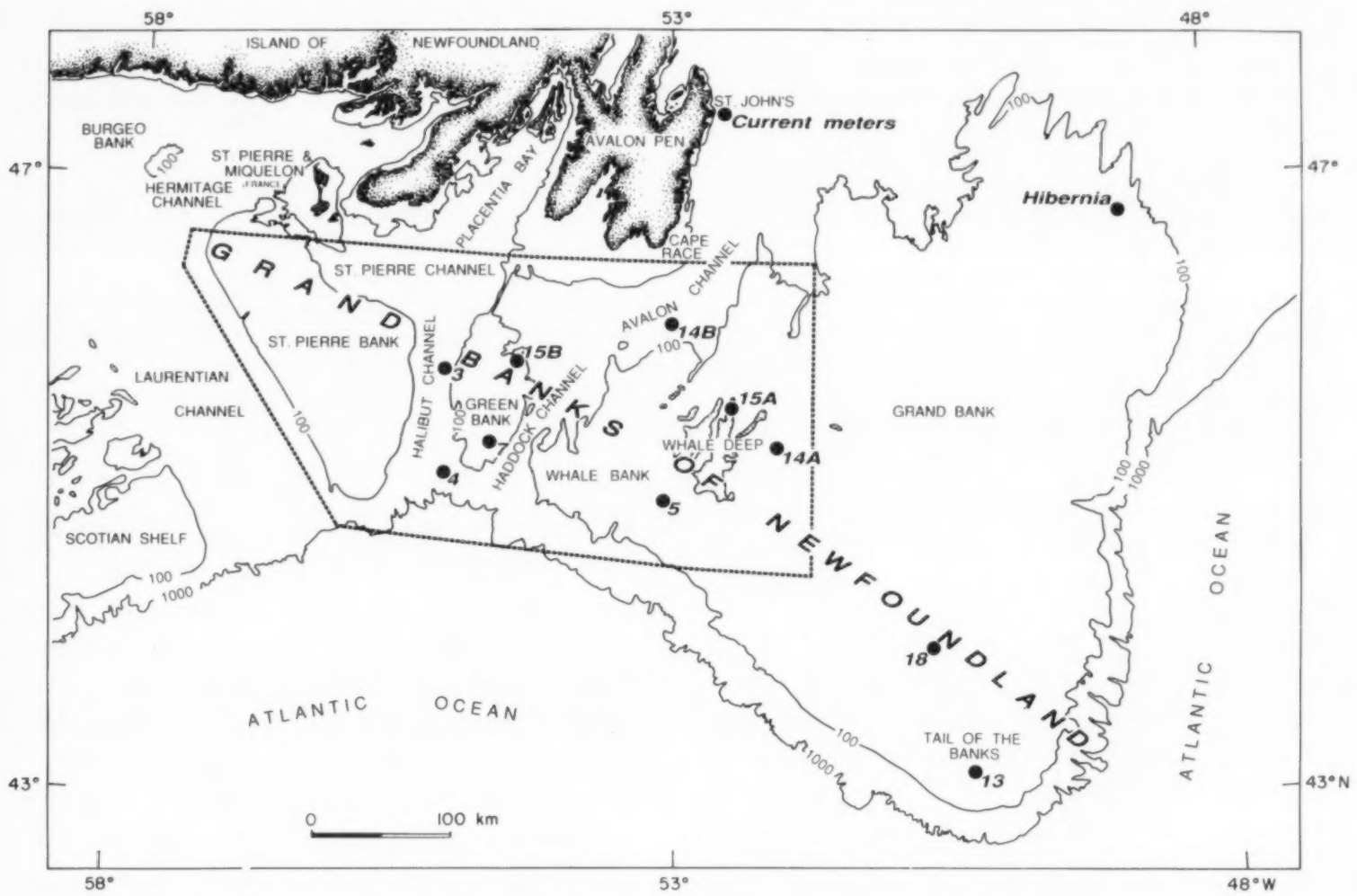

Fig. 1. Location and bathymetric map of the Grand Banks of Newfoundland, eastern Canada. The heavy dashed rectangle outlines the primary study area. The dots and adjacent numbers give the location of seismic reflection profiles, sidescan sonograms and bottom photographs shown in the paper.

Approximately 3200 km of high-resolution, seismic reflection data were collected from the area east of St. Pierre Bank using a Huntec (1970) Ltd. deep-towed, boomer system (Hutchins et al., 1976) which has a theoretical resolution of 0.3 m and a maximum penetration of 200 m in unconsolidated sediment (Fader et al., 1982). Corresponding side-scan sonar data were obtained with two systems: a BIO 70 kHz unit with a 1.5 km swath; and a 100 kHz Klein system normally operated with a 150 m swath. Most of the bedform observations reported below were derived from the Klein sonograms.

Vertical, bottom photographs were obtained on the 85-005 and 86-017 cruises using a Umel underwater camera which has a field of view measuring 120 cm by 75 cm. Oblique photographs were also obtained on Grand Bank using the *Pisces IV* submersible (Fader, 1989b).

Physiography of the study area

The Grand Banks of Newfoundland consist of a 160,000 km^2 series of shallow banks extending from Burgeo Bank in the west to Grand Bank in the east, which are separated from each other and the island of Newfoundland by deeper channels or enclosed basins (Fig. 1). This study examines the western half of the Grand Banks of Newfoundland, including St. Pierre, Green and Whale Banks, the southwestern portion of Grand Bank, and the intervening channels and basins.

Throughout the western Grand Banks, the shelf break occurs at a depth of approximately 120 m and is located more than 200 km from land (Fig. 1); by comparison, the world average shelf width is only 75 km. The banks are very flat and have typical water depths of 60–80 m. The shallowest depths on St. Pierre, Green and Whale Banks are 31 m, 53 m and 64 m respectively, and are situated approximately 135 km offshore. The banks are separated from the Newfoundland shoreline by the Avalon and St. Pierre Channels which are 50–75 km wide and up to 200 m deep (Fig. 1). Halibut and Haddock Channels, which separate St. Pierre, Green and Whale Banks, are 10–30 km wide and 120–160 m deep (i.e. 40–100 m deeper than the adjacent banks). Whale Deep, which separates Whale Bank from Grand Bank, is an irregular, elongate depression that is roughly 70 km long and 40 km wide, and about 50 m deeper than the surrounding banks.

Quaternary stratigraphy and geological history

Glacial events

During the Pleistocene, the western Grand Banks were glaciated numerous times, with glacial ice extending to the shelf break one or more times during the Wisconsinian (Fader et al., 1982; Grant and King, 1984; King and Fader, 1986; Bonifay and Piper, 1988; Josenhans and Fader, 1989; Piper et al., 1990). The Grand Banks Drift (Fader and Miller, 1986a), which consists of poorly-sorted sandy diamict with abundant gravel-sized clasts (Fader et al., 1982; Williams et al., 1985; King and Fader, 1986), contains the deposits formed by direct glacial action. This unit outcrops in the Avalon Channel east of the island of Newfoundland, and in St. Pierre Channel and Placentia Bay (Fig. 2), and is present in the subsurface throughout the area; it is recognized seismically by its acoustically-massive character and incoherent reflections (Figs. 3, 4 and 5). Where exposed, its upper surface is commonly covered by relict iceberg furrows.

The timing of glacial retreat is not well constrained. Conventional ^{14}C dates suggested that the banks were ice free during the late Wisconsinan (King and Fader, 1986), but recently-acquired AMS dates from the glaciomarine sediments which interfinger with and overlie the Grand Banks Drift indicate that ice may have extended to the shelf edge in Halibut Channel as late as 12 ka B.P. (Bonifay and Piper, 1988). The glaciomarine sediments which accumulated during and after ice retreat (King and Fader, 1986; Josenhans and Fader, 1989) are called the Downing Silt (Fader and Miller, 1986a). Texturally, they consist of well-stratified, dark grey-brown, clayey to sandy silts and silty sands with some gravel (Williams et al., 1985; Bonifay and Piper, 1988). On seismic reflection profiles this unit contains continuous coherent reflections with a pronounced, draping geometry (Figs. 3 and 5). King and Fader (1986) indicated

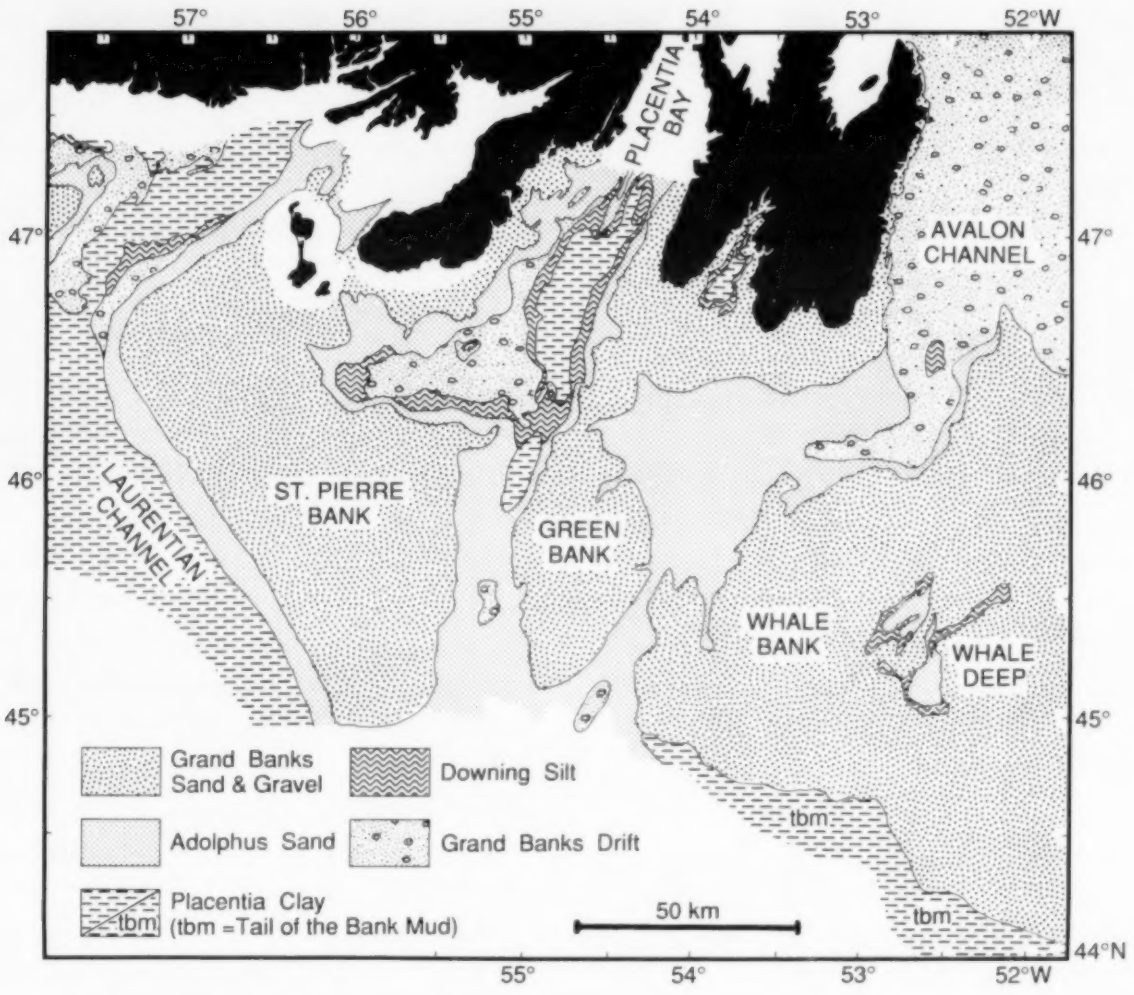

Fig. 2. Seabed geology of the study area; after Fader et al. (1982, in prep.).

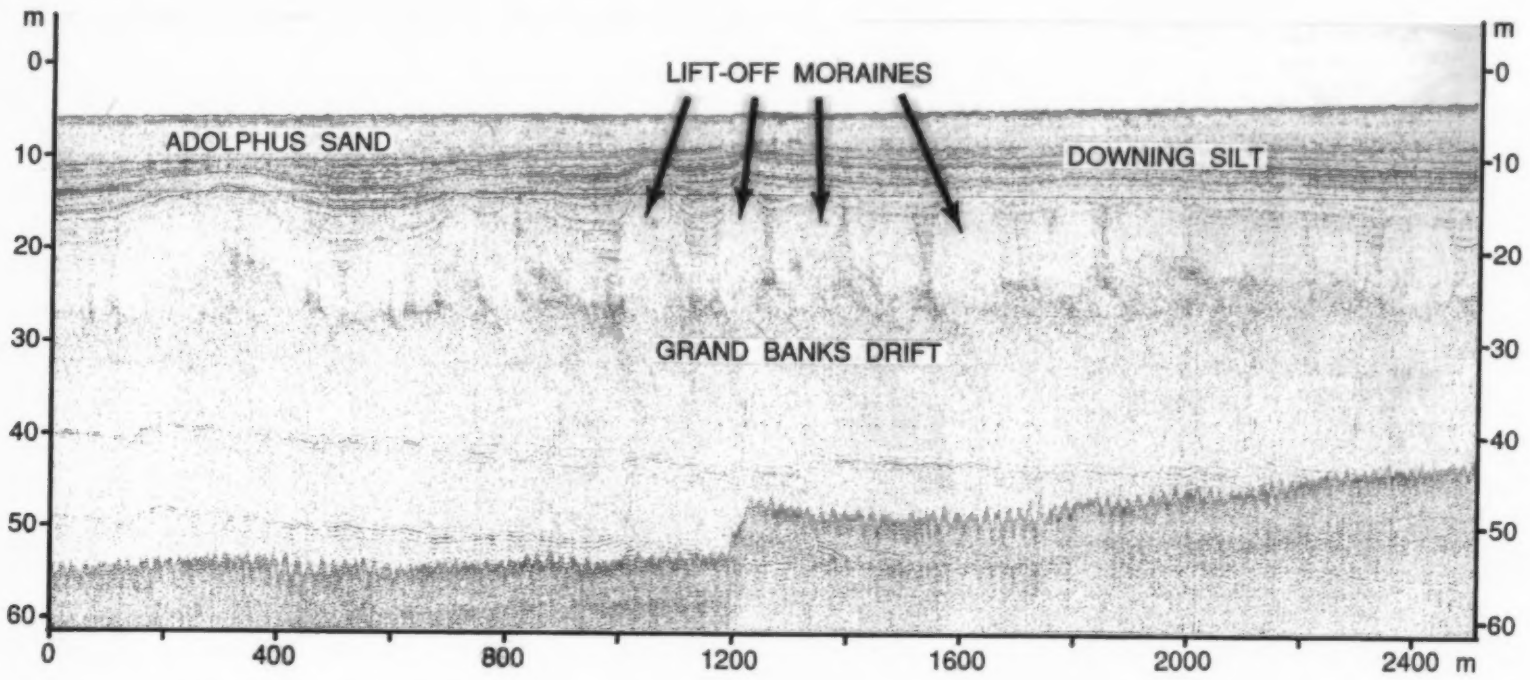

Fig. 3. High-resolution, seismic-reflection profile from the northern part of Halibut Channel, showing the acoustic character of the Grand Banks Drift, Downing Silt and Adolphus Sand. The acoustically-massive features which rise from the top of the Grand Banks Drift are interpreted as lift-off moraines (King and Fader, 1986; Josenhans and Fader, 1989). Note the draping geometry of the overlying Downing Silt. The surface undulations on this and other seismic-reflection profiles are due to wave-induced fish motion unless otherwise stated. The vertical scale in all seismic-reflection profiles assumes a speed of sound of 1500 m s^{-1}.

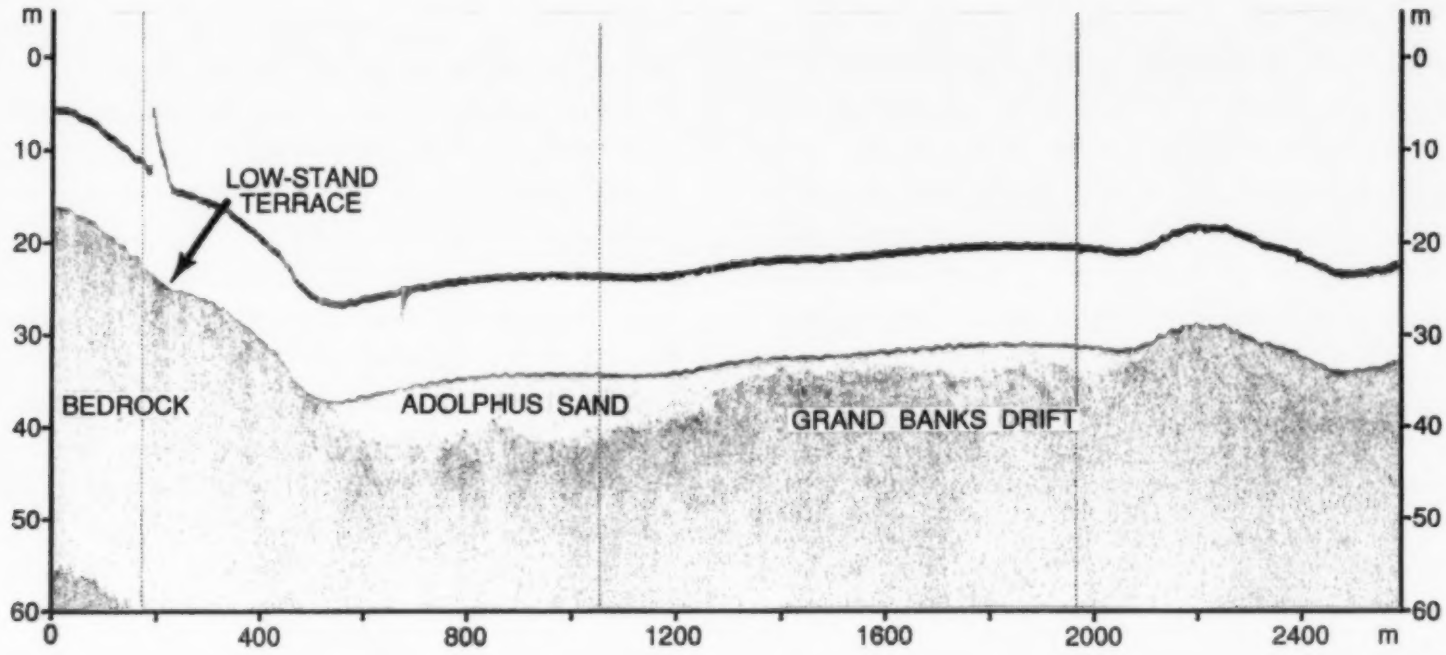

Fig. 4. High-resolution, seismic-reflection profile across the southeastern margin of Halibut Channel showing the wave-cut terrace at the low-stand elevation, and the restriction of thick accumulations of modern sediment (Adolphus Sand) to areas below this level. The sea bed above the low-stand elevation is veneered by lag gravel of the Grand Banks Sand and Gravel.

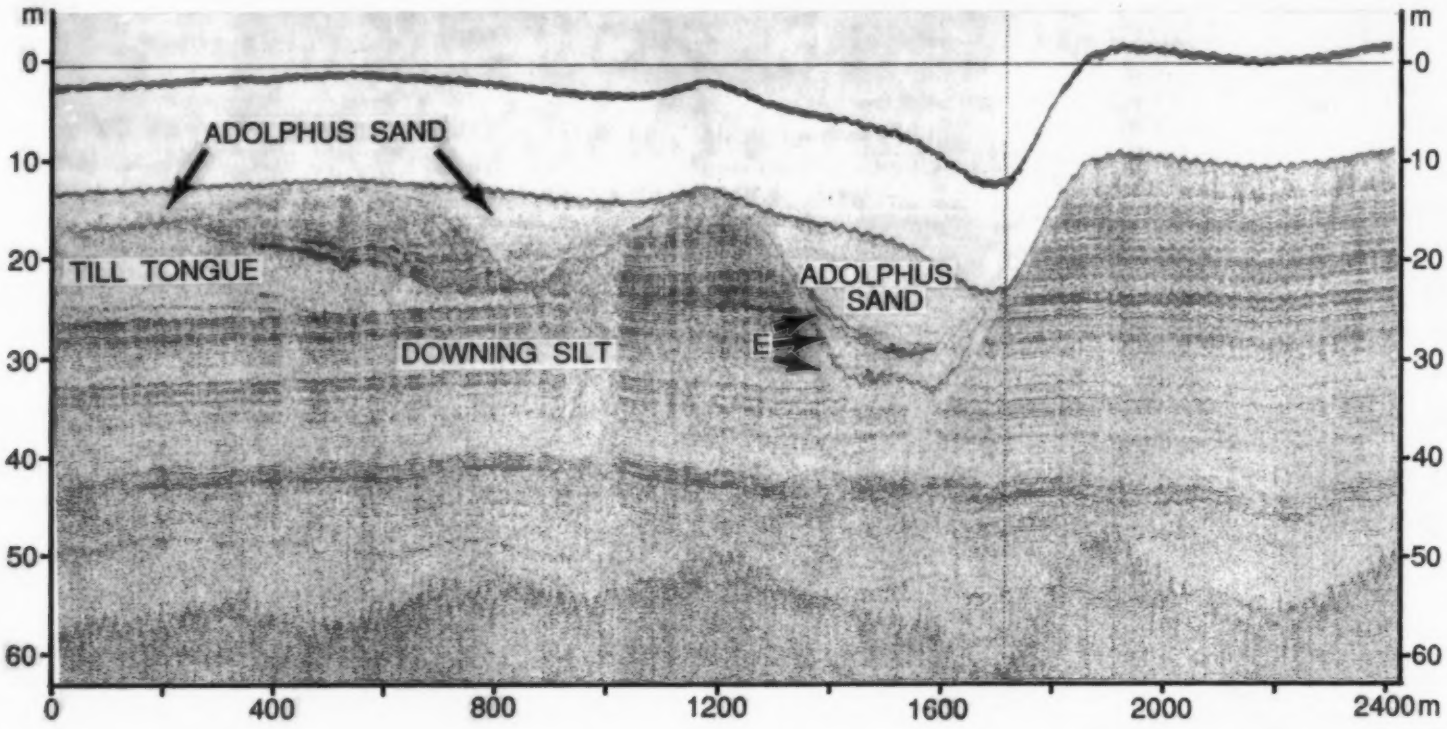

Fig. 5. High-resolution, seismic-reflection profile from the southern part of Whale Deep showing a thick section of well-stratified Downing Silt that contains a till tongue (Grand Banks Drift; King and Fader, 1986; Josenhans and Fader, 1989). One major and two minor erosional discontinuities (*E*) dissect the upper portion of the Downing Silt, removing up to 25 m of section. The origin of these is uncertain, but the possibilities include erosion by late glacial surges, current scour in narrow channels when sea level was lower than at present, and catastrophic melt-water discharges (cf. Boyd et al., 1988; Shaw, 1989). Note the restriction of the Adolphus Sand to these erosional depressions.

that glacio-marine deposition ended ca 14 ka B.P., but the more recent dating suggests that Downing Silt accumulation may have persisted until after 11 ka B.P. (Bonifay and Piper, 1988; King and Fader, 1989).

Post-glacial sea-level fluctuations

The banks were submerged during deposition of the Downing Silt, but relative sea level then fell to a −110 to −120 m lowstand at approximately

10 ka B.P. (Fader et al., 1982; Fader and Miller, 1986a) because isostatic uplift preceded much of the eustatic sea-level rise (Fader, 1989a). At this time only the deepest parts of the interbank channels were below sea level (Fig. 1). Subsequently, sea level has risen steadily (Quinlan and Beaumont, 1981; Fader et al., 1982). As a result, the entire surface of the banks has been subaerially exposed and the uppermost Wisconsinan sediments and any exposed bedrock have been subjected to shoreface and surf-zone erosion twice, once during the sea-level fall and again during the sea-level rise (Fader et al., 1982; King and Fader, 1986).

The surficial sediments deposited during the sea-level fall and rise have been divided into three formations (Fader et al., 1982, in prep.; Williams et al., 1985). The Grand Banks Sand and Gravel, which occurs as a veneer on the banks at elevations above the sea-level lowstand (Figs. 2, 6 and 7), consists of moderately- to well-sorted sands and gravels. At the lowstand elevation, there is a rapid but gradational transition into the finer-grained, muddy Adolphus Sand (Fig. 4) which occurs at elevations down to approximately −250 to −300 m in the interbank channels and on the continental slope (Fig. 2). At these depths there is a further gradation to clayey silts and silty clays termed the Placentia Clay (Fig. 2).

These three latest Wisconsinan to Holocene units are broadly time equivalent (Fader et al., 1982). As the shoreface and surf zone traversed the shallower parts of the banks during the sea-level fall, the finer fractions of the surficial material were winnowed and transported to progressively deeper water, the silt and clay accumulating in the deepest water to form the Placentia Clay while the finer sands accumulated in shallower water as the Adolphus Sand. The coarser sands and gravels that were left behind on the banks formed the Grand Banks Sand and Gravel. Cores taken across the transition between the Adolphus Sand and Placentia Clay in Halibut Channel and Whale Deep show an upward-coarsening trend (Fig. 6; LeGresley, 1988) which represents the encroachment of the Adolphus Sand onto the deeper-water clay as sea level fell. The lack of an overlying upward fining trend and the distinct textural break in the surficial sediments at the lowstand elevation (see below) suggest that little or no deposition occurred during the subsequent sea-level rise, presumably because little fine-grained material remained in the surficial lag produced during the sea-level fall. No subaerial deposits dating from the lowstand are yet known from the study area.

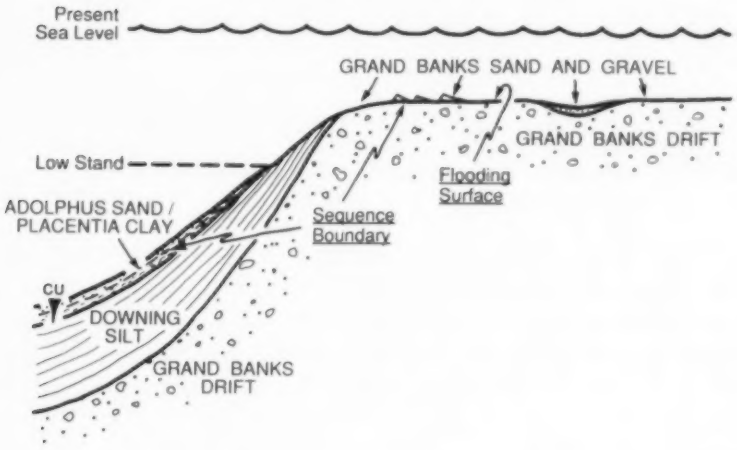

Fig. 6. Diagrammatic section showing distribution of stratigraphic units and sequence-stratigraphic boundaries. Not to true scale. The arrow head and *CU* in the modern sediments (lower left) indicates the upward-coarsening trend produced during the sea-level fall; almost no sediment accumulated during the subsequent flooding.

The thickness distribution of these latest Wisconsinan to Holocene sediments is also strongly depth dependent. Thick accumulations (up to 15 m) occur only at elevations below the sea-level lowstand (Figs. 4–6); because of this, these accumulations consist almost entirely of the Adolphus Sand and/or Placentia Clay facies. By comparison, the Grand Banks Sand and Gravel is generally thinner than the resolution of the seismic reflection systems used, except within local depressions (Fig. 6) or the body of large active bedforms (Fig. 7; see below).

Most of the surficial units also become thicker toward the south and southwest. For example, the Adolphus Sand and Grand Banks Sand and Gravel are absent from the northern portions of the Avalon Channel, except within relict iceberg scours, whereas to the south of the Avalon Peninsula, these units are widely distributed (Fig. 2). An unusually thick occurrence of a sandy facies of the Placentia Clay is also present along the southern edge of Whale and Grand Banks, in water depths as shallow as 55 m (Fig. 2). This deposit, which is termed the Tail of the Bank Mud (Fader and

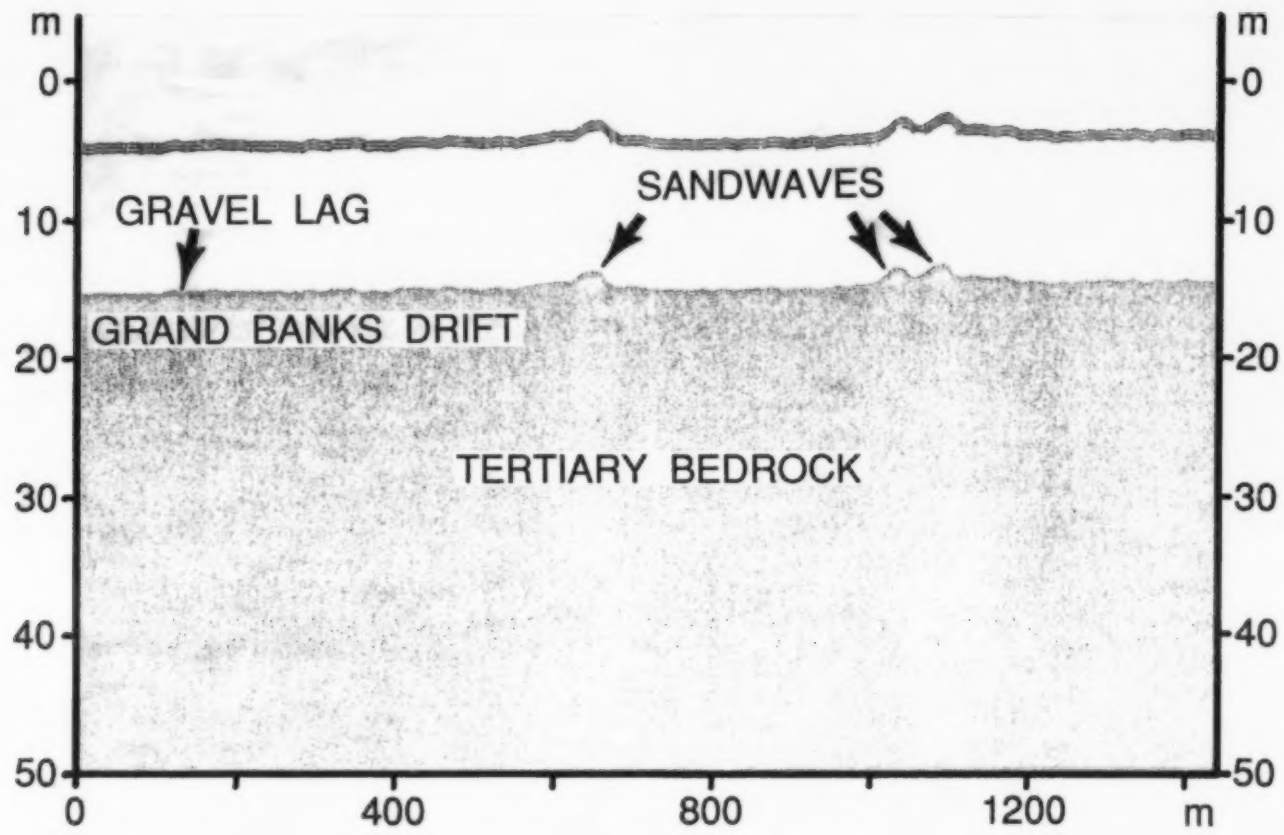

Fig. 7. High-resolution, seismic-reflection profile from southern Green Bank showing active, asymmetric sandwaves formed within the Grand Banks Sand and Gravel. In the area between the bedforms, the Grand Banks Sand and Gravel consists of a gravel lag which is less than 0.5 m thick. This material overlies a thin unit of Grand Banks Drift which rests on Tertiary bedrock.

Miller, 1986a), was originally believed to consist of glaciomarine sediment, but the observation that it locally overlies Holocene sand ridges indicates that it has accumulated since sea level has risen to near-present elevations. These distribution patterns suggest that sediment has been eroded from the more northerly parts of the Grand Banks, transported in a southerly direction, and deposited along the southern margin of the banks.

In sequence-stratigraphic terminology, the base of the Grand Banks Sand and Gravel (at elevations above the sea-level lowstand) is a combined type 1 sequence boundary (Van Wagoner et al., 1988; Fig. 6) and ravinement surface. In deeper water, the sequence boundary lies within the conformable, upward-coarsening succession from Placentia Clay to Adolphus Sand; this succession represents a parasequence (Van Wagoner et al., 1988) that formed during the sea-level fall and lowstand (i.e., a forced regression). The underlying contact between the Downing Silt and Placentia Clay does not have obvious sequence-stratigraphic significance because it is related to the degree of glacial influence rather than to sea-level changes. The present seabed represents a flooding surface (Fig. 6). In water shallower than approximately −110 m, the surficial sediments are still being reworked by modern processes (see below), but in deeper water there is little or no reworking, except by biological activity, and the rate of deposition is negligible.

Physical oceanography

Tides

Tides on the western Grand Banks are microtidal, with a maximum range associated with coincident M_2 (the largest constituent by a factor of at least 4), S_2 and N_2 tides of approximately 180 cm (Petrie et al., 1986). Tidal current speeds and directions have not been monitored systematically, but numerical model results (De Margerie and Lank, 1986; Petrie et al., 1986) indicate that the maximum, depth-averaged speeds are located just landward of the shelfbreak where maximum M_2 speeds reach 0.08 m s^{-1}. Throughout the remainder of the area, tidal-current speeds are only

0.03–0.04 m s^{-1}. The major axes of the M_2 tidal ellipses are generally oriented N–S over Green, Whale and St. Pierre Banks.

Regional currents

Regional circulation on the Grand Banks is dominated by the Labrador Current, a permanent, southerly-flowing, cold ocean current which originates in Davis Strait and the Labrador Sea as a result of freshwater outflow from the Arctic archipelago and continental runoff (Robe, 1971; Chapman and Beardsley, 1989, fig. 6; Ikeda, 1989). Most of the discharge of the Labrador Current skirts the northern and eastern margins of the Grand Banks (Fig. 8), but approximately 10% flows southward through the Avalon Channel and then southsouthwestward across the study area (Forrester and Benoit, 1981; Petrie and Anderson, 1983; Greenberg and Petrie, 1988). The closest "near-bed" current-meter moorings to the study area were located in the Avalon Channel (Fig. 1), at heights of 45–58 m above the bed (Petrie, 1991). These records (Fig. 9) show that flow to the southsouthwest is of greater duration and higher speed than movement in other directions; the vector-

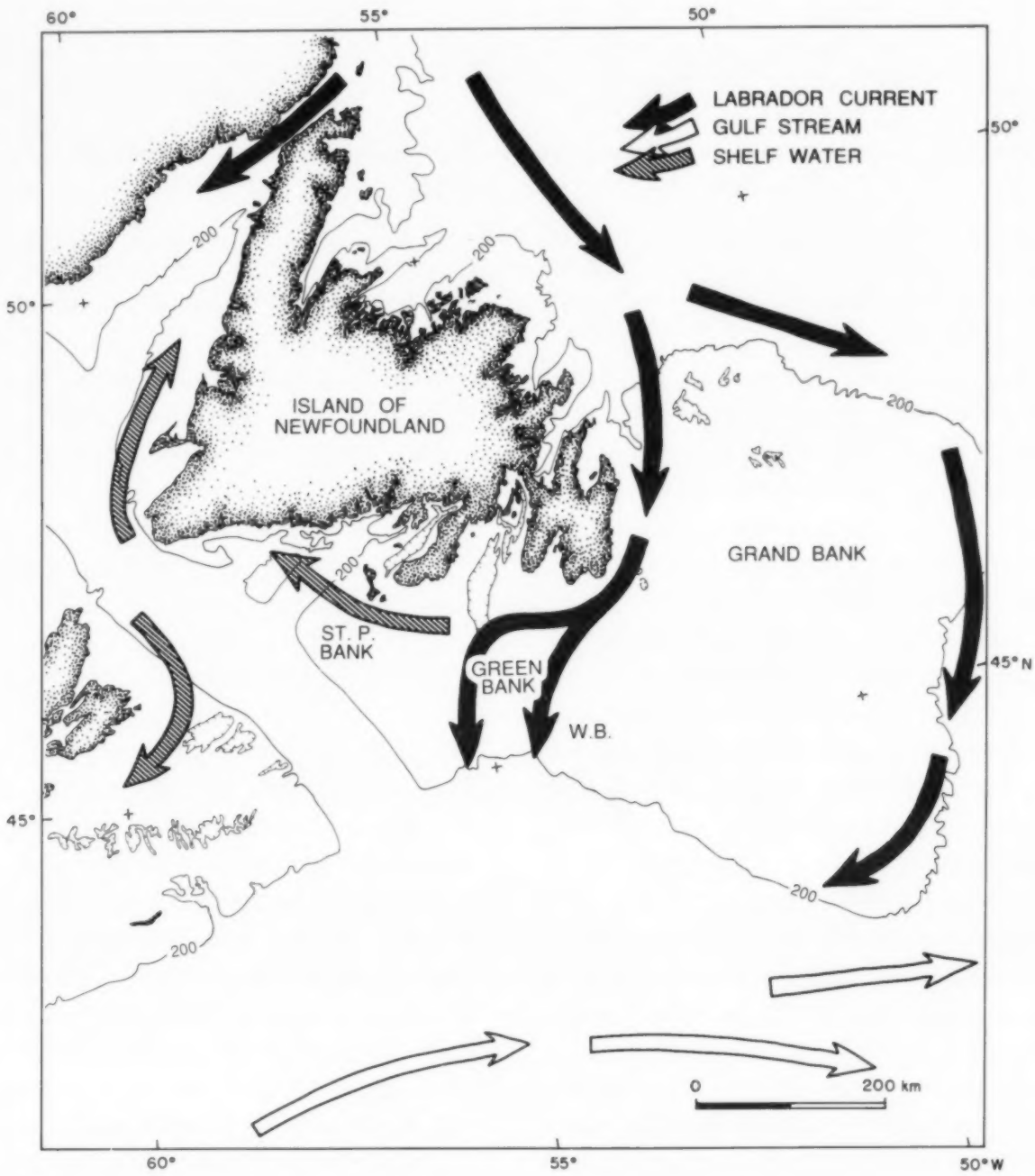

Fig. 8. Map of the Grand Banks of Newfoundland and adjacent areas showing the distribution of main surface currents. Modified after Fader et al. (1982), Petrie and Anderson (1983) and other sources. *St.P.* = St. Pierre. *W.B.* = Whale Bank.

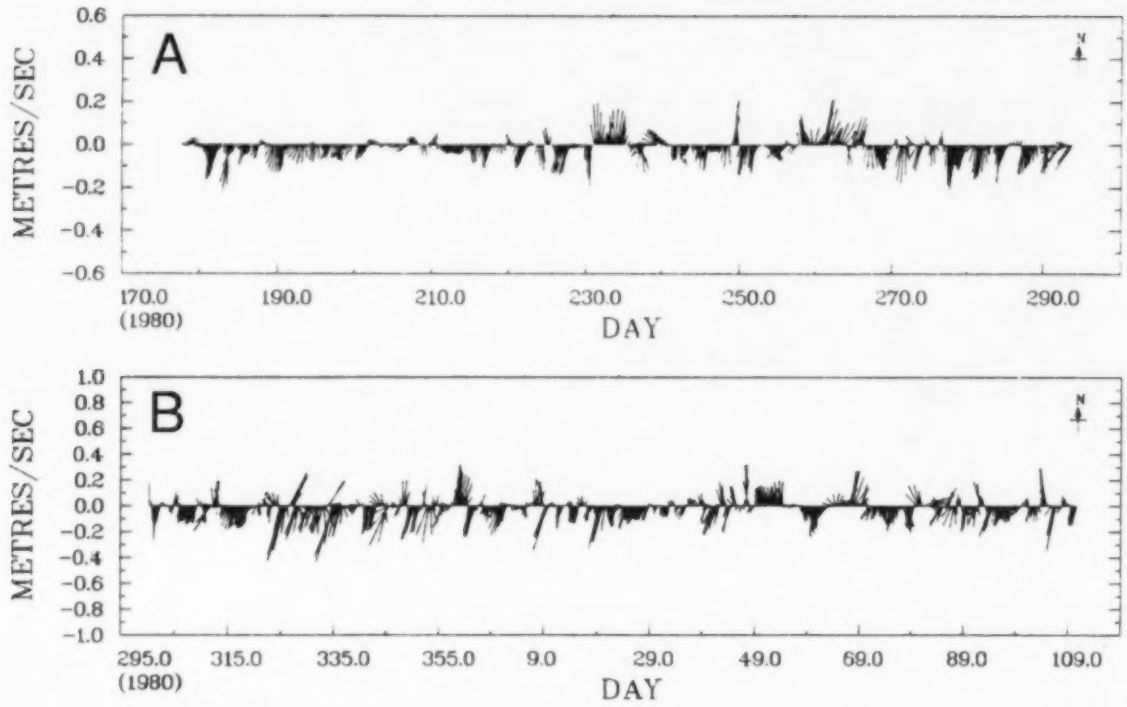

Fig. 9. Filtered, current-velocity data from the Avalon Channel (175 m of water) east of St. John's, Newfoundland (Fig. 1); all periods less than 28 hours have been removed (from Petrie, 1991). Time given in Julian days. (A) Data for the summer and early fall (late June to late October) of 1980 (mooring #393). The meter was located 130 m below the surface and 45 m above the bottom. (B) Data for the winter (late November to late April) of 1980–1981. The meter was situated 117 m below the surface and 58 m above the bottom. In both records the prevailing flow of the Labrador Current is to the south. Variability of the current speed and direction on a time scale of several days is attributed to wind-generated (storm) flow.

mean speeds for these two records are 0.034 m s^{-1} and 0.14 m s^{-1}, with mean flow directions of 195° and 203°. Typical measured speeds for the southsouthwesterly flow were 0.05–0.15 m s^{-1} (Petrie, 1991), and Petrie and Anderson (1983) report similar values for the near-surface flow. A numerical model of barotropic circulation in the study area suggests that the southsouthwesterly flow is concentrated in Halibut and Haddock Channels, while the currents over the banks are weaker and more variable in orientation (Greenberg and Petrie, 1988).

Waves and storm currents

The study area experiences strong wave action because of the large number of intense storms which cross the area from SSW–NNE (Fig. 10; Lewis and Moran, 1984). The storms are especially intense in the winter when storm-wind conditions (wind speeds >88 km h^{-1}) persist for more than 40 hours per month (Table 1; Mortsch et al., 1985). During December, January and February wave heights exceed 6 m for approximately 5% of the time and modal periods are 6–7 s; 12 s waves occur for 7–8% of the time (Table 1). Data on the joint frequency distribution of wave heights and periods are not available for the study area, but data for the Hibernia site (Fig. 1) indicate that waves with heights larger than 8 m generally have periods greater than 10 s (Neu, 1982). At the same site, more than 80% of the storm waves come from the northwest, west and southwest, but on the western Grand Banks the presence of the Island of Newfoundland may limit wave action from the northwest. Thus, the largest and longest-period waves are most likely to approach from the west and southwest.

The current-meter data from the Avalon Channel (Fig. 9) show that the current velocity is highly variable, with episodic reversals of the southerly-flowing Labrador Current. These transient currents, which are of much higher speed than the Labrador Current, are commonly associated with storms (LeGresley, 1988) and are believed to be primarily wind generated. During the summer, these storm events possess peak speeds up to 0.45 m s^{-1}, but the stronger winds which accompany

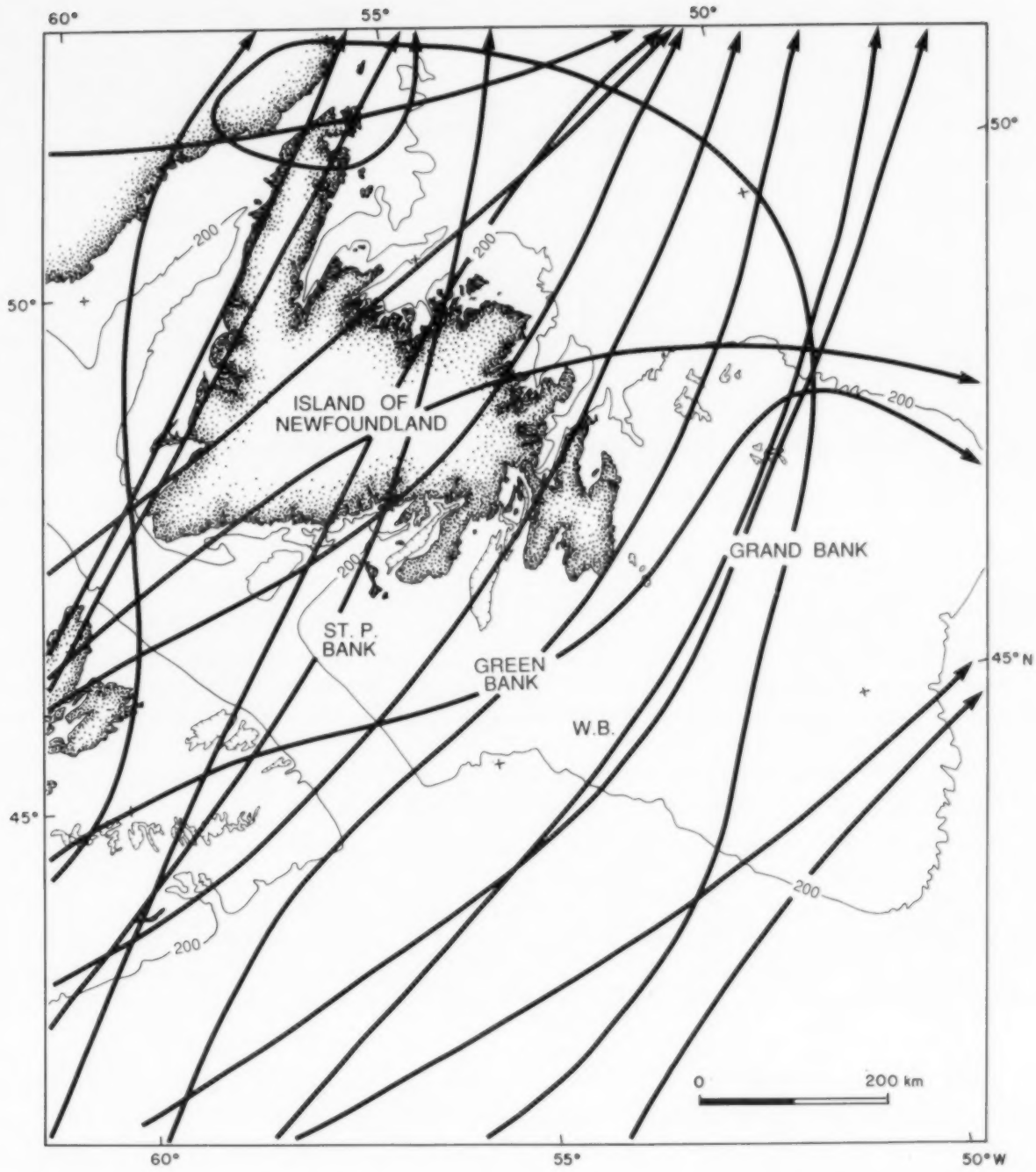

Fig. 10. Representative storm tracks from the period 1957–1983 (from Lewis and Moran, 1984), including the *Ocean Ranger Storm* which is so named because it sank the semi-submersible drilling rig of that name at the Hibernia site on February 15, 1982, killing 84 people. This storm enters the map area from the south at 60°W, passes over Cape Race (Fig. 1), and exits the area at about 48°W. The predicted storm currents for the *Ocean Ranger Storm* are shown in Fig. 11.

winter storms produce maximum speeds reaching 0.75 m s^{-1} (Petrie, 1991). Similar, but generally weaker, storm-generated currents are observed on many continental shelves (Allen, 1980; Swift and Niedoroda, 1985; Cacchione and Drake, 1990).

In the Avalon Channel, the storm-generated currents flow approximately northnortheast and southsouthwest (Fig. 9), parallel to the nearby shoreline, but this need not be the case in the study area which is far removed from the constraining influence of a coast (i.e., beyond the Rossby deformation radius; cf. Allen et al. (1983) who report a similar situation on the Bering Sea shelf). No measurements of storm currents exist for the western Grand Banks, but a numerical model has been used to determine the depth-averaged, wind-generated currents which would have been associated with past storms having recurrence intervals ranging from 1 to 32 years (LeGresley, 1988; Amos and Judge, 1991; Petrie, unpubl. results). This model shows that the current patterns differ between storms due to differences in storm speed,

TABLE 1

Annual summary of wind and wave characteristics for the study area. Data from Mortsch et al. (1985)

Month	Mean wind speed (km h^{-1})	Duration of storm winds[1] (h)	% Waves >6 m high	10 Yr. return wave height (m)	100 Yr. return wave height (m)	Modal wave period (s)	% Periods >12 s
January	16	40	5	11.5	14	6–7	8
February	16	45	5	11	14	6–7	8
March	9	50	3	11	13	6–7	6
April	7	40	2	10.5	13	<6	4
May	4	30	<1	8	10	<6	3
June	9	20	<1	7.5	10	<6	2
July	11	10	<1	7	11	<6	2
August	9	20	<1	7.5	9	<6	2
September	7	10	1	7.5	10	<6	4
October	9	30	2	8	11	<6	4
November	9	40	4	9	11	6–7	7
December	14	60	5	11	13	6–7	7

[1]Wind speeds >88 km h^{-1}.

magnitude and path (Fig. 10). The predictions show, however, that the current directions generally rotate clockwise progressively through nearly 360° during the passage of a storm, unlike the more rectilinear pattern commonly observed in near-coast locations (Fig. 9; Lavelle et al., 1978; Vincent et al., 1981). Initially there is weak flow to the north as the storm approaches from the southwest (Fig. 11), but the speeds increase rapidly as the storm centre passes and the current swings first to the east and then to the south. As the storm moves off to the northeast, the current speed decreases gradually, with the final flow being to the west or northwest. Current dissipation occurs by bottom friction; it is estimated that a peak flow of 0.8 m s^{-1} would decrease to background values of 0.15 m s^{-1} in about 2.5 days.

Generally, the highest speeds (0.5–0.8 m s^{-1}) occur over the shallow banks and flow either toward the east, southeast or south. During the Ocean Ranger Storm (Figs. 10 and 11), for example, predicted current speeds on Whale Bank exceeded 0.5 m s^{-1} for nearly 24 h. For more than half of this time the flow was in the southerly quadrant, but the maximum sediment-transport rates occurred when the flow was directed toward the east and southeast (Amos and Judge, 1991).

Surficial sediments

Sediment texture

As discussed above, the grain size of the surficial sediments varies systematically with depth (Fig. 12), despite considerable local variability due to hydrodynamic segregation over bedforms (see below), local outcrops of glacial sediment or bedrock, and input of coarse material by ice-rafting. In general, most of the surficial sediment above the lowstand elevation (i.e. the Grand Banks Sand and Gravel) consists of medium to coarse sand and gravel; St. Pierre and Green Banks are covered predominantly by material ranging from coarse sand to cobbles (coarser than 1 ϕ; Fig. 12A), whereas the somewhat deeper Whale Bank is covered by medium sand (1–2 ϕ; Fig. 12B). Sidescan sonograms show that in areas shallower than 110 m the sand-sized material has been hydraulically segregated into a variety of large-scale bedforms (see below), while the gravel-sized sediment remains as a lag which underlies the bedforms and outcrops between them. This lag is composed of a diverse assemblage of rock types (LeGresley, 1988), together with significant amounts (5–50%) of shell debris.

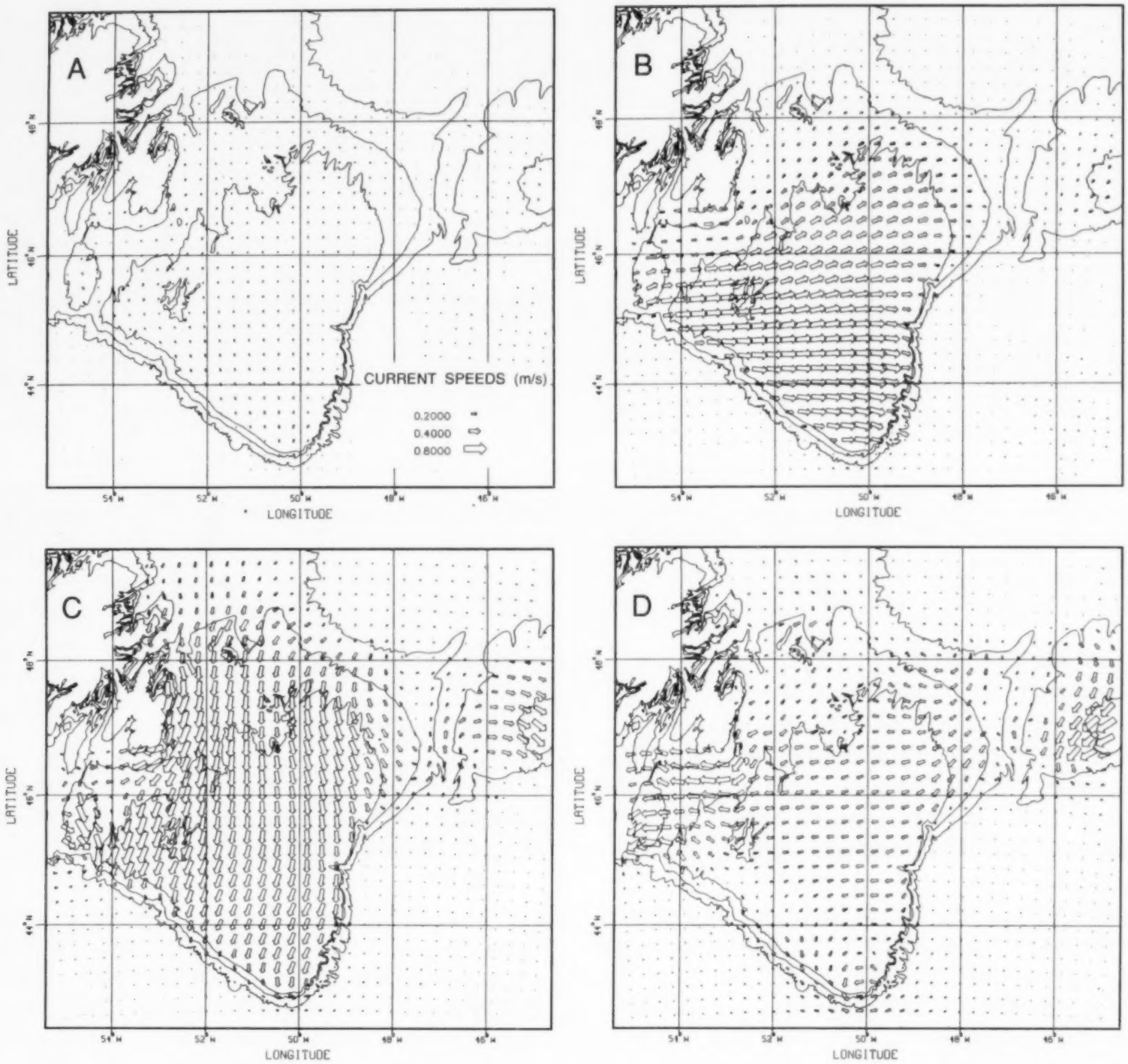

Fig. 11. Predicted wind-driven, depth-averaged current velocities on the Grand Banks during the *Ocean Ranger Storm* (February 14–15, 1982) which generated waves at the Hibernia site (Fig. 1) with a 32-year return period; see Fig. 10 for the storm's track. The 100, 200 and 1000 m isobaths are shown. (A) 0600Z, February 14. The storm centre lies approximately 500 km to the southsouthwest of the map area, and the currents are flowing weakly to the north. (B) 1800Z, February 14. The storm centre lies over the eastern end of the island of Newfoundland. (C) 0600Z, February 15. The storm centre lies a short distance north of the map area, at about longitude 46°W. (D) 1800Z, February 15. The storm centre has moved nearly 500 km to the northnortheast of the map area. Note the clockwise rotation of the current vectors, the rapid increase in speed between (A) and (B), and the slow decrease in current speed from (B) to (D).

At depths below the lowstand elevation, grain sizes become progressively finer in the transition to the Adolphus Sand (Fig. 12). The mean size of surface samples from Whale Deep range from 2 to 2.5 ϕ, or about 0.5–1.5 ϕ-units finer than sediment on the adjacent banks (Fig. 12B), whereas the channels around St. Pierre Bank typically contain fine to very fine sand (2–4 ϕ; Fig. 12A).

Coarse sediment locally extends into deeper water on the southern side of the banks than it

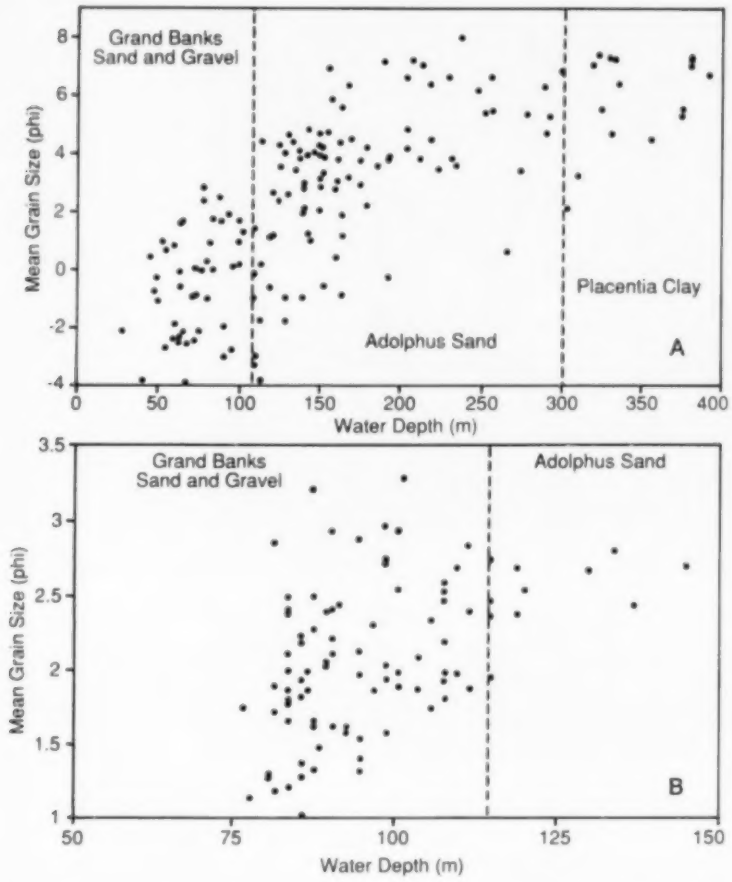

Fig. 12. Variation of mean grain size as a function of water depth on (A) St. Pierre Bank and (B) Whale Bank. For reference, the boundaries between the surficial formations (Fig. 2) are included.

does on other margins. This is particularly evident off the southern tip of St. Pierre Bank where material is approximately 2 ϕ-units coarser than sediment at comparable water depths farther to the northwest.

Bedforms

Bottom photographs and submersible observations show that small-scale wave ripples (Fig. 13) are abundant in medium, fine and very fine sand in water depths down to at least 120 m. These features are ephemeral, due to disturbance of the seabed by surface and infaunal organisms (Fig. 13). This disturbance is particularly intense in the finer sediments which occur in water depths greater than 110–120 m, and cores from the Adolphus Sand show that the sediment is thoroughly bioturbated.

Sidescan sonograms indicate that large-scale bedforms of both current and wave origin are widespread wherever the seabed is composed of Grand Banks Sand and Gravel. Following the terminology of Amos and King (1984), the flow-parallel, current-generated features are called sand ribbons, while the flow-transverse forms consist of megaripples and sandwaves. All of these bedforms are largely composed of medium to coarse sand (Fig. 12) which rests on the lag-gravel pavement. The large, wave-generated bedforms, which are here termed gravel waves, occur in slightly coarser sediment.

Sand ribbons

Sand ribbons (Kenyon, 1970; McLean, 1981) consist of straight to slightly sinuous, elongate patches of sand (Fig. 14A) that rest on the lag-gravel substrate. The width of a single ribbon averages about 100 m, whereas spacings between ribbons range from 60 m to over 800 m. Individual ribbons may be in excess of several kilometres long. The thickness of the sand forming the ribbons is not detectable on sidescan sonograms or seismic reflection profiles, suggesting that it is less than about 0.5 m; the fact that the troughs of superimposed megaripples commonly expose the underlying lag gravel (Fig. 14A) supports this interpretation. Sand ribbons are restricted to water depths of less than 100 m, and are most abundant at the northern end of Green, Whale and Grand Banks.

In areas that have a more continuous sandy cover, elongate strips of coarser material are present locally (Fig. 14B). These gravel stripes are flow parallel as indicated by adjacent megaripples, and are believed to be dynamically equivalent to the gravel areas exposed between sand ribbons. All of these current-parallel features have a pronounced SW–NE orientation.

Amos and King (1984) considered sand ribbons to be an upper-flow-regime phenomenon, and suggested that sand ribbons consisting of medium to coarse sand would require current speeds of 1 m s^{-1} or more to form. On the other hand, various authors including McLean (1981) associate sand ribbons with sediment starvation rather than a particular current speed. Indeed, the presence of superimposed and laterally-adjacent megaripples

Fig. 13. Wave ripples in silty fine sand in the Tail of the Bank Mud. The large number of brittle stars present have begun to degrade the ripples in places. An abundant infauna (species composition unknown) is also present, as evidenced by the agglutinated burrow openings. Their activity completely destroys any stratification generated by storms. The compass on the trip weight is 7.5 cm in diameter.

(Fig. 14A) suggests that the sand ribbons form under lower flow regime conditions. McLean's (1981) theory of sand-ribbon formation predicts that the optimum ribbon spacing is four times the water depth. In the study area, ratios of sand-ribbon spacing to present-day water depth average about 3, a value close to that predicted by McLean (1981). This implies that the sand ribbons are modern features, and that the effective flow depth is the entire water column. This situation is most likely to exist during the winter when the water column is unstratified.

Megaripples and sandwaves

Megaripples (Dalrymple et al., 1978; Amos and King, 1984; "medium to large, simple dunes" in the terminology of Ashley, 1990) are the most common type of large-scale bedform on the western Grand Banks. Both 2-dimensional (2D) and 3-dimensional (3D) varieties are present (Fig. 15A), although 2D forms predominate regionally. The wavelengths of 2D megaripples range from 6.5 m to over 20 m, with a mean of 12.5 m. The wavelengths of 3D megaripples are commonly smaller than those of associated 2D forms, ranging from less than 7 m to about 13 m, with a mean of 9.5 m. Most megaripple heights are below the limit of resolution on seismic-reflection records (approximately 50 cm), but heights exceeding 1 m are observed. All of the megaripples are asymmetric as indicated by acoustic shadows on sidescan sonograms or the asymmetric distribution of grain size across their crest (as interpreted from acoustic reflectivity patterns). Both 2D and 3D megaripples show a strongly preferred orientation with an average crestal *strike* of 120–125° (Figs. 16A, B), indicating that sediment transport is generally to the southsouthwest and southwest, except on the western part of Grand Bank where it is to the west (Fig. 17).

Megaripples are present in water depths of 68–113 m. They occur in discrete fields which are commonly composed of a single megaripple type, or may be superimposed on sand ribbons and sandwaves. The discrete fields are generally elongate in the direction of megaripple migration and typically have sharp boundaries. These fields are

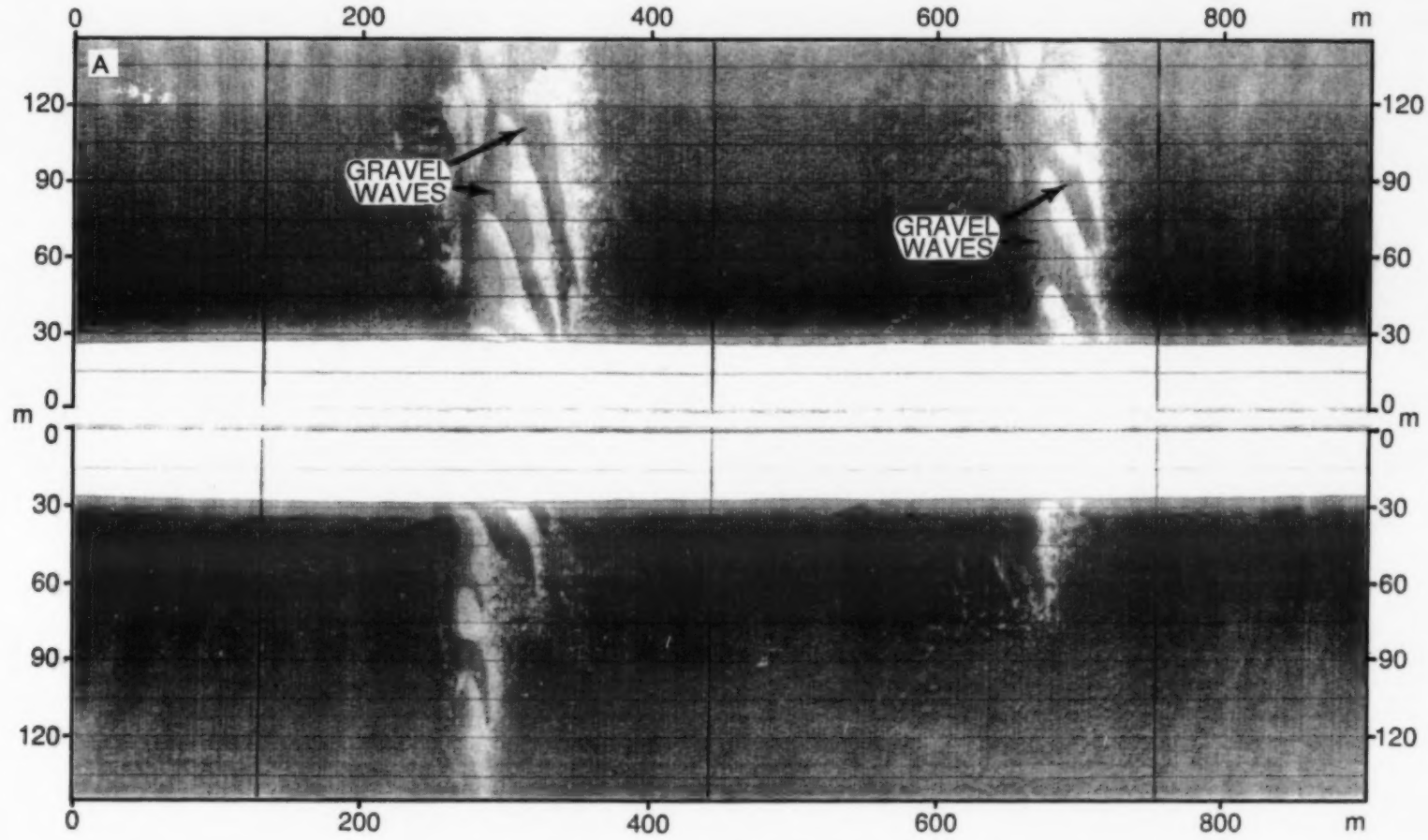

Fig. 14. Sidescan sonograms of current-parallel bedforms. (A) Sand ribbon (western part of Grand Bank) with superimposed 2D megaripples that are migrating obliquely toward the top of the figure. Gravel waves occur locally in the coarser (more reflective) sediment in the megaripple troughs. (B) Current-parallel band of fresh gravel waves on Grand Bank. Degraded gravel waves are also visible in the slightly finer (less reflective) sediment adjacent to the gravel stripe. Note that the gravel-wave crests are approximately perpendicular to the elongate band; parallel kinks in gravel-wave crestlines are due to wave-induced motion of the sidescan fish.

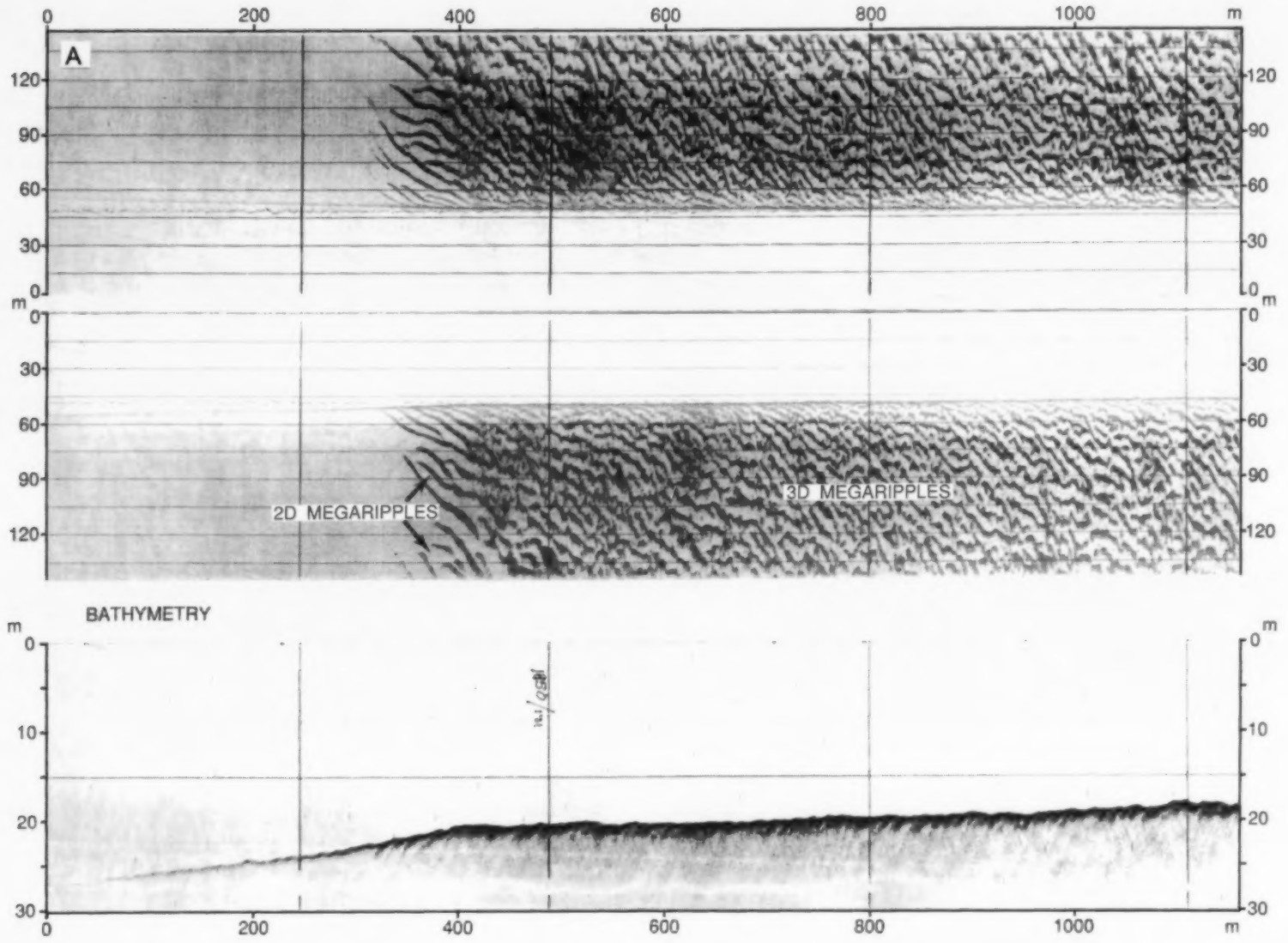

Fig. 15. Sidescan sonograms of flow-transverse bedforms. (A) Transition between 2D and 3D megaripples, northern Whale Deep. The boundary between the 2D megaripples and the featureless seabed to the left corresponds approximately with the Grand Banks Sand and Gravel–Adolphus Sand boundary.

bordered by lag gravel in areas above the sea-level lowstand, or by featureless sand in deeper water (Fig. 15A).

Sandwaves (Dalrymple et al., 1978; Amos and King, 1984; "large to very large dunes" in the terminology of Ashley, 1990) are larger than megaripples and have group-mean wavelengths of 30–200 m (average 91 m) on the western Grand Banks. Heights range from less than the limit of detection to a maximum of 2–3 m; values toward the lower end of the range are more usual. Most sandwaves are relatively straight-crested (Fig. 15B), but a few are arcuate to irregular in plan form. Sandwaves typically have megaripples superimposed on their stoss and upper lee sides (Fig. 15B; "compound dunes" of Ashley, 1990), and gravel waves may be present in the trough. These superimposed bedforms are commonly oriented at an oblique angle to the sandwave, but on average, sandwave crestlines show the same preferred orientation as the megaripples (Fig. 16C); the secondary mode at 90° to the main mode may be due to the misidentification of some sand ribbons. The asymmetry of the sandwaves indicates that they are also migrating in a southwesterly direction.

Sandwaves may occur as isolated individuals or in fields containing a small number of separate or partially-coalescing forms (Fig. 15B). Sandwaves are found throughout the study area, but are especially abundant in and around Whale Deep, occurring in water depths down to 100 m. In general, sandwaves appear to occur where there is more sand than is necessary for the formation of

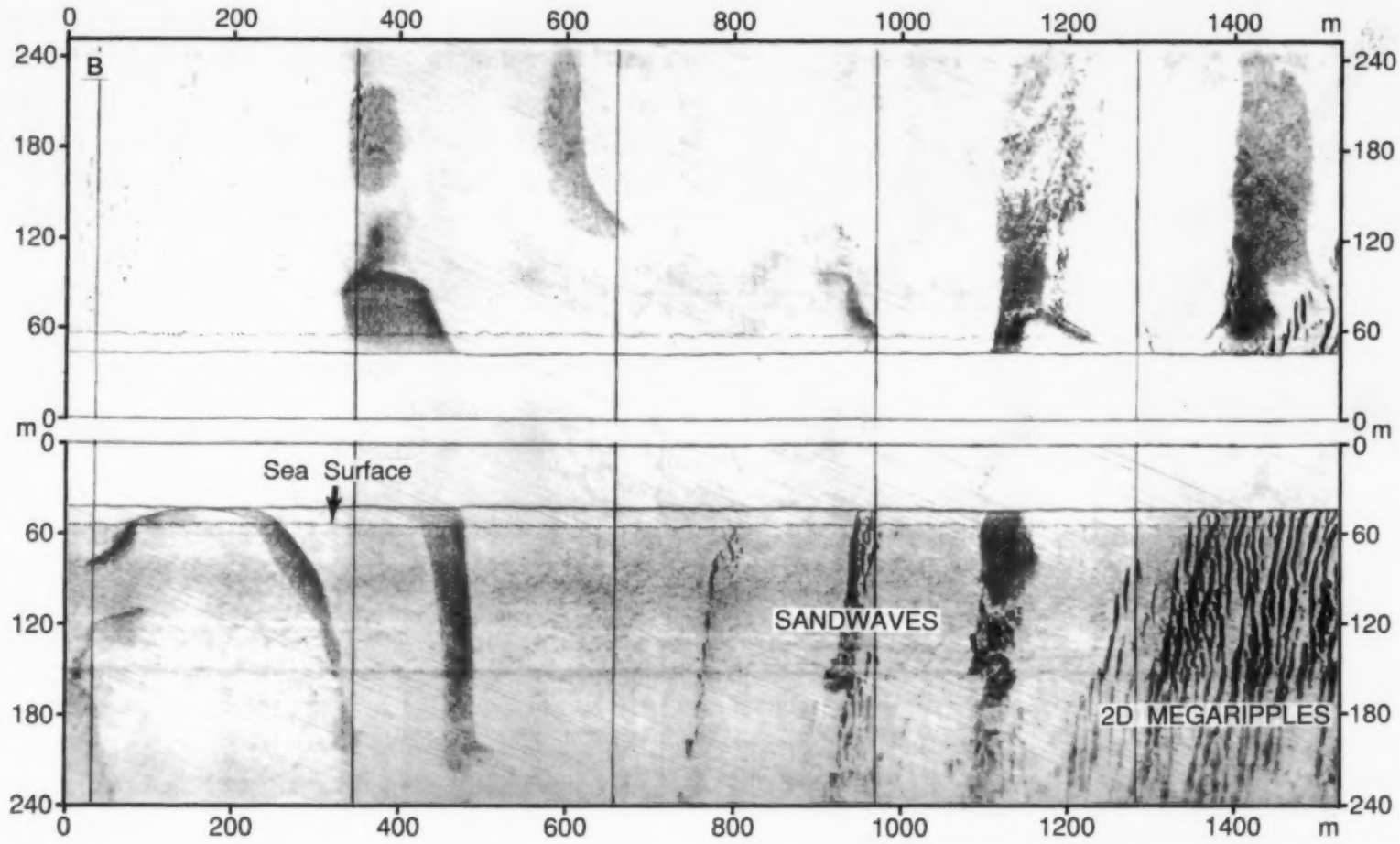

Fig. 15. (B) Straight to gently-curved sandwaves, locally with superimposed 2D megaripples, northern Green Bank. Wave noise from the sea surface has degraded the record in places.

megaripples alone (Dalrymple et al., 1978). On Green and Whale Banks, the extent of sand cover generally increases from north to south; consequently, sandwaves tend to be more abundant in the south while sand ribbons or megaripples alone predominate in northern areas.

The widespread presence of megaripples and sandwaves requires that currents with speeds of 0.5–1.0 m s^{-1} (Southard and Boguchwal, 1990) either have or still do influence all areas of the Grand Banks shallower than 100 m. The fresh appearance of these bedforms (i.e. the sharply-defined textural contrast between the bedform and the underlying gravel lag; Figs. 14A and 15), despite the presence of intense bioturbation and frequent wave action, indicate that they are modern features.

Gravel waves

On sidescan sonograms gravel waves appear as a "zebra-strip" pattern of parallel, light and dark bands (Fig. 14A and B) caused by textural differences between their crest and trough (Fig. 18). Their spacing is near the limit of resolution of 100 kHz sonars, but ranges from less than 1 m to slightly more than 2 m. Better quality sonograms show that crestal branching is common. Bottom photos indicate that these ripples have symmetrical profiles with heights of 10–20 cm (Fig. 18). They are not biologically degraded and appear to be recently formed. The sediment comprising them consists of coarse sand to gravel, commonly with a substantial component of shell hash; particles up to 16 mm in diameter have been observed within the ripples. These gravel waves have a regionally-consistent, mean crestal strike of 147° (Fig. 16D) which is almost identical to that of the megaripples and sandwaves (Fig. 16A–C). The likely cause and significance of this will be discussed below.

Gravel waves occur in water depths down to 102 m, but are most common on the shallower parts of the banks. They usually occur in current-

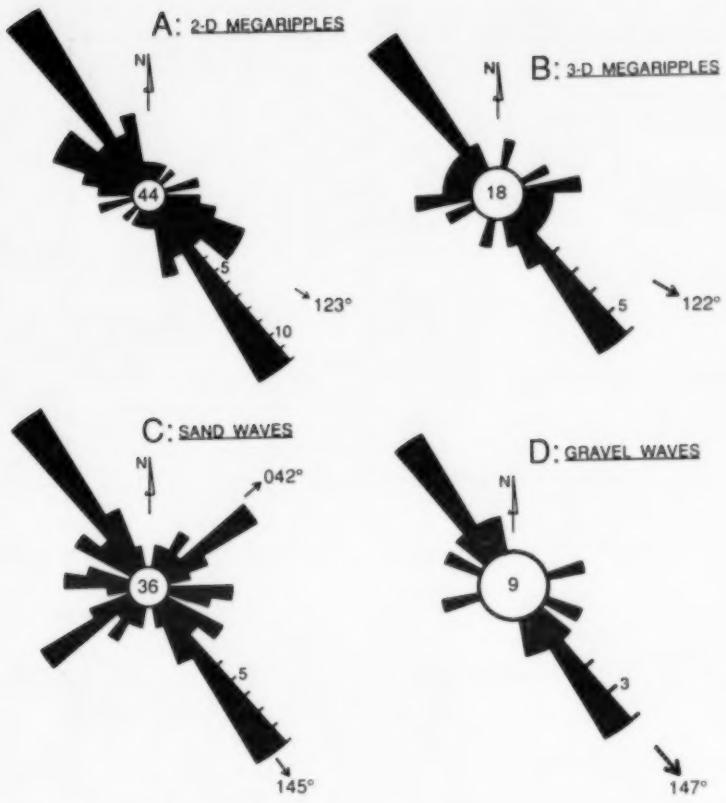

Fig. 16. Rose diagrams showing the crestline-strike orientation of: (A) 2D megaripples; (B) 3D megaripples; (C) sandwaves; and (D) gravel waves. The roses are plotted symmetrically, but the topographic and textural asymmetry displayed by numerous examples indicate that the regional migration direction is to the southwest (see Fig. 17). The number in the central circle gives the number of group-mean values plotted.

parallel, elongate fields (Fig. 14B) that average 40 m by 200 m in size. These fields represent exposed windows of the basal lag gravel which are surrounded by a thin sand cover that may contain megaripples. Gravel waves also occur on the flanks of sand ribbons (Fig. 14A) and in the troughs of current-generated bedforms.

Features which are morphologically similar to the gravel waves have been described by numerous people including Yorath et al. (1979), Forbes and Boyd (1987) and Leckie (1988), all of whom interpret them as large, coarse-grained wave ripples. Calculations using linear wave theory and the threshold for sediment motion due to wave action (Miller et al., 1977; Forbes and Boyd, 1987) indicate that waves with a period of 12 s and a height of 8.5 m (the one-year recurrence value; Mortsch et al., 1985) can move fine sand (0.175 mm) down to 100 m, but that the 16 mm pebbles which are locally present in the gravel ripples cannot be moved in water deeper than 66 m by 12 s waves with even the 100-year-return height of 14.5 m (Mortsch et al., 1985). Waves with a period of 15 s and a height of 8.5 m are capable, however, of moving 16 mm pebbles in water as deep as 110 m; therefore, such long-period waves, which comprise about 2% of the yearly wave spectrum (Mortsch et al., 1985), are apparently responsible for the gravel waves.

Sediment transport processes

The intense wave action that the study area experiences suggests that sedimentation is strongly wave-influenced if not wave-dominated. Despite this, there is abundant evidence of south to southwesterly sediment transport by unidirectional currents: the southward increase in the thickness of the Adolphus Sand and Grand Banks Sand and Gravel (Fig. 2); the possible spill-over of sediment along the southern margin of the banks; the widespread development of bedform fields, sand ribbons, megaripples and sandwaves, all indicating a strongly-preferred southwesterly flow direction (Figs. 16 and 17); and the southward progression from sand ribbons through megaripples to sandwaves on Green and Whale Banks which mimics the downstream changes that occur along tidal transport paths (Belderson et al., 1982).

From the available current data and numerical model results it is clear that only storms are capable of generating currents with speeds which are sufficiently high (0.5–1.0 m s^{-1}; Figs. 9B and 11) to create the observed bedforms. By comparison, tidal currents and the inshore branch of the Labrador Current, which rarely achieves speeds exceeding 0.1 m s^{-1}, do not generally exceed the threshold of motion of medium sand. It is not immediately obvious, however, how the storm currents, which have speeds greatly in excess of the threshold over a wide range of directions, even within a single storm (Fig. 11), are able to produce the uniform, southerly to southwesterly sediment transport indicated by the sediment-distribution patterns and bedform orientations (Figs. 16 and 17). This difficulty is particularly acute given that the maximum sediment-transport rates during storms are believed to have an easterly or southeasterly orientation in the study area (Amos and

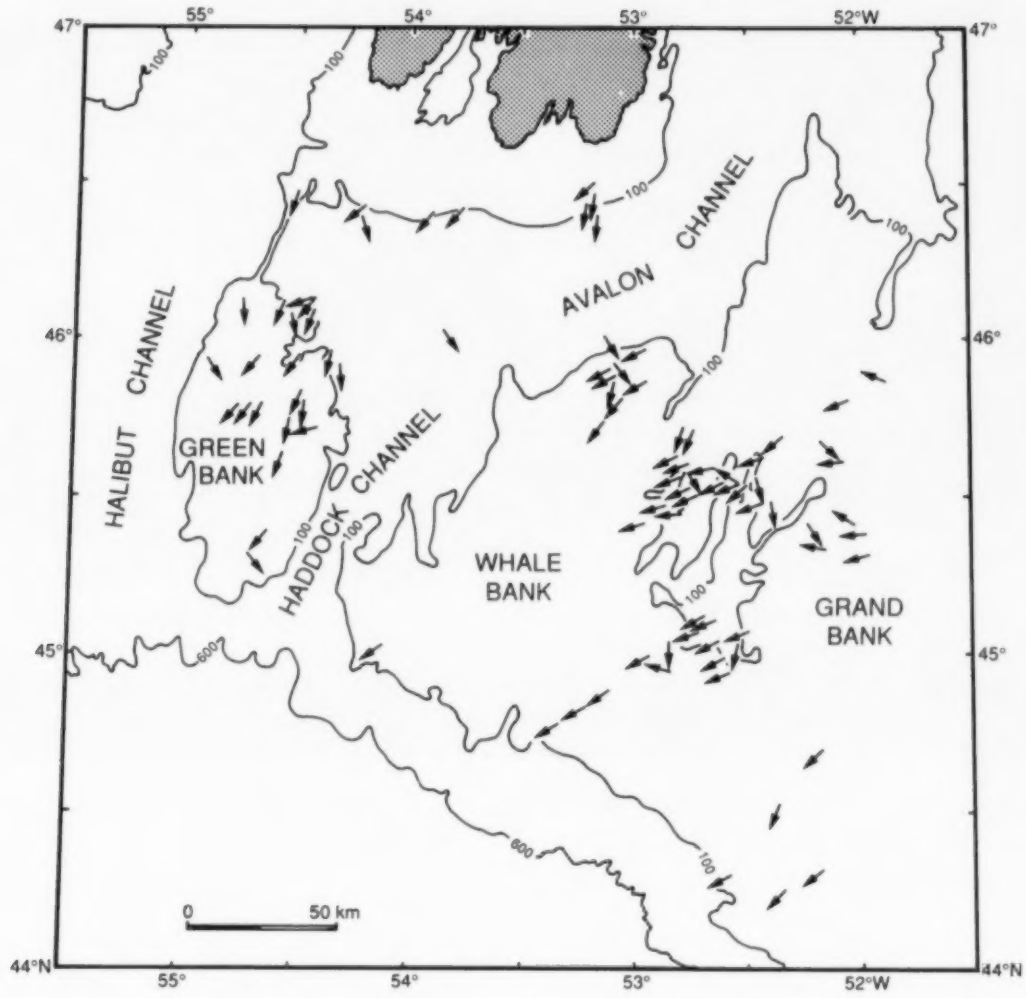

Fig. 17. Map of bedform migration directions, incorporating data for all megaripples and sandwaves where a facing direction could be determined. Each arrow is representative of many bedforms.

Judge, 1991). Unfortunately, the lack of near-bed current data precludes a definitive analysis of the reasons for this discrepancy, but we suggest that three factors combine to account for the observed transport.

Firstly, winter storms typically follow a north-northeasterly path which takes them directly over or very close to the western Grand Banks (Fig. 10; Lewis and Moran, 1984; Tucker and Barry, 1984; Brown et al., 1986). This, together with their large diameters (up to 1000 km; Lewis and Moran, 1984), ensures that storm winds commonly blow from the east and/or southeast as a storm approaches, and then swing rapidly to blow out of the west and/or northwest as the storm leaves the area. As a result of the relatively rapid change in wind direction as the storm moves over the area, storm currents directed toward the northeast, east and southeast, although having high speeds, do not act for long periods (Fig. 11). By comparison, the southerly and southwesterly currents which occur during the prolonged (2–3 day), post-storm, spin-down period act for considerably longer. Ericksen and Slingerland (1990) have concluded independently that it is the winds and currents on the trailing edge of storms which are the most sedimentologically important. Thus, it may be that the *vector-mean*, sediment transport on the western Grand Banks is in a more southerly direction than the maximum transport. There will also be a tendency for the storm currents to be preferentially channelled in a southsouthwest orientation by bathymetric features such as Halibut and Haddock Channels and Whale Deep (Fig. 1).

The second factor which promotes the consistent southwesterly transport is the Labrador Current (Fig. 8). Although this current by itself is incapable of significant transport, its presence will augment southerly- and southwesterly-flowing storm currents, but impede flow to the north and northeast.

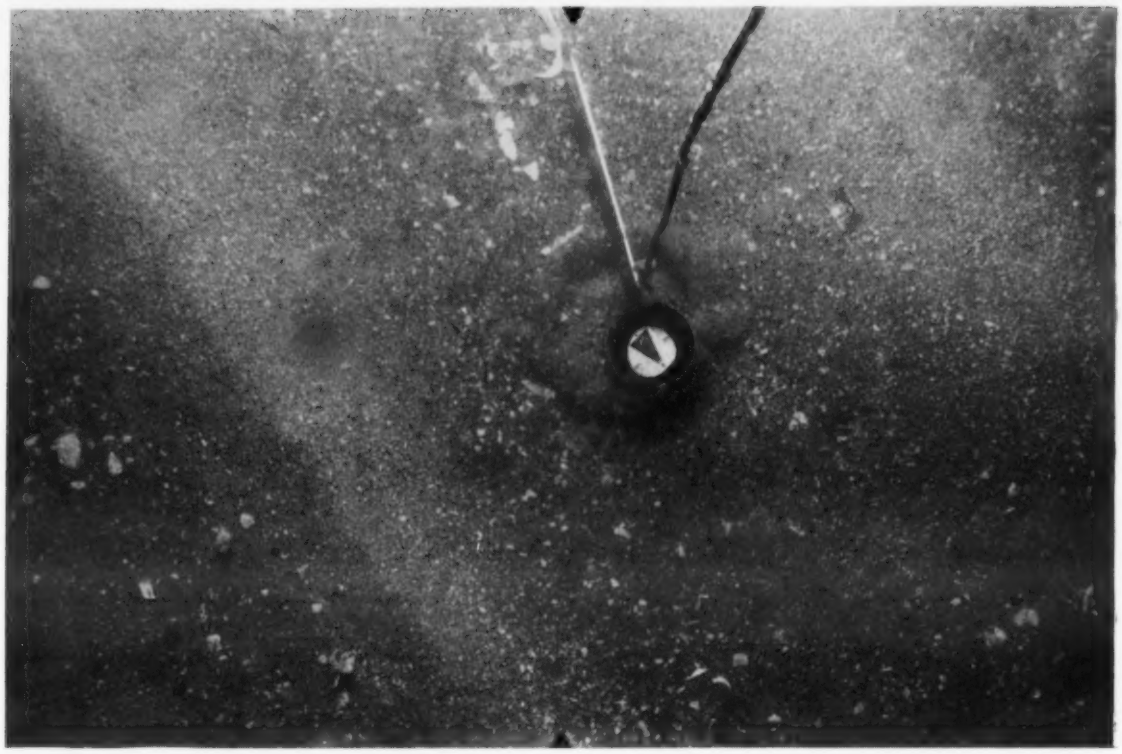

Fig. 18. Symmetrical gravel waves (Grand Bank) composed of coarse sand with minor gravel and shell debris. The ripple crests are noticeably finer than the intervening ripple trough. The vane on the trip weight is 24.5 cm long; the ripple spacing is approximately 75 cm.

Because of this, the net sediment transport will tend to be in the direction of the Labrador Current because of the exponential relationship between current speed and sediment discharge. To illustrate this, the component of storm-generated transport along the line of the Labrador Current (q_s) can be represented by the equation:

$$q_s \propto (U_{LC} \pm U_S)^3 \quad (1)$$

where U_S is the component of the storm current speed that is colinear with the Labrador Current, and U_{LC} is the speed of the Labrador Current; the plus sign is used when the storm current flows in the same direction as the Labrador Current and the negative sign is used when the two flows are in opposite directions. If U_S and U_{LC} are assigned representative values of 0.7 m s^{-1} and 0.05 m s^{-1}, equation (1) shows that transport to the south-southwest will be more than 1.5 times greater than transport to the northnortheast. Thus, the relatively weak Labrador Current has a marked influence on the direction of net sediment transport, thereby contributing to the parallelism between the flow direction of the Labrador Current (Fig. 8) and the bedform orientations (Fig. 17).

Finally, wave-orbital motion probably plays a significant role in determining the direction of net sediment movement and the orientation of the current-generated bedforms. Theoretical considerations (e.g., Davies et al., 1988; Duke, 1990), as well as the observation that gravel waves occur in coarser sediment than the megaripples and sand-waves, indicate that the peak, wave-orbital stresses are greater than those associated with the storm currents. Thus, the net sediment transport associated with the combined flow will not necessarily be in the direction of the current, but will instead lie closer to the direction of the peak wave motion because of the non-linear relationship between current speed and sediment transport [see current-vector plots for combined flows in Davies et al. (1988) and Duke (1990)]. The orientations of the gravel waves clearly show that the most intense wave-orbital motion is predominantly oriented NE–SW (Fig. 16D), perhaps because the largest waves are refracted into parallelism with the shelf edge as they advance onto the shelf. In this situa-

tion, wave motion further augments the tendency for southwestward transport due to the Labrador Current. As a result, the close correspondence between the orientations of the current-generated bedforms and gravel waves (Fig. 16) may not be coincidental, as the megaripples and sandwaves are oriented in response to the net transport direction (Duke, 1990) which is in turn approximately co-linear with the wave-orbital motion.

Discussion

In this example, the Labrador Current, wave-orbital motion, and perhaps also the vector-mean storm currents reinforce each other to generate a strongly-preferred, net sediment transport toward the southsouthwest, without the necessity of having a nearby shoreline to constrain the flow (as is the case on narrower shelves). That these three processes operate in approximately the same direction is coincidental; this need not be the case in other situations, where, for example, the wave-orbital motion might well be at right angles to the currents. The results in such cases are far from obvious, and more information on the interaction of waves and currents is needed.

The relative importance of the three processes discussed above cannot be evaluated with the available evidence. Certainly the largest near-bed shear stresses are presumably wave generated; thus, it might be argued that the directional consistency is primarily a result of the wave-orbital motion. On the other hand, the influence of the relatively weak Labrador Current should not be neglected, for as shown above, a directionally-consistent current with a speed as low as 0.05 m s^{-1} can impose a strong asymmetry to the sediment transport, in the same fashion that a small net drift does in tidal settings (Harris, 1991). Thus, weak oceanic currents may have an influence that is out of proportion with their absolute magnitude, and they should not be ignored when inferring the direction of sediment transport on modern shelves, or when reconstructing the origin of ancient shelf deposits which contain unidirectional cross bedding—e.g., the Lower Greensand, England (Allen, 1982), the Sandfjord Formation, north Norway (Levell, 1980), and the Shannon Sandstone, western USA (Tillman and Martinson, 1984).

The textural response of the western Grand Banks to the post-glacial sea-level fall and rise has also had an importance influence on the nature of the bedforms produced by the combined flows. The widespread distribution of medium and coarse sand at elevations above the lowstand (Fig. 12) promotes the formation of current-generated structures because wave-generated, hummocky cross stratification (HCS) does not form readily in such coarse sediment (Duke, 1985) while dunes have a wide stability range in these grain sizes (Southard and Boguchwal, 1990). This grain-size control on the structures may in fact explain why many relatively coarse-grained transgressive-shelf deposits are cross bedded while the associated finer-grained regressive units contain abundant HCS. There is no need to invoke a fundamental change in the hydrodynamic regime [(tidal-)current dominated as opposed to storm-wave dominated respectively] as is suggested by some workers (e.g. Walker, 1984; Tillman, 1985; Leckie, 1986).

Summary and conclusions

The surficial sediments on the western Grand Banks of Newfoundland are palimpsest, consisting of material reworked primarily from Wisconsinan glacial and glaciomarine sediments by shoreface and shallow marine processes during and after the post-glacial sea-level fall and subsequent Holocene rise. Modern sediment input is negligible and consists almost exclusively of biogenic material. Thick, Holocene deposits occur only below the lowstand elevation, and consist of fine sands, silts and clays that have been winnowed and transported from shallower areas. They accumulated mainly during the sea-level fall because most areas above the lowstand elevation became armoured and little fine material was liberated during the sea-level rise. In areas above the lowstand elevation the Holocene sediments consist of a thin, shelly gravel lag, on which lie scattered, mobile bedforms composed of medium to coarse sand.

Despite intense wave action which forms wave ripples in gravelly sands to depths of 110 m, the majority of the bedforms are current generated

because of the coarse-grained nature of the sediment (hummocky cross stratification appears not to form in these sediment sizes). Current speeds sufficient to generate the megaripples and sandwaves (0.5–1.0 m s^{-1}) occur only during storms. Sediment-transport directions during these events are variable because of the cyclonic nature of the winds, the diversity of storm tracks, and the lack of a nearby shoreline, but the maximum rate of sediment transport may be to the east or southeast (Amos and Judge, 1991). The orientation of individual megaripples and sandwaves, the presence of a north to south progression of bedform types which mimics the down-current trends in tidal transport paths, and the distribution of sediment thicknesses all indicate, however, that sediment transport is consistently to the south or southwest. We propose that the consistent south to southwesterly transport is due to a coincidental combination of factors including the occurrence of southerly- and southwesterly-directed currents during the lengthy post-storm spin-down period, and the enhancement of southsouthwesterly storm flow by the Labrador Current and wave-orbital motion.

These observations indicate that the net sediment-transport direction as recorded by large-scale bedforms and sedimentary structures is a result of the complex integration of all of the processes operating in the shelf environment. Relatively weak oceanic currents can, when superimposed on storm (or tidal) currents, have an influence that outweighs the strength of the oceanic current by itself. Similarly, wave action cannot be ignored, even if the environment appears to be current dominated.

Acknowledgments

The authors wish to thank the following people for their assistance in the various phases of the research: Mr. R.O. Miller and the technical staff of the Atlantic Geoscience Centre, Bedford Institute of Oceanography; the Captain and crew of the C.S.S. *Hudson*; and Ela Rusak Mazur, Queen's University, for drafting. The work by LeGresley and Dalrymple has been funded by grants to Dalrymple from the Canadian Department of Energy, Mines and Resources, the Natural Sciences and Engineering Research Council of Canada (Operating Grant A7553), Shell Canada Ltd. and Gulf Canada Ltd. Petrie's research was supported in part by the Panel for Environmental Research and Development (Canadian Department of Energy, Mines and Resources). We also thank Wm. Duke, D. Greenberg, B. MacLean and B. Zaitlin for their constructive comments on the manuscript.

References

Allen, J.R.L., 1982. Mud drapes in sand-wave deposits: A physical model with application to the Folkestone Beds (early Cretaceous, southeast England). Proc. R. Soc. London, A306: 291–345.

Allen, J.S., 1980. Models of wind-driven currents on the continental shelf. Ann. Rev. Fluid Mech., 12: 389–433.

Allen, J.S., Beardsley, R.C., Blanton, J.O., Boicourt, W.C., Butman, B., Coachman, L.K., Huyer, A., Kinder, T.H., Royer, T.C., Schumacher, J.D., Smith, R.L., Sturges, W. and Winant, C.D., 1983. Physical oceanography of continental shelves. Rev. Geophys. Space Phys., 12: 1149–1181.

Amos, C.L. and Judge, J.T., 1991. Sediment transport on the eastern Canadian continental shelf. Continental Shelf Res., 11: 1037–1068.

Amos, C.L. and King, E.L., 1984. Bedforms of the Canadian eastern seaboard: A comparison with global occurrences. Mar. Geol., 57: 167–208.

Arnott, R.W. and Southard, J.B., 1990. Exploratory flow-duct experiments on combined-flow bed configurations, and some implications for interpreting storm-event stratification. J. Sediment. Petrol., 60: 211–219.

Ashley, G.M., 1990. Classification of large-scale subaqueous bedforms: A new look at an old problem. J. Sediment. Petrol., 60: 160–172.

Barrie, J.V. and Collins, M.B., 1989. Sediment transport on the shelf margin of the Grand Banks of Newfoundland. Atlantic Geol., 25: 173–179.

Barrie, J.V., Lewis, C.F.M., Fader, G.B.J. and King, L.H., 1984. Seabed processes on the northeastern Grand Banks of Newfoundland; Modern reworking of relic sediments. Mar. Geol., 57: 209–227.

Barrie, J.V., Collins, W.T., Segall, M.P. and Lewis, C.F.M., 1985. Holocene development and sediment transport on the northeastern Grand Banks of Newfoundland. Bedford Inst. Oceanogr., Intern. Rep., 155 pp.

Belderson, R.H., Johnson, M.A. and Kenyon, N.H., 1982. Bedforms. In: A.H. Stride (Editor), Offshore Tidal Sands. Processes and Deposits. Chapman and Hall, London, pp. 27–57.

Bonifay, D. and Piper, D.J.W., 1988. Probable Late Wisconsinan ice margin on the upper continental slope off St. Pierre Bank, eastern Canada. Can. J. Earth Sci., 25: 853–865.

Boyd, R., Scott, D.B. and Douma, M., 1988. Glacial tunnel valleys and Quaternary history of the outer Scotian Shelf. Nature, 333: 61–64.

Brown, R.D., Roebber, P. and Walsh, K., 1986. Climatology of severe storms affecting coastal areas of Eastern Canada. Environmental Studies Revolving Funds, Rep. 20, Ottawa, Ont., 233 pp.

Cacchione, D.A. and Drake, D.E., 1990. Shelf sediment transport. In: B. LeMéhauté and D.M. Hanes (Editors), The Sea, Vol. 9B, Ocean Engineering Science. Wiley–Interscience, New York, pp. 729–774.

Chapman, D. and Beardsley, R., 1989. On the origin of shelf water in the Mid Atlantic Bight. J. Phys. Ocean., 19: 384–391.

Dalrymple, R.W., Knight, R.J. and Lambiase, J.L., 1978. Bedforms and their hydraulic stability relationships in a tidal environment, Bay of Fundy, Canada. Nature, 275: 100–104.

Davies, A.G., Soulsby, R.L. and King, H.L., 1988. A numerical model of the combined wave and current bottom boundary layer. J. Geophys. Res., 93: 491–508.

De Margerie, S. and Lank, K.D., 1986. Tidal circulation of the Scotian Shelf and Grand Banks. Contractor Rep., Contract 08SC.FP901-5-X515, Can. Dept. Fisheries and Oceans, Dartmouth, N.S. (Unpubl.).

Duke, W.L., 1985. Hummocky cross-stratification, tropical hurricanes, and intense winter storms. Sedimentology, 32: 167–194.

Duke, W.L., 1990. Geostrophic circulation or shallow marine turbidity currents? The dilemma of paleoflow patterns in storm-influenced prograding shoreline systems. J. Sediment. Petrol., 60: 870–883.

Ericksen, M.C. and Slingerland, R., 1990. Numerical simulations of tidal and wind-driven circulation in the Cretaceous Interior Seaway of North America. Geol. Soc. Am. Bull., 102: 1499–1516.

Fader, G.B.J., 1980. C.S.S. *Hudson* 80-010 Cruise Report. Bedford Inst. Oceanogr., Dartmouth, N.S., Intern. Rep.

Fader, G.B.J., 1985. C.S.S. *Hudson* 85-005 Cruise Report. Bedford Inst. Oceanogr., Dartmouth, N.S., Intern. Rep., 11 pp.

Fader, G.B.J., 1986. C.S.S. *Hudson* 86-017 Cruise Report. Bedford Inst. Oceanogr., Dartmouth, N.S., Intern. Rep., 48 pp.

Fader, G.B.J., 1989a. A Late Pleistocene low sea-level stand of the southeastern Canadian offshore. In: D.B. Scott, P.A. Pirazzoli and C.A. Honig (Editors), Late Quaternary Sea-Level Correlation and Applications. Kluwer Academic Publishers, Boston, pp. 71–103.

Fader, G.B.J., 1989b. Submersible observations of iceberg furrows and sand ridges, Grand Banks of Newfoundland. In: D.J.W. Piper (Editor), Submersible Observations off the East Coast of Canada. Geol. Surv. Can., Pap. 88-20: 27–39.

Fader, G.B.J. and King, L.H., 1981. A reconnaissance study of the surficial geology of the Grand Banks of Newfoundland. Geol. Surv. Can., Pap. 81-1A: 45–56.

Fader, G.B.J. and Miller, R.O., 1986a. A reconnaissance study of the surficial and shallow bedrock geology of the southeastern Grand Banks of Newfoundland. Geol. Surv. Can., Pap. 86-1B: 591–604.

Fader, G.B.J. and Miller, R.O., 1986b. Regional geological constraints on resource development—Grand Banks of Newfoundland. Proc., Third Can. Conf. Mar. Geotech. Eng. (St. John's, Newfoundland), 1, pp. 3–40.

Fader, G.B.J., King, L.H. and Josenhans, H., 1982. Surficial geology of the Laurentian Channel and the western Grand Banks of Newfoundland. Geol. Surv. Can., Pap. 81-22, 376 pp.

Fader, G.B.J., Lewis, C.F.M., Barrie, J.V., Parrott, D.R., Collins, W., Miller, R.O. and d'Apollonia, S., 1985. Quaternary geology of the Hibernia area of northeast Grand Bank. Geol. Surv. Can., Map 14968 QG.

Fader, G.B.J., Miller, R.O., Ruffman, A. and Wilson, E., in prep. Surficial geology of the central Grand Banks of Newfoundland. Geol. Surv. Can., Map.

Forbes, D.L. and Boyd, R., 1987. Gravel ripples on the inner Scotian Shelf. J. Sediment. Petrol., 57: 46–54.

Forrester, W.D. and Benoit, J., 1981. Physical oceanography of waters over the Grand Banks of Newfoundland. Grand Banks Oceanographic Studies 1. MacLaren Plansearch Ltd., Halifax, N.S.

Grant, D.R. and King, L.H., 1984. A stratigraphic framework for the Quaternary history of the Atlantic Provinces, Canada. Geol. Surv. Can., Pap. 84-10: 173–191.

Grant, W.D. and Madsen, O.S., 1979. Combined wave and current interaction with a rough bottom. J. Geophys. Res., 84: 1797–1808.

Grant, W.D. and Madsen, O.S., 1982. Movable bed roughness in unsteady oscillatory flow. J. Geophys. Res., 87: 469–481.

Greenberg, D.A. and Petrie, B.D., 1988. The mean barotropic circulation on the Newfoundland shelf and slope. J. Geophys. Res., 93: 15541–15550.

Harris, P.T., 1991. Reversal of subtidal dune asymmetries caused by seasonally reversing wind-driven currents in Torres Strait, northeastern Australia. Cont. Shelf Res., 11: 655–662.

Hutchins, R.W., McKeown, D.L. and King, L.H., 1976. A deep tow high resolution seismic system for continental shelf mapping. Geosci. Can., 3: 95–100.

Ikeda, M., 1989. A review of sea ice and ocean modelling relevant to the Labrador and Newfoundland shelves. IEEE Trans. Geosci. Remote Sensing, 27: 535–540.

Josenhans, H.W. and Fader, G.B.J., 1989. A comparison of models of glacial sedimentation along the eastern Canadian margin. Mar. Geol., 85: 273–300.

Kenyon, N.H., 1970. Sand ribbons of European tidal seas. Mar. Geol., 9: 25–39.

King, L.H., 1973. C.S.S. *Dawson* 73-006 Cruise Report. Bedford Inst. Oceanogr., Dartmouth, N.S., Intern. Rep.

King, L.H. and Fader, G.B., 1986. Wisconsinan glaciation of the continental shelf, S.E. Atlantic Canada. Geol. Surv. Can., Open File Rep. 1126.

King, L.H. and Fader, G.B., 1989. A comparison between the late Wisconsinan history of southwest and northeast Emerald Basin. Geol. Surv. Can., Open File Rep. 2060.

Lavelle, J.W., Jr., Gadd, P.E., Han, G.C., Meyer, D.R., Stubblefield, W.L. and Swift, D.J.P., 1978. Fair weather and storm transport on the Long Island, New York, inner shelf. Sedimentology, 25: 823–842.

Leckie, D., 1986. Tidally-influenced transgressive shelf sediments in the Viking Formation, Caroline, Alberta. Bull. Can. Soc. Petrol. Geol., 34: 111–125.

Leckie, D., 1988. Wave-formed, coarse-grained ripples and their relationship to hummocky cross-stratification. J. Sediment. Petrol., 58: 607–622.

LeGresley, E.M., 1988. Holocene sedimentation on the western

Grand Banks of Newfoundland. M.Sc. Thesis, Queen's Univ., Kingston, Ont., 316 pp. (Unpubl.).

Levell, B.K., 1980. A Late Precambrian tidal shelf deposit, the lower Sandfjord Formation, Finnmark, North Norway. Sedimentology, 27: 539–557.

Lewis, C.F.M., 1984. C.S.S. *Hudson* 84-024 Cruise Report. Bedford Inst. Oceanogr., Dartmouth, N.S., Intern. Rep.

Lewis, P.J. and Moran, M.D., 1984. Severe storms off Canada's East Coast: A catalogue summary for the period 1957 to 1983. Atmospheric Environment Serv., Can. Climate Centre, Rep. 84-13, 337 pp. (Unpubl.).

McLean, S.R., 1981. The role of non-uniform roughness in the formation of sand ribbons. Mar. Geol., 42: 49–74.

Miller, M.C., McCave, I.N. and Komar, P.D., 1977. Threshold of sediment movement under unidirectional currents. Sedimentology, 24: 507–527.

Mortsch, L.D., Agnew, T., Saulesleja, A. and Swail, V.R., 1985. Marine climatological atlas—Canadian East Coast. Atmospheric Environment Serv., Can. Climate Centre, Rep. 85-11, 343 pp.

Neu, H.J.A., 1982. Eleven-year deep-water wave climate of Canadian Atlantic waters. Can. Dept. Fisheries Oceans, Tech. Rep. Hydrogr. Ocean Sci., 13, 41 pp.

Petrie, B., 1991. Current meter and bottom pressure observations in Avalon Channel. Can. Dept. Fisheries Oceans, Tech. Rep. Hydrogr. Ocean Sci., in press.

Petrie, B. and Anderson, C., 1983. Circulation on the Newfoundland continental shelf. Atmosphere-Ocean, 21: 207–226.

Petrie, B., Lank, K. and De Margerie, S., 1986. Tides on the Newfoundland Grand Banks. Atmosphere-Ocean, 25: 10–21.

Piper, D.J.P., Mudie, P.J., Fader, G.B.J., Josenhans, H.W., MacLean, B. and Vilks, G., 1990. Quaternary geology. In: M.J. Keen and G.L. Williams (Editors), Geology of the Continental Margin of Eastern Canada. (Geology of Canada, 2) Geol. Surv. Can., pp. 475–607.

Quinlan, G. and Beaumont, C., 1981. A comparison of observed and theoretical relative sea level in Atlantic Canada. Can. J. Earth Sci., 18: 1146–1163.

Robe, R.Q., 1971. Oceanographic observations, North Atlantic standard monitoring systems A1, A2, A3 and A4, 1967–1968. U.S. Coast Guard Oceanogr. Rep. 43, 227 pp.

Shaw, J., 1989. Drumlins, subglacial meltwater floods, and ocean responses. Geology, 17: 853–856.

Slatt, R., 1977. Late Quaternary terrigenous and carbonate sedimentation on the Grand Banks of Newfoundland. Bull. Geol. Soc. Am., 88: 1357–1367.

Southard, J.B. and Boguchwal, L.A., 1990, Bed configurations in steady unidirectional water flows. Part 2. Synthesis of flume data. J. Sediment. Petrol., 60: 658–679.

Southard, J.B., Lambie, J.M., Federico, D.C., Pile, H.T. and Weidman, C.R., 1990. Experiments on bed configurations in fine sands under bidirectional purely oscillatory flow, and the origin of hummocky cross-stratification. J. Sediment. Petrol., 60: 1–17.

Swift, D.J.P. and Niedoroda, A.W., 1985. Fluid and sediment dynamics of continental shelves. In: R.W. Tillman, D.J.P. Swift and R.G. Walker (Editors), Shelf Sands and Sandstone Reservoirs. SEPM Short Course Notes, 13: 47–133.

Tillman, R.W., 1985. The Tocito and Gallup Sandstones, New Mexico, a comparison. In: R.W. Tillman, D.J.P. Swift and R.G. Walker (Editors), Shelf Sands and Sandstone Reservoirs. SEPM Short Course Notes, 13: 403–463.

Tillman, R.W. and Martinson, R.S., 1984. The Shannon shelf-ridge sandstone complex, Salt Creek Anticline area, Powder River Basin, Wyoming. In: R.W. Tillman and C.T. Seimers (Editors), Siliclastic Shelf Sediments. SEPM Spec. Publ., 34: 85–142.

Tucker, G.B. and Barry, R.G., 1984. Climate of the North Atlantic Ocean. In: H. van Loon (Editor), Climates of the Oceans. (World Survey of Climatology, 15) Elsevier, Amsterdam, pp. 193–262.

Van Wagoner, J.C., Posamentier, H.W., Mitchum, R.M., Vail, P.R., Sarg, J.F., Loutit, T.S. and Hardenbol, J., 1988. An overview of the fundamentals of sequence stratigraphy and key definitions. In: C.K. Wilgus, B.S. Hastings, C.G.St.C. Kendall, H.W. Posamentier, C.A. Ross and J.C. van Wagoner (Editors), Sea-Level Changes: An Integrated Approach. SEPM Spec. Publ., 42: 39–45.

Vincent, C.E., Swift, D.J.P. and Hillard, B., 1981. Sediment transport in the New York Bight, North American Atlantic Shelf. Mar. Geol., 42: 369–398.

Walker, R.G., 1984. Shelf and shallow marine sands. In: R.G. Walker (Editor), Facies Models. 2nd ed. Geol. Assoc. Can., Toronto, Geosci. Can. Reprint Ser. 1, pp. 141–170.

Williams, G.L., Fyffe, L.R., Wardle, R.J., Colman-Sadd, S.P. and Boehner, R.C. (Editors), 1985. Lexicon of Canadian Stratigraphy, Volume VI, Atlantic Region. Can. Soc. Pet. Geol., Calgary, Alta., 572 pp.

Yorath, C.J., Bornhold, B.D. and Thompson, R.E., 1979. Oscillation ripples on the northeast Pacific continental shelf. Mar. Geol., 31: 45–58.

Marine Geology, 105 (1992) 119–140
Elsevier Science Publishers B.V., Amsterdam

Barriers, barrier platforms, and spillover deposits in St. George's Bay, Newfoundland: Paraglacial sedimentation on the flanks of a deep coastal basin

John Shaw and Donald L. Forbes

Geological Survey of Canada, Bedford Institute of Oceanography, P.O. Box 1006, Dartmouth B2Y 4A2, NS, Canada

(Received May 6, 1991; revision accepted August 7, 1991)

ABSTRACT

Shaw, J. and Forbes, D.L., 1992. Barriers, barrier platforms, and spillover deposits in St. George's Bay, Newfoundland: Paraglacial sedimentation on the flanks of a deep coastal basin. Mar. Geol., 105: 119–140.

St. George's Bay and adjacent coastal areas of southwest Newfoundland contain thick sequences of late Quaternary glaciogenic sediments and have been subject to relative sea-level fluctuations over a range of 70 m during the past 13.5 ka. Glaciogenic sediments have been mobilized by littoral processes to form two types of deposits. These are: (1) the prograded barrier beach and spit at Stephenville and Flat Island, respectively, which are associated with large subaqueous sandy platforms; and (2) a wedge of well-stratified sand and gravel on the landward flank of the shallow sill which extends across St. George's Bay at an average depth of about 25 m.

The subaerial barriers and spits are composed of gravel beach ridges, overlain locally by thin aeolian deposits, with freshwater and salt-marsh peats in swales. These barriers developed during the last several thousand years, as relative sea level approached its present position from an early postglacial minimum of approximately −25 m. The prerequisite for beach-ridge formation was the deposition of large, sandy subaqueous platforms which appear on shallow seismic reflection records as clinoform wedges prograded into the deep basin of inner St. George's Bay. The barrier platform at Stephenville is constructed across a deep submarine valley. The Flat Island barrier platform sits on the flank of a glacially-overdeepened trough, partly filled by glacial and postglacial sediments, and envelops a delta formed during the early postglacial low stand of relative sea level. The platform and barrier together constitute a thick coastal sequence coarsening up from sandy mud at the base to gravel at the top.

The wedge of well-stratified, coarse sediment, up to 50 m thick, situated on the landward flank of the shallow sill overlies older, glaciogenic sediments and passes laterally into postglacial basin muds. Steep foreset reflections dipping 10°–20° are evident on shallow seismic reflection records, suggesting that the wedge was formed by spillover of sediment, entrained by wave and current action, into the relatively deep basins of the inner bay. Active gravel ripples testify to the continued mobility of coarse sediment on the sill. The formation of the spillover deposits, barriers and platforms demonstrates the potential for glacially -overdeepened basins to host thick, heterogeneous, coarse-grained coastal and inner-shelf deposits.

Introduction

This paper presents observations of Holocene barrier deposits and associated platform and spillover wedges on the southwest coast of Newfoundland. In the paraglacial setting of St. George's Bay, rising relative sea level, abundant sediment supply, irregular coastal topography, and differing source-sink relationships have produced a variety of barrier sequences and thick clastic wedges with contrasting progradational architecture and orientation. These results demonstrate the important role of glacial processes in the creation both of deep receiving basins and of sediment sources for the accumulation of thick and heterogeneous coastal sequences. A number of recent studies have confirmed the importance of glacial or proglacial deposits as sediment sources for coastal deposition in eastern Canada (e.g. Boyd et al., 1987; Forbes and Taylor, 1987; Forbes et al., 1989, 1990; Carter et al., 1989, 1990). Glacial erosion has also placed a strong imprint on the coast, in the form of

numerous fjords and other over-deepened basins that constitute important sediment sinks (e.g. Piper et al., 1983; Shaw and Forbes, 1990c). Forbes (1984) showed that the coastline of Newfoundland is generally deficient in sediments, except in the immediate vicinity of large ice-contact and outwash deposits. With the exception of a few locations where large sandy beaches and dunes are present (Forbes, 1984; Shaw and Forbes, 1990a), the largest coastal deposits on the island are gravel beach-ridge plains sited immediately downdrift of coastal bluffs composed of glaciogenic material (Shaw and Forbes, 1987; Shaw, 1989). Along the north and south coasts of St. George's Bay (Fig. 1), thick sections of glacial and proglacial sediments are exposed in extensive coastal bluffs (MacClintock and Twenhofel, 1940). These represent the largest coastal sediment source in Newfoundland. Much of the sediment mobilized from this source has accumulated in bayhead and extensional barriers resting on sandy subaqueous barrier platforms. Sediment derived from a related (now largely relict) source on the St. George's Bay sill (Fig. 1c) has accumulated in a large spillover wedge building into the basin on the landward side of the sill.

Barrier facies sequences, platforms, and spillover deposits

Recent decades have seen an increasing awareness of the complexity of coastal and shallow-marine clastic deposits. By the early 1970s, the classic regressive barrier island model based on the Galveston Island sequence (Bernard et al., 1962) had been augmented by studies of contrasting transgressive sequences, for example as described from the Delaware coast by Kraft (1971). Observations of tidal-inlet channel-fill units (e.g. Hoyt and Henry, 1965, 1967; Kumar and Sanders, 1974) revealed the importance of inlet migration in the development of many barrier sequences. As a result, Reinson (1979) proposed three "end-member" facies models for barrier complexes. These were: (1) the regressive or prograding model (coarsening upward); (2) the transgressive model (coarsening upward or stacked in a more complex manner); and (3) the inlet–migration model (typically fining upward). By the early 1980s, studies of coastal barrier systems in Australia were demonstrating the heterogeneity of estuarine fill and barrier complexes in a variety of coastal settings (Roy et al., 1980) and a transition from transgressive to regressive development associated with stabilization of relative sea level (Thom, 1983). Recent review papers by Reinson (1984) and Elliott (1986) have emphasized the great variety of geometries that may result from the development of barrier systems.

In some barrier systems, exemplified by the features described in this paper, the subaerial component represents only a small part of the total sediment volume. Much of the sediment occurs in a subaqueous platform that provides the foundation for development of the barrier itself. Meistrell (1966, 1972) used the term 'spit-platform' to describe this subaqueous structure constructed at the coastline as a prerequisite to spit development; here we adopt the term 'barrier platform' in an equivalent but more general sense. There are very few detailed field descriptions of barrier platform deposits. Nielsen et al. (1988) examined the morphology and internal structure of uplifted Late Pleistocene spit deposits in northern Denmark. They described a "giant-scale" cross-bedded unit, up to 10 m thick, formed by spit-platform accretion. Their results appeared to corroborate the conclusions of Meistrell (1966, 1972) that the growth rates of spit and platform structures are inversely related.

Barrier platforms are but one type of coarse-grained progradational wedge that may develop in coastal settings. Other examples include lacustrine oolitic carbonate wedges (e.g. Swirydczuk et al., 1979), clastic progradational shoreface sheets (e.g. Clifton, 1981; Cant, 1984), thick clinoform wedges such as the "giant" foreset beds of the Bohemian Cretaceous Basin (Jerzykiewicz and Wojewoda, 1986), or a Holocene "submerged spit bar" off southeast Africa (Martin and Flemming, 1986). At the extreme end of the size spectrum, there are very large clinoform debris wedges fronting carbonate platforms with relief of 200 to 1000 m or more (e.g. Enos, 1977; Hubert et al., 1977). In this paper we describe another type of marine clastic wedge, in this case a spillover feature prograding into a deep coastal basin under conditions of rising

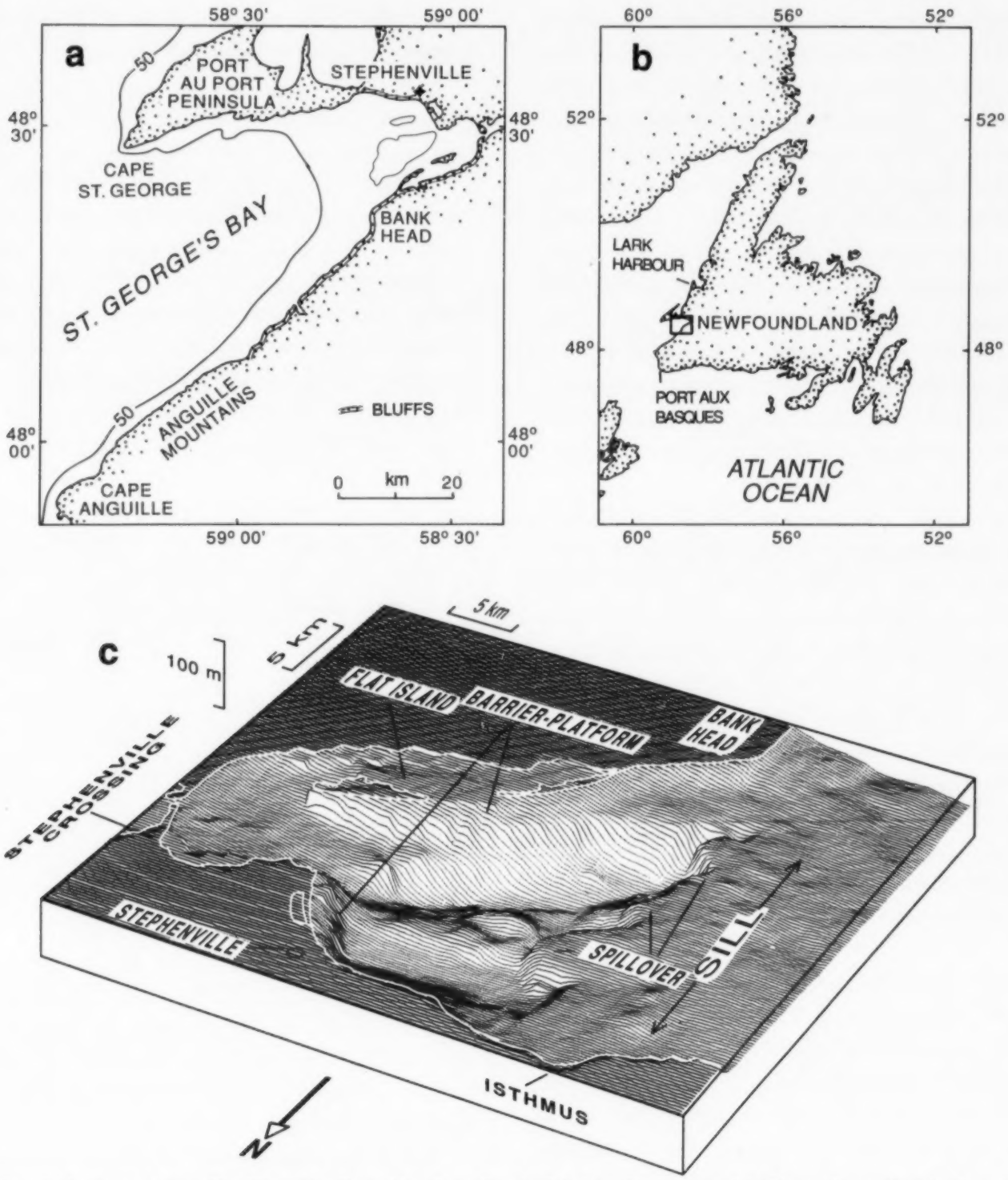

Fig. 1 (a) The study area, inner St. George's Bay, Newfoundland. (b) Location map. (c) Three-dimensional view towards the southeast, showing the bathymetry of St. George's Bay, and illustrating how the surface of the sill merges with the proximal part of the Flat Island barrier platform.

relative sea level. This spillover deposit is located on the landward flank of the shallow sill extending across St. George's Bay (Fig. 1c). Although the term 'spillover' has deep-water connotations, and was used by Stanley et al. (1973) to describe the movement of sediment over the shelf edge, we apply it here to an analogous process on the inner shelf. In this case, the spillover results from the movement of wave-entrained sand and gravel across a shallow sill into the deeper basin on its landward side, to form a coarse-grained clinoform wedge up to 50 m thick.

The study area

St. George's Bay is a large coastal embayment in southwest Newfoundland (Fig. 1), exposed to a fetch of up to 700 km to the west and southwest.

Wave hindcast estimates and limited observational data (Woodward-Clyde Consultants, 1982) show that wave energy levels are relatively high for the Gulf of St. Lawrence, with annual significant wave height exceeding 5 m. Although some long-period Atlantic swell enters the bay, modal wave periods are nevertheless relatively low, associated with local sea waves. The direction of wave approach, although variable, is predominantly from the west and southwest, as are the prevailing winds. The semi-diurnal tides have a mean range of 1 m. Sea ice exceeding 40% cover is normally present during February and March and wave activity can be restricted by ice from late December to early May (Markham, 1980; Farmer, 1981).

Tidal data from Port aux Basques (Fig. 1) show mean sea level rising at a rate of 3.04 m ka^{-1} (Shaw and Forbes, 1990b). Carrera et al. (1990) calculated a rate of 3.75 m ka^{-1} for Port aux Basques and 2.97 m ka^{-1} for Lark Harbour, in Bay of Islands (Fig. 1). Studies of recent salt-marsh deposits in St. George's Bay suggest a rate of relative sea-level rise of approximately 1 m ka^{-1} over the past 2–3 ka (Brookes et al., 1985; Shaw and Forbes, 1987, 1990b).

The outer part of St. George's Bay shallows gradually up to a sill with an average depth of 25 m, with several shoals shallower than 20 m (Figs. 1c and 2). The sill extends from Bank Head to the Port au Port isthmus. The inner side of the sill is a steep escarpment, with a slope of 10° to 20°, facing two inner basins with maximum depths of 60 and 100 m. Much of the coastline consists of eroding bluffs, typically about 30 m high, and comprising a wide range of glaciogenic sediments, including till, glaciomarine mud, and deltaic sands and gravels (MacClintock and Twenhofel, 1940; Brookes, 1974, 1987). The bluffs feed sediments to accretionary coastal systems in the inner bay (Figs. 2 and 3). The largest of these is the Flat Island barrier, a 12 km spit composed of gravel beach ridges with a thin veneer of marsh and aeolian sand deposits. The barrier at Stephenville, also composed of gravel beach ridges, encloses a tidal lagoon connected to the ocean by an artificial channel. The small spit along the southeast side of the Indian Head Range is largely intertidal. The barrier at Stephenville Crossing is composed of sand and gravel beach ridges with extensive coastal dunes and a large tidal inlet complex.

Data collection methods

Interpretations of barrier development are based partly on evidence from maps and charts dating from the mid-18th century onwards, from vertical air photographs dating from 1949 and later, and from 1985 oblique aerial photography and video imagery (Forbes and Frobel, 1986). Topographic surveys were run along selected profiles, with repetitive surveys at some sites dating back to 1982 (Forbes, 1984). Some profiles on Flat Island were extended seaward to depths of approximately 10 m using an inflatable boat equipped with a 200-kHz echo sounder. Seabed sediments along these profiles were sampled at eight locations using a small grab sampler.

A survey conducted from the research vessel *Navicula* in 1988 provided 313 line-kilometres of shallow seismic reflection data from the inner part of St. George's Bay (Forbes and Shaw, 1989). The data were obtained simultaneously with bubble-pulser and multitip-sparker shallow seismic systems. Bathymetry was recorded using a 30-kHz echosounder and sidescan sonar imagery was collected with a 100-kHz towfish and wet-paper recorder. The ship's tracks included two lines near-normal to the beach-ridge plain at Stephenville and one line through it (in a dredged channel), nine lines across the eastern (landward) edge of the sill, and fifteen lines near-normal to the Flat Island barrier. Twenty-one grab samples and two gravity cores were recovered.

Other data include several high-resolution shallow seismic reflection profiles across the sill (Josenhans et al., 1989) and seismic data gathered by Shearer (1973). Details of sampling methods used on freshwater and salt-marsh peats are given in Shaw and Forbes (1987). Computer simulations of wave refraction were obtained using a modified version of a program published by May (1974).

Late-Quaternary events and stratigraphy of St. George's Bay

Unlike most coastal areas of the island of Newfoundland, the region bordering the south coast

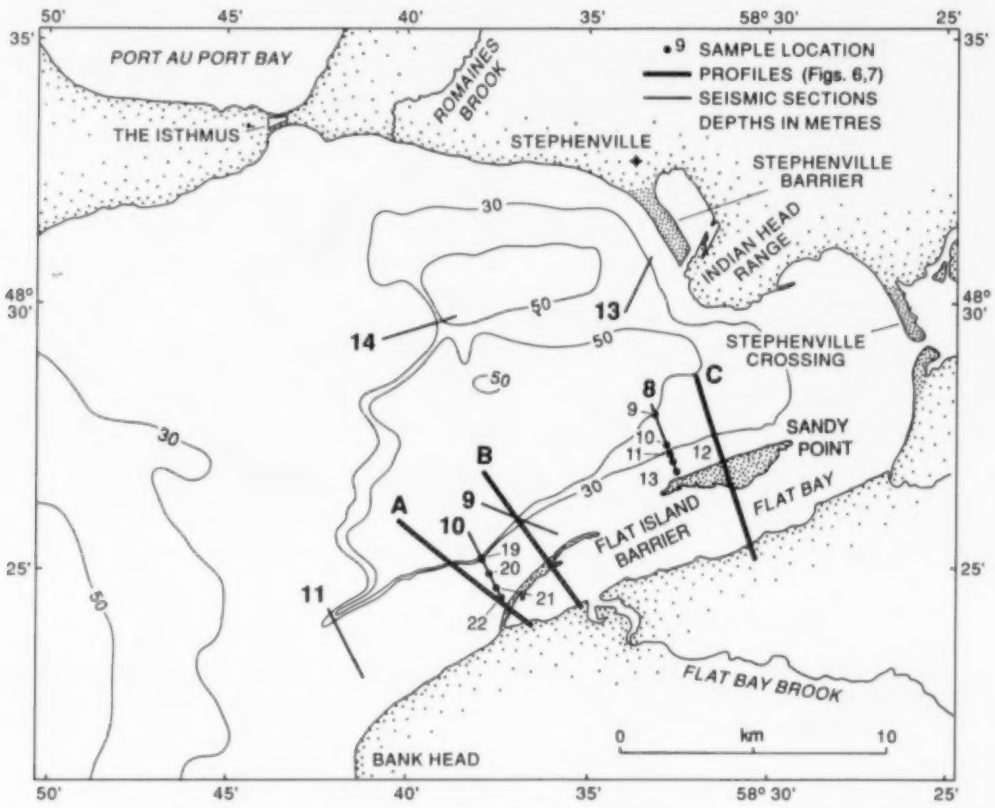

Fig. 2 Inner St. George's Bay. The drift-aligned Flat Island barrier is located on the south coast of the bay, adjacent to a basin more than 90 m deep in places. Eroding coastal bluffs extend from the attachment point a distance of 40 km in an updrift direction. In contrast the Stephenville barrier is in a compartment setting, bounded by coastal bluffs to the west (updrift), and a major bedrock headland formed by the Indian Head Range. A third barrier system is located at Stephenville Crossing, at the head of the bay. Also shows locations of profiles *A*, *B* and *C* (Figs. 6 and 7), seismic sections (Figs. 8–11, 13 and 14), and seabed samples (Fig. 12).

of St. Georges Bay has a thick and continuous cover of Quaternary sediments (Liverman and Taylor, 1990). The sediments exposed in coastal bluffs around the bay have been described and interpreted by Flint (1940), MacClintock and Twenhofel (1940), Brookes (1969, 1970, 1974, 1977, 1987) and Grant (1987). Till and ice-margin facies are overlain by marine overlap deposits which began accumulating by 13.7–13.5 ka B.P. The latter, predominantly silty clay bottomsets and sandy foresets, constitute the Bay St. George Delta, which was formed by a coalescence of deltas fed by streams draining an ice front close to the present coastline. A subsequent minor ice readvance locally capped the stratified delta deposits with ice-contact sediments (Brookes, 1974).

These events occurred against a background of changing relative sea level (Fig. 4). Relative sea level fell from a registered maximum of +44 m at 13.6 ka B.P. (Brookes, 1977) to a postglacial minimum, previously estimated at −11 to −14 m (Brookes et al., 1985), but thought by Grant (1987) to have been lower. Shaw and Forbes (1990b,c) have reported evidence for a minimum at approximately −25 m. This minimum is so far undated, but probably occurred between 9 and 10 ka B.P. Relative sea level rose to −2.8 m by 2.8 ka BP and to −1.8 m by 2.4 ka B.P. (Brookes et al., 1985).

The two basins in the inner bay (Fig. 2) are filled partly with unconsolidated sediment and underlain by deep bedrock valleys (Fig. 3). The St. George Valley runs seaward from the head of the bay and has a maximum depth of 195 m. It is located about 3 km offshore from Flat Island spit and aligned roughly parallel to the shoreline. By contrast, the Stephenville Valley extends beneath the beach-ridge plain at Stephenville, oriented normal to the shoreline, and is 180 m deep just offshore.

The inner part of St. George's Bay contains up to 180 m of late Quaternary sediments. Shaw and Forbes (1990c) have distinguished eight seismostratigraphic units according to their character on

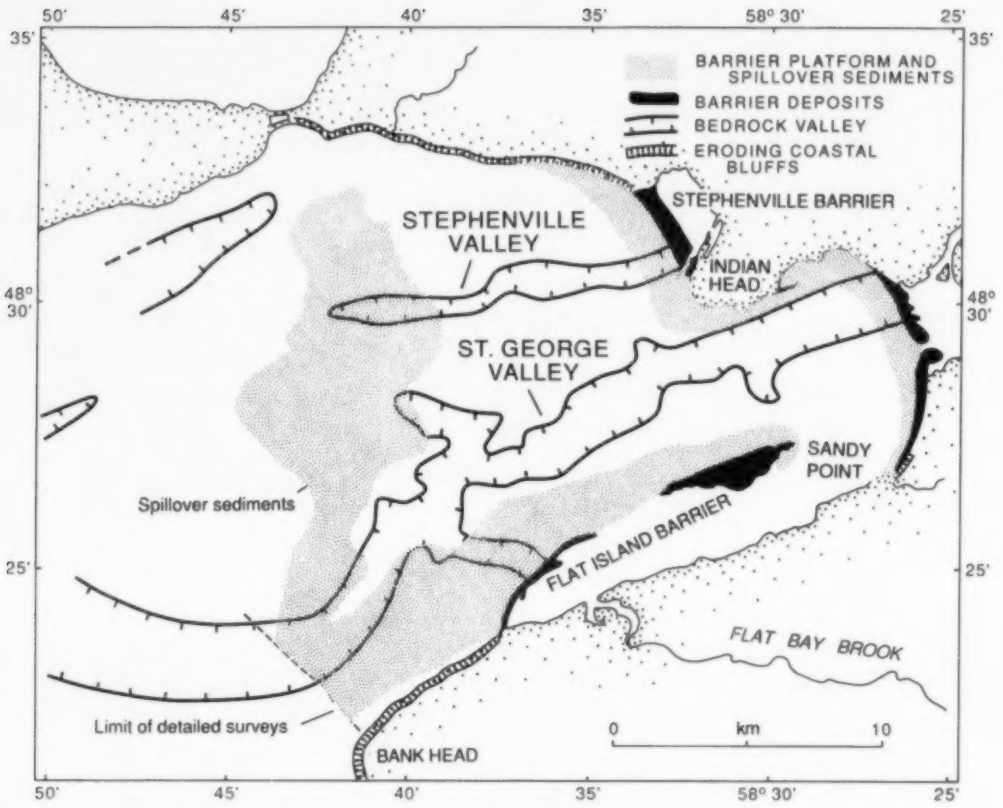

Fig. 3 Extent of barriers, barrier platforms and spillover sediments in St. George's Bay, and locations of glacially-overdeepened submarine valleys which underlie Quaternary sediments. Branching from the St. George Valley is the tributary palaeovalley of Flat Bay Brook. Barrier-platform sediments of Flat Island spit merge with spillover deposits several kilometres northwest of Bank Head, mid-way across the St. George Valley. Seabed sediment associated with the barrier platforms is predominantly sand, grading to muddy sand with depth, but the spillover structure extending across the bay is covered by rippled fine gravel. The extent of eroding coastal bluffs is also indicated. Bluffs extend to the Anguille Range, 40 km southwest of the proximal end of Flat Island spit.

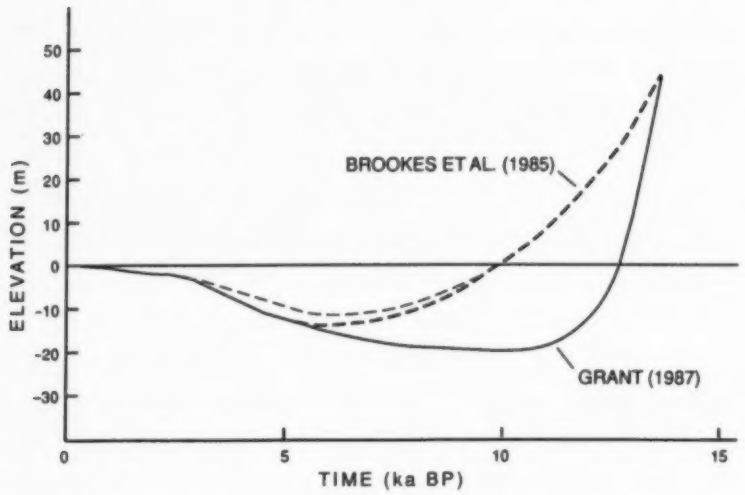

Fig. 4 Published relative sea-level curves for St. George's Bay. The dashed lines approximate the curve published by Brookes et al. (1985). Grant (1987) suggested a modified curve, shown here as a solid line. Recent shallow reflection seismic evidence (Forbes and Shaw, 1989; Shaw and Forbes, 1990c) substantiates Grant's view, but suggests that relative sea level dropped to about −25 m in the early postglacial.

acoustic records, supplemented by limited lithological data derived from grab samples and cores. The glacial units are: (1) a unit with incoherent reflections, interpreted as glacial diamict and probably correlative with the St. George's River Drift of MacClintock and Twenhofel (1940); (2) a unit, contained in the two deep submarine valleys, that displays a basin-fill acoustic style, with continuous coherent reflections of moderate amplitude, interpreted as subaqueous (possibly subglacial) outwash; (3) a unit with moderate to high-amplitude continuous coherent reflections, highly conformable to the substrate, interpreted as glaciomarine mud and sand, and dated at 13.7–11.2 ka B.P. in nearby Port au Port Bay. Postglacial units include: (4) a ponded unit either with very low-amplitude, continuous, coherent reflections or acoustically transparent, containing shallow gas in places, and believed to be mud derived largely from reworking of earlier sediments; (5) a seaward-thickening wedge on the seaward side of the sill, with low to

moderate-intensity continuous coherent reflections, interpreted as shoreface sand; and (6) seaward-thinning wedges with low to moderate-intensity continuous coherent reflections, steeply dipping and arranged in clinoform style. These are deltas, formed during the postglacial low-stand of relative sea level, and graded to −25 m.

In this paper we focus attention on the two remaining acoustic units identified in St. George's Bay. Unit 7 consists of a prograded, seaward-thinning clinoform wedge with moderate to high-intensity continuous coherent reflections. It fronts the gravel beach-ridge systems at Stephenville and Flat Island and has been interpreted as barrier-platform sand (Fig. 3). Unit 8 is a wedge with steeply-dipping moderate to strong continuous coherent reflections, located along the landward flank of the sill. We have interpreted this unit as spillover sand and gravel (Shaw and Forbes, 1990c).

Flat Island

The subaerial spit

The Flat Island barrier (Fig. 5a) is about 12 km long and can be subdivided into three sections. Close to the attachment point, the western section is a narrow gravel ridge with crest elevations up to 2.8 m (Fig. 6, profile A), capped by cobble-boulder overtop and washover deposits. Farther northeast, the beach truncates older gravel beach ridges with a thin aeolian cover and with crest heights ranging up to 1.2 m (Fig. 6, profile B). The ridges are wooded and peat is developed in places. Basal freshwater peat from the flank of a ridge is dated at 1350±70 radiocarbon years B.P. (Table 1). Swales are occupied by salt marsh, with freshwater marsh in the upper reaches. The ridges and swales decline in height towards the lagoon side of the barrier, where they are buried by up to 1 m of salt-marsh peat. Basal dates on salt-marsh peat at two sites (Shaw and Forbes, 1987) are 760±70 and 640±60 radiocarbon years B.P. (Table 1).

The middle section of the barrier (Fig. 5a) differs strongly from the east and west sections in that its morphology has been largely conditioned by overwashing. This has resulted in the destruction of the formerly continuous narrow barrier and its replacement by intertidal and shallow subtidal sand and gravel flats (mean elevation −0.5 m) penetrated by numerous deeper channels".

The eastern (distal) section of the barrier, the island of Sandy Point, is more than 1 km wide, and consists of discordant sets of gravel beach ridges (Fig. 6, profile C), with a thin aeolian veneer. Crest elevations are typically between 2 and 3 m. Most swales lie at about 1 m but some are as low as mean water level. An area of recently prograded gravel beach ridges (light coloured in Fig. 5a) is covered by dune grassland and is being colonized by spruce. The former coastline at the landward margin of this area is delineated by a wooded sandy ridge, at 3 m above mean water level. On the bay side of the barrier, ponds and freshwater marshes in the swales pass laterally into extensive salt marsh. Radiocarbon dates on basal salt-marsh and freshwater peats at two locations are 470±60 and 300±50 B.P. (Table 1).

Maps and charts dating back to 1763 show the barrier as a continuous feature. Later cartography also depicts the barrier as continuous but with a narrow middle section, breached by several minor channels. During the 1950s, the middle section was extensively breached (Fig. 2). Computer simulations of wave refraction show that with southwest approach directions, short-period waves experience little refraction, and induce longshore transport towards the northeast. By contrast, waves with periods of 7 s and longer are refracted by irregularities on the sill and focus strongly on the middle section of the subaerial barrier. This may be a significant process during storms.

The extensive overwashing and breaching of the middle section of the barrier during the 1950's allowed sediment to leak into the shallow backbarrier basin (Flat Bay). The resulting interruption of littoral drift caused severe erosion of the western end of Sandy Point. Gravel from the eroding section moved alongshore into a beach-ridge foreland. Small gravel recurves of the western section of the barrier have been extending eastward across the washover flats at a rate of approximately 50 m a^{-1}, sufficient to heal the breach in 30 years. A sandy nearshore bar fringing the eroding coastal

Fig. 5 (a) Airphoto mosaic compiled from 1949 photographs (NAPL A12241-92, -93, -95, Energy Mines and Resources Canada), showing the nearshore bar which feeds sand to the distal end of the Flat Island barrier system. The narrow central section of the barrier was washed through in the 1950's, initiating erosion at the western end of the wide distal part of the barrier. The delta of Flat Bay Brook shows clearly (bottom left). Its early-Holocene counterpart is seen in seismic records. The locations of radiocarbon-dated samples *1–5* (Table 1) are shown, as are the locations of cross-sections illustrated by Fig. 6. (b) Part of a 1949 air photograph (A-12156-166) showing the Stephenville beach-ridge plain. The earliest beach ridges are submerged. This photograph predates the navigation channel which cuts through the barrier at the south end. The location of radiocarbon sample *6* is indicated.

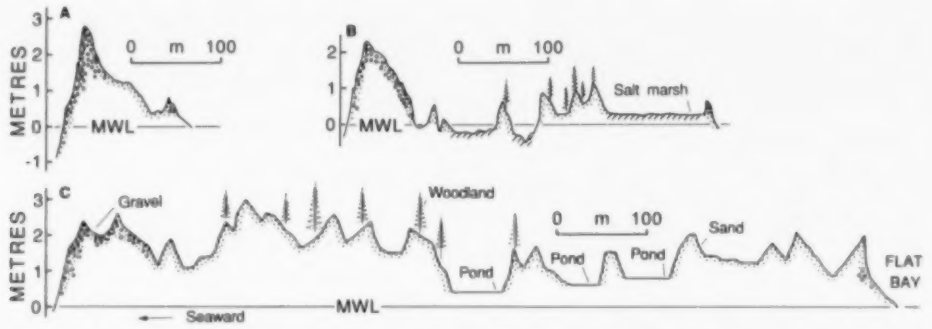

Fig. 6 Three profiles across Flat Island barrier, located on cross-sections A, B and C (Fig. 2). Profile A is on the narrow, overwashed, proximal part of the western barrier section. Profile B is located farther downdrift. Away from the overwashed storm beach, spruce woodland covers aeolian-sand decoration on the beach ridges. Gravel beach ridges at lower elevation are masked by salt-marsh peat up to 1 m deep. Profile C is on the eastern distal section of the barrier. In this area, gravel beach ridges have a thin aeolian cover. Freshwater ponds give way landward to salt marsh at the back of the barrier.

TABLE 1

Radiocarbon dates from the base of freshwater and salt-marsh peats on the Flat Island and Stephenville barriers, St. George's Bay, Newfoundland. Locations shown on Fig. 5

Site	Location	Lab. no.	^{14}C age (a B.P.)	Adjusted age (a B.P.)	$\delta^{13}C$ (‰)	Material
1	Flat Island	Beta-19583	1360 + 70	1350 + 70	−26.13	Freshwater peat
2	Flat Island	Beta-19584	740 + 60	640 + 60	−31.39	Salt-marsh peat
3	Flat Island	Beta-19585	890 + 70	760 + 70	−32.77	Salt-marsh peat
4	Flat Island	Beta-19586	400 + 50	300 + 50	−31.71	Freshwater peat
5	Flat Island	Beta-19571	350 + 60	470 + 60	−17.48	Salt-marsh peat
6	Stephenville	GSC-4730	550 + 70	–	–	Freshwater peat

bluffs to the southwest extends along the front of the Flat Island barrier (Fig. 5a). Repetitive surveys suggest that this bar is a permanent or semi-permanent feature. Sand moves on this nearshore bar system to the distal end of the spit.

The barrier platform

The beach ridges of Flat Island spit rest on a subaqueous platform (Fig. 7) with a gently shelving upper surface (typically less than 1°) and a steep seaward face (typically 9°). The break in slope between the two facets is at a depth of 25 m at the proximal end of the barrier in the southwest, where the upper surface of the platform merges with the sill, but ascends to a depth of just 5 m at the distal end of the barrier near Sandy Point. The barrier-platform sediments extend seaward onto a series of northeast to southwest-trending bedrock ridges on the south flank of the submarine St. George Valley (Fig. 3). The ridges are overlain by a variable thickness of glacial diamict and a conformable drape of glaciomarine sediment, typically 10–20 m thick (Shaw and Forbes, 1990c).

Seismic profiles (Figs. 8–11) illustrate the morphology and internal structure of the barrier platform and its relationship to the underlying sediments and topography. The acoustic structure of the platform is characterized by numerous coherent reflections, intersecting the upper bounding surface and dipping steeply seaward. Dips decrease seaward from a maximum of 9° and the reflections become more closely spaced, forming a tangential oblique clinoform pattern (Mitchum et al., 1977). This suggests progradation with little aggradation, subsequent truncation, or both.

In Fig. 8 the barrier platform appears as a 50-m thick prism of sediment. It infills a shallow valley and extends seaward onto the bedrock ridge that forms the south flank of the submarine St. George Valley. The ridge is capped by glacial diamict overlain by draped glaciomarine sediments. The clinoform reflections of the platform deposits, dipping seaward at 6°, onlap the ridge.

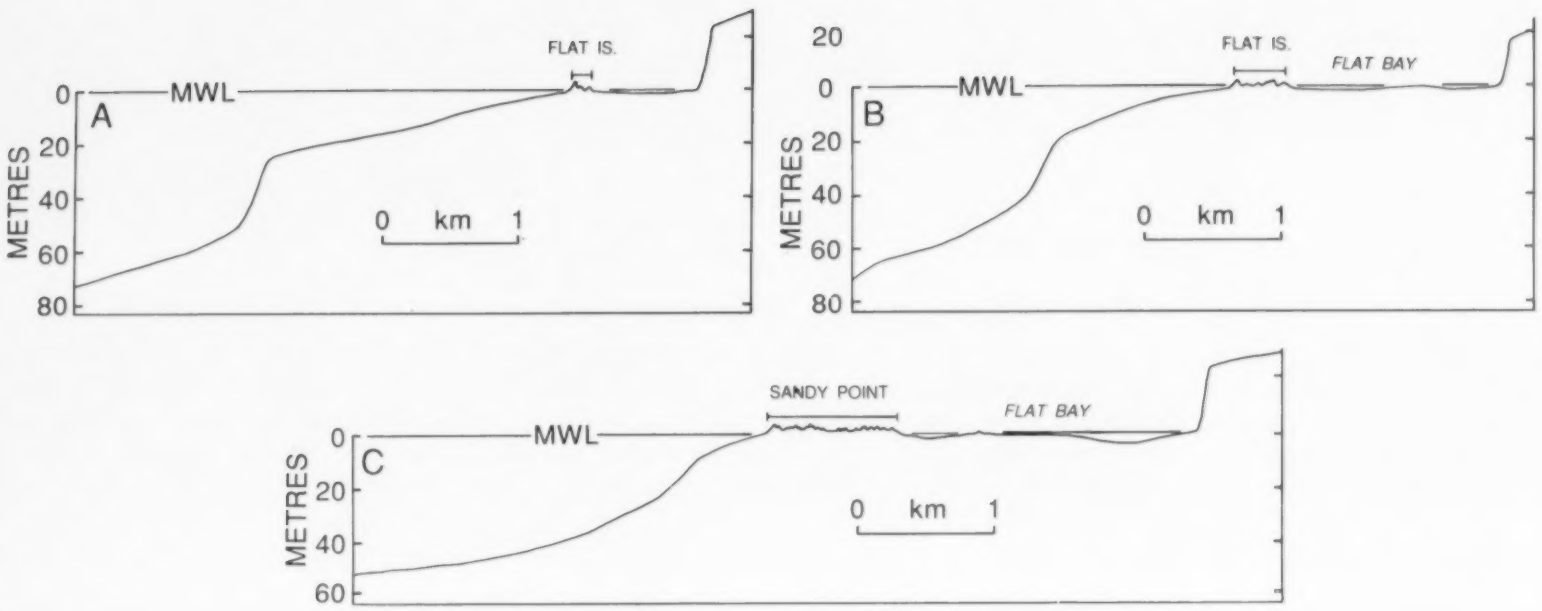

Fig. 7 Three cross-sections through Flat Island, illustrating the extent of the subaqueous barrier platform relative to the subaerial barrier. Locations are shown on Fig. 2. Profile A is close to the proximal attachment point of the subaerial barrier, profile B is across the west-central part, and profile C lies across the wide distal section.

Sidescan sonar data and samples 9–13 (Fig. 12) indicate that seabed sediments fine seaward, with well-sorted medium sand and scattered gravel patches at the landward end of the profile, fine sand at the lip of the platform (at a water depth of 25 m) and muddy sand at the base. On the ridge the postglacial mud cover is thin or absent. The dark tone on sidescan sonar records indicates the presence of patches of fine gravel on the sea bed, a lag resulting from winnowing of the exposed glaciomarine sediment by waves and currents. The postglacial mud thickens in the deep basin at the end of the section and contains gas.

In Fig. 9, the 40-m thick clinoform wedge extends seaward onto a bedrock ridge draped with glaciomarine sediment. We interpret the disrupted and chaotic internal reflection pattern near the base of the platform in this area as evidence of subaqueous slope failure. This pattern is seen on about half of the barrier-platform profiles. A prominent subsurface reflection with a break at about -25 m defines the seaward extent of the early Holocene delta of Flat Bay Brook. It extends seaward and overlies weakly-stratified, draped to ponded sediment which contains gas and is interpreted as prodelta mud.

In Fig. 10, the platform sediments partly infill a 155-m deep bedrock valley, a tributary to the St. George Valley. The platform in this area is indented in the form of an amphitheatre. The upper part of the seaward slope is relatively steep (14°), while the lower part is more gently sloping (3°), with a wrinkled appearance. This results from seabed irregularities of 1-m amplitude, which we interpret as compressional ridges generated by slumping. The underlying sediment shows a disrupted pattern of internal reflectors. The deep valley appears to have hindered alongshore extension of the barrier platform in this area. Much of the platform unit here may have been emplaced by subaqueous slope failure. Seabed sediment samples along this profile (Fig. 12) grade from well-sorted medium sand (sample 22) to muddy sand (sample 19).

Fig. 11 shows part of a seismic line located offshore from Bank Head, southwest of the present attachment point of the barrier. It depicts a narrow trough bounded to the south by barrier-platform sediments which have prograded seaward, and to the north by more steeply-dipping prograded deposits associated with spillover of sediments from the sill. A short distance to the southwest of this profile the trough is completely infilled, producing a level surface at about -27 m. The acoustic signature of the infill is a series of opposing dips in barrier-platform and spillover sediments. On an adjacent profile not shown here, shoreward-dipping reflectors are interpreted as barrier-platform

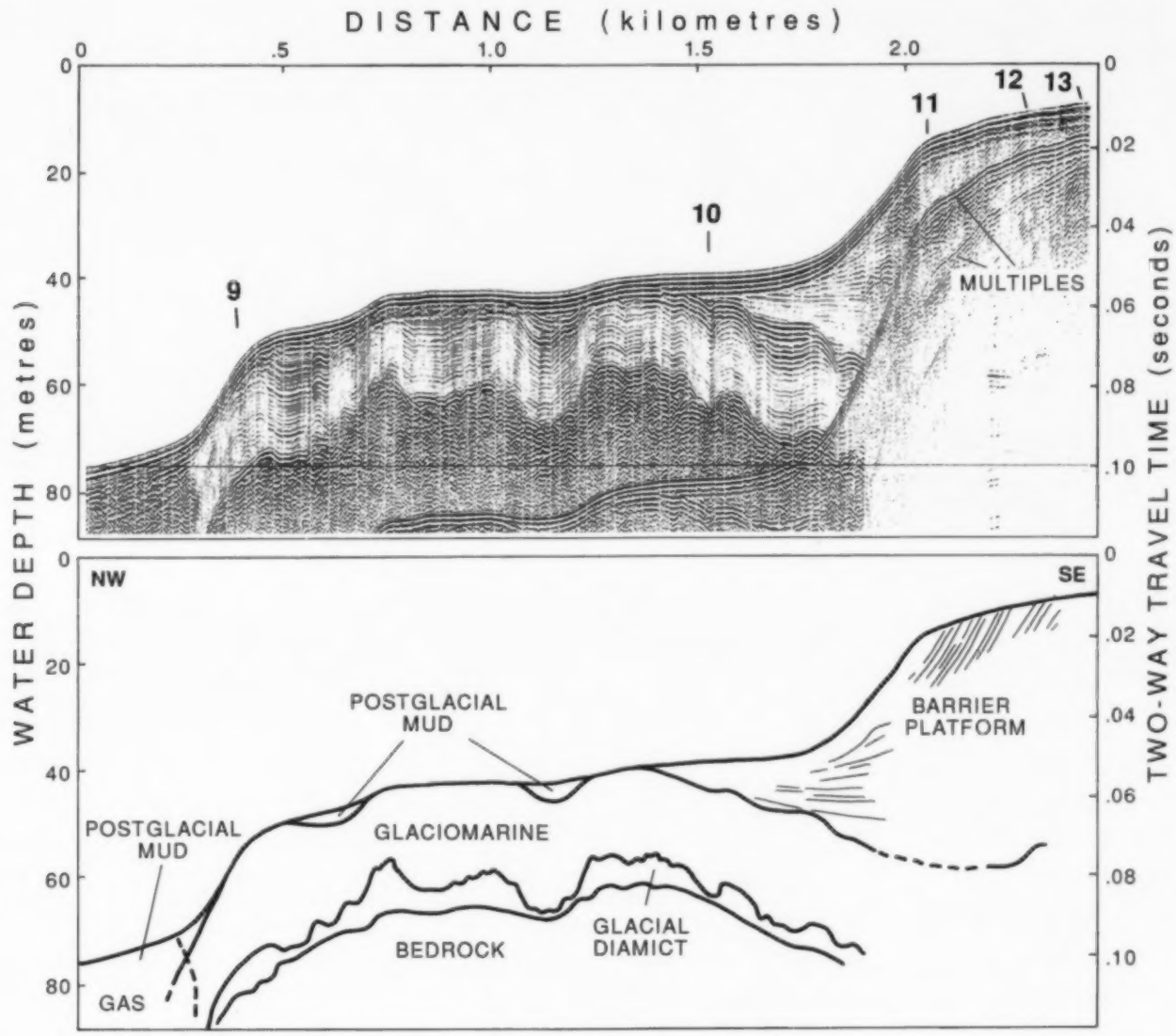

Fig. 8 Seismic reflection profile showing the Flat Island barrier platform as a seaward-thinning, tangential, clinoform prism. Platform sediments onlap glaciomarine deposits draped over glacial diamict on a bedrock ridge. Gas is present in the postglacial mud forming the uppermost sediment in the adjacent basin. Locations of seabed samples *9–13* are shown.

foresets, associated with a spit which was previously attached to Bank Head, and a −25 m terrace appears to be incised into glaciomarine sediments.

Stephenville

The subaerial barrier

The Stephenville barrier is a 1-km wide complex of parallel gravel beach ridges (Fig. 5b) enclosing a lagoon which is now connected to the ocean by an artificial channel. Air photographs show beach ridges submerged in the lagoon (Grant, 1975). The mean crest elevation of the beach ridges increases from below mean water level in the lagoon to about 3 m at the present coast. Unlike deposits behind the Flat Island barrier, the gravel beach ridges fringing the lagoon are not covered by salt-marsh sediment, possibly because there was no marine water in the lagoon until relatively recently.

Unfortunately, gravel extraction and other human activities have disturbed or removed datable organic deposits on the beach-ridge plain. Close to the dredged channel, 0.4 km landward of the modern beach (Fig 5b), thin freshwater peat overlying weathered gravel and overlain by dredge spoil has been dated at 550 ± 70 radiocarbon years B.P. (Table 1).

The barrier platform

On acoustic records, the subaqueous platform of the Stephenville barrier (Fig. 13) appears as a

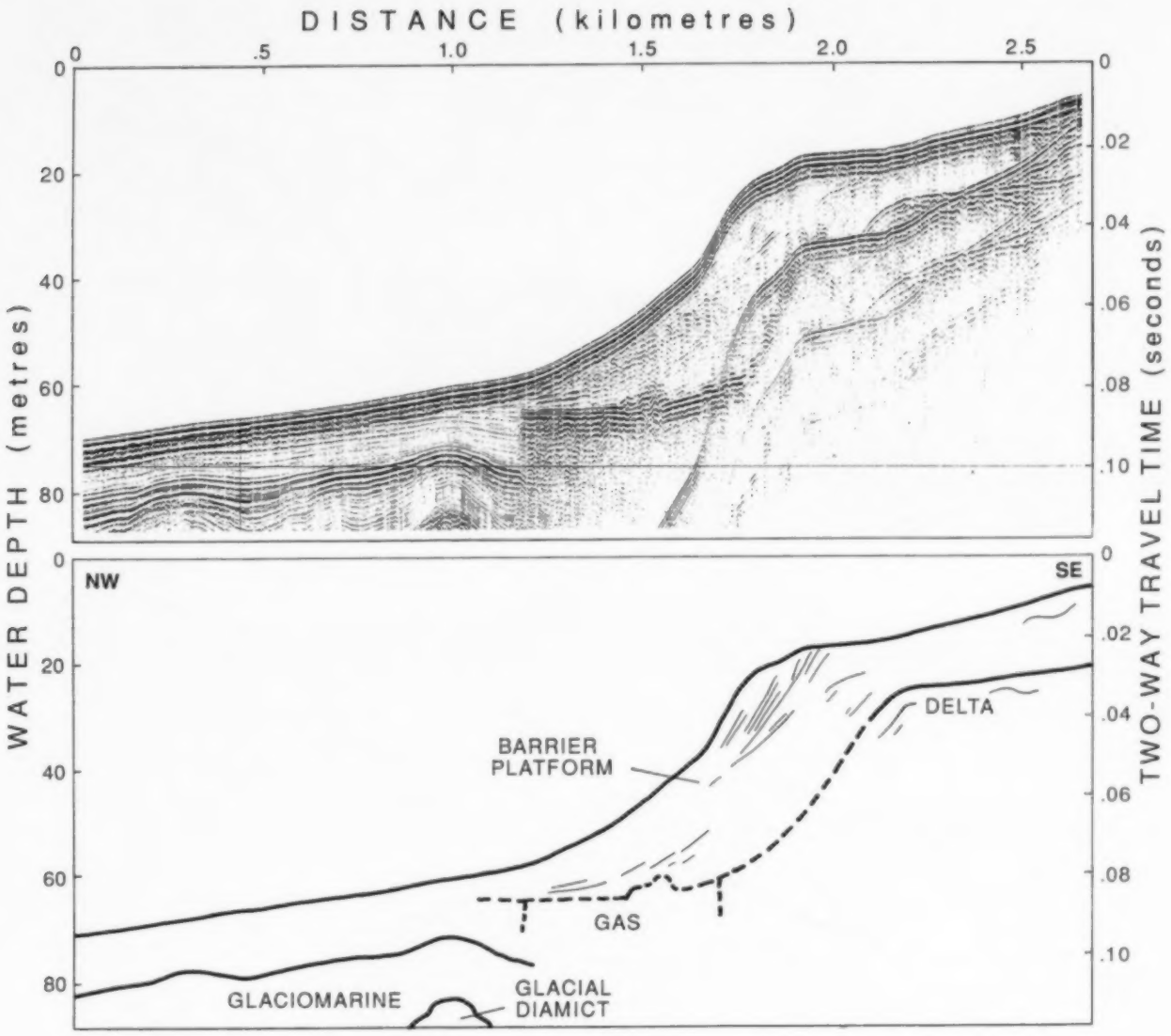

Fig. 9 Seismic reflection profile showing the early-Holocene delta of Flat Bay Brook, with topsets graded to about -25 m, buried within barrier -platform sediments.

prism containing numerous moderate to high-intensity, steeply-dipping (maximum 6°), continuous coherent reflections, forming a pattern intermediate between tangential oblique and sigmoidal (Mitchum et al., 1977). This style indicates both aggradation and progradation. The platform sediments overlie glaciomarine mud, draped over sediment interpreted as subaqueous outwash, which partly fills a valley up to 180 m deep just offshore from the barrier. The toe of the barrier-platform prism runs into a deep basin filled with postglacial mud. A prominent unconformity is developed at the top of the underlying glaciomarine sediments, at depths of 35 to 40 m. The combined thickness of the barrier and platform is almost 40 m. A seismic transect obliquely through the barrier, along the dredged channel, reveals steeply-dipping (10°) reflections extending down to about 20 m below the beach ridges, representing the upper platform at the base of subaerial barrier. Seabed sediments were not sampled in this area but sides-can sonar records indicate that sand predominates on the upper platform surface. By analogy with Flat Island, we hypothesize that the sand grades to muddy sand or sandy mud with depth.

The Stephenville barrier platform extends around the base of Indian Head (Figs. 2 and 3) and links with the barrier at Stephenville Crossing, at the head of St. George's Bay. The small spit flanking the southeast side of the Indian Head massif rests on this section, which is relatively narrow. Seismic profiles in this area show steeply-dipping internal reflections which downlap into the basin.

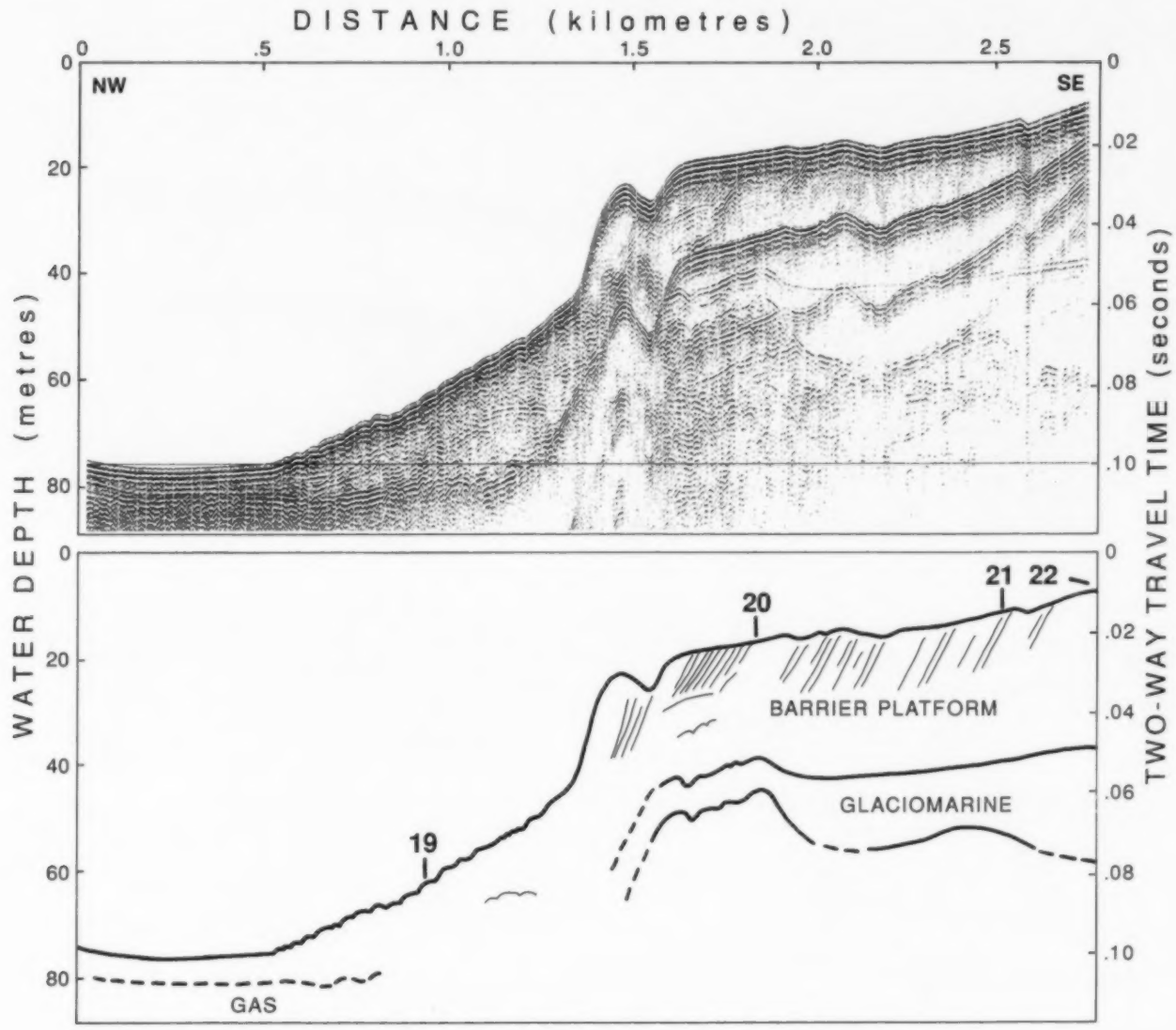

Fig. 10 Seismic reflection profile showing evidence of subaqueous slope failure. The cause was the presence of a steep-sided deep (155 m) transverse valley which hindered alongshore extension of the barrier platform. The surface of the platform has a deep indentation here. The locations of seabed samples *19–22* are shown.

St. George's Bay sill

The spillover unit

The spillover deposits occur in a wide swath extending across St. George's Bay (Fig. 3). In cross-section they form a wedge-shaped body which thickens eastward, terminating in the steep escarpment with a slope of 10° to 20° and a relief of 20 to 50 m which forms the landward boundary of the sill. It contains numerous moderate-high intensity steeply-dipping continuous coherent reflections (dips average 14° in Figure 14). The spillover sediments are located landward of a zone of glacial diamict exposed on the sill. They have prograded into the basin over glaciomarine muds. Outcrops of glacial diamict on the sill are characterized by a surficial lag of boulders and cobbles encrusted with coralline algae. This material is judged to be largely immobile. By contrast, seabed sediment on the spillover unit is predominantly fine gravel, typically poorly-sorted material ranging from very coarse to very fine pebbles, with a mean size of 10 mm. This sediment is organised into bands of ripples, with wavelengths ranging from 1 to 3 m. The gravel, at depths to 30 m, is frequently mobilized under present conditions (Shaw and Forbes, 1990c) and is covered in places by irregular ribbons of medium sand.

Discussion

Early-postglacial shoreline evolution

With falling relative sea level early in the postglacial period (Fig. 4), rivers entering the bay became

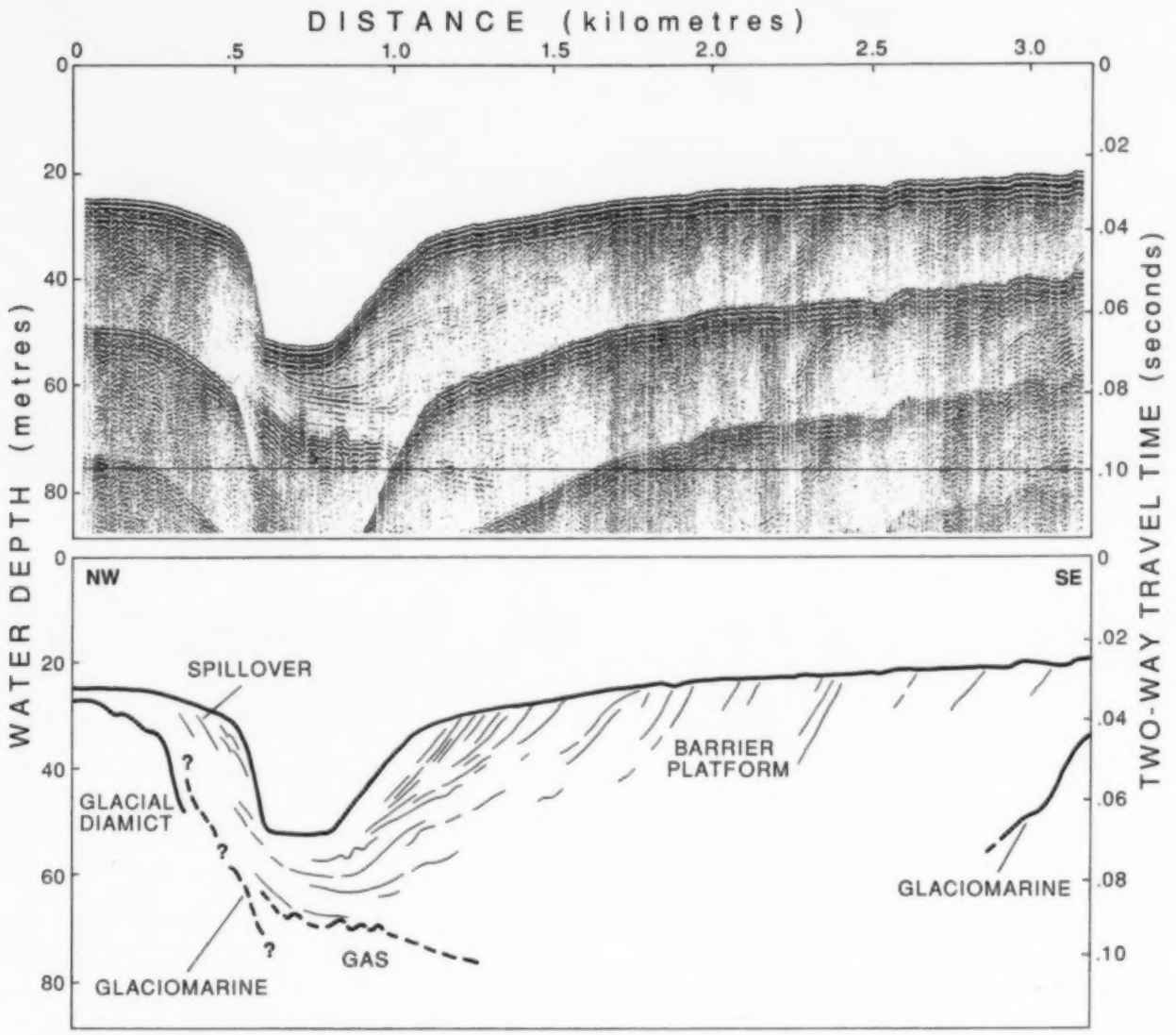

Fig. 11 Seismic reflection profile southwest of the present attachment point of the barrier. The barrier platform extends seaward, almost meeting the spillover sediments of the sill (left). Immediately south of this location, the intervening valley has been infilled by sediment from both sides.

incised into the relatively thick glaciogenic sediments of the area, producing deltas graded to the early postglacial lowstand of approximately −25 m. Wave action formed terraces graded to −25 m and winnowed the uppermost glaciomarine sediment in shallow areas. The remobilized mud accumulated in the basin landward of the sill. A suggested reconstruction of the paleogeography of inner St. George's Bay at 10 ka B.P. is shown in Fig. 15a. Much of the sill would have been subaerially exposed at this time, with a peninsula extending south from the Port au Port isthmus to within a few kilometres of the present Bank Head. The largest of the three deltas in the inner bay was that of the St. George's River, and a second was formed by Flat Bay Brook. The seismic evidence for a third delta, offshore from Romaines Brook, is less conclusive, although the river valley is incised at the present coast.

The Holocene transgression and the formation of spillover deposits

Since the early postglacial low stand, the coast of St. George's Bay has experienced progressive submergence, with relative sea level rising at a maximum rate of about 5 m ka^{-1} during the middle Holocene. Early in the transgression, the peninsula extending across the sill was probably severed into several islands (Fig. 15b), some of which may have been linked for short periods of time by small barriers. Eventually, all remaining islands and linking barriers were eroded and submerged, and the sediment within them dispersed.

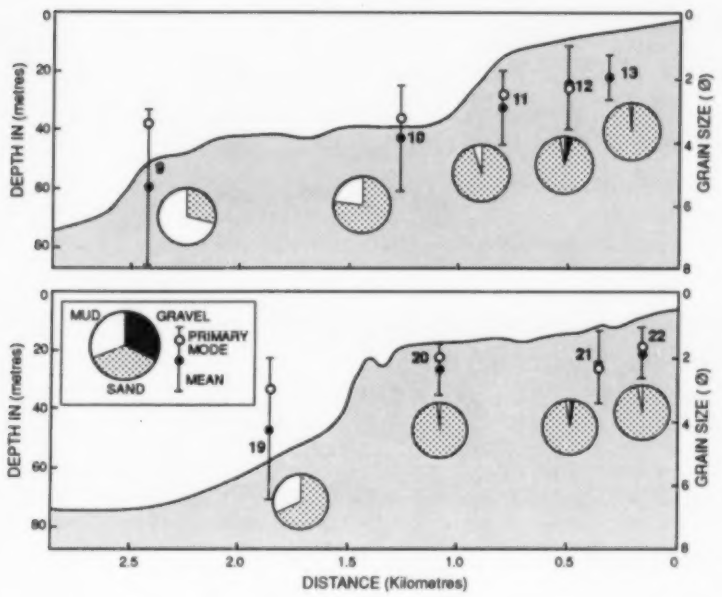

Fig. 12 Grainsize data from two profiles across the Flat Island barrier platform and into the basin of St. George's Bay. The seismic stratigraphy is illustrated by Fig. 8 (upper profile), and Fig. 10 (lower). Profile locations are indicated on Fig. 2. Well-sorted, medium-fine sand typifies the seabed on top of the platform (samples *11*, *12*, *13*, *20*, *21*, *22*). In deeper water, the seabed sediments are poorly sorted mixtures of mud (primarily silt) and fine sand (samples *9*, *10* and *19*). The difference between the mean and the primary mode increases seaward. The vertical bars represent one standard deviation either side of the mean.

Mud winnowed from seabed outcrops of glacial diamict was transported by suspension into the basin east of the sill.

Coarser material was entrained by wave action on the shallow sill, moved eastward by the dominant southwest waves, and deposited as a spillover unit along the landward flank of the sill (Fig. 15c). Thus, unlike the barrier platforms, the spillover deposits were eventually decoupled from any subaerial sediment source. Because relative sea level was rising during the mid and late Holocene, the sill has been subjected to progressively diminishing wave energy. However, the widespread occurrence of active gravel ripples indicates that sediment on the sill is still mobile.

Dispersal of sediment into barriers and barrier platforms

While the spillover deposits are a major repository for coarse-grained sediment of glaciogenic origin in St George's Bay, the bulk of such material is contained within the barriers and their associated subaqueous platforms. In contrast to the spillover, these are still linked to their sediment sources—the thick, heterogeneous glaciogenic deposits exposed in coastal bluffs along the north and south coasts of the bay. The finest material, susceptible to wave resuspension on the shallow platforms, has accumulated in the basins as gas-charged mud. Coarser material has been entrained into a littoral drift system maintained by waves approaching from the southwest and has accumulated on the barriers (predominantly gravel) and the subaqueous platforms (predominantly sand). The sandy subaqueous platforms contain more than 90% by volume of the sediment in the barrier/platform systems. The formation of the platforms was both necessitated and facilitated by the existence of deep basins adjacent to the coastline. These deposits in St. George's Bay provide a striking example of bathymetric control on the evolution and architecture of coastal deposits.

The parallel aspect of the gravel beach ridges at Stephenville may reflect onshore–offshore movement in response to seasonal variations in wave energy. Because coarse sediment could not have been moved up from the basin by any known mechanism, the source of the sediment in the Stephenville platform was not offshore. The evidence is clear that the sediment was supplied alongshore from the extensive eroding bluffs along the north shore of St. George's Bay (Fig. 3). When the platform had prograded sufficiently seaward, it allowed sediment to bypass Indian Head. The sandy barrier platform eventually extended around the headland to the head of the bay, facilitating sediment transport along a small flanking spit and onto the barrier system at Stephenville Crossing (Fig. 2). The recognition of headland bypassing at this site underlines the necessity of documenting sediment transport paths on the shoreface. These can be of critical importance to an understanding of the coastal system (Forbes, 1987).

The longshore movement of sediment in the barrier system is segregated according to grain size. The nearshore bar complex fronting the Flat Island barrier functions as an important littoral conduit, moving sand from sources many kilometres to the southwest, along the front of the barrier, to the distal end of the spit. Rip currents seen on

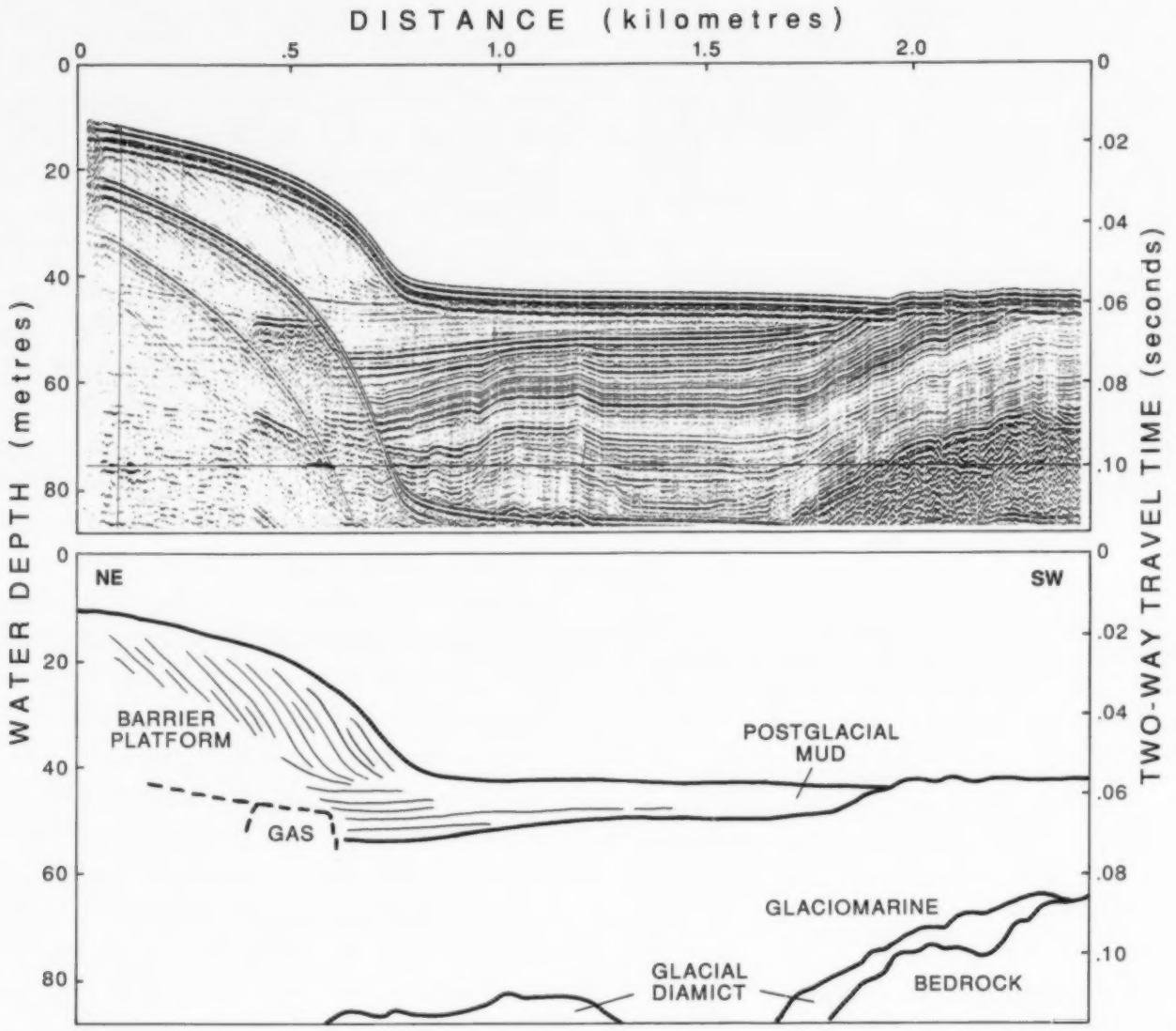

Fig. 13 Seismic reflection profile showing the clinoform prism of the Stephenville barrier platform which extends seaward into a basin in which postglacial mud overlies a thick sequence of glaciomarine sediment.

air photographs off the middle section of the Flat Island barrier undoubtedly provide a mechanism for seaward sand transport onto the platform. The frequency and magnitude of sand transport on the platform itself is largely unknown at present, but it is believed that the platform lip is still prograding seaward along its full length. The decrease in the depth of the lip towards the distal end of the spit is largely a function of platform width, so that the deepest platform edge occurs in the southwest, where the platform is widest.

In both the Flat Island and Stephenville systems, gravel moves independently of sand. Gravel transport occurs largely in the swash zone, so that swash-constructed gravel beach ridges are the chief component of the subaerial barriers. Minor landward leakage of sand across the gravel beach zone has formed a thin aeolian veneer which covers parts of the beach ridges.

The oldest radiocarbon date from the barriers is 1.35 ka B.P. on Flat Island (Shaw and Forbes, 1987). The maximum age is constrained by the elevation of the oldest ridges, which are below mean water level in the backbarrier area. Since contemporary storm beach crests on both barriers are between 2 and 3 m high (Fig. 6), the oldest ridges are unlikely to be older than about 3 ka, when relative sea level was approximately 3 m lower than today (Fig. 4). It would appear then, that the greater part of the present barrier and its associated subaqueous platform postdates about 3 ka B.P.

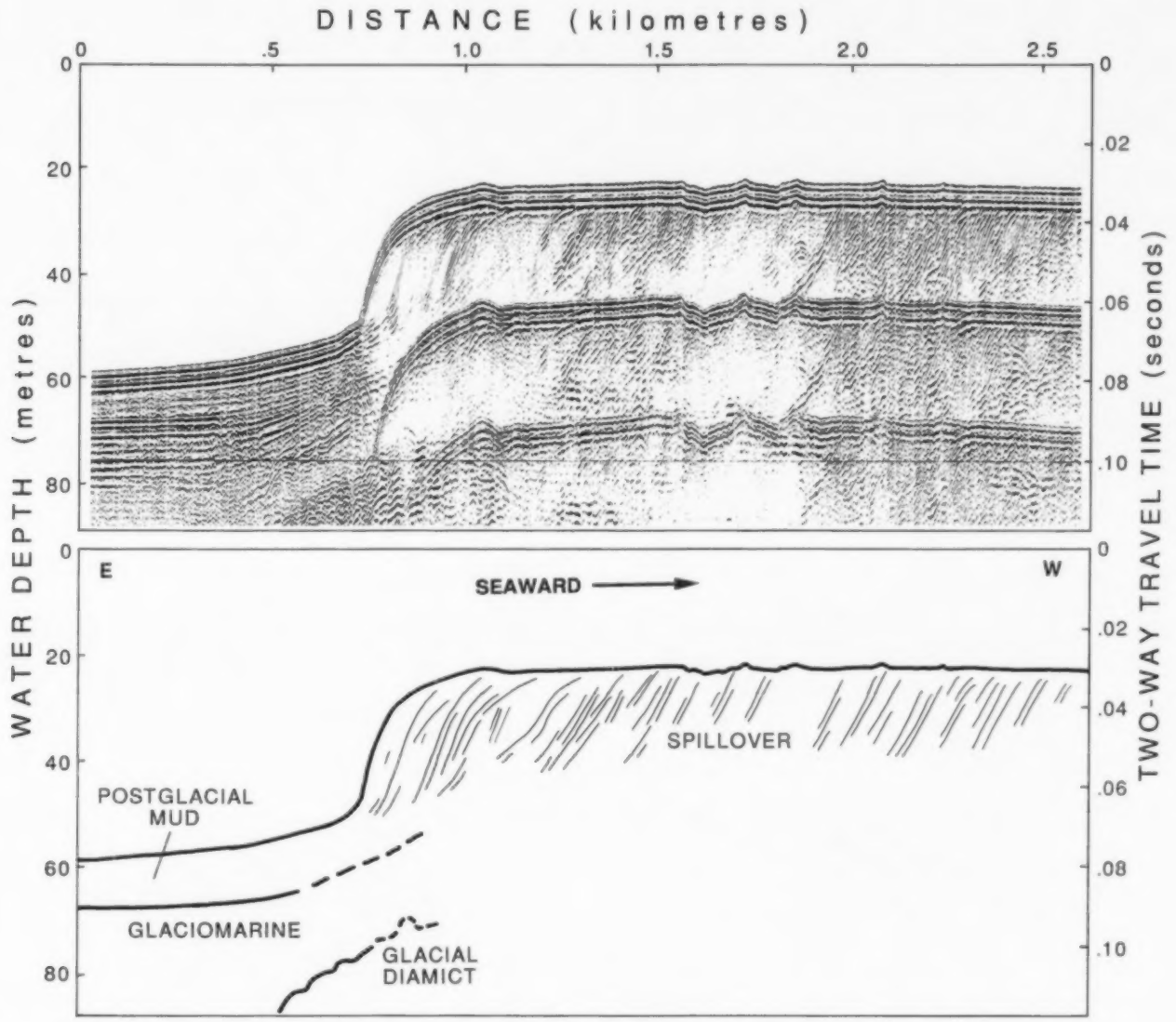

Fig. 14 Profile showing coarse spillover sediments deposited on the landward side of the sill, prograding eastward into the inner bay. The seabed sediment on the spillover structure is a mixture of sand and rippled fine gravel (see fig. 15 of Shaw and Forbes, 1990c).

Physiographic setting and depositional style

The contrasting physiographic settings at Flat Island and Stephenville have resulted in the development of different barrier and platform architecture at the two sites. The swash-aligned Stephenville barrier system lies across a deep valley that is oriented normal to the coastline and partly filled with glaciogenic sediment. The barrier platform prograded seaward into a deep muddy basin. In contrast to the setting at Stephenville, the Flat Island barrier platform is located along the basin flank, and the barrier is drift-aligned.

At Flat Island, irregularities in the pre-Holocene basin margin morphology may explain the tripartite subdivision of the barrier. In an early stage of development, sandy sediments of the extending and prograding barrier platform enveloped a series of shore-parallel bedrock ridges on the south side of a very deep (195 m) submarine depression, the St. George Valley. However, alongshore progradation was hindered when the platform encountered a 155-m deep submarine valley, tributary to the St. George Valley and oriented normal to the coast offshore from Flat Bay Brook (Fig. 3). It seems likely that the slow infilling of this deep valley allowed a more sustained period of beach-ridge progradation, initiating development of the wide western section of the barrier complex. Subsequently, the barrier platform extended alongshore more rapidly, on top of the early postglacial delta sediments. This resulted in the formation of the narrow, middle section of the barrier. The wide prograded eastern section was then formed by slow

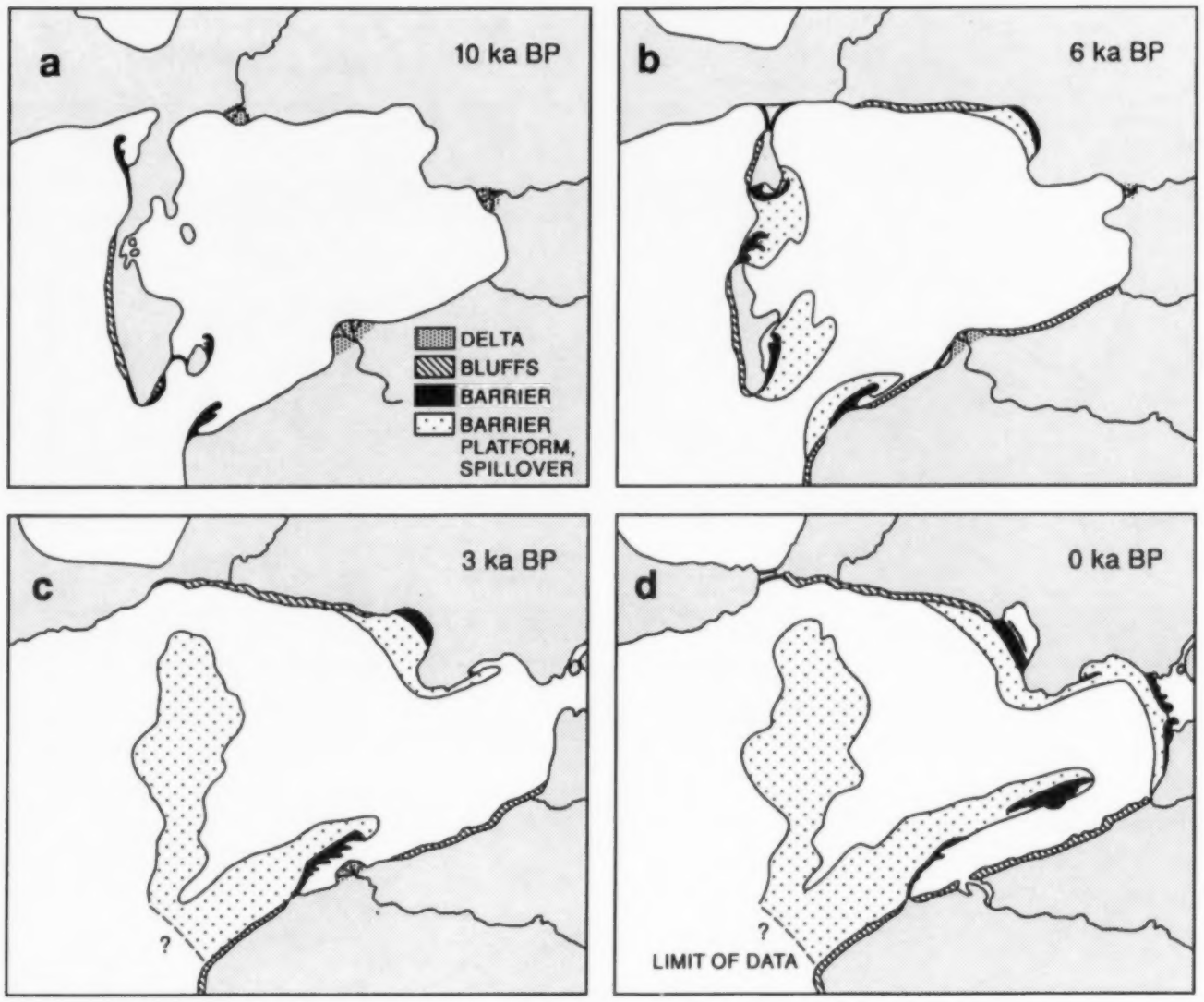

Fig. 15 Paleogeographic reconstructions of inner St. George's Bay. At 10 ka B.P., when relative sea level was at approximately −25 m, a peninsula extended across much of the bay. By 6 ka B.P. it had been severed into several parts. At 3 ka B.P. relative sea level was about 3 m below today's level and part of the Flat Island barrier was emplaced in its present position. The spillover deposits were by now disconnected from a subaerial source and the barrier platform at Stephenville is thought to have prograded sufficiently to allow bypassing around Indian Head. The 0 ka B.P. situation depicts the known extent of barrier and barrier platform deposits today.

barrier-platform infilling of a basement depression south of the ridge system which flanks the St. George Valley. These observations, like those of Nielsen et al. (1988), appear to confirm Meistrell's conclusions (1966, 1972) that growth of spit and platform structures are inversely related.

Just as basin margin morphology has determined the overall form of the Flat Island barrier, the sill extending across St. George's Bay has played a role in the evolution of the coastline. It has acted as a control on wave refraction patterns within the bay, in particular by focussing longer period wave energy on the middle section of the Flat Island spit, possibly promoting the large-scale breaching that occurred in the 1950s. This influence of the sill upon refraction patterns within the bay has presumably varied during the Holocene transgression.

Sills defining the seaward margins of glacially-overdeepened basins are often composed of, or draped by, ice-contact deposits of one kind or another. Although extensive spillover deposits such as those observed in St. George's Bay have not been widely reported, more limited features of this kind are found in other cases where fjord sills occur at or close to sea level. At Holyrood Pond in St. Mary's Bay, southeast Newfoundland (Forbes, 1984; Shaw et al., 1990), ice-contact sediments draping the fjord sill are overlain by beach and washover sands and gravels dipping in oppos-

ing directions on the seaward and landward faces of the sill. Other cases of now-submerged sills carrying relict littoral deposits have been reported by Forbes (1984) from elsewhere in St. Mary's Bay, and by Barnes and Piper (1978) from Mahone Bay, Nova Scotia.

Glaciated inner-shelf settings are typically not conducive to the formation of extensive sand sheets, except in areas of major outwash deposition, but are more likely to host patchy sand and gravel bodies with extensive bedrock outcrop (cf. King, 1970; Fader et al., 1982; Piper et al., 1986). On the other hand, fjords and other glacially-overdeepened inner-shelf basins can accumulate thick deposits, which may include large proportions of sand and conglomerate. These coarse deposits are most commonly found in deltaic and submarine-fan facies. They have been suggested as analogues for small hydrocarbon reservoirs in active graben settings (Syvitski and Farrow, 1989). Our observations in St. George's Bay demonstrate that substantial bodies of sand and gravel can also be emplaced by littoral and shoreface processes in a glacial-basin setting.

Furthermore, the combination of a basin setting, rising relative sea level, and a heterogeneous sediment supply has produced a distinctive barrier architecture which differs considerably from that observed in other settings with a predominance of sand, stationary relative sea level, or relatively shallow inner shelf shoreface bathymetry. Examples of contrasting Holocene barrier systems are numerous, but include, for example, the sand-dominated stationary barriers of eastern Australia (e.g. Thom, 1983). On the high-energy, glaciated coast of western Ireland (Shaw, 1985), stable relative sea level during the past four thousand years, high wave energy, and a westerly wind regime have allowed the transfer of considerable quantities of sand onshore. The result is that some Irish barriers are the inverse of the present examples, with large volumes of sand contained in high (>30 m) coastal dunes which cover gravel beach-ridge complexes located close to present sea level (Taylor et al., 1986; Carter et al., 1989).

The vertical scale (up to 50 m) of the clinoform units formed by barrier-platform and spillover deposition in St. George's Bay exceeds that of the "giant-scale cross-bedded foreset units" in Holocene spit platforms of northern Denmark (Nielsen et al., 1988). It is also much larger than the "giant foresets" (up to 17 m thick) reported from a tectonically-controlled inner-shelf setting in the Bohemian Cretaceous Basin (Jerzykiewicz and Wojewoda, 1986). The coastal platform sands in St. George's Bay can be related to the type-1 coarsening-upward, shoreline-attached, clastic wedges of Cant and Hein (1986), but accumulated under conditions of rising sea level and are much less extensive than many type-1 examples observed in the rock record (e.g. Cant, 1984).

In St. George's Bay, the juxtaposition of longshore transport systems and a morainal sill feeding sediment into the coastal basin has produced clinoform deposits of widely varying orientation and structure. Architectural heterogeneity of the kind observed in St. George's Bay, comparable to that encountered in some active tectonic settings (e.g. Kazanci, 1990), requires careful consideration in the interpretation and exploitation of clastic reservoirs.

Conclusions

The following conclusions are drawn from this study:

(1) During the past 13.5 ka, as relative sea level fluctuated over a vertical range of approximately 70 m, glaciogenic sediments in St. George's Bay and adjacent coastal areas have been mobilized by coastal processes and incorporated into a distinctive suite of subaerial and subaqueous depositional features.

(2) The glacially-overdeepened basin and its sill in St. George's Bay have formed a setting conducive to the formation of barrier platform and spillover wedges up to 50 m in thickness, with large-scale clinoform structure on shallow seismic records.

(3) Barriers composed of gravel beach ridges have prograded seaward and extended alongshore on top of sandy, subaqueous, barrier platforms. Radiocarbon evidence and sea-level data show that the barriers were emplaced in their present positions approximately 3 ka B.P. or later, and most

of the present barrier deposits were in place by 1.35 ka B.P.

(4) The growth of the Flat Island barrier to form relatively wide proximal and distal beach-ridge sequences, separated by a narrow middle section, may have resulted from varying rates of platform accretion associated with irregularities in the basin margin.

(5) The Stephenville barrier consists of prograded beach ridges, composed of gravel that has moved alongshore into a headland-confined coastal compartment. The seaward progradation of the barrier platform extended the littoral-drift system around the rock headland to the head of St. George's Bay.

(6) The morainal sill extending across St. George's Bay was subaerially exposed during the early-Holocene low stand of relative sea level. Subsequent submergence and landward transport of sediment across the sill resulted in the formation of extensive sand and gravel spillover deposits.

Acknowledgements

We thank Captain Neil Langille and the crew of M.V. *Navicula*, Darrell Beaver and Donald Locke for technical assistance, and David Frobel for his contribution to fieldwork in the St. George's Bay area. Sediment analyses were performed by Donald Clattenburg. We also thank D.J.W. Piper and G.E. Reinson for reviews of an early draft of the paper. Geological Survey of Canada contribution number 57090.

References

Barnes, N.E. and Piper, D.J.W., 1978. Late Quaternary geological history of Mahone Bay, Nova Scotia. Can. J. Earth Sci., 15: 586–593.

Bernard, H.A., Leblanc, R.J. and Major, C.F., 1962. Recent and Pleistocene geology of southeast Texas. In: E.H. Rainwater and R.P. Zingula (Editors), Geology of the Gulf Coast and Central Texas and Guidebook of Excursions. Houston Geol. Soc.—Geol. Soc. Am. Annu. Meet. (1962), Houston, Texas, pp. 175–205.

Boyd, R., Bowen, A.J. and Hall, R.K., 1987. An evolutionary model for transgressive sedimentation on the Eastern Shore of Nova Scotia. In: D.M. FitzGerald and P.S. Rosen (Editors), Glaciated Coasts. Academic Press, San Diego, pp. 87–114.

Brookes, I. A., 1969. Late-glacial marine overlap in western Newfoundland. Can. J. Earth Sci., 6: 1397–1404.

Brookes, I. A., 1970. New evidence for an independant Wisconsin-age ice cap over Newfoundland. Can. J. Earth Sci., 7: 1374–1382.

Brookes, I. A., 1974. Late-Wisconsin glaciation of southwestern Newfoundland (with special reference to the Stephenville map-area). Geol. Surv. Can. Pap., 73–40, 31 pp. plus maps.

Brookes, I.A., 1977. Radiocarbon age of Robinson's Head moraine, west Newfoundland, and its significance for post-glacial sea level changes. Can. J. Earth Sci., 14: 2121–2126.

Brookes, I. A., 1987. Late Quaternary glaciation and sea-level change southwest Newfoundland, Canada. Centennial field guide-Northeastern Section. Geol. Soc. Am., pp. 445–450.

Brookes I. A., Scott, D. B. and McAndrews, J. H., 1985. Postglacial relative sea-level change, Port au Port area, west Newfoundland. Can. J. Earth Sci., 22: 1039–1047.

Cant, D. J., 1984. Development of shoreline-shelf sand bodies in a Cretaceous epeiric sea deposit. J. Sediment. Petrol., 54: 541–557.

Cant, D.J. and Hein, F., 1986. Depositional sequences in ancient shelf sediments: some contrasts in style. In: R.J. Knight and J.R. McLean (Editors), Shelf Sands and Sandstones. Can. Soc. Pet. Geol. Calgary Mem. 11: 303–312.

Carrera, G., Vaníček, P. and Craymer, M.R., 1990. The compilation of a map of recent vertical crustal movements in Canada. DSS Res. Contract 50SS.232344-7-4257.

Carter, R.W.G., Forbes, D.L., Jennings, S.C., Orford, J.D., Shaw, J. and Taylor, R.B., 1989. Barrier and lagoon coast evolution under differing relative sea-level regimes: examples from Ireland and Nova Scotia. In: L.G. Ward and G.M. Ashley (Editors), Physical Processes and Sedimentology of Siliciclastic-Dominated Lagoon Systems. Mar. Geol., 88: 221–242.

Carter, R.W.G., Orford, J.D., Forbes, D.L. and Taylor, R.B., 1990. Morphosedimentary development of drumlin-flank barriers with rising sea level, Story Head, Nova Scotia. Sediment. Geol., 69: 117–138

Clifton, H.E., 1981. Progradational sequences in Miocene shoreline deposits, southeastern Caliente Range, California. J. Sediment. Petrol., 51: 165–184.

Elliot, T., 1986. Siliciclastic shorelines. In: H.G. Reading (Editor), Sedimentary Environments and Facies. Blackwell, Oxford, pp. 155–188.

Enos, P., 1977. Tamabra Limestone of the Poza Rica Trend, Cretaceous, Mexico. In: H. E. Cook and P. Enos (Editors), Deep-Water Carbonate Environments. Soc. Econ. Paleontol. and Mineral., Tulsa, Spec. Publ. 25: 273–314.

Fader, G.B., King, L.H. and Josenhans, H.W., 1982. Surficial geology of the Laurentian Channel and the western Grand Banks of Newfoundland. Geol. Surv. Can., Pap. 81–22; Mar. Sci. Pap., 21, 37 pp.

Farmer, G.H., 1981. The cold ocean environment of Newfoundland. In: A.G. Macpherson and J.B. Macpherson (Editors), The Natural Environment of Newfoundland, Past and Present. Mem. Univ. Newfoundland, St. John's, pp. 56–82.

Flint, R.F., 1940. Late Quaternary changes of level in western and southern Newfoundland. Geol. Soc. Am., Bull., 51: 1757–1780.

Forbes, D.L., 1984. Coastal geomorphology and sediments of

Newfoundland. In: Current Res. Part B, Geol. Surv. Can. Pap., 84-1B: 11–24.

Forbes, D.L., 1987. Shoreface sediment distribution and sand supply at C^2S^2 sites in the southern Gulf of St. Lawrence. In: Proceedings, Coastal Sediments 87 (New Orleans). Am. Soc. Civ. Eng., New York, pp. 694–709.

Forbes, D.L. and Frobel, D., 1986. Coastal airvideo and ground survey, west Newfoundland and southern Labrador. Operations Report, Atlantic Geosc. Centre, Geol. Surv. Can., Bedford Inst. Oceanogr., Dartmouth, 13 pp. (Unpubl.)

Forbes, D. L., and Shaw, J., 1989. Cruise report 88018 (E): *Navicula* operations in southwest Newfoundland coastal waters: Port au Port Bay, St. George's Bay, La Poile Bay to Barasway Bay and adjacent inner shelf. Geol. Surv. Can. Open File, 2041, 57 pp.

Forbes, D.L. and Taylor, R.B., 1987. Coarse-grained beach sedimentation under paraglacial conditions, Canadian Atlantic coast. In: D.M. FitzGerald and P.S. Rosen (Editors), Glaciated Coasts. Academic Press, San Diego, pp. 51–86.

Forbes, D.L., Taylor, R.B. and Shaw, J., 1989. Shorelines and rising sea levels in eastern Canada. Episodes, 12: 23–28.

Forbes, D.L., Taylor, R.B., Shaw, J., Carter, R.W.G. and Orford, J.D., 1990. Development and stability of barrier beaches on the Atlantic coast of Nova Scotia. Proc., Can. Coastal Conf. 1990 (Kingston, Ont.). Natl. Res. Council, Ottawa, pp. 83–98.

Grant, D.R., 1975. Recent coastal submergence of the Maritime Provinces. Nova Scotian Inst. Sci. Proc., 27 (3): 83–102.

Grant, D.R., 1987. Quaternary geology of Nova Scotia and Newfoundland, XIIth INQUA Congress field excursion A-3/C-3. Natl. Res. Council, Ottawa, 62 pp.

Hoyt, J.H. and Henry, V.J., Jr., 1965. Significance of inlet sedimentation in the recognition of ancient barrier islands. Wyoming Geol. Assoc., Guidebook 19th Field Conf., pp. 190–194.

Hoyt, J.H. and Henry, V.J. Jr., 1967. Influence of island migration on barrier-island sedimentation. Geol. Soc. Am. Bull., 78: 77–86.

Hubert, J. F., Suchecki, R.K. and Callahan, R.K.M., 1977. The Cow Head Breccia: sedimentology of the Cambro-Ordovician continental margin, Newfoundland. In: H. E. Cook and P. Enos (Editors), Deep-Water Carbonate Environments. Soc. Econ. Paleontol. Mineral., Tulsa, Spec. Publ., 25: 125–154.

Jerzykiewicz, T. and Wojewoda, J., 1986. The Radków and Szczeliniec sandstones: an example of giant foresets on a tectonically controlled shelf of the Bohemian Cretaceous Basin (Central Europe). In: R.J. Knight and J.R. McLean (Editors), Shelf sands and sandstones. Can. Soc. Pet. Geol. Mem., 11: 1–15.

Josenhans, H. W., Sanford, B. V., Sparkes, R., Johnston, B. L., Boyce, A., Nielsen, J., and Belliveau, M., 1989. *Baffin* 89-008 cruise. Geol. Surv. Can., Open File, 2115, 68 pp.

Kazanci, N., 1990. Fan-delta sequences in the Pleistocene and Holocene Burdur Basin, Turkey: the role of basin-margin configuration in sediment entrapment and differential facies development. In: A. Colella and D.B. Prior (Editors), Coarse-grained deltas. Int. Assoc. Sedimentol. Spec. Publ., 10: 185–198.

King, L.H., 1970. Surficial geology of the Halifax-Sable Island map area. Mar. Sci. Pap., 1: 16 pp.

Kraft, J.C., 1971. Sedimentary facies patterns and geologic history of a Holocene marine transgression. Geol. Soc. Am., Bull., 82: 2131–2158.

Kumar, N. and Sanders, J.E., 1974. Inlet sequence: a vertical succession of sedimentary structures and textures created by the lateral migration of tidal inlets. Sedimentology, 21: 491–532.

Liverman, D. and Taylor, D., 1990. Surficial geology map of insular Newfoundland. Current Res. Newfoundland Dep. Mines Energy, Geol. Surv. Branch Rep., 90-1, pp. 39–48

MacClintock, P. and Twenhofel, W. H., 1940. Wisconsin glaciation of Newfoundland. Geol. Soc. Am., Bull., 51: 1729–1756.

Markham, W.E., 1980. Ice atlas: eastern Canadian Seaboard. Atmospheric Environment Service, Environment Canada, Toronto, 96 pp.

Martin, A.K. and Flemming, B.W., 1986. The Holocene shelf sediment wedge off the south and east coast of South Africa. In: R.J. Knight and J.R. McLean (Editors), Shelf Sands and Sandstones. Can. Soc. Pet. Geol. Mem., 11: 27–44.

May, J.P., 1974 WAVENRG: A computer program to determine the distribution of energy dissipation in shoaling waves, with examples from coastal Florida. In: W.F. Tanner (Editor), Sediment Transport in the Nearshore Zone. Florida State Univ., pp. 22–61.

Meistrell, F.J., 1966 The spit-platform concept: laboratory observation of spit development. Ms thesis, Univ. Alberta, Edmonton, Alb., 46 pp. (Unpubl.)

Meistrell, F.J., 1972. The spit-platform concept: laboratory observation of spit development. In: M.L. Schwartz (Editor), Spits and Bars. Dowden, Hutchinson and Ross, Stroudsburg, P.A., pp. 225–283.

Mitchum, R.M. Jr., Vail, P.R. and Sangree, J.B., 1977. Seismic stratigraphy and global changes of sea level, Part 6: stratigraphic interpretation of seismic reflection patterns in depositional sequences. In: C.E. Payton (Editor), Seismic Stratigraphy-Applications to Hydrocarbon Exploration. Am. Assoc. Pet. Geol. Mem., 26: 117–133.

Nielsen, L.N., Johannessen, P.N. and Surlyk, F., 1988. A late Pleistocene coarse-grained spit-platform sequence in northern Jylland, Denmark. Sedimentology, 35: 915–937.

Piper, D.J.W., Letson, J.R.J., De Iure, A.M. and Barrie, C.Q., 1983. Sediment accumulation in low-sedimentation, wave-dominated, glaciated inlets. Sediment. Geol., 36: 195–215.

Piper, D.J.W., Mudie, P.J., Letson, J.R.J., Barnes, N.E. and Iuliucci, R.J. 1986. The marine geology of the inner Scotian shelf off the South Shore, Nova Scotia. Geol. Surv. Can. Pap., 85-19.

Reinson, G. E., 1979. Facies Models 6. Barrier island systems. In: R.G. Walker (Editor), Facies Models. Geol. Assoc. Can., pp. 57–74.

Reinson, G. E., 1984. Barrier-island and associated strandplain systems. In: R.G. Walker (Editor), Facies Models. Geol. Assoc. Can., pp. 119–140.

Roy, P.S., Thom, B.G. and Wright, L.D., 1980. Holocene sequences of an embayed high-energy coast: an evolutionary model. Sediment. Geol., 26: 1–19.

Shaw, J. 1985. Holocene coastal evolution, Co. Donegal,

Ireland. D.Phil thesis, Univ. Ulster, Coleraine, 278 pp. (Unpubl.)

Shaw, J., 1989. Beach ridge sedimentation and morphology in Newfoundland: a preliminary review. In: Proc. Second Regional Workshop on Atlantic Shorelines (Charlottetown), pp. 114–121.

Shaw, J. and Forbes, D.L., 1987. Coastal barrier and beach-ridge sedimentation in Newfoundland. Proc. Can. Coastal Conf. 1987 (Québec). Natl. Res. Council, Ottawa, pp. 437–454.

Shaw, J. and Forbes, D.L., 1990a. Relative sea-level change and coastal response, northeast Newfoundland. J. Coastal Res., 6: 641–660.

Shaw, J. and Forbes, D.L., 1990b. Short- and long-term relative sea-level trends in Atlantic Canada. Proc. Can. Coastal Conf. 1990 (Kingston). Natl. Res. Counc. Ottawa, pp. 291–305.

Shaw, J. and Forbes, D.L., 1990c. Late-Quaternary sedimentation in St. George's Bay, southwest Newfoundland: acoustic stratigraphy and surficial deposits. Can. J. Earth Sci., 27: 964–983.

Shaw, J., Taylor, R.B. and Forbes, D.L., 1990. Coarse clastic barriers in eastern Canada: patterns of glaciogenic sediment dispersal with rising sea levels. In: P. Bruun and N.K. Jacobsen (Editors), Proc. Skagen Symp., J. Coastal Res. Spec. Issue., 9: 160–200.

Shearer, J. M., 1973. Bedrock and surficial geology of the northern Gulf of St. Lawrence as interpreted from continuous seismic reflection profiles. In: P.J. Hood (Editor), Earth Science Symp. on Offshore Eastern Canada. Geol. Surv. Can. Pap., 71-23: 285–304.

Stanley, D.J., Swift, D.J.P., Silverberg, N., James, N.P. and Sutton, R.G., 1973. Recent sand spill-over off Sable Island Bank, Scotian Shelf. In: P.J. Hood (Editor), Earth Science Symp. on Offshore Eastern Canada. Geol. Surv. Can., Pap. 71-23: 167–194.

Swirydczuk, K., Wilkinson B.H. and Smith, G.R., 1979. The Pliocene Glenns Ferry Oolite: lake margin carbonate deposition in the southwestern Snake River Plain. J. Sediment. Petrol., 49: 995–1004.

Syvitski, J.P.M. and Farrow, G.E., 1989. Fjord sedimentation as an analogue for small hydrocarbon-bearing fan deltas. In: M.K.G. Whateley and K.T. Pickering (Editors). Deltas: sites and traps for fossil fuels. Geol. Soc. Spec. Publ., 41: 21–43.

Taylor, R.B., Carter, R.W.G., Forbes, D.L. and Orford, J.D. 1986. Beach sedimentation in Ireland: contrasts and similarities with Atlantic Canada. In: Current Research, Part A, Geol. Surv. Can., Pap. 86–1A: 55–64.

Thom, B.G., 1983. Transgressive and regressive stratigraphies of coastal sand barriers in southeast Australia. Mar. Geol., 56: 137–158.

Woodward-Clyde Consultants, 1982. A study of the accessibility of three small craft harbours- western Newfoundland. Rep. prepared for Dept. Fisheries Oceans, St. John's, Newfoundland.

Marine Geology, 105 (1992) 141–154
Elsevier Science Publishers B.V., Amsterdam

Multiple sediment sources and a cellular, non-integrated, longshore drift system: Northwest Florida and southeast Alabama coast, USA

Gregory W. Stone[a1], Frank W. Stapor Jr.[b], James P. May[c] and James P. Morgan[d]

[a]*Department of Geography and Anthropology, Louisiana State University, Baton Rouge, LA 70803, USA*
[b]*Department of Earth Sciences, Tennessee Technological University, Cookeville, TN 38505, USA*
[c]*Department of Geology and Chemistry, The Citadel, Charleston, SC 29409, USA*
[d]*Institute for Coastal and Estuarine Research, The University of West Florida, Pensacola, FL 32514, USA*

(Received June 25, 1991; revision accepted August 18, 1991)

ABSTRACT

Stone, G.W., Stapor, F.W., Jr., May, J.P. and Morgan, J.P., 1992. Multiple sediment sources and a cellular, non-integrated, longshore drift system: Northwest Florida and southeast Alabama coast, USA. Mar. Geol., 105: 141–154.

The morphosedimentary maintenance of a 225 km stretch of coast along the northeast Gulf of Mexico, from Grayton Beach, Florida, to Morgan Point, Alabama, has been interpreted previously within the framework of a unidirectional, integrated, monotonic longshore drift model, with a single headland source of sediment located east of Grayton Beach. Net longshore transport and the granulometry and composition of some 2000 foredune, beach and step samples indicate a cellular net drift system, supplied by three independent sources of sediment. One source is provided by the Pleistocene barrier island complex along Grayton–Mirimar Beach, the second at Pensacola Beach on Santa Rosa Island, and the third is onshore transport across the inner shelf between Pensacola, Florida, and Morgan Point, Alabama. The Pleistocene "headland" and Pensacola Beach supply two cells along Santa Rosa Island, whereas onshore transport from the low gradient inner shelf supplies sediment to three cells along the largely accretional beach-ridge-dominated coast from Pensacola Pass to Morgan Point. Drift cells along this coast experience negligible net sediment exchange. These findings have significant implications for both the late Holocene evolution and the morphodynamic maintenance of this coast.

Introduction

Late Quaternary deposits along the 225 km length of Northeast Gulf coast from Morgan Point (Alabama) to Grayton Beach (Florida) (Fig.1), display a distinctly variable geomorphology. Well-preserved beach ridge plains interspersed by a series of modern spit, barrier island and baymouth barrier formations fronting shallow lagoons, characterize the coast from Morgan Point to Pensacola Pass (Fig.1). East of the Pass, the 95 km-long late Holocene barrier of Santa Rosa Island (Otvos, 1982), extends east to Destin East Pass and a Pleistocene headland at Grayton Beach (Fig.1). Beach sediments along the entire reach are almost entirely monomineralic, medium-grained quartz sand, with few heavy minerals. West of Santa Rosa Island, a noticeable increase in shell material occurs in beach and nearshore deposits.

Net longshore sediment transport along this coast has long been interpreted as westward (Johnson, 1956; Gorsline, 1966; U.S. Army, 1972; Balsillie, 1975; Walton, 1976), supplied by a single sediment source—the Pleistocene "headland" at Grayton Beach (Kwon, 1969). However, distinct gradational changes in the ambient wave field, and in the composition and texture of nearshore, beach and foredune sediments, indicates a non-integrated or cellular longshore sediment transport system, supplied by multiple sediment sources.

Correspondence to: G.W. Stone, Wetlands Research Institute, The University of West Florida, 11000 University Parkway, Pensacola, FL 32514-5751, USA.

0025-3227/92/$05.00 © 1992 — Elsevier Science Publishers B.V. All rights reserved

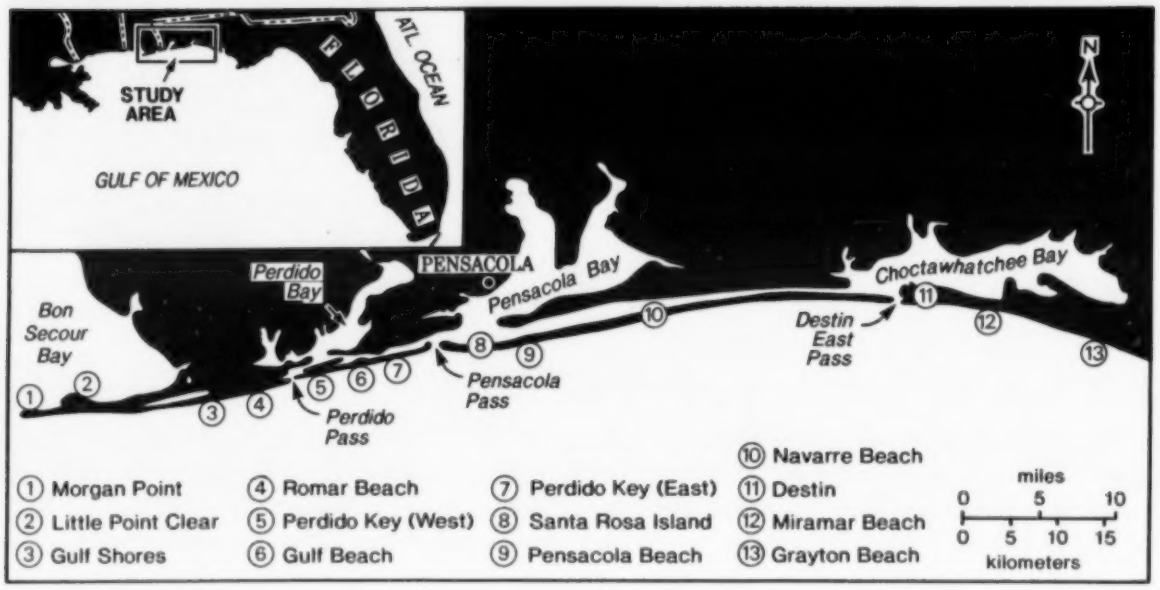

Fig.1. Map of the study area.

It is the objective of this paper to present and elucidate an alternative to the currently-held monotonic, integrated, single sediment source model, based on evidence obtained from (1) computer simulated net longshore transport predictions, and (2) analyses of the composition and texture of foredune-beach and nearshore sediments. The methodology used in this study was carefully considered so as to provide two independent data sets, the combination of which result in the most comprehensive data set available for the study area from which to draw interpretations of net longshore transport and sources of sediment supply.

Methods

Net longshore transport prediction

Since the seminal exposition of Munk and Traylor (1947), the utility associated with wave refraction analyses in predicting nearshore processes and sedimentation has become well established in the literature (Dobson, 1967; Goldsmith et al., 1974; May, 1974; Lowry and Carter, 1981; Carter et al., 1982; Stapor and May, 1983; Stone, 1991). A modified version of wave refraction program WAVENRG, developed by May (1974), was used in the present study to simulate the nearshore wave field, and predict net longshore transport rates. WAVENRG is described in detail in May (1974) and the modified version in Stone (1991).

Given a deep water wave height, period, direction of approach and frequency of occurrence, WAVENRG tracks a wave ray shoreward over a known bathymetry from a known deep water origin. As the wave ray is tracked shoreward, a companion ray is monitored to compute wave ray convergence or divergence due to refraction. The effects of shoaling on wave height and wavelength are constantly monitored due to changes in water depth as well as the dissipation of wave energy due to frictional drag. As the ray progresses shoreward, spatial coordinates, wave angle (direction), time elapsed, depth, wavelength, wave height, energy dissipation rate, refraction coefficient, bottom orbital velocity and the depth-to-wavelength ratio are computed at frequent intervals. Using the McCowan (1894) criterion, the wave is presumed broken at $0.78d$, where d is the water depth, and the breaker power, longshore component of wave power (P_L), group velocity (ECn), breaker angle (β), breaker height (H_b) and net longshore transport volume (Q_L) are computed. P_L is obtained by:

$$P_L = 0.5ECn \sin 2\beta \quad (1)$$

where wave energy density (E) is:

$$E = 0.125pgH_b^2 \quad (2)$$

and p is the mass density of water, g is gravity.

Q_L is given by:

$$Q_L = 1000 P_L \ (m^3/yr) \quad (3)$$

The coefficient 1000 is based on $k = 0.31$ in the relationship:

$$I_L = k P_L \quad (4)$$

where

$$Q_L = I_L / [(p_s\text{-}p) g a] \quad (5)$$

where p_s is mass density of sediment and a is a packing coefficient, 0.6. Inputs to WAVENRG in its modified form, consist of a bathymetric matrix of the study area, extending offshore to depths of at least $0.5L$, where L is the wavelength of the shoreward propagating deep water wave, and deep water wave statistics including wave height, period, angle of approach by percent frequency of occurrence.

Two sets of nautical charts with scales of 1:20,000 and 1:80,000 were initially used as input to WAVENRG to compare respective breaker wave statistics, particularly breaker height and angle, along Santa Rosa Island (Fig.1). No significant difference in outputs was observed, and thus the scale of 1:80,000 was used to conserve time and expense in running the program along the entire study area. Approximately 42,000 depth values were digitized and assembled in an X-Y-Z matrix format.

Two sets of deep-water wave inputs were used for simulation purposes. The first set (Table 1) was obtained from visual shipboard observations over the period 1953–1968 for Pensacola (U.S. Naval and Oceanographic Office, 1970). The U.S. Navy data (hereafter referred to as USN) suggest a mean deep-water wave height and period of 1 m and 5.8 s respectively, given fair weather conditions. The nature of the USN data permitted extraction of a wave height and period indicative of storm conditions (winter squalls as opposed to tropical storms or hurricanes). These were taken as 2 m and 8 s respectively, and are weighted by percent occurrence (Table 1).

The second data set was obtained from the Coastal Engineering Research Center's (CERC) Wave Information Study (WIS). The WIS data were produced by numerical simulation of wave growth, propagation and decay using historical wind fields in the Gulf of Mexico (Corson et al., 1980; Reiso et al., 1982; Hubertz et al., 1989). WIS inputs to WAVENRG are based on hindcasts for the period 1956–1975, computed at three hour intervals. Six stations are located along the study area in depths ranging from 18 to 37 m (Mean Low Water). The nature of the WIS data permits greater insight into the deep water wave field along the study area since directional information is obtained from a series of six stations, versus an overall regional average by direction obtainable from the USN data. Seven approach angles were selected to simulate the deep water wave approach spectrum, responsible for longshore transport along the study area (Fig.2).

Similar to the USN data (Table 1), the WIS statistics show the highest percent of occurrence for waves approaching from the southeast quadrant. However, the latter data indicate a pronounced, 0.4 m increase in height, and a 1.6 s increase in southeasterly waves south of Pensacola (station 28 on Fig.2) over those immediately west of Panama City (station 31). Thus, a corresponding westward increase in the wave energy density is to be expected, which in turn will give rise to a gradational westward increase in wave power along the adjacent coast.

TABLE 1

Deep water wave data derived from summary of synoptic meteorological observations over the period 1953–1968[1]

Dir. wave approach occurrence	Azimuth (degrees)	Wave height (M)	Wave period (s)	%
Fair weather conditions				
SE	135	1.0	5.8	16.00
S	90	1.0	5.8	6.70
SW	45	1.0	5.8	3.30
Storm conditions				
SE	135	2.0	8.0	2.10
S	90	2.0	8.0	0.90
SW	45	2.0	8.0	1.04

[1]Data obtained from U.S. Naval and Oceanographic Office (1970).

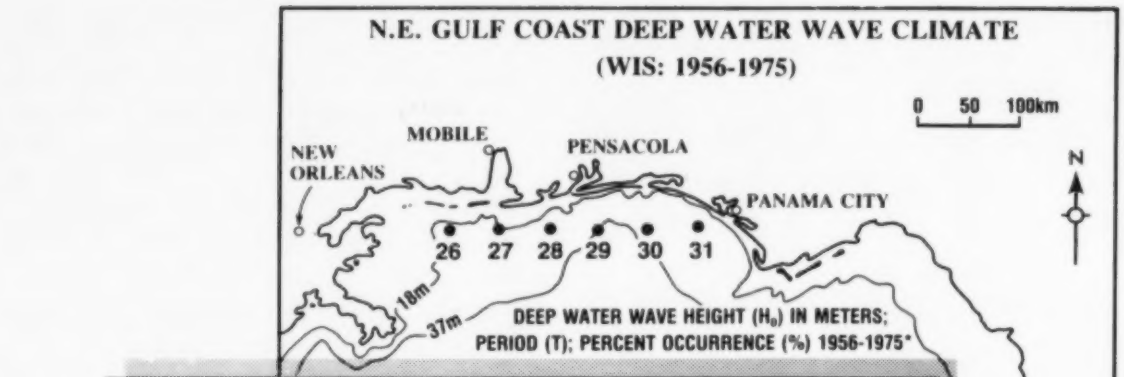

	STATION	26 (30N88.5W)			27 (30N88W)			28 (30N87.5W)			29 (30N87W)			30 (30N86.5W)			31 (30N86W)		
DIR	AZIMUTH	H_o	T	%	H_o	T	%	H_o	T	%	H_o	T	%	H_o	T	%	H_o	T	%
ESE	112.5	1.1	5.4	11.1	1.1	5.5	8.7	1.1	5.3	8.2	1.0	5.1	7.4	0.8	5.0	8.4	0.8	4.2	10.1
SE	135.0	1.1	5.7	23.6	1.1	5.7	17.1	1.1	5.6	16.2	1.0	5.5	16.3	0.8	5.2	15.5	0.7	4.2	7.0
SSE	157.5	1.0	5.4	9.6	1.2	5.8	16.1	1.2	5.8	15.3	1.0	5.6	15.8	0.9	5.4	15.7	0.7	4.3	6.4
S	180.0	0.8	4.6	3.1	1.0	5.4	7.4	1.1	5.5	8.8	1.0	5.3	10.3	0.9	5.4	9.9	0.7	4.7	7.0
SSW	202.5	0.8	4.3	1.9	0.9	5.0	3.9	0.9	5.3	5.2	0.9	5.2	6.3	0.8	5.2	6.6	0.8	5.1	5.6
SW	225.0	0.8	4.3	1.8	0.9	4.8	2.4	0.9	5.1	4.4	0.9	5.2	4.9	0.7	5.0	5.6	0.8	5.0	6.7
WSW	247.5	0.8	4.3	2.2	0.9	4.8	1.9	0.9	4.9	2.1	0.8	5.0	2.1	0.8	4.8	2.7	0.8	4.7	5.0

*HINDCAST WAVE INFORMATION SUPPLIED BY THE COASTAL ENGINEERING RESEARCH CENTER, VICKSBURG

Fig.2. Northeast Gulf coast deep water wave climate obtained from six Wave Information Study stations over the hindcast period 1956–1975.

Granulometry and composition of sediments

Sediments were sampled at 3.2 km (2 mile) intervals along the study area to describe their granulometry and composition. A total of approximately 2000 samples were collected during the winter of 1987 and summer of 1988. Four samples were obtained from the foredune crest, beach mid-tide position and beach step. Only the upper 2 cm-thick layer was sampled. Foredune and mid-tide samples were washed, decanted and dried in an oven in preparation for settling tube analyses. The finer fraction (silts and clays), and organics were removed during this process. Step samples were digested with hydrochloric acid to remove the carbonate (shell) fraction. Samples were essentially free of clay and silt. Heavy minerals composed generally less than 1%. The remainder of the samples were essentially 100% quartz sand.

Mean settling speeds were obtained for all 2000 samples using the Citadel Settling Tube (CST). Tap water was used for the settling medium. Variations in water temperature were corrected for by standardizing to 20°C according to eqn. (4) in May (1981, p.609). After temperature correction, settling speeds were calculated using the parameter *chi* after May (1981) and computed by:

$$chi = -\log_2(S/S_o)$$

where S is settling speed (m/s), and S_o is a standard speed (1 m/s). Following the relationship between particle size and settling velocity of a sphere at a given temperature, developed by Gibbs et al. (1971), settling speeds were transformed to grain size for those readers more accustomed to working with PHI, according to the equation:

$$r = 0.055804V^2P_f + 0.003114V^4P_f + [g(P_g - P_f)](4.5nV + 0.008705V^2P_f)\,[g(P_g - P_f)]$$

where r is the sphere radius (cm), V is velocity (cm/s), n is dynamic viscosity of fluid (poises), g is gravity (m/s^2), P_g is sphere density (g/cm^3).

Results

Net longshore sediment transport

The magnitude of the predicted net longshore sediment transport rate is highly dependent on the breaker wave height [eqn. (2)]. The validity of

various wave theories to accurately predict wave propagation from deep water to the break point, has received considerable attention (Dean, 1970, 1974; Le Mehaute, 1976; Cokelet, 1977; Horn and Hardisty, 1990), resulting in a lack of consensus (cf. Dean, 1974; May, 1974; Cokelet, 1977; Chaplin, 1980; Horn and Hardisty, 1990). WAVENRG simulates wave conditions based on small amplitude wave theory. Breaker heights predicted by WAVENRG show favourable agreement when compared with Littoral Environment Observations made along four sites in northwest Florida (Fig.3) by Balsillie (1975) over the period September 1969–August 1970. Similar conclusions have been reached in Australia (Bryant, 1979) and India (Kurian et al., 1985) under variable shelf gradients.

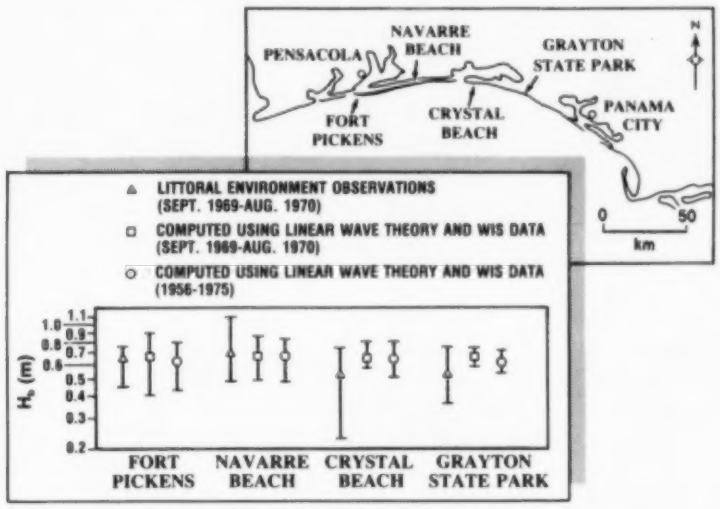

Fig.3. Comparisons of average breaker wave heights (m) obtained from LEO and computed by WAVENRG using small amplitude wave theory. Deep water wave inputs were obtained from Fig.2.

Net longshore transport rates computed using WIS and USN inputs are superimposed in Fig.4 (upper). The curves show a degree of variability in the magnitude of net transport along some portions of the study area. This is due primarily to variations in the deep water wave height where, along the eastern half of the study area, WIS generated waves are as much as 0.3 m less than those of the USN data. Similarly, along the western half of the study area, WIS generated waves are as much as 0.2 m higher than the USN data. Net transport trends, however, show good agreement,

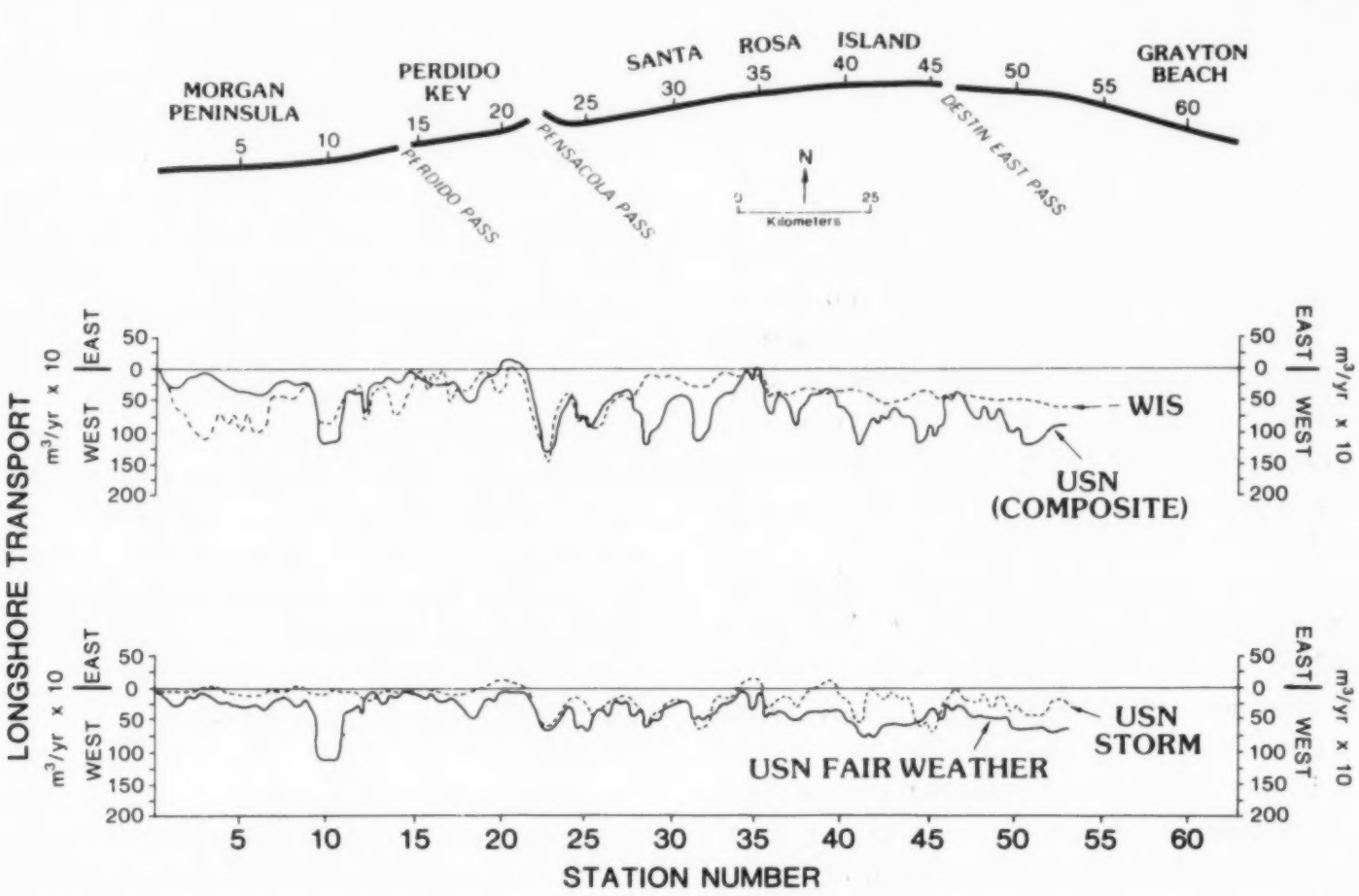

Fig.4. WAVENRG-predicted net longshore transport rates computed using WIS and USN (composite) deep water wave data and USN storm and fairweather inputs (lower) from *Grayton Beach* to *Morgan Peninsula*.

and it is reasonable to assume that "actual" transport rates should lie between the curves.

Both curves indicate dominant net westward longshore transport with the exception of a localized reversal along the eastern end of Perdido Key. Transport rates (m^3/yr) show a general decrease from Grayton Beach (site 55) to Navarre Beach (site 35) varying between 80,000 (USN) and 60,000 (WIS) at Grayton Beach, to between 25,000 (USN) and 5,000 (WIS) at Navarre Beach. West of Navarre, net transport rates increase to a maximum of between 125,000 (USN) and 150,000 (WIS) at Fort Pickens and decrease to zero at Pensacola Pass. Eastward transport along eastern Perdido Key ranges between 2,000 (WIS) and 20,000 (USN) decreasing to zero at Pensacola Pass. Along the remainder of Perdido Key net westward transport averages 25,000 before gradually increasing to between 90,000 (WIS) and 120,000 (USN) at Gulf Shores (site 10) and decreasing to zero at Perdido Pass. West along Morgan Peninsula, drift varies from an average of 75,000 (WIS) to 40,000 (USN) before decreasing to zero at Morgan Point.

Previous estimates of net longshore transport show poor agreement (Table 2). Estimates by Gorsline (1966) and Balsillie (1975) are based on Littoral Environment Observations (LEO) obtained over a one-year period. The estimate of Johnson (1956) was derived from impoundment studies at Perdido Pass whereas the U.S. Army (1972) used dredge records at Perdido and Destin East passes. Walton (1973) computed transport rates from shipboard wave observations. WAVENRG-predicted values, when compared with the above cited transport estimates, show close agreement with Gorsline (1966), and the U.S. Army (1972), and to a lesser extent Balsillie (1975) (Table 2). The estimates of Johnson (1956) and Walton (1973) are significantly higher than WAVENRG-predicted values (Table 2).

Net transport rates during storms are lower when compared with fair weather conditions (Fig.4, lower). Estimated transport rates are typically 25,000 and 50,000 m^3/yr, respectively from Grayton Beach to Pensacola Pass. West of Pensacola Pass to Morgan Point, net drift volumes are typically 5,000 and 30,000 respectively. Fair weather predictions indicate dominant net westward transport whereas the storm curve predicts three transport reversals—eastern end of Perdido Key, Navarre Beach and 16 km east of Navarre. Only one of those reversals remains on combining both storm and fairweather curves—eastern Perdido Key—thus providing the composite curve on Fig.4.

TABLE 2

Comparison of net westward longshore transport rates along the northeast Gulf Coast

Location	Net longshore transport (west m^3/yr)	WAVENRG-predicted longshore transport (west m^3/yr)	
		WIS	USN
Grayton Beach	50,000[1]		
	17,000[2]	60,000	80,000
Destin	60,000[1]		
	50,000[3]	40,000	50,000
	194,000[4]		
Navarre Beach	132,000[2]	5,000	25,000
Pensacola Beach	60,000[1]	50,000	50,000
Fort Pickens/	183,000[2]		
Pensacola Pass	223,000[4]	150,000	125,000
Gulf Beach	75,000[1]	50,000	25,000
Perdido Pass	50,000[3]		
	210,000[4]	75,000	25,000
	153,000[5]		
Gulf Shores	150,000[1]	90,000	120,000

[1]Gorsline (1966); [2]Balsillie (1975); [3]U.S. Army (1972); [4]Walton (1973); [5]Johnson (1956).

The cellular structure of the coast is also indicated by variations in the magnitude of net longshore transport rates (Fig.5). An absolute increase in the volume of transported sediment constitutes a zone of potential erosion (solid line). Conversely, an absolute decrease constitutes a potential zone of deposition (dotted line).

Composition and texture of sediments

Settling speeds (expressed as chi and phi units) are shown on Fig.6 for winter and summer beaches and the foredune as bands of $\pm$one standard deviation values about the four replicate-means at each sample site. Respective site means were

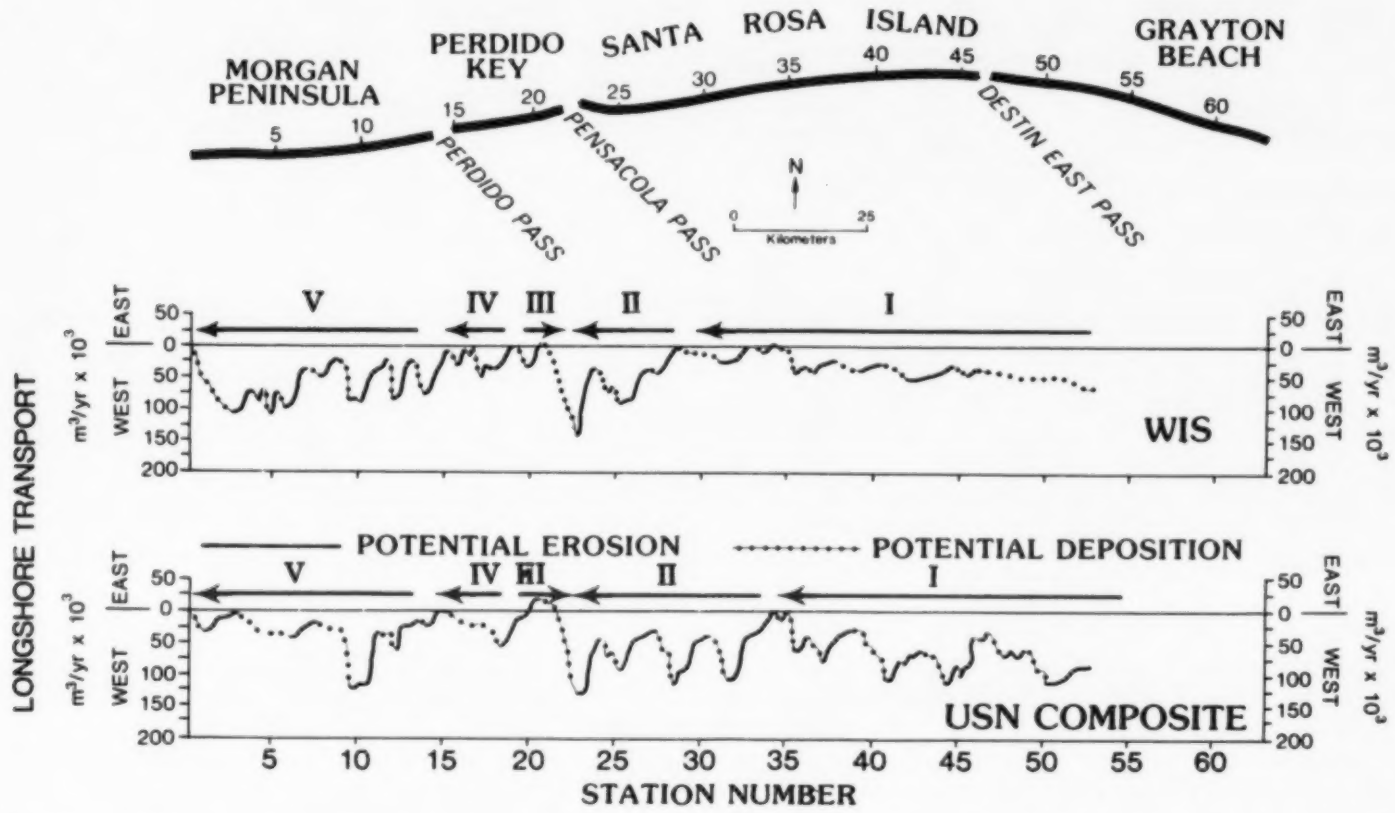

Fig.5. WAVENRG-predicted net longshore transport rates computed using WIS and USN (composite) deep water wave data illustrating zones of potential erosion (solid line) and deposition (dotted line) and cell delineation.

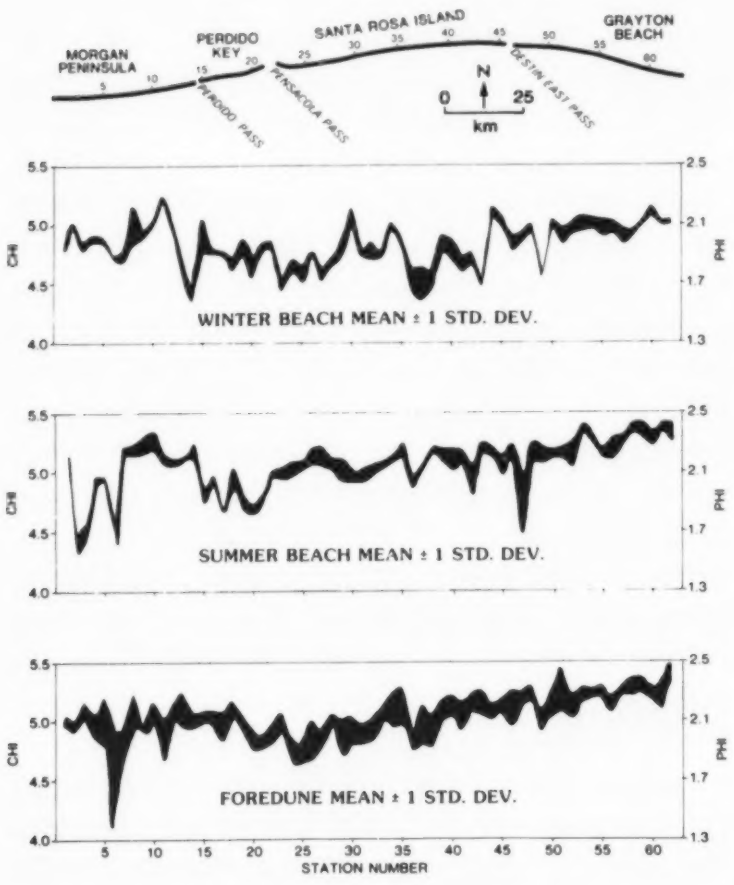

Fig.6. Mean chi and phi values ± one standard deviation for winter and summer beaches and foredune sediments.

smoothed by a three-point moving average to remove noise (Fig.7). Winter beaches show generally lower chi values (faster settling speeds/coarser sediments) than summer beaches, whereas the foredune tends to be intermediary with the exception of Perdido Key. This is expected in that foredunes continually receive sediment from the beach and have, therefore, the potential to average-out winter and summer conditions (i.e. storm versus calm conditions) (cf. Stapor and May, 1983). No statistically significant regional trend extending from Grayton Beach to Morgan Point could be identified in the data. However, statistically significant local gradients do occur. Sediments coarsen west of Grayton Beach to Pensacola Pass. Along Perdido Key they remain fairly constant and show some fining towards Morgan Peninsula. Shell content in step samples (Fig.8, upper) increases significantly (1% to 6% ± by weight) west of Pensacola Pass for summer and winter conditions. Similar to beach and foredune samples, step sediments coarsen from Grayton Beach to Pensacola Pass before finning towards Morgan Peninsula (Fig.8, lower).

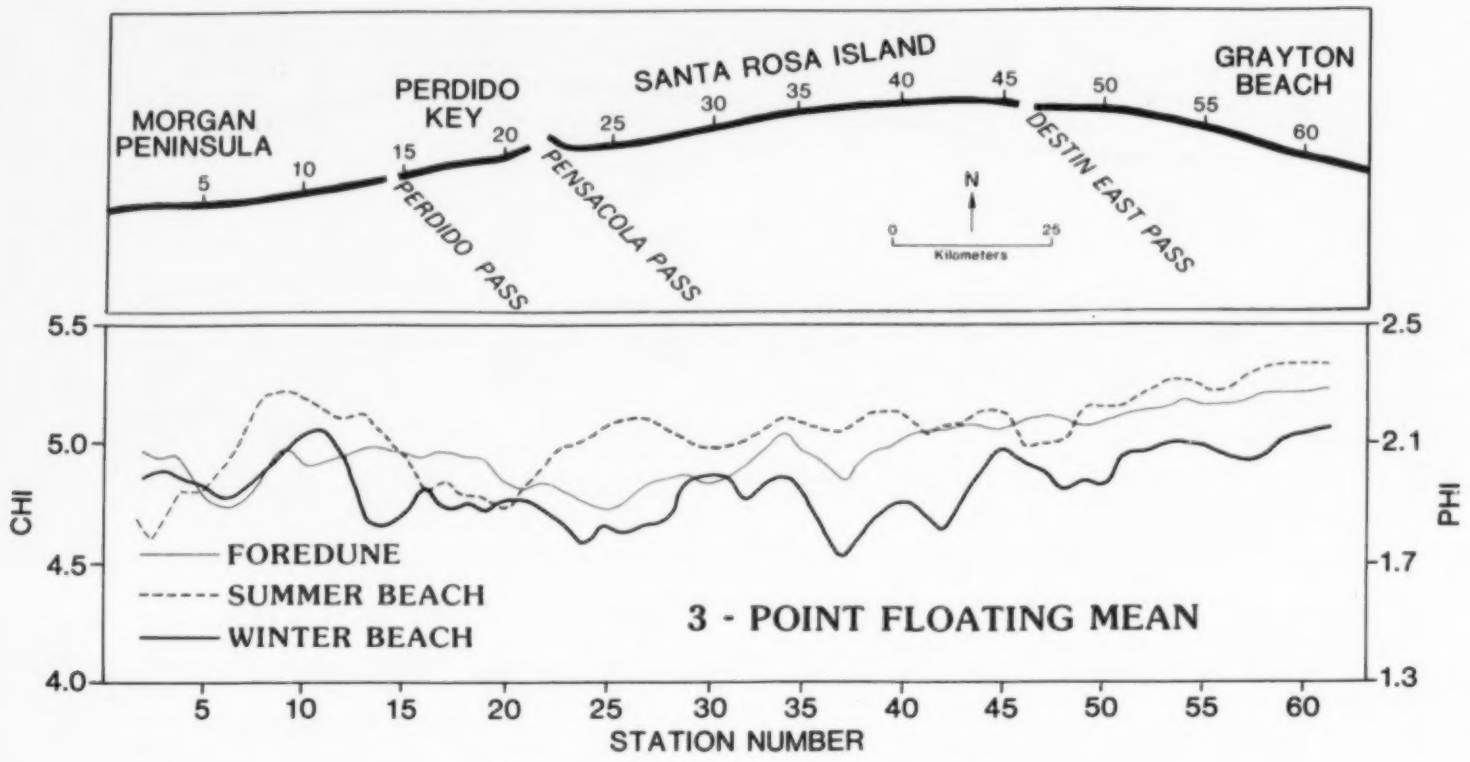

Fig.7. Smoothed mean chi and phi values for summer and winter beach and foredune sediments.

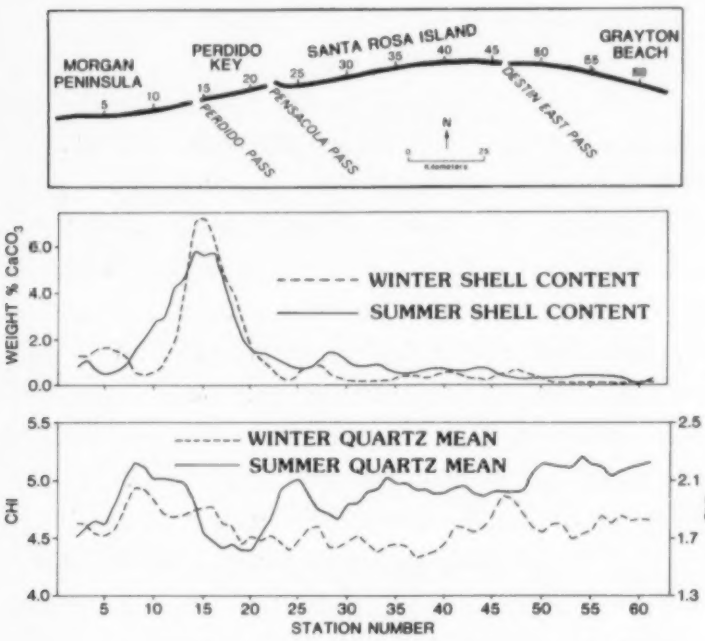

Fig.8. Winter and summer shell content (upper) and mean quartz chi and phi values for step sediments (lower).

Discussion

Longshore transport simulations indicate the existence of five littoral cells along this 225 km stretch of coast (Fig.5). Cell I extends from Mirimar to the Navarre–Pensacola Beach region and experiences net westward transport which uniformly decreases in magnitude downdrift. Cell II, in which net transport is westward, occurs along the remainder of the coast to Pensacola Pass. Cell III, located along the eastern few kilometers of Perdido Key, experiences net easterly drift indicating the importance of Pensacola Pass as a net sediment sink. Cell IV extends from eastern Perdido Key to Perdido Pass and experiences net westward transport. Finally, cell V extends from Romar Beach to the western tip of Morgan Peninsula and experiences net westward transport.

The degree of cell maturation as well as sources of sediment supply can be discerned from historic shoreline trends. Ideally, a mature sediment source constituting the updrift cell boundary should exhibit erosion, assuming negligible inputs to the source. Given the net westward transport of sediment predicted by WAVENRG along Grayton Beach and the historical (1872–1965) net erosion (0.7 m/yr) of this Pleistocene "headland" (Stapor, 1975), it is concluded that this section of coast is a mature source of sediment for Cell I along Santa Rosa Island.

Historic shoreline trends indicate stability along the vast majority of Santa Rosa Island (Stapor, 1975; Stone, 1991) with the exception of a localized, zone of net erosion west of Pensacola Beach identified by WAVENRG (stations 25–30 on Fig.5)

and characterized by extensive overwash during hurricanes (Stone, 1991). It is apparent that this localized erosional area is a mature source of sediment allowing westward progradation of the western tip of Santa Rosa Island.

Analyses of sediment samples from Santa Rosa Island reveal a settling speed increase (coarsening) in the downdrift direction (westward). This textural trend can be attributed to either an increasingly coarse contribution from an offshore source (Schalk, 1938; Carter, 1975) or an increase in the energy of the transporting medium (Evans, 1939; Carr, 1969; Komar, 1977; McCave, 1978). There exists no data to support the former along Santa Rosa Island, nor does it appear to be a logical explanation in this instance. It only begs the question by proposing (1) the existence of westward-coarsening sediments in the nearshore being uniformly delivered to the beach or (2) an increasing proportion of sediments delivered from a uniformly offshore sediment source. Furthermore, there is no independent evidence to support the suggestion of onshore transport along Santa Rosa Island.

The alternative interpretation, increasing wave energy to the west, is supported by both field observation (LEO data; Fig.3) and computer simulation (WAVENRG; Figs.9 and 10). As the wave approaches are dominantly from the southeast (Fig.2) and the coastline curves toward the south at the eastern end of the study area, it stands to

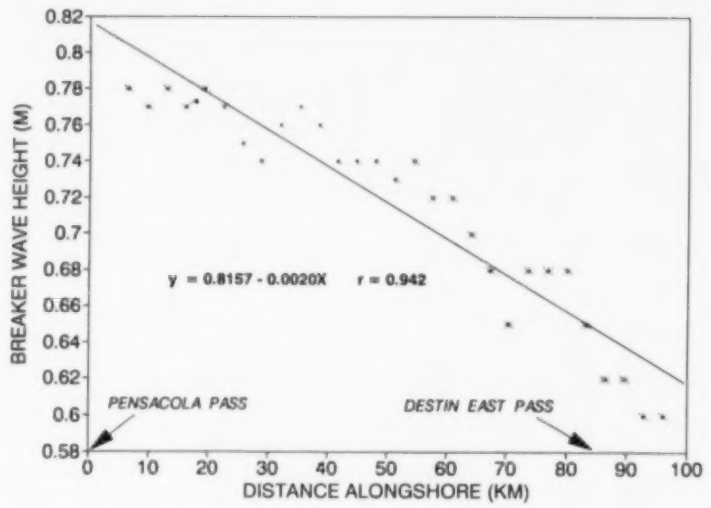

Fig.10. Relationship between breaker wave height (m) and distance from Destin to Pensacola Pass.

reason the dominant wave heights and periods, therefore total wave energy, would increase towards the west due to the increased fetch. Given that a good relationship exists between the mean settling speed and breaker wave height for both winter and summer beaches (Figs.11 and 12), it is concluded that the observed westward coarsening of beach and dune sediments results from the westward increase in wave energy.

The implications for hydraulic grading or sorting are highly significant. The vast majority of studies on longshore beach sediment grading infer either the absence of a nearshore wave energy gradient or the coincidence of that gradient with the direction of longshore transport. Consequently, it is

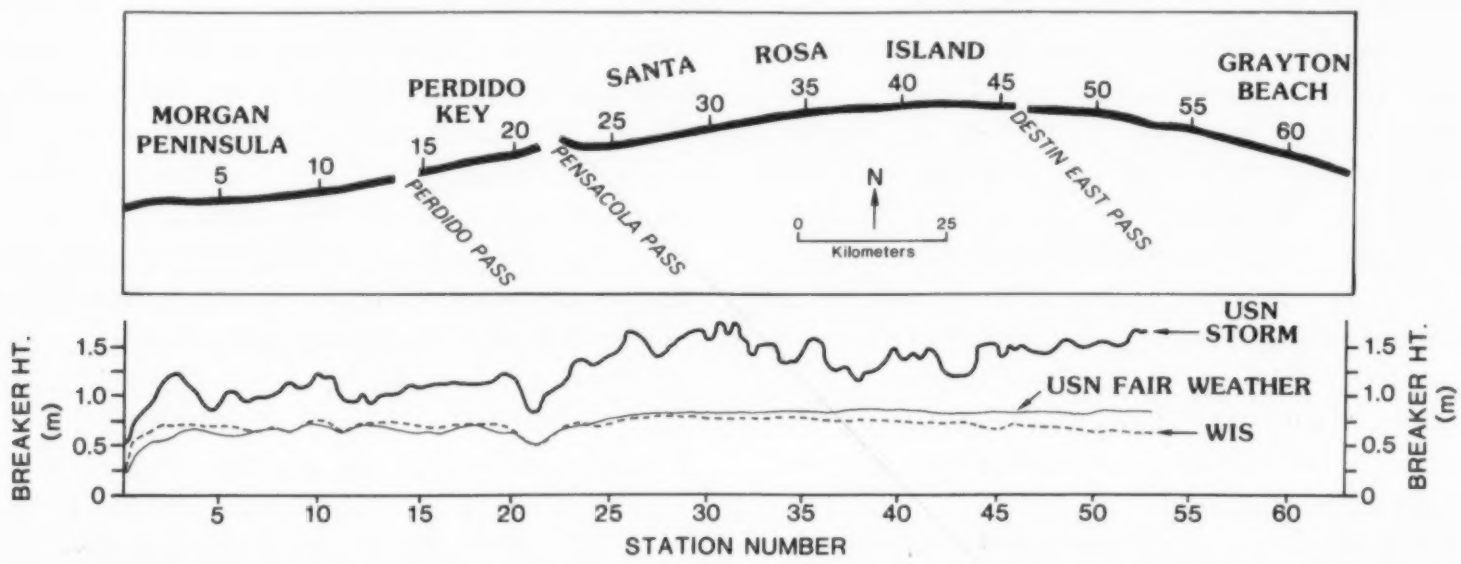

Fig.9. WAVENRG-predicted breaker wave height (m) using USN storm (upper curve) and fairweather and WIS (lower curves) deep water wave inputs.

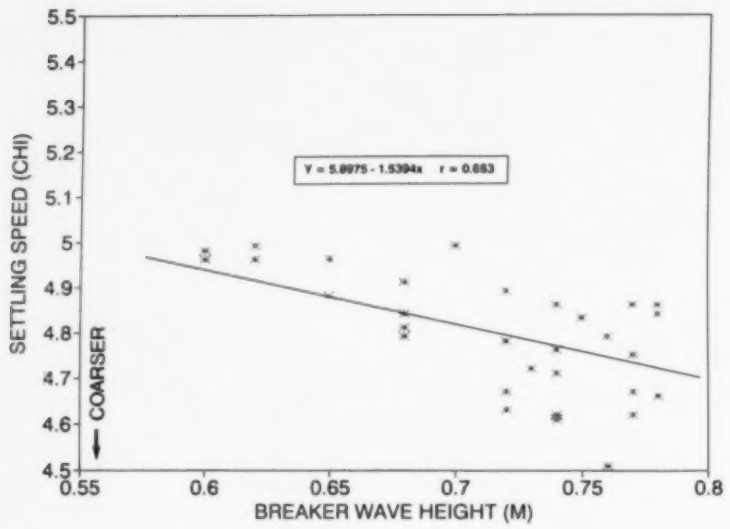

Fig.11. Comparison of breaker wave height (m) with winter beach mid-tide settling velocities (CHI).

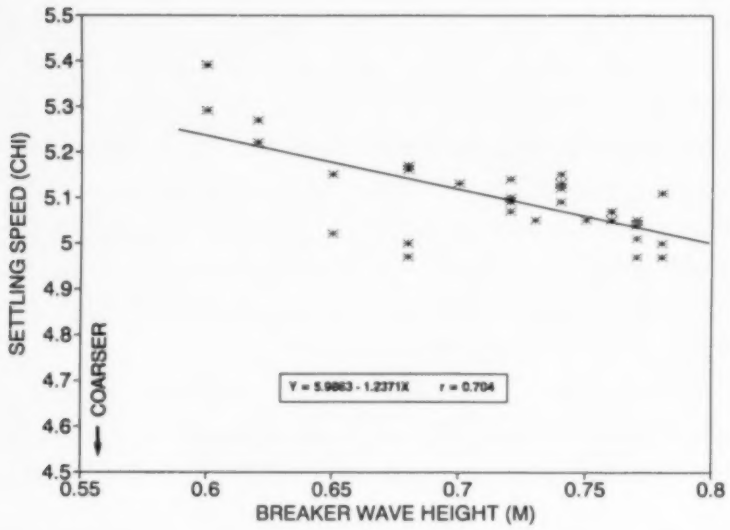

Fig.12. Comparison of breaker wave height (m) with summer beach mid-tide settling velocities (CHI).

generally accepted that textural grading is a function of grain size and distance from the primary source. Coarser material is deposited closer to the source. Fining downdrift is equally evident in fluvial systems where the slope-energy decrease downstream introduces an hydraulic gradient resulting in preferential fining downstream. Clearly the data presented here indicate the importance of the nearshore wave energy gradient in elucidating textural variability. Further, and unlike a river channel, the energy available for sediment entrainment on a beach is independent of the direction of the regional transport.

A cell terminus can be represented in the historic record by net deposition because littoral transport goes to zero, i.e. spit progradation and aggradation and/or seaward elongation of the ebb tidal delta. Westward progradation of Santa Rosa Island (1.25 km between 1771–1981) and historic net accretion along its western end, attests to its longevity as a sediment sink and cell terminus. A sediment budget constructed for Pensacola Pass (Fig.13) over the period 1856–1981, indicates net depositional rates approximating 30,000 m^3/yr between 1856–1940, and near equilibrium from 1940–1981. Historically, the vast majority of sediment has been transported from the east along Santa Rosa Island, prior to deposition in the inlet and on the adjacent ebb tidal-delta.

The eastward reversal of net sediment transport in cell III along eastern Perdido Key also appears to be mature given historical evidence. Approximately 0.36×10^6 m^3 of sediment accumulated in cell III over the period 1890–1965 (Fig.14) supplied primarily by sediment from the west flank of the Pensacola Pass ebb tidal-delta and the adjacent beach on Perdido Key. The location and maturity of this cell is in response to an established refraction pattern across the ebb shoal, prevalent during predominant southeast deep water wave approaches (Stone, 1984, 1991; Stapor and May, 1985). Elongation of the shoal offshore by approximately 1.5–2 km (1940–1981), supplied by sediment from the inlet throat during equilibration in response to throat constriction (12.5 m/yr), has enhanced the predominant refraction pattern. Therefore, and as established in other areas (Lowry and Carter, 1982; Carter et al., 1982), the drift divide or western terminus of cell III is a free boundary prone to migration in response to long-term changes in the refraction pattern associated with the Pensacola Pass ebb tidal-delta.

The data suggest that significant net transfer or sediment between Santa Rosa Island and Perdido Key does not appear to exist. Pensacola Pass receives inputs of sediment from Santa Rosa Island and Perdido Key and in doing so, serves as a sink and fixed depositional boundary for cells II and III. This finding has, therefore, important implications for the source of sediment supply to the remainder of the coast to the west comprising cells IV and V. With the exception of two frequently overwashed, localized net erosional areas—eastern Perdido Key (Fig.14) and south of Little Point

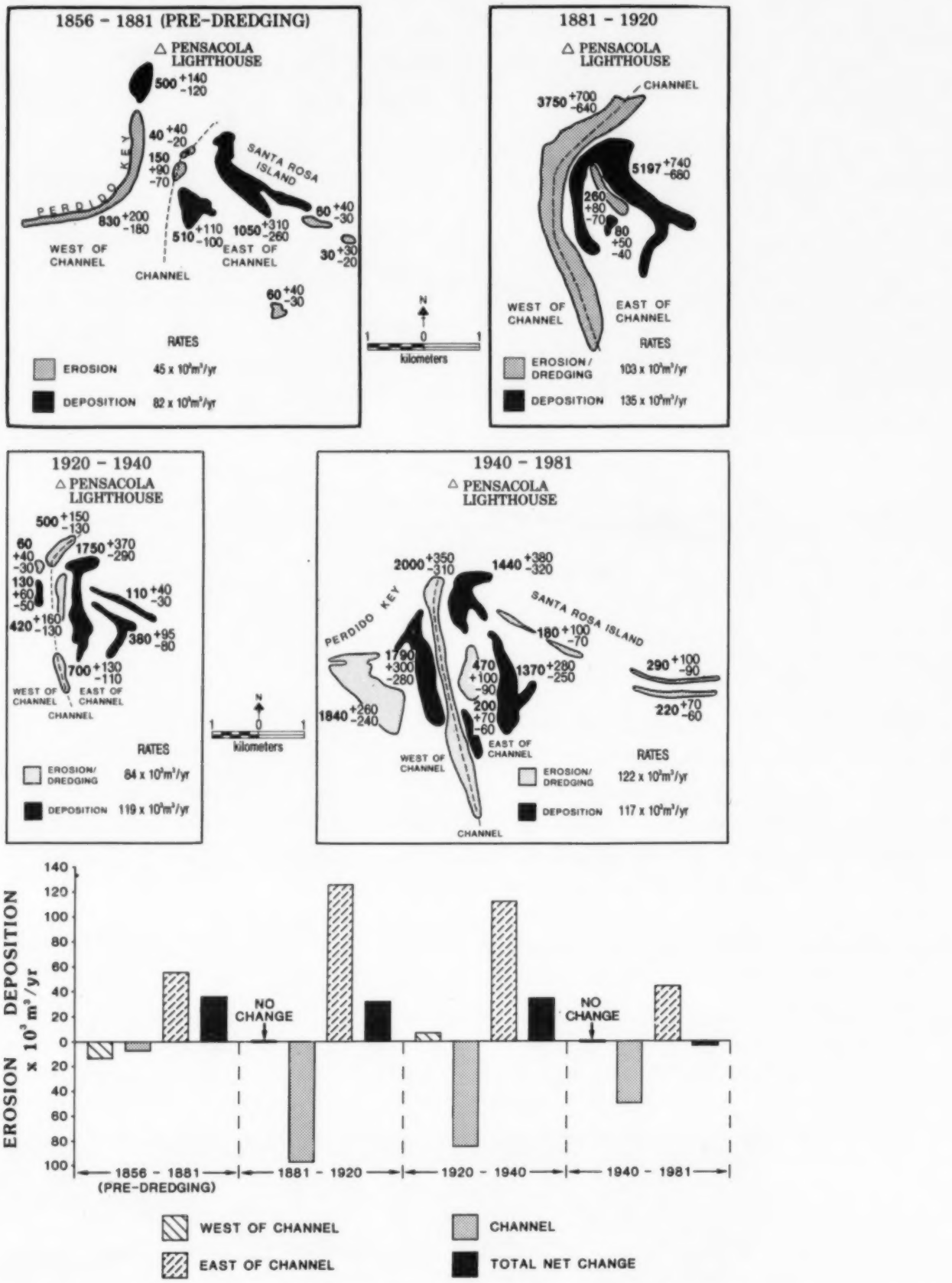

Fig.13. Sediment budget for Pensacola Pass for the periods 1856–1881; 1881–1920; 1920–1940; and 1940–1981, and summarized in m^3/yr west, east and in the channel proper, and total net change.

Clear (Fig.1)—this stretch of coast is stable to progradational (Stone, 1991). Net longshore transport is westward along this coast and diminishes to zero at Perdido Pass and Morgan Point (Fig.4).

In the absence of primary, localized, headland sources of sediment supply, inputs must, therefore, be received from the inner shelf along this stretch of coast. Various lines of evidence support this

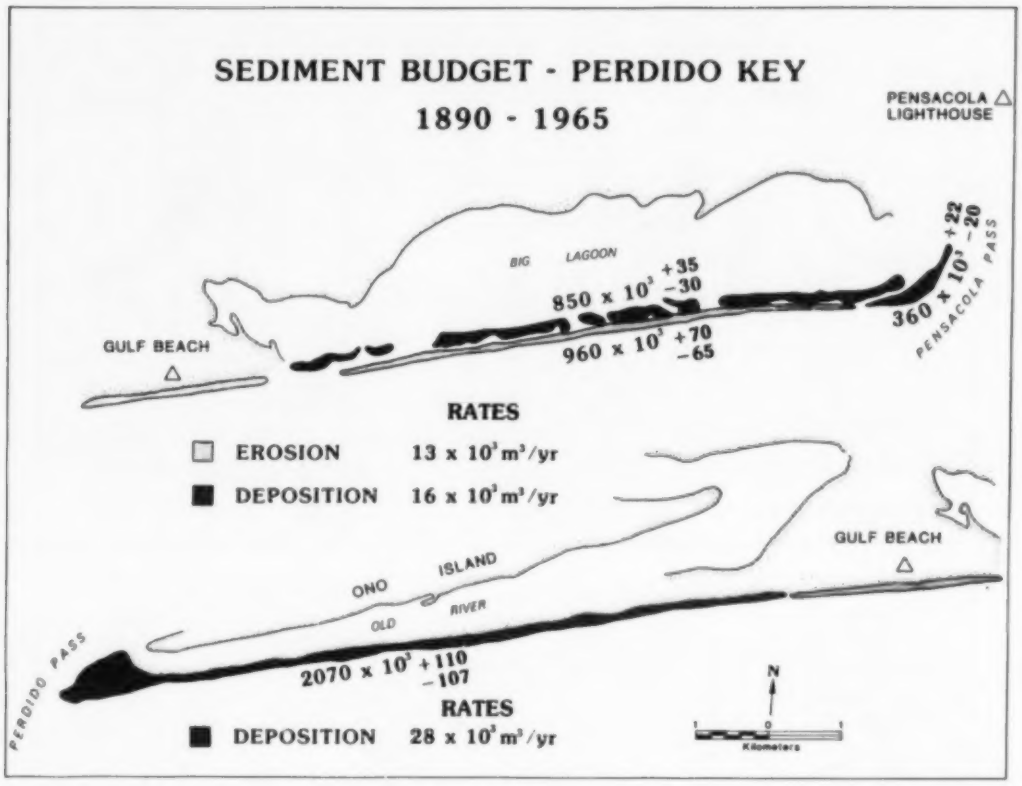

Fig.14. Net and rates of volumetric change (m^3/yr) along Perdido Key based on topographic survey comparisons over the period 1890–1965.

statement further: (1) a significant increase in the carbonate fraction found in "winter" and "summer" step samples (Fig.8) could only have been derived from offshore; (2) considerable variations in grain size/settling speeds found in foredune, beach and step sediments indicates littoral disintegration and injections of variably-sorted material from offshore; (3) a significant reduction in the adjacent inner shelf slope relative to the remainder of the coast along Santa Rosa Island (1:625 versus 1:156 respectively) (Fig.15) suggests a direct increase in the potential for transport from offshore; and (4) the concave seaward nature of four juxtaposed beach ridge plains indicates the propensity for beach ridge construction due to onshore transport from the shelf during the late Holocene (Stone, 1991).

Conclusions

Previous studies (Johnson, 1956; Gorsline, 1966; Kwon, 1969; Balsillie, 1975; Walton, 1976; Dean and O'Brien, 1987) have interpreted the morphosedimentary maintenance of the 225 km-long

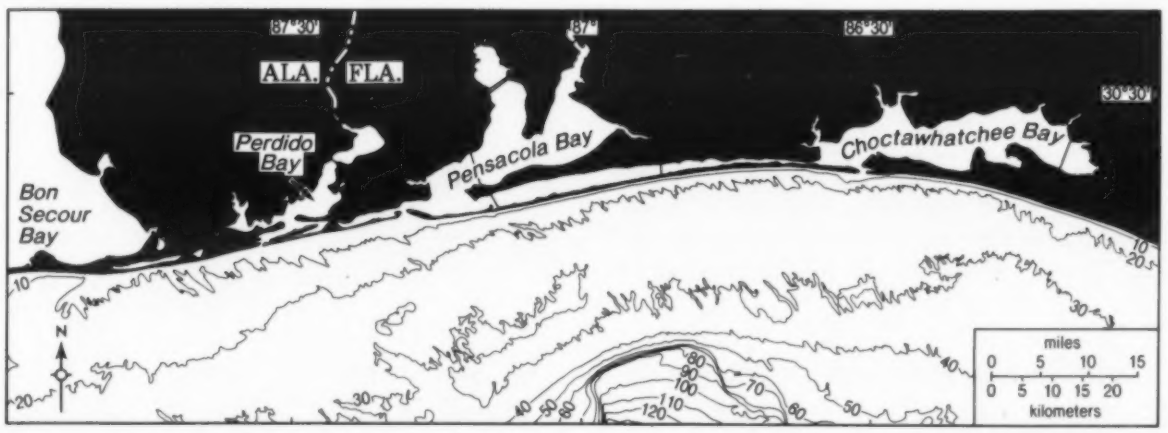

Fig.15. Bathymetric map from Grayton Beach to Morgan Point illustrating the significant decrease in inner shelf slope along the Alabama coast (isobaths in meters).

stretch of coast from Grayton Beach to Morgan Point within the framework of an integrated, unidirectional (E–W) longshore transport system, with a single source of sediment supply. Evidence presented here suggests that the net longshore transport system is composed of five mature cells, in one of which net drift is directed eastward. Net sediment transport is non-integrated since transfer between cells is insignificant. The eastern half of Santa Rosa Island (cell I) receives sediment from a Pleistocene coastal deposit east of Destin that acts as an eroding "headland." Western Santa Rosa Island (cell II) is supplied by an "internal" source at Pensacola Beach. The three remaining cells, extending from Pensacola Pass west to Morgan Point, receive material by direct onshore transport from the inner shelf.

Acknowledgements

This research was funded by the Coastal Engineering Research Center, Vicksburg, MS.. Additional funds were obtained from the National Park Service and Sigma Xi, The Scientific Research Society. The writers wish to extend their thanks to the following people who assisted in the study: Karen Moore (UWF) for support in computer modelling; Deputy Dennis Peek (Baldwin County Sheriffs Department) for field transport; Rebecca Brooks (CERC) for supplying wave data; Charles Connolly, Steve Modica and Vincent Gill for field support. Thanks also to the University of Maryland Sea Grant for vehicle use and Eglin Air Force Base personnel for coordinating field access and transport.

References

Balsillie, J.H., 1975. Analysis and interpretation of LEO and profile data along the western Panhandle coast of Florida. CERC Tech. Mem., 49.

Bryant, E., 1979. Comparison of computed and observed breaker wave heights. Coastal Eng., 3: 39–50.

Carr, A.P., 1969. Size grading along a pebble beach: Chesil Beach, England. J. Sediment. Petrol., 41: 395–409.

Carter, R.W.G., 1975. Recent changes in the geomorphology of the Magilligan foreland, County Londonderry. Proc. R. I. Acad., 75: 469–497.

Carter, R.W.G., 1988. Coastal Environments. London, Academic Press.

Carter, R.W.G., Lowry, P. and Stone, G.W., 1982. Ebb shoal control of shoreline erosion via wave refraction, Magilligan Foreland, Northern Ireland. Mar. Geol., 48: M17–M25.

Chaplin, J.R., 1980. Developments of stream function theory. Proc. 17th Conf. Coastal Eng., ASCE, 3: 179–205.

Cokelet, E.D., 1977. Steep gravity waves in water of arbitrary uniform depth. Philos. Trans. R. Soc. London, Ser. A, 286: 183–230.

Corson, W.D., Reiso, D.T. and Vincent, C.L., 1980. Wave Information Study of the U.S. Coastlines; Surface Pressure Field Reconstruction for Wave Hindcasting Purposes. TR HL-80-11, 1: USAE, Waterways Expt. Station, Vicksburg, Miss.

Dean, R.G., 1970. Relative validity of water wave theories. J. Waterways Harbors Div., ASCE, 96: 105–119.

Dean, R.G., 1974. Evaluation and Development of Water Wave Theories for Engineering Applications. Vols.1 and 2, Spec. Rep. 1, CERC, Fort Belvoir, Va.

Dean, R.G. and O'Brien, M.P., 1987. West Coast Inlets Shoreline Effects and Recommended Action. Dept. Coastal Oceanogr. Eng., Univ. Florida, Gainesville, Fla.

Dobson, R.S., 1967. Some Applications of a Digital computer to Hydraulic Engineering Problems. Tech. Memo. 80: 7–35, Dept. Civil Eng., Stanford Univ.

Evans, D.F., 1939. Sorting and transportation of sediment in swash and backwash. J. Sediment. Petrol., 9: 28–31.

Gibbs, R.J., Matthews, M.D. and Kink, D.A., 1971. The relationship between sphere size and velocity. J. Sediment. Petrol., 41(1): 7–18.

Goldsmith, V., Colonell, J.M. and Byrne, R.J., 1974. The Causes of Non-uniform Wave Energy Distribution over the Shelf and Along the Shoreline. V. Inst. Mar. Sci., Contrib. No. 559.

Gorsline, D., 1966. Dynamic characteristics of Gulf Coast beaches. Mar. Geol., 4: 187–206.

Horn, D.P. and Hardisty, J., 1990. The application of Stokes' wave theory under changing sea levels in the Irish Sea. Mar. Geol., 94: 341–351.

Hubertz, J.M., Abel, C.E., Jensen, R.E. and Vincent, C.L., 1989. Gulf of Mexico Hindcast Wave Information. Waterways Expt. Station Rep. 18, USAE, Coastal Eng. Res. Center, Vicksburg, Miss.

Johnson, J.W., 1956. Dynamics of nearshore sediment movement. Am. Assoc. Pet. Geol. Bull., 40: 2211–2232.

Komar, P.D., 1977. Selective longshore transport rates of different grain-size fractions within a beach. J. Sediment. Petrol., 47: 1444–1453.

Kurian, N.P., Baba, M. and Shahul Hameed, T.S., 1985. Prediction of nearshore wave heights using a refraction programme. Coastal Eng., 9: 347–356.

Kwon, H.J., 1969. Barrier Islands of the Northern Bulf of Mexico Coast: Sediment Source and Development. Coastal Studies Inst. Louisiana State Univ., Baton Rouge, La., TR 75.

Le Mehaute, B., 1976. An Introduction to Hydrodynamics and Water Waves. Springer, Dusseldorf.

Lowry, P. and Carter, R.W.G., 1982. Computer simulation and delimitation of littoral power cells on the barrier coast of southern County Wexford, Ireland. J. Earth Sci. R. Dublin Soc., 4: 121–132.

May, J.P., 1974. WAVENRG: A computer program to deter-

mine the distribution of energy dissipation in shoaling water waves with examples from coastal Florida. In: W.F. Tanner (Editor), Sediment Transport in the Nearshore Zone. Florida State Univ., Tallahassee, Fla pp.22–61.

May, J.P., 1981. Chi (χ): A proposed standard parameter for settling tube analysis of sediments. J. Sediment. Petrol., 51(2): 607–610.

McCave, I.N., 1978. Grain-size trends and transport along beaches: Examples from eastern England. Mar. Geol., 28: M43–M51.

McCowan, J., 1894. On the highest wave of permanent type. Philos. Mag. J. Sci., 38.

Munk, W. and Traylor, M.A., 1947. Refraction of ocean waves: A process linking underwater topography to beach erosion. J. Geol., 54: 1–26.

Otvos, E.G., 1982. Santa Rosa Island, Florida Panhandle, origins of a composite barrier island. Southeast Geol., 14: 241–250.

Reiso, D.T., Vincent, C.L. and Corson, W.D., 1982. Objective specifications of Atlantic ocean wind fields from historical data. WIS Rep. 4, USAE Waterways Expt. Station, Vicksburg, Miss.

Schalk, M., 1938. A textural study of the outer beach at Cape Cod, Massachussets. J. Sediment. Petrol., 8: 41–54.

Stapor, F.W., 1975. Shoreline changes between Phillips Inlet and Pensacola Inlet, Northwest Florida coast. Trans. Gulf Coast Assoc. Geol. Soc., 25: 373–378.

Stapor, F.W. and May, J.P., 1983. The cellular nature of littoral drift along the northeast Florida coast. Mar. Geol., 51: 217–237.

Stapor, F.W. and May, J.P., 1985. Sediment budgets at Santa Rosa Island and Perdido Key, Florida. Geol. Soc. Am., Abstracts Programs, Vol.17, p.726.

Stone, G.W., 1984. Mathematical modeling of the nearshore and implications for coastal management, northwest Florida. M.S. thesis, Coastal Studies, Univ. West Florida, Pensacola, Fla., (Unpubl.).

Stone, G.W., 1991. Differential sediment supply and the cellular nature of coastal northwest Florida and southeast Alabama during the late Quaternary. Ph.D. dissert., Dept. of Geography, Univ. Maryland, College Park, MD, (Unpubl.).

U.S. Army, 1972. Evaluation of weir-jetty systems at Perdido Pass, Alabama, and East Pass, Florida. U.S. Army, Mobile District, Mobile, Ala.

U.S. Naval and Oceanographic Office, 1970. Summary of synoptic meteorological observations: North American coastal marine area. 5: (Area 16-Pensacola).

Walton, T.L., 1973. Littoral drift computations along the coast of Florida by means of Ship Wave Observations. TR-15, University Florida, Gainesville, Fla.

Walton, T.L., 1976. Littoral drift estimates along the coastline of Florida. Florida Sea Grant, Univ. Florida, Gainesville, Fla.

Marine Geology, 105 (1992) 155–168
Elsevier Science Publishers B.V., Amsterdam

Physical processes and sedimentary record of a modern, transgressive, lacustrine barrier island

Thomas F. Bray Jr.[1] and Charles H. Carter
Department of Geology, University of Akron, Akron, OH 44325-4101, USA

(Received March 18, 1991; revision accepted August 7, 1991)

ABSTRACT

Bray, T. F., Jr. and Carter, C. H., 1992. Physical processes and sedimentary record of a modern, transgressive, lacustrine barrier island. Mar. Geol., 105: 155–168.

High water levels, storms, and a sparse sand supply have led to the formation and episodic migration of this 30 km-wide, foredune-lacking, lacustrine barrier. Transgression is dominated by overwash and by channels cut during storms that transport sand to the lagoon.

The barrier system is characterized by five environments: near-shore, foreshore, backshore/washover terrace, channel, and lagoon. The nearshore consists of irregular bars that overlie a Holocene peat and/or clay. The bars are characterized by low-angle stratification, and ripples, and landward-dipping tabular sets. The foreshore consists of a smooth, plane surface and internally by lakeward-dipping (3° to 12°) laminations that truncate one another and thin towards the berm. The backshore/washover terrace consists of a gently (1° to 2°) landward-dipping surface that changes at the lagoon margin to a steeply (30°) landward-dipping surface. Stratification consists of subhorizontal, landward-dipping laminations and thin beds that are thinnest nearer the berm and gradually thicken toward the lagoon, and by avalanche foresets. Washover fans coalesce to form the terrace. The channels, which are commonly less than a few tens of meters wide and a meter deep, form during storms when wave energy is concentrated by refraction around nearshore bars. The channel facies consists of nearly horizontal beds and laminations of gravel and coarse sand. The lagoon consists of mud that overlies a Holocene peat; the lagoonal mud is eroded during transgression.

The vertical sequence which is 1–2 m thick, consists from the base up of horizontal laminations of coarse sand and gravel of the channel facies, the landward-dipping foresets of the washover fan margin, and the gently landward-dipping laminations and landward-dipping avalanche foresets of the backshore/washover terrace. The preservation potential is considered low, although Pleistocene and Holocene coastal deposits have survived for up to 15,000 years in the Great Lakes region.

Introduction

The sedimentology of modern marine barriers has been extensively studied by workers such as Van Straaten (1954), Reineck (1967), Davies et al. (1971), Kraft and John (1979), Kahn and Roberts (1982), Oertel (1985), and Leatherman and Zaremba (1986). These and other modern studies have, in turn, been used by sedimentologists in the interpretation of ancient marine barriers. There are however, no comprehensive studies of the sedimentology of modern lacustrine barriers to help in the interpretation of ancient nonmarine barriers. Important lacustrine studies have been done by Martini (1975), Fraser and Hester (1977), and Thompson (1989) who reported on fossil Holocene lacustrine barriers, and Davis et al. (1972) who compared ridge and runnel systems from the modern nearshore/foreshore of Lake Michigan to that of a modern oceanic nearshore/foreshore, and Schwartz (1982) who studied modern small-scale washover sand bodies at Presque Isle Peninsula, Lake Erie. This study of the processes and sedimentary record of a modern Lake Erie barrier at Sheldon's Marsh is an attempt to bridge this modern to ancient gap.

This barrier is an excellent example of a trans-

[1]Present address: Lamont-Doherty Geological Observatory, Rt. 9W, Palisades, NY 10964, USA

0025-3227/92/$05.00 © 1992 — Elsevier Science Publishers B.V. All rights reserved

gressive barrier system. The combination of high water levels, a scarce supply of sand, and intense windstorms have led from 1972 to 1986 to the formation (by the breaching of a dune and tree covered baymouth spit), and episodic, 240 m landward-migration of the barrier. Washover and channel processes have created a nearly featureless, denuded barrier island that resembles some of the modern transgressive barriers along the Gulf and Atlantic coasts of the U.S.

Procedures

The barrier processes and sedimentary record were studied in 1986 and 1987, and diverse geomorphic and geologic studies over nearly a century provided the background for the overall setting and processes (e.g., Moseley, 1905; Pettijohn and Ridge, 1933; Pincus et al., 1951; Carter and Guy, 1980).

Trenches were cut to lake level into the different environments both parallel and perpendicular to the barrier. The facies were photographed, described, and sampled; a dip indicator was used to measure the true strike and dip of the sedimentary structures. Six, oriented vibracores (7.5 cm in diameter) were taken down to peat and/or clay. Smaller hand-driven cores were taken in the nearshore and lagoon. The vibracores were split, photographed, described, and sampled. Radiographs were made of the fine-grained facies in the cores with a medical X-ray unit. Sieves were used for the grain size analyses of the sands, and the mineralogy of the clays was determined by X-ray diffraction. Echo-sounder profiles were run both parallel and perpendicular to the barrier in the lagoon and the nearshore. A transit was used to complete the profiles across the barrier.

Observations and measurements were made during two northeast storms. Velocities of overwash sheetflows, and inlet channel flows were measured by timing wooden floats between markers, and barrier migration was measured by using markers emplaced prior to the storms. Observations and measurements were also made during southwest storms that lowered the lake level and exposed the lagoon and nearshore environments.

General setting and processes

Lake Erie is a low energy, microtidal (less than 5 cm astronomic tide) environment. Nonetheless, infrequent northeasters, which have a fetch of about 400 km, have a profound effect on the barrier because of its location and orientation (Fig. 1). For example, strong northeast winds produce storm surges in this area of the lake of as much as a meter. Moreover, surf zone storm waves a meter high with periods of 7–10 s are superimposed on the surges. However, although the northeast storms are an integral part of barrier transgression, sand supply and water level are just as important. The supply of sand to the barrier from the net E–W longshore transport system has essentially been cut off by the harbor jetties at Huron (about 3 km to the east) and by seawalls between Huron and the barrier. This loss of sand, coupled with record high water levels in 1972–73 and in 1985–86, caused by above average precipitation over the Great Lakes basin, allowed major northeast storms in the fall of 1972 and the spring of 1973 to breach the sand-starved barrier for the first time since the early 1860s (Mosely, 1905; Carter and Guy, 1980). Overwash and secondary sand transport through the channels and alongshore have caused accelerated transgression of the barrier. In the short term, transgression is greatest in the spring and fall because of the storms associated with the changing of the seasons. Shorefast ice, which forms around mid-December, and persists with open lake ice until around mid-March, damps the waves and armors the shore to protect the barrier in the winter.

The 2 km-long barrier was formerly a part of the eastern end of Cedar Point spit that formed in the Holocene by the net southeast to northwest longshore transport and deposition of sand across the mouth of Sandusky Bay. It consists of a tabular body of largely medium-grained sand with a maximum thickness of about 3 meters (Fig. 2). The barrier overlies a Holocene peat up to 15 cm thick, and/or a gray, interlaminated silt and clay. On the landward side, the lagoonal sediment consists of an organic-rich mud that overlies the peat, and on the lakeward side the nearshore sediment consists of fine to medium grained sand in the form of

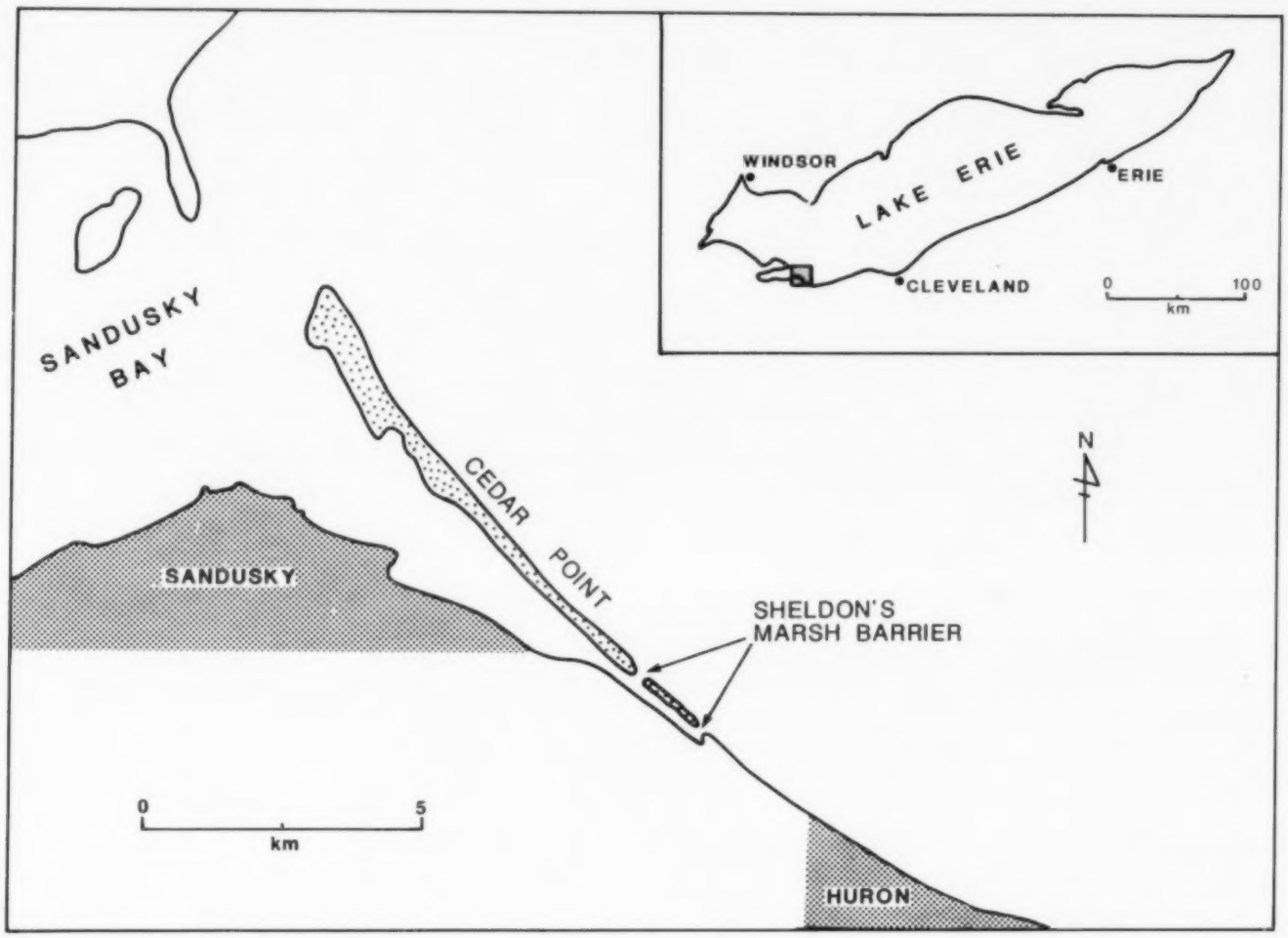

Fig. 1. Location map of Sheldon's Marsh barrier. The location and orientation of the barrier make it vulnerable to surges and waves created by northeast windstorms.

thin, irregular bars with intervening/underlying peat and/or interlaminated silt and clay.

Environments and facies

The environments and associated facies in this barrier system are: nearshore, foreshore, backshore/washover terrace, channel, and lagoon. The major sedimentological characteristics of these facies are shown on Table 1.

Nearshore

The nearshore consists of a layer of sand less than one meter thick sculpted into bars that roughly parallel the shoreline (Figs. 2 and 3). There is generally a segmented, main bar, with a relief of up to one meter, about 30 m from the shoreline. The bar segments, which lie adjacent to the foreshore, have irregular, arcuate shapes up to 30 meters long by one meter thick and relatively steep slipfaces adjacent to the runnel. The runnel surface is rippled. The facies consists of asymmetrical, ripple cross-stratification in the runnel, low-angle laminations at the bar surface and tabular sets at the slipface. These nearshore forms and associated stratification appear quite similar to the ridge and runnel systems of Lake Michigan (Davis et al., 1972).

We did not observe the formation of the bars. However, observation of the surf zone during storms suggests that wave ray convergence toward the bars may lead to elevated water levels and the development of overwash, and if of sufficient duration, of channels. This process has been described by Leatherman (1985) along the Atlantic Coast.

Foreshore

The foreshore, which is separated from the nearshore by the plunge step, consists of a narrow (a few meters wide), plane to slightly concave-up surface that dips lakeward at 3° to 12° (Fig. 4).

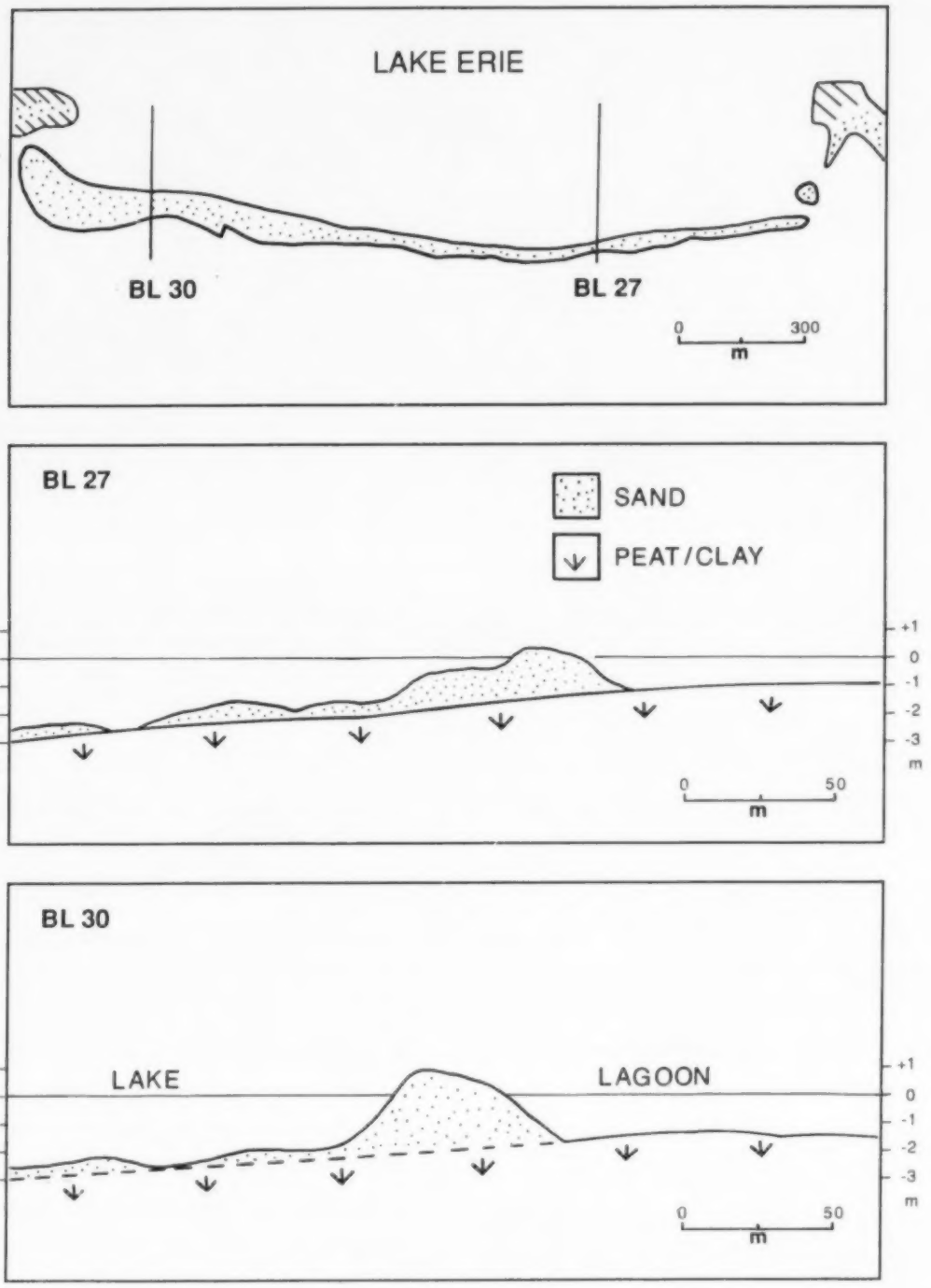

Fig. 2. Barrier plan and cross-section in 1986. The nearshore surface has a "ridge and runnel" topography that indicates the presence of nearshore bars. The horizontal line in the cross-sections represents water level at the time of the survey. The hachured pattern in the plan view represents seawalls built to try to protect adjacent parts of the barrier. Two vibracores adjacent to BL 27 provide good control for the sand-peat/clay contact whereas the closest vibracore to BL 30 was 300 m to the east.

The plunge step consists of granules and pebbles, whereas the foreshore consists of a well sorted, medium-grained sand. The sand makes up thin, lakeward-dipping laminations (Fig. 5). The laminations may be inversely graded with heavy mineral grains grading up into quartz, feldspar, and rock fragment grains but more commonly the individual laminations are hard to define or are incomplete. The laminations commonly pinch-out updip and may truncate other laminations at low angles. They are roughly horizontal in sections parallel to the shoreline.

The landward-most plunge of the waves concentrates the coarser clasts at the plunge step (Davis et al., 1972) and foreshore laminations are produced by wave backwash (Clifton 1969). The low-angle discontinuities are likely caused by changes in wave climate that modify the slope of the

TABLE 1

Characteristics of the sedimentary structures

Environment/ facies	Type	Thickness and lateral extent	Orientation and dip; other characteristics
Nearshore	Tabular sets	Several centimeters to a few decimeters; several meters parallel to shoreline	Landward, 20° to 30°; bar slip faces of a few decimeters
	Asymmetric ripples	A few centimeters to several centimeters; a few meters parallel to shoreline	Landward and alongshore; ripples in runnels
	Laminations	A few centimeters; a few meters parallel to shoreline	Lakeward, unknown
Foreshore	Laminations	A few millimeters to one centimeter; a few meters normal to the shoreline and several meters parallel to the shoreline	Lakeward, 3° to 12°; laminations are commonly inversely graded, and may truncate one another
Backshore/Washover Terrace	Laminations	A few millimeters to two centimeters; a few to several meters both normal and parallel to the shoreline	Landward within a 120° sector, 1° to 3°; laminations are normally and inversely graded. Heavy mineral laminations and concentrations in places
	Solitary trough sets	A few centimeters; up to one meter normal and several centimeters parallel to the shoreline	Landward
	Tabular sets	Several centimeters to a few decimeters; a few to several meters both normal and parallel to the shoreline. Sets thicken abruptly at fan margin	Landward, 24° to 32°; sets and cosets in places separated by subhorizontal laminations (topsets). Reactivation surfaces are common; deformed bedding
Channel	Laminations	Several millimeters to a few centimeters; unknown	Horizontal; coarse sand with granules and pebbles

foreshore (generally, the larger the waves, the steeper the foreshore). Erosion of this facies takes place during storms when the uprush and/or waves (when the barrier is submerged) transport nearshore and foreshore sand beyond the berm, onto or beyond the backshore/washover terrace. The foreshore is then reformed during fairweather periods.

Backshore/washover terrace

This environment, which is separated from the foreshore by the berm, consists of a relatively wide (meters to a few tens of meters), plane to gently undulating surface that dips landward at 1° to 3° to a slipface at the margin of the lagoon (Fig. 6). In general, a well sorted, medium-grained sand makes up the facies, but shale and peat clasts, fish skeletons, and tree branches are also present.

The facies is characterized by gently landward-dipping laminations and very thin beds (Fig. 7). The individual laminations are hard to define, but many appear to be inversely graded and/or incomplete. Heavy-mineral rich laminations are most common near the berm. Grain size, on the other hand, increases toward the lagoon (Harrell and Braun, 1987). Stratification generally thickens toward the lagoon and the dips become steeper (up to 10°) as the overlying laminations/beds commonly truncate the underlying ones. Locally, shallow (less than 2 cm thick) scours, infilled with coarse sand, granules, and pebbles form a part of the facies.

Sheetflow with velocities ranging from 1 to almost 3 m s^{-1} at water depths less than 10 cm during

Fig. 3. Storm-modified nearshore bars exposed during a major setdown. Wind-driven waves and currents have smoothed and flattened the bars. Treelines, from left margin to center (just above the foreshore/berm) and in the right quarter are about 2 km to the west. The trees in the right center cover the westernmost portion of the barrier that is separated from the main part of the barrier by a channel.

Fig. 4. Steep, storm-sculpted foreshore, berm, and backshore/washover terrace. Swash marks consisting of gravel and peat fragments cap the foreshore surface and coarse, light-colored quartz and feldspar grains mark the margins of the small fans on the backshore/washover terrace surface. The terrace is bordered by water lilies (*Nymphaea* sp.) in the lagoon and the large dark blocks in the distance are peat clasts that have been eroded from the nearshore.

overwash events produces the gently dipping laminations and beds. The coarser, light minerals and rock fragment grains apparently are concentrated near the surface of the sheet flows and are transported farther than the finer, heavy minerals across the barrier surface toward the lagoon. The downdip thickening of the stratification may reflect a landward decrease in flow strength caused by a decrease in the slope of the barrier. The barrier surface during fair weather is modified by wind that sculpts the fine to medium grains into small-scale ripples and deflation surfaces.

Individual washover fans and associated cross-stratification are most easily recognized near the lagoon margin. The upper portion of each fan consists of a gently dipping, convex-up surface, a few to several meters across, that slopes toward the lagoon. At the lagoon's edge, the fan margins are arcuate in plan view and the slipface surfaces dip landward at about 30° (Fig. 8). These fan

Fig. 5. Foreshore laminations truncating backshore/washover terrace laminations. Laminations are defined primarily by heavy minerals.

Fig. 6. Backshore/washover terrace during the waning stage of a moderate northeast windstorm. Note thin washover deposits adjacent to a wind and rain modified surface in the foreground, and a prominent washover lobe beyond the shovel in an area covered by washover deposits from the storm.

margin surfaces and associated stratification commonly are modified by waves from the lagoon.

The stratification of a fan near the lagoon margin consists of laminations and thin beds that dip gently away from the fan axes (Fig. 9) and more steeply parallel to the fan axes (Fig. 10). The contacts are well-defined between the laminations/beds and internally the grain size in the foresets increases downdip. Reactivation surfaces which are produced by wave erosion, commonly truncate the foresets. Also, overturned foresets were observed in places, and at one fan margin, a turtle nest with a width of about 20 cm and a depth of about 30 cm, which completely destroyed the stratification, was found in the sand.

The well-developed fans at the lagoon margin are produced by semi-confined flows, and the cross-stratification (avalanche foresets) is produced by grain flow down the slipface. Confinement of the sheetflow to swales between existing fans leads

Fig. 7. Backshore laminations defined by textural and mineralogic differences. Note the nearly horizontal nature of the stratification; the coarser laminations probably represent higher energy events and/or more distal portions of the individual fans.

Fig. 8. Fan margins modified by waves during a drop in water level. Dark area in the lagoon in the middle distance is a clump of water lilies (*Nymphaea* sp.).

to overlapping stratification with subhorizontal erosional contacts between the fans. Coalescence of the washover fans leads to the development of the fan terrace.

Channel

The channels range from several meters to a few hundred meters wide, but are usually no more than about one meter deep (the depth to peat and/or clay). The sediment making up the channel floor consists largely of coarse sand although pebbles and cobbles are concentrated at the channel throats. Partially filled channels observed following storms are covered by 2- and 3-dimensional ripples with heights of a few centimeters and spacings of 10 to 20 cm.

Channel floor stratification, inferred from vibracores, consists of horizontal laminations and thin beds of poorly sorted coarse sand, with minor granules, and pebbles.

Landward flow velocities in the channels during

Fig. 9. Strike section through a fan limb; fan axis is to the right with flow toward the observer,. Heavy minerals help define the stratification; holes in the trench wall are former locations of pebbles. Note reactivation surfaces, and truncation of the fan margin stratification by another fan.

Fig. 10. Dip section (flow toward lagoon, parallel to trench face) through superimposed fans. Note the reactivation surfaces, relict lagoon foreshore laminations, and thicker foresets at the lagoon margin. The uppermost unit illustrates the change from sheetflow (dips of a few degrees) to grain flow (dips of 24°–32°) produced during the last washover event.

northeast storms ranged from about 0.6 to 2.0 m s^{-1} and averaged about 1.2 m s^{-1}. These velocities in conjunction with the coarse sand and shallow channel depths appear to meet the requirements for upper plane bed conditions (Rubin and McCulloch, 1980) which are consistent with the horizontal laminations. The sand transported landward through the channels during storms is deposited as deltas in the lagoon. These deltas are eventually welded to the lagoon side of the barrier by the landward migration of the barrier. The stratification of the deltas is probably quite similar to the washover fans with low angle laminations on the delta surface and landward-dipping foresets along the delta front.

Lagoon

The lagoon is about 2 km-wide and has an average depth of about 1m. It is characterized by

fine-grained, organic-rich sediment and along its margins by plants such as cattails, (*Typha* sp.) and water lilies (*Nymphaea* sp.). Small roots, mollusk shells, and fish bones are present, and in places, the winnowing of the mud produces thin laminations of fine sand. The sediment is probably derived from both the lakeward side and the landward side of the barrier. The silt, clay, and plant debris settles and accumulates by vertical accretion whereas the sand is concentrated by small waves and currents along the margins of the lagoon.

Facies architecture

The barrier cross-section is roughly rectangular. The foreshore intersects a sand sheet/bar or Holocene peat/clay, and the washover terrace intersects the fine-grained sediment of the lagoon or Holocene peat/clay. The barrier has an average thickness of about 1 m and a maximum thickness of about 3 m. Its width, which is quite variable, measured from washover margin to plunge step averages about 30 m, and its length is about 1,800 m for a sand volume of about 54,000 m^3.

The backshore/washover terrace facies dominates the sedimentary record (Fig. 11). Crucial to the process that produces this facies is the low energy lagoon in which there is little modification of the sand eroded from the shoreface and transported by storm overwash or by channels to the lagoon.

Thin horizontal beds of coarse sand and gravel of the channel facies (and possibly lower foreset/bottomset of the backshore/washover terrace facies) overlie the Holocene peat/clay with a sharp contact. This indicates erosion of the organic-rich lagoonal mud by the channels and/or by turbulence produced by overwash. The coarse sand and gravel is usually overlain in sharp to gradational contacts, by tabular sets and gently landward-dipping laminations of medium sand of the backshore/washover terrace facies (Fig. 12). The interbedded nature of the sets and laminations reflects the influence of the barrier topography and storm surge water levels. Cosets are produced when the backshore/washover terrace is partly submerged and a new set of avalanche foresets are deposited over an existing set during overwash. Naturally, the steeper the backshore/washover terrace slope and the higher the water level the thicker the set. The thickest sets form at the lagoon margin where the slipface extends to the lagoon bottom. The common occurrence of gently dipping laminations (topsets) interbedded with the foresets indicates the largely depositional nature of the overwash process and the significance of water level in the deposition of the topsets and foresets. Overall, there is an upward decrease in set thickness and an upward increase in topset laminations. This reflects the landward migration of the higher, lakeward side of the barrier and greater deposition from sheetflow on the topographically highest portions of the barrier. In addition, winnowing of the backshore/washover terrace by wind produces a coarser deposit.

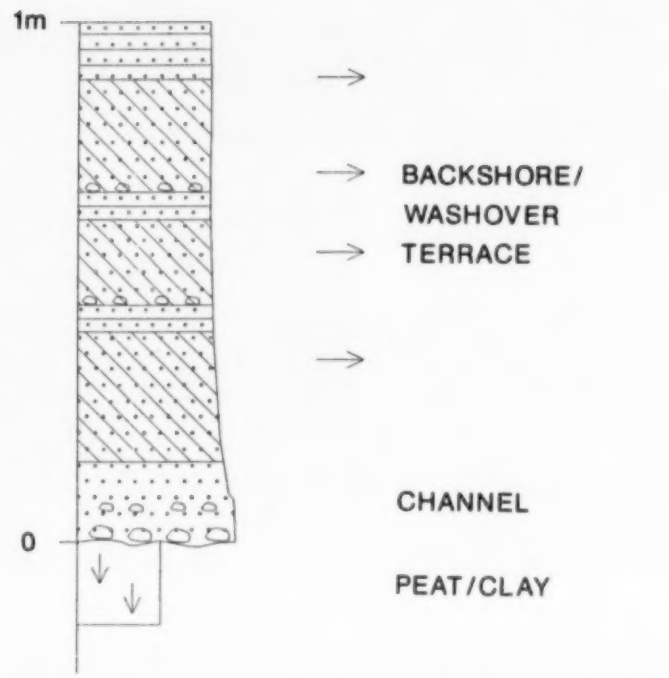

Fig. 11. Idealized transgressive barrier sequence unconformably overlying Holocene peat/clay. Arrows represent flow directions measured from the gently dipping laminations of the barrier surface and the avalanche foresets from the washover fan margins.

The nearshore ridge and runnel environment migrates landward during fairweather and becomes welded to the foreshore. The low angle laminations and tabular sets of this environment can be distinguished from the low angle laminations and tabular sets of the backshore/washover terrace facies by the lakeward-sloping contact that separates the ridge and runnel from the foreshore and/or back-

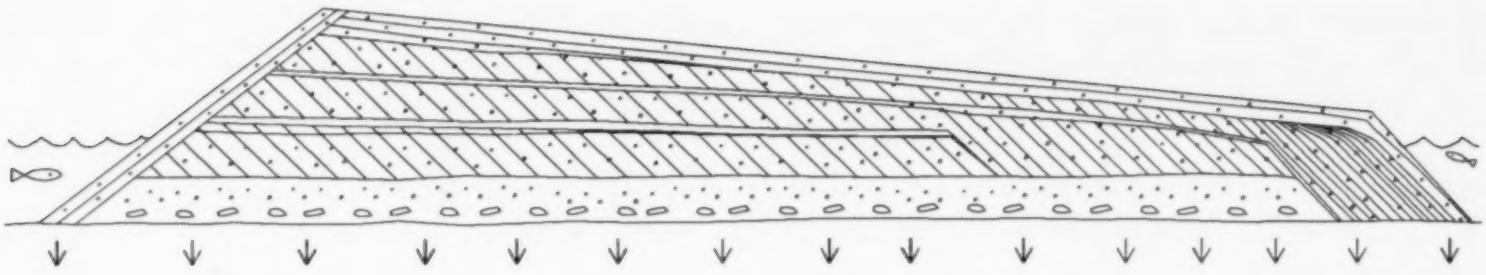

Fig. 12. Idealized transgressive barrier cross-section with foreshore, backshore/washover terrace, and channel facies overlying Holocene peat/clay. Note the thick foresets at the lagoon margin (right side) and the predominance of washover cross-stratification.

shore/washover terrace facies and by ripples developed in the runnel. Like the foreshore facies, this facies is quite ephemeral as it is the first facies to be eroded during transgression of the barrier with its sand transported across the barrier by washover during periods of high lake level, or offshore during periods of low lake level when the storm surges are too low to cause overwash. Foreshore laminations truncate the stratification of the backshore/washover terrace and welded nearshore facies producing a characteristic, angular contact. However, the foreshore facies is only present along the lakeward margin of the barrier because strong offshore winds lack the fetch and depth to produce sufficiently large waves for appreciable uprush along the lagoon margin, and offshore winds lead to a drop in water level that also restricts wave size.

The welding of the backshore/washover terrace to the deltas deposited in the lagoon by flow through the channels was not observed. However, the migration and welding of the facies would likely produce the record of a small delta encompassed within the washover fan, with the orientation and thickness of the washover foresets modified to accommodate the delta giving thinner sets over the delta surface enclosed by thicker sets around the delta margin.

Discussion and conclusions

High water levels coupled with windstorms and a sparse sand supply have led to the formation and landward migration of a nearly featureless, overwash-dominated barrier island from a portion of a baymouth spit formerly characterized by well-developed foredunes. The 30 m wide barrier has retreated about 240 m in a 15 year period; the migration rate is nonlinear with the greatest migration occuring during storms at the highest water levels. Retreat has been rapid enough that foredunes have had insufficient time to become established. However, except for the net east to west longshore transport of sand along the barrier island, the barrier has maintained roughly its same shape, orientation, and mass because of the shore-normal processes of overwash, bar welding, and inlet filling. A drop in lake level of about 60 cm from 1986 has greatly reduced the landward migration of the barrier, and plants and small wind blown dunes are now present on the barrier surface. Lakeward of the barrier are nearshore bars that overlie Holocene peat and clay.

The overall sedimentary record of this barrier is similar to the transgressive model summarized in Franks (1980, fig. 3A). In this classic model, the barrier migrates landward over lagoon deposits until water level stops rising, there is a marked increase in the supply of sand to the barrier, and/or there is a marked decrease in storm activity.

In spite of water level rises of 6 to 11 cm/yr for periods of several years, the barrier has migrated landward without a loss of mass. This indicates that erosion and landward sediment transport have been sufficiently rapid to prevent submergence and drowning of the barrier. There are at least two causes for this: one, the low relief of the barrier that has facilitated overwash and the cutting of channels, and two, sufficient wave energy to erode and transport the sediment landward. Of utmost importance to barrier relief and wave energy has been the high water levels of the lake. If high water levels and storms had continued, the barrier would have migrated to the landward margin of the

lagoon where the migration of the barrier would have slowed and eventually stopped because of a greater landward slope. This scenario is somewhat akin to modern barriers along the Atlantic Coast where a rise in water level and a decrease in sand is leading to the erosion and landward migration of the barriers. In a natural lacustrine system unencumbered by the jetties, groins, and seawalls that reduce, restrict, and/or block the longshore transport of sand along the Lake Erie shore, a high lake level would usually lead to a higher sand supply because of accelerated shore erosion. Then the nature and rate of barrier migration could be markedly changed because of the increased sand flux. Holocene transgressive lacustrine shoreface deposits reported from Lake Michigan overlie "...forested land surface or back-beach marsh sediments." (Fraser and Hester, 1977, p. 1197) or "...washover and eolian foresets." (Thompson, 1989, p. 720). If sufficient sand were transported to the barrier, we think that the formation of a sequence of land or marsh sediments overlain by shoreface deposits is most likely, unless there was a marked decrease in wave energy associated with a rapid water level rise and then possibly the barrier could be drowned with washover and eolian deposits capped by shoreface deposits.

In a mesoscopic sense the coarse sand, granules, and pebbles of the channel facies at the barrier–Holocene lake/lagoon contact might well be interpreted as a transgressive lag. However, the scarcity of coarse sediment in the lagoon and underlying Holocene peat and clay indicates that the sediment is not a lag, but has been deposited and redeposited by the highest energy waves and currents. The channels by reworking the barrier concentrate the granules and pebbles over the floor of the channel, and the abundance of this coarse sediment at the base of the barrier suggests the importance of inlet/channel processes to sedimentation.

The formation of the landward-dipping laminations and tabular sets from washover events is particularly important because the sets form such a major part of the sedimentary record. Crucial to set formation is the gentle, one to two degree surface from the berm to the lagoon on the washover terrace. This surface, which develops due to greater deposition near the berm during fair-weather and minor storm conditions, has the potential on this 30 m wide barrier, for accommodating sets as thick as one meter at the terrace surface near the lagoon. However, the tabular sets found in the barrier are, in general, no more than a few decimeters thick and several meters long. These thin sets reflect the dynamic equilibrium among storm surge levels, washover terrace slope, and barrier width. For example, water level data from a major storm in November 1972 showed durations ranging from 1 to 9 h where the water level stayed within a 15 cm range. If overwash were relatively uniform, a tabular set a few meters long could be built up in a few hours in this way. Assume that overwash frequency equals wave period, then for a 6 s period wave if a 5 mm lamination is deposited on the avalanche face each overwash a set 6 m long can form in one hour. Cosets can develop during a rise to another somewhat stationary water level, or by compaction of the loosely deposited sand of a previous event, and solitary sets can develop during a drop in water level. Set thickness increases downslope up to the margin of the terrace where the thickness of the avalanche foresets are only constrained by the relief of the barrier at the terrace margin. The narrower the barrier, the greater the length of the thick sets that form at the terrace margin for a similar flux of sand. The thickest sets that form on the washover terrace simply represent the greatest still water level for a given slope and sand flux and not necessarily the intensity of the storm. Also, the thicknesses of the sets at the terrace margin are largely independent of the storm intensity for as long as there is overwash, the relief at the terrace margin controls the set thickness, unless set migration on the terrace reaches the lagoon margin at which time the relief equals the former relief plus the new set thickness. This relief decreases with time as the avalanche foresets at the terrace margin are initially poorly compacted, but become more compact leading to thinner sets.

The sediment from the channel is much coarser (median equals coarse sand) than the sediment from the backshore/washover terrace, and the sediment from the backshore/washover terrace is coarser than the sediment from the foreshore. However, the differences are small and the medians

picked from cumulative curves are almost identical especially for the washover terrace where samples were analyzed from the washover surface and also from the washover margin. For example, from five transects across the barrier, the median foreshore grain size is fine–medium sand, and the median grain size for both the washover surface and washover margin is medium sand. We think that the small difference in grain size is probably due to the rapid migration of the barrier which limits the development of somewhat stable environments, i.e. the nearly constant erosion and transport of the foreshore and underlying and laterally adjacent washover and channel deposits precludes the development of any type of equilibrium condition and a grain size/texture that could be indicative of a specific environment. However, if deposition from the less frequent but higher energy events is the rule, perhaps in transgressive deposits such as this one the lack of well-defined textural trends is not surprising. The scattered pebbles in the washover environment are useful, however, in that they indicate deposition from water, and not from wind.

What is the likelihood of preservation of this barrier island? At first glance, preservation of this relatively narrow, thin sand barrier seems unlikely, however, there are Pleistocene sand deposits that have been interpreted as beach ridges in the Great Lakes area (Leverett and Taylor, 1915; Totten, 1982). Moreover, Holocene coastal lacustrine deposits have been described from areas adjacent to Lake Michigan (Fraser and Hester, 1977; Thompson, 1989) and Lake Huron (Martini, 1975). And although continental deposits are less likely to be preserved in the rock record than marine deposits, if there were a marked change in the tectonic setting, these deposits could well be preserved.

Aside from the overall geologic setting, what key features would characterize this lacustrine barrier in the rock record? The base of the barrier is characterized by thin (one to two decimeters in scale) horizontal laminations of coarse sand, granules, and pebbles of the channel floor that overlie with a sharp, erosional contact the transgressed surface. These laminations are overlain by structures of the washover terrace consisting of subhorizontal laminations on the scale of centimeters interbedded with tabular sets that range in thickness from a few to several decimeters. The laminations dip in the same direction (onshore) as the foresets in the tabular sets. In a dip section the laminations can be traced downdip into the foresets, and in places (terrace margin) the foresets abruptly increase in thickness. In a strike section, the laminations of both the subhorizontal laminations and foresets display horizontal to gentle convex-up shapes with a lateral extent of a few to several meters that conform to the form of the individual washovers. In addition, on the other side of the barrier the gently dipping laminations of the foreshore, which dip lakeward in the opposite direction from the washover terrace structures, may truncate the washover terrace stratification and/or the welded nearshore bar stratification.

The scarcity of bioturbation in the Lake Erie barrier is largely the result of rapid erosion and redeposition. If the barrier stops transgressing, plants, such as willows (*Salix* sp.), and animals, such as turtles, would presumably destroy the stratification, however the Holocene examples from the Great Lakes (Martini, 1975; Fraser and Hester, 1977; Thompson, 1989) exhibit well-preserved stratification which suggests that the sedimentary structures would largely be preserved.

Acknowledgments

This article is based on a Masters thesis by Thomas F. Bray, Jr. We wish to thank the Ohio Department of Natural Resources for a grant that made this project possible, and to Gene Wright, David Klarer, and Scott Hoffman of the Old Woman Creek National Estuarine Sanctuary for their support and assistance. We are grateful to Don Guy, Jr., Nate Fuller, and Dale Liebenthal of the Ohio Geological Survey for the echo sounding and for the loan of maps, aerial photographs, and equipment and to Ted Shaw, Tom Brocculeri, Roque Rokovich, and David Bray who helped in the mapping, coring, and trenching. Jim Harrell, Peter Martini, Bob Morten, and Bob Schwartz provided constructive reviews. Sharon Steuart ably did the word processing.

References

Allen, P.A. and Collinson, J.D., 1986. Lakes. In: H.G. Reading (Editor), Sedimentary Environments and Facies. Blackwell, Oxford, pp. 63–94.

Boothroyd, J.C., Friedrich, N.E. and McGinn, S.R., 1985. Geology of microtidal coastal lagoons: Rhode Island. In: G.F. Oertel and S.P. Leatherman (Editors), Barrier Islands. Mar. Geol., 63: 35–76.

Carter, C.H. and Guy, D.E., Jr., 1980. Lake Erie shore erosion and flooding, Erie and Sandusky Counties, Ohio: setting, processes, and recession rate from 1877 to 1973. Ohio Geol. Surv. Rep. Invest., 115, 130 pp.

Clifton, H.E., 1969. Beach lamination: nature and origin. Mar. Geol., 7: 553–559.

Davies, D.K., Ethridge, F.G. and Berg, R.R., 1971. Recognition of barrier environments. Am. Assoc. Pet. Geol. Bull., 55: 550–565.

Davis, R.A., Fox, W.T., Hayes, M.O. and Boothroyd, J.C., 1972. Comparison of ridge and runnel systems in tidal and non-tidal environments. J. Sediment. Petrol., 42: 413–421.

Franks, P.C., 1980. Models of marine transgression-examples from the Lower Cretaceous fluvial and paralic deposits, north-central Kansas. Geology, 8: 56–61.

Fraser, G.S. and Hester, N.C., 1977. Sediments and sedimentary structures of a beach-ridge complex, southwestern shore of Lake Michigan: J. Sediment. Petrol., 47: 1187–1200.

Galloway, W.E. and Hobday, D.K., 1983. Terrigenous Clastic Depositional Systems. Springer, New York, 423 pp.

Harrell, J.A. and Braun, R.B., 1987. Roller micrometer analysis of grain size and shape sorting within sand laminae from lacustrine barrier islands. Am. Assoc. Pet. Geol. Bull., 71: 564.

Heron, S.D., Jr., Moslow, T.F., Berelson, W.M., Herbert, J.R., Steele III, G.A. and Sussman, K.R., 1984. Holocene sedimentation of a wave-dominated barrier-island shoreline. Cape Lookout, North Carolina. Mar. Geol., 60: 413–434.

Kahn, J.H. and Roberts, H.H., 1982. Variations in storm response along a microtidal transgressive barrier-island arc. Sediment. Geol., 33: 129–146.

Kraft, J.C., 1971. Sedimentary facies patterns and geologic history of a Holocene marine transgression. Geol. Soc. Am. Bull., 82: 2131–2158.

Kraft, J.C. and John, C.J., 1979. Lateral and vertical facies relations of a transgressive barrier. Am. Assoc. Pet. Geol. Bull., 63: 2145–2163.

Leatherman, S.P., 1976. Barrier island dynamics: overwash processes and eolian transport. Proc., 15th Int. Coastal Eng. Conf., Honolulu, Hawaii, 1958–1974.

Leatherman, S.P., 1978. Migration of Assateague Island, Maryland, by inlet and overwash processes. Geology, 7: 104–107.

Leatherman, S.P., 1985. Barrier Island Handbook. Natl. Park Service, Boston, 109 pp.

Leatherman, S.P. and Williams, A.T., 1977. Lateral textural grading in overwash sediments. Earth Surface Processes, 2: 333–341.

Leatherman, S.P. and Zaremba, R.E., 1986. Dynamics of a northern barrier beach: Nauset Spit, Cape Cod, Massachusetts. Geol. Soc. Am. Bull., 97: 116–124.

Leverett, F. and Taylor, F.B., 1915. The Pleistocene of Indiana and Michigan and the history of the Great Lakes. U.S. Geol. Surv. Monogr. 53, 529 pp.

Martini, I.P., 1975. Sedimentology of a lacustrine barrier system at Wasaga Beach, Ontario, Canada. Sediment. Geol., 14: 169–190.

Moseley, E.L., 1905. Formation of Sandusky Bay and Cedar Point. Proc. Ohio Acad. Sci., 5: 79–238.

Oertel, G.F., 1985. The barrier island system. Mar. Geol., 63: 1–18.

Pettijohn, F.J. and Ridge, J.D., 1932. A textural variation series of beach sands from Cedar Point, Ohio. J. Sediment. Petrol., 2: 76–88.

Pettijohn, F.J. and Ridge, J.D., 1933. A mineral variation series of beach sands from Cedar Point, Ohio. J. Sediment. Petrol., 3: 92–94.

Picard, M.D. and High, L.H., 1972. Criteria for recognizing lacustrine rocks. In J.K. Rigby and W.K. Hamblin (Editors), Recognition of Ancient Sedimentary Environments. Soc. Econ. Paleontol. Mineral. Spec. Publ., 16: 108–145.

Pincus, H.J., Rosenbloom, M.L. and Humphris, C.C., 1951. 1950 investigation of Lake Erie sediments, vicinity of Sandusky, Ohio. Ohio Geol. Surv. Rep. Invest., 9, 37 pp.

Reineck, H.E., 1967. Layered sediments of tidal flats, beaches, and shelf bottoms of the North Sea. In: G. Lauff (Editor), Estuaries: Am. Assoc. Adv. Sci., Publ., 83: 191–206.

Reineck, H.E. and Singh, I.B., 1973. Depositional Sedimentary Environments. Springer, New York. 439 pp.

Rubin, D.M. and McCulloch, D.S., 1980. Single and superimposed bedforms: a synthesis of San Francisco Bay and flume observations. Sediment. Geol. 26: 207–231.

Schwartz, R.K., 1982. Bedform and stratification characteristics of some modern small-scale washover sand bodies. Sedimentology, 29: 835–849.

Thompson, T.A., 1989. Anatomy of a transgression along the southeastern shore of Lake Michigan. J. Coastal Res., 5: 711–724.

Totten, S.M., 1982. Pleistocene beaches and strandlines bordering Lake Erie. In G.W. White (Editor), Glacial Geology of Northeastern Ohio. Ohio Geol. Sur. Bull., 86: 52–60.

Van Straaten, L.M.J.U., 1954. Composition and structure of recent marine sediments in the Netherlands. Leidse Geol. Meded., 19: 1–110.

Marine Geology, 105 (1992) 169–209
Elsevier Science Publishers B.V., Amsterdam

Carbonate platforms along the southeast Bahamas–Hispaniola collision zone

Henry T. Mullins[a], Nancy Breen[b], James Dolan[c], Robert W. Wellner[d], John L. Petruccione[d], Mark Gaylord[d], Brannon Andersen[d], Allan J. Melillo[e], Anita D. Jurgens[e] and Daniel Orange[f]

[a]*Department of Geology, Syracuse University, Syracuse, NY 13244, USA*
[b]*Department of Geology, Stanford University, Palo Alto, CA 94305, USA*
[c]*Division of Geological and Planetary Science, California Institute of Technology, Pasadena, CA 91125, USA*
[d]*Department of Geology, Syracuse University, Syracuse, NY 13244, USA*
[e]*Chevron U.S.A., New Orleans, LA 70112, USA*
[f]*Earth Sciences Board, University of California, Santa Cruz, CA 95064, USA*

(Received June 6, 1991; revision accepted August 18, 1991)

ABSTRACT

Mullins, H.T., Breen, N., Dolan, J., Wellner, R.W., Petruccione, J.L., Gaylord, M., Andersen, B., Melillo, A.J., Jurgens, A.D. and Orange, D., 1992. Carbonate platforms along the southeast Bahamas–Hispaniola collision zone. Mar. Geol., 105: 169–209.

The southeast Bahama banks have been colliding with the island of Hispaniola along a restraining bend within the northern Caribbean plate boundary zone since the late Miocene. A SeaMARC II/seismic reflection investigation was conducted along the deep-water flanks of Mouchoir Bank, Silver Bank, and Navidad Bank to evaluate the response of these carbonate platforms to active plate tectonic collision. Overall, our data provide evidence of large-scale platform margin retreat which contrasts sharply with the prograding platform margins in the tectonically passive northwest Bahamas.

North of Silver Bank there is a large ($\sim$5,000 km^2), deep-water (3,000–4,000 m) plateau that records the drowning and step-back ($\sim$50 km) of an Early Cretaceous carbonate platform margin. Intact (uneroded) segments of this Cretaceous platform margin may occur along the seaward edge of the deep-water plateau (Bahama Escarpment) separated by large (20 km across) erosional reentrants. A coalescing system of broad (up to 10 km), shallow (<200 m relief) canyons, akin to mountainous avalanche chutes, funnel debris into the reentrants from the flank of Silver Bank. The reentrants are interpreted as zones of structural weakness produced by passage of the Atlantic spreading center along a transform plate boundary during the Late Jurassic–Early Cretaceous. Drowning and step-back appear to be part of a global response of carbonate platforms to a mid-Cretaceous tectonic pulse of ocean crust formation, and relative sea-level rise.

The southern margin of Mouchoir Bank has also been drowned and has stepped-back by about 30 km. This event occurred during the Late Tertiary prior to the mid-Pliocene and is attributed to tectonic tilting and subsidence resulting from oblique underthrusting of the southeast Bahamas beneath Hispaniola. The southern margin of Mouchoir Bank is also characterized by large ($\sim$20 km across) amphitheater-shaped "scallops" that expose Tertiary shallow-water limestones along their deep-water flanks. Seaward of one scallop is a large (25 km wide, 50 km long) mass movement with flow lines preserved on the seafloor. We interpret these scallops as catastrophic collapse structures triggered by large earthquakes generated along the collision zone since the Late Tertiary.

South of Navidad and Silver banks is a very complex seafloor morphology resulting in part from the accretion of a portion of the Bahamas onto Hispaniola. There is also a series of E–W oriented down-to-basin normal faults that have caused the platform margin to retreat. Extensional stress along this predominantly transpressive plate boundary may be a consequence of rotation of the nearby Puerto Rico block or lithospheric bending during oblique subduction.

This study provides an initial framework within which to view the actualistic response of carbonate platforms to plate tectonic collision.

Introduction

The Bahamas have long been used as a modern analog for the interpretation of the structural and stratigraphic development of carbonate platforms in the rock record (Mullins and Lynts, 1977; Schlager and Ginsburg, 1981; Sheridan et al., 1988). The northwest Bahamas, which consist of

0025-3227/92/$05.00 © 1992 — Elsevier Science Publishers B.V. All rights reserved

large, coalesced banks (Eberli and Ginsburg, 1987), are a part of the passive continental margin of eastern North America (Fig. 1). Numerous studies here have investigated the response of carbonate platforms to passive margin subsidence, eustacy, and oceanographic processes (see review by Sheridan et al., 1988) and documented the overall progradational nature of the platforms.

However, as pointed out by Uchupi et al. (1971), the southeast Bahama Banks appear to be fundamentally different from their northwestern counterparts, both morphologically and structurally. Rather than large coalesced banks, the southeastern Bahamas consist of a series of small isolated platforms with "scalloped" bank margins which led Mullins and Hine (1989) to speculate that the southeast Bahamas may be undergoing erosional retreat.

Today, the southeast Bahamas are actively colliding with the island of Hispaniola along a restraining bend within the northern Caribbean plate boundary (Fig. 2; Mann et al., 1984). Collision began in the late Miocene (Sykes et al., 1982) and since then a well-developed fold and thrust belt has evolved along an accretionary prism north of Hispaniola (Austin, 1983; Dillon et al., 1987, 1992). Collision continues today as evidenced by high seismicity along the northeast margin of Hispaniola, including large earthquakes such as the 8.1 Ms event which occurred in 1946 (McCann and Pennington, 1990). Data on earthquake focal depths and mechanisms define a subducted slab beneath northeast Hispaniola resulting from oblique underthrusting of the southeast Bahamas (McCann and Sykes, 1984). Clusters of earthquake epicenters occur offshore where Silver Bank and Navidad Bank indent the northern margin of Hispaniola (Bracey and Vogt, 1970). On-land, the dominant neo-tectonic structures in northern Hispaniola are left-lateral strike-slip faults which are a response to overall plate motions in the northern Caribbean (Mann et al., 1990).

The objective of this study is to define the response of carbonate platforms to this active plate tectonic collision. Previous studies of carbonate platform evolution in the Bahamas have focused on passive margin platform response in the northwest (Sheridan et al., 1988). In the rock record,

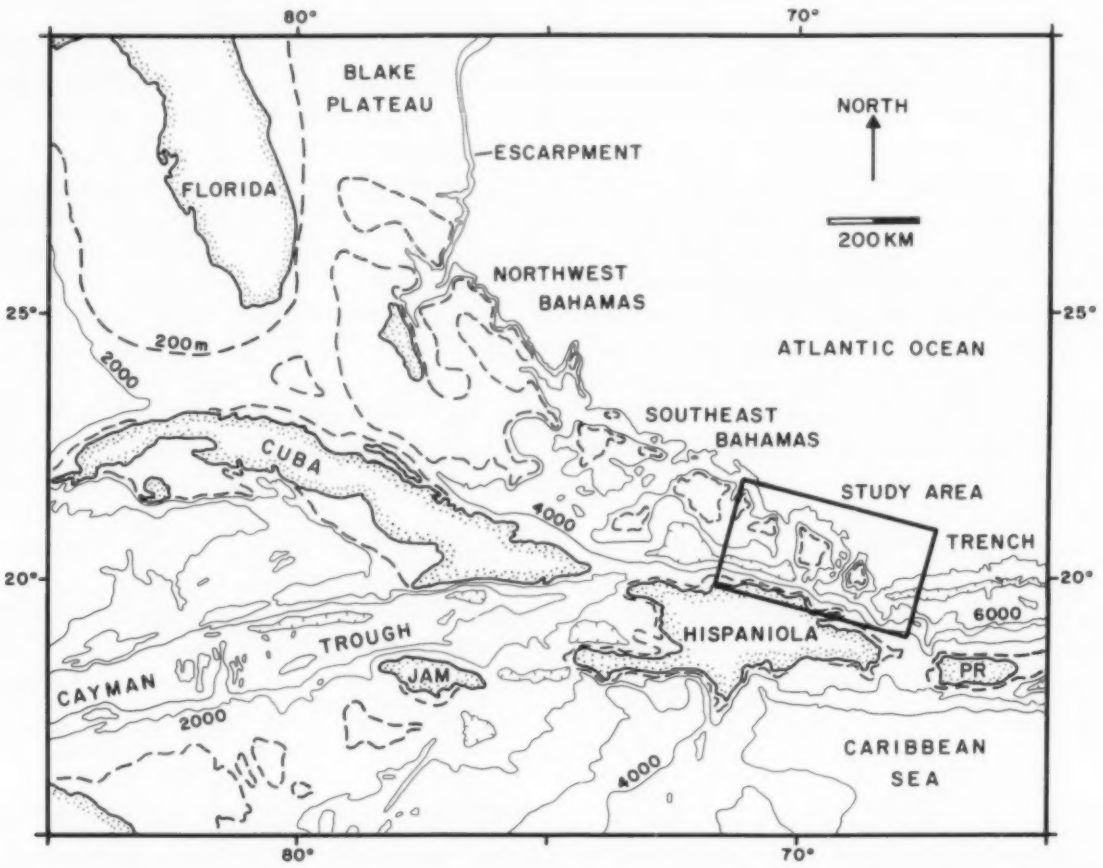

Fig. 1. General index map of Bahama–northern Caribbean region illustrating location of study area (outlined). Bathymetric contours at 2000 m intervals; *PR* = Puerto Rico; *JAM* = Jamaica.

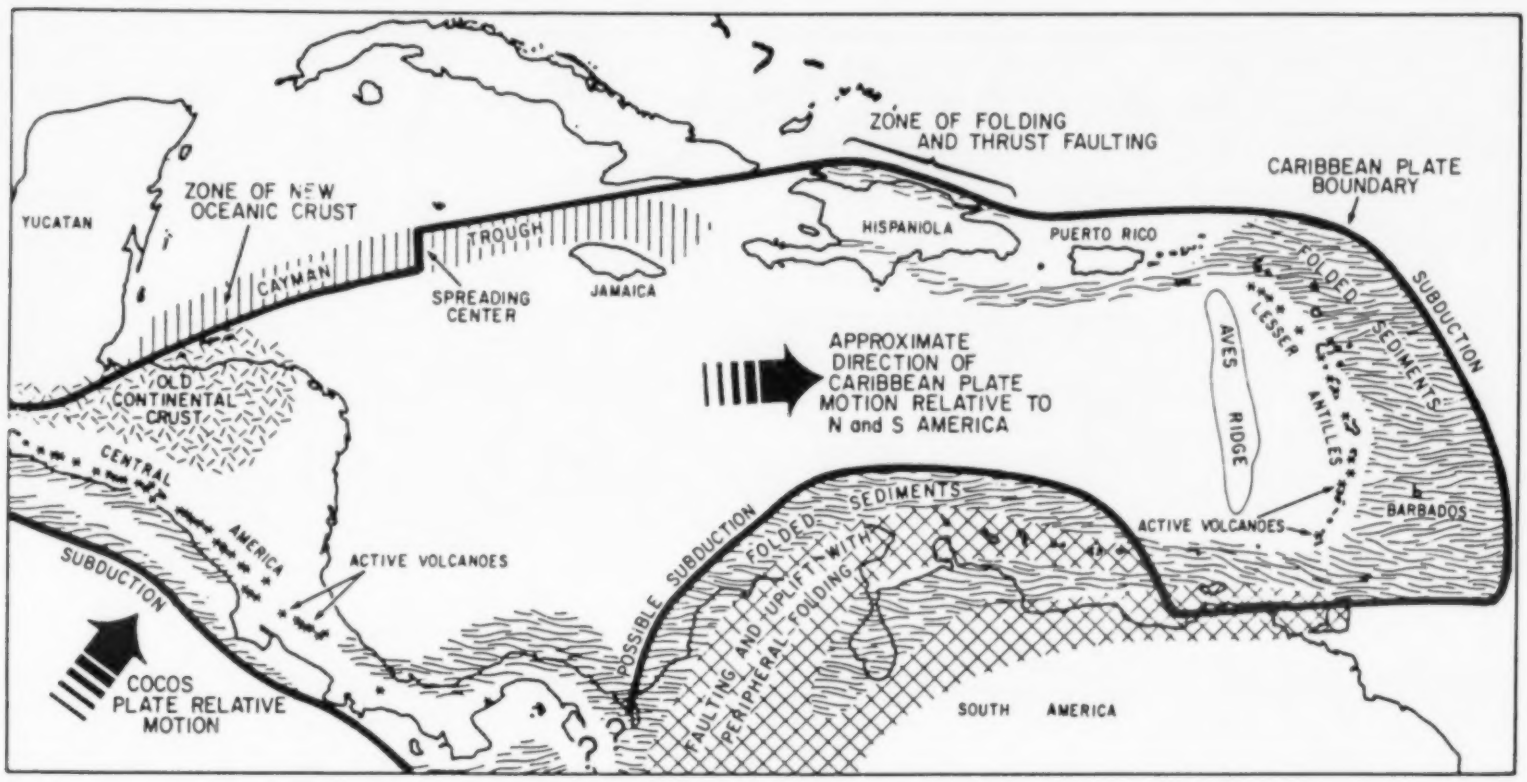

Fig. 2. Present-day boundaries of the Caribbean Plate illustrating restraining bend north of Hispaniola and collision of southeast Bahamas (from Dillon et al., 1987).

the collapse and retreat of carbonate platforms is commonly linked to tectonic processes (Bosellini, 1989) although modern analogs have not previously been developed. This study is the first to investigate carbonate platform evolution in an *active* plate tectonic collision zone and thus provides an initial framework within which to view the dynamic response of carbonate platforms to tectonic processes. Ball et al. (1985) have previously investigated the Late Mesozoic–Early Cenozoic collision of the southwestern Bahamas with Cuba.

Methods

During a 30-day research cruise aboard the R/V *MOANA WAVE* (8908) in July 1989 we collected approximately 5000 line km of geophysical data (Fig. 3) from the southeast Bahamas and its collision zone with Hispaniola. SeaMARC II, single channel air-gun seismic reflection, and 3.5 kHz PDR data were acquired simultaneously.

SeaMARC II is a deep-water seafloor-mapping, side-scan sonar system capable of acquiring up to 10 km wide swaths of quantitative bathymetric data and qualitative data on seafloor reflectivity (Tyce, 1987; Davis et al., 1987). Raw data were digitally recorded and inherent distortions corrected via on-board processing (Reed and Hussong, 1989; Malinverno et al., 1990). Dark areas on the reflectivity images correspond to relatively high seafloor reflectivity whereas light areas denote relatively low reflectivity. Single channel seismic reflection data were collected simultaneously and recorded in both analog and digital format using two 120 in^3 air-guns as a sound source. Navigation was by transit satellites and the Global Positioning System (GPS).

In addition to our geophysical data base four piston cores (up to 6 m long) and four rock dredge hauls were recovered. Rock samples have been slabbed, thin-sectioned and dated biostratigraphically. We have also integrated data from rock dredge hauls and submersible observations previously acquired from the study area (Fox and Heezen, 1975; Freeman-Lynde et al., 1981; Freeman-Lynde and Ryan, 1985; Heezen et al., 1985).

Results

Based on regional geologic variation, the study area has been divided into three sub-areas (Fig. 3):

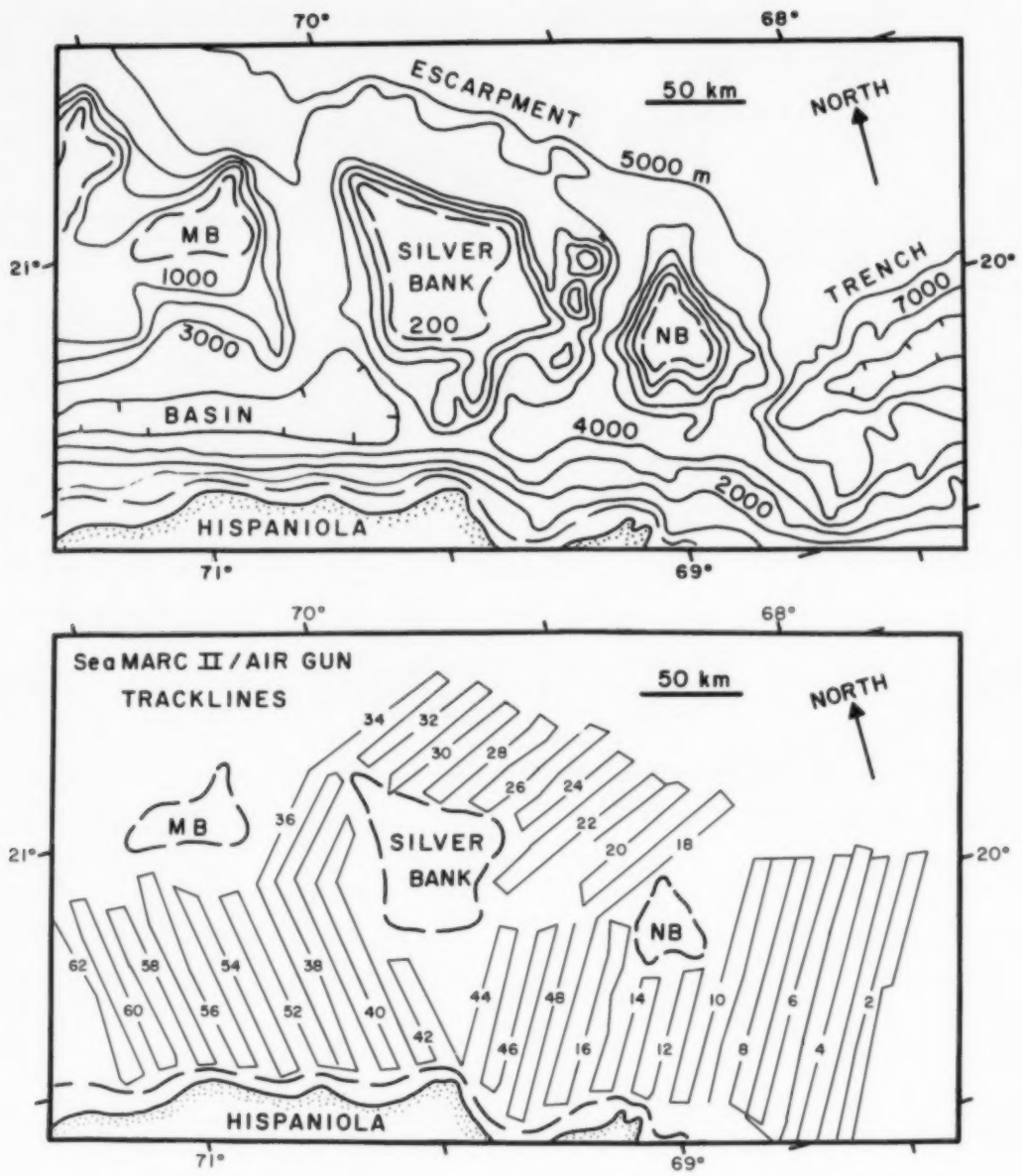

Fig. 3. (Top) Generalized bathymetry of study area (1000 m contour interval) illustrating carbonate platforms of southeast Bahamas north of Hispaniola near the western terminus of the Puerto Rico Trench; *MB* = Mouchoir Bank; *NB* = Navidad Bank. (Bottom) Geophysical trackline map of study area. Numbers correspond to individual profiles. SeaMARC II, air-gun seismic reflection, and 3.5 kHz data were collected simultaneously along all tracklines.

(1) north of Silver Bank (tracklines 18–34); (2) south of Mouchoir Bank (tracklines 37–41 and 52–62); and, (3) south of Navidad Bank (tracklines 8–17 and 44–48).

North of Silver Bank

Bathymetric data (Fig. 4) reveal a large (~5000 km^2) deep-water plateau between steep slopes associated with the Bahama Escarpment and Silver Bank. Seismic reflection profile 30 (Fig. 5) clearly illustrates this plateau at water depths of 3000–4000 m.

The Bahama Escarpment, along the seaward margin of this deep-water plateau (Fig. 5), is not a continuous feature but rather is interrupted by at least two large (~20 km wide) reentrants that extend as much as 15 km into the plateau (Figs. 4 and 6). These reentrants, which strike NE–SW, are oriented perpendicular to the trend of the Bahama Escarpment. Seismic reflection profiles (Fig. 7) reveal that the scarp at the heads of these reentrants is significantly lower in relief and declivity than the slope associated with the Bahama Escarpment (compare profiles 28 and 30; Figs. 5 and 7). SeaMARC II reflectivity data (Fig. 6) indicate slide scarps at the heads and margins of the reentrants and reflection profiles (Fig. 7) reveal

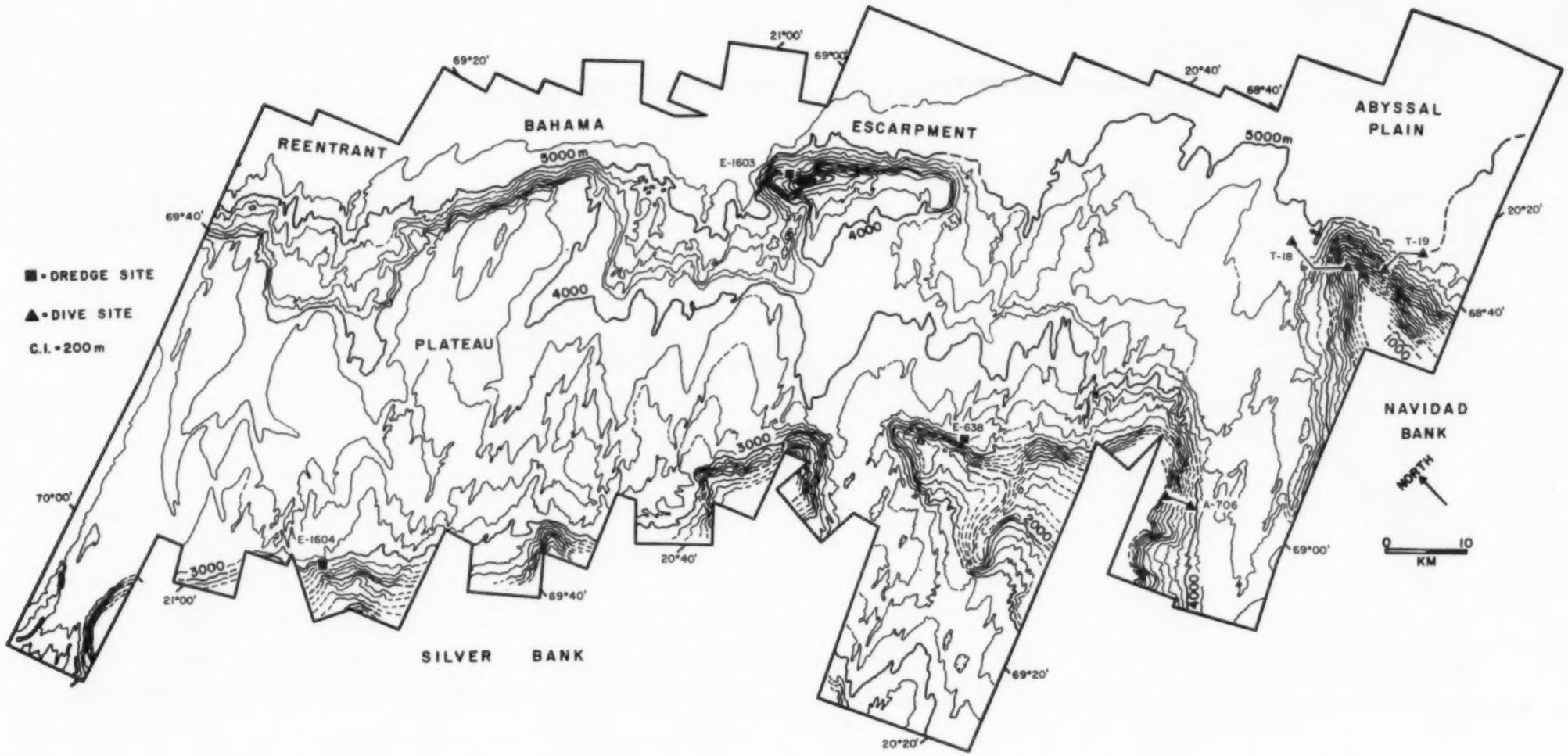

Fig. 4. Bathymetry (200 m contour interval) of the northern margin of Silver Bank based on SeaMARC II data (tracklines 18–34; Fig. 3); *T* = *Trieste*; *A* = *Alvin*. Bottom samples 600-series from Fox and Heezen (1975); 1600-series from Freeman-Lynde (1981).

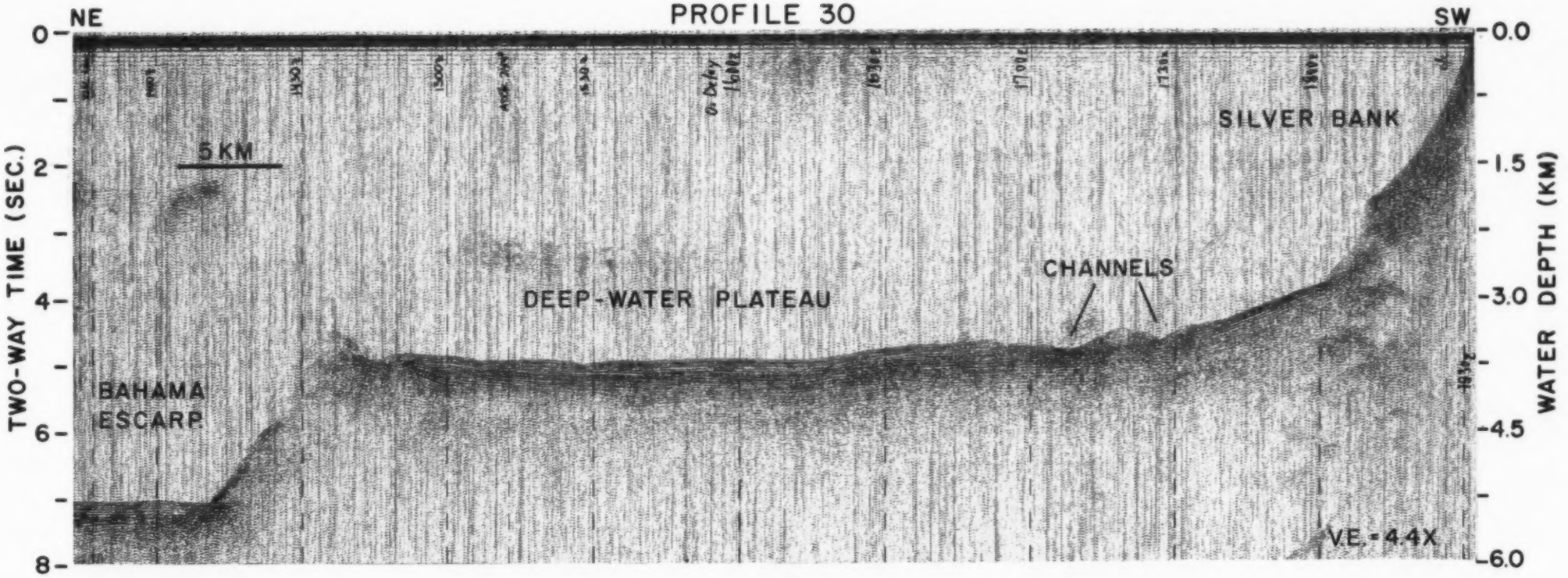

Fig. 5. Seismic reflection profile 30 from north of Silver Bank (Fig. 3). *V.E.* = vertical exaggeration.

a mounded-chaotic seismic facies at their base suggesting large scale slumping and mass movements.

In contrast to the reentrants, the escarpments between them are much steeper and lack debris piles at their base (Fig. 5). Only one rock dredge haul (E-1603) has been recovered from these steep seaward escarpments north of Silver Bank and it contained shallow-water, fore-reef limestones of mid-Cretaceous (Barremian–Aptian) age (Freeman-Lynde, 1981). In addition, digitally processed seismic reflection profiles (Fig. 8) across the steep portions of the escarpment document an acoustic facies change from even, parallel continuous reflectors beneath the plateau's interior to a reflection-free ("transparent") facies at its seaward margin. Other profiles (Fig. 9) reveal a raised-rim or late growth "reef" (Erlich et al., 1990) along the escarpment. These geophysical data, coupled with the recovery of high-energy fore-reef facies by Freeman-Lynde (1981), argue that the steep escarpments between the reentrants represent intact (uneroded) segments of a mid-Cretaceous carbonate platform margin. Such an interpretation contrasts with the overall erosional nature of the Blake–Bahama Escarpment (Paull and Dillon, 1980; Freeman-Lynde and Ryan, 1985) but is consistent with other studies that have documented isolated segments of Cretaceous platform margin facies along the Bahama Escarpment (Corso et al., 1985). In addition, talus recovered from the northern escarpment of Navidad Bank during Trieste dives 18 and 19 (Fig. 4) is largely high-energy Cretaceous biolithites and biosparrudites of reefal affinity (Freeman-Lynde, 1981).

Bathymetric and seismic reflection data also reveal a steep escarpment at the southwest end of this deep-water plateau which rises about 3000 m to the top of Silver Bank (Figs. 4 and 5). Fox and Heezen (1975) recovered shallow-water bioturbated pelmicrites (age unknown) from this escarpment (sample E-638; Fig. 4) suggesting that it is in part an erosional feature. This has been confirmed by *ALVIN* dive 706 which recovered Early–middle Cretaceous lagoonal and peritidal limestones capped by Eocene pelagic drape (Freeman-Lynde and Ryan, 1985). *ALVIN* photographs (Fig. 10) reveal shattered outcrops of shallow-water limestones below about 3400 m overlain by bedded outcrops of bank-interior facies which in turn are draped by pitted pelagic limestones.

One of the more intriguing features identified on the SeaMARC II reflectivity data from north of Silver Bank is a series of unusual canyons and channels (Fig. 11). These canyons extend down the steep slope of Silver Bank, across the relatively flat deep-water plateau and empty into the reentrants along the Bahama Escarpment. They are broad (up to 10 km across), shallow (<200 m relief) features (Fig. 5) that converge downslope and display a distinctive pattern of alternating high and low seafloor reflectivity (Fig. 11). Such a reflectivity pattern could be a result of rock outcrops alternating with sediment covered seafloor or perhaps large sediment waves. The 3.5 kHz PDR profiles across these canyons reveal hyperbolic reflections indicating an irregular surface.

Due to a lack of samples and direct seafloor observations from these canyons their origin is uncertain. However, they are clearly feeding debris into the reentrants along the Bahama Escarpment and they are not deeply incised features like many submarine canyons. The canyons north of Silver Bank are more reminiscent of avalanche chutes along steep mountain fronts. If so, they may be the result of intermittent, catastrophic slope failure or collapse of the steep escarpment north of Silver Bank (Mullins and Hine, 1989). An alternative explanation is that these canyons represent a line-source (Schlager and Chermak, 1979) for the downslope transport of excess sediment produced along the northern windward margin of Silver Bank.

A final feature identified on the SeaMARC II reflectivity data north of Silver Bank are abyssal sediment waves (Fig. 6). Northeast of the Bahama Escarpment, seafloor reflectivity is generally low with the exception of more highly reflective ridges which seismic profiles indicate are sediment waves. In the western part of our study area these sediment waves are fairly regular and strike NW–SE to E–W, oblique to the strike of the Bahama Escarpment. However, to the east, their orientation becomes much more chaotic (Fig. 6). Schneider and Heezen (1966) have previously documented

A

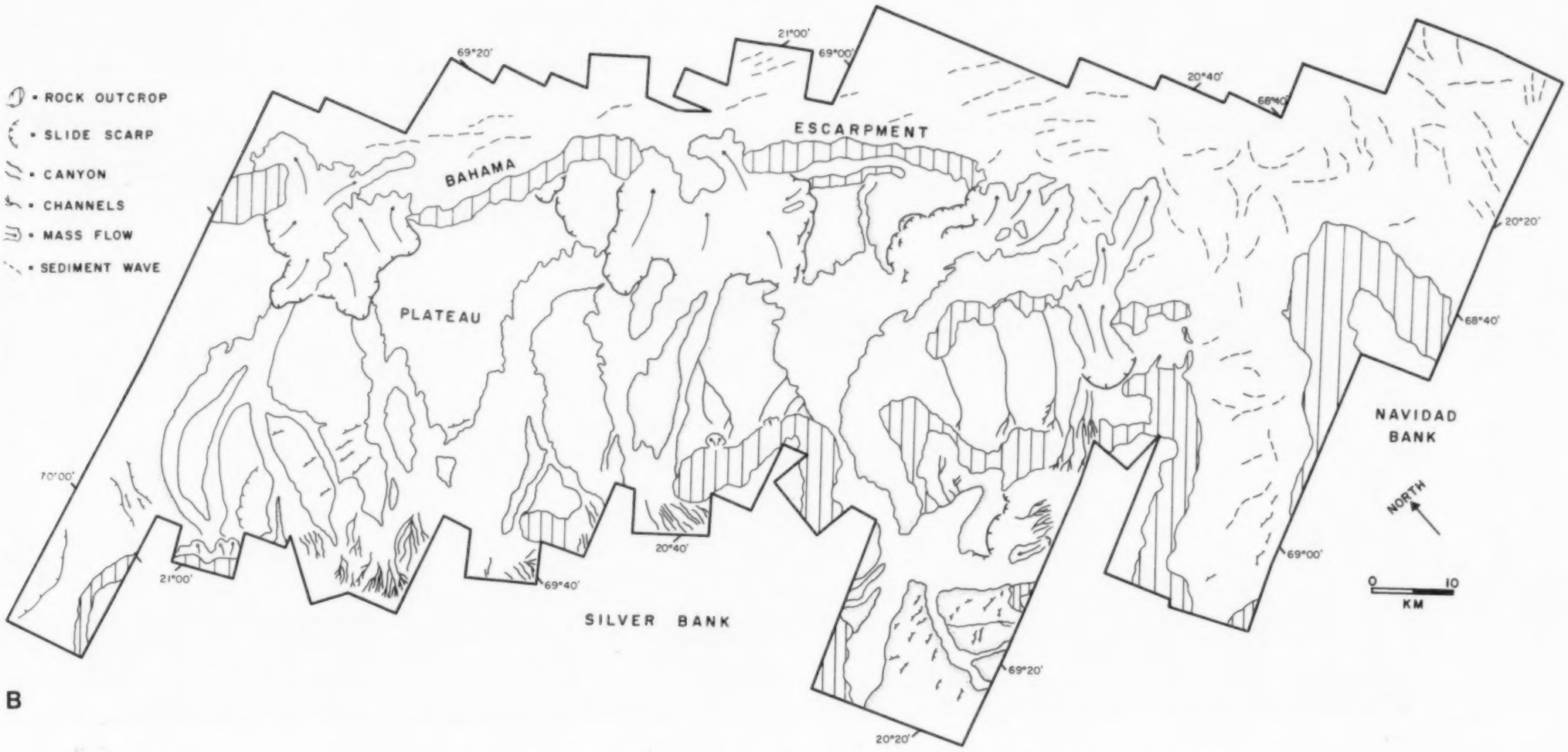

Fig. 6. (A) SeaMARC II reflectivity data mosaic from north of Silver Bank (tracklines 18–34). (B) Line drawing interpretation of data in (A).

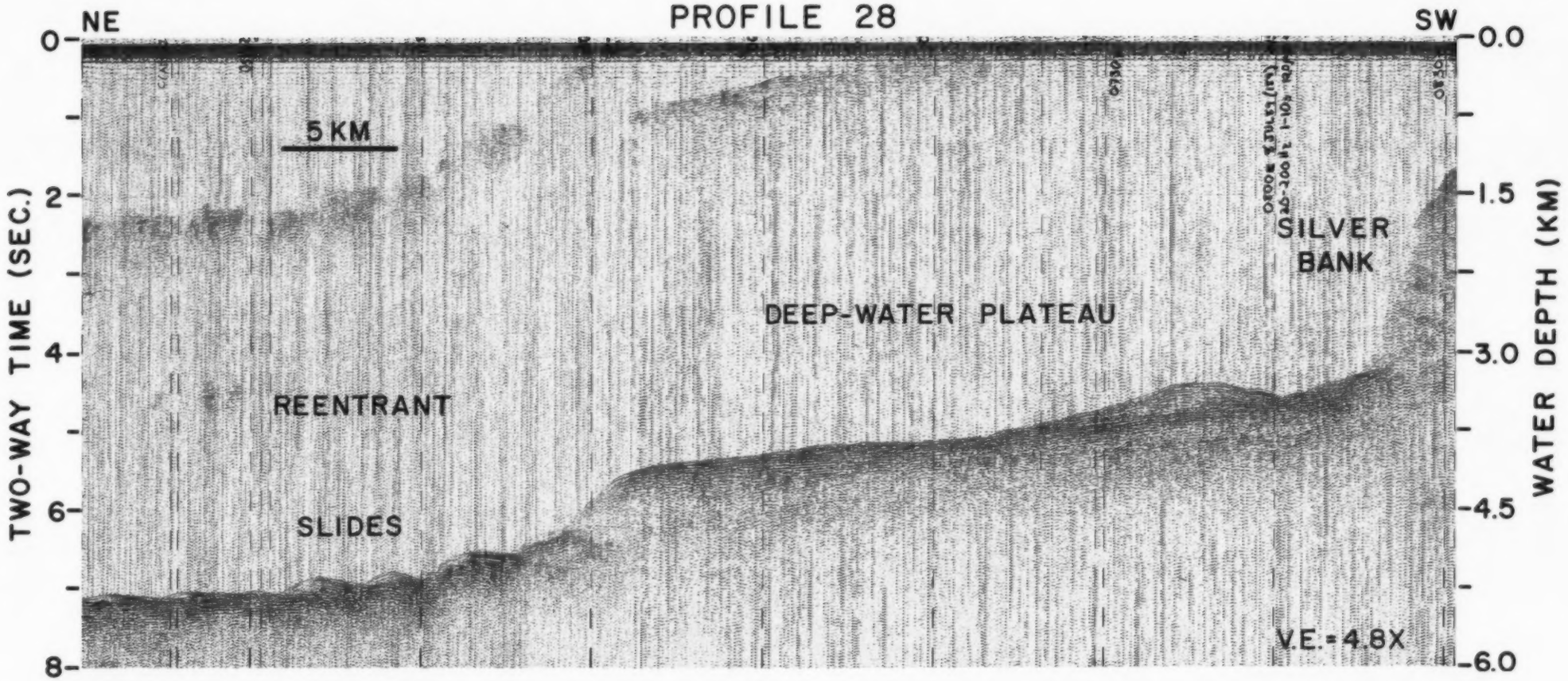

Fig. 7. Analog seismic reflection profile 28 from north of Silver Bank (Fig. 3).

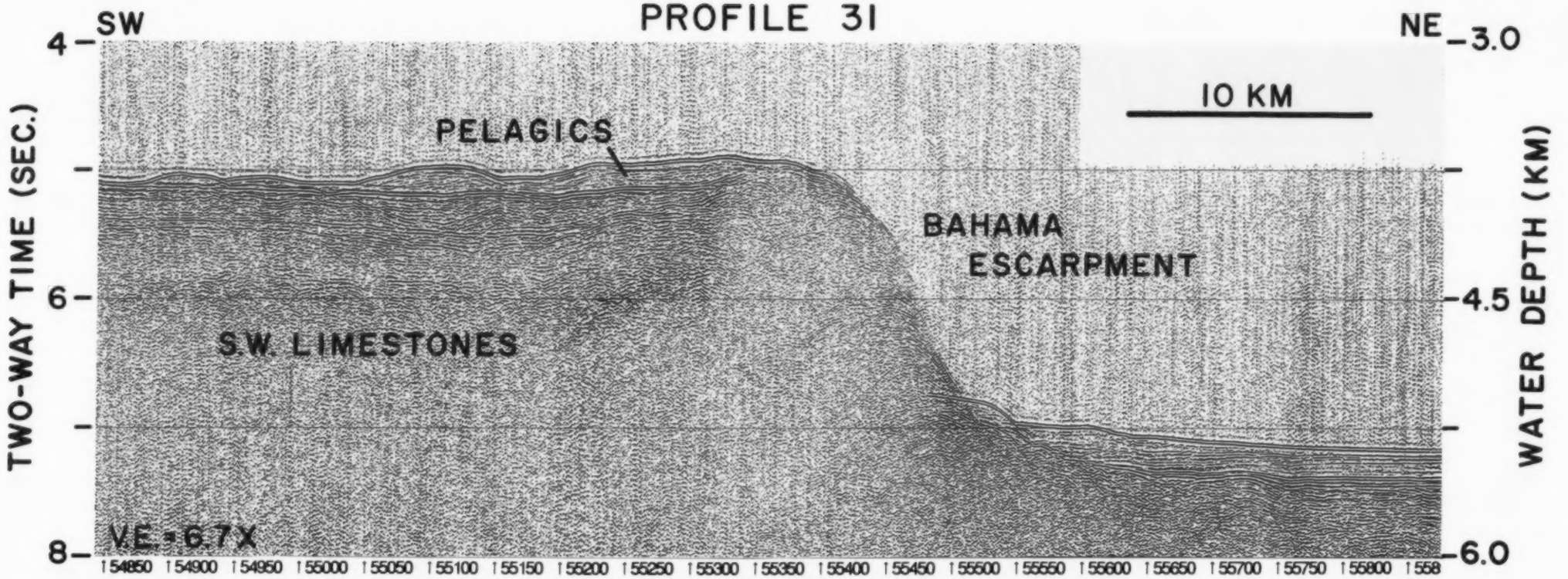

Fig. 8. Part of seismic reflection profile 31 (Fig. 3) from north of Silver Bank that has been digitally processed. Large numbers along base are shot points; *S.W.* = shallow-water.

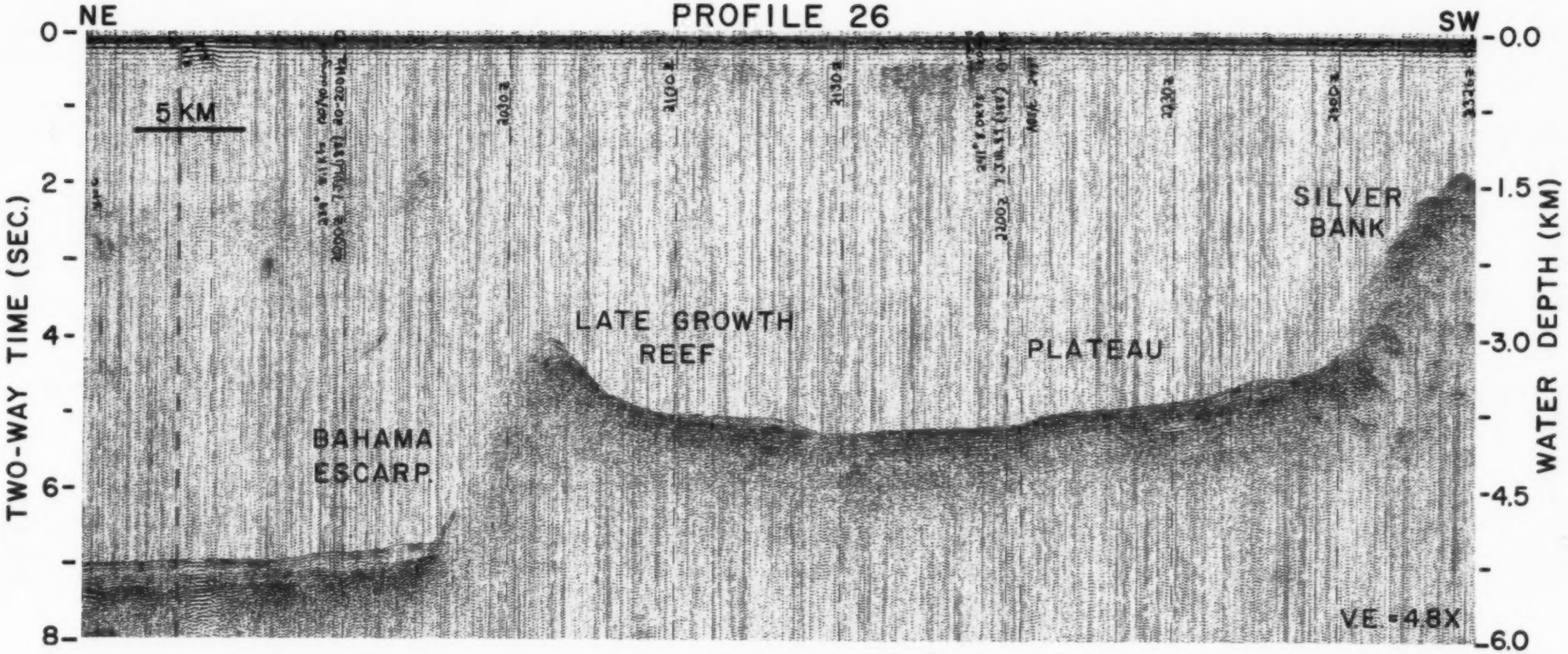

Fig. 9. Analog seismic reflection profile 26 from north of Silver Bank (Fig. 3).

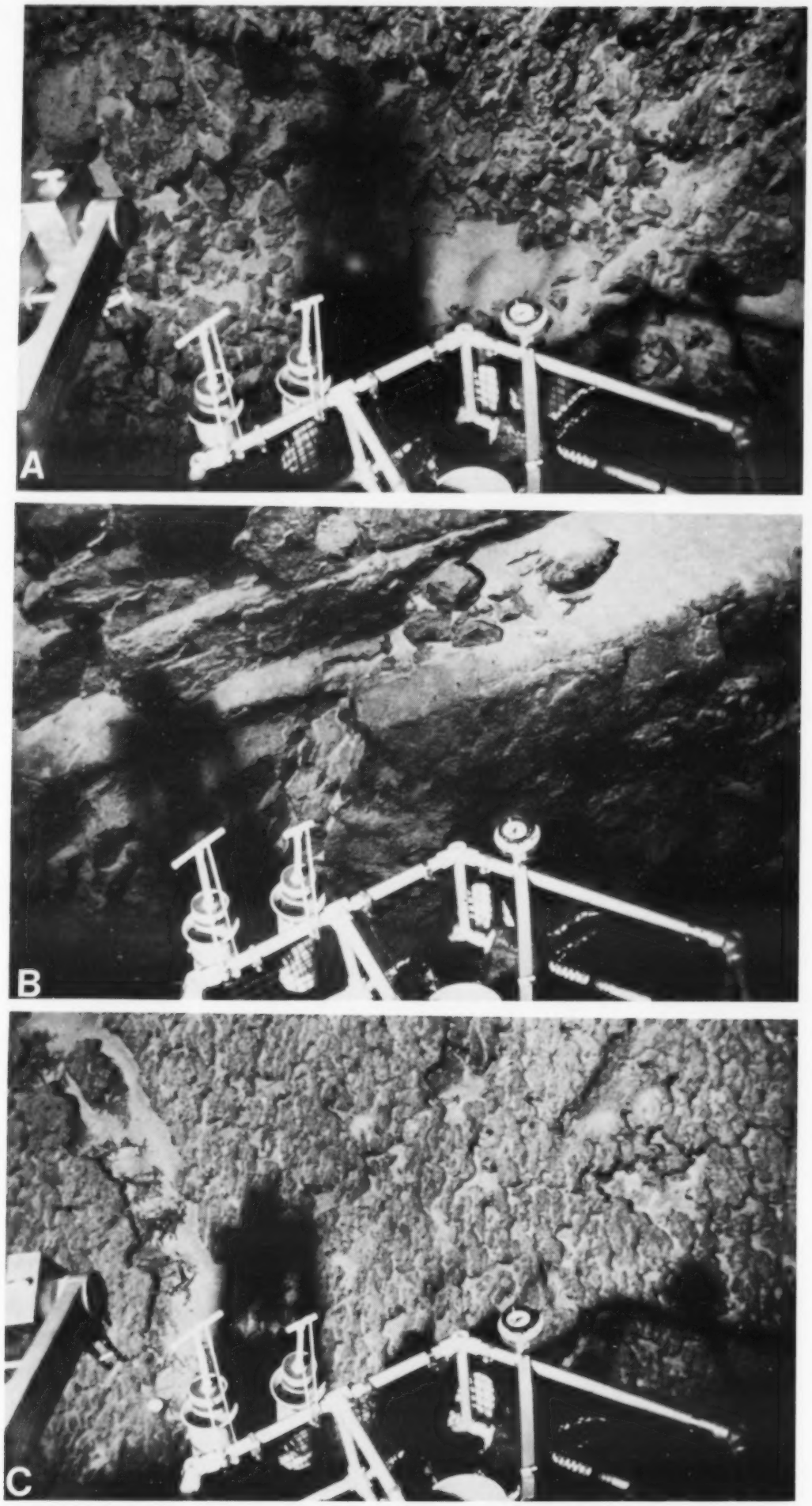

Fig. 10. Photographs of Silver Bank slope taken during *ALVIN* dive 706 (Fig. 4); (A) shattered outcrop of Cretaceous shallow-water limestones at 3547 m; (B) bedded outcrop of Cretaceous shallow-water limestones at 3015 m; (C) pitted surface of Eocene pelagic limestones at 2199 m. *ALVIN* holding cage is approximately 1.5 m across.

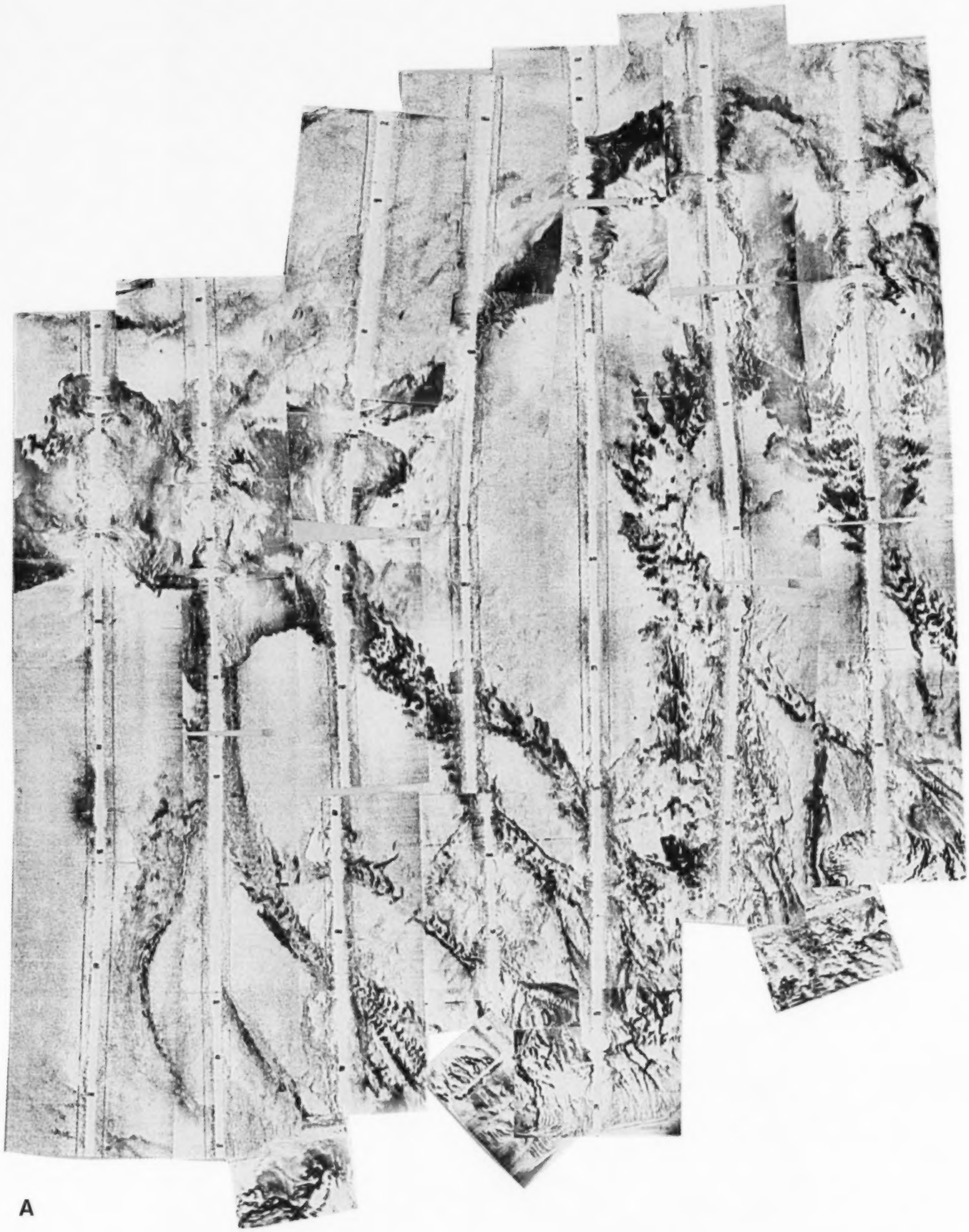

A

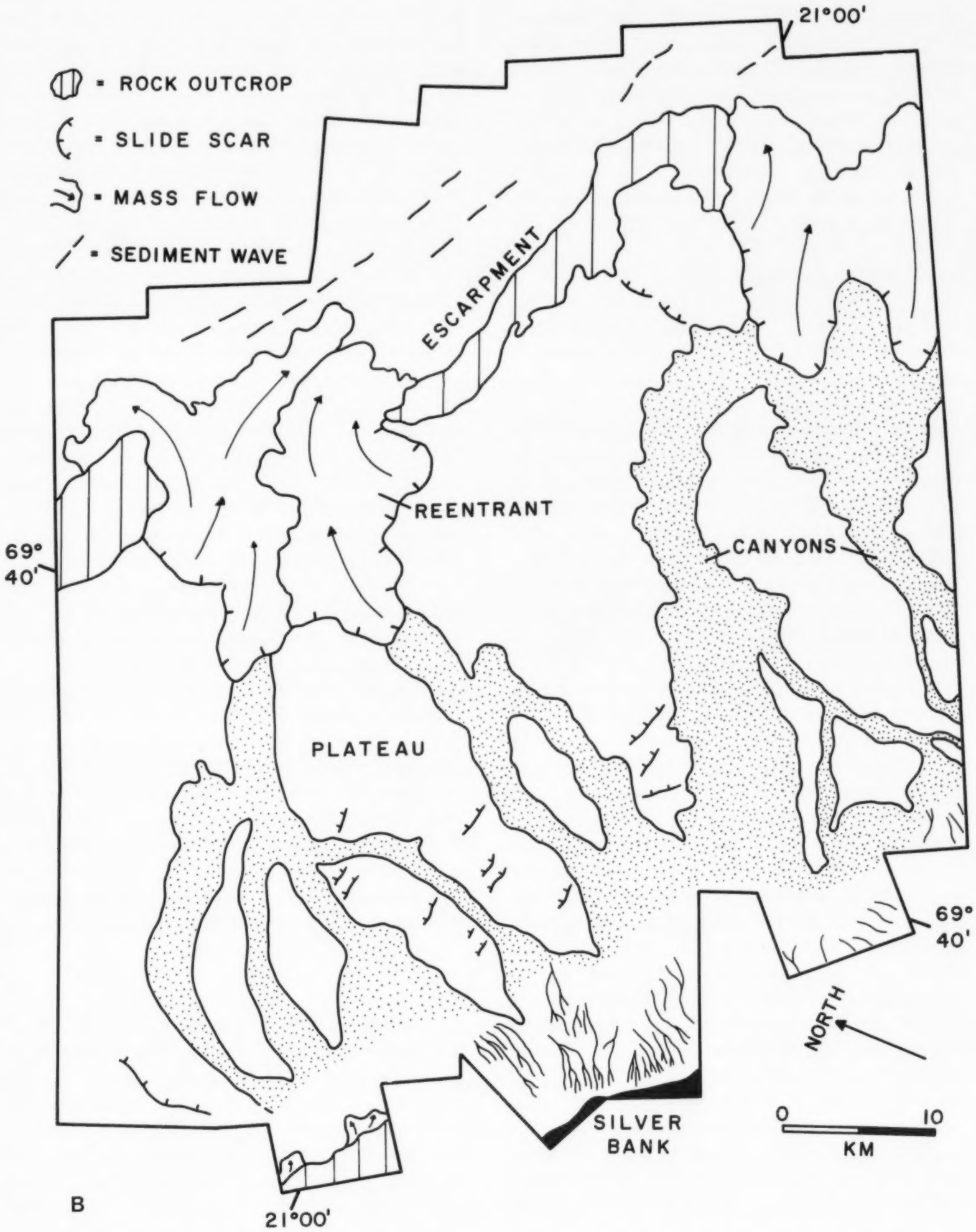

Fig. 11. (A) Close-up of SeaMARC II mosaic of northern margin of Silver Bank (tracklines 26–32) illustrating submarine channels ("avalanche chutes"). (B) Line drawing interpretatino of data in (A).

an abyssal sediment drift seaward of the southeast Bahamas produced by southeasterly flow of the Western Boundary Undercurrent. The sediment waves which we observe were likely produced by the same abyssal currents. However, their chaotic distribution between Silver and Navidad banks (Fig. 6) suggest possible topographically induced turbulence in the flow or perhaps the interaction of different currents.

South of Mouchoir Bank

Mouchoir Bank is a relatively small, irregular carbonate platform that has been built on top of a regional deep-water (~1000 m) plateau which in turn rises from a depth of about 4000 m (Fig. 3). South of Mouchoir Bank, and separating it from the northern insular slope of Hispaniola, is the flat-floored Hispaniola–Caicos basin filled with up to 3 km of mixed terrigenous–carbonate turbidites (Ditty et al., 1977; Austin, 1983). Oblique convergence of Mouchoir Bank along the Bahama–Hispaniola collision zone has generated an active fold and thrust belt along the accretionary prism north of Hispaniola (Figs. 12 and 13; Dillon et al., 1987, 1992).

Bathymetric data (Fig. 14) reveal a highly irregular drowned platform margin south of Mouchoir Bank with at least three large (~20 km across) amphitheater-shaped embayments or "scallops" (Mullins and Hine, 1989). A well-developed slope apron extends seaward from the scallops down to the Hispaniola Basin (Fig. 14). The scalloped margin south of Mouchoir Bank is also clearly imaged by SeaMARC II reflectivity data (Fig. 15). Seismic profiles across the western scallops display well-developed terraces that are as much as 15 km across (Fig. 16) and separated by steep escarpments, which produce a highly reflective seafloor. At the base of the eastern scallop, which indents the platform margin by about 20 km, SeaMARC II data reveal chaotic reflectivity which passes downslope into a seafloor with well-developed lineations which we interpret as flow-lines produced by a large (50 km long, 25 km wide) debris flow (Fig. 15). A seismic reflection profile across this feature (Fig. 17) documents a steep, irregular slope in the headward region of the scallop which passes downslope into a relatively smooth, broad slope where sediments are at least 1.5 km thick (1.5 s two-way travel time assuming $V_p = 2.0$ km s^{-1}). A well-developed submarine canyon system appears to truncate the eastern edge of this large debris flow (Figs. 14 and 15). A series of gullies and channels extend downslope from other amphitheater-shaped scallops along the eastern edge of the southern margin of Mouchoir Bank and may be contributing to erosional retreat of the platform.

Rock outcrops along steep scarps are common south of Mouchoir Bank including a highly reflective block located between tracklines 58 and 59 (Figs. 3 and 15). Three rock dredge hauls were recovered from these scarps along profile 58 (Figs. 14 and 18). Dredge D-1 (3730–2825 m) from the isolated block recovered a single sample of very well-indurated periplatform limestone containing a mix of shallow- and deep-water allochems. Red algal fragments and benthic foraminifers are common as are planktonic foraminifers which indicate a Tertiary age. Dredge D-2 (1510–800 m) recovered both shallow- and deep-water limestones. The shallow-water limestones are grainstones and rudstones with coral, red algae, green algae (*Halimeda*) (Fig. 19), mollusks, echinoiderms and benthic foraminifers of Late Tertiary age. The deep-water limestones are planktic foram packstones (Fig. 19) of mid-Pliocene (*Globorotalia miocenica* Zone) age. Dredge D-3 (2850–1825 m) recovered only shallow-water limestones including coral boundstones, skeletal grainstones and wackestones with abundant moldic porosity. Green algal fragments (dasyclades) are common (Fig. 19) as are alveolinid and dictyoconid benthic foraminifers indicating a Paleogene (late Eocene–Oligocene?) age.

South of Navidad Bank

Navidad Bank is the southeastern-most carbonate platform in the Bahamas (Fig. 1) located at the western end of the Puerto Rico Trench (Fig. 3). Bathymetric data (Fig. 20) reveal a very complex seafloor morphology that shoals to the west. Here, collision of Navidad and Silver banks with Hispaniola has segregated the Hispaniola Basin to the west from the Navidad Basin and Puerto Rico Trench to the east. Seismic profile 44 (Fig. 21)

Fig. 12. Analog seismic reflection profile 52 from south of Mouchoir Bank (Fig. 3); M_1 = first water–bottom multiple.

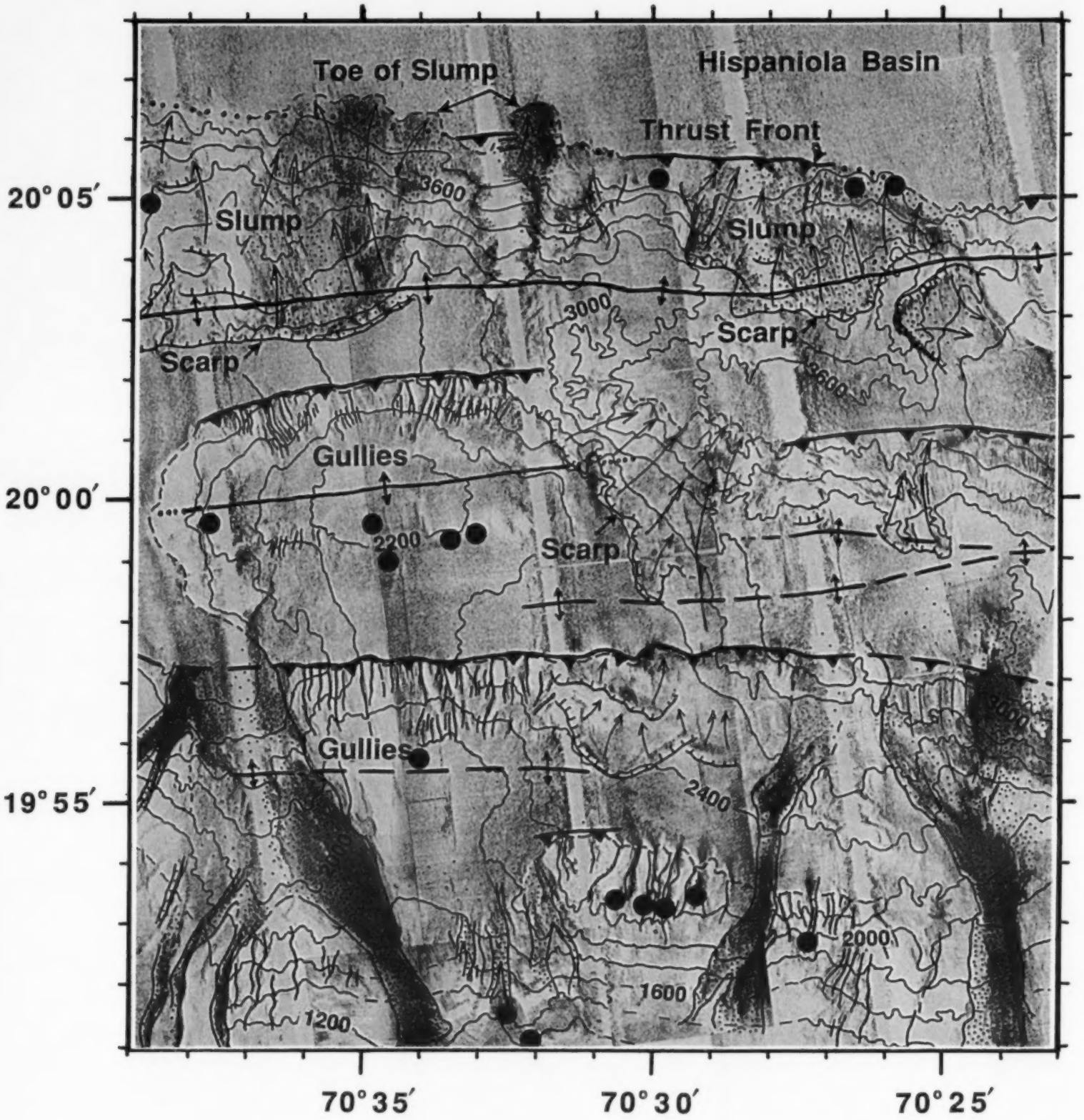

Fig. 13. Close-up of SeaMARC II mosaic (tracklines 52–54) from northern margin of Hispaniola illustrating (with interpretive overlay) fold and thrust belt along accretionary complex. Bathymetry (m) superimposed; black dots represent anomalous zones of high seafloor reflectivity which may be groundwater seeps. For scale, 1° latitude = 60 nautical miles (111 km).

illustrates the proximity of Silver Bank to the northern slope of Hispaniola and the absence of an intervening basin. Rock dredge hauls E-429 (3800–3550 m; Fox and Heezen, 1975) and D-4 (3400–2580 m; this study) have recovered shallow-water limestones as young as early Miocene from the north slope of Hispaniola indicating very rapid subsidence and perhaps accretion of part of the Bahamas onto Hispaniola. McCann and Sykes (1984) have previously suggested that a portion of the Bahama Banks was accreted to the northern Caribbean plate boundary in the Late Tertiary.

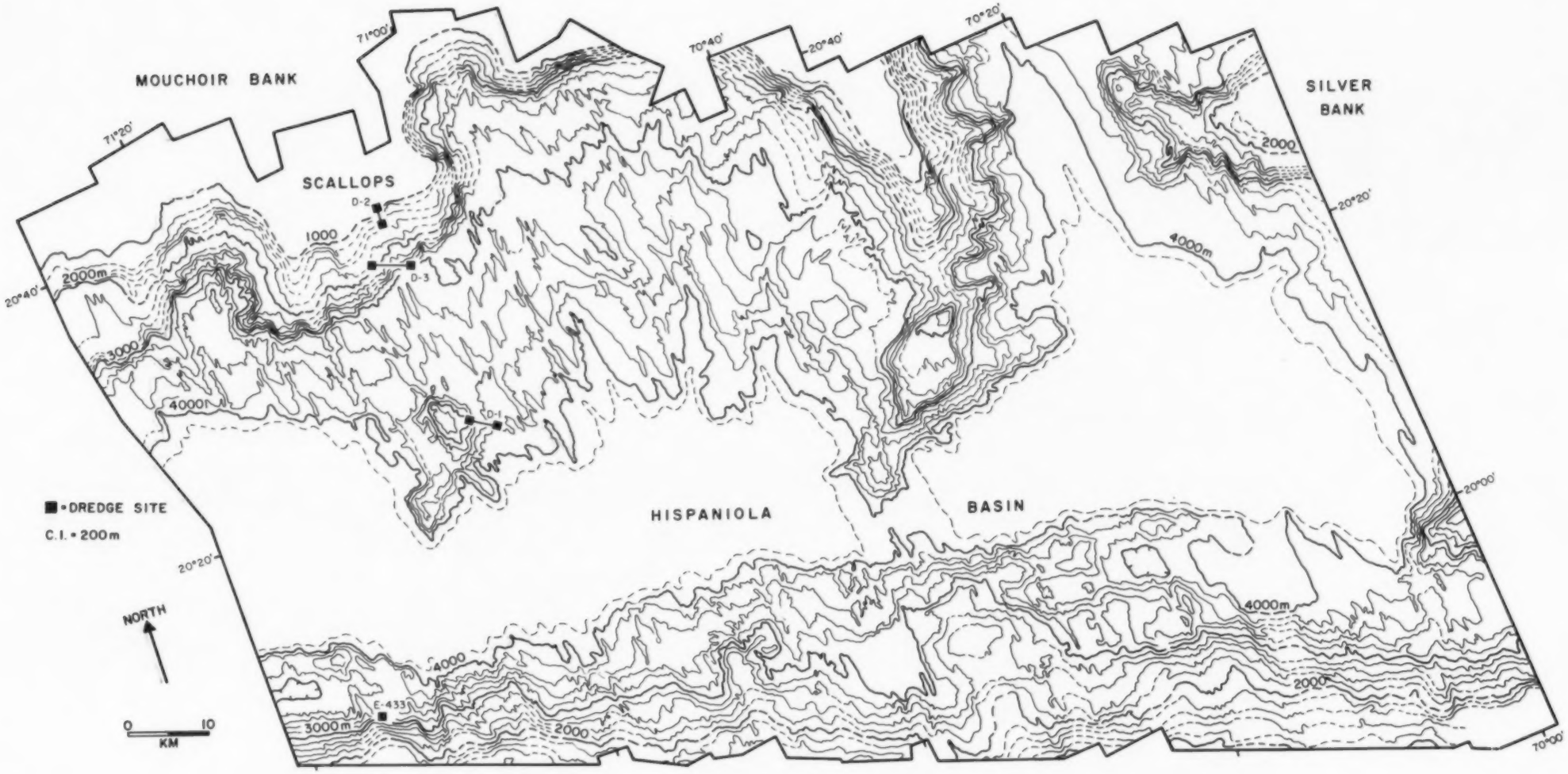

Fig. 14. Bathymetry of southern margin of Mouchoir Bank based on SeaMARC II data from tracklines 37–41 and 52–62 (Fig. 3). Dredge E-433 from Fox and Heezen (1975); dredges *D-1–D-3* from this study.

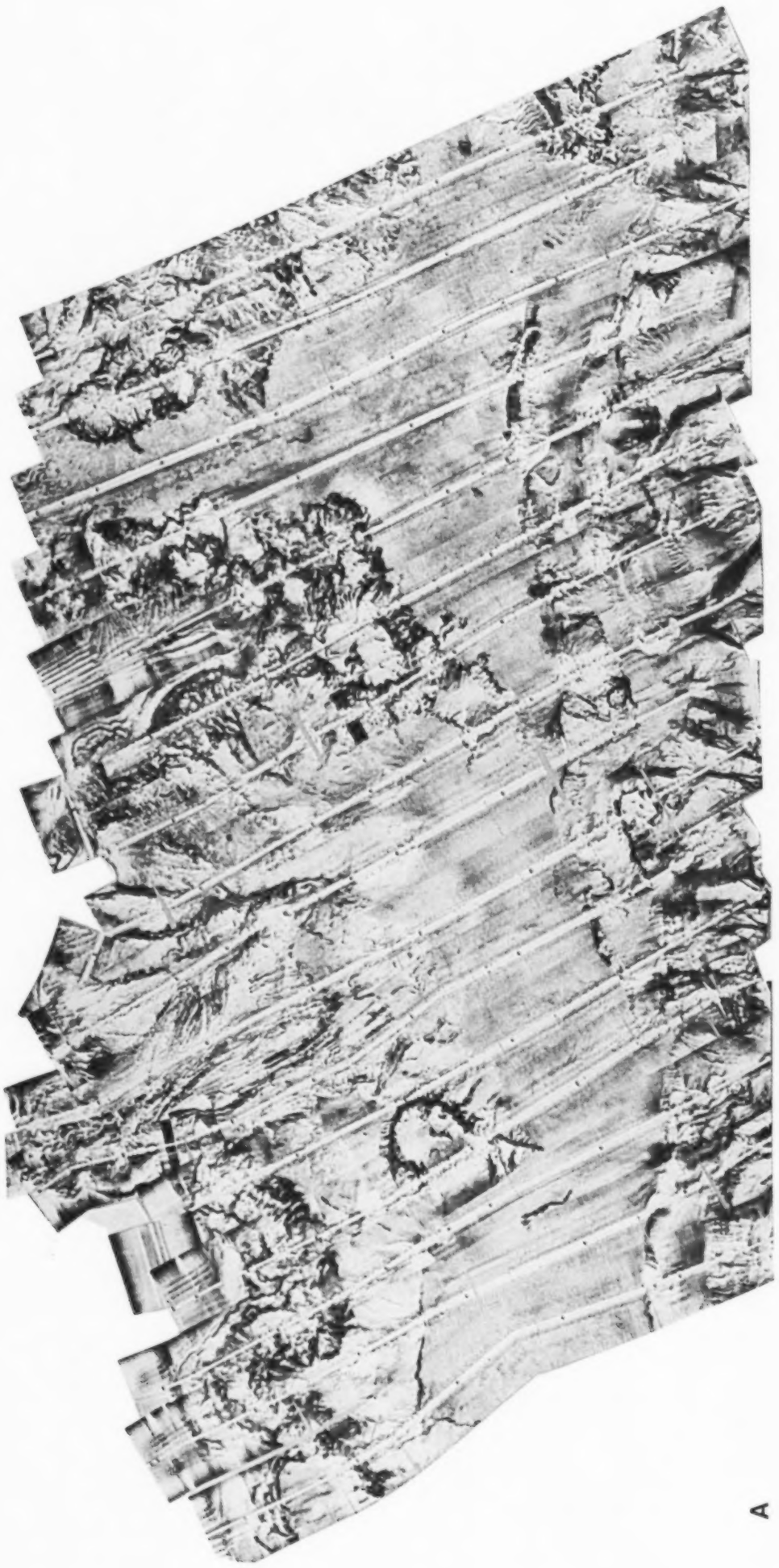
A

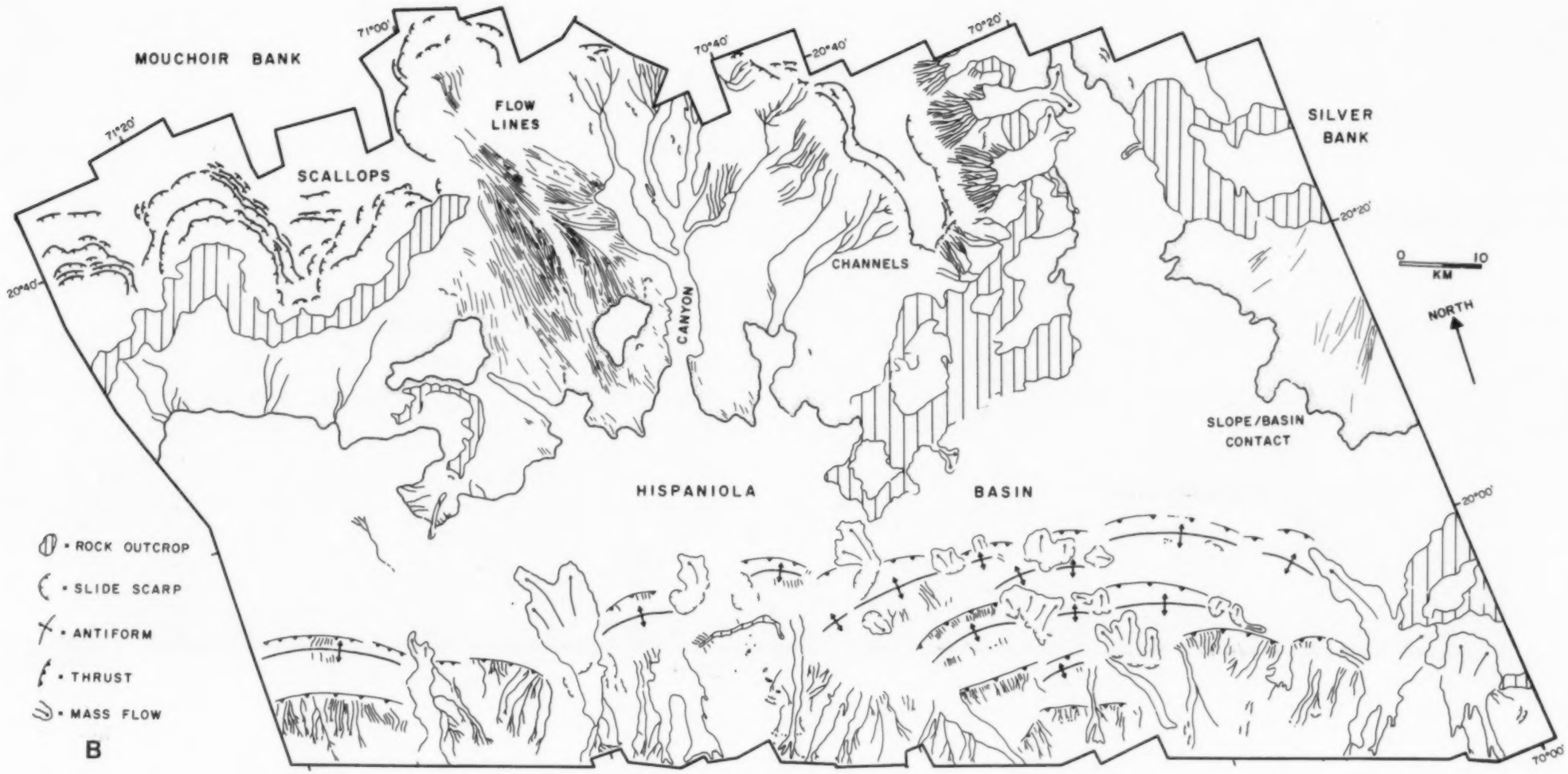

Fig. 15. (A) SeaMARC II reflectivity data mosaic from south of Mouchoir Bank (tracklines 37–41 and 52–62; Fig. 3). (B) Line drawing interpretation of reflectivity data in (A).

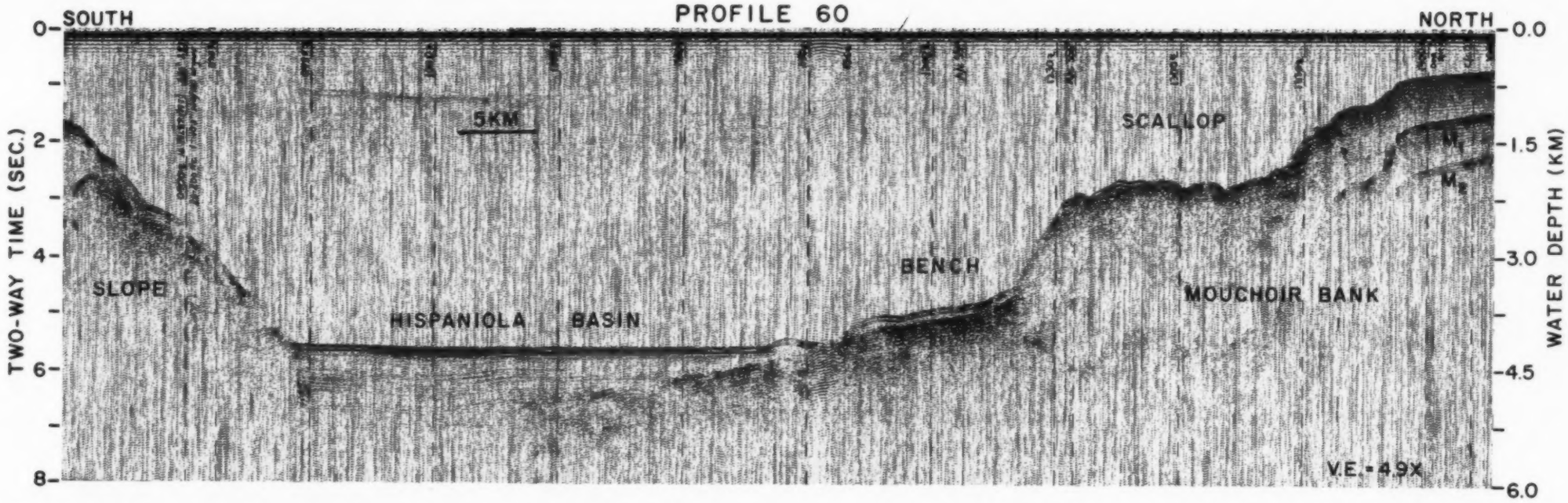

Fig. 16. Analog seismic reflection profile 60 from south of Mouchoir Bank (Fig. 3).

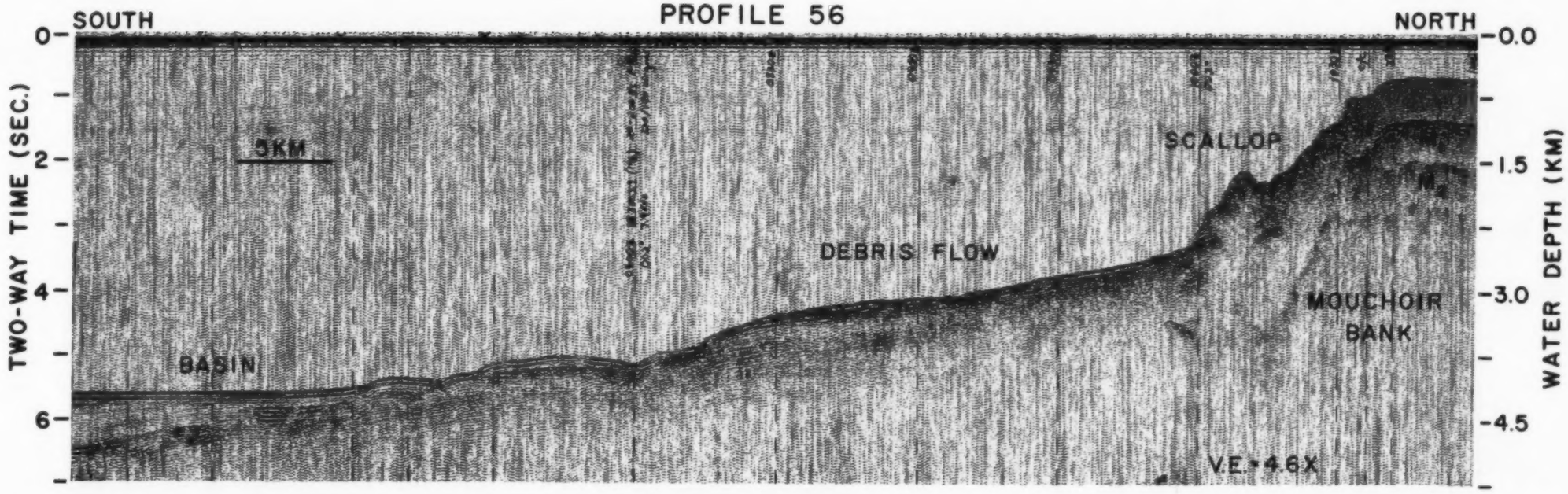

Fig. 17. Analog seismic reflection profile 56 from south of Mouchoir Bank (Fig. 3).

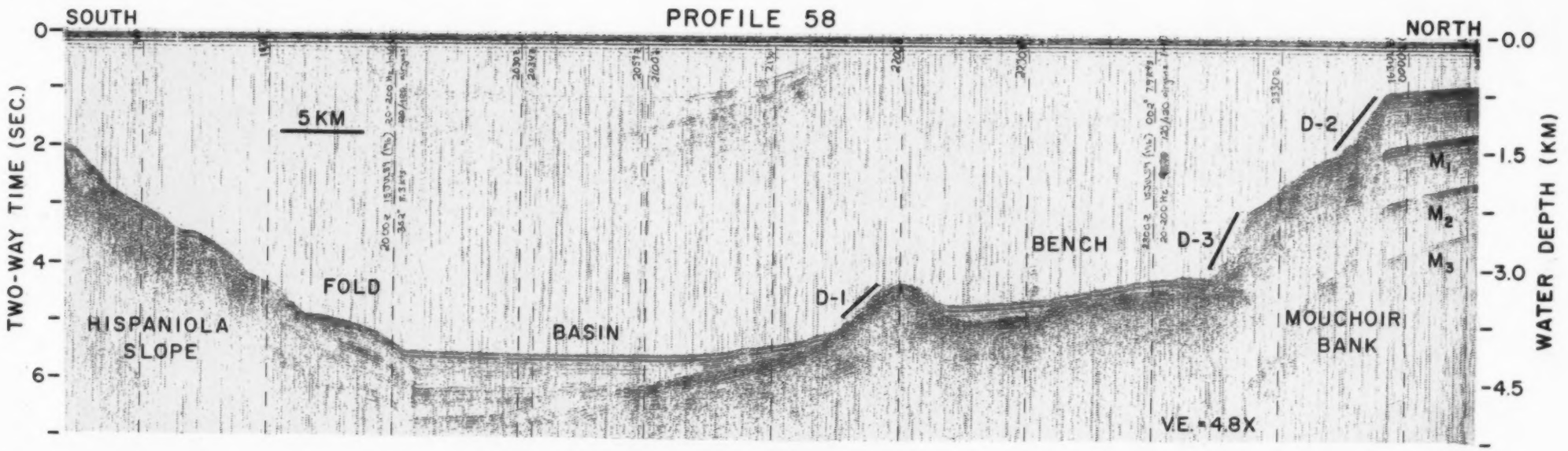

Fig. 18. Analog seismic reflection profile 58 from south of Mouchoir Bank (Fig. 3) illustrating location of rock dredge hauls *D-1* to *D-3*.

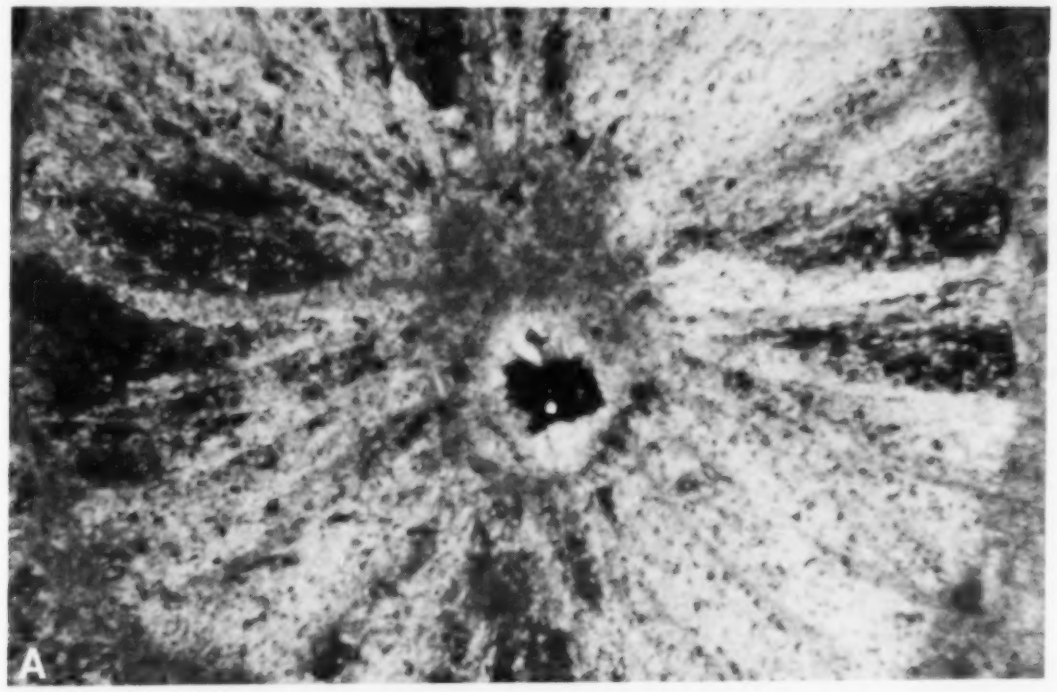

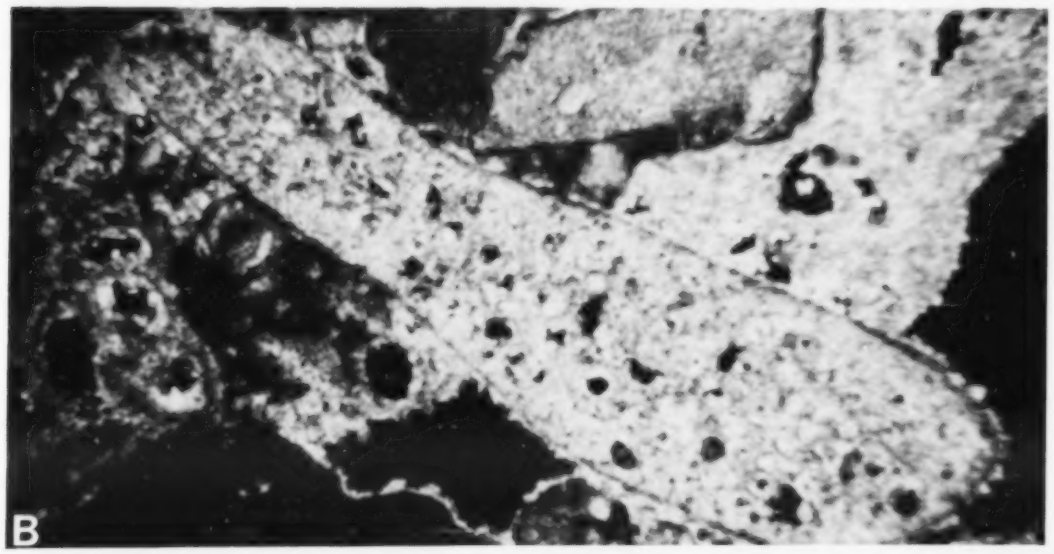

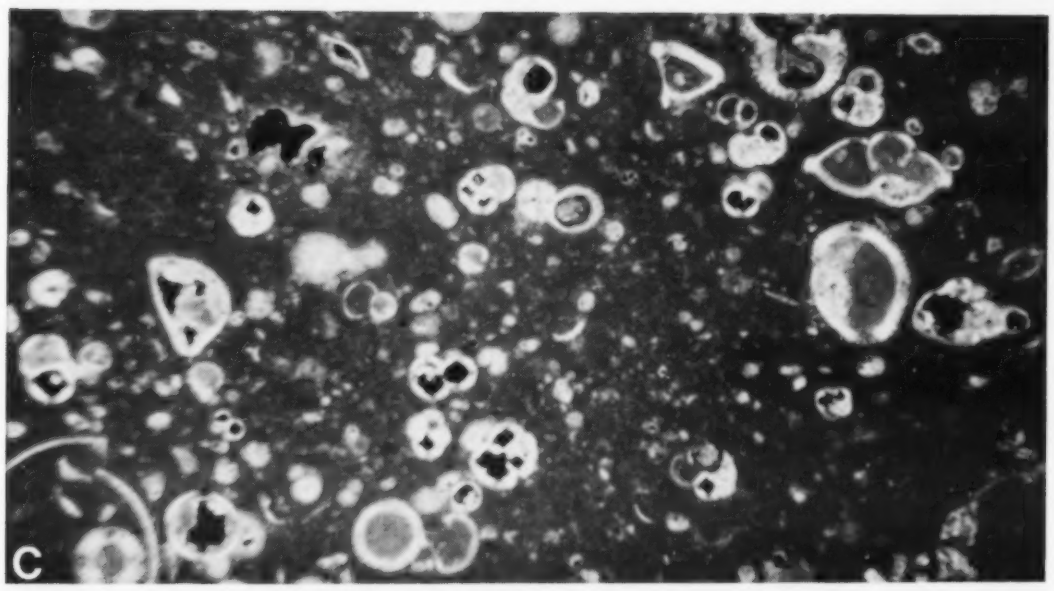

Fig. 19. Thin-section photomicrographs of limestones dredged south of Mouchoir Bank (Figs. 12 and 16): (A) daysclade fragment in Early Tertiary shallow-water limestone from D-3; 100×; cross polarized (XP) light; (B) green algal (*Halimeda*?) fragment from Late Tertiary shallow-water limestone in D-2; XP; 25×; (C) planktonic foram packstone of mid-Pliocene age from D-2; XP; 25×.

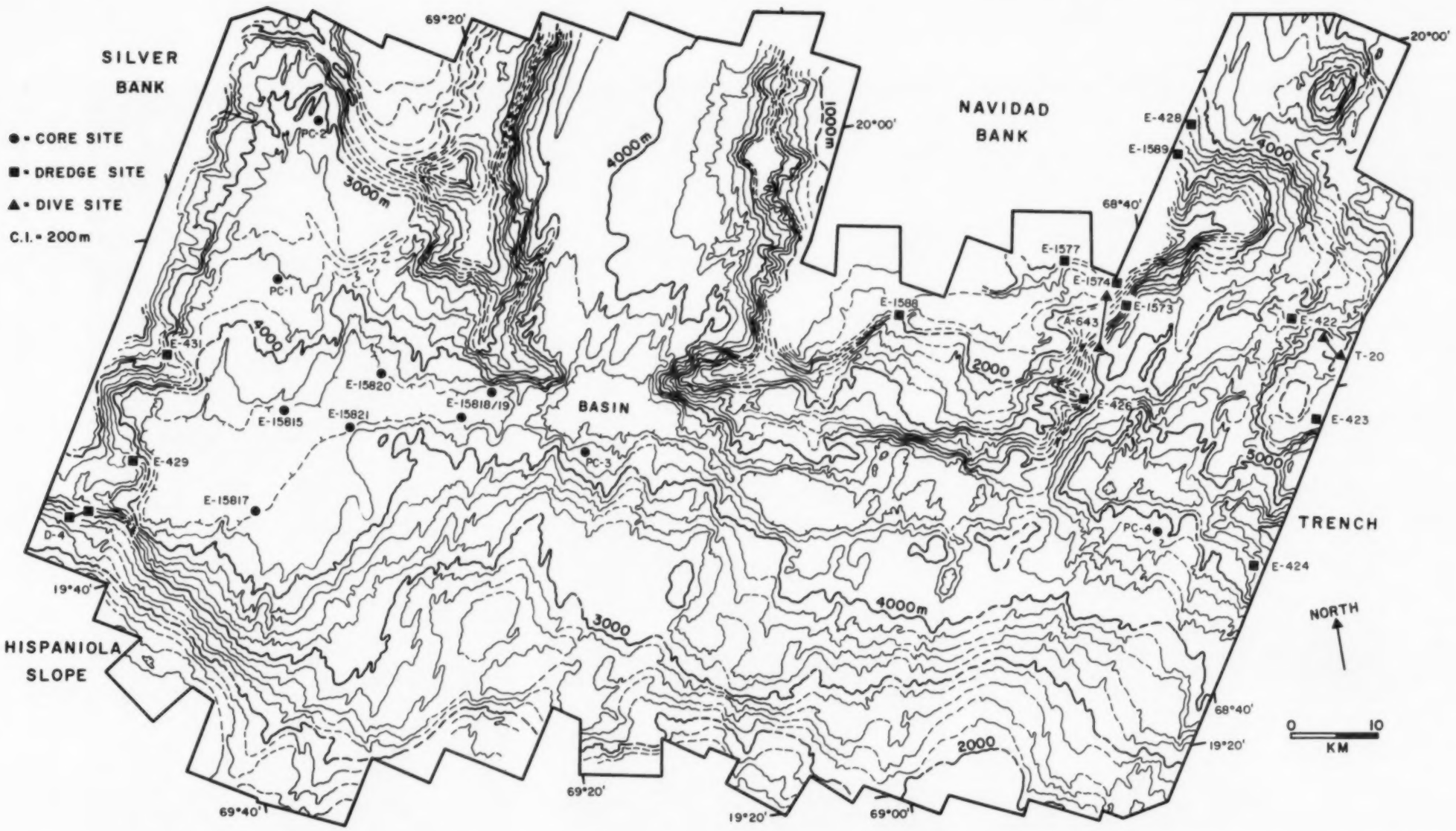

Fig. 20. Bathymetry of southern margin of Navidad Bank based on SeaMARC II data (tracklines 8–17 and 44–48); *PC* = piston core, this study; *E-15800* series are cores from Seiglie et al. (1976); *D-4* = dredge, this study; *E-1500* series are dredges from Freeman-Lynde (1981); *E-400* series are dredges from Fox and Heezen (1975); *A* = *ALVIN* dive; *T* = *Trieste* dive.

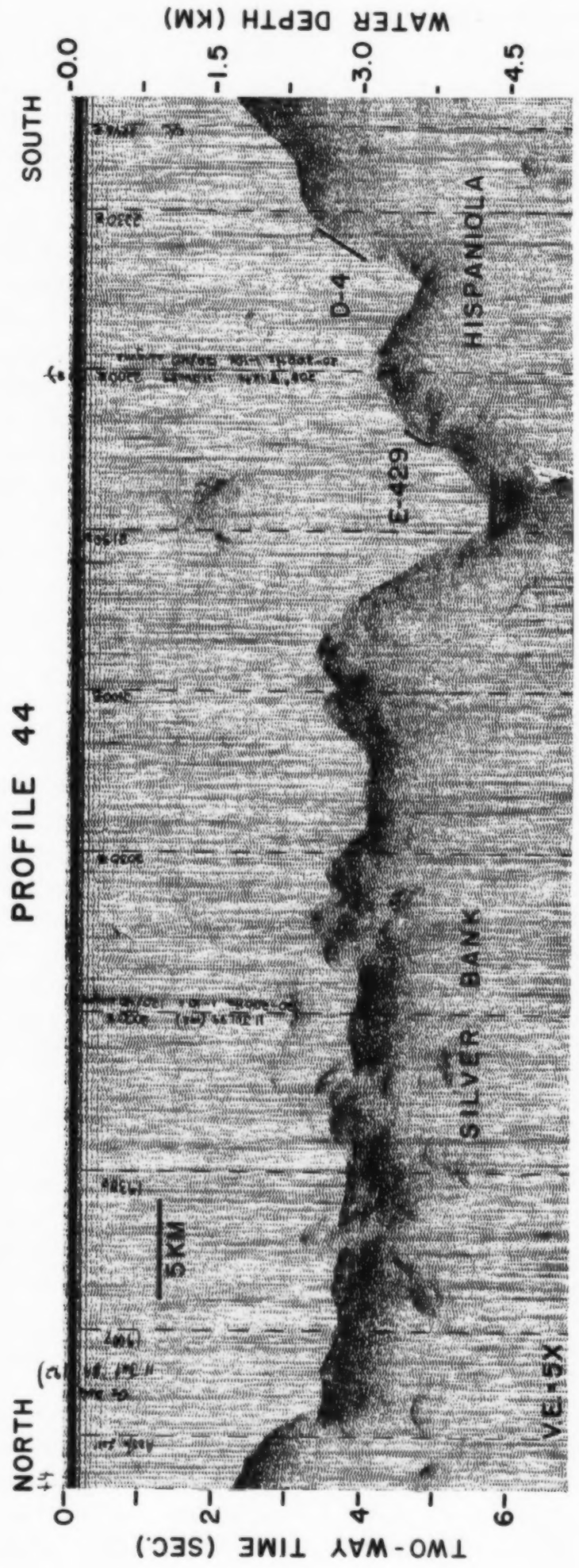

Fig. 21. Analog seismic reflection profile 44 from south of Silver Bank (Fig. 3). Note lack of basin between Bahama Bank at north and Hispaniola slope. Dredge *D-4* from this study; dredge *E-429* from Fox and Heezen (1975).

The proximity of Navidad Bank to the Puerto Rico Trench and adjacent slope of Hispaniola is well illustrated by seismic profile 10 (Fig. 22).

SeaMARC II reflectivity data document the indentation of Navidad Bank along the northern slope of Hispaniola and near closure of the intervening turbidite basin (Fig. 23). The accretionary prism here lacks obvious folds but does have a well-defined deformation front (Fig. 23). Tectonic oversteepening of the slope north of Hispaniola has also resulted in numerous, surficial submarine slides (Fig. 23).

Along the western margin of Navidad Bank and the eastern margin of Silver Bank there are thick (>1 km) sequences of carbonate slope deposits (Fig. 24). Reflectivity data from both areas (Fig. 23) display an intricate system of gullies and canyons which act as a line source (Schlager and Chermak, 1979) for the downslope transport of shallow-water debris. Piston cores (PC) document a proximal to distal transition across these carbonate slopes that correlate with acoustic facies. PC-1, from a distal seismically transparent part of the slope (Fig. 24), recovered fine-grained, rhythmically-bedded periplatform carbonates of Pleistocene–Holocene age, whereas PC-2 from a proximal high-amplitude acoustic facies, recovered only coarse-grained periplatform carbonates, also of Pleistocene–Holocene age based on the occurrence of *Globorotalia truncatulinoides* (A.F. Gardulski, pers. commun., 1991). These findings are consistent with the concept of carbonate apron deposition along the lower slope of carbonate platform margins (Mullins and Cook, 1986) as well as "self-erosion" and retreat of upper slopes (Schlager and Camber, 1986). Sediments in the adjacent basin plain (Navidad Basin) consist of thin turbidites interbedded with pelagic sediment (Seiglie et al., 1976). The carbonate turbidites in this basin-fill have likely bypassed the carbonate slope apron via a well-developed canyon system which extends down to Navidad Basin from the southeast margin of Silver Bank (Fig. 23).

A somewhat surprising feature along this transpressional plate boundary is the occurrence of normal faults. Seismic profile 13 (Fig. 25) illustrates a series of terraced "steps" that extend down the southeastern flank of Navidad Bank. Digital processing of profile 12 revealed a normal (down-to-basin) offset of a shallow subsurface reflector (Fig. 26, arrow) along one of these scarps. SeaMARC II reflectivity data indicate that these scarps strike E–W to NE–SW (Fig. 23). This interpretation of normal faulting is supported by rock dredge data from this area which indicate Cretaceous shallow-water limestones at water depths (3950–3700 m) *less* than Eocene shallow-water limestones (5700–5500 m; Fox and Heezen, 1975). In addition, there is direct evidence of faulting from observations made during *ALVIN* dive 643 (Figs. 20 and 27; Heezen et al., 1985). The slope here consists of Early Cretaceous shallow-water limestones (bank-interior facies) that are characterized by "intense shattering and faulting" below about 3100 m water depth (Freeman-Lynde, 1981, p. 42). Vertical fault planes are present between 3470 and 3450 m and fault gouge occurs between 3170 m and 3100 m (Fig. 27; Freeman-Lynde, 1981).

Discussion

Mullins and Hine (1989) previously speculated that the southeast Bahamas were once part of much larger carbonate platforms that have since retreated to their present positions. Geophysical data from this study, integrated with available dredge and dive data, confirm this speculation and provide insight to the processes by which carbonate platforms retreat in response to tectonic processes (Fig. 28).

Drowning and step-back

There appears to have been at least two drowning and step-back (Playford, 1980) events in the southeastern Bahamas that were responsible for the formation of regional deep-water plateaus presently at depths of about 3500 m (north of Silver Bank) and 1000 m (south of Mouchoir Bank; Fig. 3).

North of Silver Bank the deep-water plateau is underlain by shallow-water limestones of Early Cretaceous (Barremian/Aptian) age and capped by pelagic limestones of Late Cretaceous (Maastrichtian)–Tertiary age (Freeman-Lynde and Ryan,

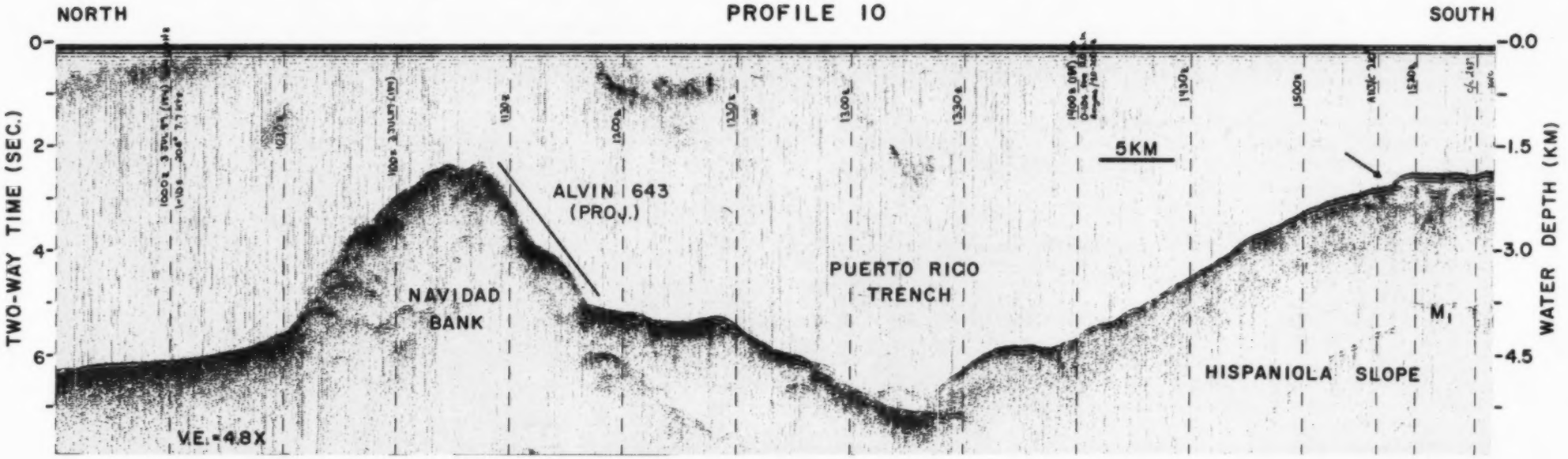

Fig. 22. Analog seismic reflection profile 10 from south of Navidad Bank (Fig. 3) illustrating proximity of bank to western terminus of Puerto Rico trench. *ALVIN* dive 643 projected from actual location along strike of outcrop mapped by SeaMARC II data; arrow points to small thrust fault along upper slope of Hispaniola.

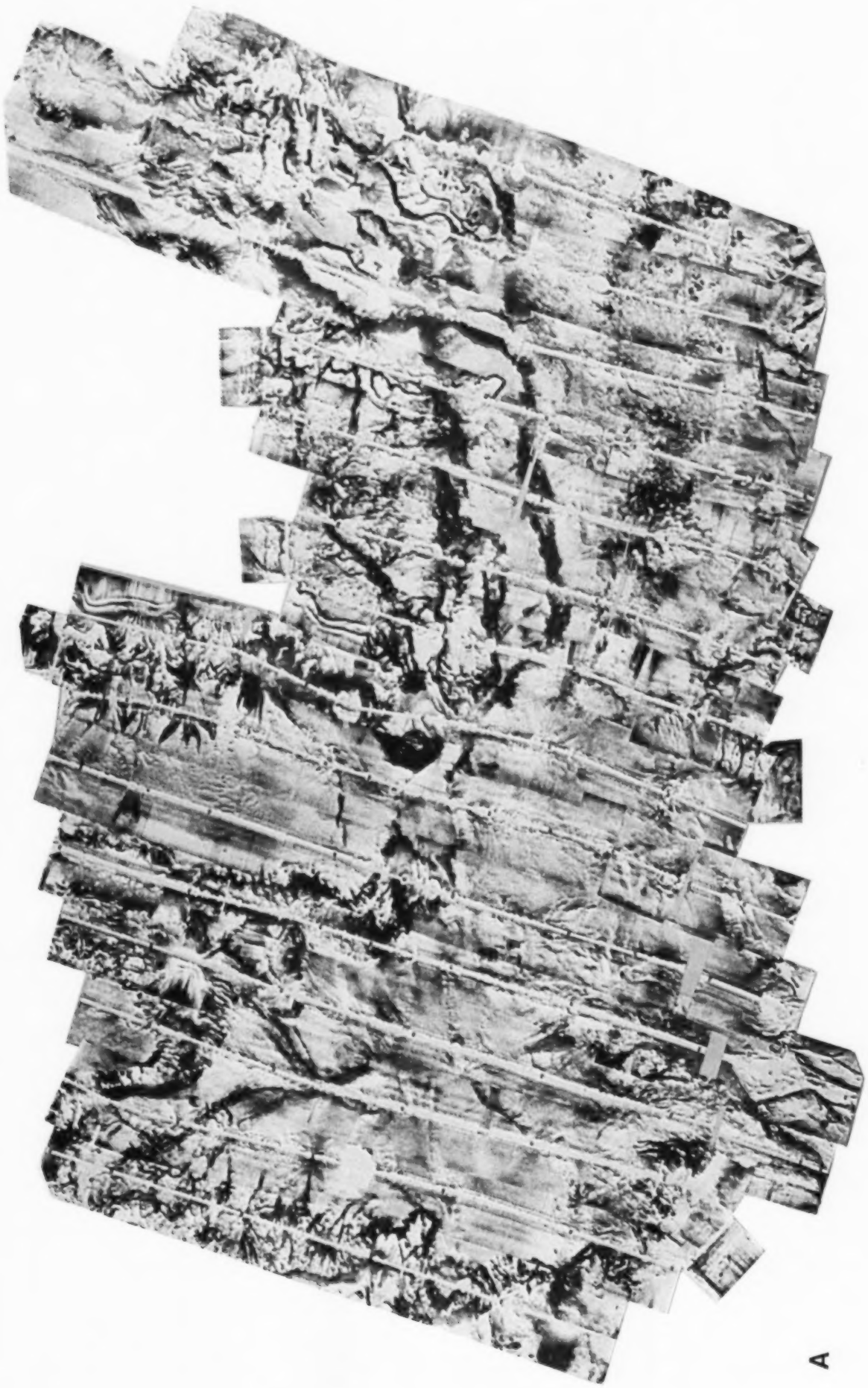

A

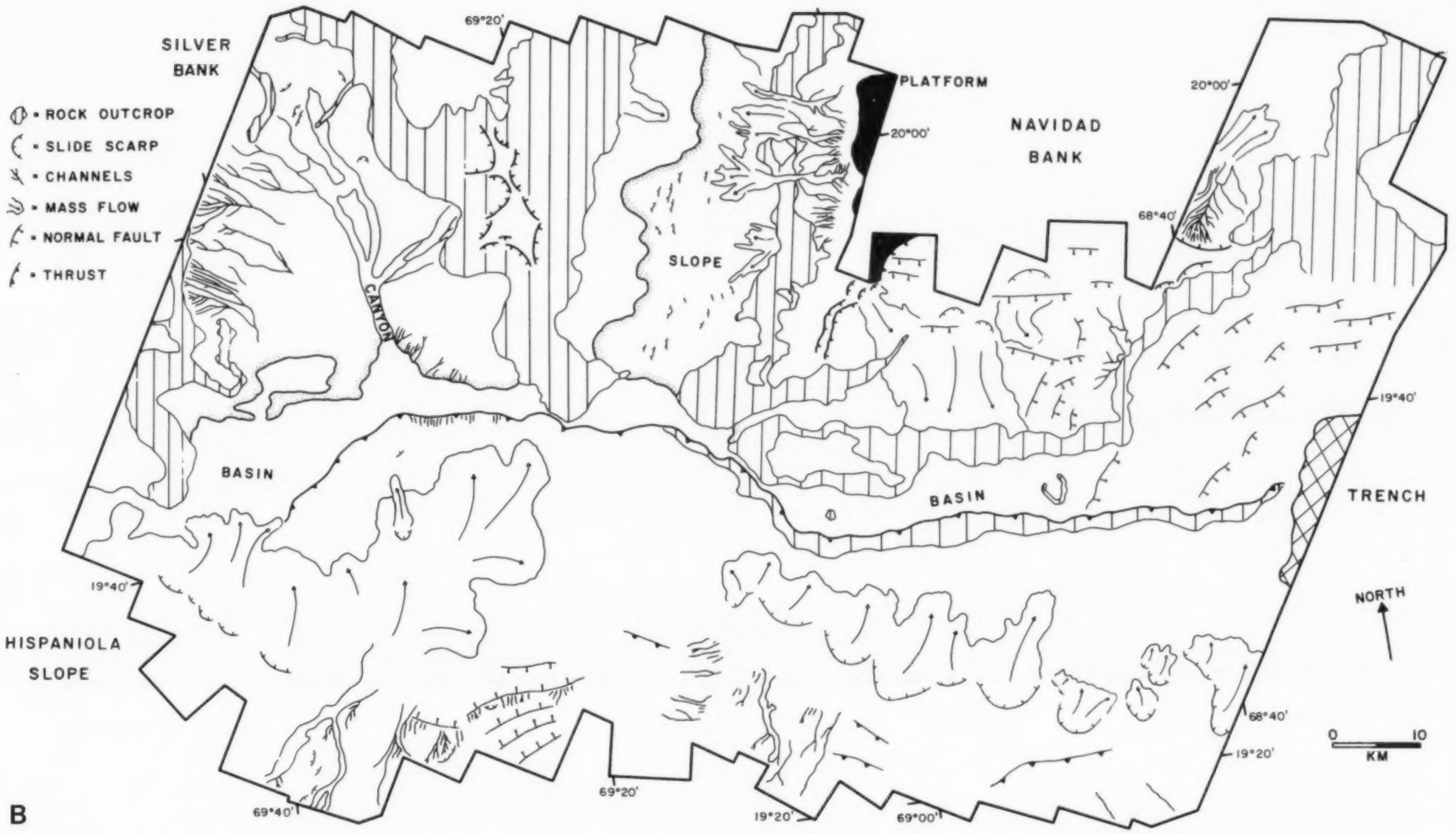

Fig. 23. (A) SeaMARC II seafloor reflectivity mosaic from south of Navidad Bank (tracklines 8–17 and 44–48, Fig. 3). (B) Line drawing interpretation of data in (A).

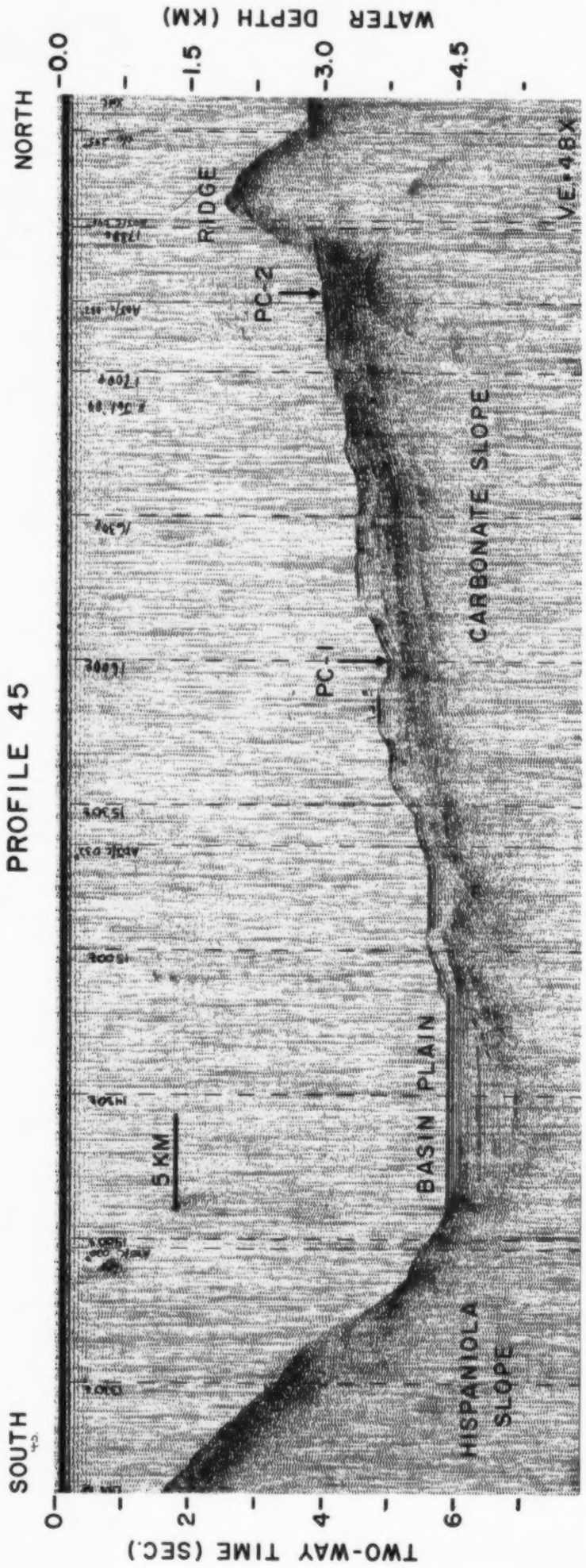

Fig. 24. Analog seismic reflection profile 45 from south of Silver Bank (Fig. 3). Location of piston cores (*PC*) *1* and *2* also shown.

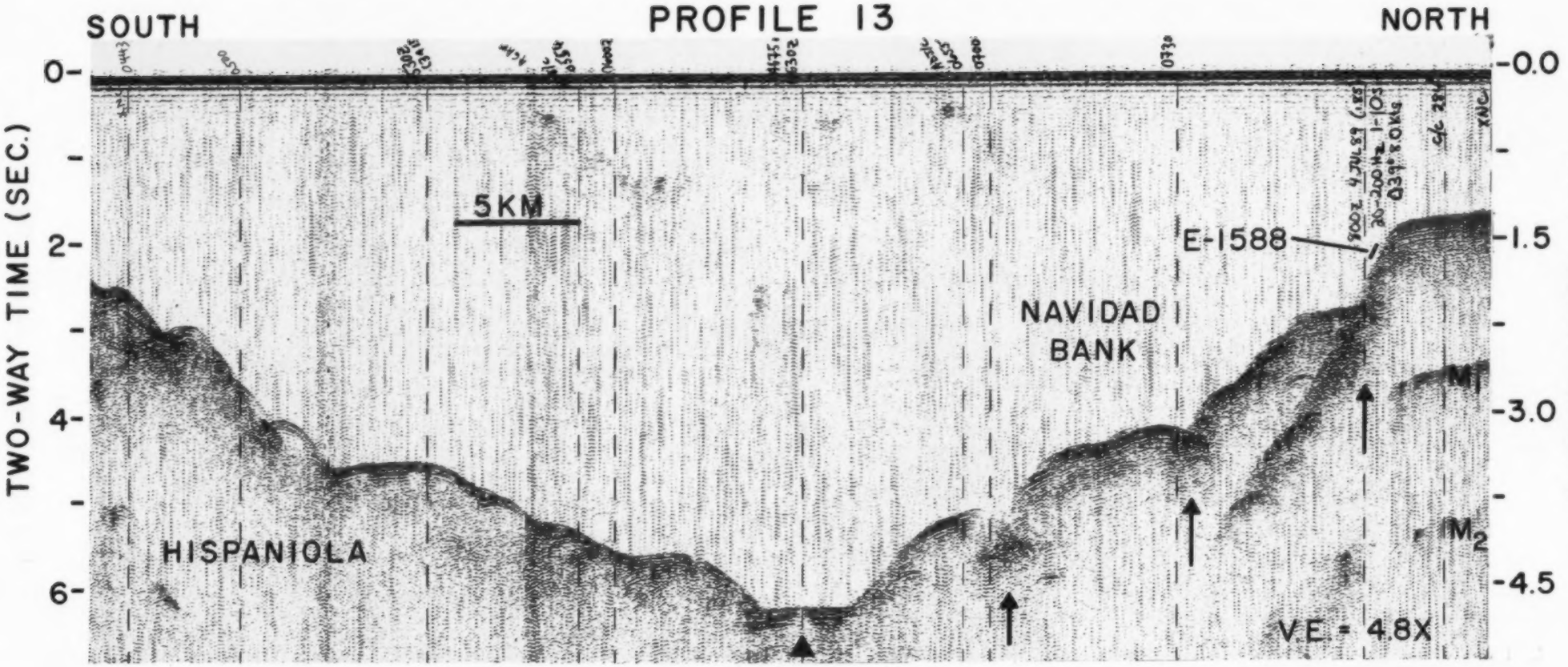

Fig. 25. Analog seismic reflection profile 13 from south of Navidad Bank (Fig. 3). Arrows mark probable normal faults; triangle marks collisional contact between Bahamas and Hispaniola. Dredge *E-1588* from Freeman-Lynde (1981).

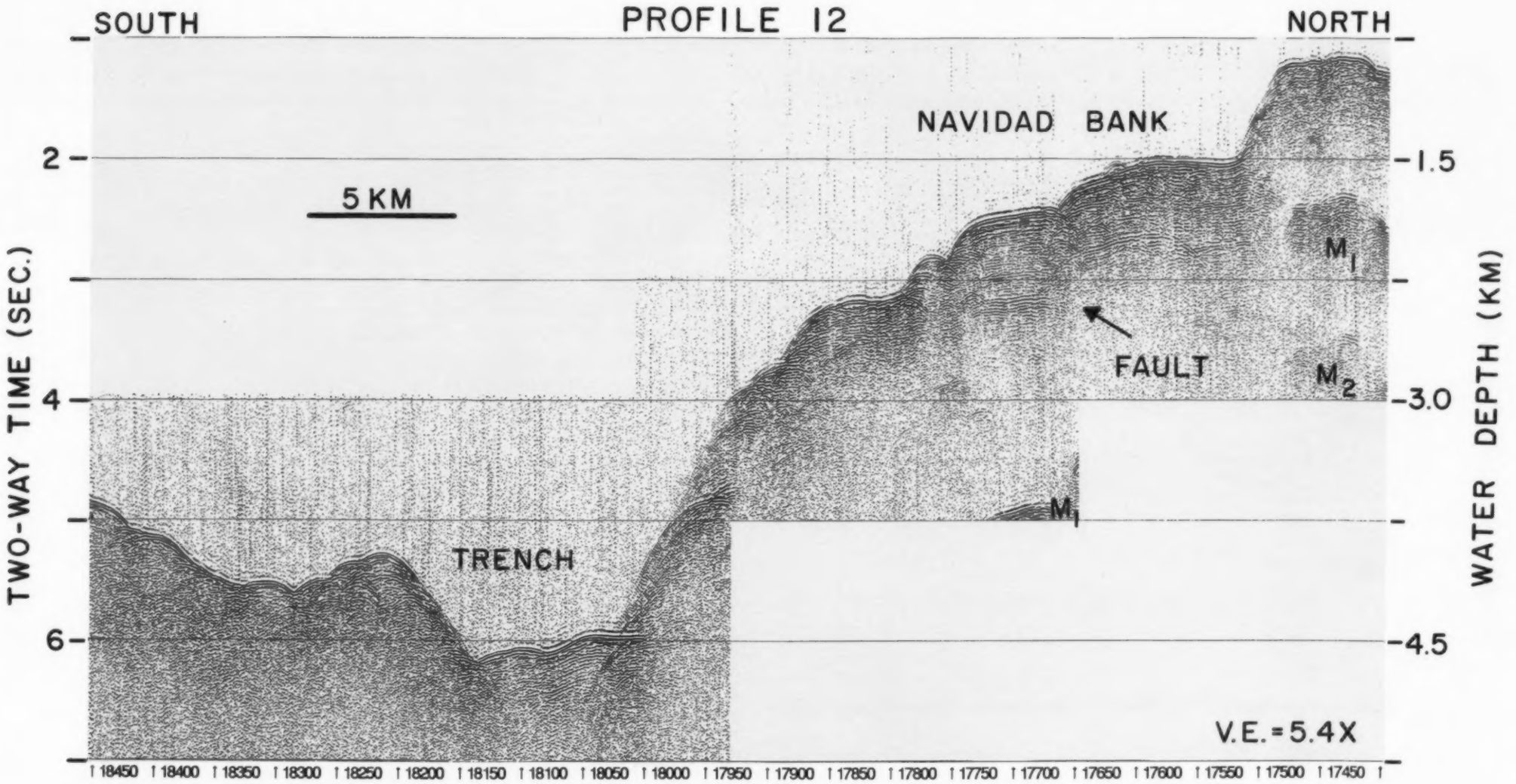

Fig. 26. Northern portion of digitally processed single channel seismic reflection profile 12 from south of Navidad Bank (Fig. 3) illustrating normal (down-to-basin) offset (arrow). Large numbers along base are shot points.

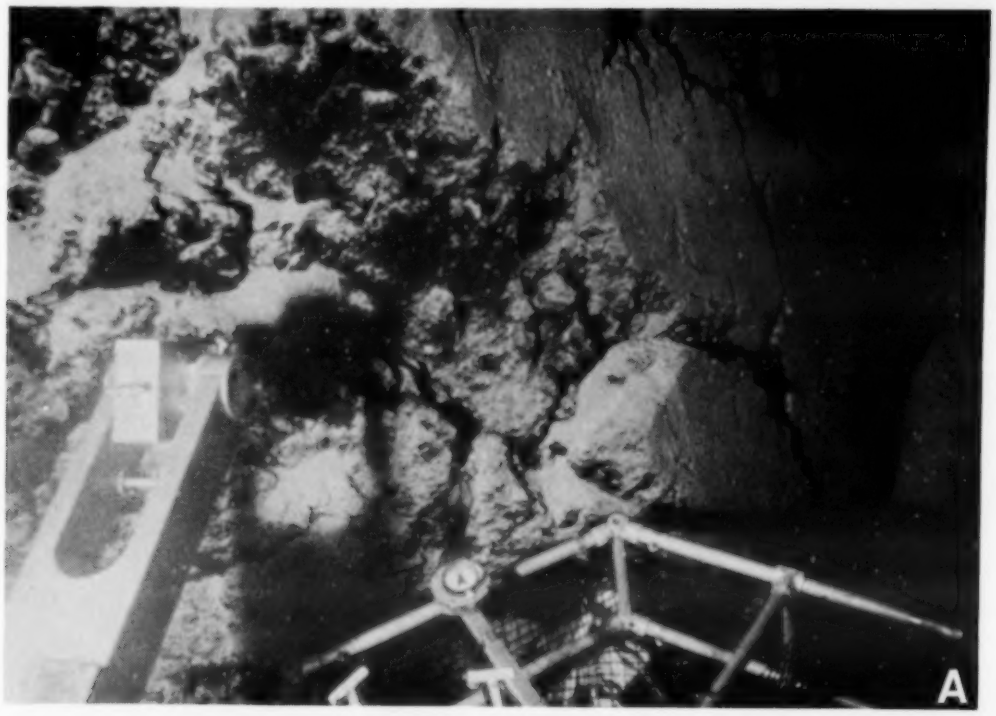

Fig. 27. Photographs of southern margin of Navidad Bank taken during *ALVIN* dive 643 (Fig. 18): (A) fault scarp cutting Cretaceous shallow-water limestones at 3465 m; (B) fault gauge within Cretaceous shallow-water limestones at 3140 m. *ALVIN* holding cage is approximately 1.5 m across.

1985). Our geophysical data (Figs. 6, 8 and 9) coupled with the recovery of fore-reef shallow-water limestones (Freeman-Lynde, 1981) suggest that there are intact sections of an Early Cretaceous carbonate platform margin exposed along the Bahama Escarpment separated by erosional reentrants. The reentrants are oriented NE–SW perpendicular to the strike of the Bahama Escarpment yet parallel with the trend of marine magnetic lineations in the North Atlantic (Klitgord et al., 1984). The Bahama Escarpment is believed to mark the trace of a transform plate boundary during early phases of Atlantic opening (Uchupi et al., 1971; Mullins and Lynts, 1977; Klitgord et al., 1984). Ross and Scotese (1988) depict an eastward migrating intersection of the North Atlantic spreading center with the Bahama Escarpment fracture zone during the Late Jurassic–Early

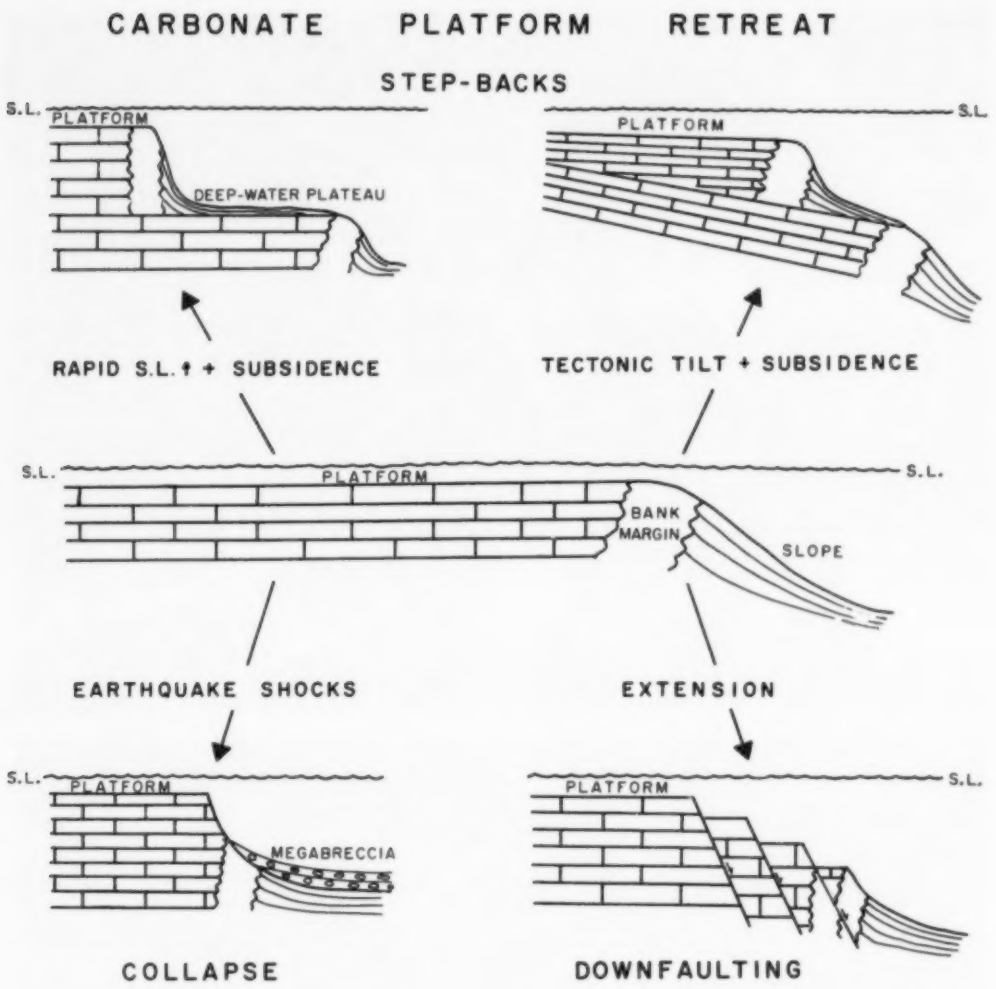

Fig. 28.Schematic cartoon illustrating fundamental concepts of bank margin step-back, collapse and downfaulting.

Cretaceous. The reentrants we observe being preferentially eroded along the Bahama Escarpment may represent zones of structural weakness generated by this passing ridge-transform juncture. If correct, it would not only provide an explanation for the origin of the escarpment reentrants, but may also provide a first-order mechanism for the origin of segmented bank and basin physiography in the southeast Bahamas (Freeman-Lynde and Ryan, 1987). That the banks respond as individual tectonic elements is evidenced by variations in the thickness of Late Cenozoic shallow-water carbonates in the southeast Bahamas (Pierson, 1982).

During the mid-Cretaceous the carbonate platform margin north of Silver Bank was drowned and stepped-back (retreated) approximately 50 km to the southwest where it realigned itself parallel to its former trace, perhaps along a tectonic lineament. Dredge and submersible samples loosely constrain this drowning/step-back event as occurring some time after the Barremian–Aptian (youngest shallow-water carbonates) and prior to the Maastrichtian (oldest deep-water carbonates; Freeman-Lynde and Ryan, 1985), or between ~120–75 Ma. This step-back is an order of magnitude greater than the 5 km of erosional retreat of the Bahamas Escarpment suggested by Freeman-Lynde and Ryan (1985).

The mid-Cretaceous drowning and step-back of the platform margin north of Silver Bank appears to have been part of a global response of carbonate platforms (Schlager, 1981), and thus can not be ascribed to a local or even regional process. Schlager (1981) has compiled evidence for the drowning of Pacific guyots as well as carbonate platforms throughout the North Atlantic between about 105–85 Ma, and suggested either a rapid pulse of relative sea level rise or deterioration of the environment as plausible explanations for their global demise. ODP Leg 101 drilling at site 627 on the southern Blake Plateau north of Little Bahama Bank has documented drowning at about

100 Ma, near the Albian–Cenomanian boundary (Scientific Party, 1985).

Although the exact cause of the drowning of mid-Cretaceous carbonate platforms has yet to be resolved, recent hypotheses have favored deterioration of the environment as a primary control. Hallock and Schlager (1986) have suggested that excess nutrients in marine waters during the mid-Cretaceous led to the demise of carbonate platforms which are adapted to oligotrophic conditions. However, modern carbonate platforms on the Nicaragua Rise which have increased trophic resources (Hallock et al., 1988) continue to be prolific sediment producers (Glaser and Droxler, 1991) despite the fact that coral-reef communities are largely absent. Vogt (1989) has recently expanded the Hallock and Schlager (1986) model to include deep anoxic (and toxic) waters brought to the surface of the ocean via volcanogenic hydrothermal upwelling during the mid-Cretaceous. And, most recently, Jenkyns (1991) has argued in favor of a combination of rapid sea level rise and anoxia, whereas Eberli (1991) has suggested global plate rearrangement as a contributing cause for platform demise.

It has also been known for some time that the mid-Cretaceous was a time of rapid sea-floor spreading on a global basis (Larson and Pitman, 1972), perhaps in response to a "pulse" of the Earth's internal tectonic system (Sheridan, 1983). Larson (1991) has recently calculated a 50–70% increase in the rate of formation of ocean crust during the mid-Cretaceous. He suggests an abrupt onset with peak production rates between 120 and 100 Ma in response to a "super plume" that rose from the core/mantle boundary and erupted beneath the mid-Pacific (Larson, 1991). Increased volume of oceanic plateaus at this time coupled with an increase of global spreading rates would result in a relative rise of sea level (Pitman, 1978) which was at a maximum between about 105–75 Ma (Haq et al., 1987). Although previous calculations of the average rate of mid-Cretaceous sea-level rise suggest that it was insufficient to drown carbonate platforms (Schlager, 1981), a short, rapid rise due to an abrupt tectonic pulse may have submerged carbonate platforms below the euphotic zone. Regardless of the exact mechanism of drowning, step-back of the northern margin of Silver Bank in the mid-Cretaceous was likely part of a global, rather than regional, response and resulted in large-scale retreat.

Mouchoir Bank, which rests on top of a regional deep-water plateau at about 1000 m (Fig. 3), similarly records a drowning and step-back event. However, our dredge results, as well as differences in water depth, document this as a considerably younger event than the drowning and step-back north of Silver Bank. Dredge D-2 (Fig. 14; 1510–800 m) recovered shallow-water limestones of Late Tertiary age capped by deep-water limestones of mid-Pliocene age, indicating drowning and step-back during the Late Tertiary prior to the mid-Pliocene. Although a portion of the Florida platform was drowned during the mid-Miocene in response to an intensification of the Gulf Stream (Mullins and Neumann, 1979), seismic profiles from Great Bahama Bank indicate extensive progradation and aggradation during this interval (Eberli and Ginsburg, 1989). Thus, drowning and step-back of southern Mouchoir Bank appears to have been a local rather than regional or global event.

The timing of the step-back of Mouchoir Bank is consistent with its linkage to the collision of the southeast Bahamas with Hispaniola, which began in the late Miocene (Sykes et al., 1982). A multichannel seismic reflection profile across this drowned platform which continues south of the Caicos–Turks banks (just west of Mouchoir Bank) documents that it is tilted to the south and perhaps downfaulted (Wanless et al., 1989). This is consistent with our data (profile 52; Fig. 12) which also indicate a southward tilt of a drowned platform. We suggest that tectonic tilting and subsidence, related to the collision and oblique underthrusting of the southeast Bahamas with Hispaniola in the late Miocene–early Pliocene was responsible for the drowning and step-back of southern Mouchoir Bank.

Collapse of platform margins

Large, amphitheater-shaped embayments (i.e., scallops) are common along the bank margins of carbonate platforms in the southeast Bahamas

(Mullins and Hine, 1989). Our bathymetric and reflectivity data (Figs. 14 and 15) have defined three large (~20 km across) well-developed scallops south of Mouchoir Bank. Rock dredges (D-2, D-3) confirm the erosional nature of these scallops via recovery of shallow-water limestones from their steep, deep-water scarps. Dredge D-2 recovered shallow-water limestones of Late Tertiary age indicating slope failure during Late Tertiary or younger time. In addition, the eastern scallop (Fig. 15) has a large debris flow associated with it complete with flow-lines exposed on the seafloor. Although the exact timing of this debris flow is not presently known, it must have been a relatively recent event if flow lines are still evident on the seafloor.

It is our interpretation that these large scallops and debris flow are the product of large scale catastrophic collapse, similar to that documented along the west Florida platform margin (Mullins et al., 1986). The exact mechanism of failure continues to be debatable (Mullins and Hine, 1989) but the timing of collapse south of Mouchoir Bank is consistent with the collision of the southeast Bahamas and Hispaniola. Large earthquake shocks associated with plate collision, such as the 8.1 Ms event in 1946, may have triggered these large-scale failures.

Downfaulting

Seismic reflection data (Figs. 25 and 26) coupled with submersible observations (Freeman-Lynde and Ryan, 1985; Heezen et al., 1985) and rock dredge results (Fox and Heezen, 1975) all indicate post-Eocene downfaulting along the southern and southeastern margin of Navidad Bank. This is a somewhat surprising result considering the overall transpressional nature of the current plate boundary here. However, Masson and Scanlon (1991) have also identified E–W oriented normal faults north of the Puerto Rico Trench along its western reaches. To explain this extension, Masson and Scanlon (1991; Fig. 29) have proposed a model of counterclockwise rotation of the Puerto Rico block within the broad, left-lateral shear zone of the northern Caribbean plate boundary. Such rotation would produce extensional stress along the southern and southeastern margin of Navidad Bank. Counterclockwise rotation of the Puerto Rico block is supported by paleomagnetic data. Vincenz and Dasgupta (1978) have documented "large" anticlockwise rotation of eastern Hispaniola since the Late Cretaceous and Van Fossen et al. (1989) have shown that Puerto Rico has undergone 45° of post-Eocene counterclockwise rotation of which 24.5° occurred during the late Miocene (Reid et al., 1991).

An alternative explanation for the downfaulting observed south of Navidad Bank might be extension associated with lithospheric bending of the southeast Bahamas as it was obliquely underthrust beneath northeast Hispaniola during a phase of attempted subduction (Heezen et al., 1985). Earthquake focal data document the presence of an underthrust (subducted) slab beneath eastern Hispaniola that extends to depths at least 150 km (McCann and Sykes, 1984).

Conclusions

A SeaMARC II seismic reflection investigation of the southeast Bahamas–Hispaniola collision zone has documented the first-order response of carbonate platforms to active plate tectonic collision and global tectonic processes. The isolated banks in the southeast Bahamas were once part of larger carbonate platforms that have retreated to their present positions since the mid-Cretaceous.

North of Silver Bank, an Early Cretaceous carbonate platform was drowned during the mid-Cretaceous and stepped-back approximately 50 km leaving behind a deep-water plateau. The seaward edge of this deep-water plateau locally contains intact sections of an Early Cretaceous carbonate platform margin separated by erosional reentrants that may mark ancient spreading center-transform intersections. Drowning and step-back in the mid-Cretaceous appear to have been part of a global response of carbonate platforms to a rapid pulse of sea level rise driven by the Earth's interior tectonic system. A number of broad, shallow canyons, akin to mountainous avalanche chutes, extend down the steep northern scarp of Silver Bank and funnel debris into the erosional reentrants. These chutes may be a product of

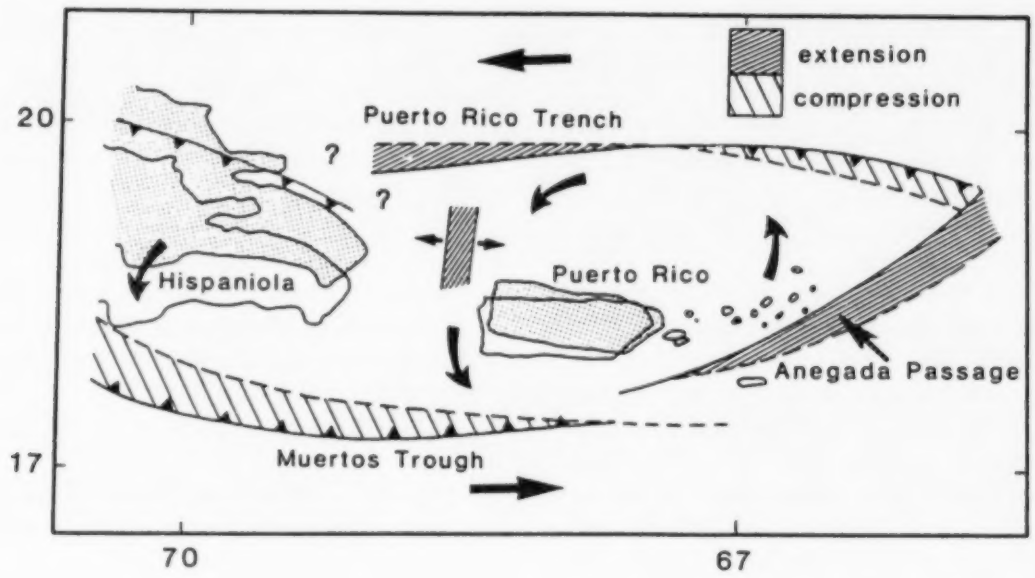

Fig. 29.Schematic model of possible plate interactions in northern Caribberan resulting in counter-clockwise rotation of Puerto Rico block and extension along western reaches of Puerto Rico Trench and southern Navidad Bank area (from Masson and Scanlon, 1991).

collapse of the platform margin due to seismic shaking.

The southern margin of Mouchoir Bank has also been drowned and has stepped-back by about 30 km. This event occurred during the Late Tertiary due to southward tilting of the southeast Bahamas in response to oblique underthrusting along the Bahamas–Hispaniola collision zone. In addition, large (~20 km across) scalloped embayments occur along the southern margin of Mouchoir Bank which have contributed to the erosional retreat of this carbonate platform. Seaward of one of these scallops is a large debris flow complete with flow-lines exposed on the seafloor. These features are interpreted as catastrophic submarine landslides that failed during Late Tertiary or younger time as a consequence of large earthquake shocks along the Bahamas-Hispaniola collision zone.

South of Navidad Bank portions of carbonate platforms appear to have been accreted to the northern slope of Hispaniola during the collisional process. In addition, the platform margin of Navidad Bank has retreated via post-Eocene downfaulting which may be a consequence of the counterclockwise rotation of the Puerto Rico block within the broad left-lateral shear zone of the northern Caribbean plate boundary or lithospheric bending during oblique subduction.

Overall, these results provide an initial framework to view the dynamic response of carbonate platforms to active plate tectonic collision. The fundamental response of carbonate platforms in the southeast Bahamas has been retreat which contrasts sharply with the progradational nature of carbonate platforms in the tectonically passive, northwestern Bahamas.

Acknowledgements

We thank Alexander Shor, his SeaMARC II personnel, and the entire crew of the R/V *MOANA WAVE* for a very successful research cruise (MW 8908). Supported by NSF grant OCE-88-12720. We also thank CHEVRON USA for allowing AJM and ADJ to participate in this project and comments by two anonymous reviewers.

References

Austin, J.A., 1983. Overthrusting in a deep-water carbonate terrane. In: A.W. Bally (Editor), Seismic Expression of Structural Styles, Am. Assoc. Petrol. Geol. Stud. Geol. 15: 3.4.2-167–3.4.2-172.

Ball, M.M., Martin, R.G., Bock, W.D., Sylvester, R.E., Bowles, R.M., Taylor, D., Coward, E.L., Dodd, J.E. and Gilbert, L., 1985. Seismic structure and stratigraphy of northern edge of Bahaman-Cuban collision zone. Am. Assoc. Pet. Geol. Bull., 69:1275–1294.

Bosellini, A., 1989. Dynamics of Tethyan carbonate platforms. SEPM Spec. Publ., 44:3–13.

Bracey, D.R. and Vogt, P.R., 1970. Plate tectonics in the Hispaniola area. Geol. Soc. Am. Bull., 81:2855–2860.

Corso, W., Schlager, W., Flugel, E. and Buffler, R.T., 1985. A reinterpretation of an Early Cretaceous carbonate platform on Abaco Knoll, northern Bahamas. Trans. Gulf Coast Assoc. Geol. Soc., 35:29–38.

Davis, E.E., Currie, R.G., Sawyer, B.S. and Kosalos, J.G., 1987. The use of swath bathymetric and acoustic image mapping tools in marine geoscience. Mar. Tech. Soc. J., 20:17–27.

Dillon, W.P., Edgar, N.T., Scanlon, K.M. and Klitgord, K.D., 1987. Geology of the Caribbean. Oceanus, 30:42–52.

Dillon, W.P., Austin, J.A., Scanlon, K.M., Edgar, N.T. and Larson, L.M., 1992. Accretionary margin of northwestern Hispaniola: Morphology, structure, and development of part of the northern Caribbean plate boundary. Mar. Pet. Geol.

Ditty, P.S., Harmon, C.J., Pilkey, O.H., Ball, M.M. and Richardson, E.S., 1977. Mixed terrigenous-carbonate sedimentation in the Hispaniola-Caicos turbidite basin. Mar. Geol., 24:1–20.

Eberli, G.P., 1991. Growth and demise of isolated carbonate platforms: Bahamian controversies. In: Controversies in Modern Geology: Academic Press, New York, Chap. 12, pp. 231–248.

Eberli, G.P. and Ginsburg, R.N., 1987. Segmentation and coalescence of Cenozoic carbonate platforms in northwestern Great Bahama Bank. Geology, 15:75–79.

Eberli, G.P. and Ginsburg, R.N., 1989. Cenozoic progradation of northwestern Great Bahama Bank, a record of lateral platform growth and sea-level fluctuations. SEPM Spec. Publ., 44:339–351.

Erlich, R.N., Barrett, S.F. and Ju, G.B., 1990. Seismic and geologic characteristics of drowning events on carbonate platforms. Am. Assoc. Pet. Geol. Bull., 74:1523–1537.

Fox, P.J. and Heezen, B.C., 1975. Geology of the Caribbean crust. In: A.E.M. Nairn and F.G. Stehli (Editors), The Ocean Basins and Margins, Vol. 3, The Gulf of Mexico and the Caribbean, Plenum, New York, pp. 421–466.

Freeman-Lynde, R.P., 1981. The marine geology of the Bahama Escarpment. Ph.D. Dissert., Columbia Univ., New York, 284 pp.

Freeman-Lynde, R.P. and Ryan, W.B.F., 1985. Erosional modification of Bahama Escarpment. Geol. Soc. Am. Bull., 96: 481–494.

Freeman-Lynde, R.P. and Ryan, W.B.F., 1987. Subsidence history of the Bahama Escarpment and nature of the crust underlying the Bahamas. Earth Planet Sci. Lett., 84:457–470.

Freeman-Lynde, R.P., Cita, M.B., Jadoul, F., Miller, E.L. and Ryan, W.B.F., 1981, Marine geology of the Bahama Escarpment. Mar. Geol., 44:119–156.

Glaser, K.S. and Droxler, A.W., 1991. High production and highstand shedding from deeply submerged carbonate banks, northern Nicaragua Rise. J. Sediment. Pet. Geol., 61:128–142.

Hallock, P. and Schlager, W., 1986, Nutrient excess and the demise of coral reefs and carbonate platforms. Palaios, 1: 389–398.

Hallock, P., Hine, A.C., Vargo, G.A., Elrod, J.A. and Jaap, W.C., 1988. Platforms of the Nicaragua Rise: Examples of sensitivity of carbonate sedimentation to excess trophic resources. Geology, 16:1104–1107.

Haq, B.U., Hardenbol, J. and Vail, P.R., 1987. Chronology of fluctuating sea-levels since the Triassic. Science, 235:1156–1166.

Heezen, B.C., Nesteroff, W.D., Rawson, M. and Freeman-Lynde, R.P., 1985. Visual evidence for subduction in the western Puerto Rico Trench. Carb. Geodyn. Symp., Paris, p. 287–304.

Jenkyns, H.C., 1991. Impact of Cretaceous sea level rise and anoxic events on the Mesozoic carbonate platforms of Yugoslavia. Am. Assoc. Pet. Geol. Bull., 75:1007–1017.

Klitgord, K.D., Popenoe, P. and Schouten, H., 1984. Florida: A Jurassic transform plate boundary. J. Geophys. Res., 89:7753–7772.

Larson, R.L., 1991. Latest pulse of the Earth: Evidence for a Cretaceous super plume. Geology, 19:547–550.

Larson, R.L. and Pitman, W.C., III, 1972, World-wide correlation of Mesozoic magnetic anomalies and its implications: Geol. Soc. Am. Bull., 83:3645–3662.

Malinverno, A., Edwards, M.H. and Ryan, W.B.F., 1990. Processing of SeaMARC swath sonar data. J. Ocean. Eng., 15:14–23.

Mann, P., Burke, K. and Matumoto, T., 1984. Neo-tectonics of Hispaniola: Plate motion, sedimentation, and seismology at a restraining bend. Earth Planet Sci. Lett., 70:311–324.

Mann, P., Schubert, C. and Burke, K., 1990. Review of Caribbean neotectonics. In: G. Dengo and J.E. Case (Editors), The Geology of North America, Vol. H, The Caribbean Region. Geol. Soc. Am., Boulder, CO, pp. 307–337.

Masson, D.G. and Scanlon, K.M., 1991. The neo-tectonic setting of Puerto Rico: Geol. Soc. Am. Bull., 103:144–154.

McCann, W.R. and Pennington, W.D., 1990. Seismicity, large earthquakes, and the margin of the Caribbean plate. In: G. Dengo and J.E. Case (Editors), The Geology of North America, Vol. H, The Caribbean Region, Geol. Soc. Am., Boulder, CO, pp. 291–305.

McCann, W.R. and Sykes, L.R., 1984, Subduction of aseismic ridges beneath the Caribbean plate: Implications for the tectonics and seismic potential of the northeastern Caribbean. J. Geophys. Res., 89:4493–4519.

Mullins, H.T. and Cook, H.E., 1986. Carbonate apron models: Alternatives to the submarine fan model for paleoenvironmental analysis and hydrocarbon exploration. Sediment. Geol., 48:37–79.

Mullins, H.T. and Hine, A.C., 1989, Scalloped bank margins: Beginning of the end for carbonate platforms? Geol., 17:30–33.

Mullins, H.T. and Lynts, G.W., 1977, Origin of northwestern Bahama Platform: Review and reinterpretation. Geol. Soc. Am. Bull., 88:1447–1461.

Mullins, H.T. and Neumann, A.C., 1979. Geology of the Miami Terrace and its paleo-oceanographic implications. Mar. Geol., 30:205–232.

Mullins, H.T., Gardulski, A.F. and Hine, A.C., 1986. Catastrophic collapse of the west Florida carbonate platform margin. Geology, 14:167–170.

Paull, C.K. and Dillon, W.P., 1980. Erosional origin of the Blake Escarpment: An alternative hypothesis. Geology, 8:538–542.

Pierson, B.J., 1982. Cyclic sedimentation, limestone diagenesis and dolomitization in Upper Cenozoic carbonates of the southeast Bahamas. Ph.D. Dissert., Univ. Miami, 294 pp.

Pitman, W.C. III, 1978. Relationship between eustacy and stratigraphic sequences of passive margins: Geol. Soc. Am. Bull., 89:1389–1403.

Playford, P.E., 1980. Devonian "Great Barrier Reef" of Canning Basin, western Australia. Am. Assoc. Pet. Geol. Bull., 64:814–840.

Reed, T.B. and Hussong, D., 1989. Digital image processing techniques for enhancement and classification of SeaMARC II side scan sonar imagery. J. Geophys. Res., 94:7469–7490.

Reid, J.A., Plumley, P.W. and Schellekens, J.H., 1991. Paleomagnetic evidence for late Miocene counterclockwise rotation of north coast carbonate sequence, Puerto Rico. Geophys. Res. Lett., 18:565–568.

Ross, M.I. and Scotese, C.R., 1988. A hierarchical tectonic model of the Gulf of Mexico and Caribbean region. Tectonophysics, 155: 139–168.

Schlager, W., 1981. The paradox of drowned reefs and carbonate platforms. Geol. Soc. Am. Bull., 92:197–211.

Schlager, W. and Camber, O., 1986. Submarine slope angles, drowning unconformities and self-erosion of limestone escarpments. Geology, 14:762–765.

Schlager, W. and Chermak, A., 1979. Sediment facies of platform-basin transition, Tongue of the Ocean, Bahamas. SEPM Spec. Publ., 27:193–208.

Schlager, W. and Ginsburg, R.N., 1981. Bahama carbonate platforms—The deep and the past. Mar. Geol., 44:1–24.

Schneider, E.D. and Heezen, B.C., 1966. Sediments of the Caicos Outer Ridge, the Bahamas. Geol. Soc. Am. Bull., 77:1381–1398.

Scientific Party, 1985. Rise and fall of carbonate platforms in the Bahamas. Nature, 315:632–633.

Seiglie, G.A., Froelich, P.N. and Pilkey, O.H., 1976. Deep-sea sediments of Navidad Basin: Correlation of sand layers. Deep-Sea Res., 23:89–101.

Sheridan, R.E., 1983. Phenomena of pulsation tectonics related to the breakup of the eastern North American continental margin. Tectonophysics, 94:169–185.

Sheridan, R.E., Mullins, H.T., Austin, J.A., Ball, M.M. and Ladd, J.W., 1988. Geology and geophysics of the Bahamas: In: J.A. Grow and R.E. Sheridan (Editors), The Geology of North America, Vol. I-2, The Atlantic Continental Margin. Geol. Soc. Am., Boulder, CO, p. 329–364.

Sykes, L.R., McCann, W.R. and Kafka, A.L., 1982, Motion of Caribbean plate during last 7 million years and implications for earlier Cenozoic movements: J. Geophys. Res., 87:10656–10676.

Tyce, R.C., 1987. Deep seafloor mapping systems—A review. Mar. Tech. Soc. Jour., 20:4–16.

Uchupi, E., Milliman, J.D., Luyendyk, B.P., Bowin, C.O. and Emery, K.O., 1971. Structure and origin of southeastern Bahamas: Am. Assoc. Pet. Geol. Bull., 55:687–704.

Van Fossen, M.C., Channell, J.E.T. and Schellekens, J.H., 1989, Paleomagnetic evidence for Tertiary anticlockwise rotation in southwest Puerto Rico. Geophys. Res. Lett., 16:819–822.

Vincenz, S.A. and Dasgupta, S.N., 1978. Paleomagnetic study of some Cretaceous and Tertiary rocks on Hispaniola. Pure Appl. Geophys., 116:1200–1210.

Vogt, P.R., 1989. Volcanogenic upwelling of anoxic, nutrient-rich water: A possible factor in carbonate bank/reef demise and benthic faunal extinctions?. Geol. Soc. Am. Bull., 101:1225–1245.

Wanless, H.R., Tedesco, L.P., Rossinsky, V. and Dravis, J.J., 1989. Carbonate environments and sequences of Caicos Platform. 28th Int. Geol. Cong. Field Trip Guideb. T374, Am. Geophys. Union, Washington, D.C., 75 pp.

Marine Geology, 105 (1992) 211–224
Elsevier Science Publishers B.V., Amsterdam

Basin changes in Jervis Bay, New South Wales: 1894–1988

J.K. Bowyer

Centre for Resource and Environmental Studies, Australian National University, G.P.O. Box 4, Canberra, A.C.T. 2601, Australia

(Received February 19, 1991; revision accepted September 16, 1991)

ABSTRACT

Bowyer, J.K., 1992. Basin changes in Jervis Bay, New South Wales: 1894–1988. Mar. Geol., 105: 211–224.

A qualitative assessment of the stability of the Jervis Bay basin, based on the hydrological and physical characteristics of the bay, suggests that the basin, as a whole, should be a relatively stable unit in the long-term. Through the employment of a geographic information system (GIS), a quantitative comparison of a historical, hydrological chart, dated 1894, and a recent hydrological survey of 1988, was performed. The comparison revealed that the basin has in fact deepened by 0.41 m over the 94 year period. The significance of this change was assessed in the light of the many errors inherent in the old chart. The error analysis indicated that the basin change was significant. Further hydrological comparisons based on the subdivision of the basin into smaller 'geomorphic' units, indicated that the magnitude and direction of basin change was not uniform over the entire basin. Over the 94 year period, a substantial portion of the northern basin has shallowed whilst the southern basin was dominated by deepening. The latter deepening was more pronounced along the nearshore margins and through the entrance channel. This spatial pattern of basin change was readily explicable through the spatial expression of the energy regime in Jervis Bay.

Introduction

Jervis Bay is a broad embayment bounded by the rocky headlands of Bhewerre and Beecroft Peninsulas on the central New South Wales coast (Fig. 1). The basin originated through the gentle folding of Permian strata (Perry and Dickins, 1952). The central axis of the synclinal valley is aligned along the N–S axis of Jervis Bay while the anticlinal axis is aligned with the two headlands of Beecroft and Bherwerre Peninsulas (Walker, 1967). Periods of lower sea level in the early Pleistocene and Late Tertiary initiated a phase of stream incision within the synclinal valley. The ancestral form of Currumbene Creek, guided by the Currumbene Fault, carved much of the present day basin. It eventually breached the anticlinal ridge linking Bowen Island to Beecroft Peninsula, thereby forming the entrance to the embayment (Albani et al., 1972). A minor drainage system drained the uppermost northeastern section of the embayment known as Hare Bay (Johnson and Albani, 1975).

Marine sediment within the basin is associated with two distinct influxes (Albani et al., 1972). The older, underlying sediment was suggested to be of aeolian origin deposited subsequent to the erosion of the basin through stream incision (Albani et al., 1972). The younger, overlying sediment is considered to be of marine origin, deposited during marine transgressions. Walker (1967) suggested that these marine transgressions were responsible for transporting marine sediment into the shallow, secondary embayments of Jervis Bay, thereby enabling the development of beaches, foredunes and barriers. Remnants of the bedrock shoreline are still prominent in Jervis Bay though. The southern section of Beecroft Peninsula is characterised by steeply cliffed, resistant Jervis Bay sandstone. According to Walker (1967, p. 46) the sandstone has undergone only minor, recent modification in comparison to the less resistant, Wandrawandian siltstone expressed in bedrock outcrops on the northern and western shorelines.

Whilst the natural history of Jervis Bay portrays an era of considerable physical change and devel-

0025-3227/92/$05.00 © 1992 — Elsevier Science Publishers B.V. All rights reserved

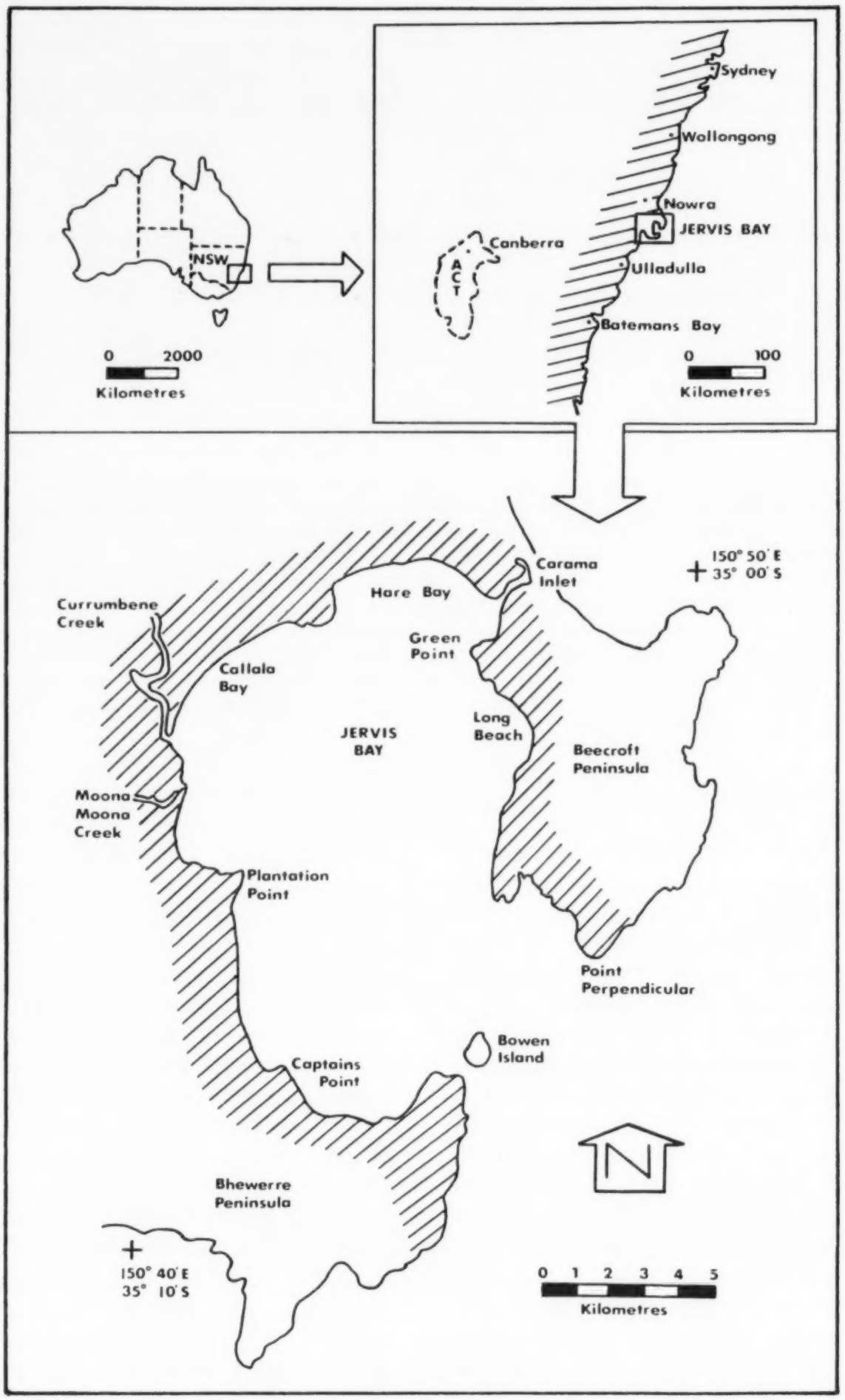

Fig. 1. Regional setting of Jervis Bay, New South Wales.

opment, the situation today is quite the contrary. Both the fluvial and marine sources of sediment to the bay are very limited. Only three drainage systems, of any notable size, enter Jervis Bay. These drainage systems, namely, Moona Moona Creek, Currumbene Creek and Carama Inlet, have small catchment areas and contribute very little sediment load to the basin of Jervis Bay. There is a small influx of marine sediment into the embayment through the narrow channel between Bowen Island and Bherwerre Peninsula. This sediment, however, only has a localised significance since it is confined to a tidal delta in the lee of Bowen Island. The introduction of marine sediment through the main channel between Bowen Island and Point Perpendicular is inhibited by the extreme depths which attain 40 metres (see Fig. 2).

In this paper, the volumetric changes of the Jervis Bay basin and a number of 'geomorphic' sub-units have been determined so as to illustrate the spatial variability of basin changes within Jervis Bay. The spatial variability may indicate patterns of sediment movement within the bay, which in turn may reflect upon mechanisms for adjacent shoreline movements.

The study environment

The fringing shorelines of Jervis Bay are characterised by shallow, secondary embayments

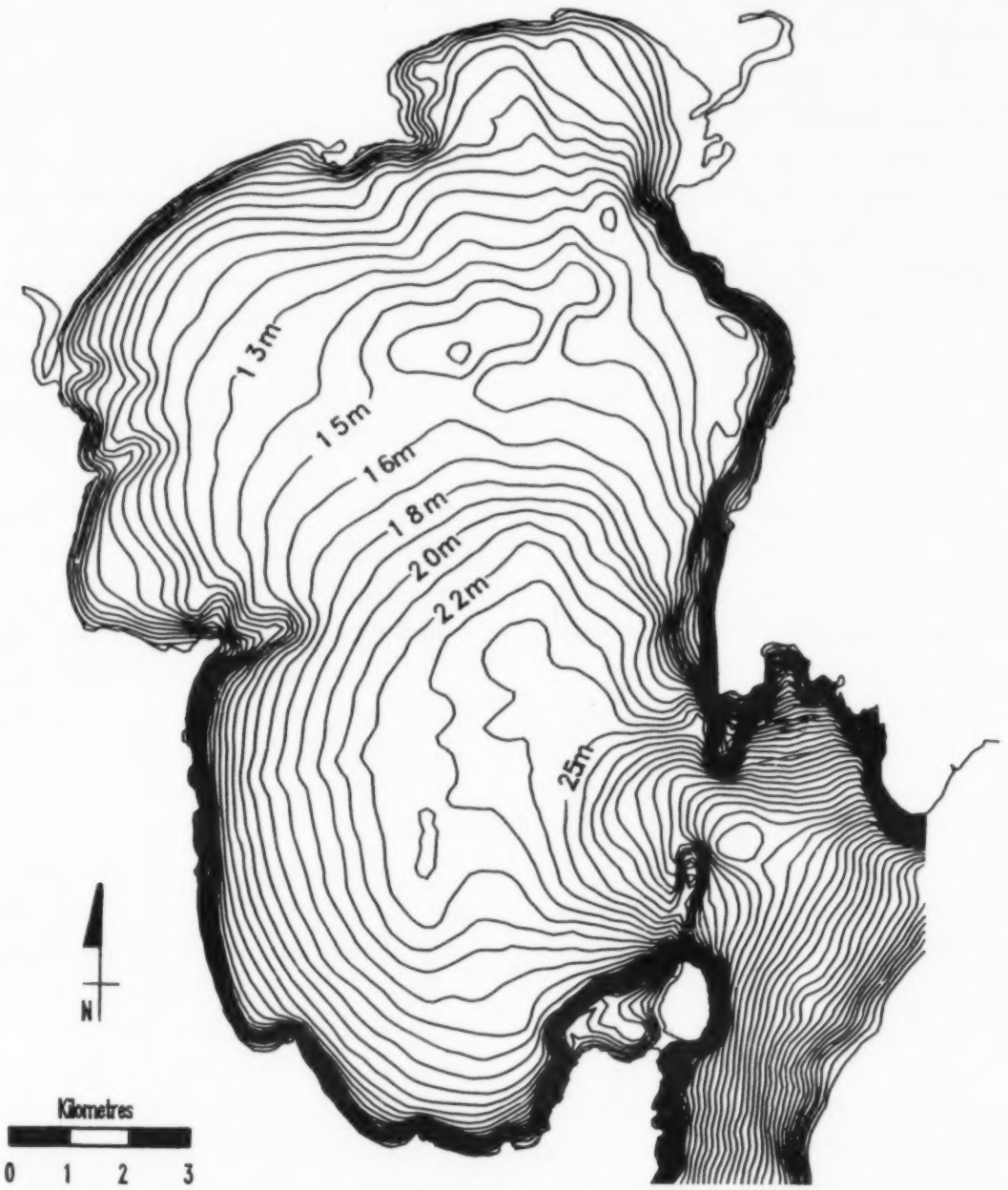

Fig. 2. Bathymetric expression of the Jervis Bay basin.

bounded by rocky headlands. The cellular beaches are fringed by foredunes and barrier systems, the latter being composed of numerous, parallel beach ridges or relict foredunes (Thom et al., 1986). In general, these are of low relief, with the exception of Callala Bay, wherein the strong influence of southeasterly swell waves has enabled the formation of an extensive barrier system. It measures 3 km in length, 0.5 km in width and attains heights of up to 3 m above mean sea level (Thom et al., 1986). Sediment characteristics within the basin exhibit a strong zonation between the centre and the margins. According to Taylor (1971), the more intense working of wave activity in the marginal zone leads to the removal of silt, clay and carbonates to the central zone. That is, the sediment of the marginal zone is typically coarser and better sorted than that of the central basin.

Wave action within Jervis Bay is characterised by both local wind-wave activity and swell waves. Wind-wave activity is generated by three dominant wind systems. Northeasterly seabreezes operate from early spring, through summer, until middle autumn. Strong southerly winds occur all year round, varying in speed and frequency on a diurnal basis. Storm events of the winter period are characterised by strong westerly and northwesterly winds. The recorded occurrence of highest wave energy in the bay is at Captains Point where significant wave height exceeds 1.0 m approximately 1% of the time and 0.2 m approximately 80% of the time. In comparison, offshore from Jervis Bay the significant wave height exceeds 1.0 m approximately 80% of the time and 4.0 m approximately 0.5% of the time (Department of Administrative Services-Construction Group, 1988). The swell regime of Jervis Bay is characterised by a persistent southerly to southeasterly swell generated in the oceanic waters off Jervis Bay. This swell is typically low in amplitude and long in length. The refraction of the dominant southeasterly swell in the Jervis Bay basin results in its energy being received predominantly along the shorelines of Callala Bay and Hare Bay (Fig. 3).

Major water circulation patterns within Jervis Bay are driven by tides, wind and variations in water temperature. Tides offshore from Jervis Bay are predominantly semidiurnal. The microtidal condition is characterised by Mean Higher Low Water to Mean Lower High Water neap tides of 0.9 m and Mean Lower Low Water to Mean Higher High Water spring tides of 1.3 m. The astronomical tidal range, from highest to lowest, is 2.0 m (Department of Defence, 1989). Clarke and Eliot (1984) established that Jervis Bay was dominated by a clockwise circulation in the winter and an anticlockwise circulation in the summer. The direction of the circulation was governed by tidal exchange interacting with a temperature gradient between waters inside the bay and those offshore. Currents around the margins of the bay are predominantly wind-driven with speeds attaining between 10 and 20 cm/s (Charash, 1972). Sediment movement within the marginal zones is almost entirely governed by energy regimes, of which wave activity is the dominant variable (Taylor, 1971).

Basin change studies for the central New South Wales coastline

Degrees of embayment infilling have been evaluated for several central New South Wales coastal embayments. Roy and Crawford (1979) evaluated changes of the Botany Bay basin from hydrographic charts dated 1871, 1930 and 1962/1963. Their volume estimation only included isobaths above 10 m and excluded the Georges River mouth and dredged areas. The results of their comparison suggested that the basin changes have been dominated by a long-term erosional trend over the past 150 years, reflected in a basin deepening of up to 1.0 m. Basin deepening in Botany Bay was explained by Roy and Crawford (1979) to be the result of sediment moving seaward from the bay to deeper water offshore. The conclusions of their study do not, however, consider what portion of the gross change in basin depth may be attributable to mapping errors on the old hydrographic charts.

Basin changes in Botany Bay have been similarly evaluated by Bryant (1980). In his study, the gross basin changes were evaluated by comparing basin depths on 60 m and 120 m grids from hydrographic charts dated between 1871 and 1950. Bryant (1980) considered positive and negative depth measurement errors at common grid points on the two

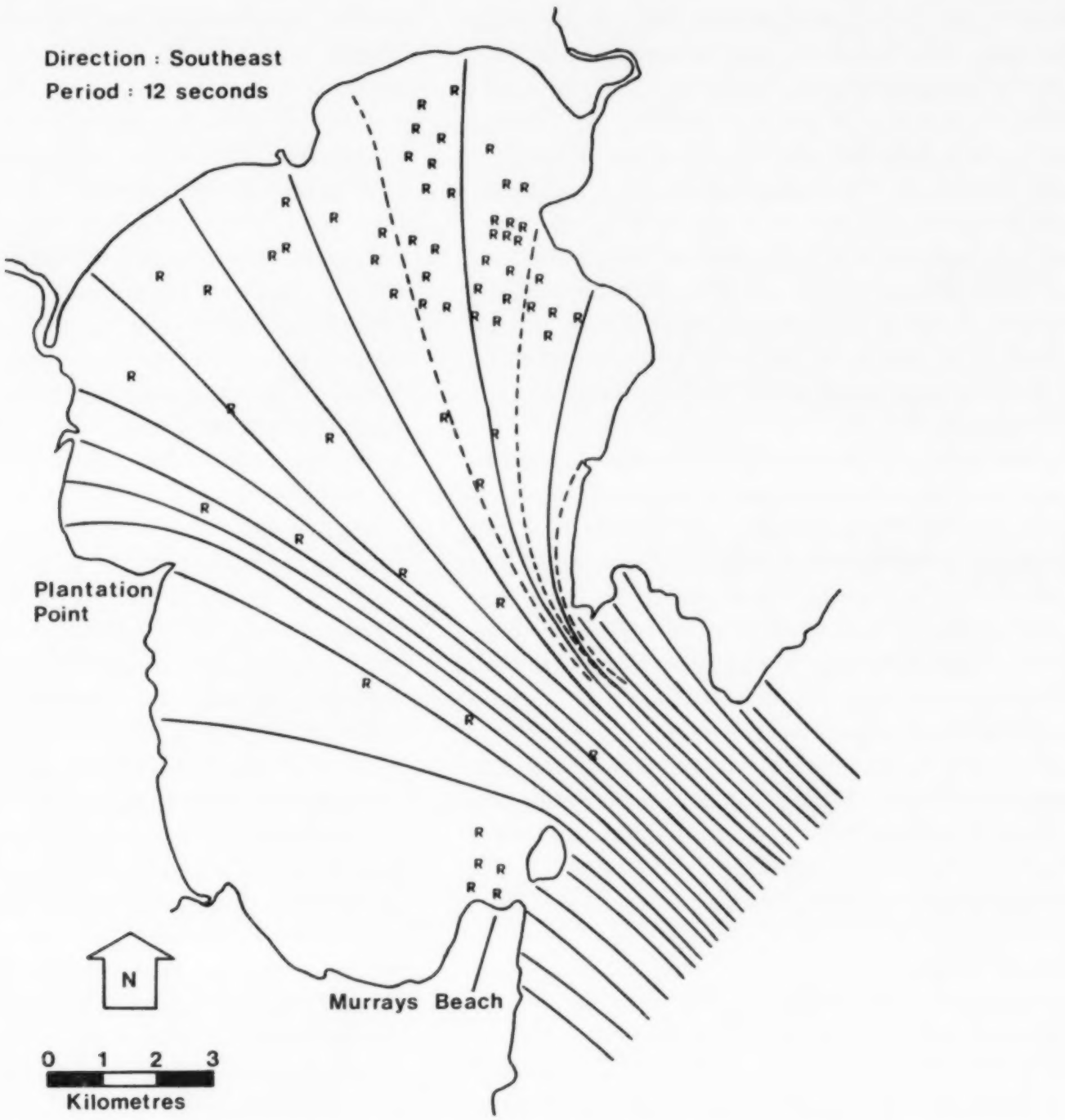

Fig. 3. Refracted wave orthogonals for a 12-s, southeasterly swell wave (Walker, 1967) and observations of swell-generated ripples on the seabed (Dames and Moore, 1985).

charts being compared. If two adjacent values of depth change alternated spatially in sign within ± 1.0 m the changes were considered insignificant. The results of the comparison suggests that basin changes in Botany Bay have been minor. Bryant (1980) concluded that "the seaward portion of the bay has remained topographically stable, while very little accretion has occurred elsewhere." The net depth change over the 79 year period of survey was evaluated as -0.1 m.

In the same study of Botany Bay, Bryant (1980) evaluated volume changes in the basins of Broken Bay and Port Jackson. Broken Bay has been dominated by accretion with a long term infilling over 78 years of approximately 0.2 m. The volume changes in Port Jackson have been dominated by erosion, most of which appears attributable to dredging activities (Bryant, 1980).

The separate studies of Botany Bay have produced different estimates of basin deepening. Significant methodological differences between the studies which may contribute to this difference are

survey extent and error analysis. The varying basin extents over which the depth change estimates were calculated only serves to increase the difference. If the Georges River mouth and the dredged areas had been included by Roy and Crawford (1979) then the 1.0 m deepening would have effectively increased. That is, both the Georges River mouth and the dredged areas are dominated by erosion (Bryant, 1980, p. 560). Including depths below 10 m would also increase the deepening result. The ocean entrance is the only region to exceed 10 m in depth and is dominated by erosion (Bryant, 1980).

The two studies described above have served to illustrate that there are methodological questions that need to be addressed when evaluating basin changes from historical charts. It is possible that the 1.0 m long-term deepening of Botany Bay, determined by Roy and Crawford (1979), incorporates significant mapping errors which have been partially removed in the latter study by Bryant (1980). The basin changes in Jervis Bay have been evaluated in association with an analysis of the mapping errors. A geographic information system (GIS) was employed to enable the development of a standardised and repeatable methodology. The GIS utilised was ARC/INFO.

Methodology

Data sources

Through consultation with the personnel of the Hydrographic Office of the Royal Australian Navy, it was established that seven hydrographic surveys existed for Jervis Bay, of which only three, dated 1867, 1894 and 1988, covered the entire extent of the basin. Although the partial surveys have a small spatial overlap with the complete surveys, it was decided not to draw depth comparisons between them due to the incompatible spatial resolution of their depth measurements. The partial surveys, without exception, had a very high density of depth measurements per unit area compared to the complete surveys. Of the three complete surveys, the 1867 chart also presented a problem in terms of the spatial resolution of depth measurements. The chart covers a stretch of coastline between Red Point and Ulladulla, and consequently has a point density of approximately 6 depth values per km^2. This data density was considered to be too sparse to enable significant depth comparisons with latter surveys such as the 1894 survey which recorded 116 depth values per km^2. As a result of these constraints, only the two surveys of 1894 and 1988 were found to be compatible in terms of point resolution and therefore suitable for analysis of basin change. The height datum for these two complete coverages was judged as being equivalent for both, although the datum for the 1894 survey could not be calculated exactly (see below). Both the 1894 and 1988 surveys were conducted and published in the same year.

Error handling

When using historical data sources in comparative analysis, acknowledgement must be given to the mapping technique employed to construct the older charts. There are three aspects of the mapping technique which enable significant horizontal and vertical errors to accrue.

First, concerning horizontal errors, the historical charts do not exist within the coordinate system of the modern-day charts, that is, Australian Map Grid (AMG). As such they must be transformed to this coordinate system before their features can be compared temporally. The horizontal accuracy of the transformation is dependent on the degree of detail by which the historical coastline is defined. The 1867 hydrographic chart, extending from Red Point to Ulladulla, for instance, is of a smaller scale than those maps encompassing only the Jervis Bay basin. As such, the Jervis Bay coastline is much more generalised in the 1867 chart, making it difficult to identify features of the coastline which could be used as control points for subsequent coordinate transformation. It was fortunate, however, that the scale of the 1894 survey supported a well-detailed coastline from which numerous control points could be positioned. Since accurate AMG coordinates could be derived for these control points from the 1988 survey, the transformation of the 1894 chart into the 1988 coordinate system was quite tightly controlled.

The second source of error is concerned with

the vertical error introduced by tidal referencing. The main concern here is that tidal datums for historical charts are difficult to trace. For example, the 1894 hydrographic chart contains soundings that have been reduced to the lowest water obtained during one lunation. Tidal records are not available for 1894 and the hydrographer can only estimate the level of the tidal datum.

The tidal datum for the 1894 survey was estimated to be approximately 0.2 m above the 1988 datum (Royal Australian Navy, Hydrographic Office, pers. commun., 1989). This error is however partially cancelled by a rising sea level. Monthly mean sea levels available for Fort Denison indicate that the mean sea level for June 1894 was 842 mm. Likewise, the mean sea level averaged over February and March, 1988 was 930 mm. The gross difference in sea level of 88 mm between the two survey times reduces the tidal datum error to approximately 0.1 m. This remaining error fraction is not a large contributor to the overall mapping error of the 1894 chart. (Tidal material for Fort Denison was supplied by the Tidal Laboratory-F.I.A.M.S. The Flinders University of South Australia, copyright reserved.)

The third source of error is also a vertical source, concerning the depth measurement techniques. The measurement of depths has developed from lead-lining for the earlier charts to echo sounding for recent charts. There is a significant increase in the accuracy of depth measurements with the advent of echo sounding as well as an improvement in the resolution of echo sounding since they were first utilised (Goudie, 1981). Bryant (1980) judged old British Admiralty charts (1871/1872) for Port Jackson, Broken Bay and Botany Bay to have an accuracy of within 0.5 m for depths less than or equal to 10 m and within the nearest 1.0 m for depths exceeding 10 m.

The errors associated with the measurement techniques of the 1894 and 1988 hydrographic surveys require separate styles of evaluation. The lead lining technique employed in the 1894 hydrographic survey contains two elements of error. The first element of error results from the application of the technique in the field, such that, the recorded depth varies from the actual depth. This could result from:

(1) the line not being taut at the time of measurement.

(2) the line does not come to rest on the actual basin floor, such as within areas covered by seagrass meadow.

(3) the line not being perpendicular to the water surface at the time of measurement.

In the case of (1) the actual depth would be over-estimated whilst the error of (2) would constitute an under-estimation. The opposing nature of these two errors and their random distribution causes them to have a negligible effect if depths are averaged over a large sample. The sample size for the basin areas used in average depth evaluation are listed in Table 1. In the case of (3) the error would be an over-estimation of the actual depth. The magnitude of error in case (3) can be evaluated through a cosine function if a maximum angle of deviation was considered to be 5°. Under such conditions, the maximum measurement error only constitutes 0.4% of the actual depth measurement and was therefore judged to be negligible.

The second element of error results from the use of the hydrographic charts for ship navigation. The depths for the 1894 hydrographic survey were only measured to the quarter fath (0.5 m) for depths less than or equal to 10 fath (18.3 m) and to one fath (1.8 m) for the remaining depths. In all instances, the rounding of the measure was downward, ensuring that the recorded depth would always be shallower than the actual depth. For example, 5.3 fath would be rounded to 5.25 fath while 12.6 fath would be rounded to 12 fath. This action was taken to prevent ships, navigating by the resulting chart, from running aground due to over-estimated depths. In order to compensate for the uni-directional error, half of this maximum error margin was added to the relevant depth measurements of the 1894 hydrographic survey. That is, one-eighth of a fath was added to all depths less than or equal to 10 fath and half a fath added to all remaining depths. Thus, the error handling procedure was deliberately biased in a conservative fashion. That is, error margins measured for the survey data would be larger than the actual errors.

The standard error of measurements less than or equal to 10 fath was estimated conservatively

TABLE I

Hydrographic sample sizes for area-averaged calculations

Area description	Area (m^2)	Number of depth measurements		
		1894		1988
		n_1	n_2	n
Whole basin	1.16×10^8	9613	3137	15617
Sub-areas:				
Hare Bay*1	9,236,125	1213	–	1214
Callala Bay*2	30,008,682	3447	70	3539
Long Beach*3	7,620,130	990	1	836
Entrance*4	4,969,143	13	409	474
South1*5	827,852	–	88	79
South2*6	819,977	4	76	2205
Bowen*7	1,607,815	15	122	159
Southwestern*8	3,611,089	403	–	1134
Basin*9	45,302,980	2750	2177	6418

Symbols correspond to sub-areas displayed in Fig. 5.
n_1 = Number of depth measurements less than or equal to 10 fath.
n_2 = Number of depth measurements exceeding 10 fath.

to be:

0.25/2 fath = 0.125 fath = 0.20 m

and the standard error of measurements exceeding 10 fath estimated to be:

1.0/2 fath = 0.5 fath = 0.9 m

These standard errors are about twice as large as the maximum range would suggest for a standard normal variable.

The echo-sounding technique employed in the 1988 hydrographic survey has been evaluated as having a maximum error of ± 0.44 m (Bryce, 1988). The standard error of all measurements in the 1988 survey was then estimated conservatively to be:

0.88/2 m = 0.44 m

The quantitative assessment of temporal and spatial basin changes in Jervis Bay will be based on average values of basin depth change. As such, the effect of this error on average basin depth values was crudely assessed by determining the standard error (S.E.) of the mean of the samples. Given a sample of n points $x_1, x_2, \ldots x_i, \ldots x_n$, the mean of the values is simply:

$$x = \sum_{i=1}^{n} x_i / n \tag{1}$$

Since the depth points of each hydrographic survey have an error component, a suitable model for each sample is:

$$x_i = \mu_i + E_i \tag{2}$$

where μ_i is the actual depth and E_i is the error component which has zero expectation and standard error as described above. Assuming that the errors E_i are independent, the variance of the total of all sample values is:

$$\text{var}\left(\sum_{i=1}^{n} x_i\right) = \sum_{i=1}^{n} \text{var}\,(x_i) \tag{3}$$

Thus the variance of the sample mean is:

$$\text{var}\,(x) = \sum_{i=1}^{n} \text{var}\,(x_i)/n^2 \tag{4}$$

and the standard error is given by:

$$S.E.(x) = \left[\sum_{i=1}^{n} \text{var}\,(x_i)\right]^{1/2} \Big/ n \tag{5}$$

Therefore, in the case of the 1894 survey, the standard error of the sample mean is:

$$(n_1\sigma_1{}^2+n_2\sigma_2{}^2)^{1/2}/(n_1+n_2) \quad (6)$$

where n_1 is the number of measurements less than 10 fath, each with standard error $\sigma_1=0.2$ m, and n_2 is the number of measurements exceeding 10 fath each with standard error $\sigma_2=0.9$ m. In the case of the 1988 survey, the standard error of the sample mean is simply:

$$(n\sigma^2)^{1/2}/n=\sigma/n^{1/2} \quad (7)$$

where n is the total number of measurements, each with standard error $\sigma=0.44$ m.

Equations (6) and (7) were used to determine the standard errors for the average depth measures calculated separately for the entire basin and each of nine 'geomorphic' sub-areas for each survey. To test for a significant difference between x_1 with standard error σ_1 and x_2 with standard error σ_2 the standard error of x_1-x_2 was estimated as:

$$S.E.(x_1-x_2)=(\sigma_1{}^2+\sigma_2{}^2)^{1/2} \quad (8)$$

These estimates of standard error were then checked against the standard normal distribution. The application of this error analysis is presented in the results section.

Data capture and processing

The primary objective of data capture and processing was to produce an ARC/INFO lattice for each of the two hydrographic surveys. The lattice is the basic requirement for further surface analysis procedures. The preliminary steps required to produce an ARC/INFO lattice, as displayed in Fig. 4, were as follows:

(1) The depth information of the 1894 hydrographic survey was digitised. The coordinate positions of each depth point were transformed from chart coordinates to Australian Map Grid (AMG) coordinates through the employment of an in-house programme called DIGINV. This programme evaluates the translation, rotation and scaling parameters required for the transformation through a set of five control points, that is, points on the chart for which AMG coordinates are known.

(2) The 1988 hydrographic survey was acquired in a digital format with AMG coordinates.

(3) The captured and transformed point data of the 1894 and 1988 hydrographic surveys were processed through the ANUDEM programme (Hutchinson, 1989). This programme calculates values on a regular grid for a discrete smooth surface fitted to the irregularly spaced depth data points. The output from this programme is in an ARC/INFO supported format.

(4) The gridded hydrographic surveys were converted to a lattice using the ARC/INFO procedure DEMLATTICE (Environmental Systems Research Institute, 1988a). The difference between a lattice and a grid is the manner in which the depth surface is represented. The former consists of a collection of point values calculated at each grid intersection whilst the latter is a collection of cell values averaged across a grid area.

Basin volumes

The evaluation of basin volumes was a four step procedure, employing the capabilities of the ARC/INFO surface analysis and modelling module called TIN. The steps, as illustrated in Fig. 4, are as follows:

(1) Contour coverages were interpolated from each of the hydrographic lattice files, with a base value of zero and a contour interval of one metre. The contours were slightly angular in appearance and a filter was thereby applied to each lattice. TIN supports only two forms of filter, a low pass filter for the removal of high frequency components from the data set, and a high pass filter for edge enhancement when a lattice represents arcs of sharply varying relief (Environmental Systems Research Institute, 1988b). A low pass filter with one iteration was applied to the hydrographic lattices, having the desired effect of smoothing the contour lines.

(2) The smoothed contour coverages for each hydrographic survey were clipped to an area representing the least spatial extent of both surveys. This process was incorporated so that volumes would be generated only for areas that have actual data as opposed to interpolated data, thus making the volumetric comparisons valid.

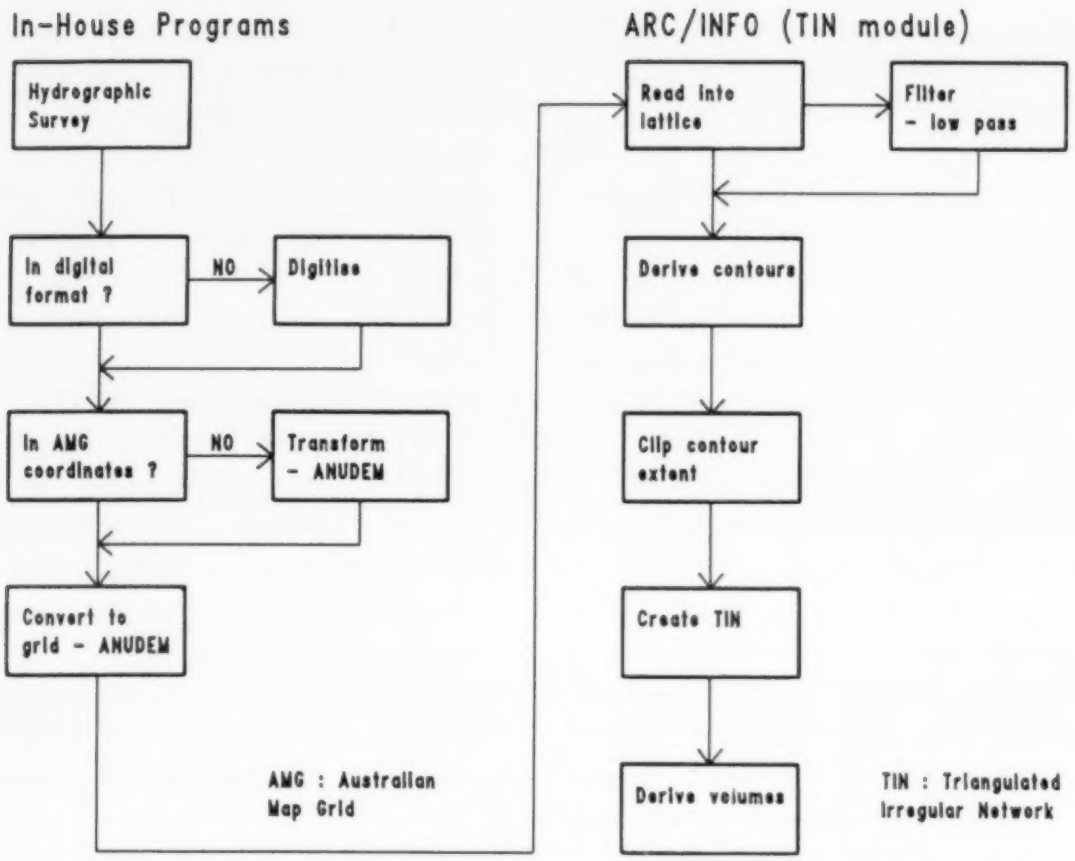

Fig. 4. The methodological steps employed to derive basin volumes from hydrographical surveys of Jervis Bay.

(3) The clipped contour coverages were each converted to a Triangulated Irregular Network (TIN). That is, the depth surface is represented by a set of non-overlapping triangles, connecting each (x,y,z) point with its neighbours (Environmental Systems Research Institute, 1988b).

(4) A basin volume was derived for each TIN, between the minimum (datum) and maximum depth value of the surface.

Spatial patterns of long-term sediment movement

The TIN package enables mathematical operations to be performed on one lattice or between two lattice files. The command, LATTICEOPERATE, was thereby used to subtract the depth values of the 1894 hydrographic survey from those of the 1988 survey. The resulting lattice was then categorised into polygons (Environmental Systems Research Institute, 1988b) to draw a spatial distinction between the different rates of basin change. Given this distinction, it became evident that nine sub-areas existed within the jervis bay basin. For each sub-area, an estimate of change in the average basin depth was evaluated through the following steps:

(1) Nine polygons were constructed to represent each of the distinct sub-areas.

(2) Each of these sub-area polygons was used to clip the relevant area of the contour coverages for both the 1894 and 1988 hydrographic surveys.

(3) The clipped contour coverages were converted to TINs and volumes derived for each TIN.

(4) Volumes were divided by respective areas to yield an estimate of average basin depth for each sub-area. The difference in average basin depth between the 1894 and 1988 surveys was evaluated for each of the nine sub-areas.

Results

Basin volumes

The first broad-scale measurement of basin change in Jervis Bay, without any spatial discrimination, revealed an increase in the gross volume of the basin by 48,000,000 m^3 over the 94 year period. Averaged over the entire basin these volu-

metric changes represent a basin deepening in the order of 0.41 m. The standard error of this estimate, when checked against the standard normal distribution indicates that the estimate is significant.

Average depths of 'geomorphic' sub-areas

The estimate of basin-wide volume change is a misleading measurement if the basin is not accreting or eroding uniformly in both the spatial and temporal dimensions. In the temporal context, if the basin eroded 1 m in the first 50 years and then accreted the same amount in the second 50 years, then the observation of basin change over the total 100 years will yield no overall volumetric change. Unfortunately, in Jervis Bay there are no acceptable, intermediary hydrographic sets between 1894 and 1988 which provide a full coverage of the bay, so this aspect of basin change can only be acknowledged.

A full coverage must be utilised to identify overall changes within the basin because of the potential bias imposed by partial coverages. For example, if the northern portion of the basin was shallowing at a more rapid rate, relative to a deepening in the southern basin, then the accretion would bias the estimate of average basin depth changes, such that the deepening of the basin could go unnoticed and the shallowing would be underestimated. For this reason, average changes in basin depth were evaluated in a spatial context.

Nine distinct regions of sedimentary change were evident in the Jervis Bay basin. Average depth changes were determined for each of these sub-areas and have been illustrated in Fig. 5. In general, the major distinction in basin changes lies between shallowing in the northern portions of the basin and deepening in the more southern portions. The shallowing is strongly evident in three offshore sub-areas, in the vicinities of Callala Bay, Hare Bay and Long Beach, and also has minor expression in the lee of Bowen Island. Basin deepening dominates south of Plantation Point, and incorporates four notable sub-areas which are of a greater magnitude of deepening than the surrounding basin. The standard errors of the average basin depth changes were checked against the standard

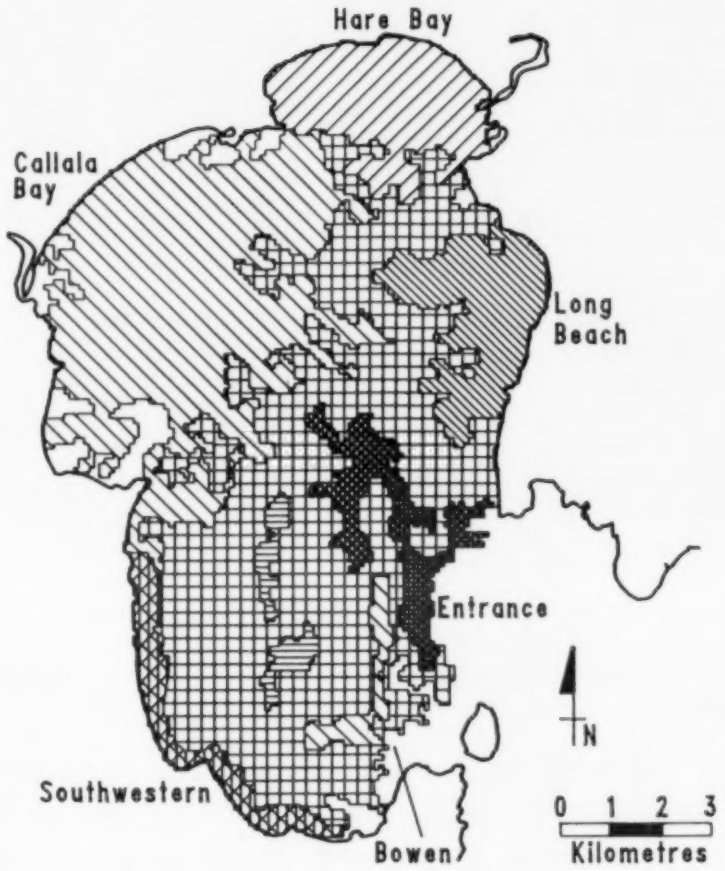

Fig. 5. Average depth changes for each geomorphic sub-area identified in the Jervis Bay basin.

normal distribution, and all measures of change were shown to be significant (Table 2).

Discussion

A very distinct spatial pattern of sediment mobility is indicated from the spatially-sensitive volumetric analysis of the Jervis Bay basin. The most evident spatial disparity occurs between the north and south portions of the embayment, the former being dominated by shallowing and the latter by deepening. The physical mechanisms responsible for this spatial disparity can be evaluated qualitatively through the spatial variation of the energy regime in Jervis Bay.

TABLE 2

Changes in average basin depth and associated standard errors

	1894		1988		Difference	
	x_1 (m)	σ_1	x_2 (m)	σ_2	$x_1 - x_2$ (m)	$S.E.(x_1 - x2)$
Whole Basin	27.32	0.004	27.73	0.003	−0.41	0.003
Sub-areas:						
Hare Bay	32.55	0.012	32.45	0.006	0.10	0.018
Callala Bay	27.09	0.007	26.89	0.004	0.20	0.011
Long Beach	26.80	0.015	26.51	0.006	0.29	0.021
Entrance	15.02	0.020	16.26	0.043	−1.24	0.063
South1	17.00	0.050	18.00	0.096	−1.00	0.146
South2	17.25	0.050	18.24	0.098	−0.99	0.148
Bowen	18.55	0.035	18.34	0.073	0.21	0.108
Southwestern	28.82	0.013	29.40	0.010	−0.58	0.023
Basin	21.61	0.005	21.98	0.090	−0.37	0.095

The dominant variable of the energy regime in Jervis Bay, as surmised by Taylor (1971), is wave activity, either swell waves or locally-generated wind-waves. In Callala Bay and Hare Bay, the beach outlines have become well-aligned to the prevailing southeasterly swell, thereby initiating a predominantly onshore–offshore transport of sediment. In the past, this mode of sediment transport has enabled the formation of a barrier system (Thom et al., 1986). The influence of swell waves is also apparent in the basin. Seabed surveys conducted by Dames and Moore (1985) and Sinclair, Knight and Partners (1988), both indicated the frequent occurrence of swell-generated ripples in that portion of the basin lying north of a line between Murrays Beach and Plantation Point (Fig. 3). The location of these ripples coincides, as expected, with the path of the southeasterly swell waves as they enter the basin and refract into Callala Bay and Hare Bay.

Changes in sediment levels of the Jervis Bay basin appear to collaborate with swell wave influence. In the southern portion of the basin the swell waves operate in an eroding environment, suggesting that they may be responsible for the entrainment of sediment as they traverse. This erosional environment persists until water depths within the Callala Bay/Hare Bay sub-areas decrease to approximately 14 or 15 m. At this depth, a depositional environment begins and extends shoreward to the land–sea interface. The depositional environment may be contributable to diminishing swell wave energy, resulting from increasing frictional drag between the swell waves and the seabed. The decreasing wave energy would encourage the deposition of entrained sediment, thereby creating a dominantly depositional environment.

In addition to the suggested depositional influences of swell waves in Hare Bay, there is the possibility of a stream, load contribution to the nearshore. Carama Inlet enters at the northwestern corner of Hare Bay and has associated with its entrance extensive tidal flats. Under 'normal' conditions, stream flow is not very significant, however, it could be expected to flow much faster and contribute a more significant sediment load after heavy rains. There have been no studies to quantify the stream load contribution of Carama Inlet, however, the burial of seagrasses in the vicinity has been observed (P. Waterman, pers. commun., 1991).

Local wind-wave activity is spatially restricted to the southwestern and eastern shorelines of Jervis Bay. Although both shorelines receive the same form of wave energy, they are not displaying the same directional changes in sediment levels of their nearshore basin environments. The southwestern shoreline exhibits an eroding nearshore basin whilst the eastern shoreline has an accreting nearshore. The physical characteristics of each of these locations does offer some explanation for this dichotomy. The eastern sub-area, for instance, receives high energy, local wind-wave activity generated by west and northwesterly winds during storm events. This activity has been responsible for the severe erosion of the seaward foredune face along Long Beach, which has been observed to have a very slow recovery potential (Posford, Pavry, Sinclair and Knight, 1975; Shoalhaven and Nowra News, 1980; Thom et al., 1986). If sufficient quantities of dune sediment are removed during these events, and deposited in the nearshore, then this may account for part of the increasing sediment levels in this sub-area. In addition, the Long Beach nearshore (specifically between low water and a depth of 12 m), is the only location in Jervis Bay where extensive meadows of *Posidonia australis* occur. This seagrass specie has strap-like

blades and develops an extensive rhizome root mat. As such, it is capable of both entrapping (blades) and binding (root mat) suspended sediments. If the seagrasses can grow apace with the sediment contributions delivered during storm events, then they may be creating a depositional environment wherein sediment is unavailable for return to the eroding beach system.

In contrast, the southwestern shorelines of Jervis Bay receive wind-wave activity generated by the northeasterly seabreeze. Such activity is of a lower energy than that received during storm events along the eastern shorelines, however, it is more persistent, occurring daily for approximately 8 months of the year. Coastal orientation and wind direction ensure that these locally-generated wind-waves arrive obliquely to the shoreline. As such, a longshore current develops in response to the longshore component of the radiation stress of the waves (Komar, 1976). Such a current would initiate sediment movements which would be erosive in nature to the nearshore environment. The seagrass community in this sub-area has a much reduced entrapping/binding capacity in comparison to those of the eastern sub-areas. The *Posidonia australis* is intermixed with two other species (*Halophila ovalis* and *Zostera capricorni*) which have leaf structures much less capable of baffling wave energy, due to their size and shape. In addition, the plants in these mixed communities of seagrass are generally of a moderate to sparse density.

The environmental setting of the Jervis Bay entrance is a complex one, as reflected in the complex pattern of changes in sediment levels in this area. It is a high energy environment, being on the direct path of deep-water waves. It is thought that the widest part of the entrance, between Point Perpendicular and Bowen Island, is influenced by coastal-trapped waves (CSIRO, 1989). These waves are generated through vertical density gradients on the continental shelf outside of Jervis Bay. The CSIRO (1989) has pointed out that "these waves are too large to enter the bay, but the vertical movements of the isotherms at the mouth induces a response that can lead to significant currents inside the bay." These currents may be responsible for the sub-area of deepening within the embayment entrance. The narrow entrance channel between Bowen Island and Bherwerre Peninsula influences the flow of tidal currents to produce a depositional environment in the lee of Bowen Island, expressed in the form of a tidal delta.

Conclusions

The long-term changes of sediment levels in the Jervis Bay basin were evaluated in order to establish whether any distinct pattern of spatial variability was discernible. The evaluation indicated that there were at least nine distinct basin sub-areas displaying varying levels of sedimentary change. At the basin-wide scale, the most apparent distinction was between the northern and southern portions of the basin, the former being an erosional environment and the latter being a depositional environment. In addition, there were several smaller sub-areas of the basin which were of significant size to warrant some form of explanation for their distinct sedimentological change characteristics.

The environmental settings of each sub-area were considered, specifically in relation to the physical processes that may be operating as a result of this setting. The distinction between wave forms, that is swell waves or local wind-waves, yielded a spatially variable model of sediment mobility which corresponded favourably with the sediment level changes. In the majority of the sub-areas, there were additional factors which could be contributing to the wave energy model, such as, the influence of stream loads or the entrapping/binding capabilities of seagrasses. In all cases these additional influence served to provide further support for the spatial differentiation discerned in basin sediment levels. While few of the physical influences on sediment mobility have been quantified, their correspondence to the quantified basin changes, provides some grounds for confidence in the quantification procedure.

The employment of a geographic information system in determining basin-wide changes in average sediment levels in Jervis Bay, has served to construct a method of environmental monitoring which is rigorous and repeatable. Once the

initial steps of the analytical routine have been established, as this research has specified, the method can be repeated in a very time-efficient manner, while maintaining a high level of analytical flexibility should it be required. This computerised method of hydrographical analysis is complimented by the advent of a digital mode of hydrographic surveying in the past few years.

Acknowledgements

Personnel of the Hydrographic Office, Sydney, of the Royal Australian Navy made available the digital survey information for the 1988 hydrographic survey. They also discussed the data sources and provided insight into the problems that may be encountered in the analysis of the old charts. Mr. Doug Crabb, from the Department of Housing and Construction, Canberra, allowed the loan of the 1894 hydrographic chart and also provided some informative discussion. Dr. Michael Hutchinson, of the Centre for Resource and Environmental Studies, Australian National University, provided patient instruction on the mathematics behind the error analysis. Dr. Ian Eliot, of the Centre for Resource Planning and Urban Development, Western Australia, assisted generously in the criticism and construction of this paper.

References

Albani, A.D., Carter, A.N. and Johnson, B.D., 1972. The bedrock topography of Jervis Bay, New South Wales. In: R. Fraser (Editor), Oceanography of the South Pacific. N. Z. Natl. Comm. UNESCO, Wellington, pp. 179–184.

Bryant, E., 1980. Bathymetric changes in three estuaries of the central New South Wales coastline. Aust. J. Mar. Freshwater Res., 31: 553–571.

Bryce, D.C., 1988. Australia-East Coast, Jervis Bay. R. Aust. Navy, Hydrogr. Office, Detached Surv. Unit.

Charash, E., 1972. Turbulent diffusion in the ocean and bay in the Jervis Bay area. Aust. Mar. Sci. Bull., pp. 10–19.

Clarke, D.J. and Eliot, I.G., 1984. Jervis Bay: Water temperature and salinity observation, 1976–1977. Dep. Math., Univ. Wollongong, Coastal Res. Rep., 5/84 (Prepared for the Dep. of Housing and Construction).

CSIRO, 1989. Jervis Bay Baseline Studies. Division of Fisheries, Third Progress Rep., 336 pp.

Dames and Moore, 1985. Jervis Bay sediment and seagrass study. Rep. to the Dep. of Housing and Construction, 3 vols.

Department of Administrative Services-Construction Group, 1988. Jervis Bay fleet base planning study.

Department of Defence, 1989. Australian National Tide Tables 1990. Aust. Gov. Publishing Serv., Canberra.

Environmental Systems Research Institute, 1988a. ARC/INFO, Volume 2, Command References, Geogr. Inf. Syst. Software, Users Guide, Redlands, Calif.

Environmental Systems Research Institute, 1988b. TIN, ARC/INFO Surface Modelling Display, Users Guide, Redlands, Calif.

Goudie, A., (Editor), 1981. Geomorphological Techniques. Allen and Unwin, London.

Hutchinson, M.F., 1989. A new procedure for gridding elevations and stream line data with automatic removal of spurious pits. J. Hydrol., 106: 211–232.

Johnson, B.D. and Albani, A.D., 1975. Bedrock topography in northern Jervis Bay. J. Proc. R. Soc. N. S. W., 108: 12–15.

Komar, P.D., 1976. Beach Processes and Sedimentation. Prentice-Hall, Englewood Cliffs, N.J., 429 pp.

Perry, W.J. and Dickins, J.M., 1952. Report on a geological survey of Commonwealth territory, Jervis Bay. Rec. Commonw. Bur. Miner. Resour., Geol. Geophys., 1952/88.

Posford, Pavry, Sinclair and Knight, 1975. Coastal zone management study, Culburra, Callala and Callala Beach. Rep. for the Shoalhaven Shire Council.

Roy, P.S. and Crawford, E.A., 1979. Holocene geological evolution of the southern Botany Bay–Kurnell region, central New South Wales. Rec. Geol. Surv. N. S. W., 20(2): 159–250.

Shoalhaven and Nowra News, 1980. Sand dune restoration a success. May 14.

Sinclair, Knight and Partners, 1988. Coastline stability within Jervis Bay, Jervis Bay environmental studies. Prepared for Dep. Defence, 2 vols.

Taylor, G., 1971. Sedimentation in Jervis Bay. Proc. Linn. Soc. N. S. W., 96(4): 297–306.

Thom, B.G., Roy, P.S., Short, A.D., Hudson, J. and Davis, R.A., 1986. Modern coastal and estuarine environments of deposition in southeastern Australia. Guide for Excursion 4a, 12th Int. Sedimentol. Cong., Canberra, pp. 175–188.

Walker, G.T., 1967. The coastal geomorphology of the Jervis Bay area. M.Sc. Thesis, Australian National Univ., Canberra.

Marine Geology, 105 (1992) 225–240
Elsevier Science Publishers B.V., Amsterdam

The geomorphology of the Southwest Guinea Margin: tectonic, volcanic, mass movement and bottom current influences

S. Rossi[a], F. Westall[b] and J. Mascle[c]

[a]*Istituto per la Geologia Marina, C.N.R., via Zamboni 65, 40127 Bologna, Italy*
[b]*Laboratoire de Biosédimentologie, Sciences de la Terre, Université, 2 chemin de la Houssinière, 44072 Nantes, France*
[c]*Laboratoire de Géodynamique sous marine, B. No. 48, Villefranche s/m, France*

(Received February 6, 1991; revision accepted August 19, 1991)

ABSTRACT

Rossi, S., Westall, F. and Mascle, J., 1992. The geomorphology of the Southwest Guinea Margin: tectonic, volcanic, mass movement and bottom current influences. Mar. Geol., 105: 225–240.

Slope morphology controls were examined in two topographically different areas on the southern transform margin of the Guinea Plateau (Sectors G1 and G2). Tectonic control is manifested by steep, faulted slopes in both study areas, and by basement warping in Sector G1 and magmatic emplacements in Sector G2. Sediment deposition and the formation of bedforms such as sediment waves on the margin are influenced by topographically intensified bottom currents within the intermediate–deep water mass, the North Atlantic Deep Water (NADW), as well as in the shallower Equatorial Surface Water (ESW)/Antarctic Intermediate Water (AAIW) at the uppermost slope/plateau-edge level. Thus, unconsolidated sediments are eroded from steep slopes (the upper and lower continental slopes, canyon walls and the slopes of the volcanic cones) and concentrated into slope-parallel depocentres in Sector G1, and ponded in moats between the volcanic cones in Sector G2. Surficial sediment waves, which are apparently oriented at an angle to the slope, range from 0.5 to 2 km in wavelength and up to 100 m in height. Mass movement of the sediment cover is significant on the lower slopes of both sectors and is the result of slope steepness and instability caused by the continuing tectonic activity.

Introduction

This paper presents an interpretation of the geomorphology of two areas on the southern margin of the Guinea Plateau (Figs. 1 and 2) in the context of tectonic, mass-wasting and bottom-current controls. The study is based on 12 kHz Seabeam echosounding and on 3.5 kHz and seismic reflection data from the EQUAMARGE II cruise (February–March, 1988) of R.V. *J. Charcot* (Mascle et al., 1989). Although the two sectors are close together (Sector G1 is only about 50 km to the west of Sector G2) the geomorphology of the two areas is quite different. Sector G1 presents a faulted, gently warped profile, whereas the margin in Sector G2, although also faulted, is dominated by volcanic cones. The sediment cover superimposed on these morphologically different margins has been strongly influenced by bottom-current activity and slumping.

Geological setting

The Guinea Plateau Margin was strategically positioned during the opening of the Central and Equatorial Atlantic (Fig. 1) and is, therefore, an important study area for investigation of the effects of the complex rifting process on the continental margin (Jones and Mgbatogu, 1982; Marinho, 1985; Mascle et al., 1986, 1988; Ciais, 1988). Its intricate morphology has been strongly influenced by two phases of opening, the Central Atlantic during the Jurassic and the Equatorial Atlantic during the Cretaceous, with each tectonic episode

0025-3227/92/$05.00 © 1992 — Elsevier Science Publishers B.V. All rights reserved

Fig. 1. General map of the Equatorial Atlantic showing location of the Guinea Marginal Plateau.

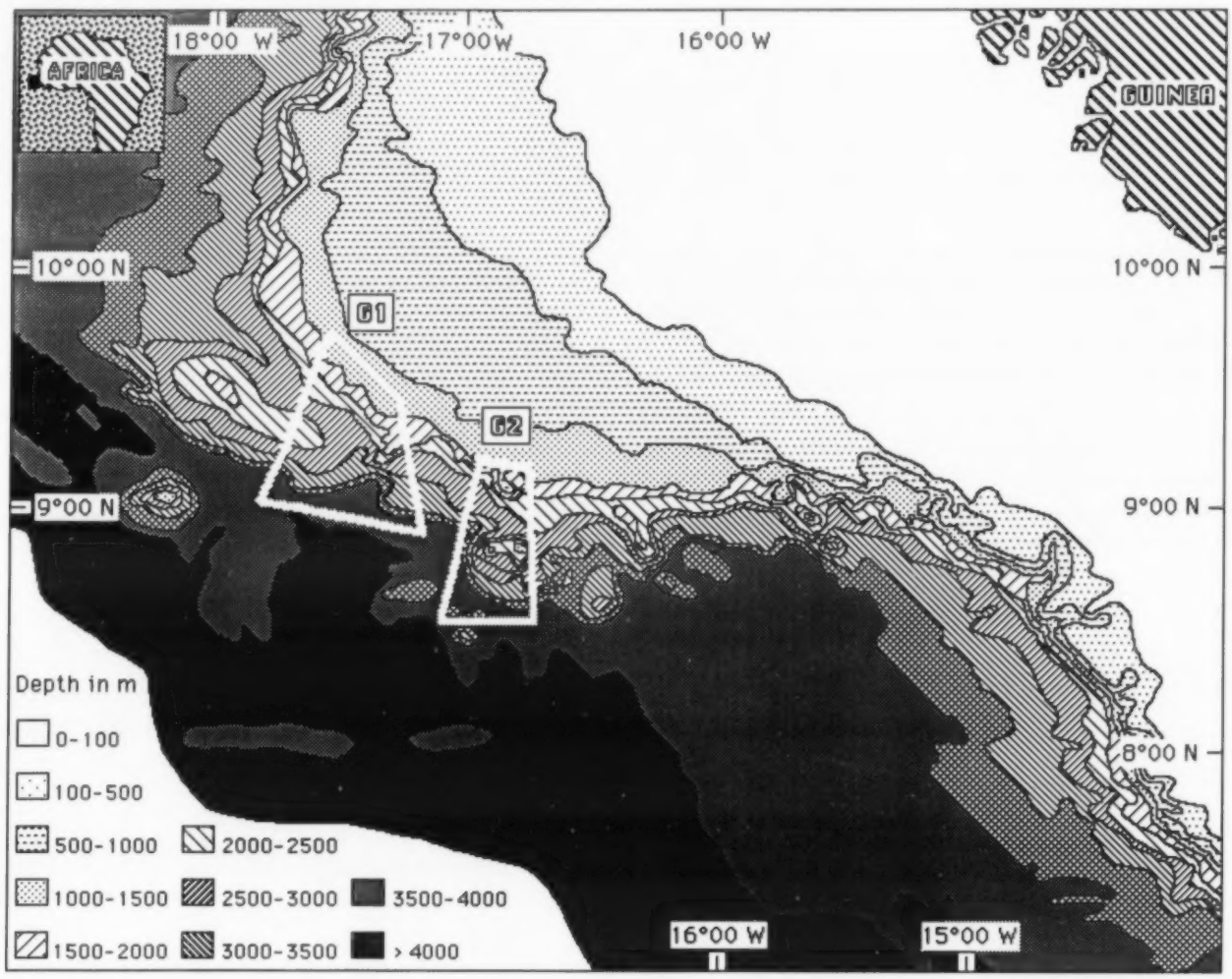

Fig. 2. Bathymetry and location of the two areas of study on the southern margin of the Guinea Marginal Plateau.

reactivating pre-existing structures (Ciais, 1988). During the Jurassic, passive margin phase of development the Guinea Plateau and its southern margin probably constituted the upper part of the divergent Central Atlantic Margin (Ciais, 1988). This phase was followed by renewed seafloor spreading activity during the Cretaceous when strike-slip stresses on the already fractured margin resulted in magmatic activity superimposed on the E–W trending slope (Jones and Mgbatogu, 1982; Marinho 1985; Mascle et al., 1986, 1988; Ciais, 1988). In the Cretaceous period, transform motion was additionally accompanied by local compressional movements at the extreme southwestern end

of the Guinea Plateau Margin, resulting in the formation of a mid-slope basin (Ciais, 1988).

The fractured southern margin represents a structural continuation of the Guinea Fracture Zone and is probably conjugate with the Demerara Margin in the Western Atlantic at the Brazil/Guyana boundary (Marinho, 1985).

Further modification of the slope morphology was caused by volcanic activity and by bottom-current moulding and slumping of the sedimentary cover.

Sector G1 is chiefly characterised by a thickly sedimented mid-slope basin containing several acoustic sequences. The deepest layer is intensely fractured, with normal and reverse faults, and is gently folded (Figs. 3 and 4) (Benkhelil et al., 1989; Tricart et al., 1991). This sequence is probably of pre-Cenomanian age, and is covered by a ca. 2 s (TWT) wedge of sediments containing a number of hiatuses and erosional surfaces.

The continental margin in Sector G2 is influenced by both tectonic and magmatic events (Figs. 4 and 5). Magmatic activity was on a large enough scale to completely disrupt most of the litho-acoustic succession (Bertrand et al., 1989). Much of the slope is dominated by a large volcano of 16 km in diameter which rises up to −840 m; there are also five smaller cones. Sequences interpreted as interbedded lava flows and volcaniclastic layers are presumed to be Upper Cretaceous in age (Benkhelil et al., 1989).

Oceanography

The majority of the continental slope between 1500 and 4250 m comes under the influence of the North Atlantic Deep Water (NADW), the most important intermediate to deep water mass in the Atlantic Ocean (Fig. 6a). This water mass spreads southwards from its origin in the Labrador Sea–Greenland–Iceland–Scotland sector of the North Atlantic. In the region of the Guinea Plateau, it swings east-southeast and follows the West African continental margin (Defant, 1941). At depths greater than 4250 m, it mixes with the Antarctic Bottom Water (AABW) (Lynn and Reid, 1968), a deep-water mass originating in Antarctic waters which spreads northwards along the western boundary of the Atlantic Ocean. At the Equator a part of this water mass passes through the Romanche Fracture Zone in the Mid-Atlantic Ridge and enters the Sierra Leone Basin, where it mixes with the NADW and spreads both north and south. Thus, along the southern margin of the Guinea Plateau, mixed AABW/NADW moves north-northwest along the foot of the continental slope to the Kane Gap (between the Guinea Plateau Margin and the Sierra Leone Rise), through which it passes into the Gambia Basin to the north.

Equatorial Surface Water (ESW) is the major water mass at depths shallower than about 1500 m and moves in a southeasterly direction (Fig. 6b). There is possibly a thin layer of Antarctic Intermediate Water (AAIW) sandwiched between the ESE and the NADW: Sverdrup et al. (1942) show AAIW turning east-southeast in a gyre-like motion along the eastern boundary of the Atlantic at the Guinea Plateau latitude.

Instrumentation

This study is based on data from 47 Seabeam profiles and on seismic reflection and 12 kHz and 3.5 kHz records. Most of the tracklines are oriented normal to the slope, although there are a few tielines (Fig. 7). Track coverage totalled 3900 km for the two areas studied. In addition, four dredge stations were observed and three cores were taken.

The following instruments were used:

(1) A 12 kHz transducer for the bathymetric profiles.

(2) A Seabeam with multiphase transducer for detailed bathymetric surveying. Depth charts were plotted in real time.

(3) A Sub-Bottom Profiler with 3.5 kHz transducer for profiling the seafloor surface as well as some tens of meters of the subbottom.

(4) Two 1.5 litre TWG waterguns producing single-track seismic reflection profiles that were recorded both graphically and magnetically.

(5) A Geometrics (G801) magnetometer with a precision of 1 nT and a measurement interval of 3 s.

(6) A gravimeter.

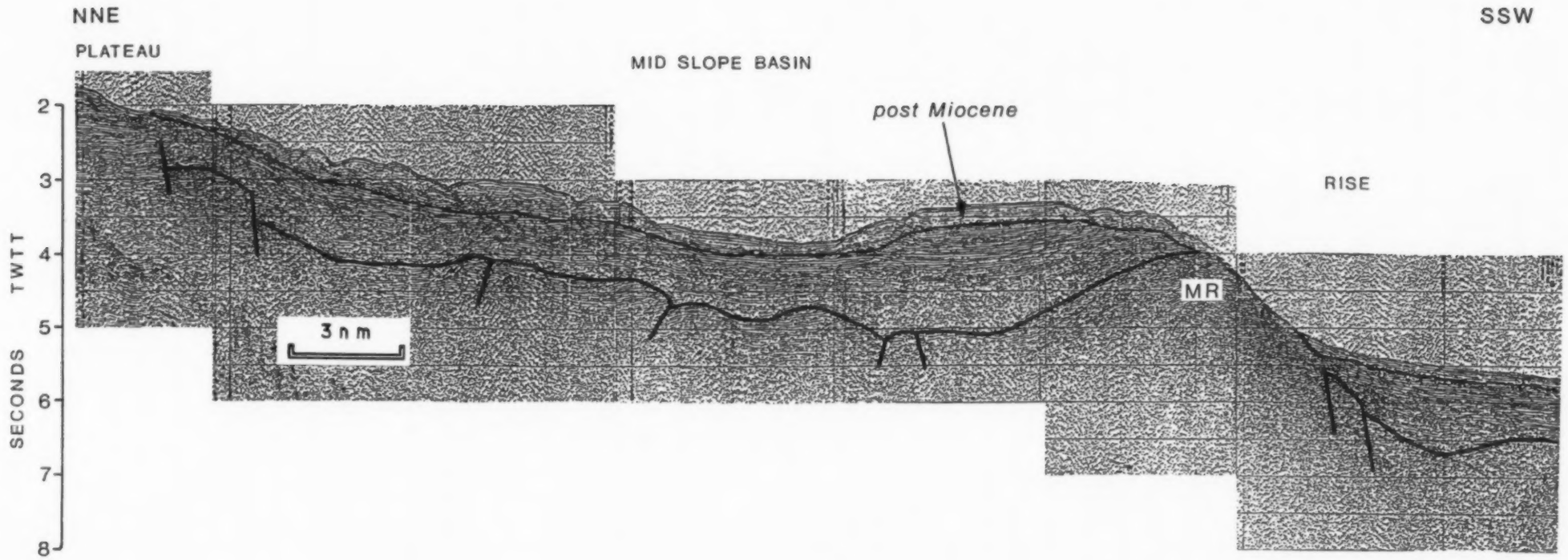

Fig. 3. N–S seismic cross section through Sector G1 showing the tectonised basement (faults, folding and marginal ridge (*MR*)) and the current-moulded sediment cover. Unconsolidated, post-Miocene sediments are indicated. Trackline shown in Fig. 7.

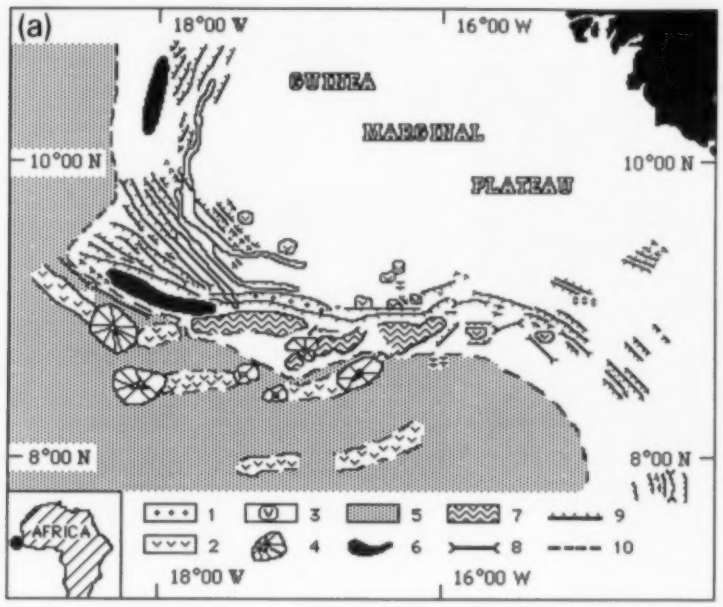

Fig. 4. (a) General tectonic map of the Guinea Marginal Plateau after Mascle et al. (1988). *1* = southern slope upper scarp; *2* = oceanic crust ridges; *3* = volcanics detected on the seismic profiles; *4* = subcircular seamounts; *5* = inferred oceanic crust; *6* = lower scarp basement highs (western slope segment); *7* = lower to middle slope basement ridges (southern slope segment); *8* = axis of main sedimentary basins; *9* = main fault systems; *10* = extent of oceanic crust (as deduced from seismic reflection data). (b) Detail of the tectonic structures along the southern Guinea Margin after Marinho (1985). *1* = normal fault; *2* = reverse fault; *3* = axis of intermediate basin; *4* = synclinal axis; *5* = anticlinal axis; *6* = volcanic crest; *7* = crater; *8* = volcanic flows; *9* = limit of magmatism; *10* = base of margin ridge (oceanic); *11* = escarpment zone.

(7) An integrated satellite navigation system (UMB) was used.

Sector G1

Bathymetry and morphology

The three-dimensional image of the margin in Fig. 8 is based on Seabeam data. It shows the following morphological characteristics (Rossi et al., 1989):

(1) The southern part of the Guinea Plateau Margin (−1250 to −2000 m) has a relatively smooth surface and presents a regularly deepening profile gently inclined to the southeast at angles of 2–3°.

(2) The upper slope (−2000 to −2500 m), which is oriented NNW–SSE in the western part of the sector and swings around to NW–SE in the eastern part, is moderately steep, with inclinations of 4°–6°. The uppermost part of the slope is deeply incised by a number of canyons and, lower down, is characterised by small-scale irregularities of the order of 50–100 m in height. At a depth of about 2500 m, the upper slope is truncated by two converging slope-parallel valleys, one from the west and one from the east; these valleys converge towards a large, central slope-normal valley on the lower slope.

(3) On either side of this central valley the continental margin is cut by an intermediate basin (−2500 to −3250 m) oriented parallel to the slope. To the west of the central valley the intermediate basin contains two large sediment drifts, which form broad swells which diverge slightly towards the northwest (Westall et al., in press). The sediment drift immediately adjacent to the upper slope follows a NW–SE trend, whereas the drift at the outer edge of the intermediate basin is oriented WSW–ESE. They are separated by a valley underlain by a condensed sequence. Above −3250 m the floor of this valley appears flat. On the eastern side of the central, lower slope valley the crest of the swell in the intermediate basin is curved, and follows the bathymetric contours with an overall E–W trend. The valleys in the intermediate basin commonly exhibit erosional features, especially in their lower, steeper, canyon-like parts.

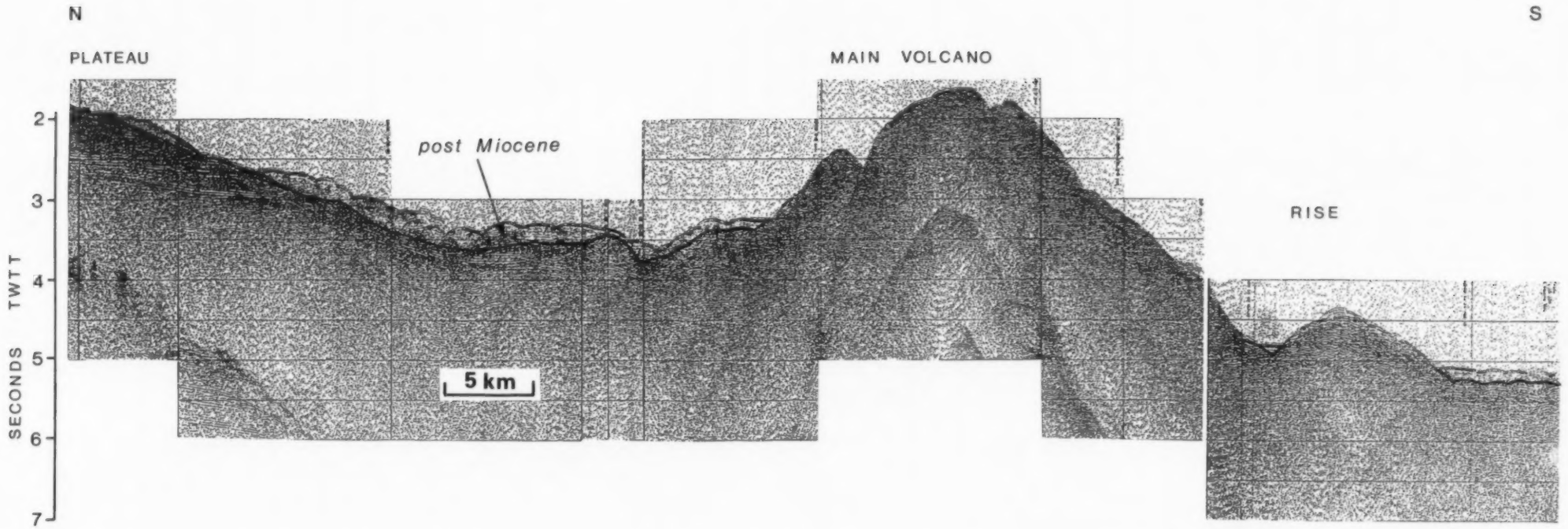

Fig. 5. Seismic cross section through Sector G2 showing steep upper scarp, volcanic emplacements and current-moulded sediment cover. Unconsolidated, post-Miocene sediments are indicated. Trackline shown in Fig. 7.

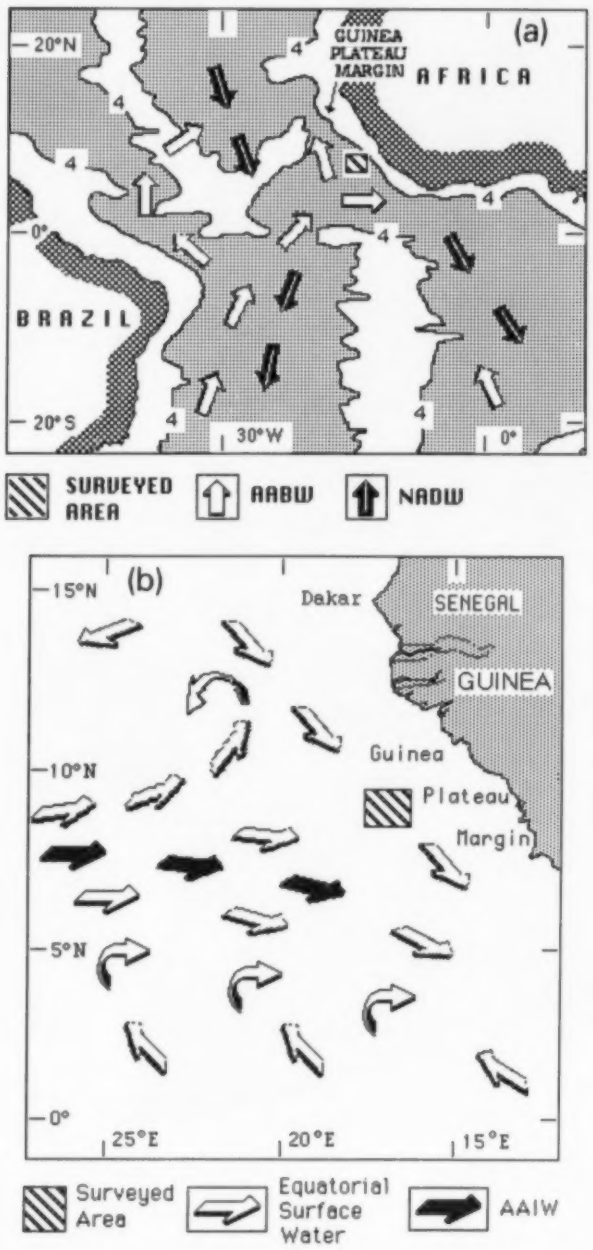

Fig. 6. (a) Direction of flow of the AABW and NADW in the Equatorial Atlantic (compiled from Defant, 1941; Lynn and Reid, 1968). (b) Flow directions of the Equatorial Surface Water (after Mienert, 1986) and AAIW (after Sverdrup et al., 1942).

With the exception of the extreme western part of the sector where the surface of the swell on the southwestern edge of the intermediate basin is planed, small-scale irregularities (up to 100 m high) cover the surfaces of the swells.

(4) The lower slope (−3250 to −4000 m) is steeply inclined, at angles ranging from 8° to 14°. It is oriented WNW–ESE in the west and swings around to a more or less E–W direction in the east. At 17°30'W, the lower slope is sharply dissected by a large NNE–SSW oriented flat-bottomed valley cutting across the regional slope. The

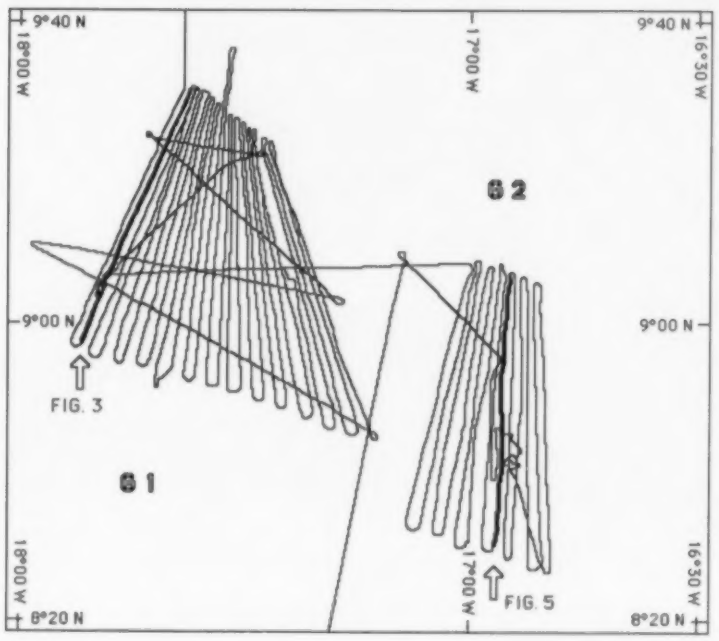

Fig. 7. Tracklines for Sectors G1 and G2. Thickened lines represent the line of section of the seismic reflection profiles displayed in Figs. 3 and 5.

walls of this valley are steep and are cut by a number of canyons with eroded walls, some representing the extensions of the valleys in the intermediate basin. The lower slope itself is also cut by numerous shallow canyons.

(5) The continental rise (−4000 to −4500 m) is inclined very gently towards the south-southwest at an angle of 0.7°–2.5°. Its fairly regular morphology is disrupted to the southeast by slightly rugged topography.

Unconsolidated sediment thickness and acoustic facies

Five seismic units were identified on the southern Guinea Margin on the basis of the seismic reflection records (Mascle et al., 1989). In the intermediate basin, the lowermost unit, consisting of tectonically deformed pre-Cenomanian(?) sediments (Benkhelil et al., 1989; Moullade et al., in prep.) (Fig. 3), is overlain by four sedimentary units with a maximum thickness of about 2 s (TWT). A plot of the thickness of the unconsolidated post-Miocene sediments is displayed in Fig. 9. The locations and orientations of the sediment drifts underlying the swells in the intermediate valley are clearly delineated by sediment thicknesses of >300 ms (TWT; all thicknesses

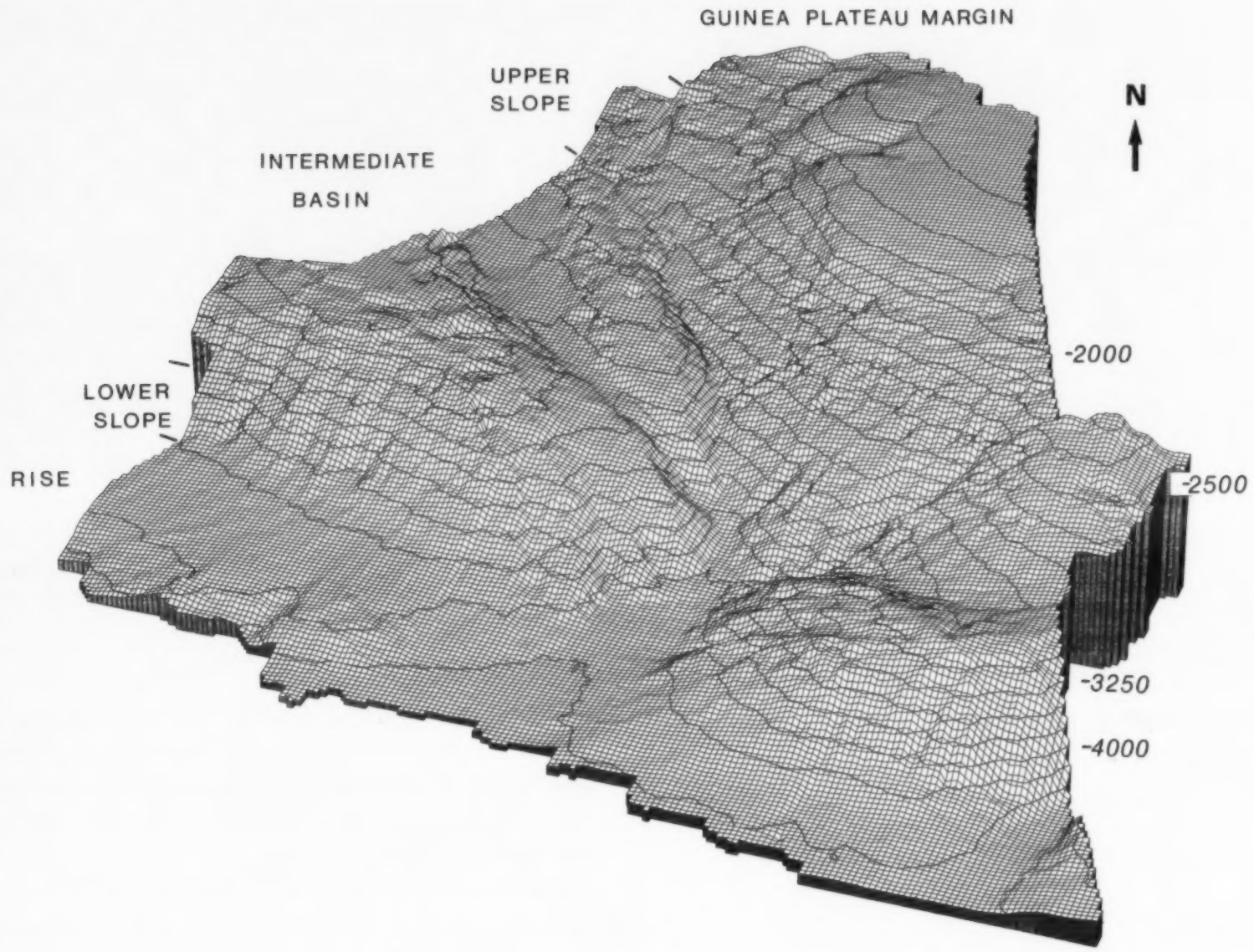

Fig. 8. Three-dimensional image of the continental slope in Sector G1 based on Seabeam data. Bathymetry in metres.

given here are in TWT). Another thick accumulation of unconsolidated sediment (>400 ms) underlies the continental rise to the southeast.

Zones with little or no unconsolidated sediment cover (0–100 ms) occur on the uppermost part of the slope and at the edge of the Guinea Plateau, in a band along the steep lower slope, and on the slope of the main central valley cutting the lower slope. Unconsolidated sediment thickness in the slope-parallel valleys in the intermediate basin and in the central valley on the lower slope is also low, <200 ms.

The acoustic responses of the 3.5 kHz records in this paper have been classified following to Damuth (1975), Jacobi and Hayes (1982), Courp (1984), Mienert (1986) and Marinho (1987). Examples observed on the Guinea Margin are shown in Fig. 10:

Echo type 1A: continuous, sharp bottom echo with no subbottom reflectors.

Echo type 1A': continuous, sharp bottom echo with discontinuous subbottom reflectors, often undulating and truncated by the sediment surface.

Echo type 1B: continuous, sharp bottom echo with continuous subbottom reflectors.

Echo type 2B: weak reflectors, sometimes with transparent sediment wedges of varying thicknesses between individual reflectors.

Echo type 3A: large hyperbolic echoes.

Echo type 3B: small, narrow, hyperbolic echoes.

Echo type 3D: standing sediment waves.

Echo type 3F: migrating sediment waves.

The distribution of these echo types in Sector G1 is shown in Fig. 11. Echo types 1A and 1A' are restricted to the edge of the Guinea Plateau

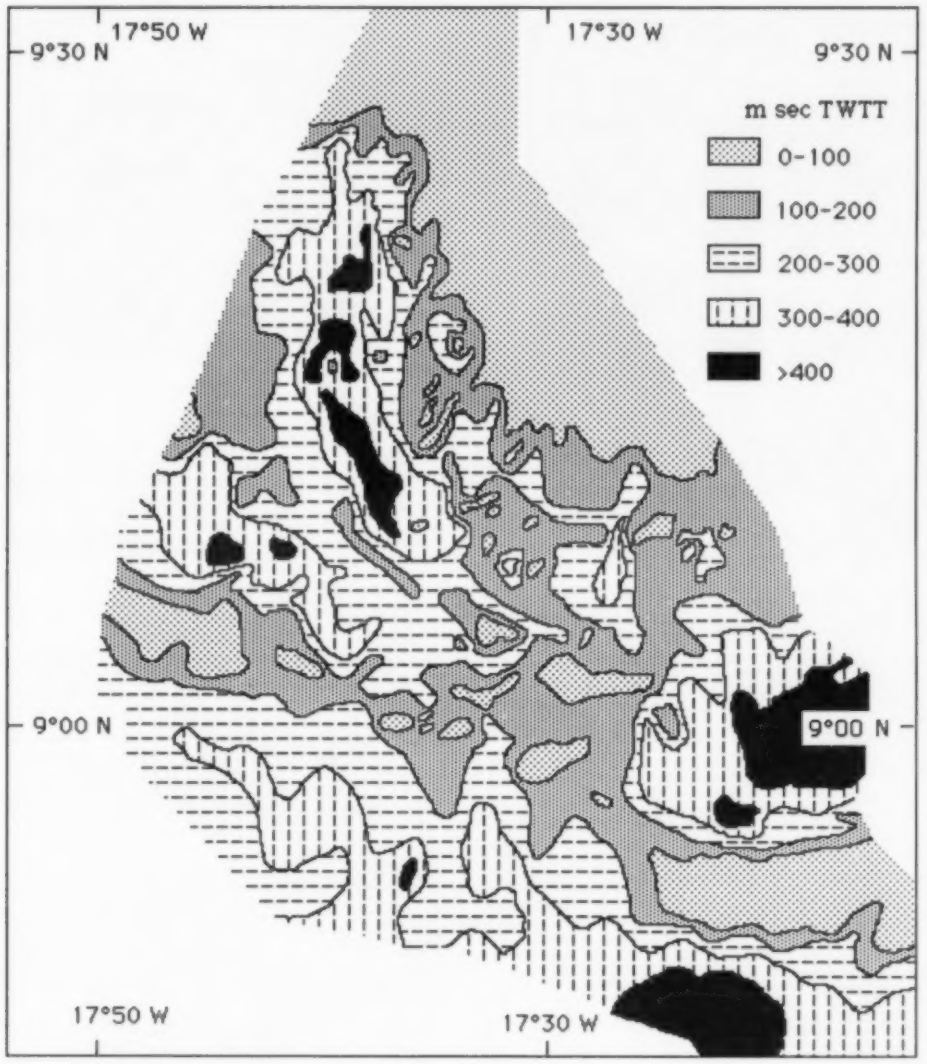

Fig. 9. Thickness of unconsolidated post-Miocene sediments in Sector G1.

and, on the basis of the seismic reflection data, are interpreted as erosional surfaces. All steep slopes, including most of the upper slope and almost all of the lower slope, are covered with the large hyperbolae of Echo type 3A. Comparison with the seismic reflection records shows that this echo character is produced by sediment waves and by irregular eroded surfaces of steep slopes. Sediment waves on the steeper slopes have small wavelengths (0.5 km) and are <100 m in height. The entire intermediate basin and upper continental rise region is characterised by standing sediment waves (Echo type 3D) of slightly longer wavelength (1 km). Areas of flatter topography in the intermediate basin, such as the wide, upper parts of the valleys and the flat portion of the sediment drifts, are covered by Echo type 2B, representing sediments deposited under stronger, and possibly erosive, bottom-current regimes. The seismic reflection records show planed, eroded sediments on the crest of one of the drifts at the extreme western end of the study area, whereas in the valleys sediments are underlain by condensed sequences. Small pockets of migrating sediment waves (Echo type 3F) are located on the walls of the central, lower slope valley and its subsidiary canyons on the lower slope. A disturbed echo response (Echo type 3B), which is typical of slumped sediments, is almost ubiquitous on the upper continental rise, whereas flat-surfaced sediments with conformable subbottom reflectors (Echo type 1B) cover the lowermost part of the rise.

Most of the tracklines in Sector G1 run approximately N–S (Fig. 7). Analysis of echo types on the few NW–SE tielines demonstrates that the type of echo character registered often depends on the orientation of the trackline with respect to the slope and the sedimentary bedform on the slope. Three areas have been delineated in Fig. 11 where superimposed echo types were observed on the

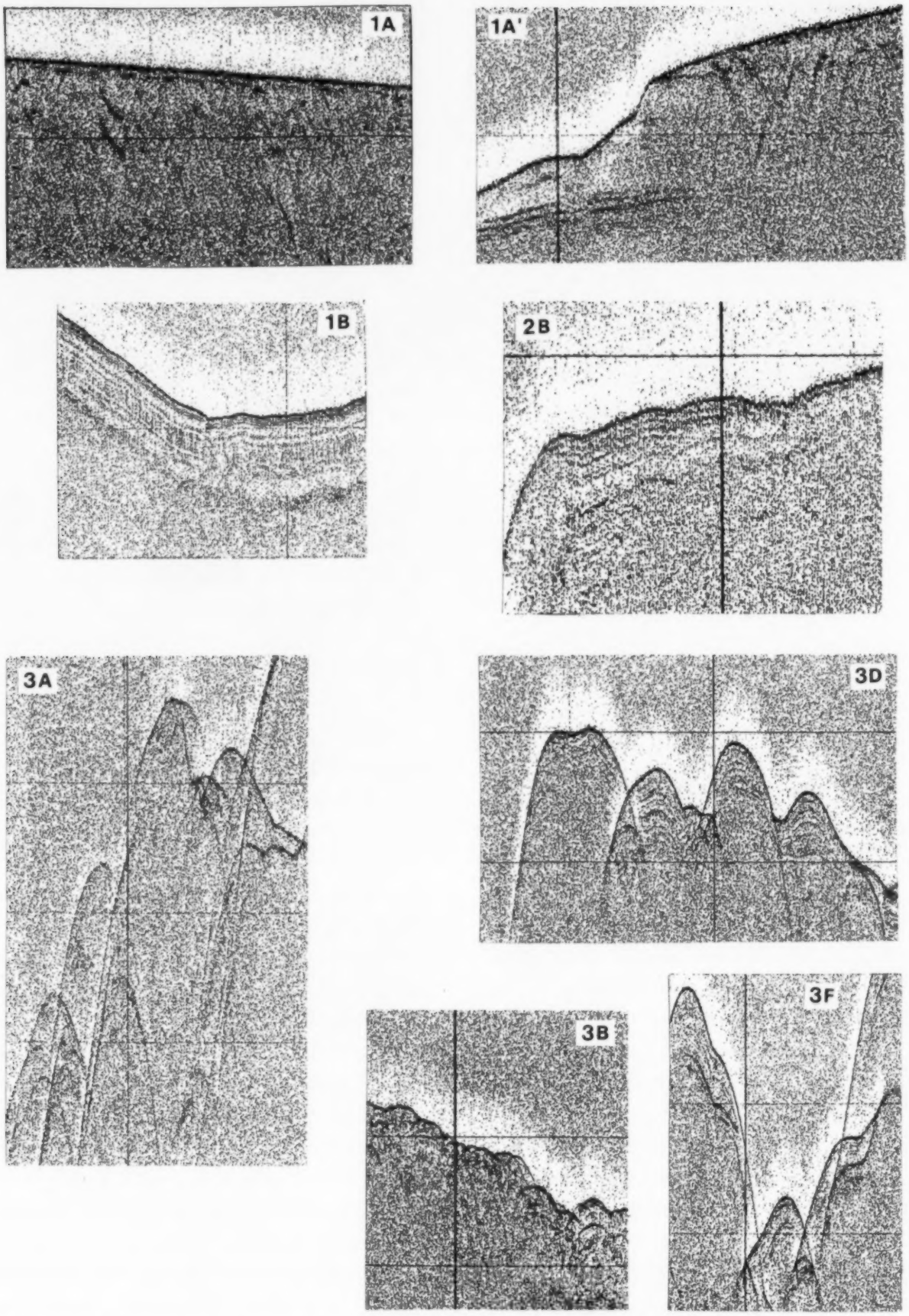

Fig. 10. Examples of 3.5 kHz responses on the Guinea Plateau Margin.

tielines. In areas 1 and 2 on the steepest part of the upper slope, the N–S tracklines record the hyperbolic structures of Echo type 3A, whereas standing waves (Echo type 3D) were registered on the NW–SE tieline. Superimposed echo types also occur on the lower slope in area 3: on the eastern wall of the large valley cutting the lower slope, the N–S tracklines show standing waves (Echo type

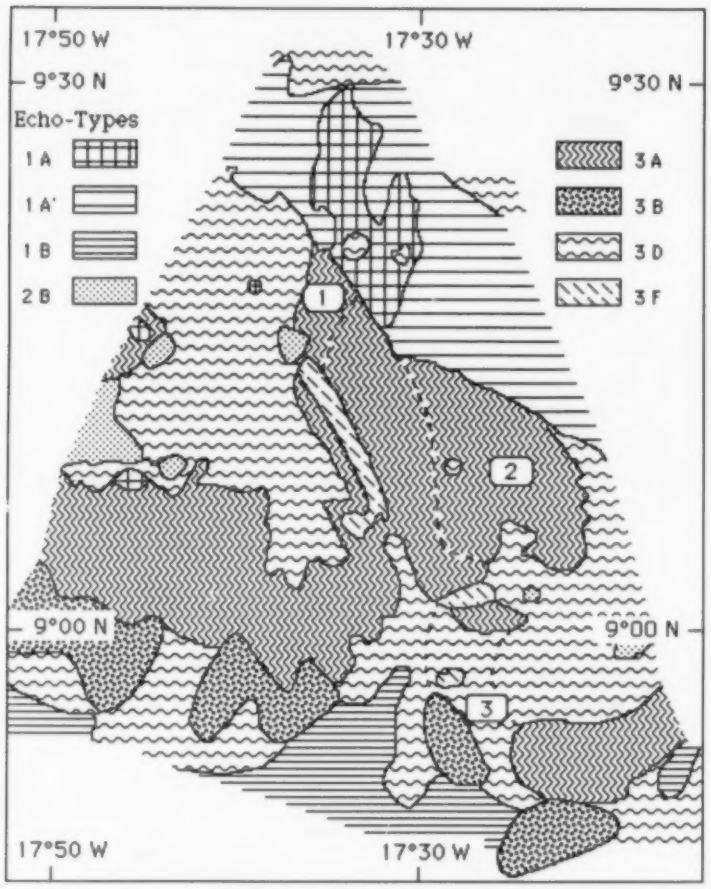

Fig. 11. Distribution of 3.5 kHz responses in Sector G1. Numbered areas with dashed outlines are those where the acoustic response varies depending on trackline orientation (see text).

3D), whereas hyperbolic echoes (Echo type 3A) were observed on the NW–SE tieline.

Sector G2

Bathymetry and morphology

The continental margin in Sector G2 (Fig. 2) comprises the following morphological elements (Rossi et al., 1989) (Fig. 12):

(1) The southern margin of the Guinea Plateau (above −1500 m) displays a regular topography and slopes gently to the south at an angle of 1.5°. It is incised by a number of slope-normal canyons.

(2) The steeper upper slope (−1500 to −2200 m) presents a more irregular topography (on a scale of <100 m) and is cut by a deep canyon with a curved N–S orientation originating on the plateau; there is a second, broader canyon to the west.

(3) The mid-slope region (−2200 to −3250 m) in Sector G2 is complicated by the presence of a number of volcanic cones of varying sizes. A large volcano, which is 2400 m in height and 16 km in diameter and topped by an eroded summit, occupies much of this region (Bertrand et al., 1989). The sides of the volcano are cut by radiating valleys. We will refer to this structure as the "main volcano". Smaller volcanic cones up to 250 m in height occur on a plateau at −2500 m in the eastern part of the mid-slope region. The latter is sandwiched between the upper slope and the main volcano and presents a small-scale (<100 m), irregular topography. Towards the west, the plateau passes into a fairly steep, very irregular, canyon-incised slope.

(4) The topography of the lower slope (−3250 to −3700 m) and the continental rise (deeper than −3700 m) is also complicated by the presence of volcanic structures (Fig. 4). The orientation of the lower slope and upper continental rise follows the base of the (main) large, circular, mid-slope volcano, rather than the regional E–W trends. Slope topography is slightly smoother than at shallower depths on the margin.

(5) At depths >4500 m the Sierra Leone abyssal plain is gently inclined towards the southeast and presents a regular topography.

Unconsolidated sediment thickness and acoustic facies

The thickness of post-Miocene unconsolidated sediments in Sector G2 is plotted in Fig. 13. In contrast to Sector G1 the unconsolidated sediment thicknesses in Sector G2 are generally low. The outer edge of the Guinea Plateau Margin and the upper slope are covered by <200 ms of unconsolidated sediments, with the main canyon clearly outlined by thinned, eroded sediment (0–100 ms). Numerous pockets of thinned sediments (<200 ms) or exposed basement in the mid-slope region mark the heads of valleys, steep slopes or volcanic cones.

The isochronopach map clearly illustrates a N–S axis of thinned sediment and exposed volcanic basement along 16°55'W. This axis runs from the main volcano and links up with other structures to the south.

Unconsolidated sediment cover in the rest of

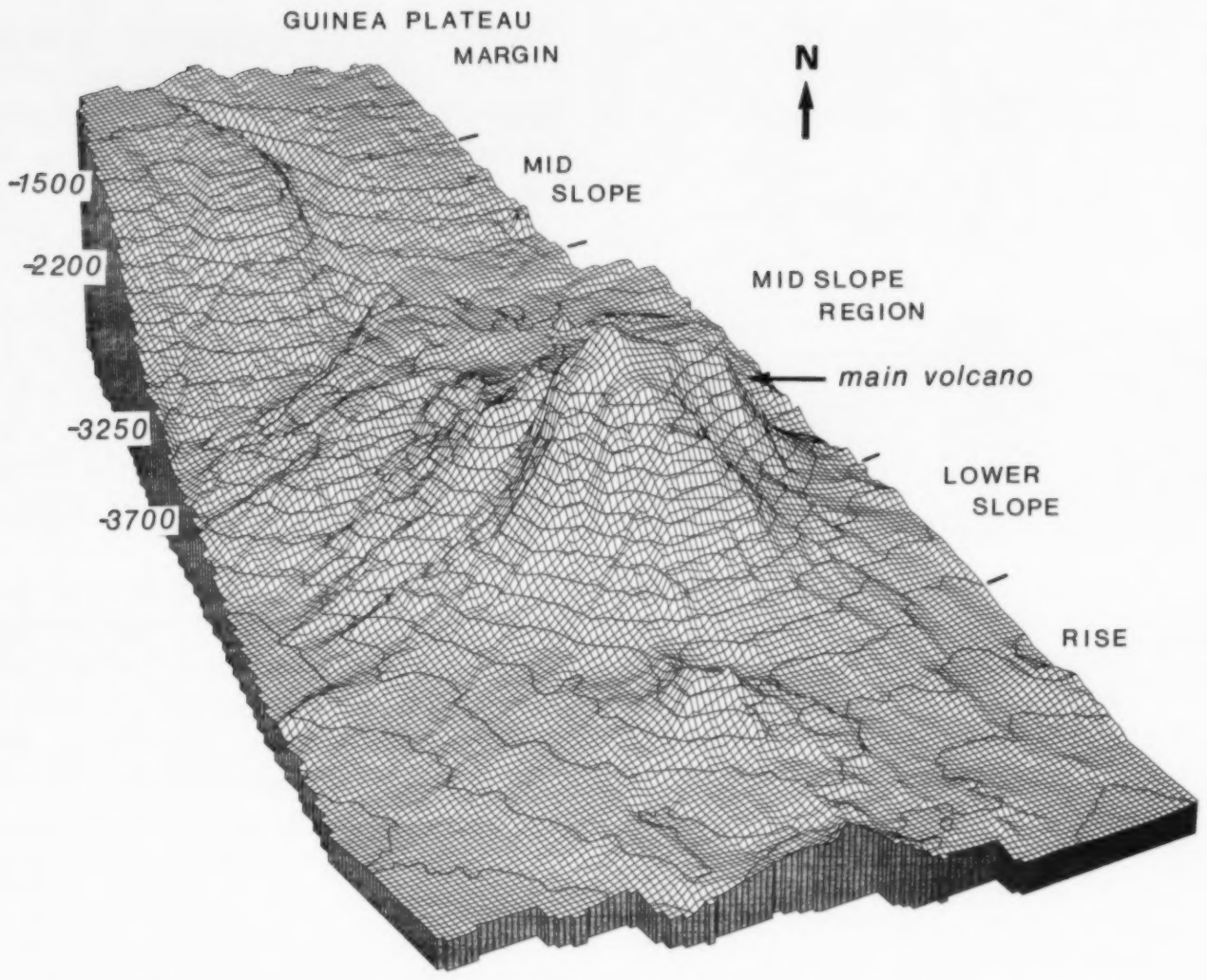

Fig. 12. Three-dimensional image of the continental slope in Sector G2 based on Seabeam data. Bathymetry in metres.

the mid-slope region is moderate, generally ranging from 200 to 300 ms, with a few small pockets of thicker sediments (>300 ms) ponded in moats between the volcanic cones. The greatest accumulations of unconsolidated sediments in Sector G2 occur on the lower slope and continental rise area, where sediments of >400 ms in thickness have been ponded on either side of the above-mentioned N–S volcanic axis. It was noted above that the surface topography of the two depocentres is fairly regular in comparison to the rest of the mid-slope area. The extreme southwestern part of this sector (the lower continental rise/abyssal plain) is characterised by a slightly thinner covering of unconsolidated sediments (200–300 ms).

The distribution of the acoustic facies is diplayed in Fig. 14. The outer ridge of the Guinea Plateau and the uppermost part of the upper slope are characterised by Echo types 1A and 1A', produced by the eroded surface of consolidated sediments. Additional occurrences of Echo type 1A are found in the eroded moat between the main volcano and the upper slope, on the summit of the main volcano, on the steepest part of the lower slope, and at the head of the valley between the main volcano and a smaller cone on the lower slope.

The dominant acoustic facies in Sector G2 is Echo type 3A, representing the large, overlapping hyperbolae which are typical of steep slopes. The seismic reflection profiles indicate that this echo response is produced by steep volcanic basement, and by sediment waves in the surficial sediment cover. On steep surfaces, wavelengths are small to medium (0.5–1 km), and heights range up to 100 m. Sediment waves of 1 km in wavelength (Echo type 3D) occur on the mid-slope plateau and on the SW-facing lower slope. Thus, as in Sector G1, there is an apparent correlation between sediment wave size and steepness of slope, with the smallest waves occurring on the steepest slopes and the

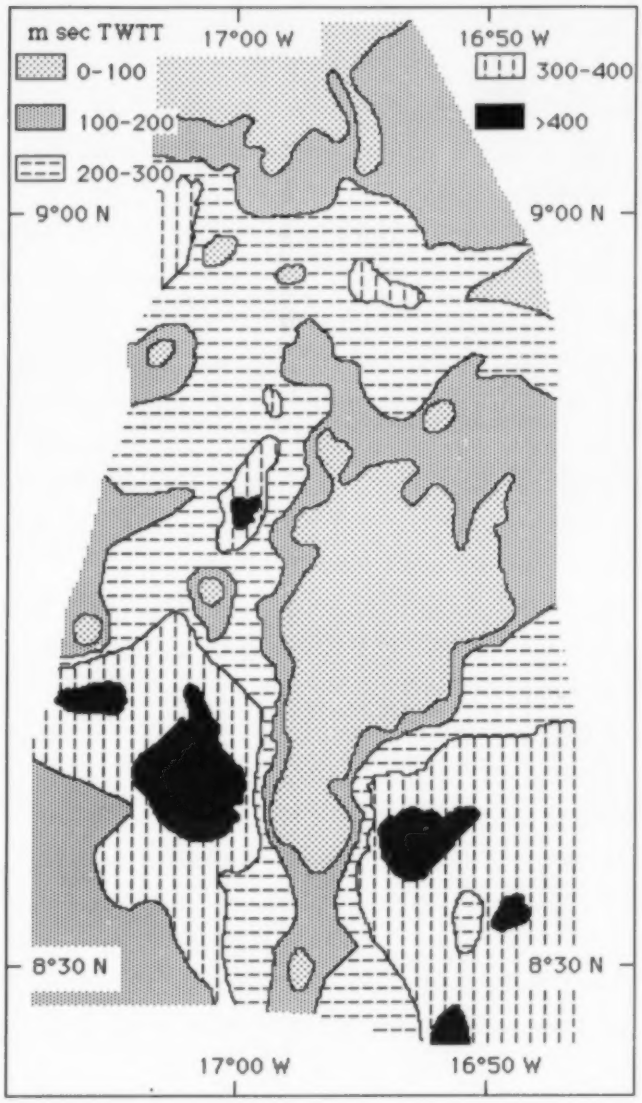

Fig. 13. Thickness of unconsolidated post-Miocene sediments in Sector G2.

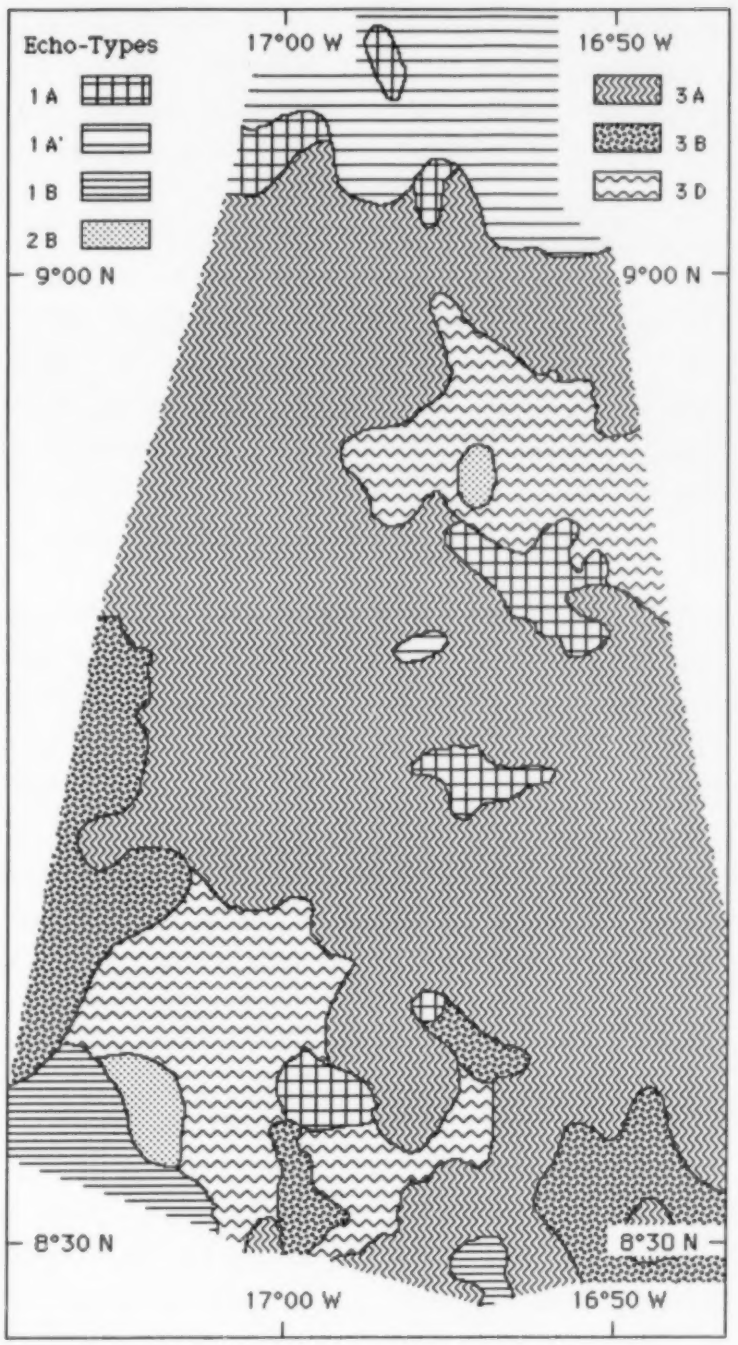

Fig. 14. Distribution of 3.5 kHz responses in Sector G2.

largest on the gentler slopes. The sediment waves appear to be oriented at an angle to the slope.

Much of the lower slope around the main volcano is covered by Echo type 3B, representing the irregular surfaces of slumped sediments. Towards the southwest, smooth-surfaced contourite sediments represented by Echo type 2B occur on the gentle slope of the continental rise. This acoustic facies grades into the pelagic facies of Echo type 1B on the abyssal plain of the Sierra Leone Basin. There is a further, isolated occurrence of Echo type 2B on the flattest part of the mid-slope plateau. In Sector G2, the sediment surface morphology producing this echo type seems to result from bottom currents that are weaker than those affecting the steeper slopes. In the intermediate basin in Sector G1, on the other hand, Echo type 2B was interpreted as resulting partly from bottom current erosion.

Discussion

Tectonic and magmatic control of the continental slope morphology in Sector G1 is reflected by (1) slope trends (NW–SE for the western margin, swinging around to the E–W for the southern margin), (2) steep, faulted upper and lower slopes, and (3) gentle folding of the pre-Cenomanian strata beneath the western part of the lower slope,

resulting in a downwarped intermediate basin and a marginal basement ridge, behind which a great thickness of sediments is trapped (Fig. 3). The faulting and folding of the lower strata have not continued into the overlying layers.

Tectonic activity has also strongly influenced the morphology of the continental margin in Sector G2, resulting in a steep, faulted upper slope. SSW–NNE and E–W fractures appear to have guided subsequent Late Cretaceous volcanic emplacements (Bertrand et al., 1989), leading to the creation of very irregular topography in the mid- and lower slope regions, which are dominated by volcanic structures.

The morphology of the sediment cover in the two sectors is controlled by bottom currents and mass-wasting processes, the latter predominating on the lower slope (Westall et al., in press). On the upper slope and the lower slope canyon and valley walls, relatively strong currents, due to topographic intensification, are responsible for the erosion of unconsolidated sediment. Slope steepness and tectonic activity are additional controls of sediment deposition and erosion on the lower slope. The canyons cut into the upper slope do not appear to be structurally controlled and are presumably caused by erosive turbidity currents.

In Sector G2, bottom-current induced erosion was also noted on the saddle between the main volcano and the upper slope, and on the steepest part of the lower slope. Erosion of the summit of the main volcano was apparently due to subaerial exposure, as shown by the indurated shallow-marine and littoral deposits recovered from the crest (Mascle et al., 1989; Bertrand et al., 1989; Cousin et al., in prep.).

Sediments in the intermediate valley in Sector G1 are concentrated into slope-parallel sediment drifts separated by valleys underlain by zones of condensed or eroded sediment. These zones continue into the deepest layers of the sediment cover and obviously mark the axes of higher velocity current cores which have been present throughout almost the whole of the history of sedimentation on the margin (Westall et al., in press). These current cores occur within the NADW, which influences most of the margin. Average velocities for the NADW in this region are very low (< 2 cm/s; Hogg et al., 1982), and therefore increases in velocity must be caused by topographic intensification and possibly by the passage of deep-water eddies (Sarnthein et al., 1982).

The sediment surfaces in both sectors are almost ubiquitously covered by current-moulded sediment waves. These bedforms appear to be stationary, except in the lower parts of the valleys and canyons where migrating sediment waves (in conjunction with erosion) indicate higher current velocities. In G2, shallower sediment waves (3D) appear to have the same trend as the prominent N–S submarine canyon, suggesting that the waves may be the product of turbidity current overspill. The apparent correlation of wave size with steepness of slope (smaller waves on steeper slopes and larger waves on gentler slopes) may be due to a change in orientation of the bedforms with respect to slope trends, as suggested by data from the tielines.

The morphology of much of the lower slope is controlled by the emplacement of mass-movement deposits, the latter being caused by instability due to the continuing tectonic activity on this transform margin in conjunction with the steepness of slope.

Conclusions

This study shows that tectonic control of the morphology is strong in both Sectors G1 and G2. In both regions, the upper slope is steepened by faulting. However, whereas transpressional forces in Sector G1 resulted in gentle folding, thus deforming the intermediate basin, extensional forces on the probably transtensionally faulted margin in Sector G2 caused major magmatic emplacement. Sector G2 is thus dominated by magmatic structures, with much of the mid-slope region being taken up by a large, 16 km diameter volcano reaching to 840 m below sea level and by a number of smaller cones. Other small cones also occur on the lower slope.

Bottom-current control of the entire margin in both sectors may be demonstrated by the topographically induced erosion on the uppermost slope/Guinea Plateau edge, as well as on steeper

parts of the lower slope, and on the walls of canyons incised into the margin. Bottom currents within the NADW are responsible for moulding the sediment cover, producing sediment waves ranging from 0.5 to 1 km in wavelength and up to 100 m in height and oriented at an angle to the slope. They are also responsible for much of the erosion over this part of the margin, in conjunction with bottom currents in the shallow-water masses at the edge of the Guinea Plateau (ESW/AAIW). Mass movement in both sectors, caused by steepness of slope and slope instability due to the continuing tectonic activity of the margin, has considerably modified the lower slope/upper rise areas.

Acknowledgements

The authors are very grateful to E. Bonatti and A. Castellarin for valuable discussion and to the anonymous reviewers for critically reading the paper.

This is contribution 809 of the *Istituto per la Geologia Marina*, CNR, Bologna and contribution 552 of GEMCO (URA CNRS 718).

References

Benkhelil, J., Mascle, J., Villeneuve, M., Tricart, P., Auroux, C., Basile, C., Ciais, G. and *Groupe Equamarge*, 1989. La marge transformante sud-guinéenne: premiers résultats de la campagne Equamarge II (février 1988). C.R. Acad. Sci. Paris, Sér. II, 308: 655–661.

Bertrand, H., Mascle, J., Villeneuve, M., Robert, C., Cousin, M., and *Groupe Equamarge*, 1989. Le volcanisme de la marge sud-guinéenne, implications pour l'ouverture de l'Atlantique équatorial: résultats de la campagne Equamarge II. C.R. Acad. Sci. Paris, Sér II, 309: 1703–1708.

Ciais, G., 1988. Contribution à l'étude de la marge sud-guinéenne: morphologie, sédimentologie et structure. (Campagne Equamarge II, février 1988). Mém. D.E.A., Univ. Paris, pp. 1–78.

Courp, T., 1984. Interprétation acoustique des profils 3.5 kHz de la zone Guinéee–Côte d'Ivoire. Mém. D.E.A., Univ. Paris, pp. 1–51.

Cousin, M., Mascle, J., El Mouichni, A., Moullade, M. and Bertrand, H., in prep. Sedimentary record of recent foundering along the Guinean Margin.

Damuth, J.E., 1975. Echo character of the western equatorial Atlantic floor and its relationship to the dispersal and distribution of terrigenous sediments. Mar. Geol., 18: 17–45.

Defant, A., 1941. Die absolute Topographie des physikalischen Meeresniveaus und der Druckflachen, sowie die Wasserbewegungen im Atlantischen Ozean. Wiss. Ergeb. Dtsch. Atl. Exped. 'Meteor', 1925–1927, 6/1(5): 191–260.

Hogg, N., Biscaye, P., Gardner, W. and Schmitz, Jr., W.J., 1982. On the transport and modification of Antarctic Bottom Water in the Vema Channel. J. Mar. Res., 40(Suppl.): 231–263.

Jacobi, R.D. and Hayes, D.E., 1982. Bathymetry, microphysiometry and reflectivity characteristics of the West African Margin between Sierra Leone and Mauritania. In: U. von Rad, K. Hinz, M. Sarthein and E. Seibold (Editors), Geology of the Northwest African Continental Margin. Springer, Berlin, pp. 182–212.

Jones, J.W. and Mgbatogu, C.C.S., 1982. The structure and evolution of the West African continental margin off Guinea, Guinea Bissau and Sierra Leone. In: R.A. Scrutton and M. Talwani (Editors), The Ocean Floor. Wiley, pp. 165–202.

Lynn, R.J. and Reid, J.L., 1968. Characteristics and circulation of deep and abyssal waters. Deep-Sea Res., 15: 577–598.

Marinho, M.O., 1985. Le plateau marginal de la Guinée—transition entre Atlantique central et Atlantique équatorial. Thèse 3ème Cycle, Univ. Paris, 183 pp.

Marinho, M.O., 1987. Le plateau marginal de Guinée. Evolution de la marge Guinéenne du Crétacé supérieur à l'Actuel. D'après des données sismiques. Tome II°. Thèse Doct., Univ. Paris, 130 pp.

Mascle, J., Marinho, M.O. and Wannesson, J., 1986. The structure of the Guinean continental margin: implications for the connection between the Central and the South Atlantic oceans. Geol. Rundsch., 75: 57–70.

Mascle, J., Blarez, E. and Marinho, M., 1988. The shallow structures of the Guinea–Ivory Coast transform margins: Their bearing on the Equatorial Atlantic Mesozoic evolution. Tectonophysics, 155: 193–209.

Mascle, J., Auroux, C. et al., 1989. Les marges continentales transformantes ouest-africanes: Guinée, côte d'Ivoire, Ghana et la Zone de Fracture de la Romanche. Campagne Equamarge II. COF/IFREMER, 8, pp. 1–150.

Mienert, J., 1986. Akustostratigraphie im äquatorialen Ostatlantik: Zur Entwicklung der Tiefenwasserzirkulation der letzen 3,5 Millionen Jahre. 'Meteor' Forshungsergeb., Reihe C, 40: 19–86.

Moullade, M., Mascle, J., Tricart, P., Benkhelil, J. and Cousin, M., in prep. Middle Albian sediments on the Guinean Margin: implications concerning the evolution of the area.

Rossi, S., Mascle, J. and Westall, F., 1989. Studio geomorfologico di due aree lungo il margine trasforme della Guinea (Africa Equatoriale). Rend. Soc. Geol. Ital., 12: 33–36.

Sarnthein, M., Thiede, J., Pflaumann, U., Erlenkeuser, H., Fütterer, D., Koopmann, B., Lange, H. and Seibold, E., 1982. Atmospheric and oceanic circulation patterns off Northwest Africa during the past 25 million years. In: U. von Rad, K. Hinz, M. Sarnthein and E. Seibold (Editors), Geology of the Northwest African Continental Margin. Springer, Berlin, pp. 545–604.

Sverdrup, H.U., Johnson, M.W. and Fleming, R.H., 1942. The Oceans: Their Physics, Chemistry, and General Biology. Prentice Hall, 1087 pp.

Tricart, P., Mascle, J., Basile, C., Benkhelil, J., Ciais, G. and Villeneuve, M., 1991. La tectonique d'inversion médio-crét-

acée de la marge sud-guinéenne (campagne Equamarge II). Bull. Soc. Géol. Fr., 162: 91–99.

Westall, F., Rossi, S. and Mascle, J., 1990. Current-controlled sedimentation in the Equatorial Atlantic: examples from the southern margin of the Guinea Plateau and the Romanche Fracture Zone. In: D.A.V. Stow and J.C. Faugères (Editors), Proc. Contourites Symp. (Nottingham). Int. Assoc. Sedimentol., in press.

Marine Geology, 105 (1992) 241–252
Elsevier Science Publishers B.V., Amsterdam

Indications of hydrothermal activity at the Chile Ridge spreading centre

P. Marienfeld[a] and V. Marchig[b]

[a]*Alfred-Wegener-Institut für Polar- und Meeresforschung, Bremerhaven, Germany*
[b]*Bundesanstalt für Geowissenschaften und Rohstoffe, Alfred-Bentz-Haus, Postfach 510153, 3000 Hannover 51, Germany*

(Revision accepted August 19, 1991)

ABSTRACT

Marienfeld, P. and Marchig, V., 1992. Indications of hydrothermal activity at the Chile Ridge Spreading Centre. Mar. Geol., 105: 241–252.

A small section of the Chile Ridge spreading zone has been investigated. This area is composed of three short spreading segments offset by fracture zones, and this section of the ridge is hydrothermally active. The basalts investigated are of the MORB type and indicate that this part of the Chile Ridge is a normal oceanic spreading zone. A dredge from the spreading axis recovered rock samples containing hydrothermal sulphide lenses enriched in galena.

Sediments near the ridge reveal hydrothermal contamination an order of magnitude lower than in the sediments surrounding the southern part of the East Pacific Rise. The hydrothermal material is characterized by strong diagenetic changes which have not been previously reported.

Introduction

The Chile Ridge has been recognized by Herron (1972) as a divergent plate boundary oriented NNW–SSE. The concentration of earthquake epicentres (Fig. 1) shows that it is a tectonically active spreading zone. The spreading rates for the last 5 m.y. are 3–4 cm/yr (Forsyth, 1972; Klitgord et al., 1973; Herron et al., 1981).

During cruise GEOMETEP 4 on the *Sonne*, a part of the Chile Ridge between 36.5° and 39°S was investigated with the aim of determining whether the Chile Ridge at this latitude is hydrothermally active and, if so, how intense this activity is.

We attempted to achieve this goal by means of Seabeam mapping of the seafloor, by TV and photographic surveys in the spreading zones, and by investigations into sediment and rock samples.

Bathymetric investigations on Chile Ridge

Bathymetric investigations were performed using the Seabeam automatic mapping system (Wilke, 1986). The part of the ridge that we investigated is divided into three segments oriented approximately NNW–SSE. Each segment is offset by groups of parallel E–W striking transform faults (Fig. 2).

The southern ridge segment extends from 38°24'S to 38°56'S, and in this area we found a graben oriented 176° and bounded by a series of dip-slip faults. Two tracks by the photographic and TV observation system showed that the bottom of the graben is covered with sediments which are so thick that the tops of pillows protrude only occasionally from the sediment cover (Holler, 1987). This indicates that the graben is devoid of recent volcanic activity and thus probably represents a fossil spreading zone (dashed line in Fig. 2).

Eleven nautical miles (20 km) to the west another graben was found. This graben has a central horst about 40 m high and is also framed by numerous dip-slip faults. Fresh glassy basaltic material was obtained by dredging and gravity coring within this graben. We therefore believe that this graben, and not the one in the east, is the active spreading

0025-3227/92/$05.00 © 1992 — Elsevier Science Publishers B.V. All rights reserved

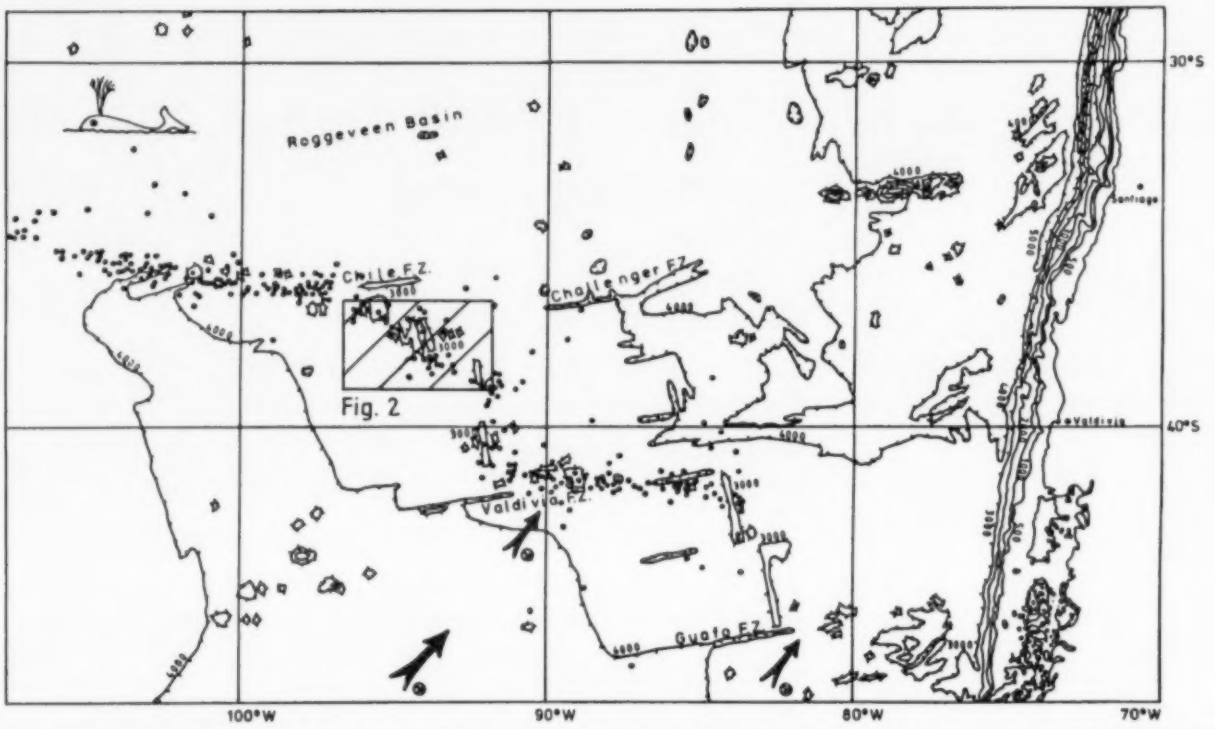

Fig. 1. Map of the southeast Pacific. The locations of near-surface earthquakes of the last 40 years west of 83°W are indicated by dots. The arrows show the prevalent direction of bottom currents (after Lonsdale, 1976).

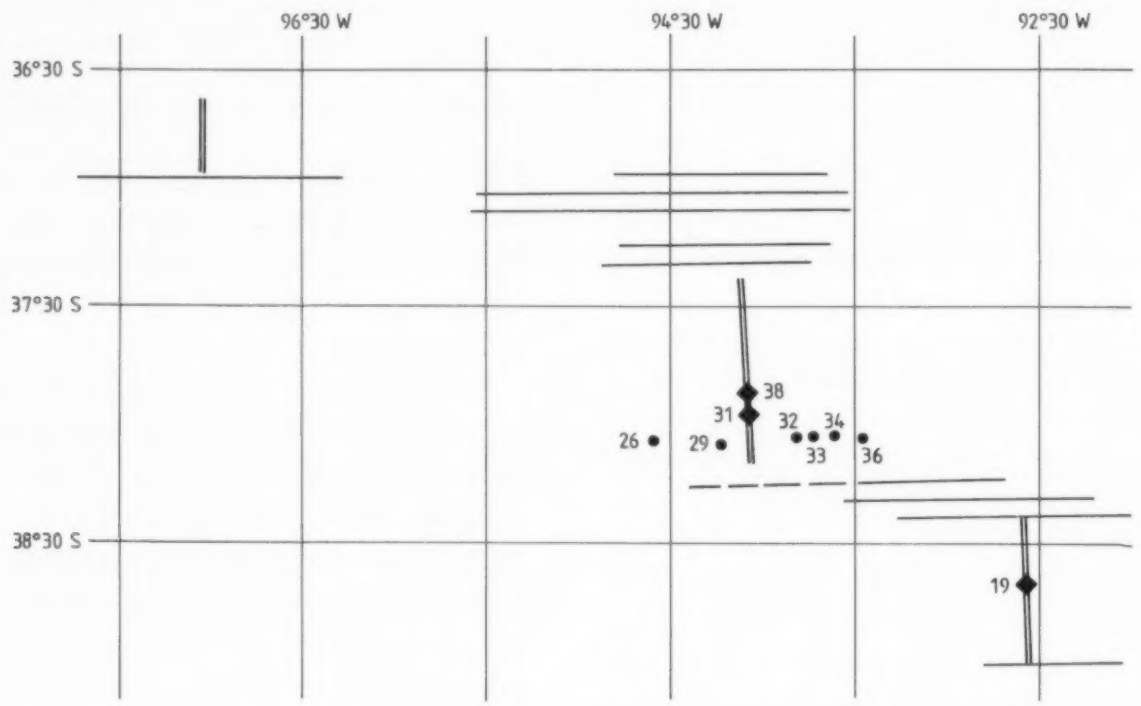

Fig. 2. Sketch map of the investigated area with three segments of the spreading zone (double lines) and a series of fracture zones between them. The dashed line indicates a fossil fracture zone. Sites of sediment cores are marked by dots, sites of dredged rock samples are marked by diamonds.

zone of the southern segment of the Chile Rise (Fig. 2).

The middle segment of the three investigated (Fig. 2) is offset from that in the south by a 12 n mile (22 km) wide zone dominated by a series of E–W striking faults, which offset this segment to the west by 70 n mile (130 km). The segment is defined by a graben 3200–3800 m below sea level (bsl) which is, like that in the southern segment, framed by a series of dip-slip faults. A profile across the Chile Ridge was obtained at 38°4'S (Fig. 3). Fresh basalts collected from the axis show

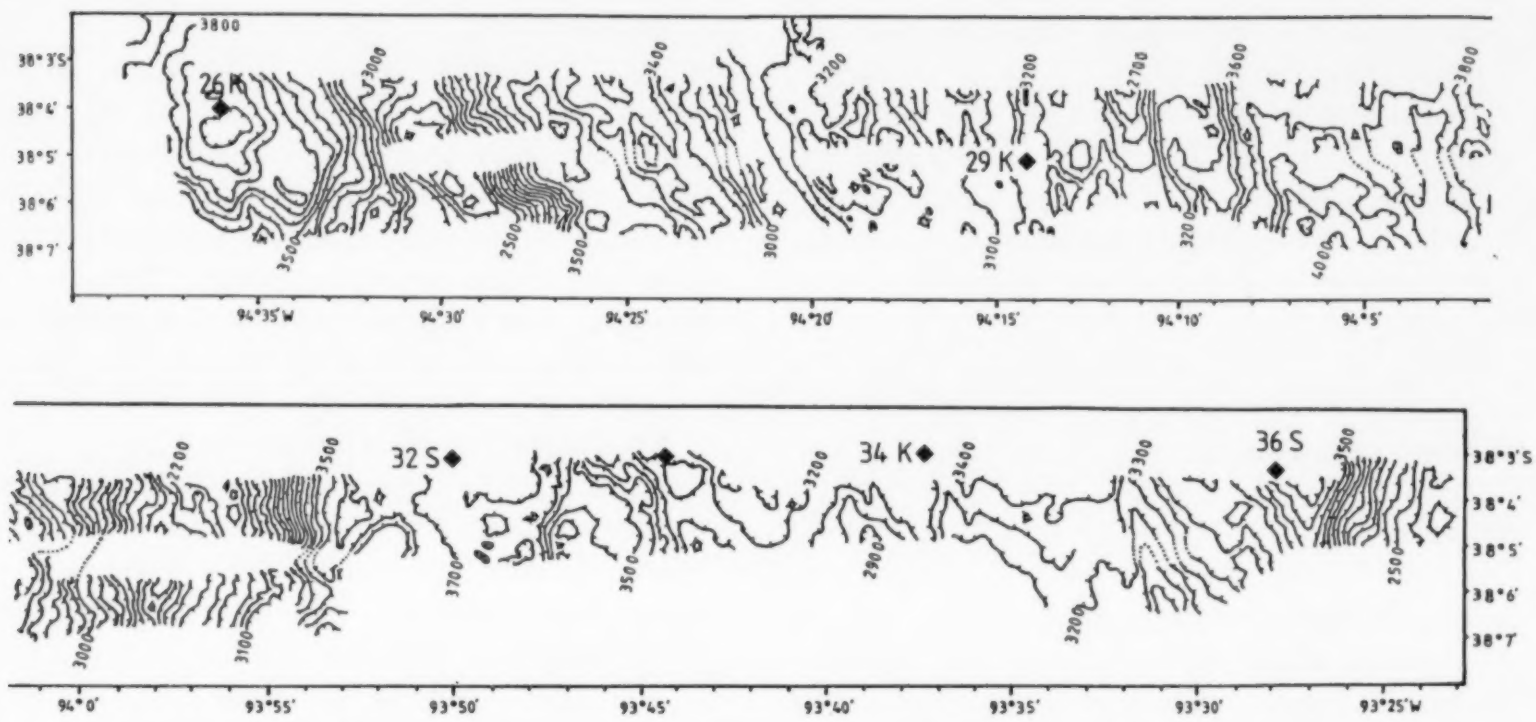

Fig. 3. Bathymetric map of the investigated core profile across the Chile Ridge between 38°2'S and 38°8'S. Core sites 26K, 29K, 32S, 33S, 34K and 36S are marked by diamonds. The spreading zone is between *29 K* and *32 S*.

that the graben has recently been volcanically active. We were able to follow this graben as far as 37°20'S.

The northern ridge segment extends from 36°40'S to 36°57'S and is offset to the west by a series of E–W striking faults by 141 n mile (261 km), as in the previous two ridge segments. The northern segment is defined by a 3500–4100 m (bsl) deep graben with a discontinuous central horst and, again as in the other two segments, by a frame of dip-slip faults. In this spreading zone we observed small volcanoes and fresh pillow lavas, features which are characteristic of other medium- to slow-spreading ridges.

Methods

Sediment

Six sediment cores were obtained by means of piston corer and gravity corer along a profile of about 90 km in length. The positions of the cores are shown in Fig. 2. On average, all cores were sampled at intervals of 10 cm. Sedimentary structures were recorded continuously.

A portion of each sample (fractions bigger and smaller than 63 μm) was wet-sieved. The >63 μm fraction was examined microscopically to determine the composition and degree of preservation of the planktonic foraminiferal assemblage. Smear slides were used for the microscopic examination of the fine-grained sediment fraction.

Thirty-five elements were determined by X-ray fluorescence analysis of the total dry sediment. The carbonate content was calculated from the amount of calcium in the samples analyzed. This method was checked by volumetric CO_2 determination after addition of acid to the sediment. Within analytical error (2%) both methods yielded the same results, indicating that the content of calcium in the non-carbonate fraction of the sediment is smaller than the analytical uncertainty. The amount of oxide and silicate was calculated from X-ray fluorescence analysis, as described in Marchig and Erzinger (1986).

Rocks

Rock samples were also dredged from within the spreading zone. Three samples from two dredges of the middle ridge segment and two samples from one dredge of the southern ridge segment have been microscopically and chemically

investigated. The positions of the dredged samples are also shown in Fig. 2.

Rock samples were cut in half. One part was ground and used for X-ray fluorescence analysis. From the other part thin sections were produced in order to microscopically examine the mineralogical composition and structural characteristics of the rocks.

Results and discussion

Rocks

The samples are fragments of pillow basalts, with glassy crusts which do not reveal any phenocrysts. Samples taken from the centres of the pillows, however, do contain some phenocrysts of plagioclase and olivine in a glassy groundmass. Plagioclase crystals are twinned, olivine often has a skeletal form.

The chemical composition of the samples is shown in Table 1, together with the average chemical composition of basalts from the extremely rapidly diverging part of the East Pacific Rise, between the equator and the Easter Plate at 22°S (author's unpublished results). Both groups of samples have a chemical composition within the range of normal MORB.

Sulphide impregnations in the rocks

In addition to fresh basalt, dredge 31 also contained several samples of alterated basalt with sulphide impregnations. They occur in the form of up to 2 cm thick lenses which consist of 40% pyrite, 25% galena, 20% sphalerite, 10% chalcopyrite and 5% covellite. (A detailed description is given by Mühe, 1987.) The ore paragenesis is typical of hydrothermally formed sulphide impregnations at diverging plate boundaries, and contrasts with the ore paragenesis occurring as massive sulphide chimneys which contains galena only in traces. These impregnations thus indicate the existence of hydrothermal activity at the Chile Ridge spreading centre.

Sediments

Sediment cores were sampled on a profile across the middle segment of the investigated part of the Chile Ridge. We had observed recent volcanic activity there, and concluded that this area represents the active spreading centre. The profile, extending over a distance of 90 km, comprises six cores between 78 cm and 500 cm long.

Observations on foraminifera

The extinction of *Pseudoemilianea lacunosa* and the first occurrence of *Globorotalia truncatulinoides* provide us with a time marker of 470,000 yrs B.P. (Haq, 1984; Heinze and Knüttel, 1986). This time marker could be observed in core 26 at a depth of 1 m and in core 36 at depth of 4.8 m. This marker was used to determine both sedimentation rates and accumulation rates of different sedimentary components.

Twenty-one species of planktonic foraminifera have been distinguished in the coarse fraction of the sediments. They are listed according to their occurrence (as determined semi-quantitatively) in Fig. 4. It can be seen that downcore the number of well-preserved foraminifera decreases. The degree of preservation worsens and the sediment is increasingly composed of fragments of foraminiferal shells. Some easily soluble species totally disappear. From this we conclude that strong dissolution of calcite takes place downcore. The calcite dissolution is connected with diagenetic processes: the growth of phillipsite (which develops at a very early stage), the complete filling of foraminiferal shells or shell fragments and their discolouration to yellow, the formation of Mn stains on the tests of foraminifera, and finally the formation of Mn micronodules and aggregates rich in Fe.

Five well-graded turbidite beds have been observed in the cores, two in each of the cores 32 and 33, and one in core 36. The four turbidite beds of cores 32 and 33 are characterized by enrichment of the volcanic glass component, whereas the turbidite bed of core 36 is an almost pure foraminiferal sand (Fig. 4). Cores 26, 29 and 34 show a continuous decrease in carbonate content downcore. This trend is interrupted in

TABLE 1

Chemical composition of basalts

Sample:	31/1	31/2	38	19/1	19/2	Chile Ridge	East Pacific Rise
%							
SiO_2	49.17	48.56	49.12	49.10	49.24	49.04±0.17	48.88±0.89
TiO_2	1.39	1.23	1.38	1.33	1.35	1.34±0.06	1.99±0.83
Al_2O_3	16.35	15.84	16.38	15.69	15.63	15.98±0.36	14.11±1.52
Fe_2O_3	9.82	9.89	9.81	9.24	9.48	9.65±0.28	12.77±2.81
MnO	0.17	0.18	0.18	0.17	0.17	0.17±0.01	0.25±0.12
MgO	7.63	7.47	7.52	8.29	8.19	7.82±0.39	7.00±1.60
CaO	11.51	10.07	11.58	11.69	12.00	11.37±0.75	10.86±1.41
Na_2O	2.83	3.16	2.83	3.17	3.01	3.00±0.17	2.64±0.25
K_2O	0.12	0.14	0.10	0.11	0.06	0.11±0.03	0.23±0.13
P_2O_5	0.14	0.10	0.12	0.11	0.13	0.12±0.02	0.19±0.09
mg/kg							
Cu	63	60	67	80	68	68±8	71±14
Ni	105	58	107	94	89	91±20	89±49
Sr	119	121	122	127	127	123±4	114±34
Y	32	32	35	30	32	32±2	47±18
Zn	69	75	71	68	67	70±3	103±38
Zr	87	62	84	81	78	78±10	117±54
Cr	235	183	251	312	293	255±51	241±124
Sc	37	40	39	38	42	39±2	52±4
V	260	289	252	253	251	261±16	398±121
LOI (%)	0.05	2.06	0.03	0.36	0.10	0.63±1.11	0.62±0.10
FeO/FeO+MgO (rate of liquid/solid differentiation in the magma chamber)						0.53	0.62
Spreading rate (cm/yr)						3–4	16–19

cores 32, 33 and 36 by the turbidite beds. Directly below each turbidite bed the carbonate content is higher than directly above it. The best explanation for this is that the turbidites have sealed the sediment. In this way the possibility of exchange of matter between seawater, porewater and sediment was reduced, and the further solution of carbonate in the sediment below each turbidite bed was drastically diminished. This shows that the dissolution of calcite is a diagenetic process which takes place within the sediment column, at a depth in which porewater retains contact with seawater allowing the dissolved carbonate to be transported away. Rapid deposition of a thick turbidite layer has always stopped this process. If the dissolution of calcite had happened in seawater or at the sediment surface, the observed gradation of foraminiferal dissolution between the turbidite beds would not have been possible. Moreover, delicate species susceptible to dissolution would not have been deposited and buried, but would already have been destroyed in the seawater or at the seawater–sediment interface (Berger, 1970).

Composition of sediments: variations with depth in core and with distance from Chile Ridge

The proportions of the main sediment components, carbonate, silicates and oxides, which have been calculated from the X-ray fluorescence data are shown in Fig. 5. The observed five turbidite beds are bounded by horizontal lines.

The downcore decrease in carbonate and increase in silicates and oxides is obvious in all cores. These changes are caused by diagenetic dissolution of calcite, as described in the previous section. An increase in silicate and oxide content with depth in core is due to secondary enrichment of residue after dissolution of calcite, and not because of higher accumulation rates. The amount of oxides is relatively low in those core sections in

which diagenetic dissolution of calcite has not yet taken place. The sediment in these sections contain, on average, 7% oxide. The oxide content reaches 50% in the deeper core section with strong dissolution of calcite.

Figure 7 shows the average sediment composition of the cores in relation to their distance from the Chile Ridge spreading zone. There is no trend of decrease in oxide content with increasing distance from the spreading zone, as is the case with core profiles across the East Pacific Rise (Marchig and Erzinger, 1986). Core 26, at the end of the core profile (i.e., further from the spreading centre than the other cores investigated), reveals the opposite trend, with the greatest average enrichment in oxides (Fig. 7). This leads us to conclude that it is not the primary output of hydrothermal precipitates from the spreading zone that regulates the distribution of oxides in this part of the Chile Ridge, but rather the secondary enrichment due to diagenetic dissolution of calcite. This conclusion is confirmed by the X-ray fluorescence data calculated on a carbonate-free basis (Fig. 6). Downcore the relative proportion of silicates and hydrothermal matter changes only slightly. Hence we infer that volcanic and hydrothermal activity of the Chile Ridge did not change significantly with time.

Accumulation rates of manganese in the sediment

Areas of very low sedimentation rates can reveal strong enrichment of Fe and Mn oxides (Marchig, 1978), because the input of hydrogenous matter, which is known to be homogenous all over the ocean (Elderfield, 1977), is only weakly diluted by other sediment components. In order to determine whether the hydrothermal activity of the Chile Ridge was the source of oxides in the surrounding sediment we calculated the accumulation rates of manganese. However, this calculation could only be performed for core 36: The average sedimentation rate could be determined for this core by using the horizon dated by the extinction of *P. lacunosa* and the first occurrence of *G. truncatulinoides*. Additionally, unlike core 26 for example, which is the second dated core, core 36 shows no pronounced dissolution of calcite. The calculated average sedimentation rate for core 36 is 1 cm/1000 yrs.

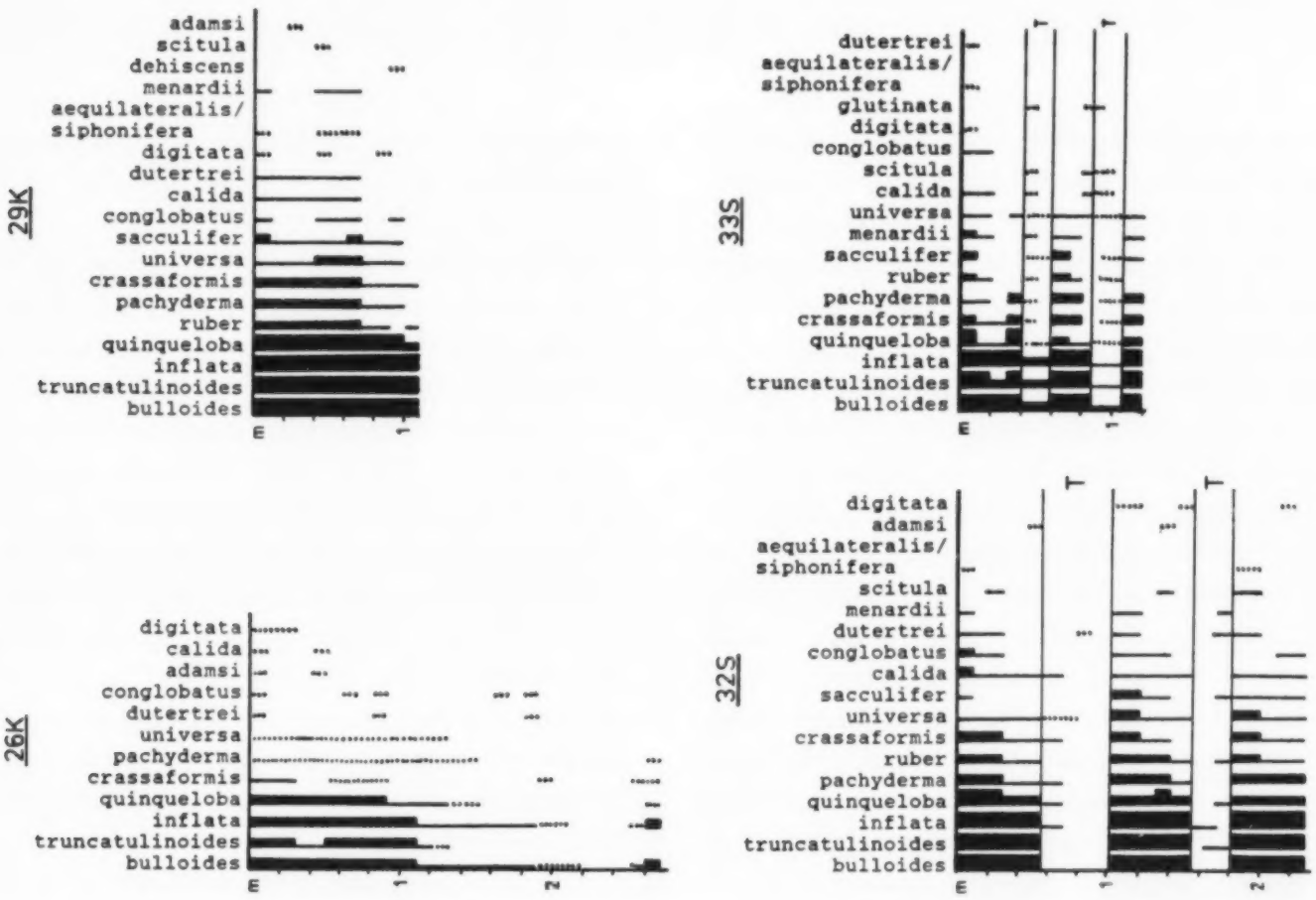

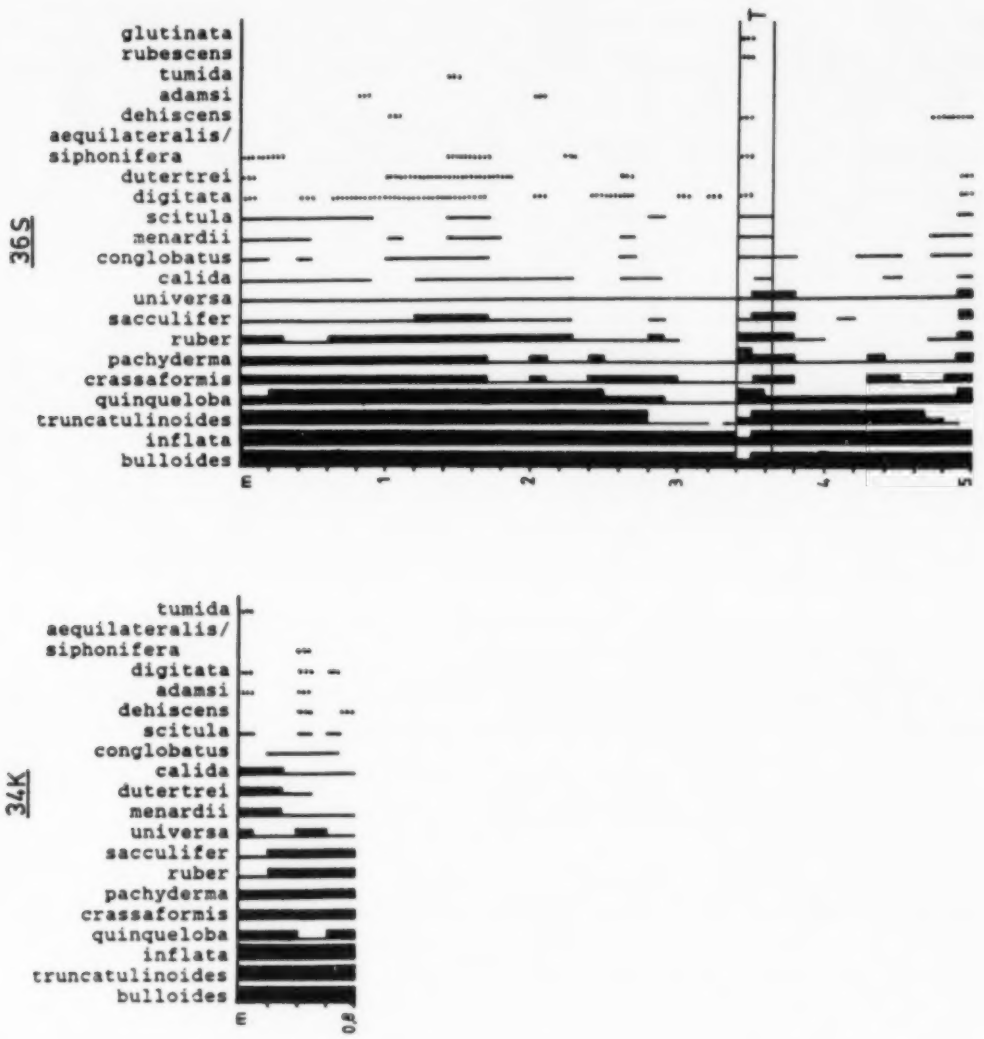

Fig. 4. Distribution of planktonic foraminifera versus depth in cores. Only well-preserved specimens have been taken into account. The width of the bar indicates the number of individuals counted in four frequency groups. Turbidite beds are marked with a *T*.

Manganese has a calculated accumulation rate of 5 mg/cm^2/yr in core 36. Only 0.2–2.1 mg/cm^2 of manganese accumulate per year worldwide by means of hydrogenous precipitation in the oceans (Elderfield, 1977). This comparison shows that not all manganese can be attributed to hydrogenous precipitation, although a significant amount may have originated in that way. This means that hydrothermal input in the sediments of the Chile Ridge is definitely taking place.

A core sampled 60 km west of the spreading zone of the East Pacific Rise at 17°S reveals an accumulation rate of hydrothermal manganese of 14 mg/cm^2/yr (Heinze, 1985). This significantly higher accumulation rate for hydrothermal manganese at the spreading zone of the East Pacific Rise corresponds to higher spreading rates in this region (18 cm/yr) compared to the Chile Ridge (3–4 cm/yr).

Correlation matrix of elements on a carbonate-free basis

The correlation matrix shown in Fig. 8 was calculated for all of the 112 sediment samples analyzed. To eliminate the different amounts of dilution of silicates and oxides by carbonate matter, it was calculated on a carbonate-free basis. The samples from turbidite beds have been excluded from the calculation because these sediments were formed under completely different physical conditions and were sorted during transport. The elements Ca and Sr have also been excluded from the calculation, as they are dominantly bound to carbonate. Included in the correlation matrix are the amounts of oxides and silicates which have been calculated from the chemical composition of the samples as described by Marchig and Erzinger (1986).

The calculated correlation matrix is rearranged

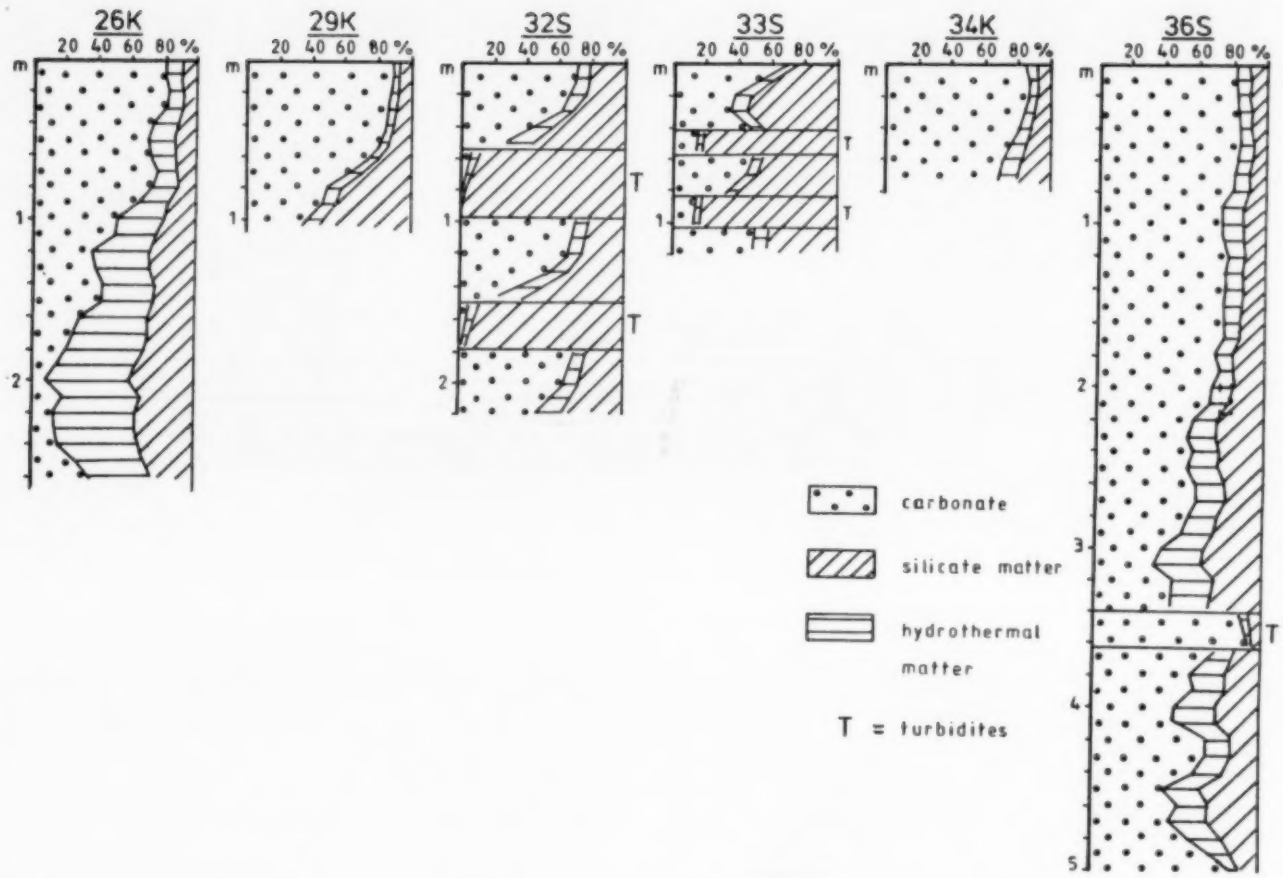

Fig. 5. Changes in the content of carbonate, silicates and hydrothermal matter of the sediment as a function of depth in core.

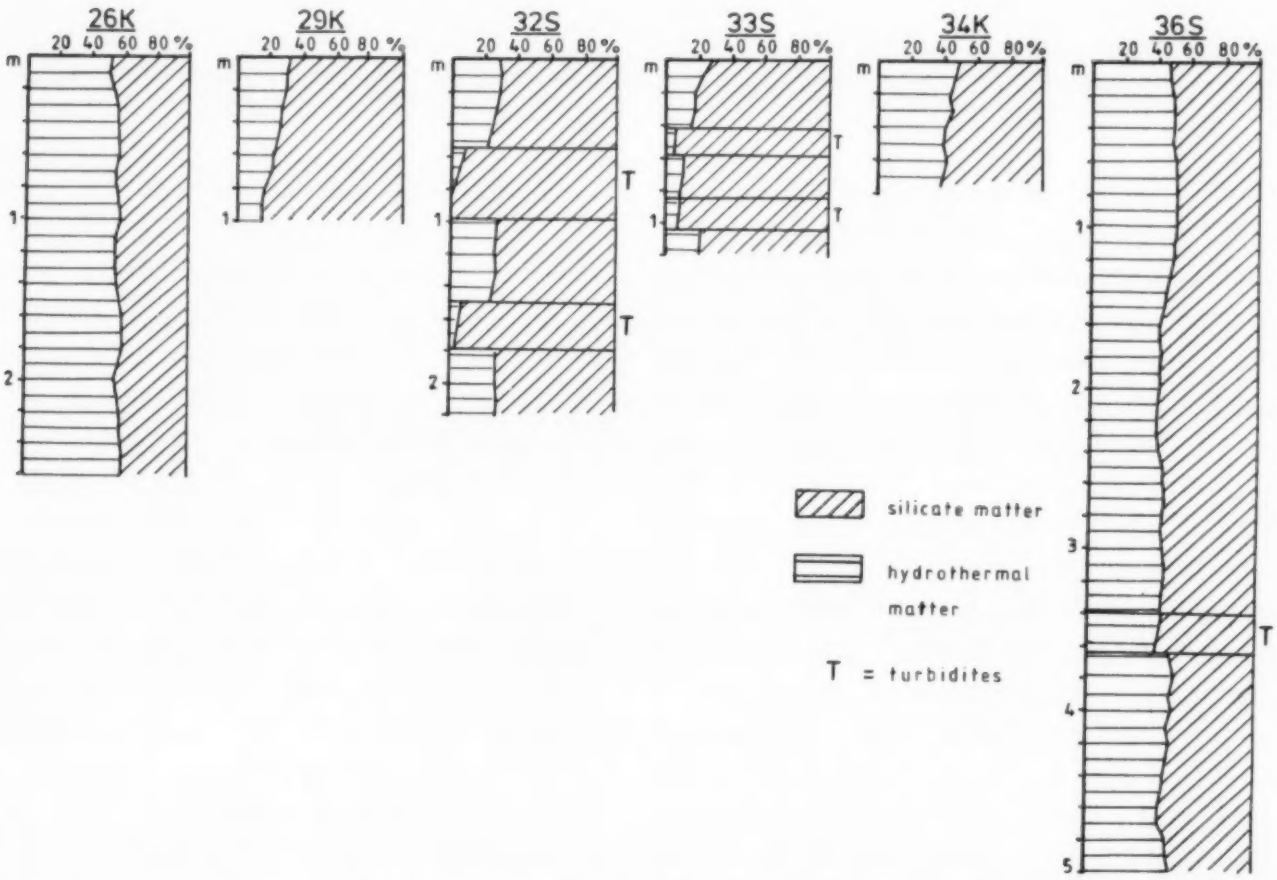

Fig. 6. Changes in the content of silicates and hydrothermal matter of the sediment as a function of depth in core. The data are calculated on carbonate-free basis.

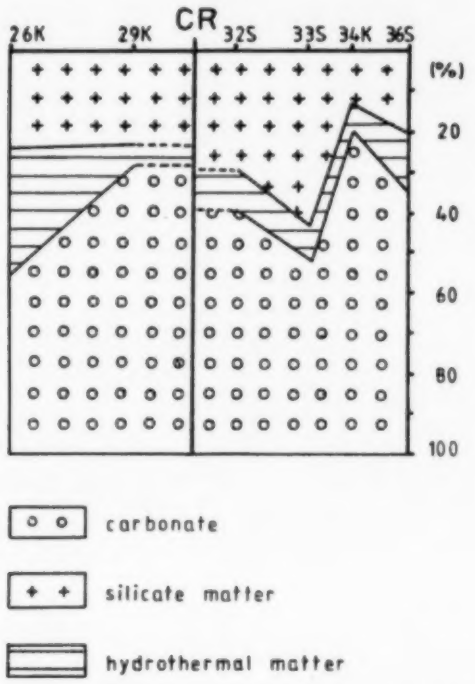

Fig. 7. Changes in the content of carbonate, silicates and hydrothermal matter in the sediment cores relative to distance from the spreading zone. Mean values of the main sediment components have been calculated for the whole cores.

in a way that the elements, which are bound with significant positive correlations to each other, are always gathered into one group. This method of presentation of a correlation matrix results in the formation of three groups of elements. The elements of one group reveal a preponderance of positive correlations between the members of the group. Between the members of different groups there is a preponderance of negative correlations as well as statistically insignificant correlations.

The first group comprises the elements Si, Ti, Al, Mg, Na, K, Cr and Sc (Fig. 8). It is known that Ti and Al cannot be mobilized from silicate rocks during hydrothermal leaching. It can be concluded, therefore, that the group containing Ti and Al is the silicate group; i.e., the elements bound to Ti and Al with positive correlations are, to a large extent, included in the silicate fraction of the sediment.

The second group comprises the elements Fe, Mn, P, As, Ba, Ce, Co, Cu, Mo, Ni, V, Zn and Zr (Fig. 8). The elements Fe and Mn are the main components of the oxide phase, regardless of

	Si	Ti	Al	Mg	Na	K	Cr	Sc	Fe	Mn	P	As	Ba	Ce	Co	Cu	Mo	Ni	V	Zn	Zr	S	Pb	Rb	Th	Y
Si																										
Ti	99																									
Al	90	99																								
Mg	84	80	76																							
Na	32			49																						
K					63																					
Cr	75	70	68	82	45																					
Sc				57			41																			
Fe	68	66	72				33																			
Mn	61	55	59	38	35	32	43		67																	
P	89	87	90	63			58		91	67																
As	74	72	75	48			54		80	65	82															
Ba	89	84	82	86	47		78	33	64	64	84	72														
Ce									72	68	57	59														
Co									55	67				79												
Cu	78	74	76	60	41		57		73	82	83	71	79													
Mo					54	43				60						49										
Ni	60	54	58	32			38		78	93	72	71	63	82	76	78	55									
V	84	81	84	57			55		92	74	94	85	81	65		83		79								
Zn	60	58	63						88	78	78	71	54	68	66	80		84	84							
Zr	70	65	69	46			48		87	81	84	82	77	79	62	78	49	91	89	80						
S	66	63	56	91	51		72	62			43		76			45			34							
Pb								50																		
Rb	32	37		48		45	33	42						37	33							54				
Th	39	38		72	38		52	72					45	42	41							82		67		
Y	85	81	79	89	47		76	52	50	47	77	54	89			74		43	68	43	56	82		42	63	
carb.				48	35			87	43					72	66			49		43	40	60	47	49	80	38
oxide	92	91	94	61			58		90	73	97	83	81	60		83		76	94	81	84	37			72	
silic.	64	64	60	80	47		65	89			42		60			47			76			80	47	49	79	76

Fig. 8. Correlation matrix for 112 sediment samples from all six cores calculated on a carbonate-free basis. The turbidite samples have not been included in the calculation. Only highly significant correlations (>0.32 and <-0.32) are plotted in the martix. The values shown are correlation coefficients multiplied by 100. Negative correlations are underlined. Below the matrix, correlations of carbonate, silicates and hydrothermal matter with the elements on a carbonate-free basis are shown.

whether they are of hydrothermal or hydrogenous origin. Thus, the elements bound to Fe and Mn with positive correlations are also expected to belong to the oxide phase of the sediment.

The third group, comprising the elements S, Pb, Rb, Th and Y (Fig. 8), is indicative of early diagenetic processes in the sediment. The prolonged contact between sediment and near-bottom seawater, which takes place when rates of sedimentation are low, promotes various processes all integrated under the term "early diagenesis". For example, the formation of clay minerals by weathering of basaltic glasses leads to the enrichment of Rb and Th, for these elements are preferentially incorporated in the newly formed clay minerals. Residual enrichment of baryte and apatite by dissolution of carbonate results in the enrichment of S and Y. Pb enrichment is caused by adsorption of Pb in the fine-grained fraction of the sediment which increases in quantity due to the early diagenetic dissolution of coarse carbonate particles.

Hydrogenous oxides are preferentially enriched where sedimentation rates are low and where sediments undergo prolonged contact with seawater. The same conditions favour the diagenetic enrichment of elements. If the oxides of the sediments investigated were of predominantly hydrogenous origin they would have positive correlations with the diagenetic group of elements. This is not the case. A separate group of oxides exists whose members reveal significant positive correlations only with other members within the group. Negative or insignificant correlations to elements of the silicate and diagenetic group exist. Therefore it can be concluded that the bulk of the oxides is not of hydrogenous origin but can be ascribed to hydrothermal processes. This supports the results of our calculations, that even the maximum possible content of hydrogenous oxides in the sediment is too low to explain the measured oxide content.

Core 26 shows the most advanced diagenesis of all the six studied cores: strong dissolution of foraminifera, and formation of philipsite and manganese micronodules. We therefore also calculated a separate correlation matrix for the samples from this core only (Fig. 9). In this correlation matrix a microscopically determined factor for the degree of preservation of the foraminifera has been included in the calculation.

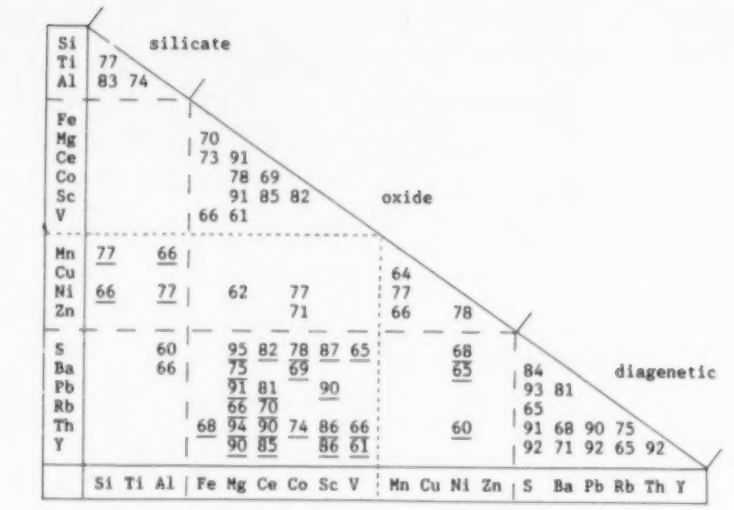

	Si	Ti	Al	Fe	Mg	Ce	Co	Sc	V	Mn	Cu	Ni	Zn	S	Ba	Pb	Rb	Th	Y
carb.				76	91	87	72	90	67					86		83		88	83
silic.				74	90	86		89	61					83		81		86	83
oxide		79		62	75	68	73		77			84	66	78	62			70	63
pres.		62			68									73	69		66	70	68

Fig. 9. Correlation matrix for 27 samples from core 26. Only highly significant correlations (>0.60 and <-0.60) are plotted in the martix. The values shown are correlation coefficients multiplied by 100. Negative correlations are underlined. Correlations of carbonate, silicates hydrothermal matter and a microscopically determined factor for the degree of preservation of the planktonic foraminifera on a carbonate-free basis are shown below the matrix.

The silicate group of elements, as well as the diagenetic group, is present. Only slight variation compared with the previously discussed correlation matrix (Fig. 8) exists, although the difference between the two correlation matrices is striking within the oxide group. In the correlation matrix for core 26 this group is divided in two subgroups (Fig. 9).

We explain this division of the oxide group by diagenetic changes within the oxide component. Due to the decay of organic matter during diagenesis, the Eh dropped to lower values. As a consequence the manganese of the oxide component, but not, at this stage, iron, could be reduced. The reduced soluble manganese was transported by porewater to higher, more oxidized horizons and reprecipitated there in the form of manganese micronodules. The elements Cu, Ni and Zn followed manganese. Mg, Ce, Co, Sc and V remained immobile together with iron.

This explanation confirms our microscopic observation of "bleached" core sections which are depleted in manganese but not in iron, and of the overlying core sections which contain manganese micronodules.

Diagenetic mobilization of manganese has been described for hydrogenous oxides in radiolarian oozes from the central Pacific and has been applied for explanation of the formation of the diagenetic phase of manganese nodules (Marchig and Gundlach, 1981). The same explanation can be applied for the formation of manganese micronodules from hydrothermal oxides in the sediments investigated here. The process does not apply to hydrothermal oxide precipitates elsewhere. At the East Pacific Rise, for example, sedimentation rates are very high and time of contact between sediment and seawater is relatively short, so that diagenetic changes in the sediment are insignificantly low (Lyle, 1986). At the Chile Ridge spreading centre, where sedimentation rates of hydrothermal precipitates are low, diagenetic changes in the hydrothermal oxide component can be observed.

Conclusions

This preliminary investigation of a segment of the Chile Ridge was performed because of the strong interest of Chilean marine geologists in the spreading zone of the Chile Ridge which partly reaches into their territorial waters. It was planned as a first test for the presence of hydrothermal activity on a spreading zone, for which until now only tectonic activity had been known. For this reason, special attention was given to the sediments, which store the history of hydrothermal discharge over a long period of time.

The sediments were shown to be strongly diagenetically changed by dissolution of carbonate and formation of new minerals. Furthermore, it could be demonstrated that a large part of the manganese is of hydrothermal origin, i.e., that hydrothermal input in the sediment is taking place.

As a byproduct of the investigation into this hydrothermally contaminated sediment, diagenetic aging of hydrothermal matter could be observed for the first time. Aging could be microscopically observed as bleached sequences overlain by sequences rich in manganese micronodules. Chemically, aging is indicated by division of elements in two groups. Cu, Ni and Zn follow manganese by diagenetic remobilization and formation of manganese micronodules. Mg, Ce, Co, Sc and V stay together with the diagenetically less mobile iron in the primary position in the bleached-sediment core sections.

The five basalts investigated are of the MORB type, showing that this segment of the Chile Ridge is a real oceanic spreading zone with no continental influence.

The leached basalts that were dredged have shown lenticular sulphide impregnations. A high galena content does not indicate that the hydrothermal activity is atypical at this spreading zone. Enrichment of galena is typical of active ocean ridge metallogenesis in trap structures, i.e., in sediment-covered ridges or impregnations in rocks. Galena is the most mobile of the typical hydrothermal sulphide minerals. It can be found only in positions where the discharge does not directly enter seawater, so that sequential deposition of the various minerals of the paragenesis can develop in the sediments. By quick discharge in form of the "black smoker" type it disappears with the black smoke and can be found only in traces in the sulphides of the top of the chimney.

The total output of hydrothermal products deposited around spreading zones depends on the spreading rate. High spreading rates cause strong hydrothermal circulation in the oceanic crust. The accumulation of metal sulphides in the spreading zone does not appear to be dependent on the spreading rate, however, as rich occurrences have been found at the slowly spreading Juan da Fuca Ridge, as well as at the Mid-Atlantic Ridge.

Our investigations of the spreading zone of the Chile Ridge have not been sufficiently exhaustive to find occurrences of massive sulphides, although one accidentally placed dredge has recovered hydrothermally altered material as well as metal sulphide impregnations in rock samples.

We propose more intensive investigation into the spreading zone of the Chile Ridge in order to evaluate the metal sulphide potential of this spreading zone.

Acknowledgements

We would like to thank the German Ministry of Research and Technology for the financial support which made the scientific cruise possible. Admiral Carlos Quinones is acknowledged for his active interest in the Chile Ridge investigations and many useful discussions during the cruise.

References

Berger, W.H., 1970. Planktonic foraminifera: selective solution and the lysocline. Mar. Geol., 8: 111–138.

Elderfield, H., 1977. The form of manganese and iron in marine sediments. In: G.P. Glasby (Editor), Marine Manganese Deposits. (Elsevier Oceanography Series, 15.) Elsevier, Amsterdam, pp. 269–289.

Forsyth, F.W., 1972. Mechanisms of earthquakes and plate motions in the East Pacific. Earth Planet. Sci. Lett., 17: 189–193.

Haq, B.U., 1984. Jurassic to Recent nannofossil biochronology: an update. In: B.U. Haq (Editor), Nannofossil Biostratigraphy. (Benchmark Papers in Geology, 78.) Hutchinson Ross.

Heinze, P.M., 1985. Vergleich zweier quartärzeitlicher Kastenlotkerne aus dem Pazifik in Bezug auf ihre geochemische und mineralogische Zusammensetzung und Bestimmung der jeweiligen Sedimentationsrate mittels biostratigraphischer Bearbeitung der planktonischen Foraminiferen (westlich des EPR bei 17°S/113°W und 13°N/104°W). Diplomarbeit Univ. Hannover.

Heinze, P.M. and Knüttel, S., 1986. Cruise report GEOMETEP 4. Bundesanst. Geowiss. Rohstoffe, Hannover.

Herron, E.M., 1972. Sea-floor spreading in the Cenozoic history of the East-Central Pacific. Geol. Soc. Am. Bull., 83(6): 1671–1692.

Herron, E.M., Cande, S.C. and Hall, B.R., 1981. An Active Spreading Center Collides with a Subduction Zone: A Geophysical Survey of the Chile Margin Triple Junction. Geol. Soc. Am. Mem., 154: 683 pp.

Holler, G., 1987. Scientific cruise report GEOMETEP 4. Bundesanst. Geowiss. Rohstoffe, Hannover, 44–178.

Klitgord, K.D., Mudie, J.D., Larson, P.A. and Grow, J.A., 1973. Fast sea-floor spreading on the Chile Ridge. Earth Planet. Sci. Lett., 20: 93–99.

Lonsdale, P., 1976. Abyssal circulation of the south-eastern Pacific and some geological implications. J. Geophys. Res., 81(6): 1163–1176.

Lyle, M.W., 1986. Major element composition of Leg 92 sediments. Init. Rep. DSDP, 92: 355–370.

Marchig, V., 1978. Brown clays from the Central Pacific—Metalliferous sediments or not? Geol. Jahrb. Reihe D, 30: 3–25.

Marchig, V. and Erzinger, J., 1986. Chemical composition of Pacific sediments near 20°S, changes with increasing distance from the East Pacific Rise. Init. Rep. DSDP, 92: 371–381.

Marchig, V. and Gundlach, H., 1981. Separation of iron from manganese and growth of manganese nodules as a consequence of diagenetic aging of radiolarians. Mar. Geol., 40: M35–M43.

Mühe, R., 1987. Scientific cruise report GEOMETEP 4. Bundesanst. Geowiss. Rohstoffe, Hannover.

Wilke, M., 1986. Cruise report GEOMETEP 4. Bundesanst. Geowiss. Rohstoffe, Hannover.

Marine Geology, 105 (1992) 253–273
Elsevier Science Publishers B.V., Amsterdam

Late Tertiary seismic facies and structures of the Levant passive margin off central Israel, eastern Mediterranean

Gideon Tibor and Zvi Ben-Avraham
Department of Geophysics and Planetary Sciences, Tel Aviv University, Tel Aviv, 69978, Israel

(Received January 21, 1991; revision accepted September 9, 1991)

ABSTRACT

Tibor, G. and Ben-Avraham, Z., 1992. Late Tertiary seismic facies and structures of the Levant passive margin off central Israel, eastern Mediterranean. Mar. Geol., 105: 253–273.

The Late Tertiary seismic facies and structures of the Levant passive margin off central Israel in the eastern Mediterranean Sea were studied by the interpretation of more than 3000 km of seismic reflection profiles, most of them previously unpublished single-channel profiles. The Neogene growth and evolution of this margin was influenced by the interaction of three main processes: (1) the outbuilding and loading of the margin by the Nile sediments since the Pliocene, (2) uplift and tectonic subsidence related to the tectonic activity along the Dead Sea Transform, and (3) the effect of the above processes on the thick Messinian evaporites which caused many salt-tectonic features including flowage, piercement diapirs, slumps, and en-echelon listric normal faults in the supra-salt sediments. We suggest that the study area may be divided into two segments, north and south of Caesarea. These segments vary in their depositional environment, the amount of sediment supply and load, salt-related features and tectonic activity. We propose that the northern segment is affected by low sediment supply and by the continued uplift of the Carmel structure, and that this segment may even be a part of this structure. The southern segment has been affected by the deposition and loading of the Nile-derived sediments since the Pliocene. Three main depositional sequences were observed in the southern segment: (1) sequence I (Early Pliocene) onlaps the top of the Messinian evaporites representing a rise of sea-level and renewed subsidence, (2) sequence II (Early Pleistocene) is lens-shaped, thinning to the north, west and east and was derived during a relatively short time interval from the Pre-Nile, and (3) sequence III (since the Pleistocene) represents a major episode of continental shelf construction.

Introduction

The Levant continental margin is a mature passive margin situated in the eastern Mediterranean off Israel, Lebanon and Syria (Fig. 1). This margin was formed by rifting during the Late Triassic to Early Jurassic (Garfunkel and Derin, 1984). The close proximity and the variety of plate boundaries, the Dead Sea Transform in the east, the Cyprian Arc in the northwest and the collision with the Taurus mountains in the north, contributed to its complicated evolution. Further complications arise from the thick sedimentary cover (about 12–15 km). In the Late Cretaceous a change in the relative motion of Africa with respect to Eurasia led to a change into a compressive regime and to the formation of the Syrian Arc fold structures. These are a series of NE–SW trending anticlines and synclines on the Levant margin and on the adjacent land (Ginzburg et al., 1975). Since the beginning of the Tertiary, active subduction and collision activity has been occurring to the north, leading to the formation of the Zagros and Taurus mountain chains. Rifting and opening of the Red Sea, together with the initiation of the Dead Sea Transform, began in the Miocene. At the end of Miocene, the evolution of the Levant margin was greatly influenced by the Messinian desiccation of the Mediterranean Sea. Although this event lasted less than one million years, it led to a major erosional phase and deposition of thick layers of salt and evaporites (Hsu et al., 1977). Subsidence along the margin increased in the Pliocene as a result of the large volumes of clay and

0025-3227/92/$05.00 © 1992 — Elsevier Science Publishers B.V. All rights reserved

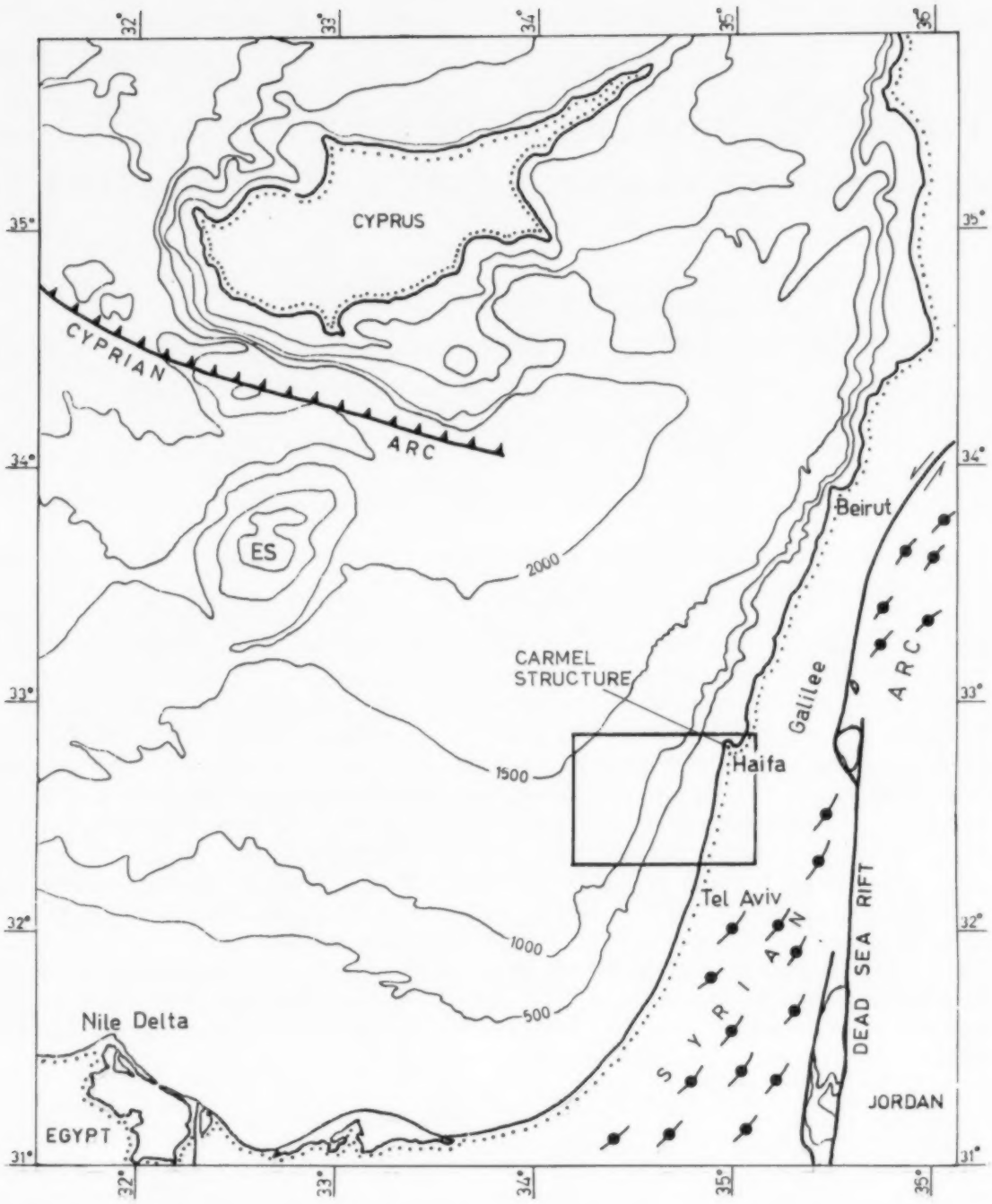

Fig. 1. Bathymetry of the eastern Mediterranean (revised from Hall, 1980). The box outlines the study area. *ES* = Eratosthenes.

silt that were transported from the Nile delta and deposited on the continental margin.

The Levant continental margin off Israel and Lebanon can be divided into two distinct provinces south and north of the Carmel structure, a NW-trending feature extending from land to the edge of the continental shelf (Fig. 1). The southern province (south of 32°40') is characterized by a relatively smooth bathymetry, with a slope that becomes steeper from south to north. The northern province (north of 32°40') is characterized by rugged bathymetric relief. The continental shelf is much narrower than in the southern province and the continental slope is cut by numerous submarine canyons (Fig. 1). Ben-Avraham and Ginzburg (1986, 1990) and Ginzburg and Ben-Avraham (1987) have suggested that marked differences in the deep crustal structure of the Levant continental margin exist between the provinces north and south of the Carmel structure.

The present study describes the late Tertiary seismic facies and structures of the northern portion in the southern province of the Levant margin. The study was based on the interpretation of single-channel seismic reflection profiles and some multichannel reflection profiles. This particular

area was picked for study because it shows the transition of shelf progradation, seismic facies and structures between the southern and northern provinces of the Levant continental margin.

Data base

More than 3000 km of seismic reflection profiles were interpreted for this study (Fig. 2). Contour and isopach maps were made for the top and base Messinian evaporites. The seismic profiles were collected during five single-channel reflection surveys conducted by Ben-Avraham in 1975, 1976, 1978 and 1979 and by Mart in 1978. Some of these profiles were published by Ben-Avraham (1978) and Mart and Eisin (1982). Four multichannel reflection profiles from a survey conducted by Seismic Geocode Ltd. in 1983 were also interpreted. The technical parameters of these surveys are summarized in Table 1.

Morphology

The bathymetry of the study area is shown in Fig. 3. The continental shelf narrows from 14 km off Netanya to 10 km off Haifa and the depth to the shelf break is about 150 m. The shelf edge is relatively abrupt in the north (Fig. 4, profiles 1–5),

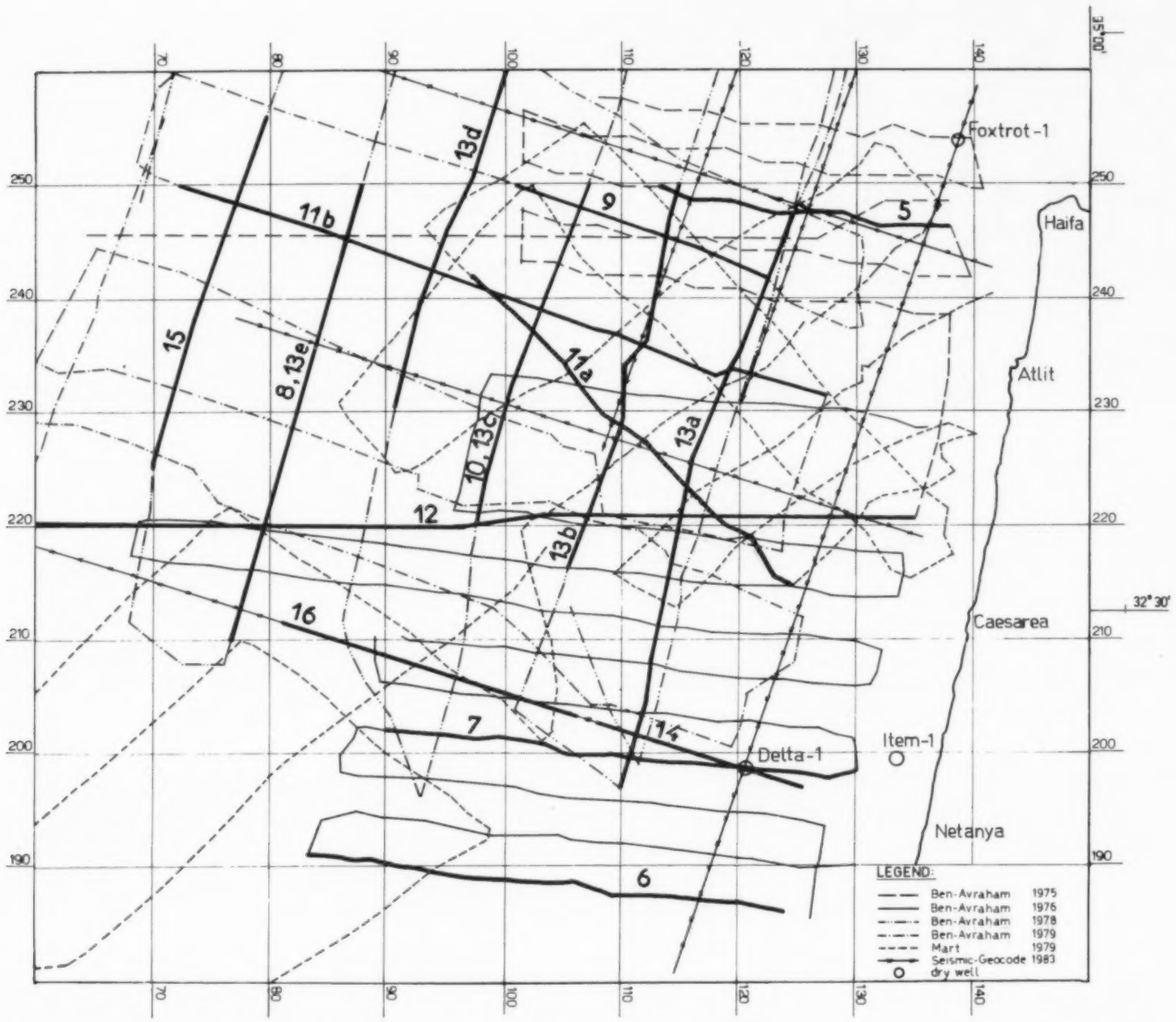

Fig. 2. Location of seismic lines used in this study. All of the lines, except for the Seismic Geocode line, are single-channel. Heavy lines indicate sections of profiles shown in the figures and are identified by figure numbers.

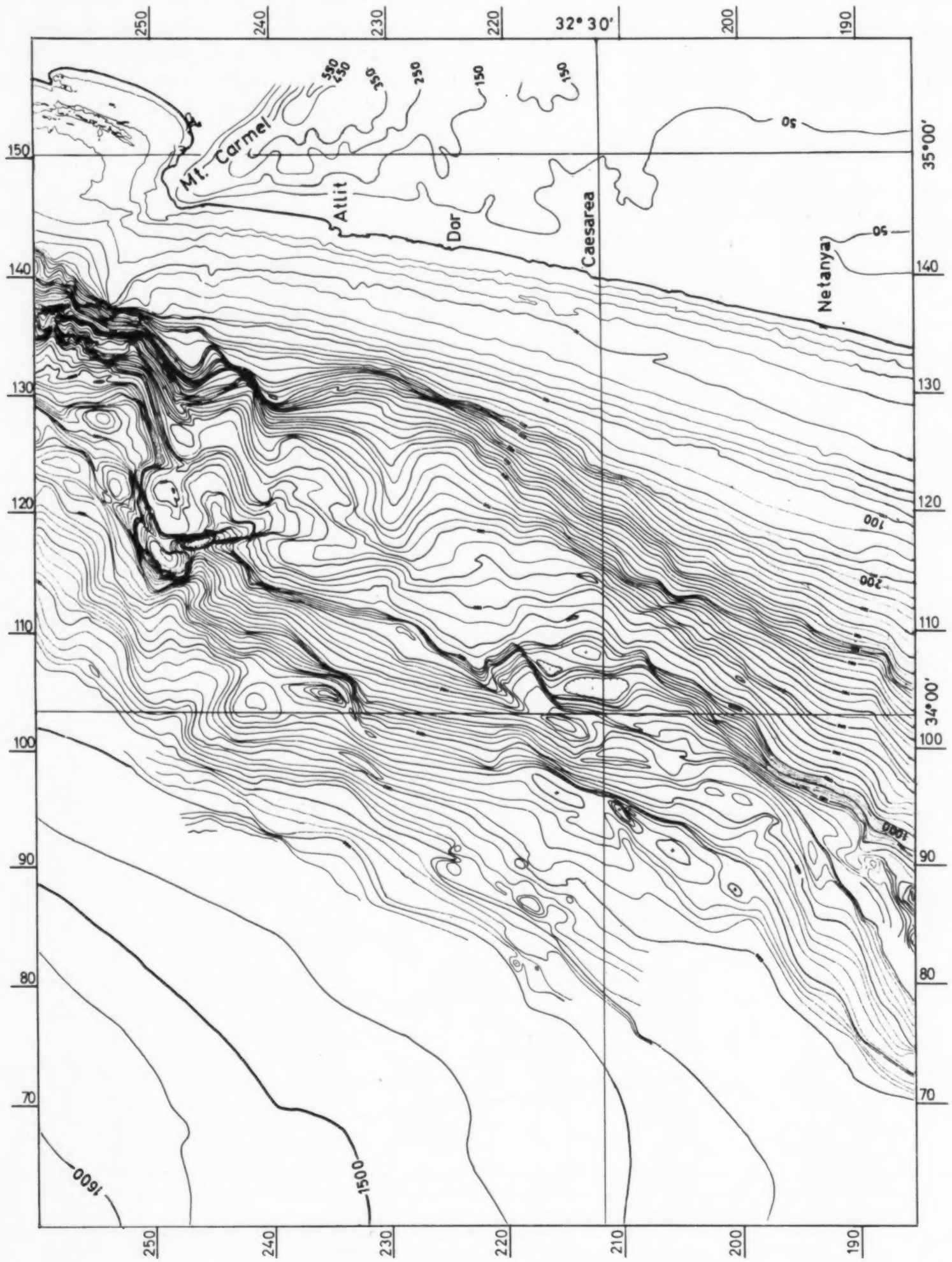

Fig. 3. Bathymetry of the study area (from Almagor and Hall, 1984). Contour interval is 10 m down to 100 m, and 25 m at depths greater than 100 m. Cassini (Israel grid) and geographic coordinates are shown.

TABLE 1

Parameters of seismic data

Survey		Source and receiver	Filter
Name	Type		
Ben-Avraham (1975)	single-channel reflection	300 in^2 airgun, 8 s inter; two 300 in^3 airgun 12–16 s inter; 4 s sweep; 48 geophones	10–200 Hz
Ben-Avraham (1976)	single-channel reflection	300 in^3 airgun, 12 s inter; 4 s sweep; 48 geophones	10–200 Hz
Ben-Avraham (1978)	single-channel reflection	600 in^3 airgun, 12 s inter; 4 s sweep; 48 geophones	20–200 Hz
Ben-Avraham (1979)	single-channel reflection	600 in^3 airgun, 12 s inter; 4 s sweep; 48 geophones	10–150 Hz
Mart and Eisin (1979)	single-channel reflection	two 300 in^3 airgun; 12 s inter; 4 s sweep; 48 geophones	15–100 Hz
Seismic Geocode (1983)	multi-channel reflection	2180 in^3 airgun; shot inter. 25 m; 120 geophones	low cut 5.3 Hz high cut 90 Hz

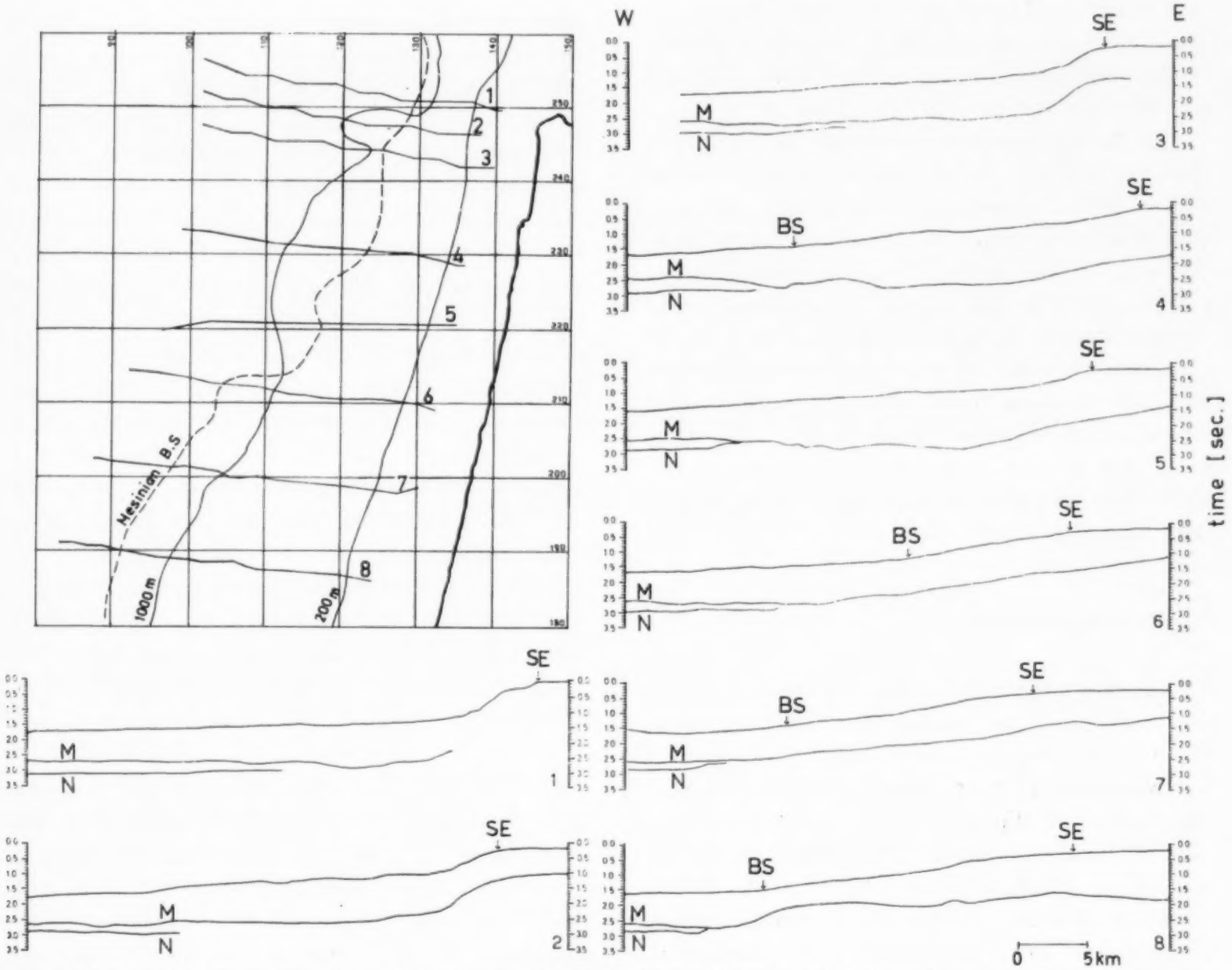

Fig. 4. Line drawings from single-channel reflection profiles across the continental margin. Shown in each profile are: the present seafloor, top of the Messinian evaporites (reflector *M*), the base of these evaporites (reflector *N*), present shelf edge (*SE*), and the base of the present-day continental slope (*BS*). The regional location of the Messinian base of slope is shown in the location map. Actual seismic profiles along several of these line drawings are shown in other figures: Part of profile 2 is shown in Fig. 5, profile 5 is shown in Fig. 12, part of profile 7 is shown in Fig. 7 and part of profile 8 is shown in Fig. 6.

but is more gradual in the south (Fig. 4, profiles 6–8). The continental slope is 18 km wide and extends from water depths of 150 m to 1000 m. In the south the slope is generally smooth, whereas to the north it becomes steep, irregular and progressively narrows. The slope in the northern area is broken by three terraces or plateaus off Dor, Atlit and Haifa (Fig. 3). The rough bathymetry off Dor was described in previous studies (e.g. Garfunkel et al., 1979; Mart and Eisin, 1982; Almagor, 1984). Garfunkel et al. (1979) named this feature the Dor disturbance and interpreted it as a complex slump feature downslope from the Caesarea drainage system. In contrast, Mart and Eisin (1982) interpreted the Dor terrace as a tectonic feature. The continental rise extends between 1000 m and 1400 m and generally merges smoothly with the abyssal plain at depths of 1100–1400 m.

The configuration and location of the Messinian erosional surfaces and the top of the evaporites as imaged on the seismic reflection profiles can provide an approximation of the Messinian paleobathymetry. In the north, the configuration of the pre-Messinian margin generally resembles that of the present-day margin (Fig. 4, profiles 1–3). In the south, from Netanya to Caesarea, the Messinian base of slope and shelf edge were located seaward of their present locations (Fig. 4, profiles 6–8). The slope was narrow and steep and the shelf extended about 10 km seaward of the present shelf edge (Fig. 6).

Sequence stratigraphy

Seismic sequence and facies analyses were conducted primarily using the single-channel reflection profiles. Acoustic penetration reaches the base of the Messinian (Upper Miocene) evaporites. The late Tertiary stratigraphy of the study area can be identified and correlated to the deep wells on the continental shelf (Fig. 2), Delta-1 and Item-1 (Derin and Reiss, 1971). In a typical profile (Fig. 5), from the northern part of the study area, the Messinian evaporitic sequence is defined by two reflectors, labelled *M* and *N*, that represent the top and the base of the sequence respectively. This evaporitic sequence thickens to the northwest into the Mediterranean basin but pinches out landward beneath the base of the continental slope, where reflector *M* is faulted. Landward of this area, reflector *M* represents an erosional surface. The relatively acoustically transparent zone above *M* is the lower Yafo formation (Pliocene), which is composed of clayey marls (Derin and Reiss, 1973). The upper Yafo formation (Late Pliocene–Early Pleistocene) is well layered and is composed of thin shale beds and sandstone layers (Derin and Reiss, 1973). The Pleistocene sediments on top of the Yafo formation are mostly unconsolidated sandstones that are well layered and downlap onto the Yafo at the base of the slope (Fig. 5). The seafloor of the continental slope in the northern part of the study area is cut by listric normal faults and by several slump scars (Fig. 5).

Two shelf depositional environments are observed above the Messinian evaporites. These environments are controlled by the amount of the Nile-derived sediments that reached them and by the rate of tectonic subsidence. In the north, the sediments show obliquely prograding clinoforms that may indicate a high-energy environment of deposition with depositional dips up to 10°, low tilt rates and low sediment supply. In contrast, in the south, a low-energy depositional environment is indicated by sigmoid prograding clinoforms (Fig. 6). This facies implies a low depositional dip of $<1°$, a relatively high tilt rate and a large sediment supply (Mitchum et al., 1977a,b).

In the southern part of the study area, which is less tectonically disturbed, three main depositional sequences can be observed in the seismic profiles (Fig. 7). Sequence I (equivalent in part to the Yafo formation) onlaps the top of the Messinian evaporites and was deposited from Late Miocene to Early Pliocene. This well-stratified sequence shows coastal onlap termination, which represents a rise in sea level and renewed subsidence. Sequence II (equivalent to the Yafo formation) is lens shaped and thins to the north, west and east (Fig. 8). This sequence has an irregular subparallel reflection configuration. The source of this sequence appears to be from the south and may represent a large supply of mainly lithified sands derived during a relatively short time interval from the Pre-Nile in

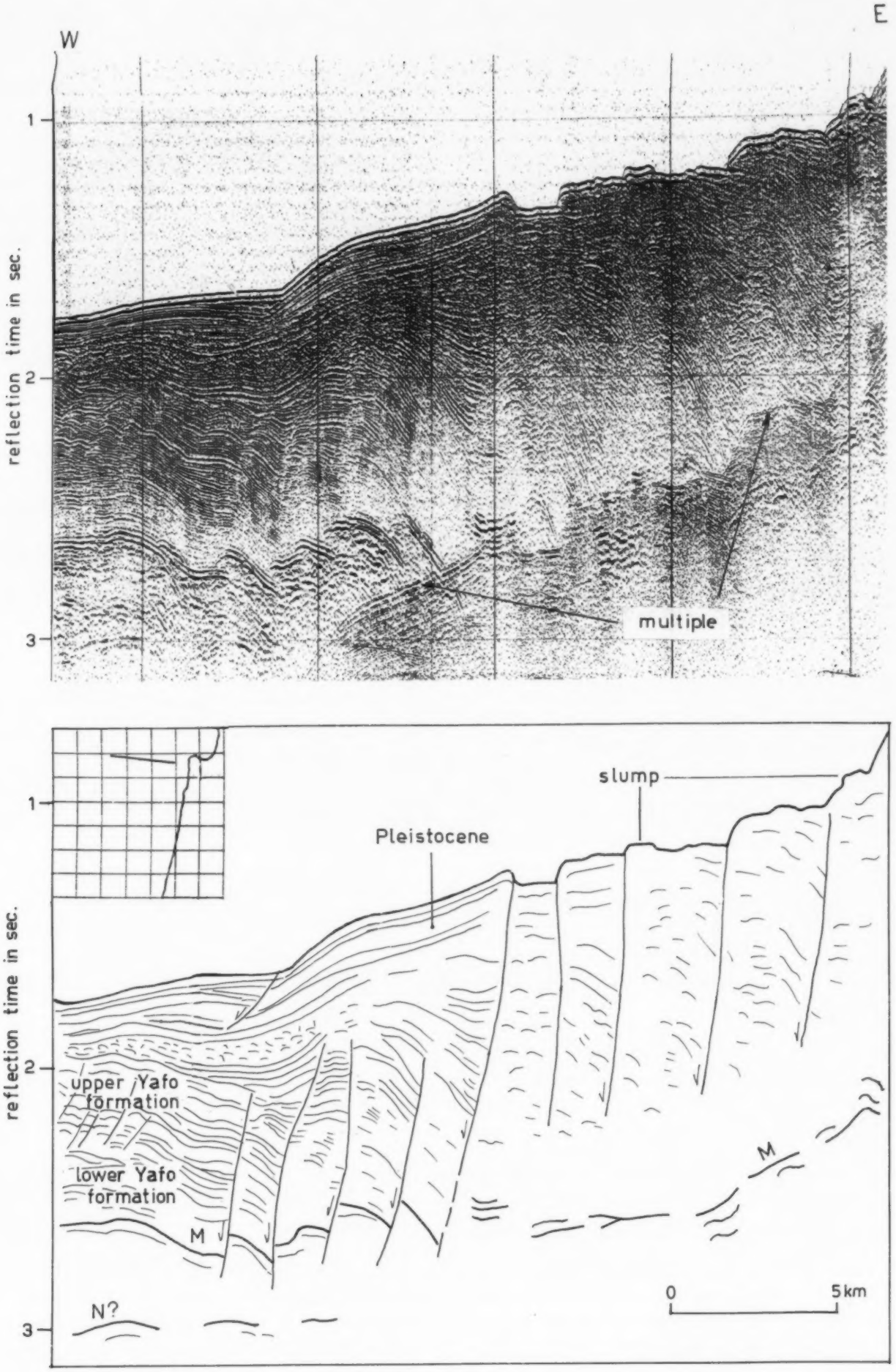

Fig. 5. Single-channel reflection profile from the northern part of the study area, off Haifa, showing the general stratigraphy in this area (location in Fig. 2). *M* = top Messinian evaporites; *N* = base Messinian evaporites (profile from Ben-Avraham 1975 survey).

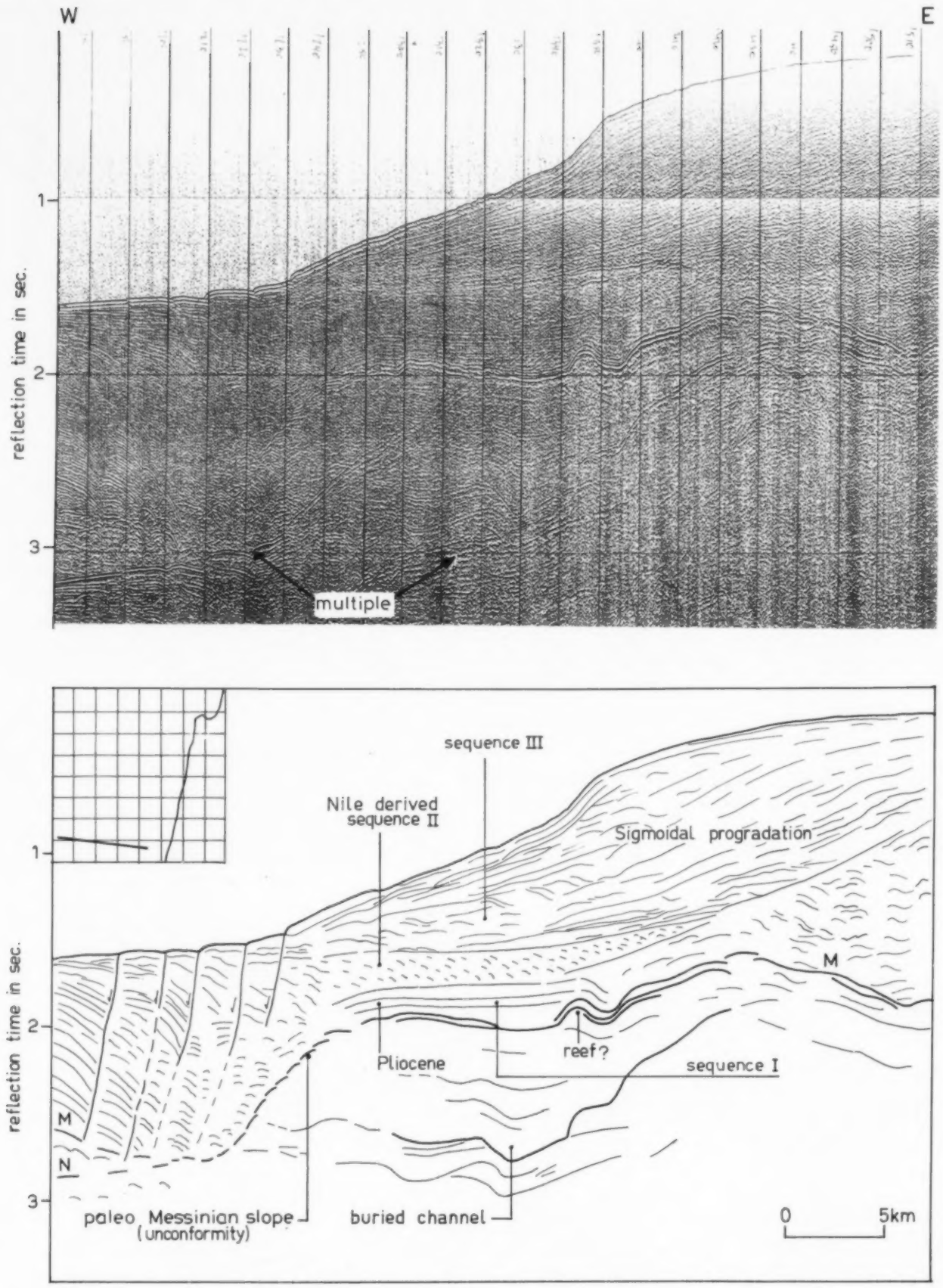

Fig. 6. Single-channel reflection profile across the southern part of the study area (location in Fig. 2). The sequence with the sigmoid progradation facies is of Pleistocene age and shows different lap-out relationships, including onlap, offlap, toplap and downlap. Note the well-stratified Pliocene sequence beneath the slope and the steep paleo-Messinian slope (*M*). A possible reef structure is observed above a tilted buried channel (profile from Ben-Avraham 1976 survey).

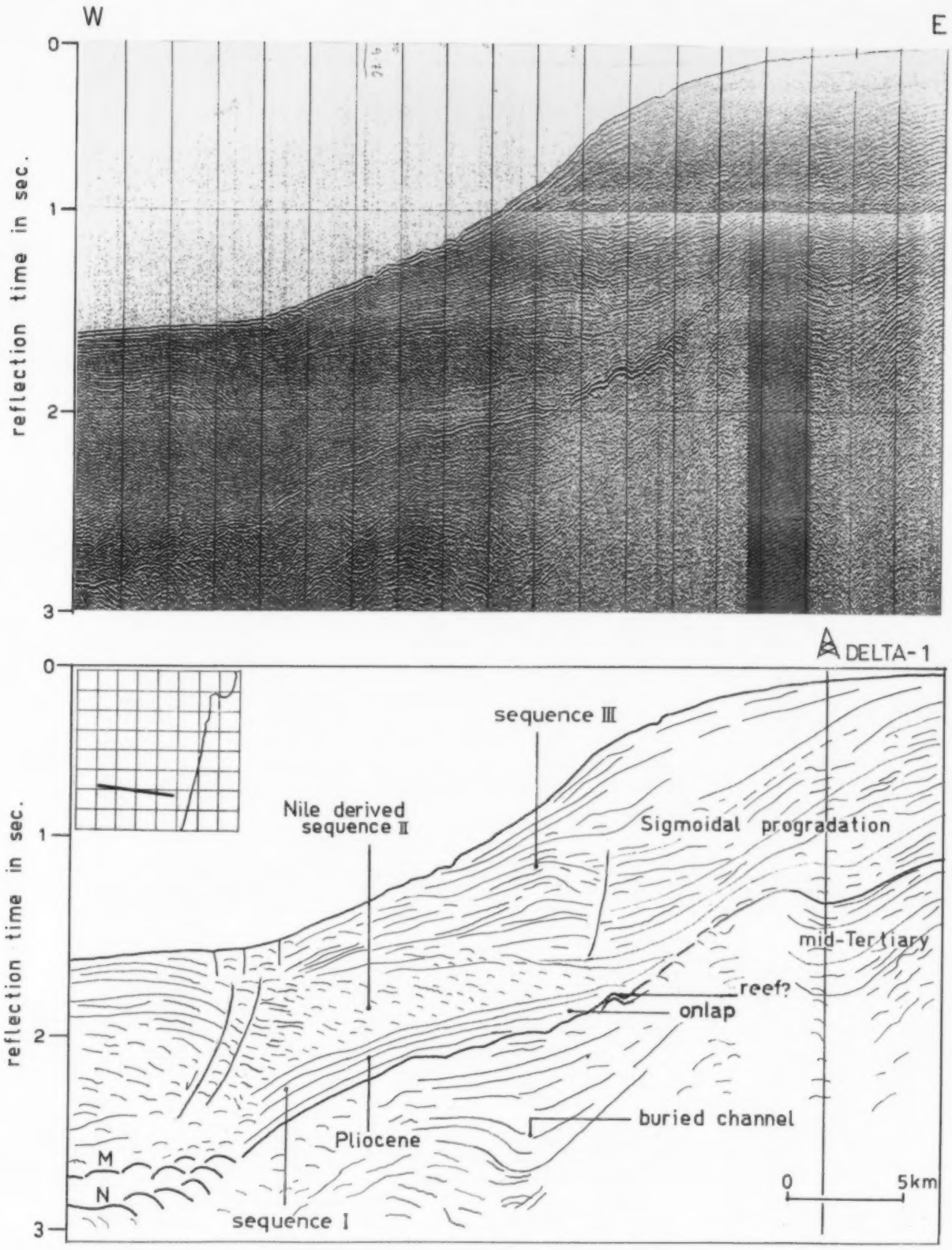

Fig. 7. Single-channel reflection profiles across the southern part of the study area (location in Fig. 2) showing the three main sedimentary sequences discussed in the text. Note the thinning of sequence II to the east (profile from Ben-Avraham 1976 survey).

Early Pleistocene (Said, 1981). Sequence III consists mainly of unconsolidated sandstones and represents a major episode of continental shelf construction during the Pleistocene. In the south this sequence has a sigmoidal progradational configuration with onlap, toplap and downlap reflection terminations. The maximum thickness of this sequence is over the outer shelf and continental slope, suggesting seaward progradation of the shelf.

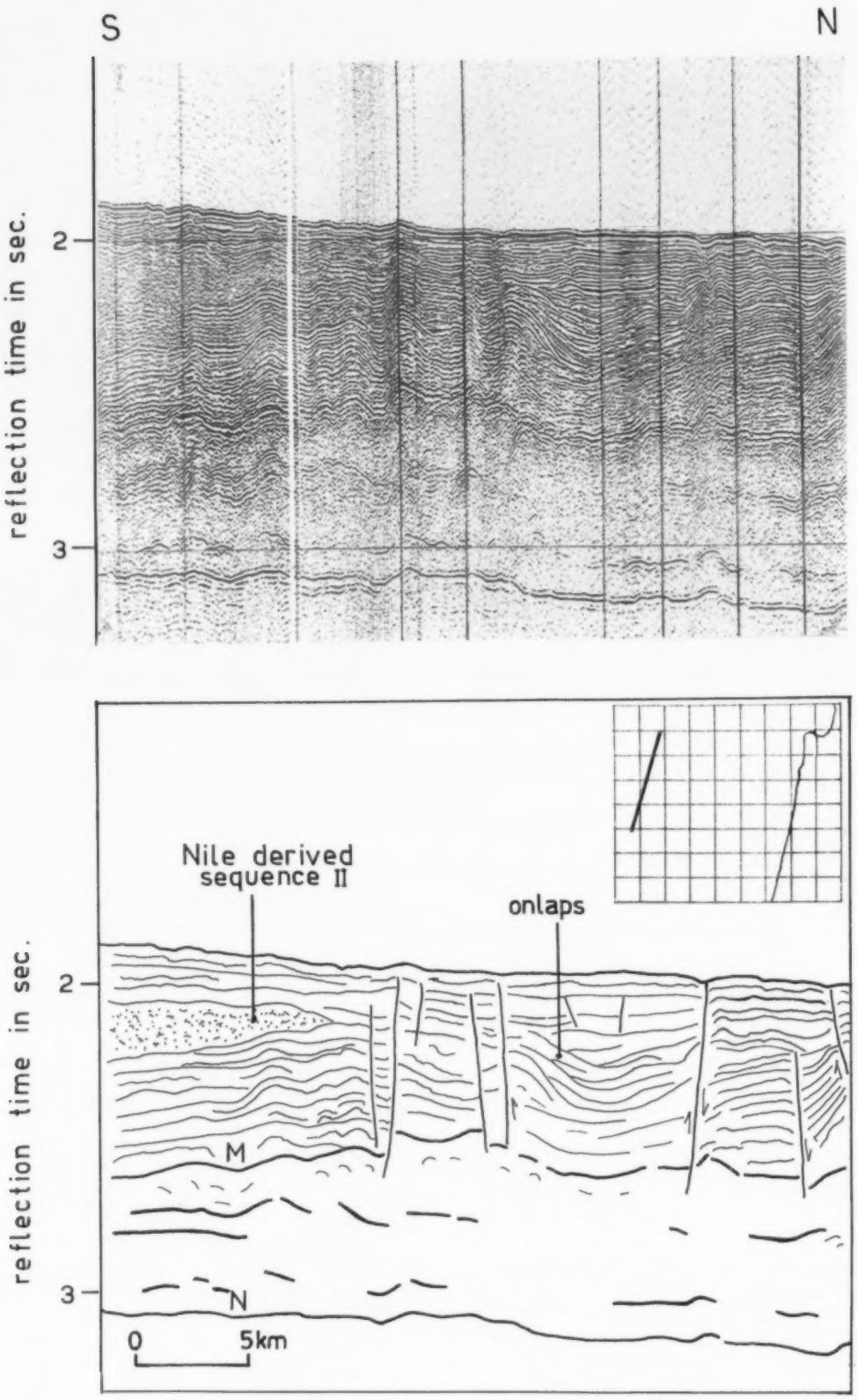

Fig. 8. Single-channel reflection profile along the western part of the study area (location in Fig. 2) showing the thinning of sequence II to the north. Note the internal reflectors within the evaporitic sequence (profile from Ben-Avraham 1978 survey).

Salt structures

The desiccation of the Mediterranean Sea during the Messinian led to the deposition of thick layers of evaporites (Hsu et al., 1977). This was accompanied by an intense erosional phase and isostatic uplift of the margin. The thick evaporitic layers served as a detachment surface and a later deformation led to the formation of listric faults, collapse features and salt structures that are all generally observed in clastic facies overlying the evaporites. In the study area, the thickness of these

evaporites, estimated from seismic reflection profiles and well data, vary from several meters on the continental shelf and slope to more then 1000 m farther to the west. The maximum thickness occurs closer to the shore in the north (1000 m thick about 40 km off Haifa) than in the south (1000 m thick about 75 km off Dor).

In general the Early Pliocene sediments are parallel to the undulation of reflector *M*, whereas the Late Pliocene sediments vary in thickness and show onlap terminations, thus indicating that the flow and migration of the Messinian evaporites probably began in the Late Pliocene (Garfunkel and Almagor, 1985). The lateral flow of these evaporites led to the collapse of the overlying section, the majority of which occurs at the base of the continental slope (Fig. 9). Salt structures and salt-related structures are observed beneath the continental rise in the central and northern parts of the study area. One of these is a salt diapir located on the northern edge of an uplifted area about 35 km off Atlit. This diapir is about 3 km wide and deforms the surrounding sediments of the Yafo Formation (Fig. 10).

Slump features

The continental margin in the central and northern parts of the study area is severely affected by mass wasting. Slump structures were formed in post-Messinian time, and continue to form today (Figs. 5, 11 and 12). A unique, elongate (17 km long × 5 km wide × 400 m thick) NW-trending "fossil" (Early Pleistocene) slump feature has been found 30 km off Atlit (Fig. 11). The internal reflection characteristics of this slump show undulations caused by en-echelon normal listric faults. The cause of this slump is unknown, but it may be related to mass failure initiated by earthquake activity along the WNW–ESE Dor fault that borders the slump on its northern side (Fig. 13c).

Faults and folds

The main faulting trend in the southern province of the Levant margin is NE–SW, parallel to the shore. Shallow normal (gravity) faults occur on the continental slope as a result of salt outflow and shelf loading. These faults cause a landward tilt of the sediments above the Messinian (Fig. 12). The limited penetration of the single-channel seismic reflection profiles makes it impossible to determine whether any of these faults continue below the Messinian sequence. A fault zone with another trend, WNW–ESE, was observed off Atlit along a length of more than 40 km (Fig. 13). This fault zone is probably post-Pliocene in age, but since its last movement it has been covered by 200 ms of sediment. The faults within this zone define a graben-like feature. The origin of this fault zone is not known, but its trend is quite common in the Galilee area, north of the Carmel structure.

The buildup of the continental shelf in the southern segment off Netanya might be influenced by an older anticlinal structure (Fig. 14). This anticline is part of the shore-parallel Syrian Arc folds that were active from Late Cretaceous time (Braun et al., 1987) to Neogene times (Eyal and Reches, 1983). On the seaward side of this anticline we observed a buried early Tertiary channel (Figs. 6, 7 and 14). The westward tilt of this channel and the erosional unconformity of the Early Pliocene sediments above the anticline may indicate its continued uplift during that period.

On the continental rise in the northern part of the study area, a folded zone with a relief of about 70 m on the seafloor was observed (Fig. 15). These structures appear in the reflection profiles as uniform folds down to the Messinian evaporites. Similar features were observed on the northern part of the Levant continental margin by Ben-Avraham (1978) and by Garfunkel and Almagor (1985). The cause and location of this zone is unknown. It may have been formed by regional compression in a manner similar to the Mexican Ridges in the Gulf of Mexico (Buffler et al., 1978), where the underlying Messinian evaporites served as a basal detachment surface during folding (Garfunkel and Almagor, 1985); salt-driven features (diapirs) may also have played a role in forming the folded zone.

Disturbed zone

A disturbed zone was observed near the base of the continental slope throughout the study area.

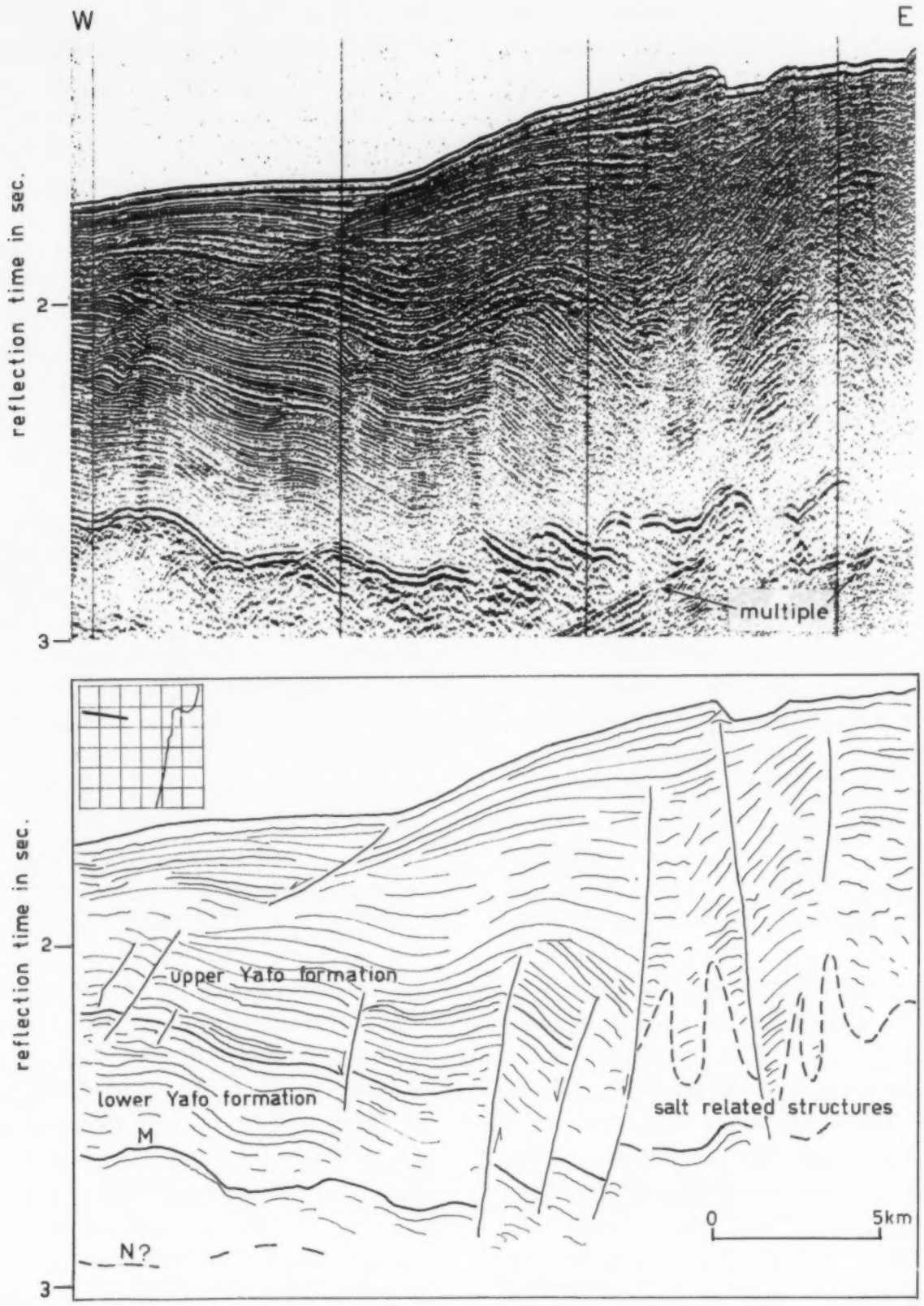

Fig. 9. Single-channel reflection profile across the northern part of the study area (location in Fig. 2) showing salt-related structures at the base of the continental slope. Note the well-stratified sediments of the upper Yafo Formation (profile from Ben-Avraham 1975 survey).

In this zone, reflector *M* is faulted, and the post-Messinian sediments are tilted to the east (Fig. 16). We defined this zone in the west on the basis of the pinch-out of the Messinian evaporites (reflectors *N* and *M* merge), and to the east by means of the changes in dip and reflection characteristics of reflector *M*, where the reflector represents an erosional surface (Figs. 6 and 7). Previous studies

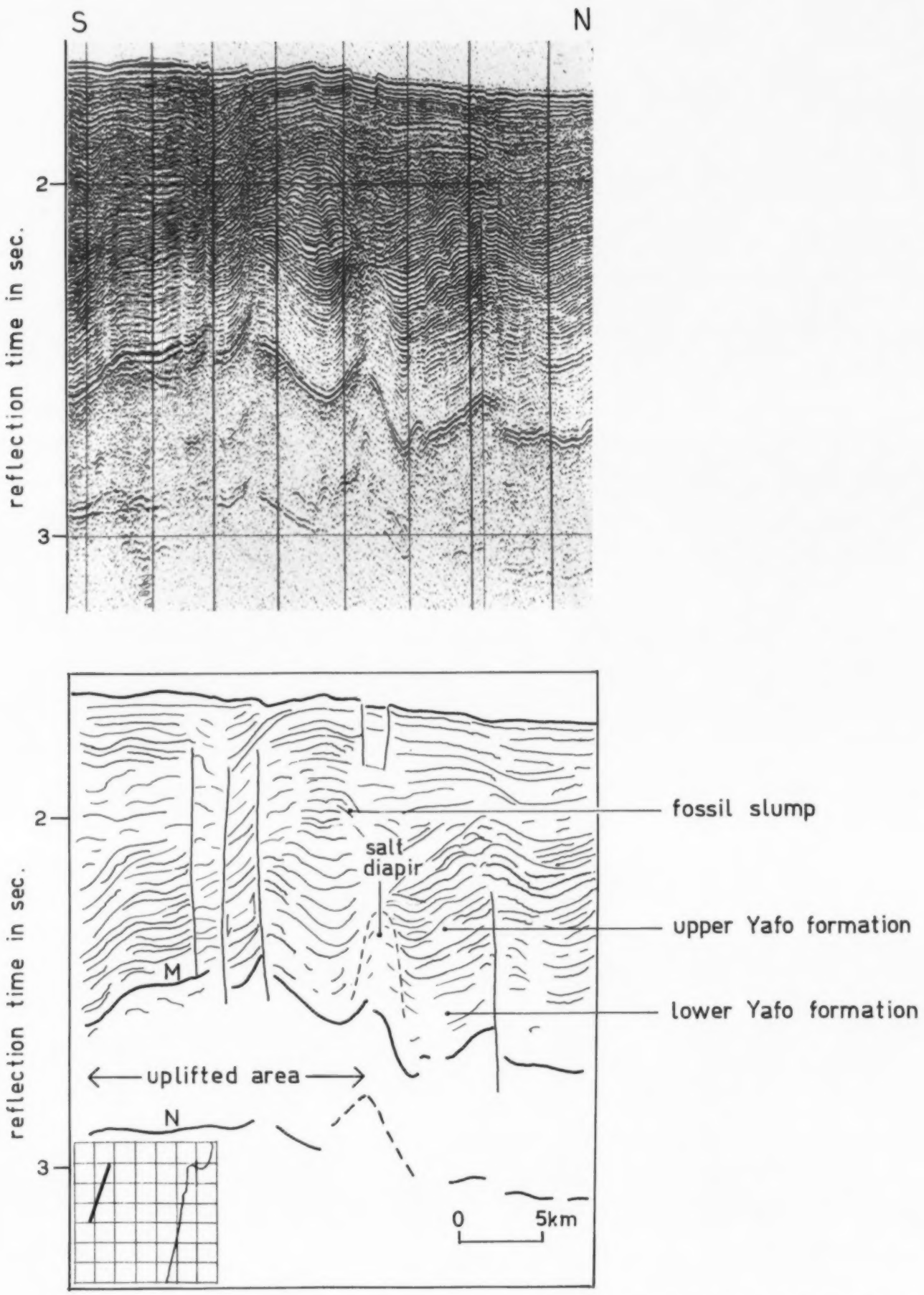

Fig. 10. Single-channel reflection profile along the western part of the study area (location in Fig. 2) showing salt diapir beneath the continental rise. Note the uptilting of the Yafo Formation; the diapir seems to emerge from the northern edge of the uplifted area (profile from Ben-Avraham 1978 survey).

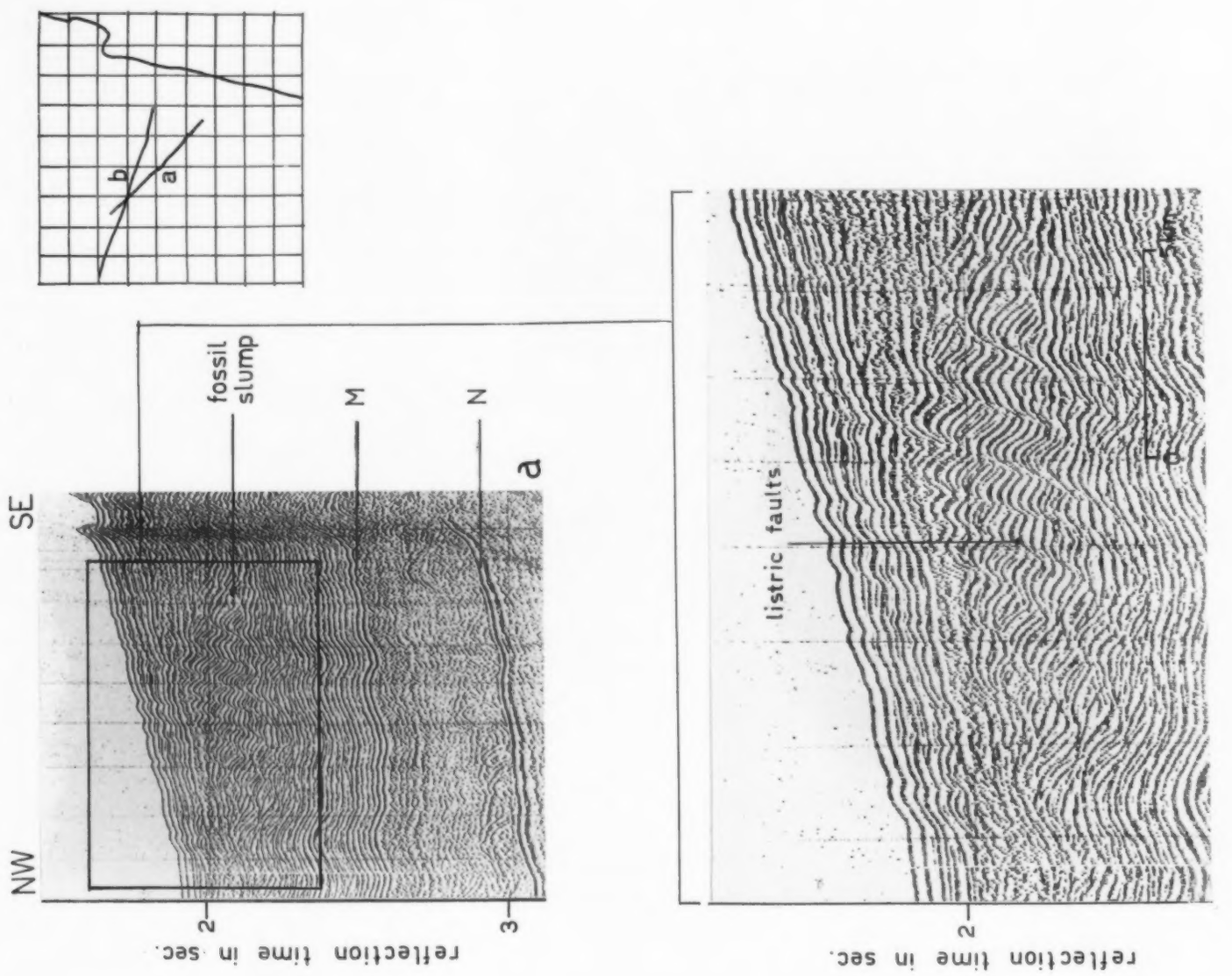

Fig. 11. Single-channel reflection profiles across the central part of the study area (locations in Fig. 2) showing Early Pleistocene slump. Note the en-echelon listric normal faults in this slump, the relatively undisturbed sedimentary layers beneath the slump and the downlap terminations of the slumped sediments onto these sediments. Profile 11a from Ben-Avraham (1978 survey) and 11b from Mart (1979 survey).

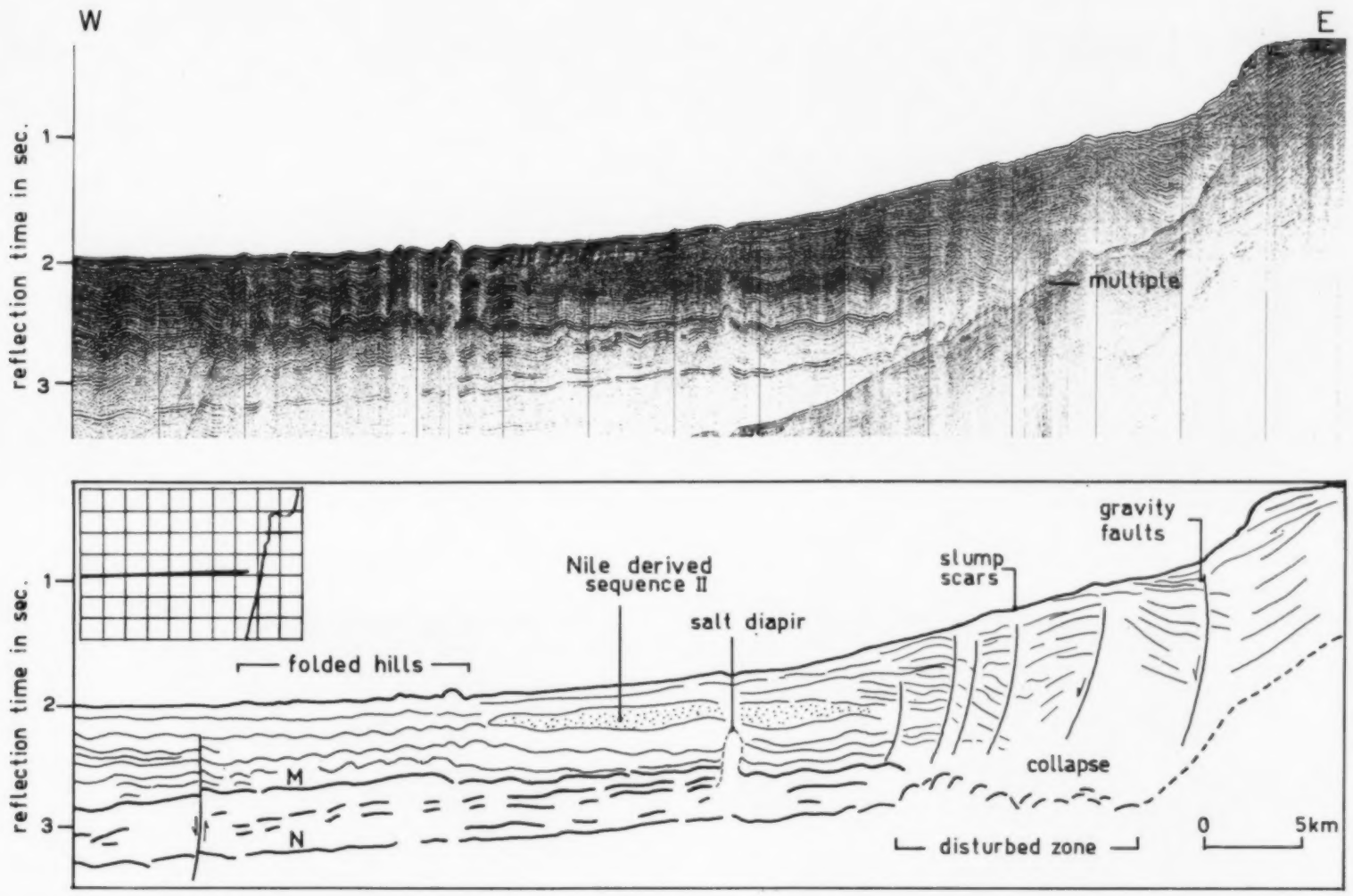

Fig. 12. Single-channel reflection profile across the central part of the study area (locations in Fig. 2) showing shore-parallel gravity faults at the continental slope, the Nile-derived sequence, and the folded hills area. Note the collapse area at the base of slope (revised from Ben-Avraham, 1978).

also recognized this zone, and have called it the "Pelusium line" (Neev et al., 1976), the "disturbed zone" (Ben-Avraham, 1978) and the "zone of discontinuity" (Folkman and Klang, 1982). Neev et al. (1976) suggested, based on their interpretations of single- and multichannel reflection profiles, that the Pelusium line is a compressive feature. We found that the width of the disturbed zone varies along the margin, from 2 km in the south to more than 20 km in the north. We suggest that the landward edge of this zone represents the Messinian base of slope. Thus, these variations in width may arise from differences in the paleobathymetry prior to the Messinian, or they may result from variations in the amounts of evaporitic migration throughout the area since the Late Pliocene. Variations in this migration may result from different sediment loads and from different rates of tectonic subsidence.

Discussion and conclusions

The late Tertiary growth and evolution of the Levant margin in the study area was influenced by the interaction of three main processes:

(1) Outbuilding and loading of the margin by the Nile sediments since the Pliocene. Sediments derived from the Nile thin to the north but have built the continental shelf of the southern Levant margin up substantially, in a way similar to that in the Mississippi Delta (Moore et al., 1978).

(2) The loading of the thick Messinian evaporites caused a variety of salt-tectonic features, including flowage, piercement diapirs, slumps and en-echelon listric normal faults in the supra-salt sediments. Similar salt-related features are found in the northern part of the Gulf of Mexico (Lamor et al., 1979).

(3) However, unlike in the Gulf of Mexico the

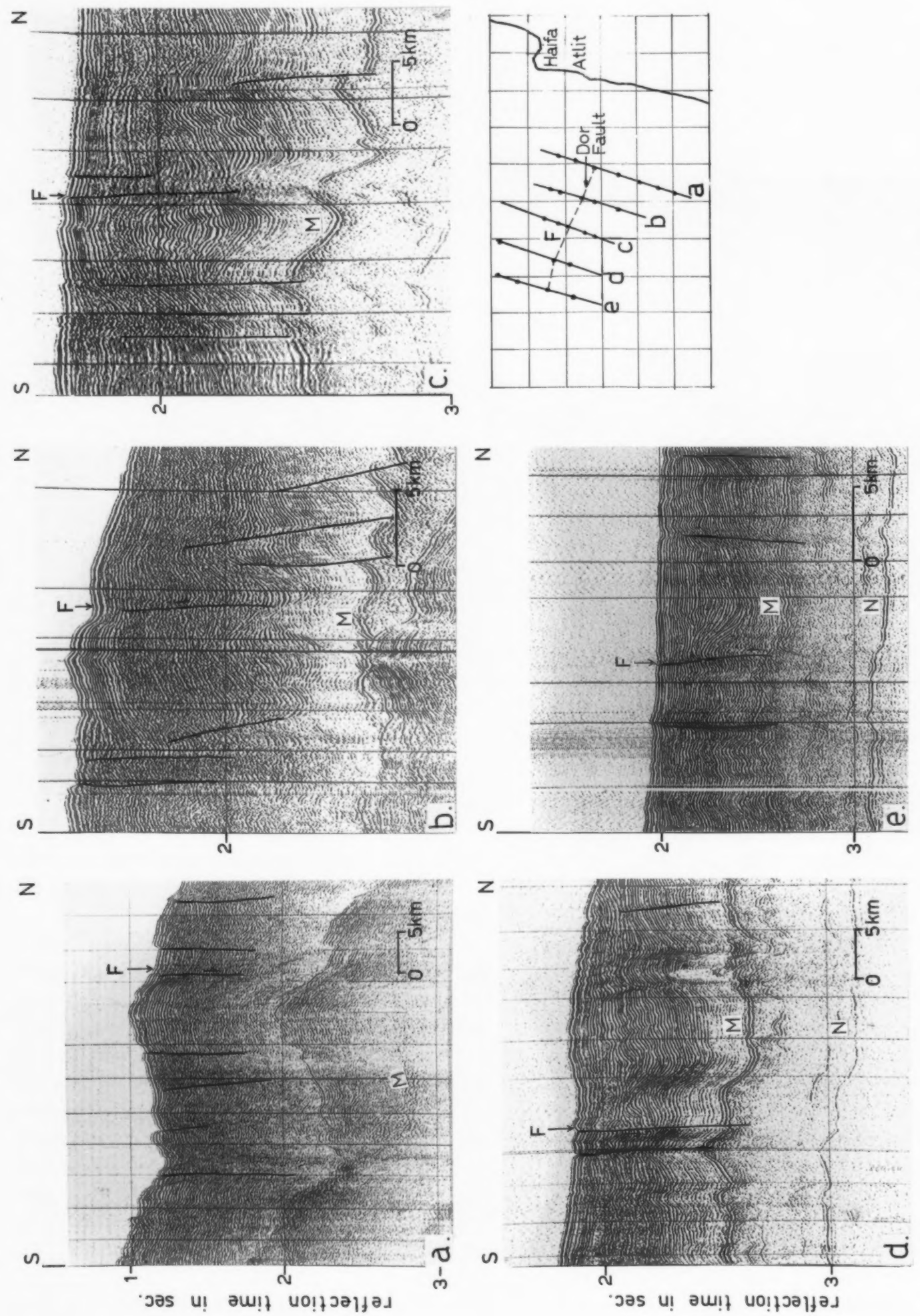

Fig. 13. Single-channel reflection profiles along the northern part of the study area (locations in Fig. 2) showing the NW–SE trending Dor fault in the post Messinian strata off Atlit. In the location map, fault locations are marked by dots and the possible correlation between them is marked by a dashed line. Note the graben-like feature in 13c and 13d (profiles from Ben-Avraham 1978 survey).

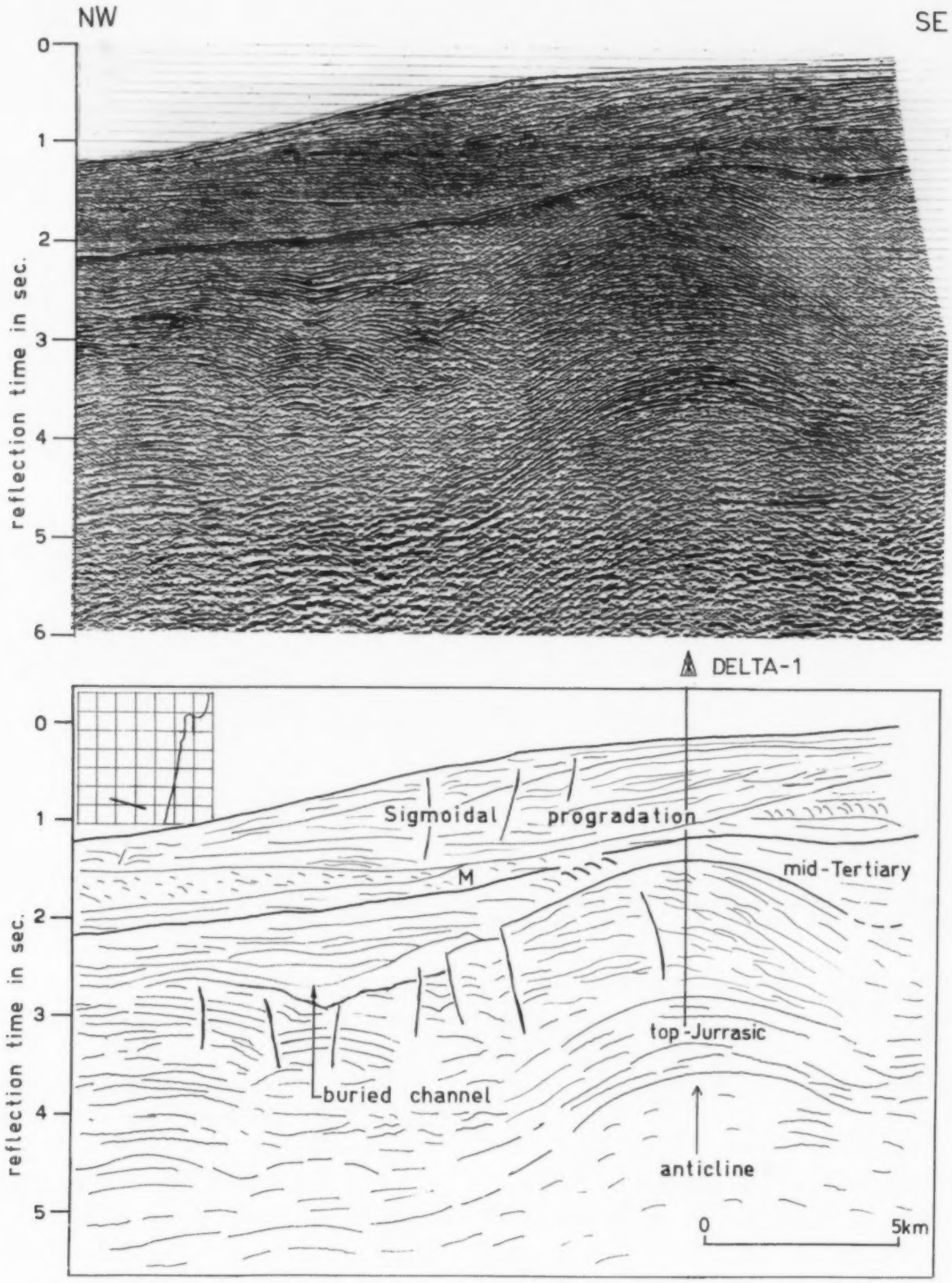

Fig. 14. Multi-channel (migrated) reflection profile off Netanya (location in Fig. 2) showing a fold which is part of the Syrian arc fold system (profile from Seismic Geocode 1983 survey). The configuration of reflector *M* and the Pliocene sediments above the fold may indicate its continued uplift into the Neogene. The interpreted reflectors were tied to the Delta-1 well.

close proximity of an active plate boundary, specifically the Dead Sea Transform, continues to influence the evolution of the margin. Stresses generated by the active plate boundary and the flexural response of the lithosphere to loading caused tectonic uplift and subsidence along the margin and triggered salt flow.

The present study of the shallow late Tertiary strata on the Levant continental margin in the northern part of the southern province indicates

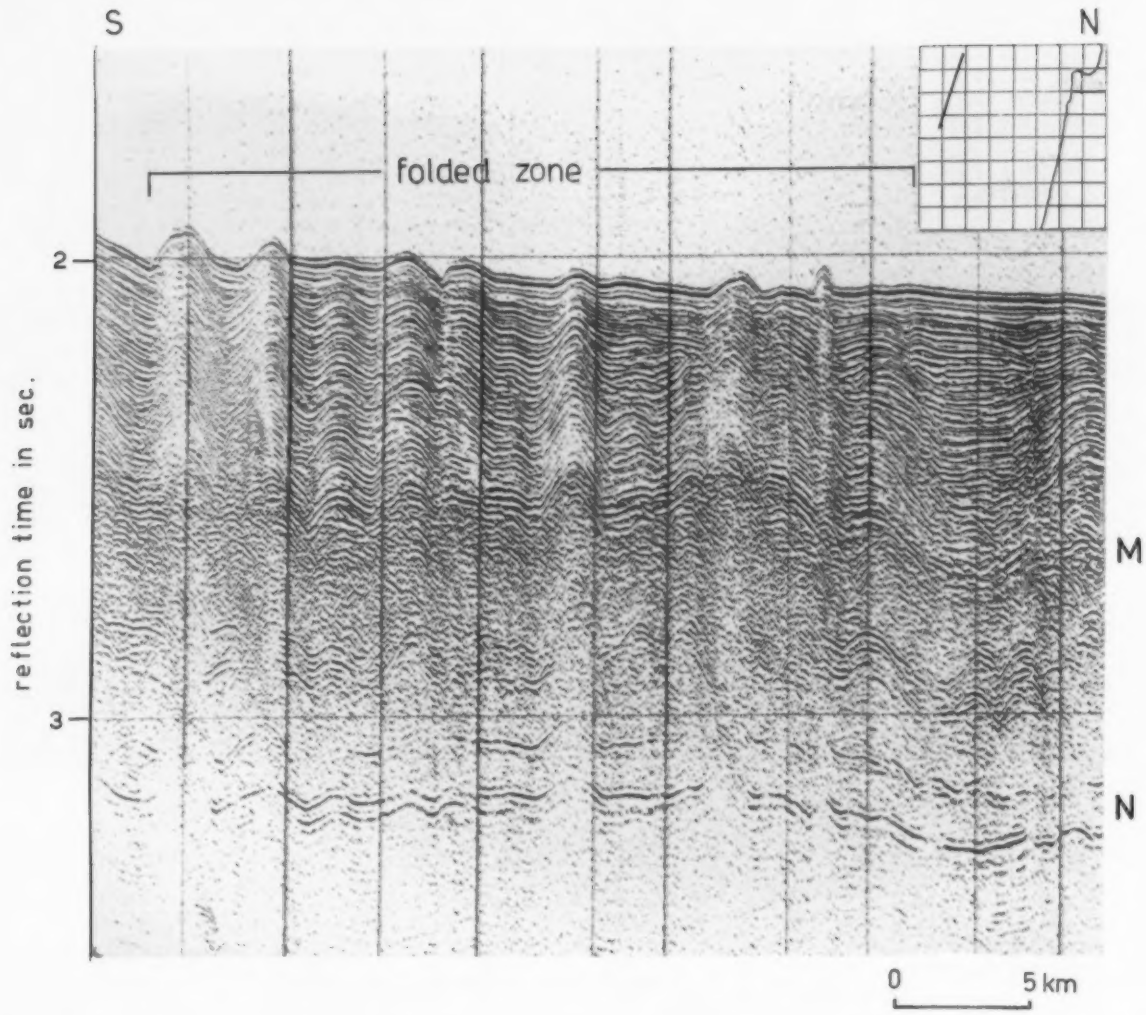

Fig. 15. Single-channel reflection profile along the northwestern part of the study area (location in Fig. 2) showing folded hills on the continental rise. Note the uniform folds down to the Messinian evaporites (profile from the 1978 Ben-Avraham survey).

that this area is composed of two segments which show different depositional environments and underwent different structural deformation (Fig. 17). This is supported by the following observations:

(1) *Physiography*: The location and nature of the physiographic units of the margin in the pre-Messinian compared to the present units varies in the two segments. The pre-Messinian base of the continental slope and shelf edge in the southern segment was located seaward of the present slope and shelf and is now filled with Nile-derived deposits. In the northern segment, where the influence of the Nile is less, the pre-Messinian and modern shelf edges are roughly in the same locations.

(2) *Depositional environment*: Two types of Pleistocene depositional environments were observed beneath the continental shelf and slope: (a) a high-energy environment (oblique progradation) in the north and (b) a low-energy environment (sigmoid progradation) in the south. These observations may indicate a larger sediment supply and higher subsidence rates in the southern segment.

(3) *Salt structures and tectonic features*: Most of the salt-related features were found in the northern segment west of the base of slope. The folded zone, which might represent compression or salt movement, seems to be limited to this segment. Faulting of the post-Messinian section and slumping activity is more evident to the north.

(4) *The disturbed zone*: The location and width of the disturbed zone at the base of the continental slope varies from south to north. This may represent different paleobathymetry during the Messinian and variation in evaporitic migration since then.

We suggest that the southern segment is influenced by the outbuilding of the shelf and loading by the Nile sediments while the northern segment is influenced by a smaller sediment supply and by

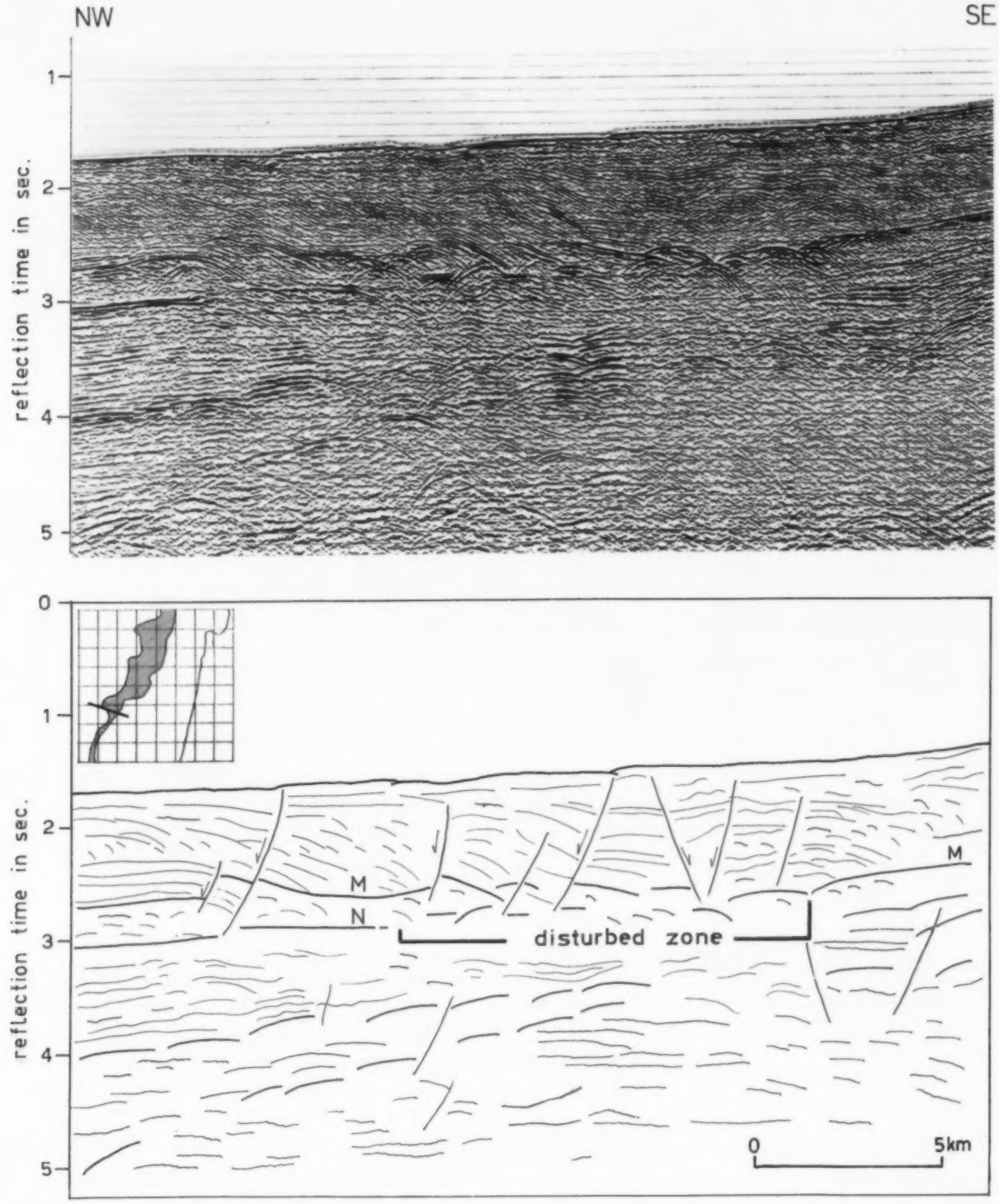

Fig. 16. Multichannel (migrated) reflection profile off Netanya (location in Fig. 2) showing the reflection characteristics of the disturbed zone at the base of the continental slope (profile from Seismic Geocode 1983 survey). The inset shows the regional extent of this zone.

ongoing tectonic activity as seen in the continuing uplift of the Carmel structure. The boundary between these two segments may mark the southern edge of the Carmel structure on the continental margin. This boundary could be the surface expression of a deep-seated fault and/or may represent deep crustal structure variations.

Acknowledgements

We thank the Ministry of Energy and the National Oil Company Ltd. who authorized the use of the Seismic Geocode (1983) profiles and the well data, Dr. Y. Mart for permission to use his 1978 single-channel seismic survey, and Dr. J.K.

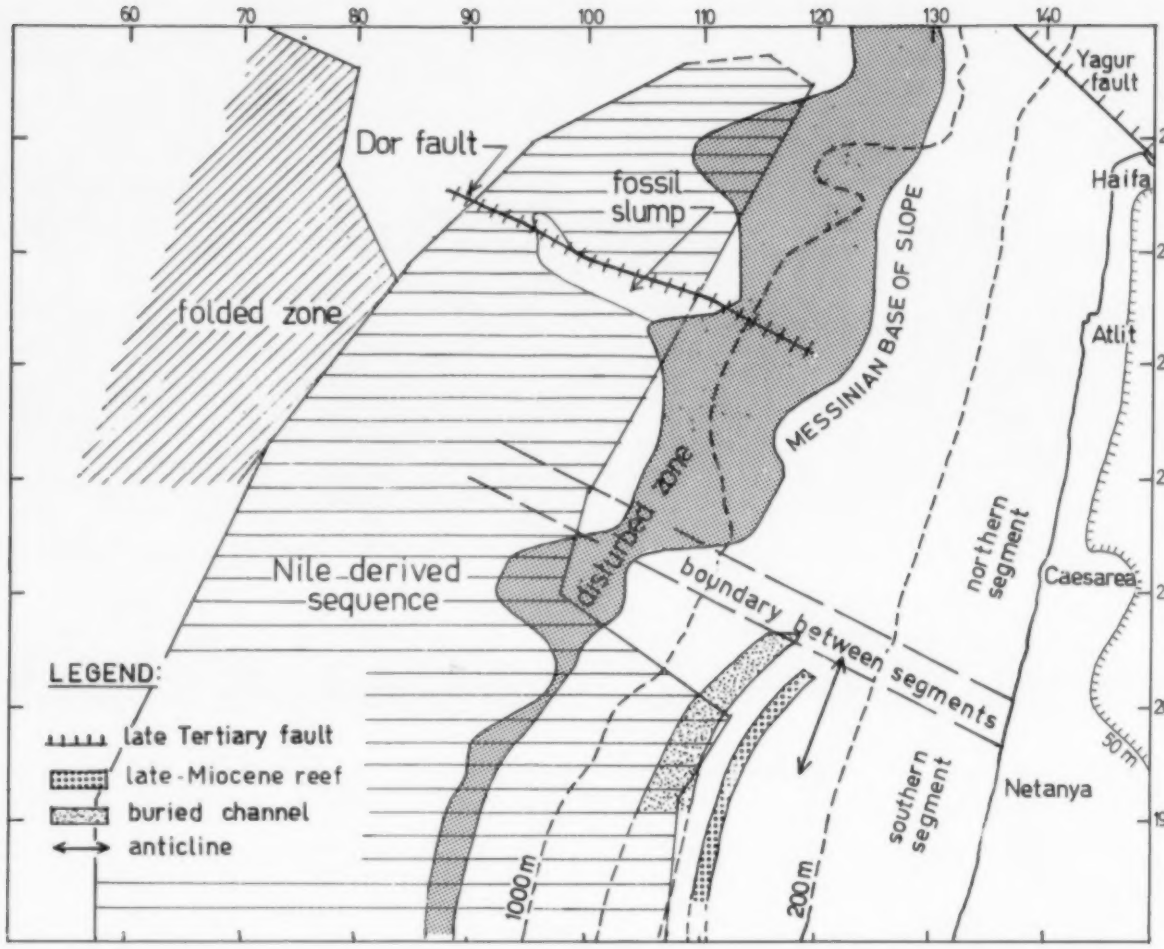

Fig. 17. Summary of the main features off central Levant continental margin discussed in the present study. Note the regional extent of the disturbed zone and the abrupt change in its width between the two segments. The buried channel and the Late Miocene reef are found only in the southern segment.

Hall for his help in the digitization of the data. We also thank J.E. Damuth of Mobil Research and Development Corp. for his constructive review.

References

Almagor, G., 1984. Salt tectonics in the Mediterranean slope off central Israel. Mar. Geophys. Res., 6: 227–243.

Almagor, G. and Hall, S.K., 1984. Morphology of the Mediterranean continental margin of Israel. Geol. Surv. Isr. Bull., 77.

Ben-Avraham, Z., 1978. The structure and tectonic setting of the Levant continental margin, Eastern Mediterranean. Tectonophysics, 46: 313–331.

Ben-Avraham, Z. and Ginzburg, A., 1986. Magnetic anomalies over the central Levant continental margin. Mar. Petrol. Geol., 3: 220–233.

Ben-Avraham, Z. and Ginzburg, A., 1990. Displaced terranes and crustal evolution of the Levant and the Eastern Mediterranean. Tectonics, 9: 613– 622.

Braun, M., Flexer, A., Honigstein, A., Rosenfeld, A. and Baida, U., 1987. Sedimentary setting of the Turonian, mainly Nezer formation in the northern Negev (Israel) structure—a precursor of the Syrian Arc folding phase. Newslett. Stratigr., 117: 57–70.

Buffler, R.T., Shaub, F.J., Watkins, J.S. and Worzel, J.L., 1978. Anatomy of the Mexican ridges, southwestern Gulf of Mexico. Am. Assoc. Pet. Geol. Mem., 29: 319–327.

Derin, B. and Reiss, Z., 1971. Remarks on the Middle Miocene–Lower Pliocene stratigraphy of the coastal plain. Isr. Inst. Pet. Res. Geophys. Rep. SMA/482/67, 66 pp.

Derin, B. and Reiss, Z., 1973. Revision of marine Neogene stratigraphy in Israel. Isr. J. Earth Sci., 22: 199–210.

Eyal, Y. and Reches, Z., 1983. Tectonic analysis of the Dead Sea rift region since the Late Cretaceous based on mesostructures. Tectonics, 2: 167–185.

Folkman, Y. and Klang, A., 1982. Seismic interpretation of the Eastern Mediterranean off Israel. Minist. Energy and Infrastructure Adm. for Earth Sci. Res. Rep. XO/590/79-82.

Garfunkel, Z. and Almagor, G., 1985. Geology and structure of the continental margin off northern Israel and the adjacent part of the Levantine basin. Mar. Geol., 62: 105–131.

Garfunkel, Z. and Derin, B., 1984. Permian–Early Mesozoic tectonism and continental margin formation in Israel and its implications for the history of the Eastern Mediterranean. In: J.E. Dixon and H.F. Robertson (Editors), The Geological Evolution of the Eastern Mediterranean. Geol. Soc. Spec. Publ., 17: 187–202.

Garfunkel, Z., Arad, A. and Almagor, G., 1979. The Palmahim disturbance and its regional setting. Isr. Geol. Surv. Bull., 72.

Ginzburg, A. and Ben-Avraham, Z., 1987. The deep structure of central and southern Levant continental margin. Ann. Tectonicae, I: 105–115.

Ginzburg, A., Cohen, S.S., Hay-Roen, H. and Rosenzweig, A., 1975. Geology of Mediterranean shelf of Israel. Am. Assoc. Pet. Geol. Bull., 59: 2142– 2160.

Hall, J.K., 1980. Bathymetry chart of southeastern Mediterranean Sea. Isr. Geol. Surv. Rep. MG/13/80.

Hsu, K.J., Montadert, L., Bernoulli, D., Cita, M.B., Erickson, A., Garrison, R.E., Kidd, R.B., Melieres, F., Muller, C. and Wright, R., 1977. History of the Mediterranean salinity crisis. Nature, 267: 399–403.

Lamor, L., Worzel, J.L. and Burk, C.A., 1979. The margins of the Gulf of Mexico. In: J.S. Watkins, L. Montadert and P.W. Dickerson (Editors), Geological and Geophysical Investigations of Continental Margins. Am. Assoc. Pet. Geol. Mem., 29: 403–420.

Mart, Y. and Eisin, B., 1982. Some faulting patterns along the continental slope of Israel and their tectonic significance. Mar. Geophys., 5: 249–262.

Mitchum, J.R., Vail, P.R. and Sangree, J.B., 1977a. Stratigraphic interpretation of seismic reflection patterns in depositional sequences. Am. Assoc. Pet. Geol. Mem., 26: 117–133.

Mitchum, J.R., Vail, P.R. and Thompson, III., S., 1977b. Stratigraphic interpretation of seismic reflection patterns in depositional sequences. Am. Assoc. Pet. Geol. Mem., 26: 53–62.

Moore, G.T., Woodbury, H.O., Worzel, J.L., Watkins, J.S. and Starke, G.W., 1978. Investigation of Mississippi Fan, Gulf of Mexico, Am. Assoc. Pet. Geol. Mem., 29: 283–302.

Neev, D., Almagor, G., Arad, A., Ginzburg, A. and Hall, J.K., 1976. The geology of southeastern Mediterranean Sea. Isr. Geol. Surv. Bull., 68: 51 pp.

Said, R. (Editor), 1981. The Geological Evolution of the River Nile. Springer, New York, 151 pp.

Marine Geology, 105 (1992) 275–284
Elsevier Science Publishers B.V., Amsterdam

The morphology of the top-Tertiary erosion surface in the Belgian sector of the North Sea

A.C. Liu[1], T. Missiaen and J.P. Henriet[2]
Renard Centre for Marine Geology, State University of Gent, Belgium

(Received June 17, 1991; revision accepted October 15, 1991)

ABSTRACT

Liu, A.C., Missiaen, T. and Henriet, J.P., 1992. The morphology of the top-Tertiary erosion surface in the Belgian sector of the North Sea. Mar. Geol., 105: 275–284.

The detailed analysis of more than 12,000 km of high resolution reflection seismic profiles has shed some new light on the morphology of the erosion surface at the top of the Tertiary substratum in the Belgian and northern French sectors of the North Sea. This morphology seems to be slightly controlled by the lithology and structure of the Tertiary substratum. Some remarkable planation surfaces, paleovalleys and other morphological features have been identified. The main planation surfaces are well defined and, subject to later chronostratigraphical control, might yield a clue to the record of Late Pleistocene postglacial sea level rises in the Southern North Sea basin. The paleovalleys seem to represent the hitherto missing link between onshore paleovalley systems and the axial paleochannel in the Southern Bight.

Introduction

High resolution reflection seismic investigations are commonly used to study the stratigraphical and structural build-up of the uppermost part of the substratum. They may however also be used to study shallow buried morphologies over large areas. The Renard Centre of Marine Geology (RCMG) of the State University of Gent, Belgium, has been carrying out high resolution reflection seismic surveys on the Belgian continental shelf and in adjacent areas of the North Sea since 1980, which has resulted in a dense grid of more than 12,000 km of good-quality seismic profiles (Fig. 1). Interpretation of these seismic profiles has led to a detailed description of the Tertiary and Quaternary sedimentary sequences (De Batist, 1989; Henriet et al., 1989a; Mostaert et al., 1989).

Based on this seismic information, a detailed reconstruction has been made of the topography of the top-Tertiary erosion surface in the Belgian and northern French sectors of the North Sea (Liu, 1990). In this area, the Paleogene strata exhibit a general strike of 40°–45°NW and a dip of 0.5°–1°NE, locally overprinted by some tectonic deformations (Henriet et al., 1982, 1988, 1989b). The erosion surface truncating these Paleogene strata largely coincides with the base of the Quaternary deposits. Intercalations of Neogene deposits are found further north. The Quaternary cover is relatively thin and mainly consists of Holocene tidal sand banks, locally overlying Pleistocene deposits.

Because sedimentological and paleontological information on the study area are still very scarse, it remains extremely difficult to link the surface morphology and the chronostratigraphy. It is in fact beyond the scope of this study, which in the first place intends to present a detailed picture of the morphological elements, thus setting the stage for further morphogenetic work.

Correspondence to: T. Missiaen, Rijksuniversiteit Gent, Geologisch Instituut, Laboratorium voor Aardkunde, Krijgslaan 281 S8, B-9000 Gent, Belgium.
[1]Present address: Ningbo Marine Survey Team, SOA Ningbo 315040, People's Republic of China.
[2]Present address: Department of Marine Geosciences, IFREMER, Centre de Brest, B.P. 70, F-29280 Plouzane, France.

0025-3227/92/$05.00 © 1992 — Elsevier Science Publishers B.V. All rights reserved

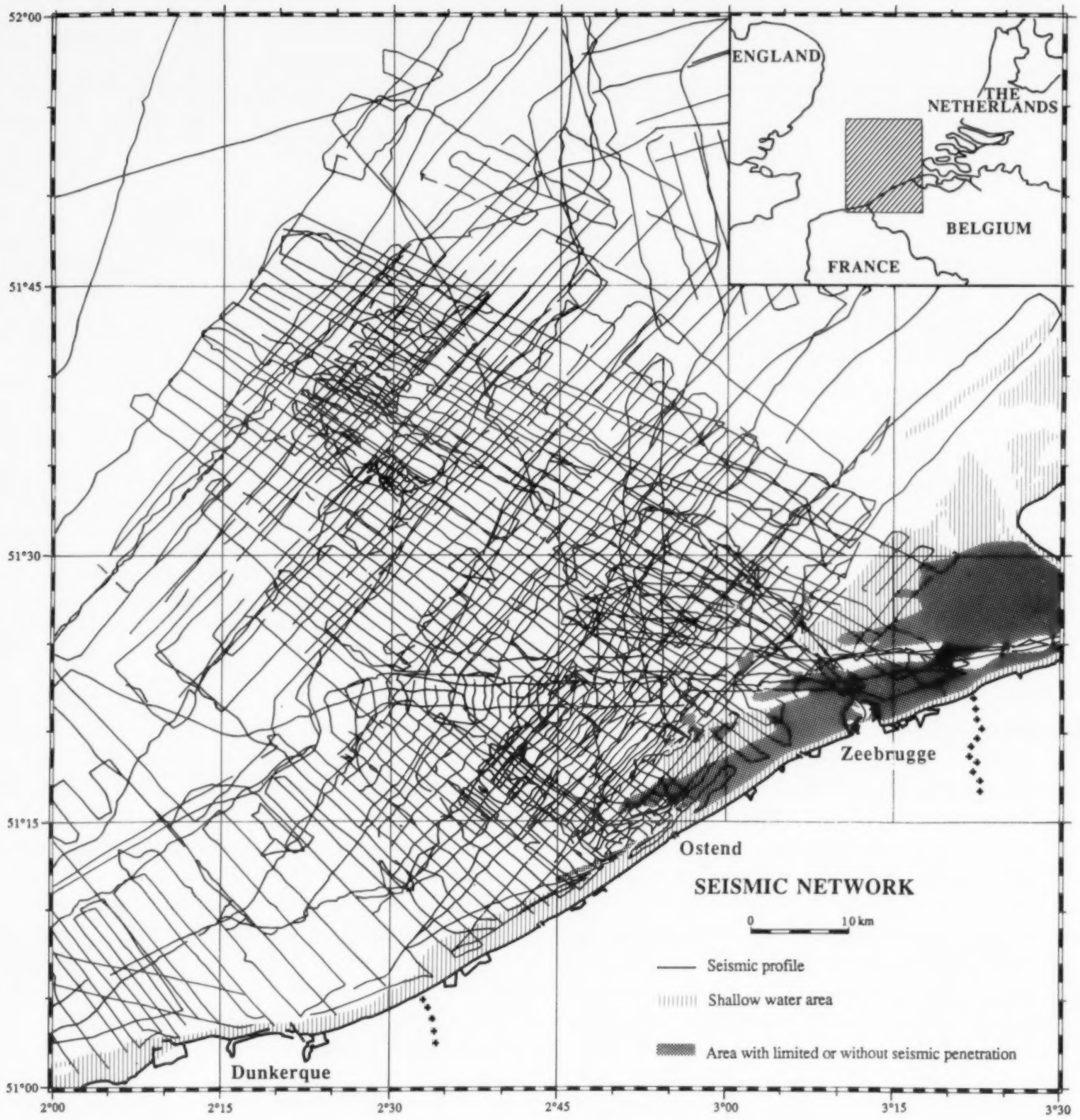

Fig. 1. Map showing RCMG's 1988 seismic coverage on the Belgian continental shelf and adjacent areas (after Henriet et al., 1988).

Morphology of the top-Tertiary erosion surface

Morphological features

The top surface of the Tertiary substratum has been known to progressively deepen under the coastal plain. This trend was expected to continue in the offshore direction (e.g. Briquet, 1931), although early reflection seismic profiles indicated bedrock highs in the immediate nearshore area (Bastin, 1974; Henriet et al., 1978). The full picture of this buried morphology clearly emerges from the isobath map in Fig. 2, on which we can see that off the Belgian coast the erosion surface first

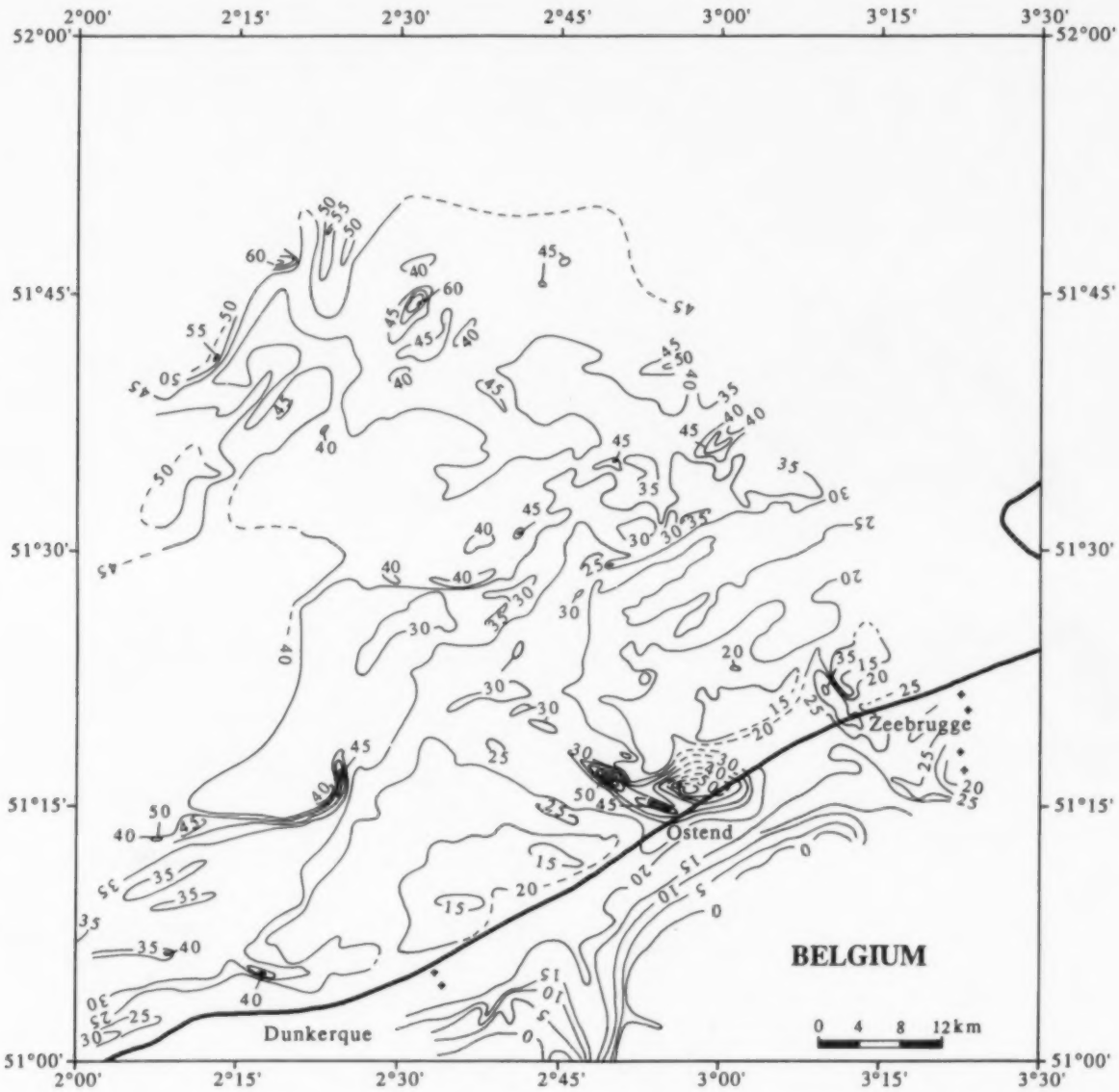

Fig. 2. Isobath map of the top-Tertiary erosion surface. Mercator projection at 51°20'N. Reference level is the mean lowest low water level at spring tide. Landward part after De Moor and De Breuck (1973), Somme (1979), Baeteman (1981), Depret (1983), Devos (1984), Mostaert (1985) and De Batist (1989).

rises to a nearly flat-topped nearshore ridge, then slowly slopes down in seaward direction, flattening again about halfway, ultimately stepping down into a major channel. Off the northern French coast the erosion surface is generally flatter.

Different morphological features show up in this erosion surface, such as planation surfaces bounded by scarps, slope breaks or ridges, and major paleovalleys, often associated with scour hollows (Fig. 3). The planation surfaces, being either horizontal ('platforms') or gently sloping ('slopes'), generally exhibit a SW–NE orientation and their boundaries are marked by drops of less than 10 metres. The paleovalleys have a depth below the surrounding surface ranging from a few metres to a few tens of metres, and contain most of the scour hollows, in which case these are generally oriented parallel to the axis of the valley.

Morphological units

Based on the identification of these morphological features, 13 morphological units have been defined in the study area: 4 planation surfaces (Offshore Platform, Middle Platform, Nearshore Slope and Marginal Platform), 3 boundaries between these planation surfaces (Offshore Scarp, Middle Scarp and Nearshore Slope Break) and 6 paleovalleys or major valley segments (Axial Channel, Northern Low Surface, Northern Valley, Ostend Valley, Western Valley and Coastal Valley) (Fig. 4).

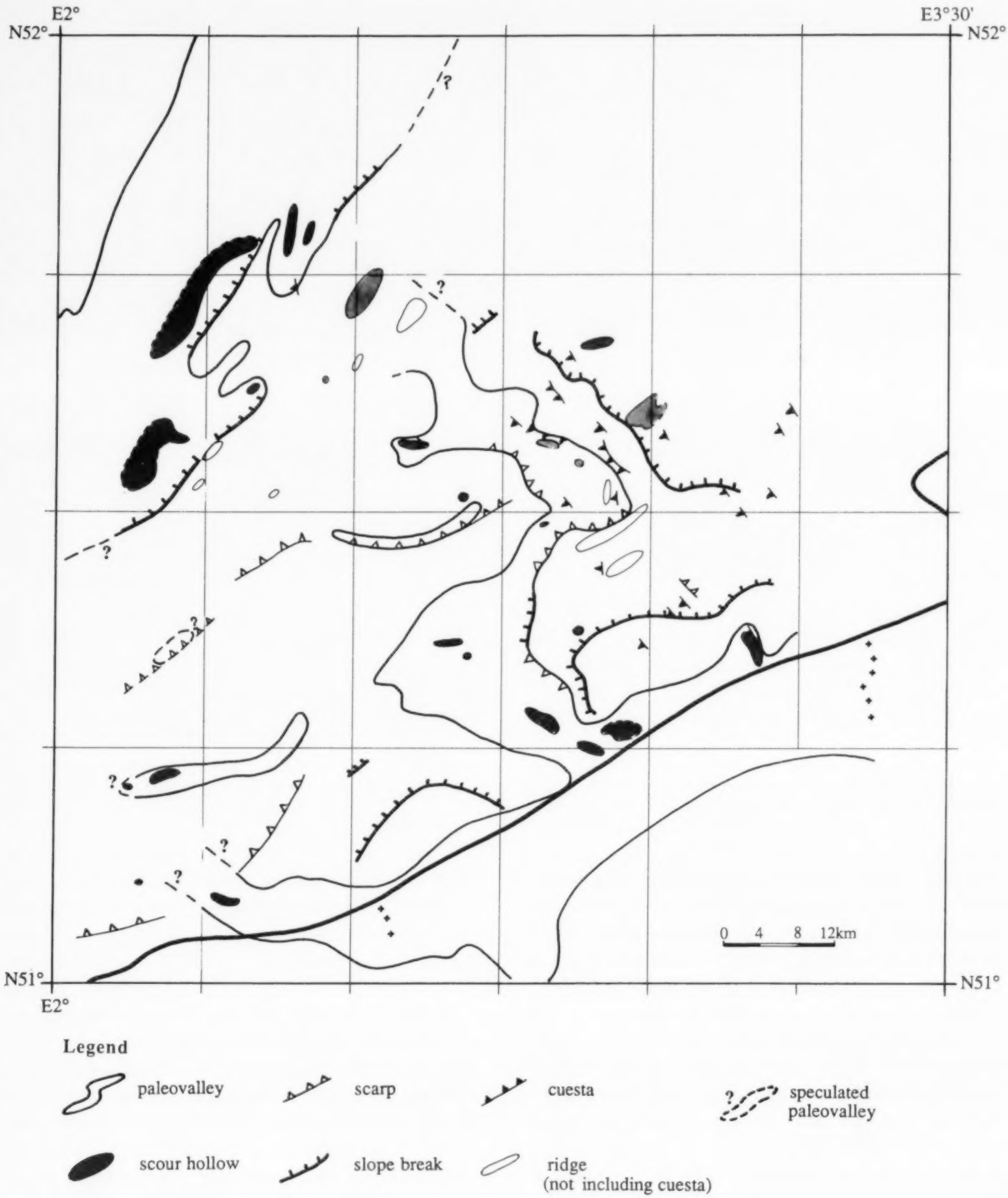

Fig. 3. Distribution of morphological features in the study area.

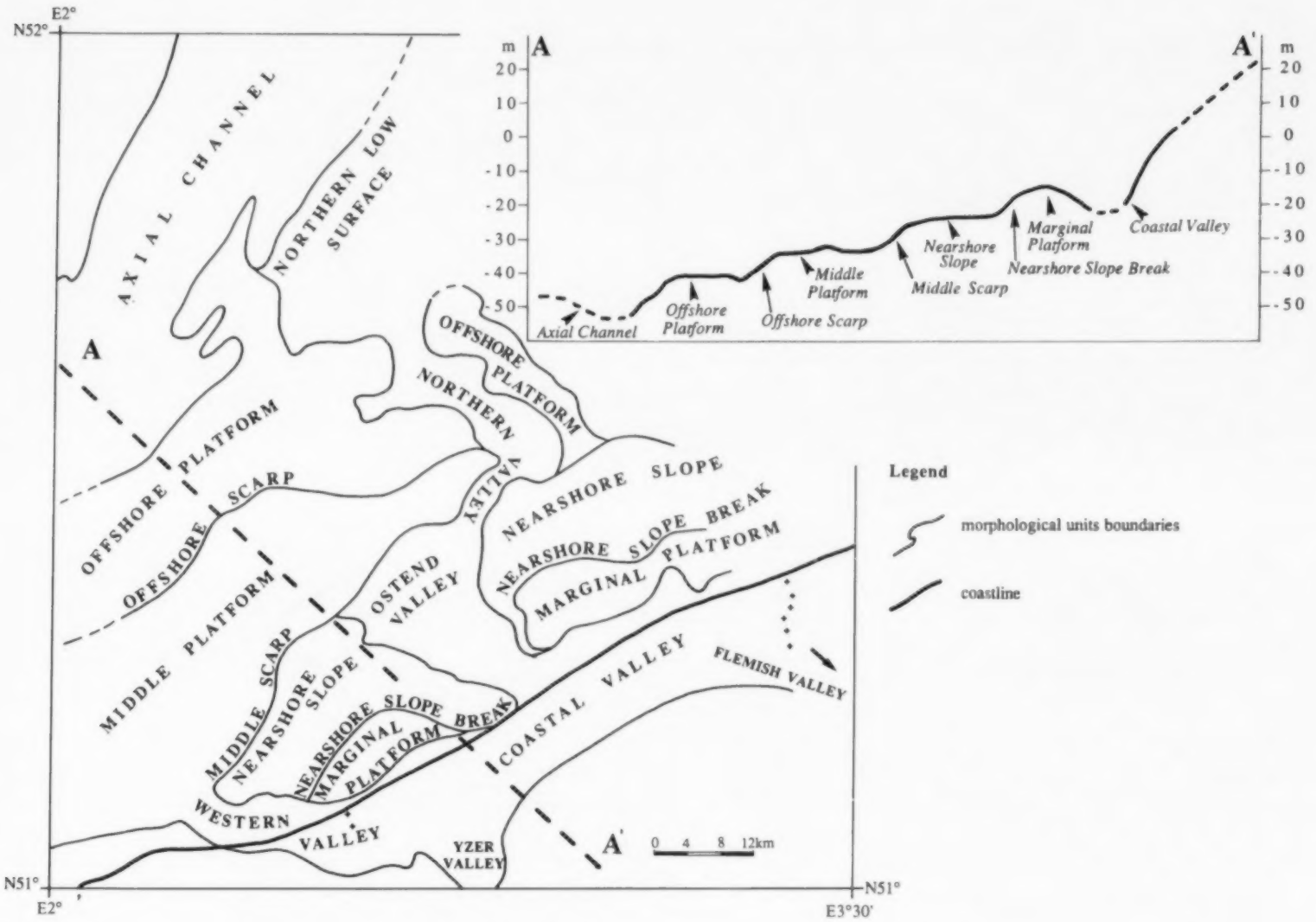

Fig. 4. The main morphological units identified in the study area.

The names of some of these morphological units have been introduced in earlier papers, such as the Ostend Valley (Henriet, 1983), the Axial Channel (Balson and D'Olier, 1988), the Coastal Valley (Mostaert and De Moor, 1989), and the Marginal Platform (Mostaert et al., 1989). All other units have been introduced by the present authors.

Planation surfaces and their boundaries

Offshore Platform and Offshore Scarp

The Offshore Platform consists of a large, SW–NE oriented western part and a small, SE–NW oriented eastern part, separated by a major paleovalley (Fig. 4). Its southern boundary is formed by the Offshore Scarp, which is characterized by a rather steep slope of some 5 to 10 m (Fig. 5, profile B–B').

The western part of the platform has a depth of some 35 to 40 m and truncates the Thanetian to Ypresian–Lutetian sequences. It is marked by a shallow valley in the south and a local high in the north (Fig. 3), the latter corresponding to a large block-faulted synclinal structure in the underlying Tertiary strata. The eastern part of the platform has a depth of some 37 m and truncates the Bartonian sequence. Its surface is marked by several cuestas and slope breaks with a strike parallel to the strike of the bedding of the substratum, suggesting differential erosion on heavy clay beds in the Bartonian sequence.

In general, the Offshore Platform is thinly covered by Quaternary sediments, except for the southern part which is overlain by the sand banks of the Hinder group. Eemian and Weichselian deposits have been observed in the Sandettié Bank area, in the southwestern part of the platform (Kirby and Oele, 1975). Nevertheless, hypotheses about the origin of the Offshore Platform/Scarp

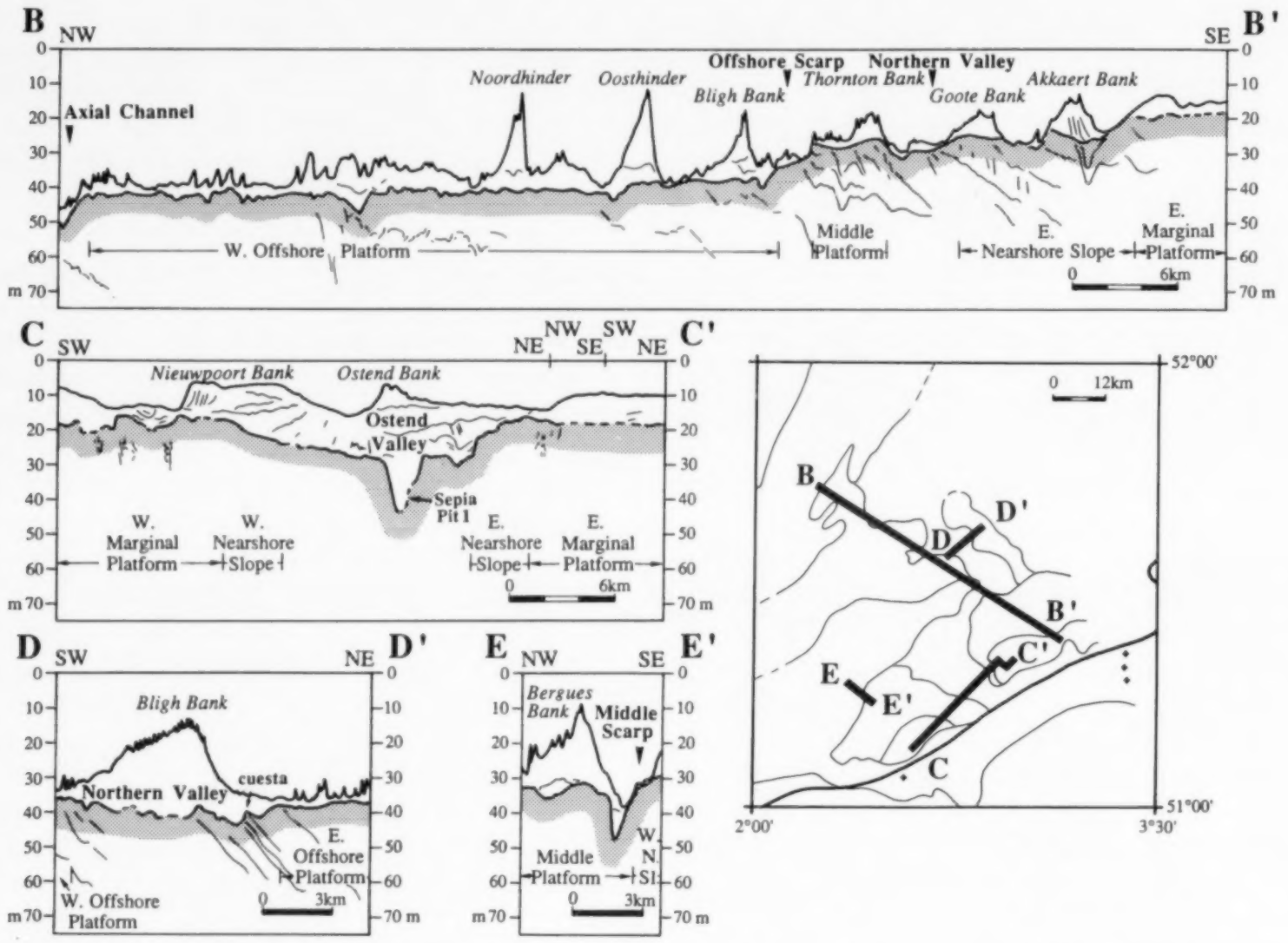

Fig. 5. Selected reflection seismic profiles across the Belgian sector showing some of the main morphological features of the top-Tertiary erosion surface.

are still highly speculative. Marine abrasion during a sea level lowstand at about −35 to −40 m might be one factor, although some glacigenic or related processes may not a priori be ruled out.

Middle Platform and Middle Scarp

The wedge-shaped Middle Platform has a depth ranging between some 35 m (in the west) to some 30 m (in the east), and truncates the Thanetian to Ypresian–Lutetian sequences (Fig. 4). Its southern boundary, the Middle Scarp, is generally marked by a gentle drop of some 5 m (Fig. 5, profile E–E'), becoming rather unclear towards the northeast where it locally fades into a slope break or a small ridge.

Towards the west the platform is cut by a large, completely buried E–W trending valley (Fig. 3; Fig. 5, profile E–E'), which may possibly have been formed by Holocene tidal currents. North of this valley the platform is rather flat, with undulations of up to a few metres in amplitude. South of the valley the platform exhibits a faint NNW dip and is incised by buried shallow gullies, more or less parallel to the valley. The eastern part of the Middle Platform is marked by several shallow depressions and an inclined surface, locally incised by gullies, which are either exposed on the seafloor or thinly covered by Quaternary sediments.

Nearshore Slope, Nearshore Slope Break and Marginal Platform

The Nearshore Slope forms a gently NW sloping surface, ranging in depth between some 20 to 25 m, locally dropping to some 15 m (Fig. 2). West

of the Ostend Valley the slope cuts the Ypresian clay, and exhibits a more or less regular surface (as indicated by the alignment of the contour lines in Fig. 2), except near Ostend where it becomes steeper. East of the Ostend Valley the slope truncates the Ypresian to Priabonian sequences, and exhibits a rather irregular and strongly eroded surface marked by elliptic depressions and a long, SW–NE oriented valley (Fig. 3).

Towards the south several bedrock highs and/or lows, scarps and cuestas can be observed, which are most likely due to differential erosion of the alternately soft and more resistant layers in the underlying Bartonian sequence. Some of the bedrock highs and/or lows may however also be structurally controlled, as they are associated with small synclines and/or anticlines in the Tertiary substratum.

The Nearshore Slope Break separates the Nearshore Slope from the Marginal Platform. West of the Ostend Valley the slope break is rather gentle and fully covered by Quaternary sediments. The eastern part however exhibits a somewhat more marked slope change and is fully exposed, probably due to the steepness of the adjacent Nearshore Slope.

The Marginal Platform has a depth of some 15 m, and truncates the Ypresian to Bartonian sequences. The eastern part is rather flat, locally marked by small cuestas and valleys, whereas the western part is rather irregular, with several highs and depressions.

Due to a lack of sedimentological and paleontological data, the exact age and origin of the Middle Platform, the Nearshore Slope and the Marginal Platform remain uncertain. However, as it is generally believed that the Early Pleistocene transgressions did not reach the study area, it seems plausible to assume that these planation surfaces may well have been formed during the subsequent Middle or Late Pleistocene transgressions.

Paleovalleys

Axial Channel

The Axial Channel forms the northern part of the Lobourg Channel, which stretches from the Strait of Dover to the Southern Bight (Balson and D'Olier, 1988). The channel has a depth of some 50 to 60 m, and contains several elongated pits oriented parallel to the channel axis (Figs. 2 and 3). Its southeastern margin is marked by three pronounced lobes (Fig. 3). The channel itself is little or not covered by Quaternary sediments, whereas the lobes are mostly completely buried.

According to Balson and D'Olier (1988) the Lobourg Channel came into existence during the Middle Miocene, when it formed the most eastward branch of a complex river system. The channel was probably further eroded during the Pliocene, as suggested by Early Pliocene infilling sediments of the Murray Pit (P.S. Balson, pers. commun., 1989). The occurrence of two horizontal internal reflectors in the lobes indicates at least three stages of infilling, the oldest one possibly being of Saalian or even older age (Balson and D'Olier, 1988), and the upper two of Eemian and Holocene age, respectively (Spaink, 1981). This indicates that further scouring of the channel probably took place during the Late Pleistocene and the Holocene, as seems to be confirmed by the lack of Quaternary sediments in the channel itself.

Coastal Valley and Western Valley

The Coastal Valley extends along the Belgian coastline, joining the Flemish Valley in the east (De Moor and Tavernier, 1978) and the Yzer Valley in the west (Fig. 4). Its cross-section is asymmetric, with a rather gentle seaward flank and a more steep landward flank which reaches a level of up to +20 m (Mostaert et al., 1989). The valley is carved into the Ypresian to Bartonian sequences, and has a depth of some 20 to 25 m, becoming locally deeper near Zeebrugge (Zeebrugge Pit) and Ostend (Fig. 2). The Zeebrugge Pit has a steep northeastern flank marked by a cuesta carved in Bartonian clay, and a very gentle southwestern flank which follows the resistant limestone and sandstone beds in the Lutetian sequence (De Wolf et al., 1981).

Towards the west the Coastal Valley extends into the Western Valley (Fig. 4), which is scoured into the Ypresian clay. Due to a lack of good quality profiles the morphology of the valley is

not very clear, except for the Dunkerque Pit area in the northwest, which is marked by SE dipping fill deposits.

According to De Moor and Tavernier (1978) the Flemish Valley formed the mouth of the River Scheldt and its tributaries during the Saalian, during which severe erosion took place in the valley. It indicates that the Coastal Valley may well have been formed by fluvial erosion of waters coming from the Flemish Valley. This seems to be confirmed by recent research by Mostaert and De Moor (1989), which states that a large valley was present under the eastern Belgian coastal plain before the Eemian. It is still unclear, however, if the western part of the Coastal Valley and the adjoining Western Valley were also formed during this period. Further marine erosion of these valley systems probably took place during the Eemian and the Holocene transgressions.

Ostend-Northern Valley System

The NW trending Ostend Valley (Fig. 4) runs more or less parallel to the strike of the underlying Ypresian clay. The valley is quite narrow near Ostend and widens towards the sea, where it also becomes shallow and flat-bottomed (25–30 m deep) (Figs. 2 and 4). It is completely covered by Quaternary sediments, and has a strongly asymmetrical profile with a gentle southwestern slope and a steeper northwestern flank (Fig. 5, profile C–C'). (Sub)horizontal internal reflectors of sometimes high amplitude (gravel beds ?) are present at least at two different levels in the sediments, indicating a minimum of three different depositional/erosional stages.

Offshore from Ostend the valley is marked by several scour hollows, the so-called Sepia Pits (Fig. 3; Fig. 5, profile C–C'). These pits probably resulted from severe marine scouring during the Eemian, as suggested by a boring carried out by the Belgian Geological survey. This also seems to be confirmed by recent research near Brugge by Mostaert and De Moor (1989).

Towards the northeast the Ostend valley extends into the southern, NE trending part of the Northern Valley. This narrow and quite shallow valley is incised into the Ypresian–Lutetian sequences, and has a rather irregular bottom which is poorly or not covered by Quaternary sediments. Its southern margin forms a local high, overlying a buried basin of Ypresian–Lutetian age (De Batist et al., 1989), and which is probably due to the presence of more resistant basin fill sediments. This basin may possibly be the cause of the offset between the Ostend Valley and the Northern Valley.

The northern, NW trending part of the Northern Valley is wider and deeper, and scoures the Ypresian to Bartonian sequences. The bottom of the valley is completely buried by Quaternary sediments, and is locally quite rough. It is marked by several cuestas which are probably related to the presence of lithified (calcareous sandstone) beds in the underlying Lutetian sequence (Fig. 3; Fig. 5, profile D–D'). The northeastern flank of the valley is formed by a cuesta scarp, and roughly coincides with the Lutetian–Bartonian sequence boundary. This indicates that it may well have been formed by differential erosion between the relatively soft Lutetian sequence and the more resistant Bartonian clays.

Towards the north the cuesta scarp fades out, and the Northern Valley widens into the Northern Low Surface. This is probably due to a lateral lithological change in the Lutetian sequence, eventually reducing the Lutetian–Bartonian lithological contrast. The Northern Low Surface has a depth of some 40 to 45 m, and is scoured into the Ypresian to Rupelian sequences. Towards the south it is marked by a large scour hollow, incised some 15 m deep into the surface (Fig. 3). According to a recent boring by the British Geological Survey (Cameron, pers. commun., 1990), the basal part of the Quaternary infilling sediments of the hollow consists of sands containing plant fragments, possibly arguing for a fluvial origin. This may confirm the primarily fluvial origin in a sea level lowstand period of the drainage system including the Ostend Valley, the Northern Valley and the Northern Low Surface.

Conclusions

Detailed analysis of a dense grid of high resolution reflection seismic profiles has yielded a coherent picture of the morphology of the erosion

surface cut in the Tertiary rocks in the Belgian sector and adjacent areas of the Southern North Sea. This surface does not dip smoothly in the offshore direction from the depth reached under the coastal plain, as originally suggested in earlier literature, but rises first to form a marginal platform, and then steps down in basinward direction via a few well defined planar elements which are incised by two major paleovalleys. These paleovalleys seem to form the hitherto missing link between the drainage systems of the Flemish Valley and Coastal Valley, known from onshore studies, and the major Axial Channel of the Southern Bight of the North Sea.

Due to a lack of sufficient sedimentological and paleontological data, the linkage of the morphological phenomena to a chronostratigraphic framework is still largely impossible. Future work in this area will now focus on the many scour hollows and paleovalleys identified in this study, which should contain the clues, if any, to the chronostratigraphic significance of these morphological units. Eventually, this should yield a better insight in the record of Late Pleistocene and Holocene sea level fluctuations in the Southern North Sea.

Acknowledgements

RCMG's seismic research in the Southern North Sea is supported by the Belgian Science Policy Office, the Management Unit of the Mathematical Model of the North Sea, the Ministry of Economic Affairs–Administration of Mines, the Belgian Geological Survey, the National Fund for Scientific Research and the Ministry of Education of the Flemish Government. A.C. Liu gratefully acknowledges research grants of the State University of Gent and of the Science Policy Office.

The authors thank their colleagues in the Renard Centre of Marine Geology, especially Dr. F. Mostaert and Dr. M. De Batist for the many fruitful discussions. They also wish to thank M. Bogaert for help in producing the figures.

References

Baeteman, C., 1981. De Holocene ontwikkeling van de westelijke kustvlakte. Doct. Thesis, Free Univ. Brussels, 297 pp. (Unpubl.).

Balson, P.S. and D'Olier, B., 1988. Thames Estuary, Sheet 51°N–00°E. Solid Geology. 1: 25000 Ser.

Bastin, A., 1974. Regionale sedimentologie en morfologie van de zuidelijke Noordzee en van het Schelde estuarium. Doct. Thesis, Catholic Univ. Leuven, 91 pp. (Unpubl.).

Briquet, A., 1931. Sur l'origine du Pas-de Calais. Ann. Soc. Geol. Nord., 46: 141–157.

De Batist, M., 1989. Seismostratigrafie en structuur van het Paleogeen in de zuidelijke Noordzee. Doct. Thesis, State Univ. Gent, 107 pp. (Unpubl.).

De Batist, M., De Bruyne, H., Henriet, J.P. and Mostaert, F., 1989. Stratigraphic analysis of the Ypresian off the Belgian coast. In: J.P. Henriet and G. de Moor (Editors), The Quaternary and Tertiary Geology of the Southern Bight, North Sea. Minist. Econ. Affairs and Belg. Geol. Surv., Brussels, pp. 75–88.

De Moor, G. and De Breuck, W., 1973. Sedimentologie en stratigrafie van enkele Pleistoceen afzettingen in de Belgische kustvlakte. Natuurwet. Tijdschr., 55: 3–96.

De Moor, G. and Tavernier, R., 1978. Periglacial and paleogeography of the Quaternary: Periglacial deposits and sedimentary structures in the Upper-Pleistocene infilling of the Flemish Valley. Excursion Guide (Unpubl.).

Depret, M., 1983. Studie van de lithostratigrafie van het Kwartiair en van het Tertiaire substraat te Zeebrugge onder meer met diepsonderingen. Belg. Geol. Dienst, Prof. Pap., 201, 235 pp.

Devos, J., 1984. Hydrogeologie van het Duinengebied ten oosten van De Haan. Doct. Thesis, State Univ. Gent, 219 pp. (Unpubl.)

De Wolf, P., De Rouck, J. and Henriet, J.P., 1981. Morfologie van het Tertiair substraat ter plaatse van de nieuwe buitenhaven te Zeebrugge. Coll. Belg. Comm. Eng. Geol., 6 pp.

Henriet, J.P., 1983. Seismisch onderzoek op het Belgisch Continentaal Plat. Eerste Faze, Ontginningszone 2. Minist. Econ. Zaken, Administratie Mijnwezen, Inter. Rep.

Henriet, J.P., Bastin, A. and De Rouck, J., 1978. Integration of continuous seismic profiling in geotechnical investigations of the Belgian coast. Proc. 7th Int. Harbour Congr., R. Soc. Flemish Eng., pp. 1.18/1–1.18/13.

Henriet, J.P., D'Olier, B. and Andersen, H.L., 1982. Seismic tracking of geological hazards related to clay tectonics in the Southern Bight of the North Sea. Symp. Engineering in Marine Environment, Brugge (Belgium), R. Soc. Flemish Eng.

Henriet, J.P., De Batist, M., Van Vaerenbergh, W. and Verschuren, M., 1988. Seismic facies and clay tectonic features of the Ypresian clay in the Southern North Sea. Bull. Belg. Ver. Geol., 97(3/4): 457–472.

Henriet, J.P., De Batist, M., De Bruyne, H., Heldens, Ph., Huylebroeck, J.P., Mostaert, F., Sevens, E., Auffret, J.P. and D'Olier, B., 1989a. Preliminary seismic-stratigraphic maps and type sections of the Paleogene deposits in the Southern Bight of the North Sea. In: J.P. Henriet and G. de Moor (Editors), The Quaternary and Tertiary Geology of the Southern Bight, North Sea. Minist. Econ. Affairs and Belg. Geol. Surv., Brussels, pp. 29–44.

Henriet, J.P., De Batist, M., D'Olier B. and Auffret, J.P., 1989b. A northeast trending structural deformation zone near North Hinder. In: J.P. Henriet and G. de Moor (Edi-

tors), The Quaternary and Tertiary Geology of the Southern Bight, North Sea. Minist. Econ. Affairs and Belg. Geol. Surv., Brussels, pp. 9–15.

Kirby, R. and Oele, E., 1975. The geological history of the Sandettie–Fairy area, southern North Sea. Philos. Trans. R. Soc. London, A279: 257–267.

Liu, A.C., 1990. A seismic and geomorphological study of the erosion surface at the top of the Tertiary in the Southern North Sea (Belgian and Northern French sectors). Doct. Thesis, State Univ. Gent, 119 pp. (Unpubl.).

Mostaert, F., 1985. Bijdrage tot de kennis van de kwartairgeologie van de oostelijke kustvlakte op basis van sedimentologisch en lithostratigrafisch onderzoek. Doct. Thesis, State Univ. Gent, 219 pp. (Unpubl.).

Mostaert, F. and De Moor, G., 1989. Eemian and Holocene sedimentary sequences on the Belgian coast and their meaning for sea level reconstruction. In: J.P. Henriet and G. de Moor (Editors), The Quaternary and Tertiary Geology of the Southern Bight, North Sea. Minist. Econ. Affairs and Belg. Geol. Surv., Brussels, pp. 137–148.

Mostaert, F., Auffret, J.P., De Batist, M., Henriet, J.P., Moons, A., Sevens, E., Van den Broeke, I. and Verschuren, M., 1989. Quaternary shelf deposits and drainage patterns off the French and Belgian coasts. In: J.P. Henriet and G. de Moor (Editors), The Quaternary and Tertiary Geology of the Southern Bight, North Sea. Minist. Econ. Affairs and Belg. Geol. Surv., Brussels, pp. 111–118.

Somme, J., 1979. Quaternary coastlines in northern France. In: E. Oele, R.T.E. Schüttenhelm and A.J. Wiggers (Editors), The Quaternary History of the North Sea. Acta Univ. Ups., 2, pp. 147–158.

Spaink, G., 1981. Boring RGD 80MK127. Rijks Geol. Dienst, Afd. Macropalaeontol., Inter. Rep. 1395.

Marine Geology, 105 (1992) 285–297
Elsevier Science Publishers B.V., Amsterdam

Predicting erosion resistance of muds

W.B. Dade, A.R.M. Nowell and P.A. Jumars
School of Oceanography, WB-10, University of Washington, Seattle, WA 98195, USA

(Received March 4, 1991; revision accepted August 15, 1991)

ABSTRACT

Dade, W.B., Nowell, A.R.M. and Jumars, P.A., 1992. Predicting erosion resistance of muds. Mar. Geol., 105: 285–297.

When measured or apparent yield stress of cohesive muds is assumed to reflect average particle-particle bond strength in network structures, critical bed shear stress required for grain-by-grain entrainment can be predicted from an analysis of the forces acting on component grains of geometrically-flat mud beds. Erosion resistance is then defined in terms of cohesive yield stress as well as nominal particle size, shape, relative density, and packing geometry. Predicted values of critical bed shear stress compare favorably with existing data from selected studies in which appropriate yield stress and hydrodynamic parameters have been reported.

Introduction

Muds are wet mixtures of silt- and clay-size particles found extensively throughout the oceans of the world. Mud transport consequently affects a wide range of benthic biogeochemical interactions and the bulk of the marine geologic record. Composition of natural muds includes clay and non-clay minerals, organic material, and water of varying pH and ionic strength. Muds can occur as suspensions with solids concentrations ranging from around 10 kg m^{-3} to that of a well-consolidated bed. Muds can be homogeneous, as in the case of a well-mixed suspension or a rapidly-emplaced bed, or exhibit strong vertical gradients in mechanical properties due to self-weight consolidation.

Fine component-particle size and presence of organic binding agents in muds result in cohesive behavior. This behavior contributes to mud erosion resistance exceeding that expected for individual component grains due to submerged particle weight alone. That cohesion contributes to mud erosion resistance is a concept learned early in the careers of many geologists by way of the Hjulstrøm plot (Fig. 1). Sundborg (1956) and Postma (1967) offered somewhat more enlightened perspectives on mud erosion resistance by suggesting that sediment concentration and consolidation history play important roles (Fig. 2). Postma fairly noted, however, that these plots did not "aim at exact hydrodynamic calculations" (p. 158) and that, "No great numerical value should be attached to [the left sides of Figs. 1 and 2] because the course of the

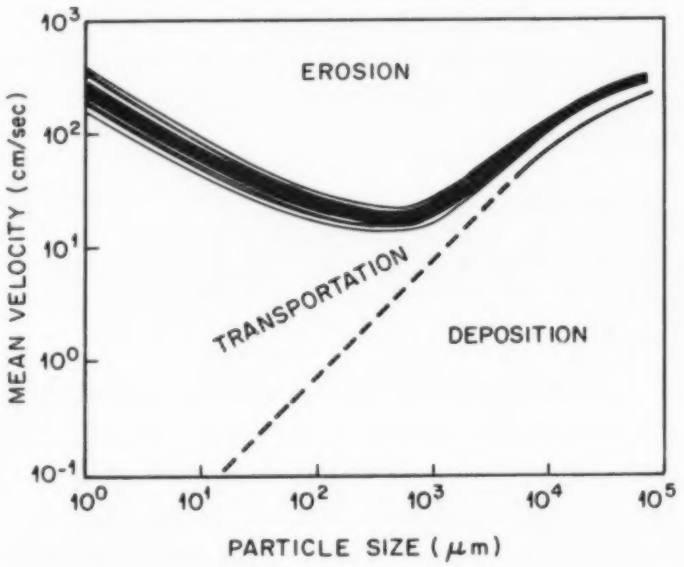

Fig. 1. Hjulstrøm plot (after Hjulstrøm, 1939).

Correspondence to: W.B. Dade, University of Washington, School of Oceanography, WB–10, Seattle, WA 98195, USA.

0025-3227/92/$05.00 © 1992 — Elsevier Science Publishers B.V. All rights reserved

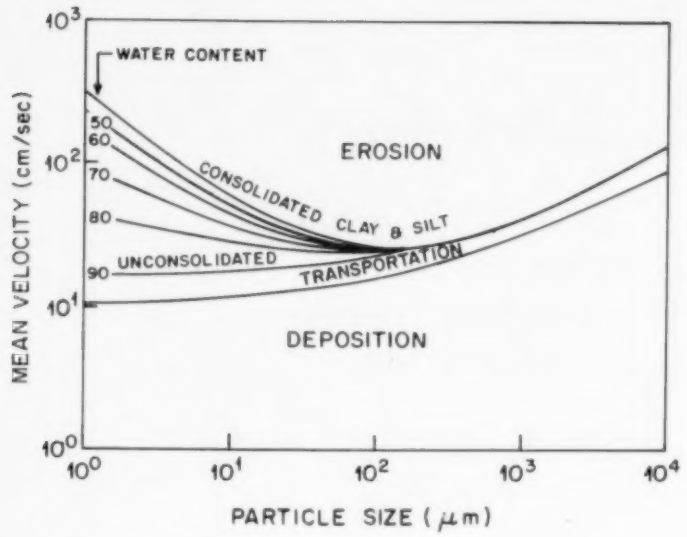

Fig. 2. Postma plot (after Postma, 1967).

lines will depend on the type of fine-grained matter under consideration." (p. 159). Practicing sedimentologists and engineers have long realized that reliable data used to construct these plots, including the discrepancy between threshold velocities for erosion and deposition, were virtually nonexistent for grain sizes finer than 100 μm, and that mud erosion resistance is too complex to be represented by unique functions of grain size and sediment concentration. These diagrams nevertheless appear in many commonly used textbooks (e.g. Blatt et al. 1980; Kennett 1982) yet incorrectly imply that erosion resistance of silts and clays can be predicted by knowledge of grain size and sediment concentration alone. Migniot (1968) made a significant contribution to an understanding of the problem by empirically correlating, for various natural muds, yield stress τ_y with critical bed shear stress required for the onset of significant transport $(\tau_o)_{cr}$. He noted in particular that for high yield strength muds

$$(\tau_o)_{cr} \approx 0.25\ \tau_y \qquad \tau_y > 1.6\ \text{Pa} \tag{1a}$$

while for weakly cohesive muds

$$(\tau_o)_{cr} \approx (0.1\ \tau_y)^{1/2} \quad \text{(in Pa)} \qquad \tau_y < 1.6\ \text{Pa} \tag{1b}$$

Subsequent attempts to characterize other cohesive mud properties giving rise to erosion resistance have included measurements of water content, bulk strength, plasticity indices, mineralogy, overlying- and pore-fluid salinity and pH, and component clay sodium adsorption ratio and cation exchange capacity. No single alternative, universally-accepted criterion has emerged. Hydrodynamic forcing employed in the determination of mud erosion resistance has included flows in open-channel and closed conduits, Couette flows, grid- or paddle-generated turbulence, and submerged jets; these devices have been designed for use in the laboratory and in situ. Discrepancies among these many different types of tests have also contributed to the confusion. In addition, very few studies have reported control of microbial growth during the course of experiments. The presence of microbes can exert significant influence on erosion resistance of otherwise non-cohesive sediments (e.g. Dade et al., 1991a), and the degree to which microbes can alter flow properties of clay-rich muds remains unclear. Summaries of a wide range of past studies conducted through the early 1980's are available in Zeman (1983) and McCave (1984).

Among the many efforts of the last two decades, those of Raudkivi and coworkers (e.g. Raudkivi and Hutchison 1974; Raudkivi and Tan 1984) stand out as useful attempts to relate in comprehensive fashion transport behavior of cohesive sediments in carefully controlled laboratory conditions to fundamental particle interactions. Although these experiments demonstrate the importance of clay mineralogy and electrochemical properties of the suspending fluid, they fall short of providing a means for straightforward prediction of mud erosion resistance. The recent efforts of D. J. A. Williams and coworkers (James et al. 1986, 1987; Williams 1986; Williams and Williams 1989a, 1991), however, represent renewed systematic analysis of mud properties contributing to mud erosion resistance. In particular, Williams and Williams (1989a) have suggested that a possible scaling for critical bed shear stress is

$$\tau_L \leq (\tau_o)_{cr} < \tau_y \tag{2}$$

where τ_L is the upper limiting stress for which surficial mud behaves in a linear viscoelastic fashion and τ_y is yield stress of the surficial material. Stresses at or slightly above τ_L but below τ_y, it is inferred, result in nonlinear viscoelastic deformation due to incipient breakdown of the weakest cohesive bonds among mud-component particles. Stresses in excess of τ_y result in unequivocal disrup-

tion of average cohesive bonds, leading to unrecoverable flow deformation. Yield stress provides an exclusive upper bound to critical bed shear stress in eqn. 2, presumably, because of particle exposure at the interface.

The purpose of this paper is to bring conceptual focus to the problem of predicting onset of mud erosion under steady, unidirectional flows. Specifically, we are interested in predictability of the left-hand limb of the erosion-resistance curves depicted in Figs. 1 and 2. To address this problem we suggest that apparent or measured yield stress of many mud suspensions represents average interparticle cohesive force per surface area of component grains. As such it can be used as a parameter in the force balance used to define critical bed shear stress required to initiate particle-by-particle entrainment of cohesive sediments. The resulting expression yields predicted values of $(\tau_o)_{cr}$ that compare favorably with the observations of Migniot (1968) and Ohtsubo and Muraoka (1986), and thus provides a physical explanation of their respective results. Consequently, the expression can serve as a basis for future attempts to predict conditions giving rise to mud erosion, and should be of value to oceanographers, geologists, and engineers alike.

We emphasize that this approach represents deterministic prediction of average conditions at the onset of significant sediment transport from geometrically flat beds underlying simple flows. Such an approach would seem to over-simplify the entrainment process in light of arguments that stochastic properties of both turbulent flow and natural, heterogeneous sediments compromise the notion of a unique critical shear stress (Lavelle and Mofjeld, 1987). The entrainment process must nevertheless remain related in well-behaved fashion to all moments of respective stochastic distributions including means, and sediment erosion rate can thus be considered to increase rapidly with average bed shear stress in slight-to-moderate excess of calculated critical values. Consequently the concept of a critical shear stress remains useful for many fine-sediment transport models (e.g. Gross and Dade, 1991). Once a meaningful deterministic expression for initial sediment motion is available, moreover, causes and implications of variance about average critical conditions can be considered in terms of variance in components of the deterministic relation (Grass 1970; Kirchner et al. 1990). Analysis of factors contributing to erosion-resistance variance may be especially important for marine sediments displaying heterogeneity due to nonuniform alteration of bed properties by biological processes (cf. Nowell et al., 1981; Self et al., 1989; Dade et al., 1991).

A balance of forces

Stationary, cohesive grains begin to move when vertical components of lift and drag imposed by near-bed flow just exceed gravitational, frictional, and cohesive forces keeping the grains in contact with the bed. For geometrically flat beds, forces on a single stationary particle resolved into the direction of initial motion are in equilibrium when:

$$F_g + F_A = F_D \cot \Phi + F_L \tag{3a}$$

In eqn. (3a), F_g' is immersed weight of the grain, F_A net interparticle adhesive/cohesive force acting in the same direction as F_g', F_D and F_L drag and lift forces due to the overlying flow, respectively, and Φ particle packing angle (Fig. 3). [The term *co*hesion is employed here to describe the predominantly *self*-sticking behavior of clay particle interactions occurring in natural muds; the term F_A is subscripted, however, in reference to the more general phenomenon of *ad*hesion applicable, for example, in the case of abundant organic binding

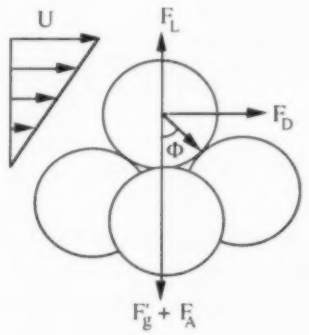

Fig. 3. Force balance for protruding particle in bed of uniformly sized, subspherical grains within the viscous sublayer; note that for simplicity $z=0$ (level of no fluid motion) taken to be bottom of protruding grain under consideration. U is flow velocity, F_D flow-induced drag, F_L flow-induced lift, F_g' submerged particle weight, F_A interparticle adhesion or cohesion force, and Φ bed packing angle.

agents or water-film surface tension in subaerial sediments.] Equation (3a) can be rearranged to yield

$$\frac{F_D}{F_g} = \frac{\tan \Phi}{1 + \frac{F_L}{F_D} \tan \Phi} \left(1 + \frac{F_A}{F_g}\right) \quad (3b)$$

Derivation and use of eqn. (3b) is a standard sedimentological approach employed to predict, in dimensionless terms, erodibility of coarse, noncohesive sediments for which F_A has been implicitly assumed to be negligible (e.g. Middleton and Southard, 1984). The modifications proposed here are explicit inclusion of the cohesion term and appropriate expressions for F_D and F_L acting on very fine particles for application to smooth beds comprising biologically-bound or clay-rich muds. Wiberg and Smith (1988) are the most recent to employ the non-cohesive force balance; they used it to examine the effects of particle packing angle Φ as it varies in coarse, heterogeneous sediments. They noted that tan Φ is analogous to a coefficient of static friction when the balance is posed as in eqn. (3b). Wiberg and Smith suggested that, in general, particle protrusion into the flow increases, and, consequently, friction-like resistance to flow-induced transport decreases, with particle size in beds of mixed sizes. As a result, particles in a heterogeneous bed can exhibit near-equal erodibility at a critical bed shear stress approximately equal to that of a well-sorted bed with similar characteristic grain size. These conditions correspond to values of packing angle Φ taken to be about 50° for spheres, 60° for natural spheroidal grains, and 70° for angular crushed quartz (Miller and Byrne, 1966).

For our purposes here, mud bed-component particles are assumed to be spheroids that are small relative to the thickness of the near-bed viscous-dominated region of overlying turbulent flows. Under these conditions, flat beds of fine sediments are said to be hydrodynamically smooth and particle Reynolds number Re_* (a dimensionless quantity defined below) is around unity or less. Turbulent stress then makes up only a fraction of total near-bed stress in flows over these hydrodynamically-smooth beds. The resulting near-viscous flow exhibits a relatively constant, linear velocity profile. Under these conditions previously existing expressions for F_D and F_L acting on spheroidal particles in viscous shear flows may be used (Table 1). The force balance of eqn. (3b) then reduces to an expression for dimensionless critical bed shear stress, or Shields parameter β_{cr} (after Shields 1936):

$$\beta_{cr} = \left(\frac{\frac{\pi}{b_1 48} \tan \Phi}{1 + 0.1 (Re_*)_{cr} \tan \Phi} \right) \left(1 + \frac{F_A}{F_g}\right) \quad (Re_*)_{cr} < 3 \quad (5a)$$

where

$$\beta_{cr} = \frac{(\rho u_*^2)_{cr}}{g(\rho_s - \rho) d_n} \quad \text{and} \quad (Re_*)_{cr} = \frac{(u_*)_{cr} d_n}{\upsilon} < 3$$

In eqn. (5a), $(\rho u_*^2)_{cr}$ is the critical bed shear stress in terms of friction velocity u_*, ρ and ρ_s fluid and sediment density, respectively, g acceleration due to gravity, d_n nominal spherical particle diameter, and υ kinematic viscosity of the entraining fluid. Shape factor b_1 relates viscous forces acting on actual spheroidal particles to that acting on nominal spheres in terms of aspect ratio $R = r_1/r_2$ with r_1 particle radius along the axis of symmetry. In

TABLE 1

Expressions for drag and lift forces due to linear-shear flows acting on very fine, spherical grains resting on geometrically smooth beds[a]

	Expression	Source	
Drag force	$F_D = 8.0 \rho \upsilon^2 Re_*^2$	O'Neill (1967)	(4a)
Lift force	$F_L = 0.81 \rho \upsilon^2 Re_*^3$	Saffman (1965)	(4b)

[a]Expressions derived from more general theoretical equations and assumption that level of no motion is the bottom of grain under consideration. Because expressions are theoretical they are, strictly speaking, only applicable for $Re_* < 0.45$ as specified by the original investigators. Coleman (1977), however, has experimentally confirmed the F_D expression (4a) for $Re_* < 2.5$. Data summarized by Lee (1982) suggest that the Saffman expression for lift is correct for a wide range of particle Reynolds numbers in linear shear flows. Hall (1988) has shown, however, that for $2 < Re_* < 40$ eqn. (4b) may underestimate by a factor of about two observed values for spheres in contact with a smooth bed, but that given this error the Saffman expression is valid for a wide range of roughness geometries.

general (Clift et al., 1978):

$$b_1 = \frac{\text{drag force acting on particle}}{\text{drag force acting on sphere of equivalent volume}}$$

and for oblate particles (discoids and blades; $R < 1$) in random orientations specifically

$$b_1 = \frac{\sqrt{1 - R^2}}{R^{1/3} \cos^{-1} R} \tag{6a}$$

or for prolate particles (rods, $R > 1$)

$$b_1 = \frac{\sqrt{R^2 - 1}}{R^{1/3} \ln [R + \sqrt{R^2 - 1}]} \tag{6b}$$

Dimensionless bed shear stresses at or in slight excess of β_{cr} calculated from eqn. (5a) are predicted to mark the onset of significant mud erosion. Unfortunately, $(u_*)_{cr}$ appears on both sides of eqn. (5a and useful solution of the equation as such requires iterative calculations. Equation (5a) can be expanded in series and solved as a quadratic expression, however, to yield β_{cr} as an explicit function of the Yalin parameter Ξ (a dimensionless submerged-particle weight; Yalin, 1972) thus eliminating $(u_*)_{cr}$ from the right side of the equation:

$$\beta_{cr} = \frac{1}{\Xi}\left[\frac{5X}{\tan \Phi}\frac{\sqrt{\frac{4}{X} - 3} - 1}{1 - X}\right]^2 \qquad (\Xi\beta_{cr})^{0.5} < 3 \tag{5b}$$

where

$$\Xi = \frac{g(\rho_s - \rho)d_n^3}{\rho v^2}$$

and

$$X = \Xi\left(1 + \frac{F_A}{F_g}\right)\frac{\pi}{b_1 4800}\tan^3 \Phi.$$

Equation (5b) can be expressed in dimensional terms as:

$$(\rho u_*^2)_{cr} = \frac{\rho v^2}{d_n^2}\left[\frac{5X}{\tan \Phi}\frac{\sqrt{\frac{4}{X} - 3} - 1}{1 - X}\right]^2 \qquad (Re_*)_{cr} < 3 \tag{7}$$

with Ξ and X are as given above. Defined in this way, critical bed shear stress is a function of submerged weight and shape of bed-component particles, relative particle protrusion (embodied in $\tan\Phi$), and magnitude of forces arising from cohesive interactions relative to submerged particle weight (F_A/F_g'). Shields (1936) did not present any data on entrainment of low Reynolds number particles. Nevertheless he did predict that β_{cr} would exhibit an inverse relationship with $(Re_*)_{cr}$ as the critical boundary Reynolds number became much less than unity. In contrast, examination of eqn. (5a) suggests that β_{cr} for non-cohesive spheroidal grains should approach a constant value of about 0.2 with diminishing $(Re_*)_{cr}$ for values of Φ between 50° and 70°. Observations unavailable to Shields indicate that the latter is indeed the case (White, 1971; Mantz, 1977; and see review of Miller et al., 1977). In fact, predicted critical bed shear stress for smooth, homogeneous beds of self-supporting, non-cohesive particles underlying turbulent flows compares favorably with available experimental observations for $(\tau_o)_{cr}$ of spheroidal and plate-like grains characterized by nominal diameter, aspect ratio, packing geometry, and density (Fig. 4). Although very little is known about particle packing angle Φ for plate-like grains in random orientation, it is interesting to note that

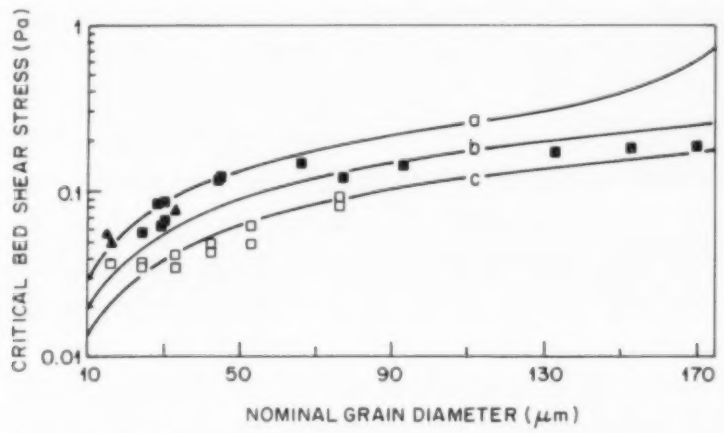

Fig. 4. Critical bed shear stress for fine, cohesionless grains in 20°C water. Solid lines represent predicted values from Eq. (7) demonstrating importance of particle shape: Spheroids ($R = 1$), (a) $\rho_s = 2650$ kg m^{-3}, $\Phi = 70°$; (b) 2650 kg m^{-3}, 60°. Plates (R = 0.05), (c) $\rho_s = 2740$ kg m^{-3}, $\Phi = 65°$. Solid squares and triangles depict data for natural quartz grains and crushed silica, respectively, reported by White (1971) and Mantz (1977). Open squares depict data for mica flakes ($\rho_s = 2740$ kg m^{-3}; $R = 0.04$–0.06) reported by Mantz (1977). Additional data are discussed in Miller et al. (1977).

eqn 7 yields reasonable predictions for onset of mica-grain entrainment with $\Phi = 65°$. This Φ value is within the range of values reported for more equant shapes by Miller and Byrne (1966). Equation 7 is thus a useful expression for simple *a priori* predictions of $(\tau_o)_{cr}$ for smooth, beds of noncohesive silt or sand with a range of primary particle shapes. This particular force balance also provides some insight into the weakly nonlinear relationship between grain size and critical bed shear stress in the low particle-Reynolds-number regime. That is, hydrodynamic lift plays an increasingly important role in the entrainment of noncohesive silts and fine sands with increasing grain size. Additionally, the effects of grain-size heterogeneity can be analyzed by varying particle packing angle Φ as described by Wiberg and Smith (1988) with similar implications for equal erodibility of most size fractions in heterogeneous mud beds. This important result means that natural mud beds, typically poorly sorted, can be analyzed in terms of a characteristic grain size and $\Phi \approx 65°$. What remains to be defined is a meaningful measure of interparticle force F_A for prediction of erosion resistance of fine-grained muds.

Fine particle interactions: a source of strength

Suspensions of fine particles in liquids flow in a variety of ways depending on the nature of particle-fluid and particle-particle interactions. Much of what is known of suspension flow behavior, or rheology, is based on theory and experiments with well-characterized laboratory suspensions. One way of summarizing rheologists' perspectives regarding mechanical response of fine-particle suspensions is in terms of measured shear stress plotted as a function of experimentally imposed steady shear rate. Many aqueous suspensions of clays and natural muds exhibit yield stresses and shear-thinning viscosities (Fig. 5, curve A; for comparison this flow behavior is qualitatively similar to that of many chocolate sauces and printing inks). At very high concentrations mud suspensions may exhibit limited shear-thickening behavior as well (curve B) (see reviews of Williams 1986; Faas, 1987; Dade and Nowell, 1991). In practice, materials exhibiting yield stress τ_y do not

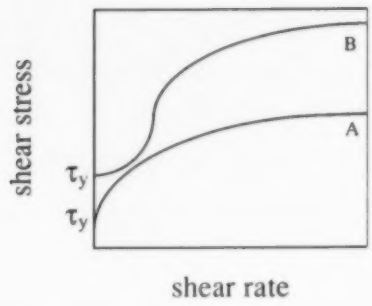

Fig. 5. Relationships between shear stress and shear rate commonly observed for aqueous suspensions of clay and natural muds. τ_y is measured or apparent yield stress, and represents average strength of cohesive bonds among fine particles. These bonds must be broken before significant flow occurs.

permanently deform when subjected to stresses less than the yield value (cf. Barnes and Walters, 1985; Hartnett and Hu 1989). This strength under shear is thus an important property in the control of mud-suspension transport behavior, whether it be for a suspension composing a thin layer at the sediment-water interface or filling the entire water column. It is most accurately measured in laboratory suspensions by way of controlled-stress and shear-vane measurements (e.g. James et al., 1986, 1987; Williams and Williams, 1989a, 1989b) and more readily by extrapolation of concentric-cylinder viscometric observations made at low shear rates (e.g. Migniot, 1968; Faas, 1985, 1987; Ohtsubo and Muraoka, 1986; also see Keentok, 1982; Yoshimura and Prud'homme, 1987). Apparent or measured yield stress τ_y is interpreted to represent average cohesive bond strength resulting from fine-particle interactions in network structures, which in turn give rise to the ability of the material to withstand shear stress without permanent strain or deformation (Dzuy and Boger, 1983, 1985; James et al., 1987, 1989; Williams et al., 1989a, 1989b). Accordingly, F_A can be defined in terms of $S\tau_y$, where S is surface area of an interfacial particle in effective contact with underlying grains.

For particle packing angle Φ between spheroidal primary grains cohesively bonded to underlying, supporting particles, the average contact surface area S is:

$$S = 2\pi \int_0^{\Phi} r \sin\theta r \, \partial\theta = \frac{\pi d_n^2}{2}(1 - \cos\Phi) \qquad (8)$$

where r is sphere radius and θ is an integration

variable (Fig. 6). Equation (8) in turn can be used to define a relevant cohesive force for particles *at* the sediment–water interface:

$$F_A = b_2 S\tau_y = \frac{b_2 \pi d_n^2}{2}(1 - \cos\Phi)\tau_y \quad (9)$$

and

$$\frac{F_A}{F_g'} = 3b_2(1 - \cos\Phi)\frac{\tau_y}{g(\rho_s - \rho)d_n} \quad (10)$$

for

$$F_g' = \frac{\pi}{6} g(\rho_s - \rho)d_n^3$$

In eqns. (9) and (10), b_2 is a shape factor that adjusts the ratio of particle surface area-to-volume as a function of platiness. Here we estimate b_2 as the ratio of (surface area / volume) quotients for cylinders and spheres:

$$b_2 = \left(\frac{R}{18}\right)^{1/3}\left(2 + \frac{1}{R}\right) \quad (11)$$

where cylinders have characteristic aspect ratio R. Defined in this way, F_A retains the effects on erodibility that arise from relative protrusion and changes in effective contact surface area (i.e., effective F_A for similarly shaped particles diminishes with decreasing Φ).

In pure clay suspensions, cohesive particle interactions are believed to result from the presence of van der Waals and electrostatic forces (Overbeek, 1982; Williams, 1986), and thus reflect controlling physico-chemical aspects of the suspension environment and surface properties of suspension particles. In seawater the scope of electrostatic forces is greatly reduced suggesting that cohesive bonds are dominated by van der Waals forces (e.g. Dade and Nowell, 1991). These interactions have characteristic bond energies given by the material-dependent Hamaker's constant $A \approx 10^{-20} - 10^{-19}$ J (Israelachvili, 1985) that can be compared to the effective potential energy of a submerged spherical grain resting on a flat bed by way of an adhesion number N_A:

$$N_A = \frac{12A}{\pi g(\rho_s - \rho)d_n^4} \quad (12)$$

N_A is greater than unity for quartz-density particles with diameters of 1–2 μm or less, indicating, not surprisingly, that clay-rich muds should exhibit cohesive behavior and erosion resistance in excess of that predicted for submerged weight of component particles. Mud at a sediment-water interface, moreover, is cohesively self-supporting when F_A exceeds F_g'. For quartz-density, 1-10 μm diameter particles in water and Φ taken to be 65°, this is the case when $\tau_y > 10^{-2} - 10^{-1}$ Pa. These values provide a lower limiting range for equilibrium surficial yield stress of clay-rich mud beds and correspond to properties of laboratory clay-and natural mud-suspensions at concentrations in slight excess of 10–20 kg m^{-3} (or the dilute limit for what is considered to be "fluid mud"; cf. Dade and Nowell, 1991).

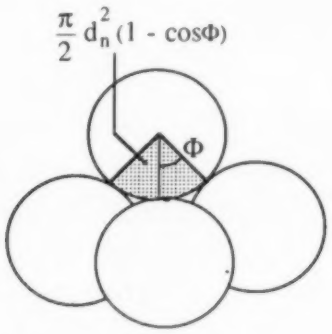

Fig. 6. Simple geometric model for relevant contact-surface area of interfacial particles cohesively bonded with underlying particles in the bed. Stippled contact surface area for protruding particle given by eqn. (8); d_n is nominal particle diameter and Φ particle packing angle.

Mud erosion resistance

Very few studies of mud erosion resistance have undertaken the tasks of reasonably accurate characterizations of mud rheology *and* bed shear stress giving rise to initial transport under conditions of steady unidirectional flow (see review of Zeman, 1983). Krone (1962, 1963), Partheniades (1965), Einsele et al. (1974) and Kelly and Gularte (1981) all, for example, measured bulk shear strengths of interfacial muds in self-weight consolidated or rehydrated, overconsolidated beds. Mud strengths reported by these workers are thus quantities averaged over the uppermost centimeters of the bed where gradients of mechanical properties are

quite severe (Einsele et al., 1974; Owen, 1975; Thorn and Parsons, 1980; Mehta et al., 1982; Parchure and Mehta, 1985; Kuijper et al., 1989). In addition, Krone (1962, 1963) and Kelly and Gularte (1981) based their interpretations on the Bingham stress, a parameter now believed to exceed considerably the sedimentologically relevant property (τ_y) of weakly-cohesive clay suspensions (cf. James et al., 1987). More likely candidates for comparison with the present approach are the studies of Migniot (1968) and Ohtsubo and Muraoka (1986); and, in fact, agreement is good between mud erosion resistance reported by these workers and predicted values from eqns. (7) and (10) (Fig. 7). The usefulness of these data sets (which include observations of all materials studied by Migniot and all natural and laboratory suspensions of kaolinite, kaolinite + organic matter, and montmorillonite studied by Ohtsubo and Muraoka) is based on design of the respective experiments. In both studies, for example, yield stress of experimentally-emplaced mud beds was correlated with bed erosion resistance defined in terms of critical bed shear stress of well-characterized flume flows. In both studies, homogeneous beds of remolded material were used. These suspensions characteristically lack strong interfacial gradients in mechanical properties (Einsele et al., 1974), indicating that reported yield stresses were representative of interfacial material. And finally, in both studies the median nominal grain size of muds was between 1 and 25 μm and all muds had large fractions of clay-sized material suggesting that cohesive particle interactions were important in transport behavior. Examination of Fig. 7 suggests that, to within the scatter of available data, model predictions are relatively insensitive to mud-component particle size and shape.

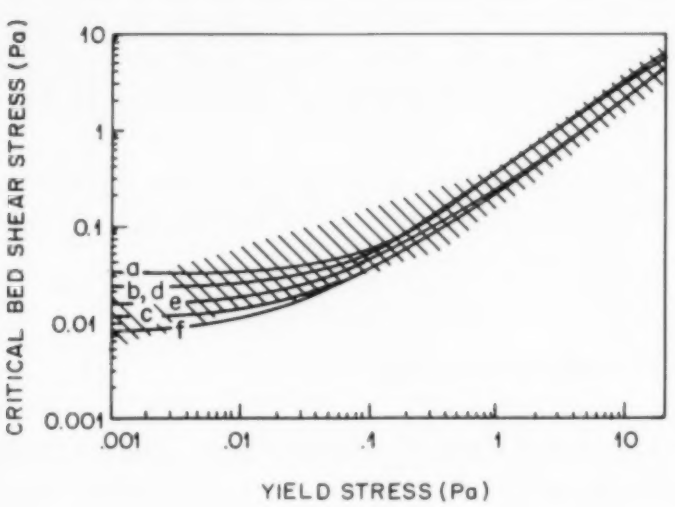

Fig. 7. Erosion resistance of mud beds with measured interfacial yield stress τ_y and $\rho_s = 2650$ kg m^{-3} in 20°C water. Solid lines represent predicted values from Eqns. (7) and (10) demonstrating model sensitivity to range of particle size and shape: Spheroids ($R = 1$, $\Phi = 65°$) (a) $d_n = 15$ μm; (b) 10 μm; (c) 5 μm. Plates ($R = 0.1$, $\Phi = 65°$) (d) $d_n = 15$ μm; (e) 10 μm; (f) 5 μm. Shaded area depicts range of observations reported by Migniot (1968) and Ohtsubo and Muraoka (1986) for muds exhibiting definite τ_y [pertaining to all materials studied by Migniot and all natural and laboratory suspensions of kaolinite, kaolinite + organic matter, and montmorillonite studied by Ohtsubo and Muraoka] and is empirically described by Eqn. (1).

Discussion

The agreement shown in Fig. 7 between predicted and observed critical bed shear stress for muds of known yield stress is arguably fortuitous. The interpretation of relevant particle surface area given in Fig. 6 and eqn. (8) is a simplistic attempt to model attenuation of mechanical bed properties on discrete particle scales at the sediment–water interface. Low yield-stress muds typically possess very high water content (much greater than 50% by volume) and arguments regarding self-supporting grains in direct physical contact are unlikely to be strictly applicable. At the very least, particle packing angle Φ as applied here should be reconsidered in terms of particle-network geometry in cohesive suspensions of very low solids content. There is no reason to expect, moreover, that all muds erode by aggregate break-up and grain-by-grain entrainment, although the observations of Allen (1969), Einsele et al. (1974), Mehta (1986), and Ohtsubo and Muraoka (1986) suggest that this is a useful first assumption for earliest transport. Some muds, particularly overconsolidated materials subjected to very high bed shear stresses, may erode by shredding and rip-up of aggregates large relative to d_n (e.g. Einsele et al., 1974; Raudkivi and Tan, 1984). Alternative choices of effective grain size (say, aggregate size) and ρ_s (bed bulk density) may then be required for successful application of eqn. (7). We hasten to point out, however, that as effective size of aggregate flow units increases, effective density decreases proportion-

ately (or nearly so). This aspect of fine-particle aggregates coupled with the difficulty of estimating aggregate properties in the bed reinforce the notion that primary particle size is a reasonable first choice for these calculations. In the case of very dense or over-consolidated muds with significant silt and sand fractions, moreover, measured yield stress may need to be partitioned into cohesive and frictional components in order to to be inserted appropriately in eqns. (7) and (10) (Kirby, 1988). As a final caveat, the approach described in this paper is as of yet only applicable to transport behavior in steady, unidirectional flow. The viscoelastic response and time-dependent breakdown of aggregate structures in cohesive suspensions subjected to oscillatory stress and strain are too poorly known at this time to recommend use of τ_y, which is a static property after all, to describe erosion resistance to dynamic forcing in wave-dominated environments. That cohesive muds respond as quasi-elastic solids with plastic yield strength τ_y to fluctuations in turbulent stress of steady flows is guaranteed by the fact that the ratio of mud viscoelastic-response time (of the order of seconds) to turbulent-fluctuation time (typically less than a second) is greater than unity. Problems associated with viscoelastic properties of mud suspensions arise when this ratio is unity or less, as in the case of wave forcing (cf. Dade and Nowell, 1991).

The strength of this approach lies in its attempt to extend noncohesive sediment transport theory to mud beds by including an additional parameter for adhesion/cohesion force F_A in a standard force balance. Such a perspective satisfyingly includes important aspects of bulk continuum behavior *and* granular properties giving rise to fine-sediment erosion resistance for materials with adhesion numbers N_A near unity. Equation. (7) can be used, for example, to evaluate the strength of adhesive bonds due to the presence of microbial exopolymers in otherwise non-cohesive fine sand (Dade et al., 1991a). The form of eqns. (5) and (7), moreover, allows incorporation of natural-bed erosion resistance arising from biological activities (pelletization through d_n, R, and tan Φ; bioturbation and microbial binding through τ_y) and vertical gradients in sediment-concentration and salinity-pH of pore-waters of the mud bed (through τ_y). Ultimately it would be useful to relate τ_y to concentrations of sediment (C_s) and biological binding agents (C_b) as well as component particle size (d_n) for any given mud mineralogy and ionic environment. Representations like the Postma plot (Fig. 2) may then be generated for a range of mud compositions and biological effects. The limited information presently available suggests that one possible scaling relationship might be (Dade and Nowell 1991):

$$\tau_y \sim (C_s)^3 (C_b)^2 (d_n)^{-2} \tag{13}$$

but confirmation of such relationships will require extensive rheological characterizations of mud suspensions.

Mud shear strengths, and thus cohesive force F_A, are also dependent on deformation history. Yield stresses of static, undisturbed clay suspensions are typically greater than yield stresses of remolded or disturbed material by a factor of two to five (making them of low to moderate sensitivity in soils engineering classification, e.g. James et al., 1987). This reduction in cohesive strength due to disturbance is probably an important factor in biological reduction of mud erosion resistance through extensive bioturbation (Singer and Anderson, 1984). It also plays a role in the difference between thresholds for onset of entrainment of resting sediments and deposition of materials already in transport. Earlier workers noted this aspect of fine sediment transport (cf. Figures 1 and 2) but offered no satisfactory physical explanations. One aspect of the problem is as follows: very fine particles in suspension, existing either as primary grains or in aggregates, will experience intermittent contact with the bed. These particles will roll or reside in temporary repose until subsequent eddies resuspend them into the flow. When in moving bed contact they are likely to experience less opposing dynamic friction (smaller tan Φ), or alternatively, increased drag than expected for static resting grains by a factor of about two (Coleman, 1977). This propensity for continued rolling motion of equivalent non-cohesive particles combined with reduction of F_A for a disturbed cohesive bed, will contribute to a threshold bed shear stress at which material already in transport will come to sustained rest $(\tau_o)_{lim}$ that is lower

than that required to initiate transport $(\tau_o)_{cr}$. When average bed shear stress of a flow falls below $(\tau_o)_{cr}$ but above $(\tau_o)_{lim}$, for example, fine material already in the water column is in wash load. A fine-sediment bedload will exist, however, unless

$$w'_{bed} \geq w_s \tag{14a}$$

where w'_{bed} is magnitude of turbulent vertical velocity fluctuations in the vicinity of the moving particle in bed contact and w_s is particle settling velocity (Middleton and Southard 1984). If eqn. (14a) obtains then upward drag due to turbulent fluctuations is greater than resisting submerged weight on average and the particle is in suspension. Assuming that $\overline{(w')^2_{bed}}$ is less than or equal to the magnitude of near-bed Reynolds stress, then for hydrodynamically smooth beds (Chapman and Kuhn, 1986; Dade et al., 1991b; Dade, 1992)

$$|w'|_{bed} \leq u_* \sqrt{10^{-3} Re_*^3} \tag{15}$$

requiring from eqn. (14a) that

$$\frac{w_s}{u_*} < \sqrt{10^{-3} Re_*^3} \tag{14b}$$

for suspension transport from the smooth bed. For fine particles adequately described by Stokes settling, the smooth-bed suspension criterion of eqn. (14b) can be expressed as

$$Re_* > 1.25\Xi^{0.4} \qquad \text{for } \Xi < 18 \text{ and } Re_* < 1 \tag{16a}$$

or

$$\beta > 1.56\Xi^{-0.2} \qquad \text{for } \Xi < 18 \text{ and } (\Xi\beta)^{0.5} < 1 \tag{16b}$$

where Ξ is the Yalin parameter, Re_* particle Reynolds number, and β the Shields parameter (cf. eq. (5)). Interestingly, eqn. (16) suggests that, due to shielding of particles from overlying turbulence by the viscous sublayer, mobile silts of quartz density in water will not go into suspension from smooth-bed contact, on average, unless $\tau_o >$ 0.4–1.2 Pa. Bed shear stresses in this range are in considerable excess of minimal τ_o required to initiate significant noncohesive, smooth-bed transport (cf. Fig. 4), and suggest that fine-particle motion over smooth beds at low transport rates includes significant bed contact. Existence of a bedload will of course give rise to bedforms with suspension occurring from the elevated surfaces, so that the criterion of eqn. (16) provides an upper estimate for onset of suspension transport. This simple observation, however, underscores the notion that in environments where average bed shear stress fluctuates in time between 0.01 and 1 Pa (corresponding to fluctuations in current speed between approximately 0.07 and 0.7 m s^{-1} at 1 m above the bed), sorting of noncohesive, fine fractions can occur by way of transport processes acting *at* a smooth bed alone. The effects of strongly cohesive and hydrodynamically rough beds are beyond the scope of this discussion but must be inferred to take on great importance in these fine-sediment sorting processes. These arguments also suggest that limiting criteria for net deposition and transport mode, presently based on smooth-bed flume experiments, remain important but as of yet poorly understood parameters in prediction of fine-sediment sorting and evolution of an initially smooth bed following the onset of transport (cf. McCave and Swift, 1976; Mehta and Lott, 1987; Self et al., 1989).

Physical models similar to that presented here for cohesive-mud erosion resistance have been advanced by Visser (1970) in his analysis of results from an experimental study of submicrometer-particle adhesion to smooth surfaces and by Iversen and coworkers (Iversen and White, 1982; Greeley and Iversen, 1985) in their discussions of surface tension of intergranular moisture films in subaerial silts and sands. In the case of marine muds, however, these simple physical arguments illustrate the principle that erosion resistance of muds with micrometer-size component grains is derived from both bio-physico-chemical particle interactions and gravitational stability. The relative importance of these factors is embodied in the ratio of intergranular cohesive force to submerged particle weight, F_A/F'_g. Strongly cohesive mud beds ($\tau_y >$ 1.0 Pa; $F_A/F'_g > 1$) exhibit erosion resistance primarily due to particle interactions. Under these conditions erosion resistance is linearly correlated with yield stress τ_y. Because large values of bed shear stress may be required to initiate erosion, critical particle Reynolds number can approach unity suggesting that particle entrainment is effected by viscous drag plus lift in excess of particle cohesion

(cf. eqns. (3b), (4), and (5a) where $F_L/F_D \sim (Re_*)_{cr}$). In weakly cohesive muds ($\tau_y < 1.0$ Pa; $F_A/F_g < 1$) erosion resistance results from the combination of fine-particle interactions *and* gravitational stability. Under these conditions erosion resistance is weakly correlated with τ_y and initiation of erosion is due to viscous drag on interfacial particles alone. Variation in particle shape and packing geometry contribute to scatter in both predicted and observed critical bed shear stresses for these weakly cohesive muds. Even if the assumptions made here regarding packing geometry and explicit correlation between F_A and τ_y do not strictly apply, one must still reconcile the combined effects of cohesive particle interactions and gravitational stability of an interface between overlying clear water and an underlying mud suspension. Undulating erosional surfaces of some weakly-cohesive muds (Raudkivi and Tan, 1984), for example, probably reflect the importance of gravitational stability contributing to bed erosion resistance. The parameter $\tau_y/g(\rho_s - \rho)d_n$ can now be measured with adequate precision in laboratory suspensions and is thus likely to appear in any useful analysis of *viscogranular* factors imparting erosion resistance to cohesive muds under experimental conditions. Application of this approach to natural sediments will require development of innovative techniques to assess in situ yield stress of interfacial muds. Work on this important aspect of predicting mud erosion resistance is presently underway.

Acknowledgements

T. Gross, P. Hill, R. Wheatcroft, P. Wiberg, and two anonymous reviewers made comments on various versions of the text. Research was supported by ONR contract N00014-90-J-1078.

References

Allen, J. R. L., 1969. Erosional current marks of weakly cohesive mud beds. J. Sedimen. Petrol., 39: 607–623.

Barnes, H. A. and Walters, K. 1985. The yield stress myth? Rheol. Acta, 24: 323–326.

Blatt, H., Middleton, G.V. and Murray, R., 1980. Origin of Sedimentary Rocks. Prentice-Hall, Englewood Cliffs, N.J., 782 pp.

Chapman, D. and Kuhn, G., 1986. The limiting behavior of turbulence near a wall. J. Fluid Mech., 170: 265–292.

Clift, R., Grace, J. R. and Weber, M. E., 1978. Bubbles, Drops, and Particles. Academic Press, New York, 380 pp.

Coleman, N. L., 1977. Extension of the drag coefficient for a stationary sphere on a boundary of similar spheres. Houille Blanche, 32: 325–328.

Dade, W. B., 1992. Near-bed turbulence and hydrodynamic control of diffusional mass transfer at the seafloor. Limnol. Oceanogr., in press.

Dade, W. B. and Nowell, A. R. M., 1991. Moving muds in the marine environment. Proc. Coastal Sediments '91 Am. Soc. Civ. Eng., pp. 54–71.

Dade, W. B., Davis, J. D., Nichols, P. D., Nowell, A. R. M., Thistle, D., Trexler, M. B. and White, D. C., 1991a. Effects of bacterial exopolymer adhesion on the entrainment of sand. Geomicrobiol. J., 8: 1–16.

Dade, W. B., Nowell, A. R. M. and Jumars, P. A., 1991b. Mass arrival mechanisms and clay deposition at the seafloor. In: R. H. Bennett, W. R. Bryant and M. H. Hulbert (Editors), The Microstructure of Fine-Grained Terrigenous Marine Sediments: From Muds to Shale. Springer, New York, pp. 161–165.

Dzuy, N. Q. and Boger, D. V., 1983. Yield stress measurement for concentrated suspensions. Rheology, 27: 321–349.

Dzuy, N. Q. and Boger, D. V., 1985. Direct yield stress measurement with the vane method. Rheology, 29: 335–347.

Einsele, G., Overbeck, R., Schwarz, H. U. and Unsöld, G., 1974. Mass physical properties, sliding, erodibility of experimentally deposited and differently consolidated clayey muds. Sedimentology, 21: 339–372.

Faas, R. W., 1985. Time and density-dependent properties of fluid mud suspensions, NE Brazilian Continental Shelf. Geo-Mar. Lett., 4: 147–152.

Faas, R. W., 1987. Viscous control of estuarine re-suspension patterns. Proc. Coastal Sediments '87. Am. Soc. Civ. Eng., 1: pp. 300–315.

Grass, A. J., 1970. Initial instability of fine bed sand. J. Hydraul. Div. ASCE, 96(HY3): 619–632.

Greeley, R. and Iversen, J. D., 1985. Wind as a Geological Process. Cambridge Univ. Press, New York, 333 pp.

Gross, T. F. and Dade, W. B., 1991. Suspended sediment storm modelling. Mar. Geol., 99: 343–360.

Hall, D., 1988. Measurements of the mean force on a particle near a boundary in turbulent flow. J. Fluid Mech., 187: 451–466.

Hartnett, J. P. and Hu, R. Y. Z., 1989. The yield stress: An engineering reality. Rheology, 33: 671–679.

Hjulstrøm, F., 1939. Transportation of detritus by moving water. In: P. D. Trask (Editor), Recent Marine Sediments. Am. Assoc. Pet. Geol., Tulsa, pp. 5–31.

Israelachvili, J. N., 1985. Intermolecular and Surface Forces. Academic Press, New York, 296 pp.

Iversen, J. D. and White, B. R., 1982. Saltation threshold on Earth, Mars and Venus. Sedimentology, 29: 111–119.

James, A. E., Williams, D. J. A. and Williams, P. R., 1986. Small strain, low shear rate rheometry of cohesive sediments. In: J. Dronkers and W. van Leussen (Editors), Physical Processes in Estuaries. Springer, New York, pp. 488–502.

James, A. E., Williams, D. J. A. and Williams, P. R., 1987. Direct measurement of static yield properties of cohesive suspensions. Rheol. Acta, 26: 437–446.

Keentok, M., 1982. The measurement of the yield stress of liquids. Rheol. Acta., 21: 325–332.

Kelly, W. E. and Gularte, R. C. 1981. Erosion resistance of cohesive soils. J. Hydraul. Div. ASCE, 107(HY10): 1211–1224.

Kennett, J.P., 1982. Marine Geology. Prentice-Hall, Englewood Cliffs, NJ, 813 pp.

Kirby, J. M., 1988. Rheological characteristics of sewage sludge: a granuloviscous material. Rheol. Acta, 27: 326–334.

Kirchner, J. W., Dietrich, W. E., Iseya, F. and Ikeda, H., 1990. The variability of critical shear stress, friction angle and grain protrusion in water-worked sediments. Sedimentology, 37: 647–672.

Krone, R. B., 1962. Flume studies of the transport of sediment in estuarial shoaling processes: Final report, Hydraul. Eng. Sanit. Eng. Res. Lab., Univ. California, Berkeley.

Krone, R. B., 1963. A study of rheological properties of estuarial sediments. U.S. Army Corps Eng., Comm. Tidal Hydraul., Vicksburg, Miss., Tech. Bull. No. 7.

Kuijper, C., Cornelisse, J. M. and Winterwerp, J. C. 1989. Research on erosive properties of cohesive sediments. J. Geophys. Res., 94: 14341–14350.

Lavelle, J. W. and Mojfeld, H. O. 1987. Do critical stresses for incipient motion and erosion really exist? J. Hydraul. Eng. 113: 370–393.

Lee, S. L., 1982. Aspects of suspension shear flows. Ad. Appl. Mech., 22: 1–65.

Mantz, P. A., 1977. Incipient transport of fine grains and flakes by fluids: extended Shields diagram. J. Hydraul. Div. ASCE, HY6: 601–615.

McCave, I. N., 1984. Erosion, transport, and deposition of fine-grained marine sediments. In: D. A. V. Stow (Editor), Fine-Grained Sediments: Deep-Sea Processes and Facies. Geol. Soc. London Spec. Publ., 15, 35–69.

McCave, I.N., and Swift, S.A., 1976. A physical model for the deposition of fine-grained sediments in the deep sea. Bull. Geol. Soc. Am., 87: 541–546.

Mehta, A. J., 1986. Characterization of cohesive sediment properties and transport processes in estuaries. In: A. J. Mehta (Editor), Estuarine Cohesive Sediment Dynamics. (Lect. Notes on Coastal and Estuarine Studies, 14.) Springer, New York, pp. 290–325.

Mehta, A.J. and Lott, J.W., 1987. Sorting of fine sediment during deposition. In: N.C. Kraus (Editor), Coastal Sediments '87. ASCE, New York, pp. 348–362.

Mehta, A. J., Parchure, T. M., Dixit, J. G. and Ariathurai, R., 1982. Re-suspension of deposited cohesive sediment beds. In: V. S. Kennedy (Editor), Estuarine Comparisons. Academic Press, New York, pp. 591–609.

Middleton, G.V. and Southard, J. B., 1984. Mechanics of Sediment Movement. Soc. Econ. Paleontol. Mineral. Short Course No. 3., 401 pp.

Migniot, C., 1968. Étude des propriétés physiques des differents sediments très fins et de leur comportement sous des actions hydrodynamiques. Houille Blanche, 7: 591–620.

Miller, M. C., McCave, I. N. and Komar, P. D., 1977. Threshold of sediment motion under unidirectional currents. Sedimentology, 24: 507–527.

Miller, R. L. and Byrne, R. J., 1966. The angle of repose for a single grain on a fixed rough bed. Sedimentology, 6: 303–314.

Nowell, A. R. M, Jumars, P. A. and Ekman, J. E., 1981. Effects of biological activity on the entrainment of marine sediment. Mar. Geol., 42: 133–153.

Ohtsubo, K. and Muraoka, K., 1986. Re-suspension of cohesive sediments by currents. Int. Symp. River Sedimentation 3rd, Univ. Mississippi, pp. 1680–1689.

O'Neill, M. E. 1967. A sphere in contact with a plane wall in a slow linear shear flow. Chem. Eng. Sci., 23: 1293–1298.

Overbeek, J. T. G., 1982. Strong and weak points in the interpretation of colloid stability: Adv. Colloid Interface Sc., 16: 17–30.

Owen, M. W., 1975. Erosion of Avonmouth mud. Hydraul. Res. St., Wallingford, Rep. INT 150.

Parchure, T. M. and Mehta, A. J., 1985. Erosion of soft cohesive sediment deposits. J. Hydraul. Eng., 111: 1308–1326.

Partheniades, E., 1965. Erosion and deposition of cohesive soils. J. Hydraul. Div. ASCE, 91(HY1):105–139.

Postma, H., 1967. Sediment transport and sedimentation in the estuarine environment. In: G. H. Lauff (Editor), Estuaries. AAAS, Washington, D.C. Publ. 83, pp. 158–179.

Raudkivi, A. J. and Hutchison, D. L. 1974. Erosion of kaolinite clay by flowing water. Proc. R. Soc. London Ser. A., 337: 537–551.

Raudkivi, A. J. and Tan, S. K., 1984. Erosion of cohesive soils. J. Hydraul. Res., 22: 217–233.

Saffman, P. G., 1965. The lift on a small sphere in a slow shear flow. J. Fluid Mech., 22: 385–400. (Corrigendum. 1968. J. Fluid Mech., 31: 624.)

Self, R. L., Nowell, A. R. M. and Jumars, P. A., 1989. Factors controlling critical shears for deposition and erosion of individual grains. Mar. Geol., 86: 181–199.

Shields, A., 1936. Anwendung der Äehnlichkeits-Mechanik und der Turbulenzforschung auf die Geschiebebewegung. Preussische Versuchsanstalt für Wasserbau und Schiffbau, Berlin, 26, 26 pp.

Singer, J. K. and Anderson, J. B., 1984. Use of total grain-size distributions to define bed erosion and transport for poorly sorted sediment undergoing simulated bioturbation. Mar Geol., 57: 335–359.

Sundborg, A., 1956. The River Klaralven, a study of fluvial processes. Geogr. Ann., 38: 125–316.

Thorn, M. F. C. and Parsons, J. G., 1980. Erosion of cohesive sediments in estuaries: an engineering guide. Int. Symp. Dredging Technology, 3rd (Bordeaux, France), pp. 349–358.

Visser, J., 1970, Measurement of the force of adhesion between submicron carbon-black particles and a cellulose film in aqueous solution. J. Colloid Interface Sc., 34: 26–31.

White, S. J., 1971. Plane bed thresholds of fine-grained sediments. Nature, 228: 152–153

Wiberg, P. L. and Smith, J. D., 1988. Calculations of the critical shear stress for motion of uniform and heterogeneous sediments. Water Resour. Res., 23: 1471–1480.

Williams, D. J. A., 1986. Rheology of cohesive suspensions. In: A. J. Mehta (Editor), Estuarine Cohesive Sediment Dynamics. Springer, New York, pp. 110–125.

Williams, D. J. A. and Williams, P. R., 1989. Rheology of

concentrated cohesive sediments: J. Coastal Res., Spec. Iss. 5: 165–174.

Williams, D. J. A. and Williams, P. R., 1991. Rheology and microstructure of concentrated illite suspensions. In: R. H. Bennett, W. R. Bryant and M. H. Hulbert (Editors), The Microstructure of Fine-Grained Terrigenous Marine Sediments: From Muds to Shale. Springer, New York, pp. 267–271.

Williams, P. R. and Williams, D. J. A., 1989b. Rheometry for concentrated cohesive suspensions. J. Coastal Res., Spec. Iss., 5: 151–164.

Yalin, M. S., 1972. Mechanics of Sediment Transport. Pergamon, New York, 290 pp.

Yoshimura, A. S. and Prud'homme, R. K., 1987. A comparison of techniques for measuring yield stresses. J. Rheology, 31: 699–710.

Zeman, A. J., 1983. Erosion of cohesive sediments: bibliography and annotated abstracts. Natl. Water Res. Inst. (Canada), Hydraul. Div., Stud. No. 354.

Marine Geology, 105 (1992) 299–304
Elsevier Science Publishers B.V., Amsterdam

Short Note

Coast-parallel palaeochannels off southern Namibia

Richard W. Day[a], Alan J. Franzsen[b] and John Rogers[c]

[a]*Geological Survey, Marine Geoscience Unit, University of Cape Town, Rondebosch 7700, South Africa*
[b]*De Beers Marine (Pty) Ltd, P.O. Box 87, Cape Town 8000, South Africa*
[c]*Geology Department, Marine Geoscience Unit, University of Cape Town, Rondebosch 7700, South Africa*

(Received October 24, 1989; revision accepted August 13, 1991)

ABSTRACT

Day, R.W., Franzsen, A.J. and Rogers, J., 1992. Coast-parallel palaeochannels off southern Namibia. Mar. Geol., 105: 299–304.

Boomer and airgun seismic data revealed ancient river channels incised into the middle shelf between Kerbehuk and Chameis Bay, Namibia. This palaeochannel complex, some 15 to 20 metres deep and often several hundred metres wide, cuts into Upper Cretaceous strata and is frequently deeply buried by sediment of Late Quaternary age. The channels were obviously formed during a sea-level regression to below −100 metres as the channels' banks lie at −90 metres off Kerbehuk and at −105 metres west of Chameis Bay. An acoustic blanketing layer south of Kerbehuk and inadequate data prevent knowledge of their true extent, but it is surmised that these channels parallel the present-day coast, perhaps for more than 50 kilometres. The reason for their strange course is not known.

Introduction

Palaeochannels off southern Namibia (Fig. 1) were first reported by Hoyt et al. (1969). These authors traced two infilled valleys from just north of the Orange River's present exit point, five and eight kilometres seaward and showed that the palaeochannels are deeply entrenched into Precambrian schists forming the inner shelf. At their deepest, the palaeochannels' axes lie more than 60 metres and at least 90 metres below sea level respectively; drilling revealed that these particular palaeochannels extend onshore under fluviatile cover (Murray et al., 1970). Isolated palaeochannels have been also recorded off Kerbehuk and Chameis Bay (Birch et al., 1991), and the course of the fossil Kaukausib River has been traced offshore down to −130 metres in Elizabeth Bay, some 40 km south of Luderitz (Murray et al., 1970). This note describes more palaeochannels incised into the seafloor off southern Namibia. These palaeochannels are remarkable in that, unlike those previously reported, they parallel the present-day coastline.

Morphologically the seafloor off southern Namibia is divisible into an inner and middle shelf. The rugged inner shelf is formed from Upper Precambrian volcanics and schists of the Grootderm Suite (South African Committee for Stratigraphy, 1980) whilst the relatively smooth middle shelf is eroded across Upper Cretaceous sedimentary rocks often concealed by an almost horizontal cover of Tertiary sediment (Dingle, 1973; McMillan, 1987). This inner shelf–middle shelf configuration was created through preferential erosion of the younger rocks, especially during sea-level regressions.

The boundary between inner and middle shelf is blurred by sediment deposits of Late Pleistocene and Holocene age (Hoyt et al., 1969; Foster, 1974). Near the Orange River mouth this sediment wedge is more than sixty metres thick and overtops the inner-shelf slope (Fig. 2). A few metres into the sand and mud which constitute the bulk of the

Correspondence to: J. Rogers, Geology Department, Marine Geoscience Unit, University of Cape Town, Rondebosch 7700, South Africa.

0025-3227/92/$05.00 © 1992 — Elsevier Science Publishers B.V. All rights reserved

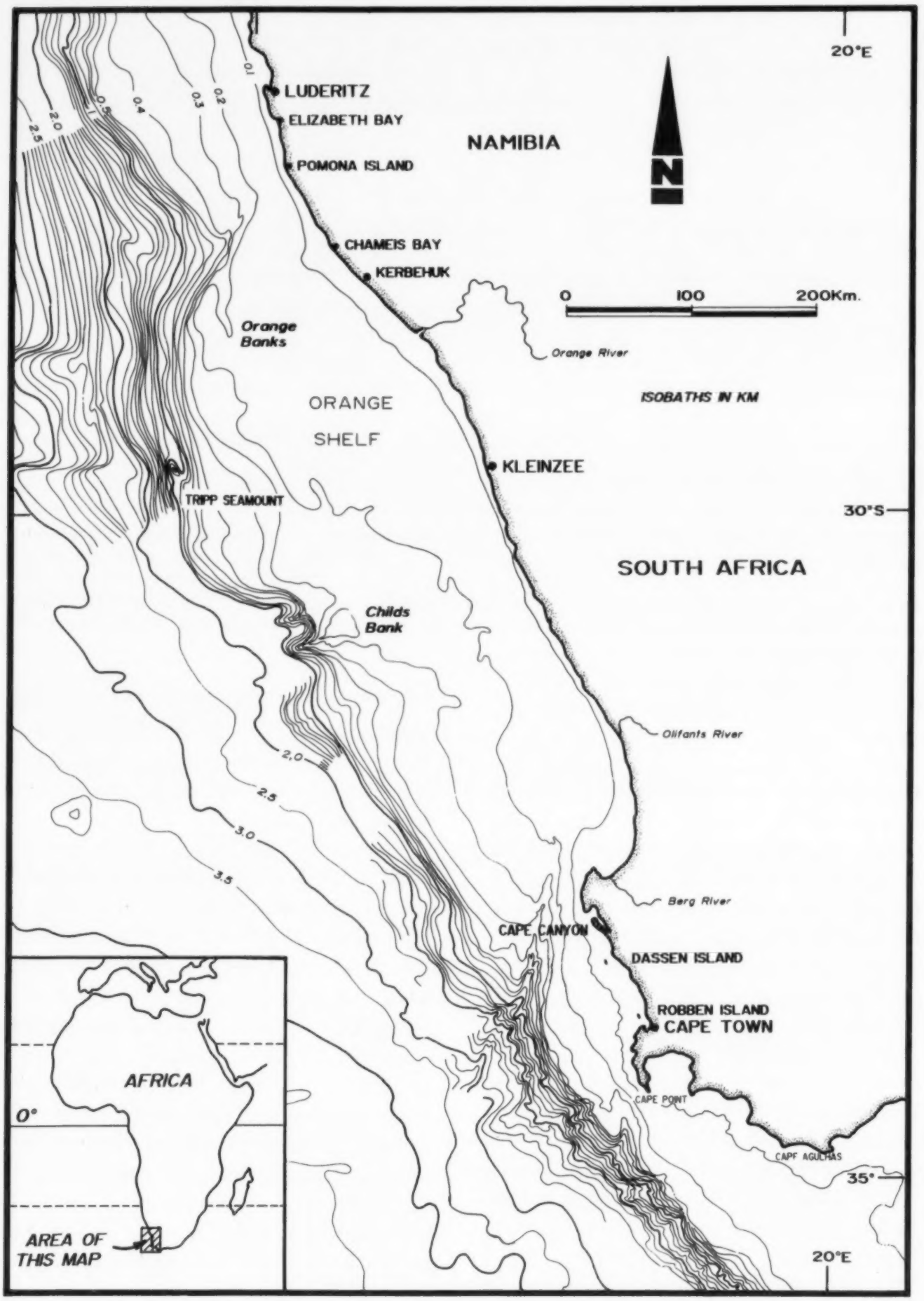

Fig. 1. Study area relative to the south-western coast of Africa.

sediments, is an acoustically impervious zone of gas-charged sediment, the Acoustic Blanketing Layer (ABL) (Foster, 1974). The ABL extends northwards to Kerbehuk, where it disappears as the sediment wedge rapidly thins. From Kerbehuk seismic sources are again able to penetrate through the sediment into bedrock.

Seismic Surveys and Results

Several seismic surveys have been carried out between Kerbehuk and Chameis Bay, of which two—one gathered using a Boomer, the other using an airgun—have records extant. Boomer lines collected in 1971 by Marine Diamond Corporation provide coverage with coast-perpendicular traverses every five kilometres. More widely spaced, but still useful, airgun lines were obtained in 1979 by the Geological Survey (Birch, 1979). Both geophysical surveys relied on the DECCA chain for positioning (Foster, 1973; Birch, 1979).

The Boomer generally penetrated 20 metres or more through the sediment wedge and its records often show detail within the Cretaceous and Tertiary basement. In some places, however, no penetration is obtained beyond basement surface. The airgun lines generally achieved better penetration into bedrock, but at the expense of resolution. Thus, to the extent that the characteristics of the seismic sources differ, the two surveys are complementary.

Two sets of palaeochannels are visible on the seismic records collected off Kerbehuk and Chameis Bay (Figs 3 and 4). These palaeochannels cut into a Late-Pleistocene platform (Fairbridge, 1961; Murray et al., 1970), are several hundred metres wide, and cut ten or twenty metres into the Cretaceous basement. As is seen in Table I, the palaeochannel thalwegs deepen to the north; off Kerbehuk, their bases lie 110 metres below sea level and off Chameis Bay at more than −120 metres. Indistinct returns on seismic line 1320 indicate that one channel may extend down to almost −140 metres.

Correlations between lines indicate that the palaeochannels parallel the present-day coastline (Fig. 4). Faint traces on a Boomer record are testimony for a channel emerging from under the northern edge of the gas layer, but no channels

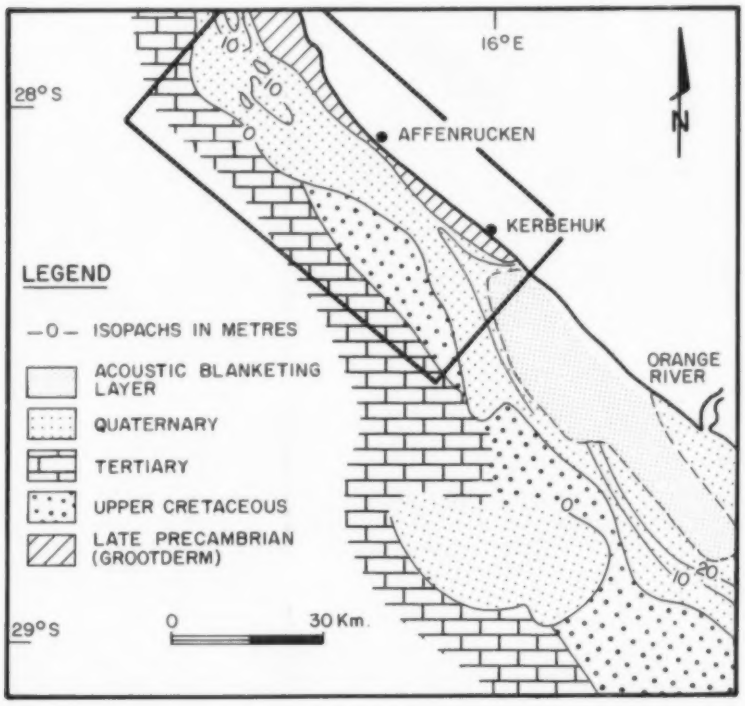

Fig. 2. Basement geology and distribution of Quaternary sediment wedge (after Birch et al., in press). Area covered by Fig. 4 outlined.

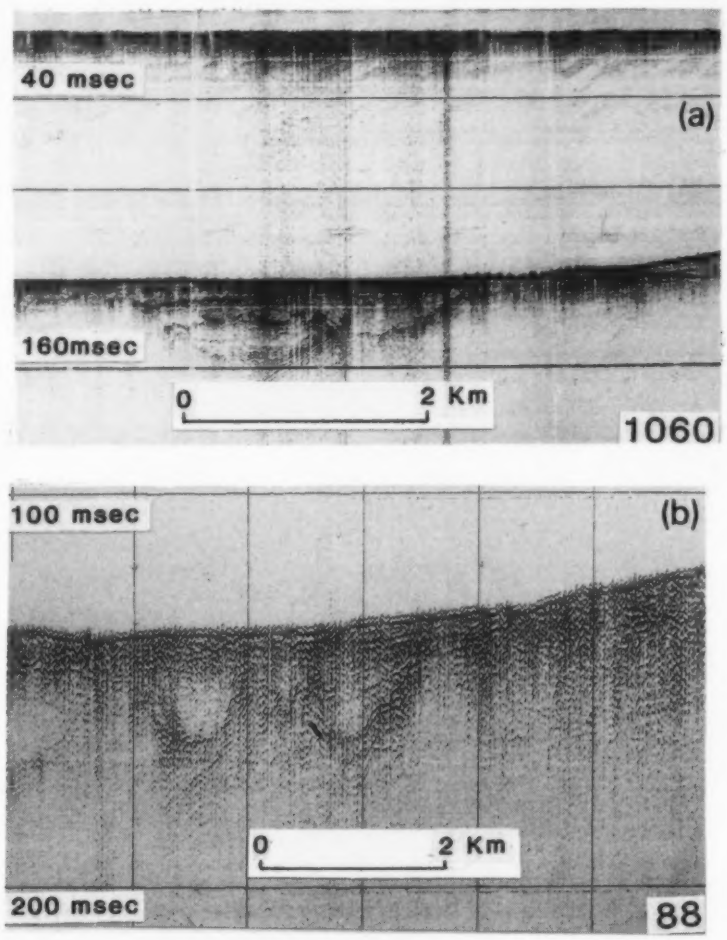

Fig. 3. Examples of boomer (a) and airgun (b) seismic records west of Chameis Bay. See Fig. 4 for locations.

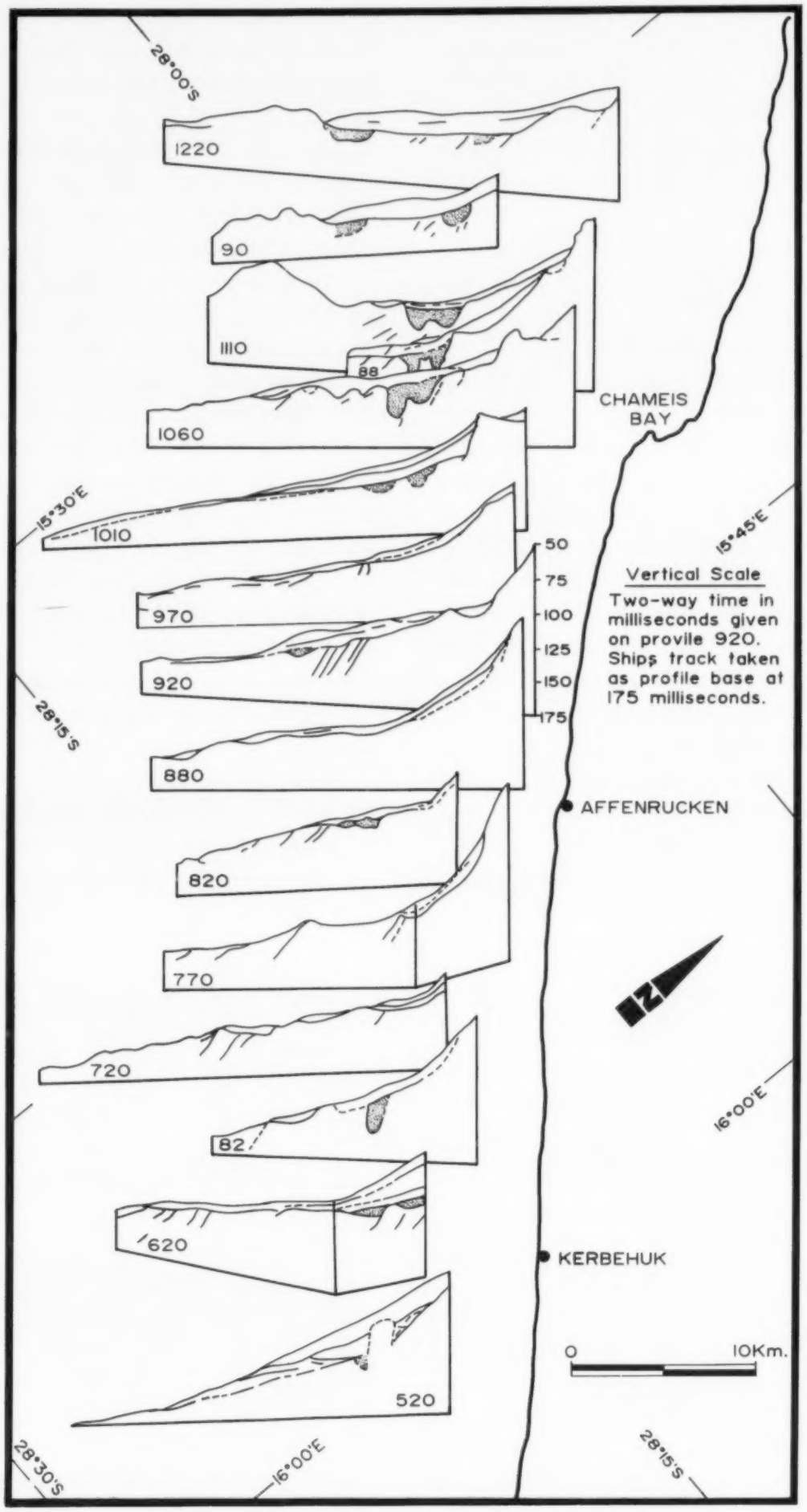

Fig. 4. Isometric projection of seismic-line interpretations. Shaded areas highlight palaeochannels.

TABLE 1

Depth of palaeochannels

Line	A	B	C	Comments
1310	120		138	Track not recovered
1310				Palaeochannels not seen on rerun
1280	106	114	138	Indistinct palaeochannels
1220	96	105	119	
90	89	103	119	Two palaeochannels
1110	87	94	110	Two palaeochannels
88	92	98?	116	Two palaeochannels
1060	90	106	123	Two palaeochannels
1010	91		114	Indistinct palaeochannels
970				Limited penetration
86				No palaeochannels observed
920				Minor palaeochannel
880				Limited penetration
820	69		80	Minor palaeochannel
770				No palaeochannels observed
84				Palaeochannel faintly observed; track coincides with line 770
720				No palaeochannels observed
680	85	92	108	Two palaeochannels
82	87	92	115	One palaeochannel observed; track coincides with line 680
620	77	89	111	Two palaeochannels
80	77	90	108	Two palaeochannels; track coincides with line 620
560				No palaeochannels observed
520	70		111	Palaeochannel partly obscured by acoustic blanketing layer

A = sea floor surface;
B = top of palaeochannel;
C = base of palaeochannel (thalweg),
Depths in metres calculated assuming a sound velocity in water and sediment of 1500 m s^{-1} and 1800 m s^{-1} respectively.

are seen immediately to the north. Opposite Kerbehuk, however, both airgun and Boomer lines show two prominent channels, which together extend five kilometres. From Kerbehuk to just south of Chameis Bay, seismic evidence for palaeochannels is equivocal but the absence of palaeochannels may be more apparent than real, dependent on equipment settings. For example, line 1350 in the north was run twice, one line recording the palaeochannels and one not (Table 1). Finally, off Chameis Bay, the palaeochannels can be traced for over 20 kilometres parallel to the coast although, according to the bedrock depth map of Foster (1974) (Fig. 4), the western channel's continuity is broken at −115 metres.

In general the palaeochannels are infilled with acoustically structureless sediment capped by an irregular surface occasionally pitted with shallow depressions, which are possibly minor channels themselves. This irregular cap stands approximately level with the basement on either side and is buried underneath at least a few metres of more recent sediment.

Discussion

The palaeochannels formed no earlier than late Pleistocene times, the age of the platform into which they are incised (Fairbridge, 1961; Murray et al., 1970). They were created during at least one sea-level regression to between −100 metres (palaeochannel top) and −140 metres (palaeochannel thalweg). Sea-level retreats to about −130 metres occurred during late Eemian and Würm IIb times (e.g. Chappell and Shackleton, 1986) and it is possible that the palaeochannels were incised during these particular events.

From the breadth of the palaeochannels and their thalweg depths, it is clear that the palaeochannels were cut by major northward-flowing river(s). If the palaeochannels are discontinuous, i.e. the gap between Kerbehuk and Chameis Bay is real, then they are the remains of several major rivers, which once flowed from the interior. No remnants of these rivers are known onshore. Alternatively, if the palaeochannels were or are continuous, then we are looking at a major northward-flowing river with its source south of Kerbehuk, towards the Orange River.

There is no obvious reason why the rivers paralleled the palaeo-(and present-day) coastline instead of flowing directly to the sea. Outcrops of Precambrian basement, probably the Grootderm Suite, may have guided the river's course in the north, but there is no physical constraint now evident elsewhere. A possible answer could lie in a back-barrier lagoon (landward of a beach-barrier) that several authors suggest, for textural (mud-sand-gravel distribution) and faunal (recovery of estuarine and sheltered-water mollusca) reasons, developed immediately prior to the Flandrian Transgression (Foster, 1973; Petersen, 1983; Price, 1984; McMillan, 1987). At that or other times,

when similar conditions prevailed, this beach-barrier may have provided the physical constraint, when it formed a temporary topographic high while exposed by a further retreat in sea level. Renewed advance by the sea overwhelmed and largely destroyed this barrier, burying the remains of the channels.

Acknowledgements

The Anglo American Corporation of South Africa, De Beers Marine (Pty) Ltd and the Director of the Geological Survey of South Africa are thanked for permission to use their data.

References

Birch, G.F., 1979. Cruise Report for Cruise 398, 12 to 22 November, 1979. Rep., Geol. Surv. S. Afr., 11 pp. (Unpubl.).

Birch, G.F., Day, R.W. and Du Plessis, A., 1991. The Quaternary marine deposits on the continental shelf off the west coast of South Africa. Bull. Geol. Surv. S. Afr., 98: 1–14.

Chappell, J. and Shackleton, N.J., 1986. Oxygen isotopes and sea level. Nature, 324: 137–140.

Dingle, R.V., 1973. The geology of the continental shelf between Luderitz and Cape Town, with special reference to Tertiary strata. J. Geol. Soc. London, 129: 337–363.

Fairbridge, R.W., 1961. Eustatic Changes in Sealevel. In: L.H. Ahrens (Editor), Physics and Chemistry of the Earth. Pergamon Press, London, 4: 99–185.

Foster, R.W., 1973. Reconnaissance geological investigation of the inshore sediment body March 1972–April 1973. Internal Report Mar. Diamond Corporation, 7 pp.

Foster, R.W., 1974. Report on the vibrocore programme March 1972 to January 1974. Internal Rep. Mar. Diamond Corporation, 35 pp.

Hoyt, J.H., Oostdam, B.L. and Smith, D.D., 1969. Offshore sediments and valleys of the Orange River (South and South-West Africa). Mar. Geol., 7: 69–84.

McMillan, I.K., 1987. Late Quaternary foraminifers from the southern part of offshore South West Africa/Namibia. Ph.D. Thesis, Univ. College Wales, Aberystwyth, 551 pp. (2 volumes). (Unpubl.)

Murray, L.G., Joynt, R.H., O'Shea, D.O'C., Foster, R.W. and Kleinjan, L., 1970. The geological environment of some diamond deposits off the coast of S.W.A. In: F.M. Delany (Editor), The Geology of the East Atlantic Continental Margin. Rep. Inst. Geol. Sci., 70(16): 119–141.

Petersen, N., 1983. Vibrocore study of sediments on the inner and middle continental shelf between the Orange River and Chameis Bay—South West Africa. B.Sc.(Hons) Proj., Geol. Dep., Univ. Cape Town, 36 pp. (Unpubl.).

Price, G.K., 1984. Lithofacies and biofacies in vibrocores from Quaternary sediments on the inner shelf north of the Orange River. B.Sc.(Hons) Proj., Geol. Dep., Univ. Cape Town, 35 pp. (Unpubl.).

South African Committee for Stratigraphy (SACS), 1980. Stratigraphy of South Africa. Part 1. Lithostratigraphy of the Republic of South Africa, South West Africa/Namibia, and the Republics of Bophuthatswana, Transkei and Venda. Handb. S. Afr. Geol. Surv., 8, 690 pp.

Marine Geology, 105 (1992) 305–308
Elsevier Science Publishers B.V., Amsterdam

Discussion

Clay mineralogy of Visakhapatnam shelf sediments, east coast of India: comment

N.V.N. Durga Prasad Rao

National Institute of Oceanography, Regional Centre, Visakhapatnam-530 023, 52, Kirlampudi Layout, India[1]

(Received October 30, 1989; accepted September 6, 1991)

In Murty and Rao's recent study of the clay mineralogy of the shelf sediments off Visakhapatnam (Marine Geology, 88: 153–165) I have noticed contradictory statements, analytical drawbacks, peculiar results which disagree with other studies from the same area, and inferences not supported by the data.

On p. 155, in the section "Earlier Studies" it was stated that "the easterly flowing rivers of the peninsula contribute detritus from humid tropical weathering to the western part of the bay". Under humid tropical conditions, chemical weathering results in high leaching of alkalies and alkaline earths and the dominant clay mineral that forms is the kaolinite. The peninsular rivers mentioned by the authors contribute abundant illite, chlorite and smectite-dominated clays.

In the X-ray diffraction techniques, the procedures adopted to identify and confirm the presence of chlorite and kaolinite were not mentioned. Further, the method used to calculate the chlorite percentage was not given. The procedure for semi-quantitative estimation refers only to the three clay minerals, but the percentages of chlorite were presented in table 3.

In the results section, the statement that illite is the dominant clay mineral in the shelf sediments is not supported by the data presented in table 1. Indeed, no mineral has a characteristically high abundance. Critical observation of the table shows that more than 30% of the surface samples, 35% between 10 and 20 cm, 60% between 30 and 40 cm and 35% between 50 and 60 cm, have more smectite than illite. Further, kaolinite is dominant in some surface sediments. Further, the data presented in the table also contradict the statement that "the concentration of illite is dominant over kaolinite and smectite at the various depths" (page 164, second column, second paragraph). The authors report the absence of chlorite in the shelf sediments, but earlier investigations (Kolla and Biscaye, 1973) reported chlorite in these sediments. Purnachandra Rao et al. (1988) have also observed chlorite in shelf sediments off Visakhapatnam. In addition, the river sediments (tables 3 and 4) which ultimately reach the sea contain chlorite too. Therefore, the absence of chlorite reported by the authors seems to be an analytical lapse. They neither tried a slow scan nor other procedures to identify chlorite.

In a semi-quantitative analysis a variation of a few percent does not make any difference. Therefore, the decreasing order of abundance of the clay minerals given by the authors simply based on the average values is not justified. An anomalous value in a sample can tilt the whole picture when only averages are considered.

In explaining the results, more stress was given to the regional distribution of clay minerals in the surface and subsurface sediments of the shelf. Such patterns provide information on the differences in the nature of the transport of the various clay minerals. Further, regional vertical variations throw some light on the diagenetic and the climatic variations in the source regions with geological time. The authors did not discuss these two points, although they did present many figures depicting

[1] Present address: Department of Geology, Kakatiya University, Warangal 506009, India.

0025-3227/92/$05.00 © 1992 — Elsevier Science Publishers B.V. All rights reserved

the distribution patterns of the clay minerals at various depths in the shelf. Attributing the observed regional variations to the circulation pattern (no pattern was given, incidently) over the shelf is baseless. Vertical variations in the clay minerals were not properly explained.

In the absence of diagenesis, the significant vertical variations in the clay minerals observed in the shelf sediments should have been produced by differences in the sources. There are no reported drastic climatic changes in the Holocene that could produce different clay minerals in the source regions within a short time interval.

The reported abundance of smectite in the nearshore sandy sediments contradicts the observation of Purnachandra Rao et al. (1988) who report abundant illite and kaolinite in the sandy sediments and smectite in the finer outer shelf sediments. Further, Reddy and Mohan Rao (1989) recorded high concentrations of kaolinite + chlorite in the nearshore sandy sediments of Visakhapatnam. The predominant kaolinite was considered to have been derived from the coastal red sediments, which are rich in kaolinite (Durga Prasad Rao and Srihari, 1980). Purnachandra Rao et al. consider that high energy conditions in the sandy zone prevent the deposition of relatively finer smectite, which will be carried to and deposited in the low energy regions along with finer sediments. Further, the larger particle size of kaolinite and illite and early flocculation of these minerals (Whitehouse et al., 1960) in saline conditions result in the enrichment of these minerals in the nearshore zone. In the light of the above, the abundant smectite reported by the authors in the nearshore sandy sediments needs a reasonable explanation.

In discussing the source of the clays (p. 161) Murty and Rao state that the khondalites are frequently covered by thick laterite and bauxites and the weathered products of these rocks are transported to the study area. Laterization is a product of intense chemical weathering under humid tropical climates and under these conditions the clay mineral that is ultimately produced is kaolinite. Durga Prasad Rao and Srihari (1980) reported abundant (>60%) kaolinite in the red soils of the Visakhapatnam coastal region. These red soils occupy large tracts of the coastal region and contribute significant amounts of kaolinite to the shelf. Even in the Gostani and Sarada rivers, which are the sources of sediments to the shelf, kaolinite constitutes a considerable proportion of the clay minerals. It is surprising that Murty and Rao record kaolinite as the least abundant clay mineral in the shelf sediments. In order to justify their results, the fate of kaolinite should have been explained.

As stated by the authors (p. 164), kaolinite is not impoverished in the Sarada, Gostani, Vamsadhara and Nagavali river sediments. In none of the samples, less than 30%. In Gostani River kaolinite has almost the same abundance as illite. Further, in two samples from the River Vamsadhara it is almost equal in abundance to illite (42% kaolinite, 46% illite). In the River Nagavali, many of the samples contain more kaolinite than illite (table 4).

Proposing a northward transport of the sediments along the Visakhapatnam coast (p. 164), the authors simultaneously consider a source of illite and kaolinite from rivers joining the bay to the north of the study area. Because of the absence of chlorite (doubtful) and the general decrease in kaolinite, they inferred that the influence of the northern rivers is negligible. Does the kaolinite decrease mean a southward movement? Does the north-flowing current terminate at Visakhapatnam and does not carry illite and kaolinite-suspended loads of the study area northwards? Added to the confusion, table 4 shows that the Mahanadi sediments have more smectite than illite, and this does not preclude a southern source for the smectite.

In addition, as stated by the authors, if Godavari River smectite-rich sediment is diluted by the Sarada and Gostani River sediment load containing about 85% kaolinite and illite, the more than 67% smectite in the nearshore shelf sediments must be an analytical error.

Conclusion (3) is rather drastic. The outer-shelf illite-dominant clays are contributed by the rivers (Sarada and Gostani) and streams draining the Eastern Ghats. In the first place, all these rivers and streams are ephemeral and their contribution to the shelf is minimal. Further, sediments from

these sources will be subjected to northward drift like those of the Godavari River. Even if it is assumed that somehow these clays escaped the northerly currents, they should instead be deposited on the inner shelf. However, the high smectite contents there show no such deposition. On bypassing the inner shelf, the clays should reach the outer shelf and be deposited there. The authors should have provided evidence in support of such a sedimentation type on the shelf. If the inner sand zone is considered to be a high-energy environment which prevents clay deposition, the same should apply for the smectite-dominant clay of the Godavari River.

Conclusion (5) states that "Provenance is the main controlling factor on the clay mineralogy of the shelf sediments". On the basis of this conclusion, the regional variations would be due to different sources through geological time. However, at one location regional variations were attributed to the surface circulation patterns in the shelf, while at another a mixing (dilution) of clays from one source with another is postulated. These two attributions contradict conclusion (5).

I conclude that the authors have not acquired their data properly and have misinterpreted the results, in particular ignoring previous investigations carried out in the area.

Reply to comment on "Clay mineralogy of Visakhapatnam shelf sediments, east coast of India"

P.S.N. Murty

Geological Survey of India, 90, Kirlampudi Layout, Visakhapatnam-530023, India

(Received November 6, 1990; accepted September 6, 1991)

From the comments offered by Mr. N.V.N. Durga Prasada Rao it appears that he may not be fully aware of the different types of investigations carried out on the sea bed sediments in the Bay of Bengal. The comments appear to be mostly based on his limited knowledge of the coastal landforms and adjoining lagoons, and the physico-chemical environments in the different domains (terrestrial and marine) have not been properly evaluated by him before putting forth his comments. We offer below our reply to the comments made:

(1) The contention of Mr. Rao that Kolla and Biscaye (1973) reported chlorite in the shelf sediments is factually incorrect since their study was confined to deep Bay of Bengal sediments, which are dominated by illite and chlorite. There is no mention of shelf sediments at all anywhere in Kolla and Biscaye's paper.

(2) The clay mineral distribution maps of Kolla and Biscaye (1973) and Goldberg and Griffin (1970) indicate that Godavari River-borne smectite has been transported as far north as off Kalingapatnam by surface currents.

(3) The statement that Purnachandra Rao et al. (1988) and Reddy and Mohan Rao (1989) have studied the nearshore sandy sediments is also incorrect as all their samples are from the area beyond the sand zone (more than 30 m deep). They have not studied any samples of nearshore sandy sediments (below the 30 m depth), where the smectite domination was reported by us.

(4) It was pointed out that we have not given the procedure followed for X-ray diffraction study. On p. 156, it is clearly stated that the procedures adopted for X-ray diffraction are after Biscaye (1965). The analysis was carried out at Scripps Institution of Oceanography, La Jolla, California by the junior author (K.S.R. Rao) himself.

(5) Mr. Rao observed that red sediments occupy large tracts of the coastal region and contribute significant amounts of kaolinite to the shelf. It should be clarified here that red sediments occur only as localised pockets along the coastal tract. The possibility of a supply of appreciable amounts of kaolinite by these red sediments is remote because (a) the existing pattern of drainage does not contribute to any such influx and (b) kaolinite is unstable in marine waters, where the pH is generally more than 7.

(6) The contention of Mr. Rao that kaolinite is the dominant clay mineral to form under humid tropical conditions is not correct. Depending on the lithology of the source area, different clay minerals form during weathering, including kaolinite as shown in table 3, of our paper. Kaolinite is unstable at high pH values in the marine environment, and apparently the relative amounts of illite and smectite tend to increase at its expense.

References

References for the comment *and* the reply

Biscaye, P.E., 1965. Mineralogy and sedimentation of recent deep-sea clay in the Atlantic Ocean and adjacent seas and oceans. Bull. Geol. Soc. Am., 76: 803–832.

Durga Prasad Rao, N.V.N. and Srihari, Y., 1980. Clay mineralogy of the late Pleistocene Red Sediments of the Visakhapatnam region, east coast of India. Sediment. Geol., 27: 213–227.

Goldberg, E.D. and Griffin, J.J., 1970. The sediments of the northern Indian Ocean. Deep-Sea Res., 17: 513–537.

Kolla, V. and Biscaye, P.E., 1973. Clay mineralogy and sedimentation in the eastern Indian Ocean. Deep-Sea Res., 20: 727–738.

Purnachandra Rao, V., Reddy, N.P.C. and Rao, Ch.M., 1988. Clay mineral distribution in the shelf sediments off the northern part of the east coast of India. Cont. Shelf. Res., 8: 145–151.

Reddy, N.P.C. and Mohan Rao, K., 1989. Clay mineral distribution from Bhimunipatnam to Pudimadaka along central eastern continental shelf of India. Ind. J. Mar. Sci., 18: 128–130.

Whitehouse, G., Jefferies, L.M. and Debbercht, J.D., 1960. Differential settling tendencies of clay minerals in saline waters. Clays Clay Miner., 7: 1–79.

NOTES FOR ELECTRONIC TEXT PREPARATION

1. General

The word-processed text should be in single column format. Keep the layout of the text as simple as possible; in particular, do not use the word-processor's options to justify the text or to hyphenate the words.

2. Text preparation

The electronic text should be prepared in a way very similar to that of conventional manuscripts (see also Guide for Authors). The list of references, tables and figure captions should be compiled separately from the main text. Do *not* reserve space for the figures and tables in the text; instead, indicate their approximate locations, either directly in the electronic text or on the manuscript.

3. Submission

The final text should be submitted both in manuscript form and on diskette. Use standard 3.5″ or 5.25″ diskettes for this purpose. Both double density (DD) and high density (HD) diskettes are acceptable. Ensure, however, that the diskettes are formatted according to their capacity (HD or DD) before copying the files onto them.

Storage of the main text, list of references, tables and figure captions in separate text files with clearly identifiable file names (for example, with extensions .TXT, .REF, .TBL, .FIG) is required.

The format of the files depends on the wordprocessor used. Texts made with DEC WPS PLUS, DisplayWrite, First Choice, IBM Writing Assistant, Microsoft Word, Multimate, PFS:Write, Professional Writer, Samna Word, Sprint, Total Word, Volkswriter, Wang PC, WordMARC, WordPerfect, Wordstar, or files supplied in DCA/RFT format can be readily processed. In all other cases the preferred text format is ASCII.

Essential is that the name *and* the version of the wordprocessing program and the type of computer on which the text was prepared is clearly indicated on the diskette label or the accompanying checklist.

Authors are encouraged to ensure that **the disk version and the hardcopy must be identical**. Discrepancies can lead to proofs of the wrong version being made.

Illustrative material (original figures or high-quality glossy prints, or photographs showing sharp contrast) should be included separately.

ELECTRONIC TEXT CHECKLIST

Please complete this list where appropriate and include it with the diskette.

Journal : _____

Title : _____

_____

Author(s) : _____

Computer

☐ IBM compatible
☐ Macintosh[1]

Diskette

☐ formatted with MS-DOS/PC-DOS
☐ formatted with Macintosh OS

File format (if different from wordprocessor's original format)

☐ ASCII
☐ DCA/RFT
☐ DEC/DX

Wordprocessor

☐ DEC WPS PLUS[2] version: _____
☐ DiplayWrite[3] version: _____
☐ First Choice version: _____
☐ IBM Writing Assistant version: _____
☐ Microsoft Word version: _____
☐ Multimate version: _____
☐ PFS:Write version: _____
☐ Professional Writer version: _____
☐ Samna Word version: _____
☐ Sprint version: _____
☐ Total Word version: _____
☐ Volkswriter version: _____
☐ Wang PC version: _____
☐ WordMARC version: _____
☐ WordPerfect version: _____
☐ Wordstar version: _____

☐ Other (specify)[4]: _____

Diskette contents : _____

_____

_____

Remarks : _____

_____

_____

[1] In view of the further text processing on a MS-DOS compatible system submission of text files on MS-DOS formatted diskettes is recommended.
[2] Files should be submitted in DX format (option "CV" from the DEC-WPS Document Processing Menu).
[3] Files created with DisplayWrite 4 should be submitted in DCA/RFT format by means of the DisplayWrite "Convert Documents" utility.
[4] Submission of the text files in ASCII format is strongly recommended.

Deep Convection and Deep Water Formation in the Oceans

Proceedings of the International Monterey Colloquium on Deep Convection and Deep Water Formation in the Oceans, US Naval Postgraduate School, Monterey, CA, USA, 26-30 March 1990

edited by **P.C. Chu** *and* **J.C. Gascard**

Elsevier Oceanography Series Volume 57

THIS BOOK contains articles presenting current knowledge about the formation and renewal of deep waters in the ocean. These articles were presented at an international workshop at the Naval Postgraduate School in Monterey in March 1990.

It is the first book entirely devoted to the topic of deep water formation in which articles have been both selected and reviewed, and it is also the first time authors have addressed both surface and deep mixed layers. Highlighted are: past and recent observations (description and analysis), concepts and models, and modern techniques for future research. Thanks to spectacular advances realised in computing sciences over the last twenty years this volume includes a number of sophisticated numerical models. Observational as well as theoretical studies are presented and a clear distinction is established between open-ocean deep convection and shelf processes, both leading to deep- and bottom-water formation. The main subject addressed is the physical mechanism by which the deep water in the ocean can be renewed. Ventilation occurs at the surface in areas called *"the gills"*, where water is mixed and oxygenated before sinking and spreading in the abyss of the deep ocean. This phenomenon is a very active area for both experimentalists and theoreticians because of its strong implications for the understanding of the world ocean circulation and Earth climate. This major theme sheds light on specific and complex processes happening in very restricted areas still controlling three quarters of the total volume of the ocean. All articles include illustrations and a bibliography. This book will be of particular interest to physical oceanographers, earth scientists, environmentalists and climatologists.

Contents: Introduction *(J.C. Gascard, C.A. Collins)*. Geophysics of Deep Convection and Deep Water Formation in Oceans *(P.C. Chu)*. Two Stable Modes of Southern Ocean Winter Stratification *(A.L. Gordon)*. Open Ocean Convection in the Southern Ocean *(D.G. Martinson)*. Relict Convective Features in the Weddell Sea *(R.D. Muench)*. Forced Convection in the Upper Ocean Near Fram Strait in Later Winter *(M.G. McPhee)*. Eddy-Related Winter Convection in the Boreas Basin *(O.M. Johannessen, S. Sandven, J.A. Johannessen)*. Upper Ocean Structures in the South-Western Iceland Sea: A Preliminary Report *(J.C. Scott, P.D. Killworth)*. An Approach to Brine and Freshwater Fluxes Interpreted from Radar and Microwave Radiometer Data *(F.D. Carsey)*. Formation of Baffin Bay Bottom and Deep Waters *(R.H. Bourke, R.G. Paquette)*. Open Ocean Convection and Deep Water Formation Revisited in the Mediterranean, Labrador, Greenland, and Weddell Seas *(J.C. Gascard)*. Equatorward Currents in Temperatures 1.8 - 6.0 °C on the Continental Slope in the Mid-Atlantic Bight *(D.R. Watts)*. Enhancements to Deep Turbulent Entrainment *(R.W. Garwood, Jr.)*. Convection in Lake Baikal: An Example of Thermobaric Instability *(E.C. Carmack, R.F. Weiss)*. The Northern Adriatic Sea as a Prototype of Convection and Water Mass Formation on the Continental Shelf *(P. Malanotte-Rizzoli)*. Thermohaline-Driven Deep Water Formation in the Northwestern Mediterranean Sea *(G. Madec, M. Crepon)*. Vertical Cells Driven by Vortices: A Possible Mechanism for the Preconditioning of Open-Ocean Deep Convection *(P.C. Chu)*. Modeling the Geostrophic Adjustment and Spreading of Waters Formed by Deep Convection *(A.J. Hermann, W.B. Owens)*. A Buoyancy-Driven Thermocline Model *(W.K. Dewar)*. Non-Hydrostatic Ocean Modelling for Studies of Open-Ocean Deep Convection *(R. Brugge, H.L. Jones, J.C. Marshall)*. Convection in the Labrador Sea: Community Modelling Effort *(CME)* Results *(E.D. Skyllingstad, D.W. Denbo, J. Downing)*. Small and Mesoscale Convection as Observed in the Laboratory *(J.A. Whitehead)*. Meteorological Triggers for Deep Convection in the Greenland Sea *(P.S. Guest, K.L. Davidson)*. Some Early Results of the Humidity Exchange over the Sea Main Experiment *(S.D. Smith)*.

1991 xii + 382 pages
Price: US $ 110.50 / Dfl. 215.00
ISBN 0-444-88764-4

Elsevier Science Publishers
P.O. Box 1930, 1000 BX Amsterdam, The Netherlands
P.O. Box 882, Madison Square Station,
New York, NY 10159, USA

The Dutch Guilder price is definitive, US $ prices are given for convenience only and are subject to exchange rate fluctuations.

World Atlas of Holocene Sea-Level Changes

by **P.A. Pirazzoli**, *C.N.R.S., Paris, France*

assisted by: **J. Pluet**, *CNRS, Laboratoire de Géographie Physique, Meudon-Bellevue,*

Elsevier Oceanography Series Volume 58

1991 300 pages
Price: US $ 100.00 / Dfl. 195.00
ISBN 0-444-89086-6

This timely study is concerned with the current record of sea-level changes during the past 10,000 years; their rates, and our ability to estimate these changes accurately. The author begins with an extensive introduction to the subject, covering the historical background and the possible causes of sea-level changes and the main methods used to reconstruct former sea-level positions. The second and main part of the Atlas provides a worldwide review of Holocene sea level changes by assembling some 800 local relative sea-level curves, deduced from field data from all parts of the world, and comparing these with over 100 curves predicted by geophysical models. This data is compiled in 77 regional plates, each containing 4-20 relative sea-level curves drawn to the same scale. These plates enable a visual assessment of geological trends in sea-level during the Holocene to be made.

Comparing this data with trends deduced from tide gauges and near-future trends predicted by climate models, should enable more accurate assessment of near future sea-level changes on a local scale. The regional plates are fully annotated with locations, authors' names, year of publication and some indicative values of the spring tidal range in the region, as well as an accompanying text of comments.

Finally, the author provides a state of the art review, proposes improvements in methodology and suggests directions for further study. An extensive bibliography of over 750 references, and two indexes complete the study. This comprehensive work contains data and interpretations of value to all those with an interest in regional geography, climatology, sea-level change, and environmental science.

Contents: **Part 1.** Historical background. Possible causes of sea-level changes. How sea-level changes are studied. Sea-level indicators. Dating Holocene shorelines. The accuracy of sea-level curves. Sea-level predictions. Aims of this Atlas. How to consult the Atlas. **Part 2: Regional Sea-Level Changes.** Svalbard. Fennoscandia. Norway. North Norway - Kola Peninsula. Central Norway. Southwest Norway. Oslofjord. Denmark - The Kattegat. Southwest & South Swe;en. Southeast Sweden. Northeast Sweden. Finland. East Baltic Coasts. Germany: Baltic. Germany: North Sea. The Netherlands. British Isles: Introduction. Southeast Britain. Scotland. Ireland. Northwest England. North and West Wales. Bristol Channel. English Channel. British Isles. Atlantic France. The Mediterranean. Central Mediterranean. The Aegean. The Levant, the Black Sea, the Caspian Sea. West Africa. West Indian Ocean. Northeast Indian Ocean. Vietnam - South China. East China - Korea. Arctic & Pacific U;SR. Japan. North Japan. Central Japan. West Japan. South Japan. Taiwan - Micronesia. Melanesia. Polynesia. New Zealand. Australia. The west coasts of the Americas. Antarctica. The east coasts of South America. West Indies - Bermuda. Guiana - Central America. The Gulf of Mexico and the Atlantic shelf of the USA. The Atlantic coast of the USA. Florida - Carolina. Virginia - Delaware. New Jersey, New York, Connecticut. Massachusetts. New Hampshire - Maine. Development and deglaciation of the Laurentide ice sheet. New Brunswick - Nova Scotia. Prince Edward Island. St. Lawrence River & Gulf. New;oundland Island. Labrador. Hudson Bay. Foxe Basin - Baffin Island. Beaufort Sea - Melville I. - Somerset I. Ellesmere and Devon Islands. Greenland **Part 3. Conclusions. Part 4. References.** Locality Index. Author Index.

ELSEVIER SCIENCE PUBLISHERS
P.O. Box 1930, 1000 BX Amsterdam, The Netherlands
In North America: P.O. Box 822, Madison Square Station, New York, NY, 10159, USA

(continued from inside front cover)

Note to contributors
A detailed *Guide for Authors* is available upon your request, and will also be printed in the first volume to appear each year. You are kindly asked to consult this guide. Please pay special attention to the following notes:

Language
The official language of the journal is English, but occasional articles in French and German will be considered for publication. Such articles should start with an abstract in English, headed by an English translation of the title. An abstract in the language of the paper should follow the English abstract. English translations of the figure captions should also be given.

Preparation of the text
a) The manuscript should be typewritten with double spacing and wide margins and include at the beginning of the paper an abstract of not more than 500 words. Words to be printed in italics should be underlined. The metric system should be used throughout.
b) The title page should include, the name(s) of the author(s) and their affiliations.

Abstract
The abstract must be an informative statement of the content of the paper, explaining what the problem is, the methods used (when appropriate), a statement of the results, and the main conclusions. Constructions using phrases such as "this paper discusses", "are described" and "is reported" have no place in an abstract: by reading the abstract, the reader should be able to understand the essential qualities of the paper without referring to the paper itself. See K.K. Landes (Bull. Am. Assoc. Pet. Geol., 1951, Vol. 35, p. 1660) for a concise statement on how to write a good abstract.

References
a) References in the text start with the name of the author(s), followed by the publication date in parentheses.
b) The reference list should be in alphabetical order and on sheets separate from the text.

Tables
Tables should be compiled on separate sheets. A title should be provided for each table and they should be referred to in the text.

Illustrations
a) All illustrations should be numbered consecutively and referred to in the text.
b) Drawings should be completely lettered, the size of the lettering being appropriate to that of the drawings, but taking into account the possible need for reduction in size (preferably not more than 50%). The page format of *Marine Geology* should be considered in designing the drawings.
c) Photographs must be of good quality, printed on glossy paper.
d) Figure captions should be supplied on a separate sheet.
e) If contributors wish to have their original figures returned this should be requested in proof stage at the latest.
f) **Colour figures** cannot normally be accepted unless the reproduction costs are to be met by the author. As a rough guide, the reproduction costs for a one-page figure are ca. Dfl. 2150 (inc. tax). Please consult the publisher for further information.

Proofs
One set of proofs will be sent to the author, to be checked for printer's errors. In case of two or more authors please indicate to whom the proofs should be sent.

Reprints
Fifty reprints of each article published are supplied free of charge. Additional reprints can be ordered on a reprint order form, which is included with the proofs.

Submission of manuscripts
a) Manuscripts originating in the Americas and Far East should be submitted in triplicate to Dr. D.A. McManus, Department of Oceanography, University of Washington, Seattle, Washington 98105, U.S.A. All other manuscripts should be sent in triplicate to the Editorial Office *Marine Geology*, P.O. Box 1930, 1000 BX Amsterdam, The Netherlands.
b) Illustrations should also be submitted in triplicate. One set should be in a form ready for reproduction: the other two may be of lower quality.
c) Authors are requested to submit the names and addresses of four potential referees with their manuscripts.
d) Letter-type contributions should be submitted in triplicate to the Editorial Office *Marine Geology, Letter Section*, P.O. Box 1930, 1000 BX Amsterdam, The Netherlands. Contributions for this section should not exceed 8 printed pages and should be complete in themselves. No foldout illustrations can be accepted. The manuscripts received will be published ca. *three months* after acceptance. In order to achieve rapid publication, no proofs will be sent to the authors. Manuscripts should therefore be prepared with the greatest possible care.
e) **The indication of a FAX number on submission of the manuscript could assist in speeding communications. The FAX number for the Amsterdam office is: 020-5862696.**
f) In order to enable publication as quickly as possible after acceptance, authors are encouraged to submit the final text also on a 3.5″ or 5.25″ diskette. Both double density (DD) and high density (HD) diskettes are acceptable. Make sure, however, that the diskettes are formatted according to their capacity (HD or DD) before copying the files onto them. As with the requirements for manuscript submission, the main text, list of references, tables and figure captions should be stored in separate text files with clearly identifiable file names. The format of these files depends on the wordprocessor used. Texts written with DisplayWrite, MultiMate, Microsoft Word, Samna Word, Sprint, Volkswriter, Wang PC, WordMARC, WordPerfect and Wordstar or supplied in DCA/RFT or DEC/DX format can be readily processed. In all other cases the preferred format is DOS text or ASCII. Essential is that the name and version of the wordprocessing program, the type of computer on which the text was prepared, and the format of the text files are clearly indicated. **Authors are requested to ensure that the contents of the diskette correspond exactly to the contents of the hardcopy manuscript. Discrepancies can lead to proofs of the wrong version being made.**

Submission of an article is understood to imply that the article is original and unpublished and is not being considered for publication elsewhere.
Upon acceptance of an article by the journal the author(s) will be asked to transfer the copyright of the article to the publishers. This transfer will ensure the widest possible dissemination of information under the U.S. Copyright Law.

MARINE GEOLOGY

International Journal of Marine Geology, Geochemistry and Geophysics

(Abstracted/Indexed in: Geoscience Contents, Geo Abstracts, Current Contents, Bulletin Signalétique, Chemical Abstracts, Marine Science Contents Tables, A.G.I.'s Bibliography and Index of Geology, Aquatic Science and Fisheries Abstracts and Oceanic Abstracts)

VOL. 105 No. 1/4 CONTENTS MARCH 1992

Regular Research Papers

Model simulations of tsunamis generated by the Storegga Slides
C.B. Harbitz (Oslo, Norway) 1

Recent environmental changes recorded in anoxic Barsnesfjord sediments: Western Norway
M. Paetzel and H. Schrader (Bergen, Norway) 23

Organic carbon distribution in the North Atlantic Ocean during the last glacial maximum
M.L. Coppedge and W.L. Balsam (Arlington, Tex., USA) 37

Early diagenesis of marine organic matter: Alteration of the carbon isotopic composition
J.M. McArthur (London, UK), R.V. Tyson (Newcastle upon Tyne, UK), J. Thomson (Wormley, UK) and D. Mattey (Egham, UK) 51

Petrology and geochemistry of a dredged clinopyroxenite–dolerite basal complex from the Jan Mayen volcanic province, Norwegian–Greenland Sea
J.C. Bailey, J. Campsie, N. Hald, F. Dittmer, S. Fine and M. Rasmussen (Copenhagen, Denmark) 63

Collapse and flow of lowstand shelf-margin deposits: An example from the eastern Tyrrhenian Sea, Italy
F. Trincardi (Bologna, Italy) and M.E. Field (Menlo Park, Calif., USA) 77

The western Grand Banks of Newfoundland: Transgressive Holocene sedimentation under the combined influence of waves and currents
R.W. Dalrymple and E.M. LeGresley (Kingston, Ont., Canada), G.B.J. Fader and B.D. Petrie (Dartmouth, N.S., Canada) 95

Barriers, barrier platforms, and spillover deposits in St. George's Bay, Newfoundland: Paraglacial sedimentation on the flanks of a deep coastal basin
J. Shaw and D.L. Forbes (Dartmouth, N.S., Canada) 119

Multiple sediment sources and a cellular, non-integrated, longshore drift system: Northwest Florida and southeast Alabama coast, USA
G.W. Stone (Baton Rouge, La., USA), F.W. Stapor Jr. (Cookeville, Tenn., USA), J.P. May (Charleston, S.C., USA) and J.P. Morgan (Pensacola, Fla., USA) 141

Physical processes and sedimentary record of a modern, transgressive, lacustrine barrier island
T.F. Bray Jr. and C.H. Carter (Akron, Ohio, USA) 155

Carbonate platforms along the southeast Bahamas–Hispaniola collision zone
H.T. Mullins (Syracuse, N.Y., USA), N. Breen (Palo Alto, Calif., USA), J. Dolan (Pasadena, Calif., USA), R.W. Wellner, J.L. Petruccione, M. Gaylord and B. Andersen (Syracuse, N.Y., USA), A.J. Melillo and A.D. Jurgens (New Orleans, La., USA) and D. Orange (Santa Cruz, Calif., USA) 169

Basin changes in Jervis Bay, New South Wales: 1894–1988
J.K. Bowyer (Canberra, A.C.T., Australia) 211

The geomorphology of the Southwest Guinea Margin: tectonic, volcanic, mass movement and bottom current influences
S. Rossi (Bologna, Italy), F. Westall (Nantes, France) and J. Mascle (Villefranche, France) 225

Indications of hydrothermal activity at the Chile Ridge spreading centre
P. Marienfeld (Bremerhaven, Germany) and V. Marchig (Hannover, Germany) 241

Late Tertiary seismic facies and structures of the Levant passive margin off central Israel, eastern Mediterranean
G. Tibor and Z. Ben-Avraham (Tel Aviv, Israel) 253

The morphology of the top-Tertiary erosion surface in the Belgian sector of the North Sea
A.C. Liu, T. Missiaen and J.P. Henriet (Gent, Belgium) 275

Predicting erosion resistance of muds
W.B. Dade, A.R.M. Nowell and P.A. Jumars (Seattle, Wash., USA) 285

Short note

Coast-parallel palaeochannels off southern Namibia
R.W. Day (Rondebosch, South Africa), A.J. Franzsen (Cape Town, South Africa) and J. Rogers (Rondebosch, South Africa) 299

Discussion

Clay mineralogy of Visakhapatnam shelf sediments, east coast of India: comment
N.V.N. Durga Prasad Rao (Visakhapatnam, India) 305

Reply to comment on "Clay mineralogy of Visakhapatnam shelf sediments, east coast of India"
P.S.N. Murty (Visakhapatnam, India) 307